UNIVERSITAT DE BARCELONA

Development of novel nanomedicines based on polyurethane-polyurea hybrid nanocapsules for cancer theragnosis

Joaquin Daniel Bonelli Blasco

ADVERTIMENT. La consulta d'aquesta tesi queda condicionada a l'acceptació de les següents condicions d'ús: La difusió d'aquesta tesi per mitjà del servei TDX (**www.tdx.cat**) i a través del Dipòsit Digital de la UB (**diposit.ub.edu**) ha estat autoritzada pels titulars dels drets de propietat intel·lectual únicament per a usos privats emmarcats en activitats d'investigació i docència. No s'autoritza la seva reproducció amb finalitats de lucre ni la seva difusió i posada a disposició des d'un lloc aliè al servei TDX ni al Dipòsit Digital de la UB. No s'autoritza la presentació del seu contingut en una finestra o marc aliè a TDX o al Dipòsit Digital de la UB (framing). Aquesta reserva de drets afecta tant al resum de presentació de la tesi com als seus continguts. En la utilització o cita de parts de la tesi és obligat indicar el nom de la persona autora.

ADVERTENCIA. La consulta de esta tesis queda condicionada a la aceptación de las siguientes condiciones de uso: La difusión de esta tesis por medio del servicio TDR (**www.tdx.cat**) y a través del Repositorio Digital de la UB (**diposit.ub.edu**) ha sido autorizada por los titulares de los derechos de propiedad intelectual únicamente para usos privados enmarcados en actividades de investigación y docencia. No se autoriza su reproducción con finalidades de lucro ni su difusión y puesta a disposición desde un sitio ajeno al servicio TDR o al Repositorio Digital de la UB. No se autoriza la presentación de su contenido en una ventana o marco ajeno a TDR o al Repositorio Digital de la UB (framing). Esta reserva de derechos afecta tanto al resumen de presentación de la tesis como a sus contenidos. En la utilización o cita de partes de la tesis es obligado indicar el nombre de la persona autora.

WARNING. On having consulted this thesis you're accepting the following use conditions: Spreading this thesis by the TDX (**www.tdx.cat**) service and by the UB Digital Repository (**diposit.ub.edu**) has been authorized by the titular of the intellectual property rights only for private uses placed in investigation and teaching activities. Reproduction with lucrative aims is not authorized nor its spreading and availability from a site foreign to the TDX service or to the UB Digital Repository. Introducing its content in a window or frame foreign to the TDX service or to the UB Digital Repository is not authorized (framing). Those rights affect to the presentation summary of the thesis as well as to its contents. In the using or citation of parts of the thesis it's obliged to indicate the name of the author.

DEVELOPMENT OF NOVEL NANOMEDICINES BASED ON POLYURETHANE-POLYUREA HYBRID NANOCAPSULES FOR CANCER THERAGNOSIS

Joaquin Daniel Bonelli Blasco

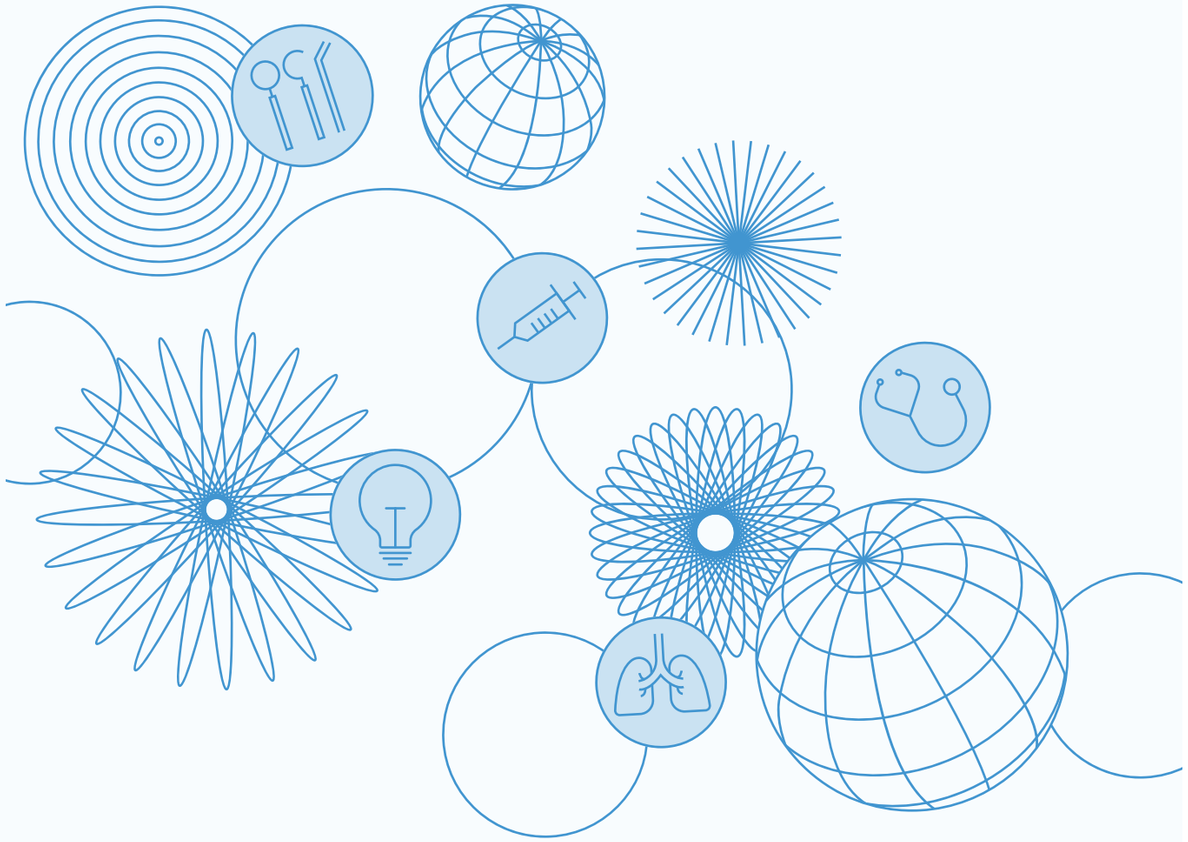

UNIVERSITAT DE BARCELONA

Joaquin Daniel Bonelli Blasco

Tesi Doctoral

2022

Programa de Doctorado en Química Orgánica

Development of novel nanomedicines based on polyurethane-polyurea hybrid nanocapsules for cancer theragnosis

Doctoral Thesis submitted by:

Joaquin Daniel Bonelli Blasco

Supervised by:

Dr. Vicente Marchán Sancho

Departamento de Química Inorgánica y Orgánica, Sección de Química Orgánica

Universidad de Barcelona

Dr. Josep Rocas Sorolla

Ecopol Tech S.L.

Barcelona, September 2022

Document signat digitalment per: JOAQUIN DANIEL BONELLI BLASCO

The present Thesis has been developed under the “Programa de Doctorado en Química Orgánica” both at the Departament of Inorganic and Organic Chemistry, Organic Chemistry section, located at the University of Barcelona and at the R&D Department of the company Ecopol Tech S.L. (April 2018-July 2022) in the framework of the Industrial PhD program, funded by Generalitat de Catalunya. This work was supported by funds from the Spanish Ministerio de Ciencia e Innovación-Agencia Estatal de Investigación (MCI/AEI/10.13039/501100011033) and FEDER funds (Projects CTQ2017-84779-R, PID2020-117508RB-I00) and the Generalitat de Catalunya (Projects RD17-1-0079 and 2017 DI 072).

Agradecimientos

Quiero empezar agradeciendo la cristalización de este trabajo a mis dos directores. Agradecerte, Josep, las oportunidades y la confianza que siempre me has brindado, tanto a nivel laboral general como en este trabajo en particular. Nunca encontré una puerta cerrada contigo. También por contagiarme tu entusiasmo y tu afán por buscar nuevas soluciones en este campo tan apasionante como es la nanomedicina.

A ti, Vicente, por aceptar tutorizarme sin apenas conocerme, por enseñarme como investigar con rigurosidad y pasión, por las largas charlas en tu despacho llenas de aprendizaje, por hacerme entender que los pequeños detalles pueden marcar la diferencia, por tu escucha, por tus consejos y, por encima de todo, por guiarme y apoyarme en aquellos momentos en los que las cosas parecían más difíciles. Siempre te estaré agradecido.

I would like to say thanks to Gilles and his research group for their amazing and warm reception, during my short stay in Paris, where I learned lot of science and good practices on scientific research, while incorporating in my life such a good people as well.

No me quiero olvidar de Pilar, Miriam y Francesc, que siempre tuvieron buenos consejos para darme, así como de Carolina y Jordi, que me introdujeron a la investigación.

A mis compañeros de Ecopol, en especial a Neus y Oriol, por respaldarme y echarme siempre una mano en todo lo que he necesitado, y a todos los compañeros del grupo de investigación de la Facultad.

Quiero hacer especial mención a Cristina y Albert, a los que admiro y con los que he aprendido tantísimo. Ellos fueron, en gran parte, quienes me motivaron e impulsaron a arrancar esta aventura.

A mis amigos y amigas, a todos; “los del barrio”, “los del pueblo”, “los de la playa”, “los de la uni” … A todas esas personas que aprecio y que forman parte de mi vida. Es un gusto compartir este éxito con vosotros.

A toda mi familia, también a la que elegí; a la cercana y a la lejana, a la que está y a la que se fue. Siempre he sentido vuestro apoyo y sé que estaréis orgullosos.

A mis padres, que simplemente han sido, son y serán una fuente de inspiración para mí.

"- Le he dicho que no es tungsteno, pero eso no significa que sepa de qué se trata.

- ¿Cómo no lo sabe?

- Me refiero a que los resultados son ridículos. (…). Imposibles, en realidad. La relación carga-masa es absurda.

- ¿Absurda en qué sentido?

- Demasiado alta. Es sencillamente imposible.

- Bien. En tal caso (…), consiga la frecuencia de su radiación característica y calcule la masa absoluta. ***No se contente con sentarse y repetir que algo es imposible***."

Isaac Asimov, (2014) [1972], *Los propios dioses*.
Barcelona. Penguin Random House. p.14

Thesis Outline

This Thesis is structured as a compendium of publications, being organized around two published articles, one article submitted for publication (see below), together with the corresponding supporting information material, and two additional sections describing non-published results. The Thesis contains a General Introduction, which includes a revision of the state-of-the-art of the previous work related with the Objectives proposed in this research project in the field of nanomedical solutions against cancer, drug delivery systems, oncological photodynamic therapy, and tumor bioimaging. Immediately after the Results and Discussion section, which has been organized in three chapters that include the three publications as well as additional non-published results, the Conclusions section can be found. Finally, according to the guidelines of the University of Barcelona for Thesis presented as a compendium of publications, a summary of the main results of the Thesis written in Spanish is provided.

List of publications:

Publication I: **Bonelli, J.**; Ortega-Forte, E.; Rovira, A.; Bosch, M.; Torres, O.; Cuscó, C.; Rocas, J.; Ruiz, J.; Marchán, V. Improving Photodynamic Therapy Anticancer Activity of a Mitochondria-Targeted Coumarin Photosensitizer Using a Polyurethane–Polyurea Hybrid Nanocarrier. *Biomacromolecules* **2022**, *23*, 2900–2913.

Publication II: **Bonelli, J.**; Ortega-Forte, E.; Vigueras, G.; Bosch, M.; Cutillas, N.; Rocas, J.; Ruiz, J.; Marchán, V. Polyurethane–Polyurea Hybrid Nanocapsules as Efficient Delivery Systems of Anticancer Ir(III) Metallodrugs. *Inorg. Chem. Front*. **2022**, *9*, 2123–2138. Highlighted on the Front Cover of the journal.

Publication III: **Bonelli, J.;** Velasco-de Andrés, M.; Isidro, N.; Bayó, C.; Chumillas, S.; Carrillo-Serradell, L.; Casadó-Llombart, S.; Mok, C.; Benítez, D.; Lozano, F.; Rocas, J.; Marchán, V. Novel tumor-targeted self-nanostructured and compartmentalized water-in-oil-in-water polyurethane-polyurea nanocapsules for cancer theragnosis. *Manuscript submitted for publication.*

Non-published results:

Chapter Ib: **Bonelli, J.** *et al*. Nanoencapsulation and biological evaluation of Ru(II)-based photosensitizers.

Chapter Ic: **Bonelli, J**. *et a*l. Encapsulation and biological evaluation of a Zn(phthalocyanine) derivative and the corresponding Ir-Zn(phthalocyanine) conjugate.

TABLE OF CONTENTS

Acronyms and abbreviations

5-ALA: 5-aminolevulinic acid

A2780: human adenocarcinoma cell line

A375: human malignant melanoma cell line

A549: human lung(carcinoma) cell line

ACS: American Chemical Society

ATP: 5'adenosine triphosphate

B16: murine melanoma cell line

BALB/C: albino, immunodeficient laboratory-bred strain of the house mouse

BODIPY: boron-dipyrromethene

BPhen: bathophenanthroline

BTCP: bicyclo-tetraazacyclo-pentaphenanthrene

C57BL/6: inbred free of genetic difference mouse strain

Ce6: chlorin e6

CHO: Chinese hamster ovary cell line

COUPY: range of coumarin-based organic fluorophores from Marchán's Lab

COVID-19: coronavirus disease of 2019

cRGDfK: cyclopeptide cyclo(-Arg-Gly-Asp-D-Phe-Lys)

CRISPR: clustered regularly interspaced short palindromic repeats

CRL-1666: rat mammary adenocarcinoma cell line

CT-26: murine colorectal carcinoma cell line

DCF: dichlorofluorescein

DCFH-DA: 2'-7' dichlorofluorescein diacetate

DMEM: Dulbecco’s modified Eagle medium

DNA: desoxyribonucleic acid

DPBF: 1,3-diphenylisobenzofuran

ECM: extracellular matrix

EDG: electro-donating group

EE: encapsulation efficacy

EPO: European Patent Office

EPR: enhanced permeability and retention

EWG: electro-withdrawing group

FA: folic acid

FDA: Food and Drug Administration

FGS: fluorescence-guided surgery

FR: folate receptor

FRET: Förster resonance energy transfer

FTIR: Fourier transformed infrared

GFP: green fluorescent protein

GSH: glutathione tripeptide

HEK293: human embryonic kidney cell line

HeLa: epithelioid cervix carcinoma cells

HER-2: human epidermal growth factor receptor 2

HGG: high-grade glioma

HIF-1: hypoxia inducible factor-1

HL-60: acute promyelocytic leukemia cell line

HLA: hyaluronic acid

HLB: hydrophilic/lipophilic balance

HOMO: highest occupied molecular orbital

HR-TEM: high-resolution transmission electron microscopy

HT-29: human Caucasian colon adenocarcinoma grade II cell line

IC_{50}: cell inhibition coefficient

ICG: indocyanine green

IR: infrared

ISC: intersystem crossing

LED: light-emitting diode

LTG: LysoTracker green

LUMO: lowest unoccupied molecular orbital

MCF-7: metastatic adenocarcinoma epithelial breast cell line

MCTS: multicellular tumor spheroids

MDA-MB-453: metastatic carcinoma of breast cancer cell line

MMP: mitochondrial membrane potential

MRC-5: human fetal lung fibroblast cell line

mRNA: messenger RNA

MSN: mesoporous silica nanoparticle

MWCO: molecular weight cut-off

NC: nanocapsule

NCO: isocyanate group

NIR: near infrared

NMIBL: non-muscle invasive bladder cancer

NSCLC: non-small cell lung cancer

O/W: oil in water

ORR: overall response rate

OXPHOS: oxidative phosphorylation

PACT: photoactivated chemotherapy

PBS: phosphate buffer saline

PCT: Patent Cooperation Treaty

PDT: photodynamic therapy

PEG: polyethylene glycol

PGPR: polyglycerol polyricinoleate

Phen: phenanthroline

PI: phototoxic index

PI3K/Akt/mTOR: phosphoinositide 3-kinase/protein kinase B/mammalian target of rapamycin

PLA: polylactic acid

PLGA: polylactic co-glycolic acid

PpIX: protoporphyrin IX

PS: photosensitizer

PTT: photothermal therapy

PTX: paclitaxel

PU: polyurethane

PUA: polyurea

OVA: ovalbumin

QD: quantum dot

QY: quantum yield

RES: reticuloendothelial system

RGD: tripeptide Arg-Gly-Asp

RNA: ribonucleic acid

ROS: reactive oxygen species

RSC: Royal Society of Chemistry

SF: selectivity factor

SK-MEL-28: human melanoma cell line

SK-OV-3: cystadenocarcinoma ovarian cancer cell line

Siglec-1: sialic acid binding Ig like lectin-1

SARS: structure-activity relationships

TEOS: tetraethyl orthosilicate

TEM: transmission electron microscopy

TLD-1433: clinical candidate photosensitizer from McFarland's Lab

TME: tumor microenvironment

TNBC: triple-negative breast cancer

TPZ: tirapazamine

UV: ultraviolet

VLP: virus-like particle

W/O: water in oil

W/O/W: water in oil in water

WHO: World Health Organization

General Introduction and Objectives

1 About nanomedicine and cancer

1.1 What is nanomedicine?

The first nanomedical study *per se* could be attributed to Nobel Prize in Medicine winners Ilya Metchnikov and Paul Ehrlich (1908) for their in-depth research on phagocytosis mechanisms, which was the basis for the further studies in immunology[1]. However, it is also well-known that alchemists of ancient civilizations were seduced by the idea of noble metals ingestion, like gold or silver, as healing agents to treat some poorly known diseases. In the same way, scientists from contemporary age worked to formulate these precious metals in colloid dispersions for improving water-solubility and administration. In the 19th Century, both Michael Faraday[2] but more intensively the physicist John Tyndall[3], elucidated how the effect of particle size produces changes in color appearance of a suspension, due to the visible-light scattering. Nevertheless, we must wait until the end of 19th Century, in 1898, when Richard Adolf Zsigmondy (Nobel Prize in Chemistry, 1925) synthesized the first colloidal gold dispersion, revealing the insets of the reddish color in ruby glass[4].

In a classical view, the term 'nano', provided by the Greeks, refers to something which is between one millionth and one billionth times smaller than a meter. The nanometer scale is abbreviated as "nm" (Figure 1). Nanomedicine can be then applied to all those research fields where nano entities, or nanoscale devices, are used to achieve innovation in healthcare and can be divided in three main areas: diagnosis, bioimaging and drug delivery. Nanostructures cannot be considered as living organisms because the minimum expression of life is a single cell (about 10 micrometers in size -10,000 nm-). Hence, in the nanomedical approach, we are dealing with rationally designed products that can internalize in live cells, through the cell membrane, causing changes or modifications on their behavior.

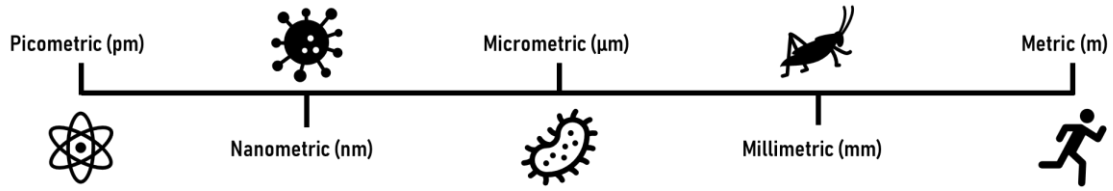

Figure 1. Size scale from picometers to meters.

In this context, cell organelles, viruses, and some types of proteins are common examples of nanometric entities which produce biological effects in cells, and here is where nanomedicine can focus the efforts by mimicking such subcellular structures to generate similar pathways for biological action. According to the European Science Foundation definition, *Nanomedicine is the science and technology of diagnosing, treating, and preventing disease and traumatic injury, of relieving pain, and of preserving*

and improving human health, using molecular tools and molecular knowledge of the human body[5].

1.2 How do nanomedicines work?

The feasibility of a molecule to be internalized from the extracellular to the intracellular medium depends on different factors: Chemical composition, molecular weight, functional groups, or potential ionization are some of the common parameters that influence cellular uptake of most bioactive molecules. Animal cell membrane is composed by a phospholipid bilayer, constructed by the assemble of lipids and cholesterol[6], where a variety of structures (mostly proteins) play a crucial role in biological recognition and membrane crossing[7] and, consequently, the cell entrance can be carried out through passive or active mechanisms (Figure 2). Common examples of small molecules that directly diffuse through cell membrane by passive mechanisms are O_2, CO_2, water, or urea, which are small enough to be internalized without requiring any energy-dependent transport. Among that, some examples reported in the literature support that the presence of specific proteins, or sterols, can also enhance the internalization of some of these small molecules through lipid bilayers[8].

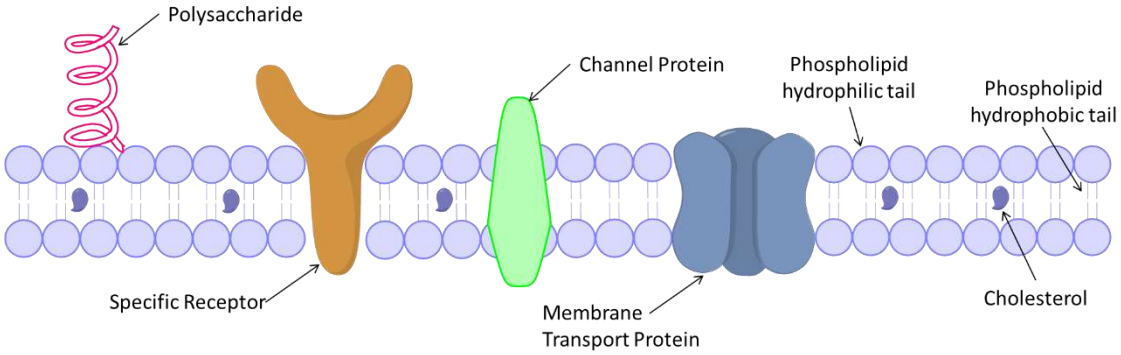

Figure 2. Simplification of the animal cell membrane composition.

On the contrary, a broad range of molecules are unable to diffuse from extracellular to intracellular media. Since most of these molecules are essential for the proper cell development and division, they must be actively transported into the cytoplasm or even to specific organelles[9]. As shown in Figure 2, the insets in lipid bilayer act as active moieties for both molecular recognition and internalization. They are highly selective for small-medium size families of molecules[10], and/or for some other specific molecules as well (for example, the Sodium Ion Channels[11], a typical way of cation-transport, or the specific receptor Siglec-1 expressed in some dendritic cells, which only recognizes sialic-acid residues contained in a ganglioside structure[12]). Large biomolecules or nano entities cannot use the above-mentioned active transport ways to internalize into the cytosol, and they can neither diffuse through lipid bilayer because of their large size. However, the

interaction of these compounds with cell membrane generates another type of active transport, the invagination or endocytic pathways[13].

Endocytic pathways are based on the principle of lipid membrane reorganization after interaction with an external artefact, which leads to the disruption of the non-covalent binding assemble between all the lipids present in the membrane with themselves, as well as with cholesterol. As shown in Figure 3, the denaturalization of this structure produces the deformation of the cell membrane, which is rearranged on the eagerness of minimizing the energy of hydro/lipophilic interactions with the external artefact, leading to the progressive formation of "holes" in the cell membrane, and becoming the precursors of intracellular vesicles, called endosomes, built up from cell membrane lysis[14,15]. These mechanisms are quite unspecific, and a wide range of supramolecular constructions can be potentially internalized into cells by this way, which has been the principal approach for traditional medical treatments. Therefore, some cells, like cancer cells or bacteria for example, have developed mechanisms to avoid the internalization of antitumoral and antibacterial agents by secreting substances that inhibit the uptake or inactivate the drug in the extracellular matrix by increasing their concentration in the cytosol, which leads to resistance[16,17]. Similarly, most of these compounds become inactive, even before they reach the target cell/tissue, since they are prematurely degraded, or opsonized and excreted by reticuloendothelial system (RES).

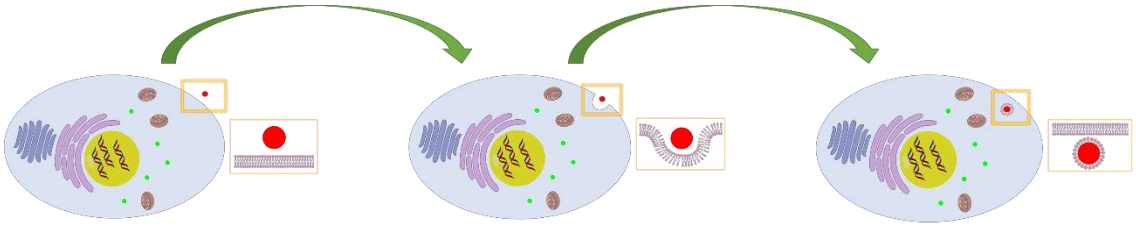

Figure 3. Simplification of an artefact (red sphere) internalizing into a eukaryote cell via endocytosis.

Nanomedicine exploits endocytosis-mediated active mechanisms to internalize bioactive molecules inside the endosomes[18,19], after preventing them from destabilization or premature degradation in bloodstream.

Is then the internalization of natural or synthetic compounds into cells a matter of size? The answer is yes, but no. It is obvious that cells are not able to ingest, without any toxicological consequence, a larger entity than itself. So, the design on the nanometric window is crucial to reach an optimum penetration in target cells, but this is not the unique factor that drives the design and the optimization of a nanomedical system. Therefore, the nanomedical approach is addressed to overcome biological barriers for an efficient action of the selected drugs, diminishing the toxicity they produce in peripheral non-target cells[20–22].

Nanomedical systems aim to improve the therapeutic index of a drug by enhancing accumulation in the target cells/tissues while minimizing their effects in "healthy" locations. Although not common, there are some examples of nanomedicines that incorporate a potential drug within their structure[23]. However, this approach could be a double-edge sword because the nanocarrier is then considered a prodrug as well, requiring a more exhaustive analysis[24].

Once a nanomedicine reaches the targeted intracellular media, it is also important to assess how the drug is released from the nanostructure to the cytosol. Although nanomedicines are prepared to specifically accumulate in target areas of the organism, achieving a 100% of cell/tissue selectivity is a real challenge. Moreover, the drug should be preferentially released in a defined biological environment, as in the intracellular media of tumor cells[25], malfunctional dendritic cells[26] or bacteria[27]. Evidently, the identification of biological differences between target and normal cells becomes crucial to provide the nanomedicine with motifs that allow to precisely recognize or/and respond to these alterations.

How can we confer specific release properties to a nanomedical design? There are different ways to achieve this goal, which are related on how the drug was incorporated in the nanocarrier and on the introduction of stimuli-responsive moieties. Indeed, the introduction of chemical, physical or biological-responsive groups in a nanomedicine could facilitate the release of the drug in specific cells, or even in subcellular organelles. That is the richness of nanomedicines' work; from a synthetic nanomedical platform, you can give solutions to different medical challenges. In this work, we have put our efforts on the development of novel nanomedicines for treatment and diagnosis in oncology.

1.3 Targeting Cancer: What should we consider in the development of oncological nanomedicines?

Cancer is the second worldwide leading cause of death, just preceded by cardiovascular diseases, in the list of World Health Organization (WHO). Generation of tumors involves about 16% of worldwide deaths, which are arisen from the combination of genetic factors and external agents affecting, with some exceptions, all types of ethnics, ages, and genders. In most of the cases, cancer development is leaded by deregulation of normal cells division pathways, which leads to an uncontrolled appearance and reproduction of malignant cells, commonly driving to death if these cells are not totally or partially removed from patient's organism. When the settlement and clustering of malignant cells is promoted in the epithelial and mesenchymal tissues, they engender a solid tumor (Carcinoma or Sarcoma), while if the appearance of malignancy does not

emerge on structural cells, but in blood, lymph, or bone marrow ones, we talk about blood cancers (Leukemia, lymphoma or myeloma).

The biological characteristics of cancer cells substantially differ from those of healthy cells. The morphology, size, the ability to clustery growing but, specially, the uncontrolled way to divide and proliferate by themselves are some of the common patterns in cancerous cells. Of course, these abnormalities are piloted by randomized mutagenic modifications in the genetic material of organism cells, that can be caused by inherited factors or leaded by external conditions exposure, promoting genotypic and phenotypic modifications that manage an extraordinary heterogenicity in the different types of cancer[28].

Interestingly, because of the dysfunctional mechanisms of cancer cell survival, the biological media enclosing tumor tissues (Tumor microenvironment or TME) exhibits unusual characteristics. Particularly, when a single tumor cell adheres over endothelium of blood vessels and enables the formation of a solid tumor, engaging its reproduction and clustering, the presence of this foreign tissue accelerates the formation of new vessels, in an angiogenesis-related process, generating structural modifications in endothelial cells that conclude in a local enhanced permeability of blood vessels to macromolecules. This phenomenon, coined by Prof. Hiroshi Maeda in 1986, is known as enhanced permeability and retention (EPR) effect, entailing an inflection point in the way on how specific tumor targeting can be achieved[29]. Prof. Maeda and his collaborators got on board in an intensive research to understand the biological pathways that manage this phenomenon, as well as its *in vitro* reproducibility and *in vivo* heterogenicity, aiming to compare the biological situation between rodents and human to elucidate if the animal modelling is a viable way to reproduce human tumors. These “perforation” phenomena in tumor closing blood vessels, cursing with the inflammation of the affected zone[30], seems to be crucial for solid tumor proliferation in the way it increases the nutrients uptake from bloodstream (Figure 4).

Many factors can be determinant at the time to evaluate the EPR effect in biological systems. The cancer type, its location, size, the grade of advance, or the receptors expressed over tumor cells, may affect the progress of the EPR effect. The conclusions extracted from the study of Prof. Maeda and co-workers revealed the heterogenicity of extravasation in different situations, identifying an enhanced EPR effect in primary tumors in comparison with metastatic ones. Prof. Maeda also suggested what could be the best approaches for an effective tumor targeting in nanomedicine-based solutions[31].

However, considering the tumor heterogeneity, other authors are reticent in that question, accepting the well-stablished explanation of extravasation but arguing that regional chemotherapy for example, can overcome several drawbacks presented on the EPR approach[32]. Shen and co-workers underlay the barriers to translate the EPR-based approach to clinical phases and have put efforts on developing novel targeted perspectives relaying on TME modulation[33].

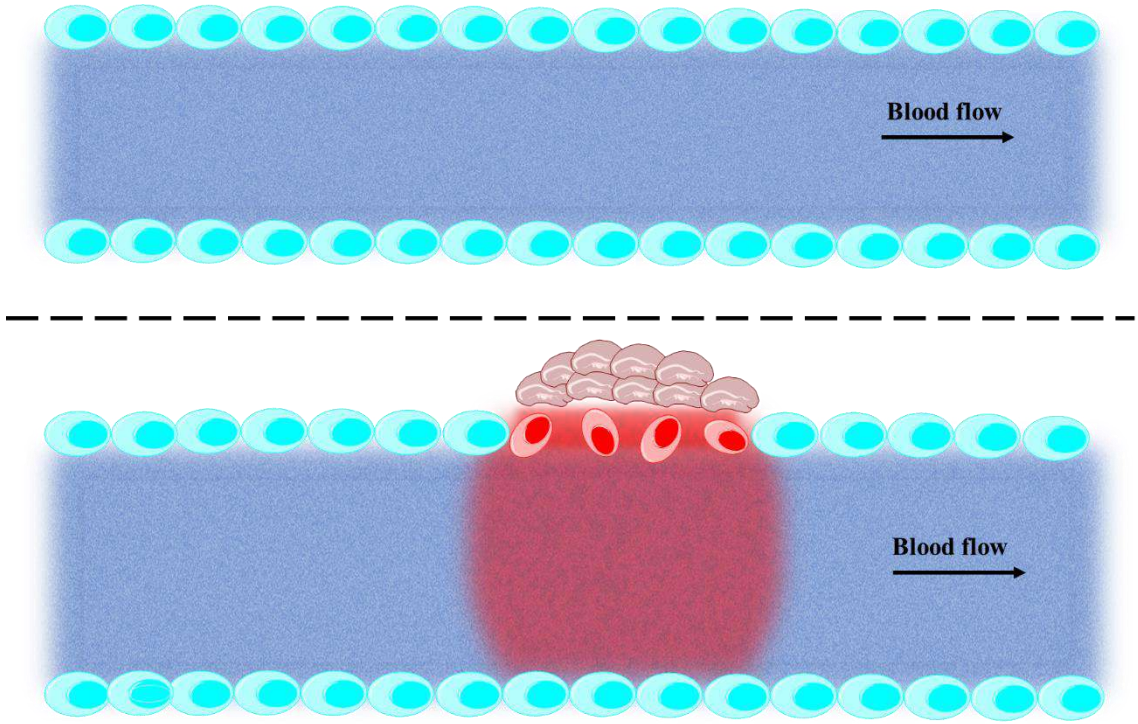

Figure 4. The EPR effect. Endothelial cells perfused by the presence of a solid tumor.

Over years of improvement by randomized mutations, cancer cells display the ability to overcome biological features that menace their survival. The persistent pro-oxidative state in cancer cells, caused by their greed metabolism and the genetic modifications, significantly increase the levels of reactive oxygen species (ROS) levels in the intracellular media of cancer cells. As it is well known, high concentrations of ROS in the cytoplasm lead to cell death through different mechanisms. This is, in fact, one of the most common approaches, that we will explore in-depth, to promote cancer cell death[34,35]. To balance this oxidative stress, cancer cells increase the intracellular concentration of the reduced form of glutathione tripeptide (GSH) to neutralize the oxidative power of ROS[36]. As a consequence of driving this dysregulated intracellular media, cancer cells suffer modifications in their metabolic and respiratory processes, being the ability to survive under hypoxic conditions, leaded by the increased glycolytic activity in these malignant cells, a common feature of cancer cells[37].

Mammalian cells mostly generate energy from both glycolysis (anaerobic respiration) and mitochondrial oxidative phosphorylation (OXPHOS, aerobic respiration). Metabolization of glucose to generate 5'-adenosine triphosphate (ATP) is carried out by glycolysis, even in the presence of oxygen, in cancer cells, leading to an increase of the ROS in the intracellular media. In the meanwhile, the lactate production levels are also increased, which is afterwards expulsed by cancer cells to the extracellular matrix (ECM)[38]. This lactate excess released outside the cancer cell, decrease the pH in close TME locations[39,40], thus leading to an acidic microenvironment that stands out from the physiological pH of bloodstream (around 7.4) and enables the possibility to design responsive nanostructures that might become cationic at acidic pH. The malfunctional cell respiration mechanism, commonly attributed to a mitochondrial dysregulation, in non-hypoxic conditions is known as aerobic glycolysis or **Warburg's effect** (Figure 5), which was discovered by Otto Warburg in 1920[41]. The regulation of the Warburg's effect is currently associated to the expression of some factors (like phosphoinositide 3-kinase/protein kinase B/mammalian target of rapamycin; PI3K/Akt/mTOR, or hypoxia inducible factor-1; HIF-1), but the complete elucidation of the biological mechanism remains, as far, unclear[42,43].

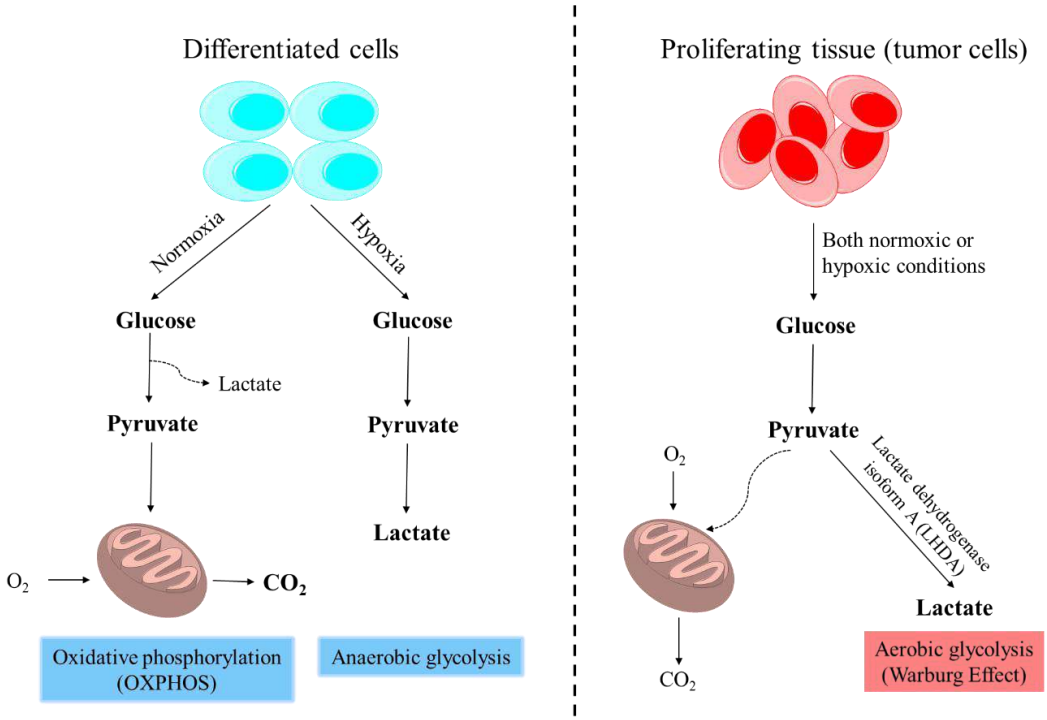

Figure 5. Warburg effect clarification. Cell respiration in healthy tissues (left) against preferential lactate production in tumor cells (right).

All of these characteristics provide the tumors with specific and unspecific ways to develop resistance to a wide range of chemotherapeutic drugs, while potentiate their ability to reproduce themselves and scale up the cancer grade in patients. The recurrent heterogeneity in different types of tumors also increases the difficulty to develop

representative *in vitro* models for primary screening of novel antitumoral agents, presenting an important challenge in anticancer drug development[44].

From a solid and well-localized tumor, some cells can soak through abnormal blood-vessels, reaching the bloodstream, and spreading malignant cells all over the organism. This phenomenon is known as **metastasis**, which is the formation of other tumor clusters in different locations from a previous solid one[45]. The identification and rapid elimination of these malignant cells, or other oncological actions, become essential to ensure the hampering of cancer spreading.

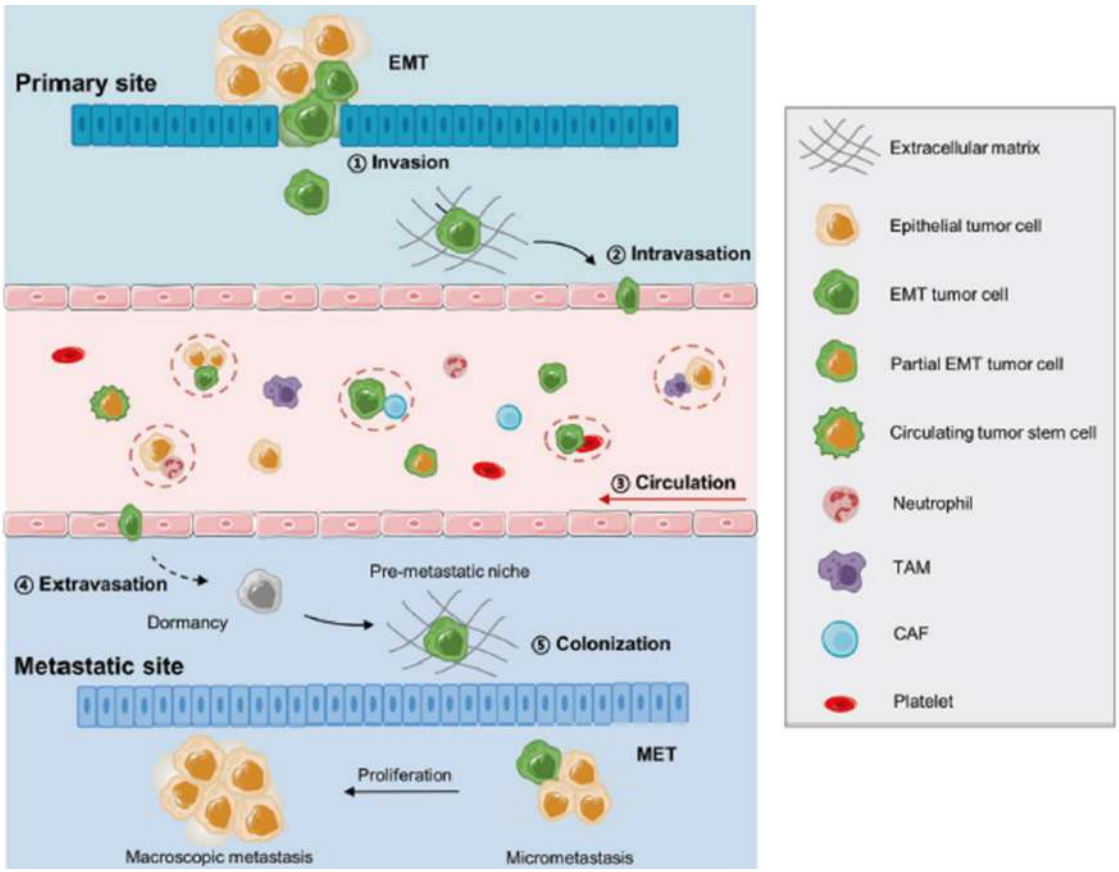

Figure 6. Metastatic process from epithelial tumor cell to circulating tumor cell. Adapted with permission from reference [45].

Currently, there are several medical approaches for the treatment of cancer. Regarding those defined by the National Cancer Institute (NCI-NIH) of the United States, we can identify nine main approaches (https://www.cancer.gov/about-cancer/treatment/types):

- Surgery: The preferred treatment. It is very useful for localized and accessible tumors, because the surgeon can remove a high percentage of cancer cells.
- Chemotherapy: Based on the administration of cytotoxic drugs that leads to cell death.

- Immunotherapy: Focused on potentiation or, *in-situ/ex-situ* training, of immune cells to enforce their biological response against cancer cells recognition.
- Photodynamic Therapy (PDT): Based on the use of photosensitizers (PS) to produce cytoxotic ROS in tumor locations. This type of treatment requires, besides the administration of a photosensitizer, the irradiation with suitable light to enable cytotoxicity.
- Stem Cell Transplant: It is commonly used as an adjuvant therapy, to restore the healthy cells damaged by immunotherapy or chemotherapy.
- Radiation Therapy: A localized therapy, which intends to produce damage in DNA sequences of cancer cells, leading to their growth slowdown or death. It differs from photodynamic therapy in the toxicity of the applied laser source *per se*, in the absence of a photosensitizer.
- Hyperthermia: Heat application, localized or global, until 45 ºC (113 ºF) to produce irreversible damage in cancer cells. It is commonly combined with the administration of heating probes to focus the effect.
- Hormone Therapy: Ingestion of determined hormones that block the membrane receptors of cancer cells, inhibiting their reproduction and impeding their survival. It can only be applicable to hormone-response tumors (very common in treatments of low aggressiveness breast cancer).
- Targeted Therapy: Rationally designed small-molecules or oligonucleotides that perform modifications in the genetic material of the cells.

In this context, depending on different factors associated with cancer category (e.g., type of tumor, size, location, phase of reproduction, cells phenotype, or patient's genetic predisposition, among others) clinicians decide the optimal treatment, to ensure as maximum tumor removal as they can with the less invasiveness or side-effects for patient.

The **vehiculization of bioactive molecules** is called to play a crucial or secondary (adjuvant) role in most of the above-mentioned ways of cancer treatment, optimizing the outcomes of therapies and improving patient's welfare. Here is where nanomedicine emerges as an important participant, filling the gap of an increased therapeutic efficacy and diminishing undesired side-effects. Nanomedical approaches can bring ground-breaking perspectives to these treatments, especially in the oncological area, due to the unique biological characteristics found in the TME of solid tumors. As previously stated, the inherited upregulation of reductive molecules generation, given the inclination of cancer cells to increase their intracellular levels of ROS[46], or the overexpression of lactic acid in the extracellular media[47] are, for example, two of the most studied and well-understood mechanisms of auto-defense of cancer cells against cell death processes. Both

factors are also attributed to promote tumorigenesis and tumor metastasis[48,49]. In 2014, when nanomedicine started to be redefined as a personalized treatment, Bertrand and co-workers collected and analyzed multiple strategies based on nanotechnology for tumor tissue targeting[50]. Some of these possibilities are exemplified in Figure 7.

As a result of the biological particularities of cancer biology, a huge amount of nanomedical approaches seek the way to stabilize, protect and selectively transport bioactive compounds through bloodstream that are widely used in the previously described oncological treatments[51,52].

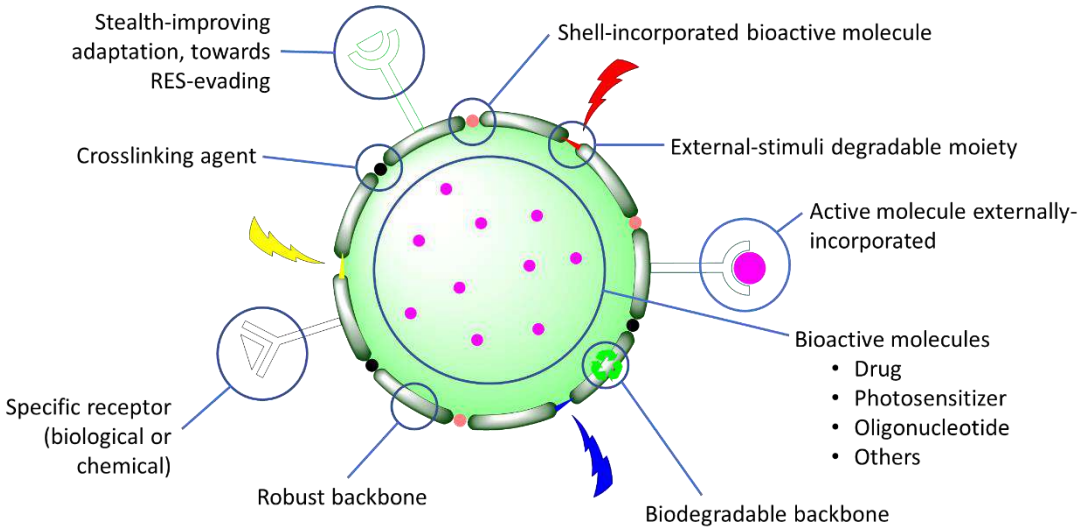

Figure 7. Functionalization possibilities of nanomedical products.

2 What kind of nanomedicines do we know?

2.1 Early phase: the first FDA-approved nanomedicine

The first developments considered as nanomedicines emerged in the figure of liposomes, as the first generation of drug-carriers for tumor treatment, being Doxil® the first liposome-based nanomedicine that was approved by FDA, in 1995, for ovarian cancer, Kaposi's sarcoma and multiple myeloma treatment[53]. Liposomes aim to recreate the structure of intracellular nanovesicles (lysosomes or other vesicles) which are responsible of the transport and release of some crucial molecules from the cell membrane to different intracellular domains. This concept, a **small-molecule confined into the core of a nanostructured composition** (lipids, in this case), opens the window for the development of chemical structures that allow the vehiculation and on-demand release of bioactive molecules. Consequently, polymeric nanocapsules[54], sugar-based nanocapsules[55], nanomicelles[56], quantum dots (QD's)[57], but also other non-encapsulating nanocarriers like shuttle-peptides[58], conjugated-antibodies[59] or virus-like particles (VLP's)[60] arose as groundbreaking nanomedical technologies.

2.2 The maturity of nanomedicine: the appearance of nAb-paclitaxel

By the beginning of the 21st Century, many research groups all over the world are working on the development of novel carriers for antitumoral drugs. In 2005, the company Abraxis BioScience developed its crown jewel, Abraxane®, which consists of a stabilized aqueous dispersion of 130 nm albumin-bound paclitaxel[61,62]. Four years later, in 2009, Abraxis announced that Abraxane had overcame the phase III clinical trials, releasing an improved overall response rate (ORR) in combination with cisplatin, for non-small cell lung cancer (NSCLC) treatment, of more than 30%[63]. This announcement rockets the value of Abraxis, which was immediately acquired by Celgene in 2010, and was later absorbed by Bristol-Myers-Squibb in 2019. The nAb-paclitaxel (the old Abraxane), considered one of the reference products in clinical trials for antitumor chemotherapy, is continuously being improved[64] and studied in combination with other new developments[65].

These results have encouraged the research and development of new nanomedicines to fight cancer, leading to the appearance, as shown in Figure 8, of various nanomedical formulations in oncology[66].

Apart from oncological-targeted products, other medical fields have also invested many efforts on the development of nanomedicine-based therapies against different diseases, and some of them are now considered the benchmark products in the market[67].

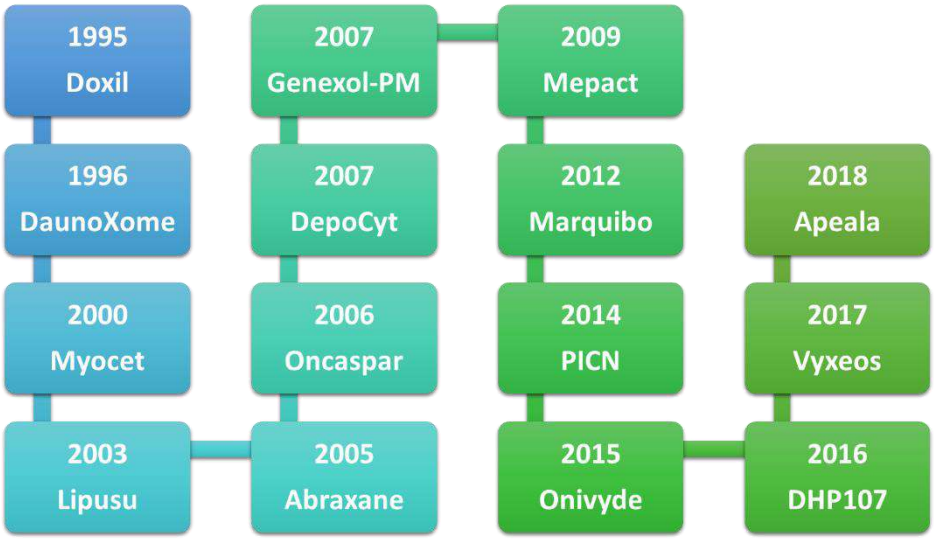

Figure 8. Nanomedical solutions for oncology approved by worldwide Regulatory Agencies.

2.3 Nanomedicine today: Open mindedness developments

Nowadays, the window of nanomedical approaches has been widely enlarged. Based on the different parameters that conform a nanomedicine (e.g., structure, synthesis, type of wall, nature of their assembled-moieties, and they degradability pathways, among others), they can be sorted in several different groups (Nanotubes, Nanodevices, Nanoparticles, Nanoshells or others). However, it is important to note that the way on a nanomedicine is designed and synthesized will define how the bioactive molecule can be introduced in the resulting nanomedical formulation. As shown in Figure 9, a drug can be confined into a core compartment, which requires a high solubility of the drug in this phase, or it can be covalently attached to any reactive point of the nanocarrier, which should not denaturalize its binding site.

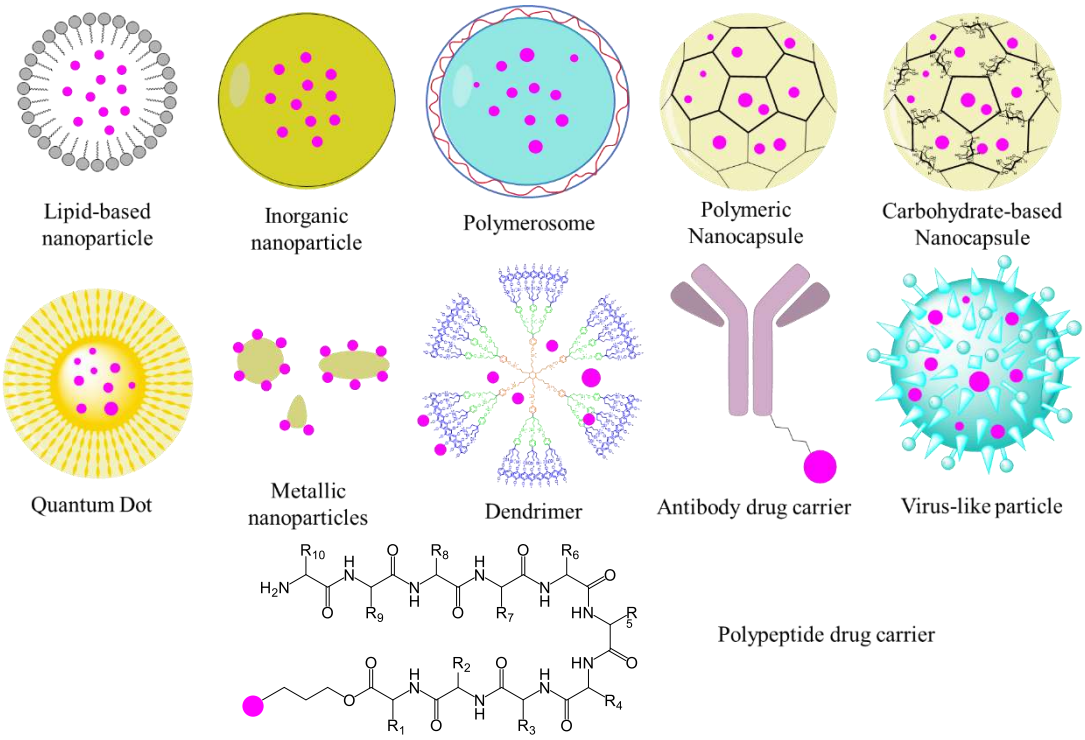

Figure 9. Some examples of nanomedical entities, where the drug (purple spheres) has been incorporated into the nano entity by different ways.

2.3.1 Lipid-based nanoparticles and liposomes

The first type of nanoparticles approved for cancer treatment was discovered by Alec D. Bangham in 1965. They consist of the assembly of a single lipid (or a mixture of different lipids) in an oil/water interface, generating an isolated liposoluble core in aqueous dispersion, where oily-soluble drugs can be confined[68]. Because of the nature of lipids that compose them, liposomes are considered high-biocompatible for human administration, not only restricted to intravenous or subcutaneous injection, but also oral administration as well[69]. Among the encapsulation and stabilization of hydrophobic drugs, the versatility of liposomes relies on mimicking lipid-bilayer, which allows the

encapsulation of hydrosoluble molecules and their isolation from the external aqueous media[70]. Then, they can be divided into unilamellar or multilamellar vesicles.

In an extensive review, published in 2016, Ventosa and collaborators compiled the use of lipid-based vesicles for nanomedical purposes[71]. They delve into the comparison between the liposomes, and those lipid-based nanoparticles that do not meet the criteria to be considered as liposomes. They argue that a liposomal construction is completely based on the lipid-bilayer emulation, putting aside those lipid-based structures that incorporate any other moieties that lead to a different biological behavior, which is the case of Doxil©.

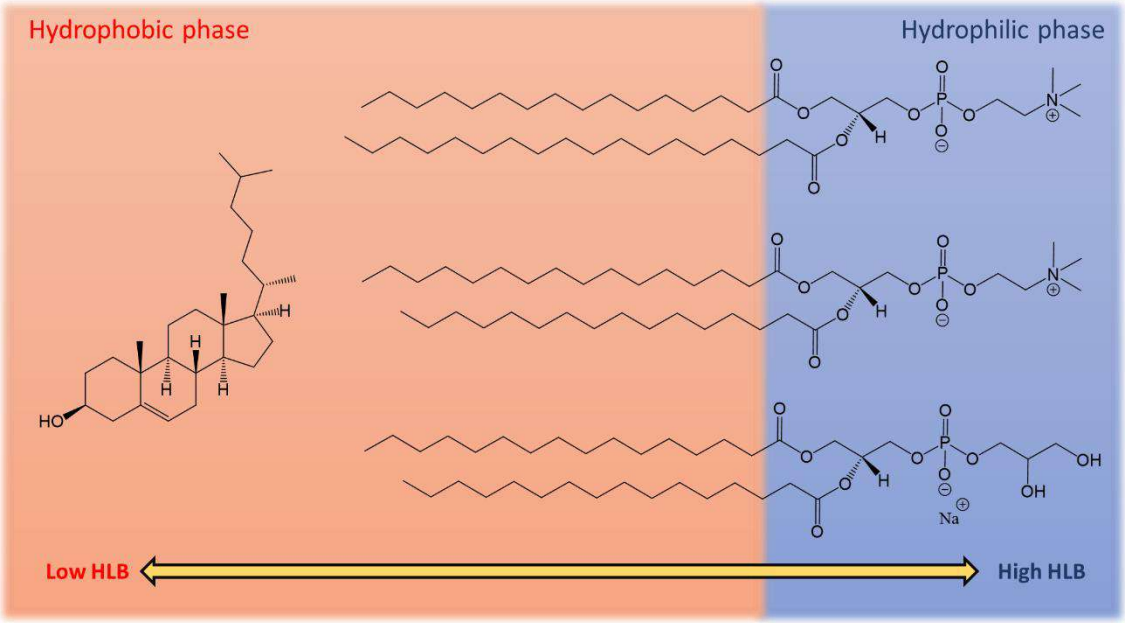

Figure 10. HLB gradient and structuration of common liposomal composition in an aqueous/organic interphase**.**

The basis of the lipid self-assembly mechanism in an oil in water interface relies on the physical manage of decrease energetic interactions between repellent sections. It is important to introduce the concept of stratification in a physic interface, which is referred to as the gradient of hydrophobicity/hydrophilicity between the most hydrosoluble point of the aqueous phase and the most liposoluble point of the oily phase. Consequently, molecules are organized and ordered in this "gradient line" decreasing, as much as they can, the potential of their repealing interactions (Figure 10). Here is where the Hydrophilic/Lipophilic Balance (HLB)[72] is stand out as a crucial parameter to understand the formation of lipidic walls because, due to their amphiphilic characteristics, lipids can act as emulsifiers in nature[73]. The arrangement of the lipids in the interphase, endorsed by cholesterol-promoted compaction of the hydrophobic tails, confers to liposomes the ability to stabilize, in their core, liposoluble compounds in aqueous media[74]. Then, liposomal formulations can be tuned, in terms of size, surface charge or compaction, using different types of lipids, and varying the ratios between them and cholesterol[75].

Despite these advantageous properties, liposomes lack of one of the most important features required for an ideal drug delivery system: robustness. Indeed, liposomes are not formed by covalently attached moieties and, consequently, hydrophobic interactions and Van der Waals forces are not strong enough to prevent lipid layers from denaturalization in biological media[76].

2.3.2 Inorganic Nanoparticles

Inorganic materials have been widely investigated as promising strategies for drug delivery systems. This collection comprises Silica-based nanoparticles, Metallic-nanoparticles, Oxide-based nanoparticles, and Quantum Dots. These types of nanocapsules incorporate rationally designed chemical groups that can be potentially affected by internal or external stimulus, leading to their degradation in specific environments.

Mesoporous silica nanoparticles (MSNs) lead the race on the inorganic nanoparticles' functionalization. They have multiple possibilities to introduce responsive moieties in their surface, providing specific ways to control the release of the drug from their core[77]. Focusing on their oncological application, given their versatile design, MSNs are being evaluated for different treatment and diagnostic areas[78,79]. Regardless these incredible properties, silica-based nanoparticles commonly display toxicological concerns and solubility limitations, which are key factors to improve the bioavailability. Some of silica-based nanomedicines are being currently evaluated in clinical trials for biomedical applications[80]. Although they released quite good results for oral administration, they are far from being completely approved for intravenous administration due to the difficult metabolization of the wall construction, which generates controversial dysregulations in excretion organs as well as in blood immune parameters[81]. In addition, they add the difficulty to encapsulate hydrosoluble compounds.

Metallic nanoparticles born from the envision of drug delivery from metallic substrates, which could incorporate bioactive molecules, drugs or targeting moieties, among others, with a view to design novel tools for theragnosis, because of the easily monitorization of transition metals in the body by using different analytical techniques[82,83]. The metal per excellence in metallic-nanoparticles synthesis is gold (Au-NPs), which is a noble metal, vested with low toxicity properties and low reactivity. This is a double-edge sword because, given its inert properties, the surface of Au-NPs is commonly modified with a large variety of chemical groups to allow their biological functionalization[84–86]. The possibility to control the morphology (spherical, rod, star, clustering…) modifies the penetration performance in certain biological domains[87]. This is an interesting point, which is being deeply investigated, that places Au-NPs in a

privileged position for specific applications, because they can induce changes at cellular and subcellular levels[88]. Regarding their possibilities in cancer therapy, they can cover most of the battle fronts in tumor therapy[89], but none of the proposed solutions has been translated to approved clinical treatments (NU-0129 is ongoing clinical early phase I against glioblastoma[90]).

Another extended metal used for metallic nanoparticles' synthesis is iron (Fe-NPs), but it is highly focused on the development of nanomedicines to treat anemia or chronic diseases[91]. Some of these solutions have been already approved by Regulatory Agencies (Ferrlecit® or Venofer®).

Talking about metallic nanoparticles, we can also include those formed by the oxidation of metals (oxide-based nanoparticles). There are also opened-research lines using this type of solutions as nanocarriers[92], but their interest is focused to use them because their semiconductive properties, which is highly attractive on nano entities or biomedical devices decorations to promote responses from external stimuli[93,94].

Evidently, the essential barrier to translate all these products to clinical phase is the lack of loading capacity and their potential undesired side-toxicities, caused by intrabody metal accumulation[95]. In addition, the drug is not confined into the core of a nanostructure, and therefore it is not isolated from the external media. In these cases, the covalent attachment to the nanoparticle surface, putting the drug in direct contact with the bloodstream media, exposes the molecule to different types of degradation as well. Other important challenges are related to difficulties associated to synthetic repeatability and expensive costs, which hinders the large-scale production of these prototypes.

Quantum Dots (QDs) are also known as nanoscale semiconductor crystals (Figure 11)[96]. They bring out their advantages from the confinement of transition metals, at different positive oxidation states, in a nano spatial volume. For this reason, they can also be considered as metallic nanoparticles, but the main difference arises in their construction. A metallic nanoparticle is composed by a solid single metal in their neutral oxidation state. On the contrary, QDs are synthesized introducing a combination of different metals in their core, and these metals exhibit different oxidation states (but all of them are oxidized).

These type of nanocarriers are commonly composed by transition metals from different groups of the periodic table, which allow the construction of an electron deficient network, leading into a stabilized and passivated semiconductor[97].

The properties exhibited by QDs suggest that their medical interest must be restricted to imaging applications, where they are able to broad the operation window towards NIR[98] and NIR-II[99], or selective electrostimulation[100]. However, they have also been evaluated as potential "substrates" for a responsive drug delivery in oncology[101,102]. Their limitations are aligned with those described for metallic nanoparticles, exhibiting a poor drug-loading capacity, and delivering animosity between researchers because of toxicological concerns.

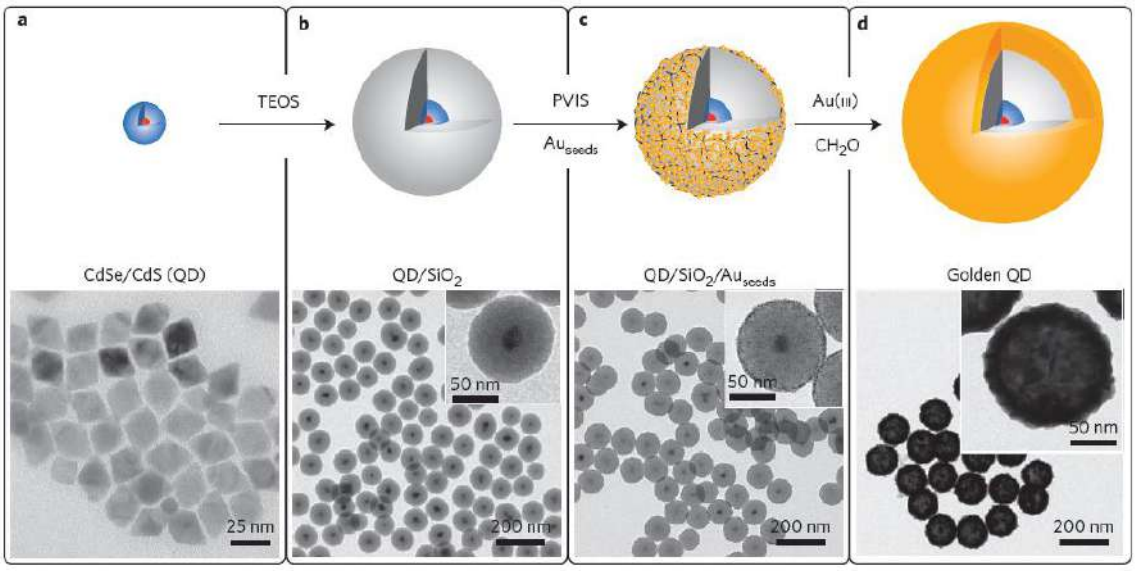

Figure 11. Schematic representation and TEM micrographs of a golden Quantum Dot synthesis. TEOS means tetraethyl orthosilicate, and PVIS, poly(1-vinylimidazole-co-vinyltrimethoxysilane). Adapted with permission from reference [96].

2.3.3 Dendrimers

This kind of nanomedicines arose from the idea to create a polymeric matrix, which present reactive points where a drug or an active substance can be potentially incorporated. They are spherically shaped amorphous assembles of linear polymers, with a regular and compact architecture, that commonly improves both aqueous and organic solubility of the actives that they incorporate (Figure 12). Dendrimers are constructed from a defined core, which is then branched and ramified by different polymers producing cavities and finalizing in peripheral groups, that define their behavior in the media where they are exposed[103]. The polymers conforming dendrimers are typically designed to be biodegradables and biocompatibles, avoiding unexpected *in vivo* side-toxicities and empowering their clinical potential in different areas[104–106].

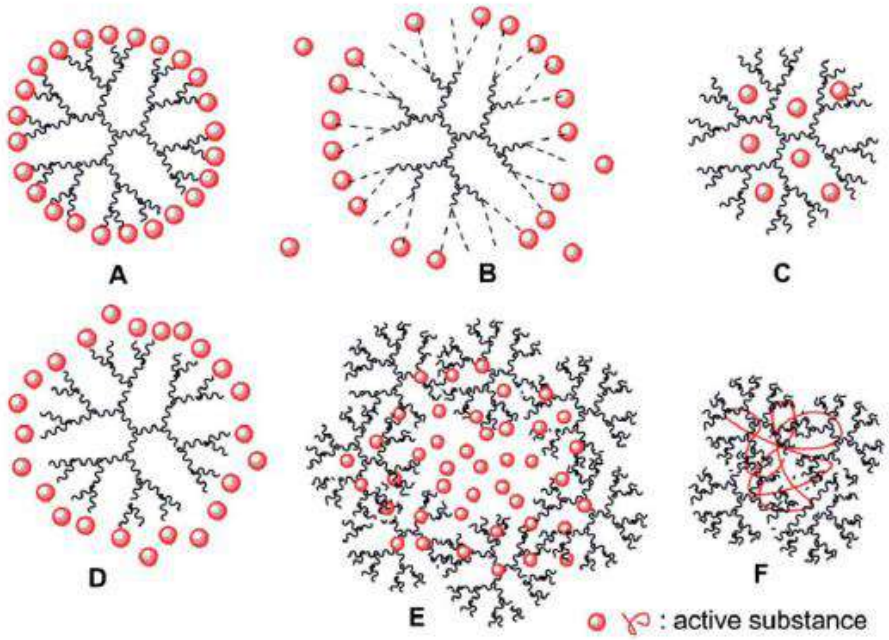

Figure 12. Different drug incorporation possibilities using dendrimers. Adapted with permission from reference [107].

The envision of the dendrimers is clearly aligned with the idea of "stealthing" the active substance during its advance through blood-vessels, avoiding premature opsonization and excretion. Another important advantage of dendrimers refers to the possibility of including different active substances, provided with different biological functionalities[107]. These resourcefulness functionalization alternatives position dendrimers as interesting tools for nanomedicine[108], and other nanomedical systems include the use of dendrimers as novel tools to improve their own performance[109].

Among the above-mentioned properties, their full-chemistry tunning possibilities, and their wide applicability, dendrimers show several drawbacks, which are very related again with a poor drug-amount incorporation, lack of symmetry, which make them low repeatable and influence their biological performance, as well as the intense effort that must be expended to elucidate the metabolic pathways of all the side-products generated during dendrimer-lysis, which difficult their translation to the pharmaceutical market[110].

2.3.4 Polymerosomes

Polymerosomal constructions are based on a similar concept than liposomes: they are built-up from an amphiphilic layer which is formed by association of synthetic polymeric entities[111] which self-arrange themselves in order to minimize the energetic interactions against water, thus generating a sort of vesicle[112].

Polymerosomes embrace the idea arisen from the combination of liposomal vesicle mimicking entities, that are made from tailored polymers, with the ability of dendrimers to introduce selective and specific moieties (Figure 13). The intelligent design of the

amphiphilic block polymers[113] allows their use in a wide range of nanomedical fields[114], based on the facility to functionalize such stable "synthetic nanovesicles" with biorelevant groups[115]. Polymerosomes refine the idea of using rationally ensembled amphiphilic and capped polymers, that were sometimes used as external emulsifiers, in the same structure they are intended to stabilize, deepen on the lipidic approach of self-emulsifiable nanostructures[116].

The research group of Prof. Battaglia (University College London – Instituto de Bioingenieria de Cataluña) has published, in recent years, different studies on the use of polymerosomes, compiling all the properties they exhibit as multifunctional nanocarriers. Besides investigating their encapsulation ability of interesting biomolecules[117], they have examined the possibility of tunning cell physiology through interaction with different polymerosomal nanoshapes[118], the specific delivery to those cells infected, for example, with intracellular pathogens[119], or their use as "nano-swimmers"[120].

Their impressive, not only physicochemical, but also biological properties, are currently positioning polymerosomes as one of the most promising nanomedical strategies for the development of fully functionalized nanomedicines. However, the concept of crosslinked compartment in the core of a nano entity, where the drug is completely isolated from outside media (achieved by inorganic nanoparticles), remains to be unattainable using block copolymers. At the end, there is also a lack of covalent binding in polymerosome constructions. This fact, together with the limited number of block copolymers that have been approved by Regulatory Agencies, make polymerosomes poorly accepted by clinicians compared with the efficacy presented by lipid-based nanomedicines[121].

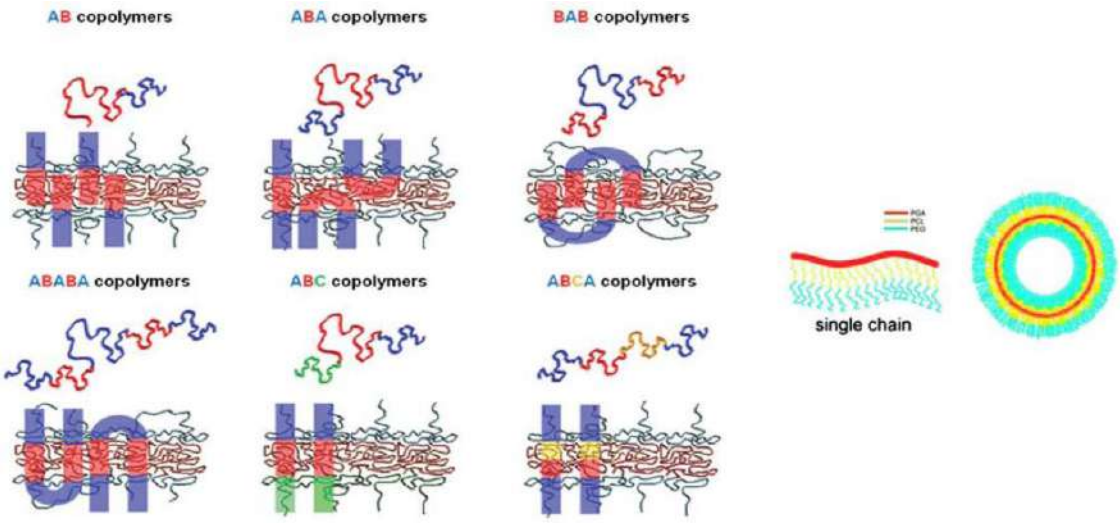

Figure 13. Different assembling possibilities of block copolymers in a polymerosome construction. On the right, a liposome-mimicking polymerosome. Adapted with permission from reference [114].

2.3.5 Polymeric Nanoparticles

From the figure of polymerosomes, with their amazing editable constructions, combined with the shielding capacity of inorganic nanoparticles, it emerges the inferable idea of covalently linking the block copolymers of polymerosomes. Indeed, the reaction of rationally incorporated reactive moieties would produce an integrated and crosslinked polymeric backbone, which will be the main part of the nanoparticle shell. By this way, polymeric nanoparticles appear in nanomedical research. We must differentiate here a nanosphere, which is an integral polymeric entity in a "bead" format (matrix system), from a nanocapsule, where the polymer is arranged surrounding a determined volume, unoccupied by any part of the polymeric construction (reservoir system)[122].

In both cases, water dispersibility of the nanostructure is achieved by introducing hydrophilic moieties into the polymer, circularly oriented outside the nanoparticles' core[123], or by using external emulsifiers, which both stabilize it in aqueous media[124]. The range of polymers that have been explored to build-up polymeric nanoparticles starts from linear constructions, without functionalities, to complex and highly ramified backbones, that incorporate different moieties to improve the performance of the nanostructure.

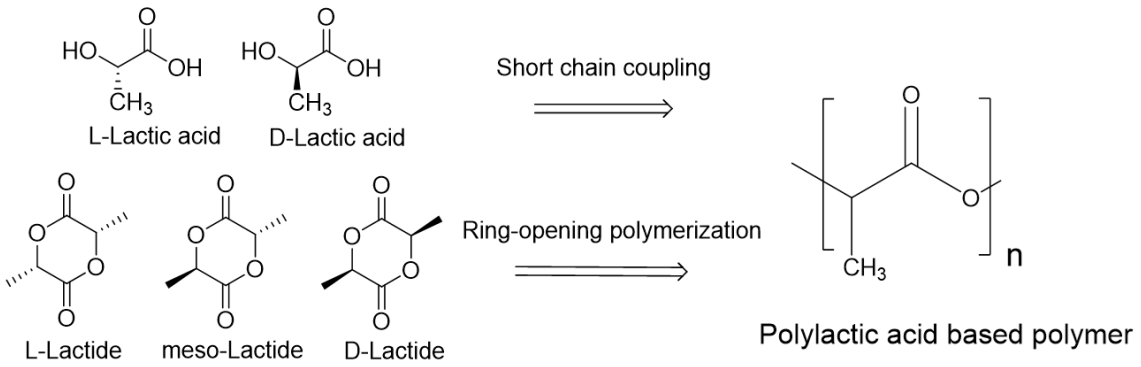

Figure 14. Polymerization reaction from lactic acid or lactide monomers.

The firsts approaches explored the chemistry between carboxylic acids and alcohols, furnishing polyester-based nanostructures, where the lactic acid polymerization was undoubtedly the "prima donna" due to its interesting polymerization properties with itself (Figure 14). Lactic acid offers different possibilities, not only because of its enantiomeric configurations (L- and D-lactic acid), but also because of the possibility of using lactide reagents as starting products[125–127].

Owing to the easiness to work with a wide range of chemical moieties that can be included using polyester chemistry, polylactic acid (PLA-polymers) have been modified with other synthetic copolymers, to increase the retention effect of the nanoencapsulation[128]. In addition, it leads to an improvement of the biocompatibility and cellular uptake[129], and some smart-designed synthetic biobased products were able to promote specific recognition by biological entities[130], among others.

The high hydrophobicity of a simple polylactic acid chain led to the exploration of different approaches to include hydrophilic motifs within the polymeric backbone, generating stratified systems (resuming the characteristics of liposomes) that provide order from the core to the external zone of nanoparticle[131,132]. The reason relies on the necessity of obtaining aqueous dispersions of the nano entities to be applied in medical fields by bloodstream injection.

Polymeric nanoparticles and polymeric nanocapsules have attracted much interest, compared with the undefined polymeric matrix in polymeric nanospheres, as a result of their improved morphological sectorization of the drug.

The sophistication of polymeric nanocapsules drove to the development of different kinds of polyester[133,134], polyethylene[135], polyamide[136], polypeptide[137–140], polypropylene[141], polyurethane[142–144], polyurea[145,146], polystyrene[147,148] and polysugar[149–151] nanoparticles, as well as synergistic strategies[152–154], which intend to enhance, in some way, the performance of the nanosystem[155].

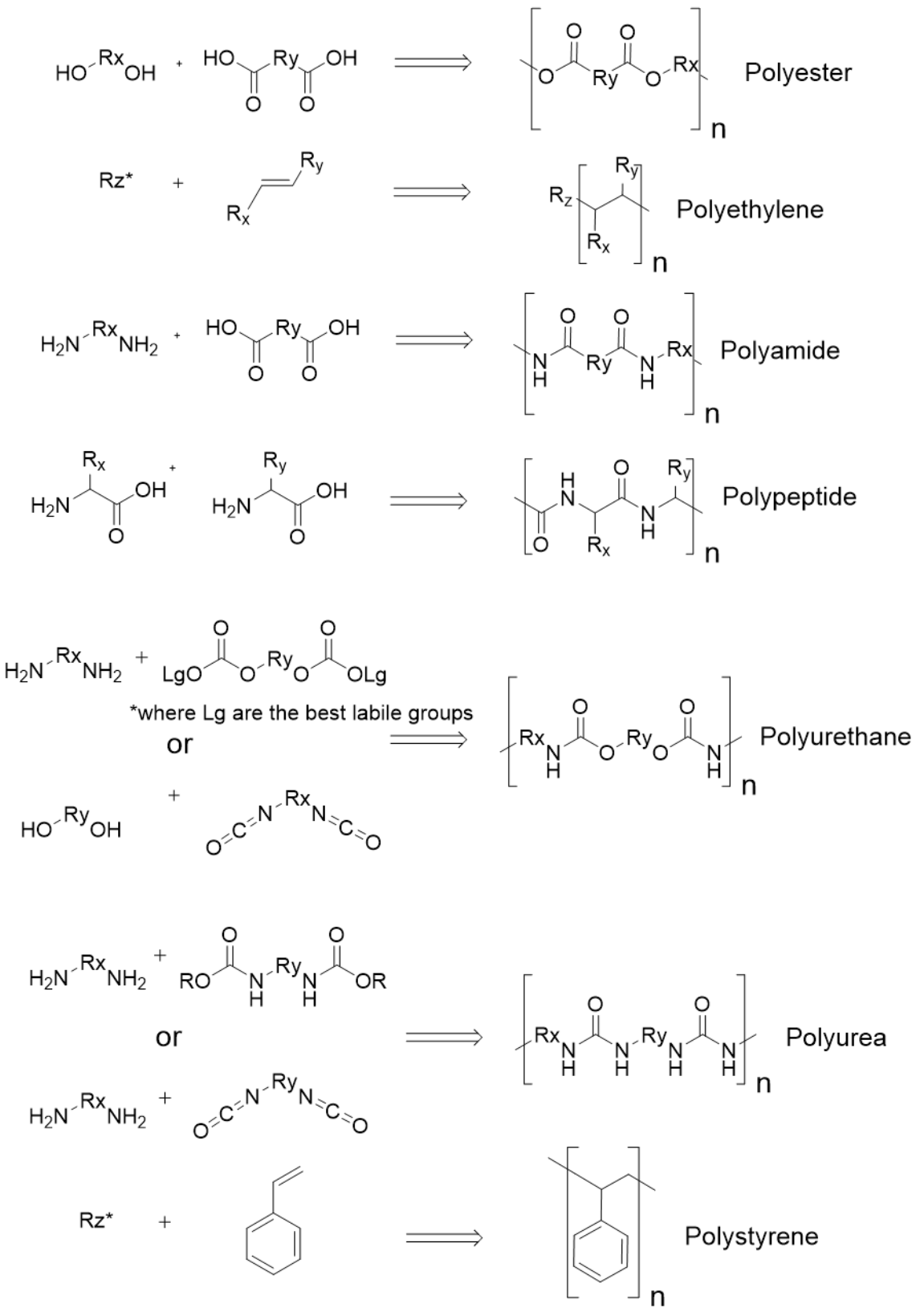

Figure 15. Different types of polymerization reactions described for the synthesis of polymeric nanoparticles.

2.4 Polyurethane-polyurea hybrid nanocapsules: towards biocompatibility, robustness, and versatile functionalization

Since Otto Bayer described the synthesis of the first polyurethane (PU) derivatives, in 1937, they have enormously evolved. Polyurethane chemistry concept comes from the polymerization reaction that leads to the formation of *n* carbamate groups. It is commonly conducted through a polyaddition reaction between an isocyanate group (NCO) from a polyisocyanate and an alcohol group from a polyol (Figure 15): the carbonyl group of the isocyanate terminal group suffers a nucleophilic attack from the hydroxyl groups of the polyol. Even so, the formation of polyurethane can also be performed by polycondensation reactions between carbon dioxide[156] or polycarbonates[157] with polyamines, as well-known alternatives for isocyanate-free polyurethane formations (Figure 15). Despite these alternative synthetic methods excluding isocyanate chemistry, it has been widely extended that polyurethane chemistry refers to the capability of NCO-reagents to easily react with alcohols.

The second most important nucleophilic groups that can react with isocyanates are amines. This reaction is commonly more vigorous and exothermically relevant than the one with alcohols due to the higher nucleophilicity of the amines compared with alcohols. In the case of the NCO/NH_2 reaction, it leads the formation of urea bonds (Figure 15), which are even more stable to hydrolysis than carbamate groups. This fact, together with the higher capability of forming intermolecular hydrogen bonds, confer polyureas (PUA) sturdier properties than their carbamate-brothers[158], and that is the reason why some approaches on materials chemistry have been focused on the design of easily hydrolysable polyurea (PUA), for example, including sterically hindered groups[159].

Under extreme synthetic conditions or high temperature processes, the excess of isocyanate groups, present in polyurethane or polyurea reactions, can react with the polymerized products, to form allophanates or biurets, respectively, as well as with themselves, giving the way to the formation of isocyanurates or diazetidine-diones[160].

The reactions that lead the formation of polyurethanes and polyureas are usually carried out under stoichiometric conditions, which ensures a full reactivity, as well as the absence of reactive groups in the final products, which could be potentially toxic. Additionally, the monitorization of isocyanate-involved reactions can be easily carried out by checking the disappearance of the band of the NCO group around 1700 cm^{-1} using Fourier Transformed Infra-Red (FTIR) spectroscopy. This easiness chemistry, and the wide range of properties they can exhibit, made polyurethanes and polyureas benchmark products in the industrial sector of surfaces and materials (adhesives, coatings, surfactants, leather products, etc). More recently, they have attracted a lot of interest in

the medical field, where their mechanical properties are also strongly appreciated[161,162]. The possibility to generate bio-based reagents or intermediates for polyurethane synthesis has been a point in favor on their acceptance for medical use[163]. Notably, the nanomedical field has received polyurethanes and polyureas as new promising biocompatible tools to perform or modulate some biological effect, not only restricted to the field of encapsulation for drug delivery, but also in polymer conjugation to active molecules, using them as efficient spacers[164].

Narrowing down on the use of PUs and PUAs for polymeric nanocapsules synthesis, the group of Prof. Landfester (Max Planck Institute for Polymer Research; Mainz, Germany) has been extremely involved in the development of ground-breaking PU-dispersions, since they described the one-step miniemulsion methodology, back in 2001[165,166], which has been further sophisticated[167]. Landfester's group started then to investigate a wide-range of applications for polyurethane-based encapsulation[168–171], but they rapidly recognized the huge potential of these nanostructures for drug delivery in medical field, bearing in mind the success of Doxil® formulation just a few years before, and they followed with the biomedical potential evaluation[172,173]. At the present time, plenty of research groups are exploring the use of polyurethanes in several nanomedical applications, like arthritis[174] or cardiovascular[175], but none compared to oncology.

2.4.1 Incorporating tumor-targeted motifs on polyurethane-polyurea hybrid nanocapsules' surface

As it has been explained before, cancer possess a special biology, as well as a great worldwide incidence, that makes it the bull's-eye for targeted-therapies research. A broad spectrum of biomarkers has been identified for cancer therapy and, for that reason, most of the efforts in the synthesis of drug-loaded PU nanocapsules have been focused on decorating them with chemical groups or ligands, aiming to target TME and/or cancer cells, which is commonly called active targeting.

Quite a few bioactive molecules have been recognized by their potential to be used in active targeting of cancer. The presence of folate receptors (FR), αvβ3 integrin or determined antigens in the membrane surface of cancer cells has respectively promoted the development of folic acid (FA)[176], RGD-peptide[177] or antibodies[178] functionalized nanomedicines.

Polyurethane-based nanomedicines have incorporated some of the above-mentioned moieties into the polymeric shell surface, with the aim of enhancing accumulation in tumoral tissues. The functionalization of the surface of these nanomedicines with active targeting moieties has been achieved by using cRGDfK-peptide for αvβ3 integrin active targeting[179], and by clickable folate-derivates aiming to

target folate-receptors (FRα, FRβ and FRγ)[180]. The incorporation of these moieties can be achieved during polyurethane shell formation by diol/diamine side-chain receptor reaction or by attachment to a reactive point of the polymeric shell, that was previously assembled.

Nevertheless, none of these active targeting approaches in polyurethane-based nanomedicines have demonstrated impressive *in vivo* accumulation in tumor-challenged mice models. This fact could be attributed to the vast heterogeneity of tumor stroma, but also to the steric hindrance that the nanocapsule itself generates around the ligand attached to the surface: the active conformation of the ligands might be distorted and, consequently, the binding towards the receptor inhibited[181]. Such limitations led to the idea of designing amphoteric entities for acidic media specific accumulation, which has raised interest within the nanomedical community. In such a context, amphoteric or zwitterionic nanostructures have been developed for an enhanced accumulation by selective cationization under acidic locations [182,183].

Applying this approach to polyurethanes, the research group of Dr. Rocas and co-workers at Ecopol Tech described the first polyurethane-polyurea based hybrid nanocapsules that promote selective accumulation in the TME and specific release into the cancer cells cytoplasm[184]. These polyurethane-based nanomedicines were designed to be superficially decorated with chemical groups that are neutral at physiological pH but become cationic below pH 7. The construction of self-ordered and self-emulsifiable polymeric structures exposes amine and acid pairs out of the NCs core, in an oil in water emulsion, making them ionizable points in aqueous dispersion. The methodology begins with the formation of a cationic and amphiphilic polyurethane-polyurea prepolymer, which contains a building block with lateral tertiary amines with different pK_b values (the first one is about pK_b 7.2 and the other one above pK_b 9). Hence, the amine of lowest pK_b is suitable to be protonated below pH ≈ 7.2, remaining neutral at physiological pH, while the highest pK_b amine is always completely protonated below pH 9. The NCO-terminal prepolymer is then used to emulsify a liposoluble fraction, where the drug is contained, into an aqueous dispersant phase, and L-lysine moieties are incorporated as diamine chain extenders, leading to the formation of urea bonds, and exposing carboxylate groups in the surface of the oil in water nanomicelles. In a final step, a polyamine is added as a crosslinking agent for a covalently attach of the polymer in the surface of nanomicelles, furnishing the stable nanocapsules.

Overall, this synthetic methodology furnishes liposoluble-drug loaded polyurethane-based nanocapsules, with no-needed of external surfactants, that have neutral surface charge at physiological pH and become cationic under acidic conditions, like the ones that are found in TME. At the same time, these constructions include

disulfide bonds along the polymeric wall, which can be selectively degraded under reductive conditions, promoting a specific release of the cargo. PEGylation and the incorporation of hydrophobic groups give the required stratification to the polymeric wall to furnish a stable oil in water emulsion, which was subsequently crosslinked by the polyamine (Figure 16). Interestingly, these nanocapsules have been tested in a non-small cell lung cancer (NSCLC) mice model, improving the therapeutic index of tambjamine, an experimental drug of difficult intravenous administration[185].

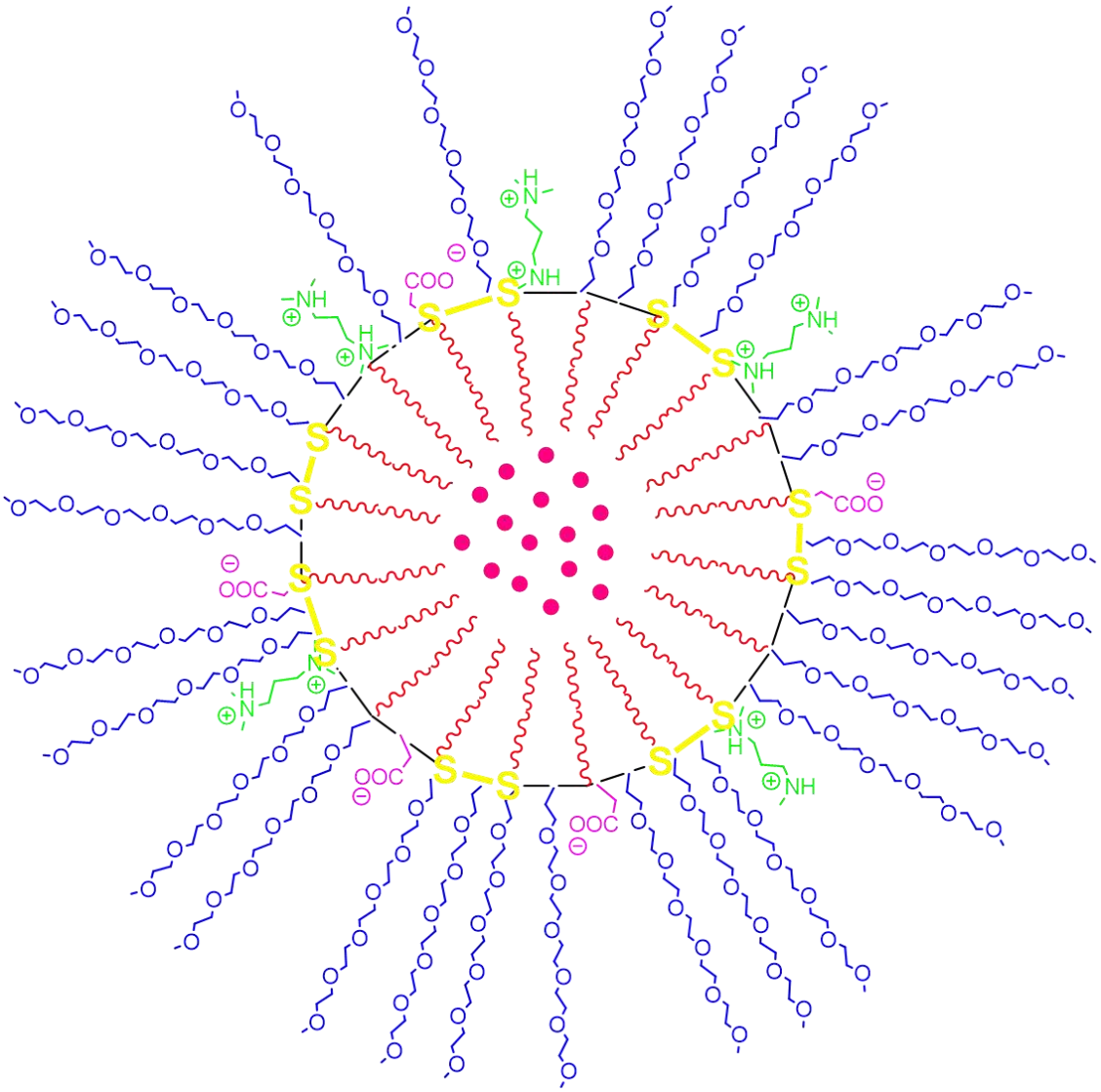

Figure 16. Simplification of the nanocapsules' decorated structure described by Cuscó and co-workers.[182] Blue PEGylated moieties increase the water dispersibility, while red hydrophobic tails enhance the retention of liposoluble drug (fuchsia spheres). Green cationizable groups and pink anionic groups promote selective accumulation in TME, and exaggerated yellow disulfide bonds are susceptible of being reduced under GSH overexpression.

2.5 Nanomedical delivery of hydrosoluble bioactive compounds

The improvement of the water solubility of bioactive agents has been one of the most studied items in the history of drug development. The aqueous nature of blood restricts the use of liposoluble compounds since they must be injected and well-distributed through the patient's body, and this is the reason why, for many years, the main approach has been the chemical modification of hydrophobic bioactive compounds for making them suitable for intravenous injection. The notorious case of paclitaxel (PTX) is one of the best examples of this problem. Not only because it was incorporated in one of the first-approved nanomedicines (nAb-paclitaxel), but also because of the large number of chemical modifications that have been investigated to design water-soluble analogues using the PTX-scaffold[186].

In recent years, innovative approaches for cancer treatment based on water-soluble therapeutic oligonucleotides and CRISPR (clustered regularly interspaced short palindromic repeats) technology[187] are knocking on the door as highly selective approaches, not only in cancer, but also for the treatment of a wide range of diseases[188].

Hence, nanomedicines for the delivery of hydrosoluble compounds are intended to bring tumor selectivity, as well as stability once intravenously injected[189]. Putting an eye on the encapsulation possibilities, the main challenge is to retain and to properly isolate the hydrosoluble cargo compound in the internal aqueous phase of the nanomedicine, while minimizing the interactions of this polar phase with the external aqueous one, which would lead to coalescence processes, and consequently to the system destabilization. In such a context, nanomedical solutions intended for the encapsulation of water-soluble molecules, such as oligonucleotides, in aqueous media have called to be ground-breaking technologies[190].

2.5.1 Current solutions for the nanoencapsulation of hydrosoluble bioactive compounds

The ability to isolate a water-soluble compound while avoiding any type of interaction from the external aqueous media has been previously well exemplified with the case of the liposomal approach. Liposomes are the corner stone of the concept of Water-in-Oil-in-Water (W/O/W) dispersions or emulsions, owing to their capacity to recreate the interactions created during an active invagination process of compounds in eucaryotic cells (Figure 3). The HLB gradient they display between their hydrophilic heads and hydrophobic tails enables their stratification position in a water in oil interface, generating a stable double-dispersion where a water droplet can be confined, thanks to the lipidic supramolecular interactions, and isolated from an aqueous system (Figure 17). By commonly adding a portion of cholesterol, the interaction between the hydrophobic

tails in the internal part of liposomal membranes can be improved. The interactions that lead to the liposome and synthetic membranes assembly have been deeply studied, envisaging to be the basis for the drug delivery developments on hydrophilic compounds[191]. The self-organization ability of the lipid to furnish multilamellar structures facilitates the use of very simple synthetic pathways to easily build-up dispersions[192]. However, as it has been mentioned in previous sections, the lack of targeting capacity, as well as the poor crosslinked membrane, compromises the liposomal approach as an integral and full-targeted nanomedical system.

A representative example of liposomes' performance on the stabilization and delivery of hydrosoluble compounds is found in the recent development of mRNA-loaded liposomes for COVID-19 vaccines[193].

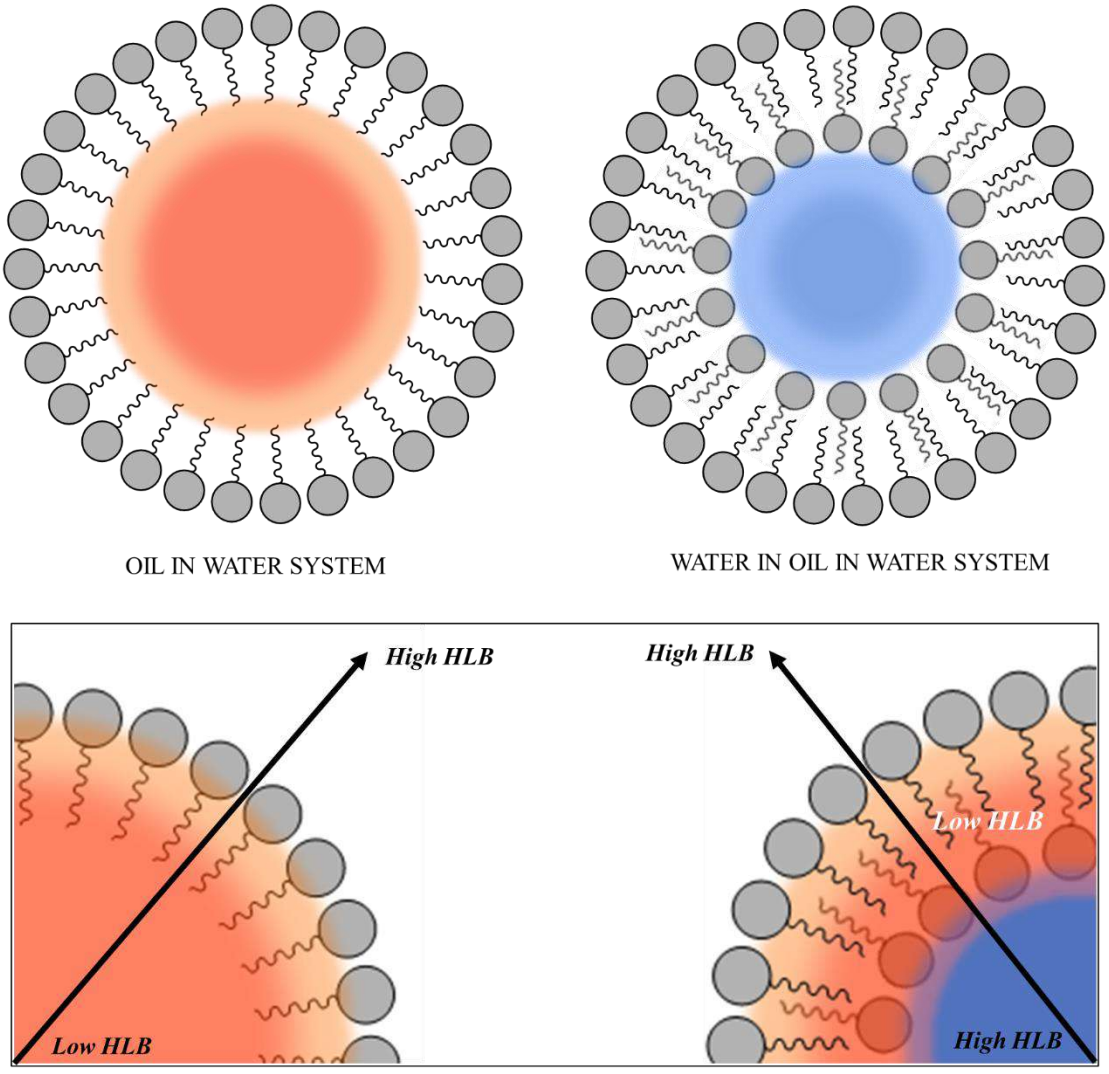

Figure 17. Comparison of the structure of liposomal Oil in Water (O/W) encapsulation *versus* Water in Oil in Water (W/O/W) encapsulation.

Based on the liposomes' route, several groups have put their efforts in applying their expertise in micelles, polymers, polypeptides, polymerosomes and biopolymers to reproduce the architectural ability of the liposomes to create water-in-oil-in water nanoemulsions.

Microfluidics technique has been one of the most fruitful methods to create stable W/O/W dispersions. The precise physical control performed in such techniques helps to define very well the ratios of each component and their proper incorporation into the dynamic system, allowing the formation of size-controlled nanodispersions[194,195].

Ultrasonic-assisted methodology also brings the possibility to create a dispersion of water in oil nanodroplets into an aqueous media, which results in a W/O/W dispersion. Prof. Landfester and co-workers have used this synthetic method to prepare cobalt tetrafluoroborate hexahydrate loaded nanoparticles by employing a polyurethane wall[196].

They also reported a combined system using polyurethane technology where a water in oil encapsulation was carried out to re-disperse the organic phase using Pickering emulsion methodology, leading to a "double-emulsion" product where the silicon nanoparticles stabilize the organic phase in the dispersant water. This is the only reported method involving self-dispersible polyurethanes to design W/O/W systems intended for nanomedical[197].

In a more recent work, Prof. Landfester and co-workers reported the encapsulation of a hydrosoluble glucocorticoid, dexamethasone, in pure silicon-oxide nanoparticles. The design embraces a pH-sensitive release of the cargo by the acidic cleavage of hydrazone bonds, which was previously used by the same group in other nanomedical approaches[198].

The sophistication of these systems arrived when the creation of a double emulsion is not supported by any other physically driven force than the organization and structuration provided by rationally designed emulsifiers. In this line, the firsts achievements were carried out with well-known amphiphilic molecules with contrary HLB; the low-HLB emulsifier promotes the formation of the first water in oil dispersion, and the second high-HLB emulsifier stabilizes the dispersion of the first emulsion in an aqueous dispersant phase. The systemic combinations of Span80/Tween80 or polyglycerol polyricinoleate (PGPR)/Tween 80 have been used, for example, by Wang and co-workers to encapsulate *trans*-resveratrol[199]. This process requires a high-pressure step, organizing the emulsifiers activity, to stabilize the nanodroplets.

In another similar approach, a combination of Span 80 with phospholipids and Tween 80 furnishes pidotimod-loaded double-walled nanodroplets for an improved

immunostimulatory therapy by oral administration[200]. This combination of emulsifiers creates de facto, through different synthetic steps, stable nanodispersions where the ratio between the amount of each dispersed compound and its corresponding emulsifier is governing the final size of the nanodroplets.

An on-demand design of co-polypeptides was described by Hanson and co-workers, generating "lipid-mimicking" polypeptides for their auto-stratification and assembly in two-step aqueous/organic and organic/aqueous interphases, providing nanocapsules smaller than 100 nm that were both loaded with hydrophobic and hydrophilic cargos[201].

In this context, a novel methodology for the synthesis of water-in-oil-in water polyurethane-polyurea based nanocapsules has been described by Ecopol Tech in the recent patent (PCT/EP2022/058801, Bonelli, J. and Rocas, J., *Nanotechnological Platform Based on Polyurethane/Polyurea Chemistry to Furnish Water-in-Oil-in-Water Multi Walled and Functionalizable Nanocapsules and Their Preparation Process*, ECOPOL TECH S.L.). This PCT submission has been recently accepted by EPO, with minor revisions. The synthetic methodology is described and discussed in the Chapter III of the Results and Discussion section of this Thesis.

3 Organic fluorophores in theragnosis

3.1 Photosensitizers based on organic fluorophores for photodynamic therapy

3.1.1 What does photodynamic therapy mean?

Photodynamic therapy (PDT) is a local medical treatment based on the irradiation of a molecule, called photosensitizer (PS), which produces cytotoxic ROS after excitation to a higher energetic state. Although PDT has been mainly used in the context of cancer treatment to generate photodamage and destroy cancer cells in a solid tumor clustering, it is also being used to remedy some skin conditions (e.g. acne or port wine stains), some fungal and microbial infections, and some age-related macular degeneration. Once the PS agent affords an excited electronic singlet state, a relaxation process begins in order to return to the ground state (minimal energy), which can be achieved under different pathways.

The photochemical process that grounds PDT is represented in Figure 18. First, the PS can return to the ground electronic state by converting energy into heat or via light emission (fluorescence). In a different relaxation process, the excited molecule can turn to a less-energetic long-lived triplet state through an intersystem crossing (ISC), that can also decay back to the ground state by emitting phosphorescence. Finally, this triplet excited state can be quenched through two photochemical pathways that produce ROS. In type I PDT, an electron is transferred to water or oxygen molecules, leading to the generation of oxygen radicals. On the other hand, type II PDT implicates the relaxation of the PS to the ground state by exciting molecular oxygen from triplet to singlet state, generating singlet oxygen ($^1O_2$). Type II PDT requires the presence of molecular oxygen

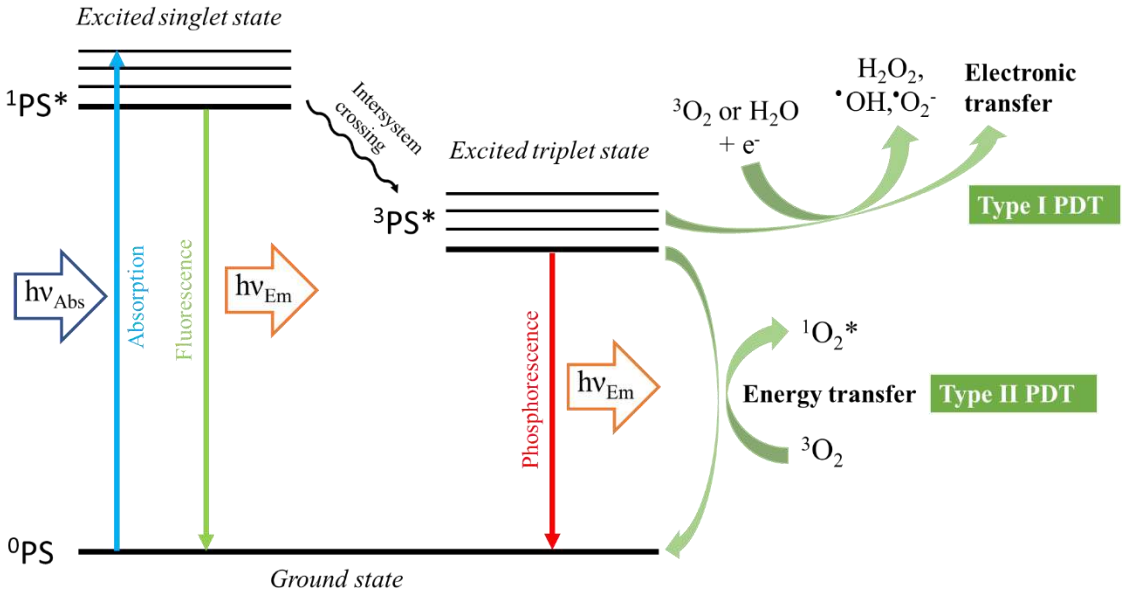

Figure 18. Illustration of ROS formation mechanisms interpreted in a Jablonski's diagram.

in the media since the only ROS that can be generated by energy transfer is singlet oxygen. Hence, besides the PS, PDT requires two additional participants to achieve cancer cell death: oxygen and light of the appropriate wavelength (Figure 19), which can also be an important factor to increase the selectivity of the treatment[202]. Indeed, the energy required to overcome the energetic gap between the ground state and the excited singlet state delimits the working operation window for each photosensitizer.

At this point, it is very important to highlight the difference between PDT and photoactivated chemotherapy (PACT). While PDT uses light to trigger the generation of ROS, PACT takes advantage of light irradiation to chemically modify a prodrug, triggering the release of a bioactive compound, which is the one that leads cytotoxicity on target cells. Therefore, not all the treatments involving light irradiation are designed for PDT purposes[203].

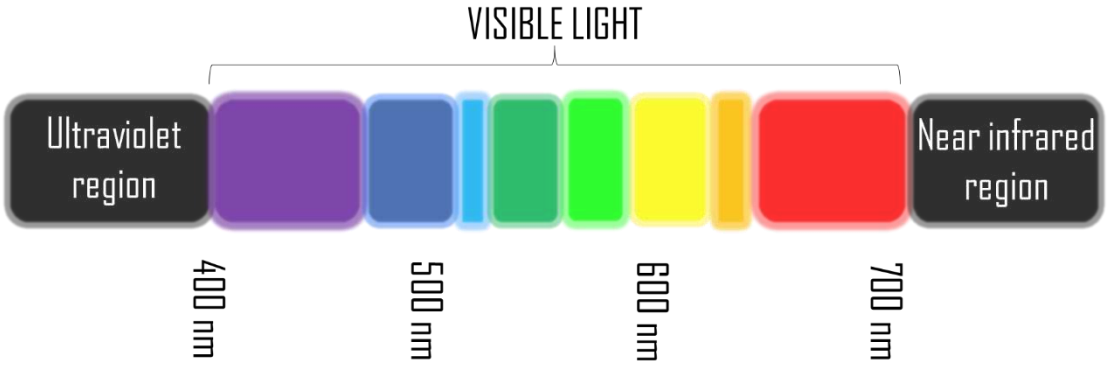

Figure 19. Dissection of the region of the electromagnetic spectra where organic fluorophores are currently working in theragnostic applications.

The ability of PSs to absorb a photon can present several limitations in terms of efficacy, depending on the media where they are dissolved. In such a context, the administration of PSs in aqueous media might lead to quenching phenomena caused by water solvation, in the same way that water quenches fluorescence in organic fluorophores. In addition, photodegradation processes (also known as photobleaching) compromise the chemical integrity of PSs, banning their long-term use.

Hypoxic conditions found in the internal media of a solid tumor are known to limit the phototoxic potential of a wide range of PSs, since the generation of singlet oxygen by type II PDT pathway is mostly blocked. This means that one of the two mechanisms that generate ROS is knocked down in most of the solid tumors. For this reason, huge efforts in oncological PDT have been put to overcome the barriers related with the poor performance of conventional PS agents in the hypoxic environment[204].

3.1.2 Organic photosensitizers

The performance of PSs as efficient PDT agents is derived from their preferential cytotoxicity under light irradiation. In particular, the dark toxicity of an ideal PS *per se*, must be as low as possible[205]. The phototoxic Index (PI) describes the ratio between the cell inhibition coefficient, IC_{50}, in the dark and the corresponding IC_{50} value after light irradiation and, consequently, higher PI values are always desired. However, it is worth noting that translation of this *in vitro* derived parameter to an *in vivo* value is not easy at all[206].

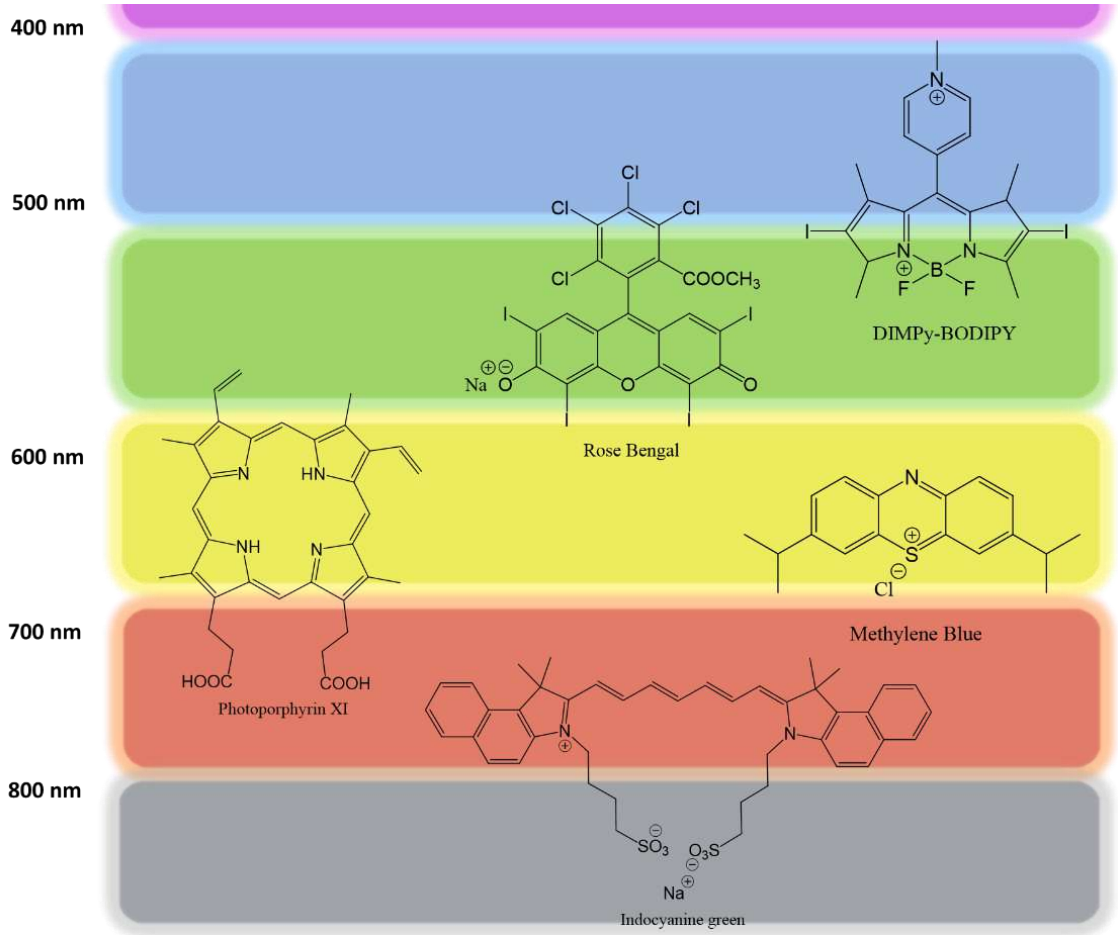

Figure 20. Overview of some organic PSs described in the literature as potential PDT agents sorted by their absorption in visible and NIR region of the electromagnetic spectrum.

In recent years, PDT has gained a lot of interest in cancer research and, specially, the use of organic fluorophores as promising PSs. In this context, an ideal PS should exhibit excellent phototoxic and biological performance within the phototherapeutic window (650-800 nm; Figure 19), organelle-targeting, improved solubility and photostability, and selectivity for cancer cells [207]. Within the electromagnetic spectrum, far-red and NIR light are low-energetic and high penetrating radiations that are able to pass through animal tissues reaching, by this way, subcutaneous locations. Hence, PSs that operate within the phototherapeutic window can be activatable using an

extracorporeal and non-toxic light irradiation, which supposes an extraordinary advantage against other highly energetic irradiation sources (e.g., blue light).

Porphyrin, chlorin, cyanine and phthalocyanine derivatives are common examples of PS scaffolds that are being studied or in clinical use. Other organic fluorophores like BODIPY, Rose Bengal or Methylene Blue have been also the starting point for the development of novel PSs in preclinical research (Figure 20). Within all these structures, porphyrin derivatives are undoubtedly occupying the first position in clinically approved PSs: Foscan®, Photofrin®, Visudyne® or Laserphyrin® are examples of porphyrin-based photosensitizers that are already approved, or in advanced phases, by Regulatory Bodies as PDT agents for anticancer treatment[208]. Even though some of these compounds exhibit some *in vitro* cancer cell specific internalization, their intravenous administration is completely unfavored compared with topical administration. Photofrin, for example, generates skin sensitization activated by sunlight. In addition, some of these organic PSs have been intended to perform subcellular targeting accumulation, which often determines the level of photodamage that is caused in cancer cells[209]. For all these reasons, the improvement of the cellular uptake and the systemic tumor accumulation of PSs is currently a promising approach that is expected to increase the selectivity and efficacy of oncological PDT in the near future.

3.1.3 Coumarin-based photosensitizers

Besides exhibiting outstanding anticancer properties[210], coumarin heterocycles have been widely studied as the basis scaffold for the generation of novel organic fluorophores and photosensitizers. At least, but not last, coumarin-based scaffolds have gained a lot of interest because of the multiple possibilities they offer for introducing chemical modifications in their primitive structure, what is of particular interest in the development of fluorescent probes that work on aqueous systems for bioimaging[211]. In this context, coumarin-based derivatives have been also envisioned for the development of novel PDT agents that operate in far-red to NIR window[212].

The group of Prof. Carotti has been working extensively on the development of coumarins for therapeutic applications[213]. From their initials, at the beginning of 21st century, Carotti's group has evaluated coumarin analogues in different medical fields, like cancer[214] or Alzheimer[215], always redefining the chemical structure of analogues based on the therapeutic performance and target. Other groups have also developed coumarin conjugates with biological moieties to drive specific fluorescent imaging to cancer cells[216].

Medina and collaborators collected in a RSC review, in 2015, the potential uses of coumarin derivatives in several biological fields, as well as their structural peculiarities, synthetic possibilities and the natural sources extraction[217].

Realizing the potential of coumarins, the group of Prof. Marchán has focused the research in recent years on this class of compounds with the aim of developing biocompatible fluorescent probes for bioimaging and photopharmacology applications that were able to operate in the far-red and NIR region of the electromagnetic spectrum. As shown in Figure 21, COUPY derivatives were designed to fulfill the criteria of an optimal organic fluorophore for bioimaging applications[218]. This was achieved in a rational synthetic way by extending the π-conjugated system of the primitive coumarin skeleton, and positioning electron-deficient pyridinium or pyrimidinium heterocycles on the positively polarized end for an enhanced "push-pull" effect.

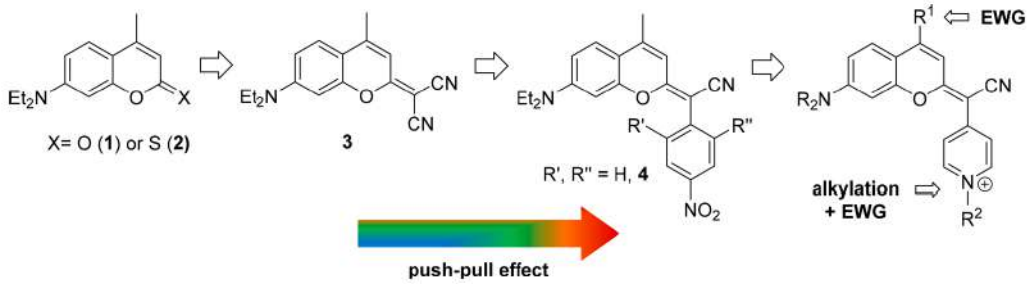

Figure 21. Rational design of the COUPY-based fluorophores described by Gandioso and coworkers. Adapted with permission from reference [218].

The synthesis of COUPY fluorophores begins with the thionation of the lactone function of commercially available coumarins (e.g., 7-diethylamino-4-methyl-coumarin, also known as *Coumarin 1*) by reaction with Lawesson's reagent, which furnishes the corresponding thiocoumarin derivative. Then, condensation of thiocoumarin with 4-pyridylacetonitrile in the presence of a strong base followed by treatment with silver nitrate affords the corresponding COUPY scaffold. Subsequent reaction with a suitable alkylating reagent such as methyl trifluoromethanesulfonate affords N-alkylpyridinium COUPY derivatives (Figure 21). Modifications over the position 4 of the coumarin scaffold were also found interesting for tuning their photophysical properties (e.g., by introduction of a CF_3 group), as well as for transforming them into visible-light sensitive caging groups[219]. As shown in Figure 22, COUPY fluorophores exhibit absorption maxima around 550-650 nm and emission in the far red and NIR region (650-750 nm).

Gandioso and coworkers studied the intracellular fate of COUPY dyes in living HeLa cells by confocal microscopy (Figure 23). The overall results demonstrated that they have excellent plasma and nuclear cell membrane permeability and accumulate preferentially in mitochondria, which can be attributed to the positively charged N-alkylpyridinium moiety, and to a lesser extent in nucleoli. In addition, COUPY dyes

exhibit high brightness, which make them monitorable at very low concentrations under green-yellow light irradiation.

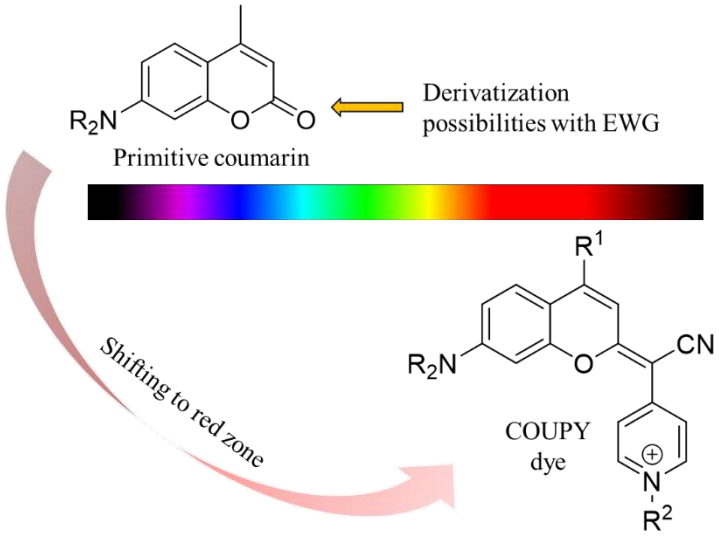

Figure 22. Comparison of the absorption region of conventional coumarins and COUPY fluorophores.

Setting out the research for bioimaging applications, Prof. Marchán's group has recently explored the potential of COUPY derivatives[220] as PSs for PDT[221]. For this reason, a deep biological study of a small library of COUPY derivatives incorporating different structural modifications was carried out in order to stablish structure-activity relationships (SARS). Among all of the compounds investigated, **COUPY 1** and **COUPY 2** (Figure 24) afforded the best phototoxic parameters under visible light irradiation, both in normoxic and hypoxic conditions. Phototoxicity studies in a panel of cancer and healthy cell lines allowed to conclude that **COUPY 2** combines the optimal phototoxicity (best PI value) with a good selectivity factor (SF) between lung cancer cell line and ovarian healthy one (A2780 vs CHO).

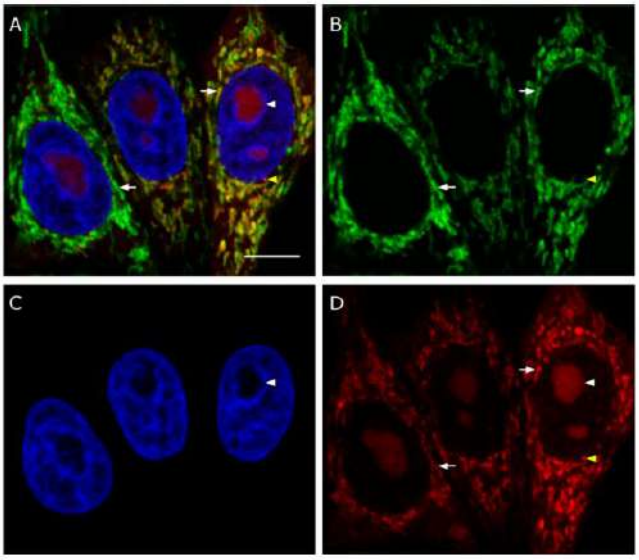

Figure 23. Confocal Microscopy analysis of COUPY 1 dye. A) Overlay of 3 channels, B) MitoTracker signaling C) Hoechst nuclei signal and D) COUPY derivative signal. Adapted with permission from reference [218].

Interestingly, the study suggested that N-hexyl pyridinium modification might be a key modulator for autophagic processes, promoting an increased damage in mitochondria. This was confirmed by the evaluation of mitochondrial membrane potential (MMP), which was clearly disturbed in presence of **COUPY 2** before irradiation.

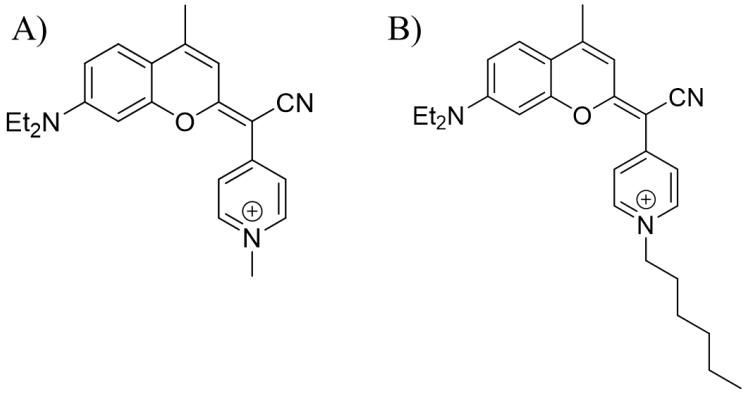

Figure 24. COUPY derivatives described by our group as phototoxic agents under green light irradiation. A) **COUPY 1** and B) **COUPY 2**

Modifications of the conventional coumarin scaffold also led to novel developments in medical fields as specific fluorescent probes[222] or as potential therapeutic agents, for example, against neurodegenerative diseases[223]. Other groups have also explored the introduction of chemical modifications, looking for an increased ROS production or operation at higher wavelengths, obtaining interesting results as well and confirming the coumarin scaffold as an encouraging starting point for ground-breaking PDT developments[224].

3.1.4 Nanomedicines encapsulating organic photosensitizers: improving their performance

Since PDT agents can be considered intrinsically selective compounds owing to their ability to trigger cell-death exclusively under light irradiation in a specific area, nanomedical research has paid attention on improving the pharmacokinetic profile of those PSs exhibiting interesting *in vitro* ROS production under different conditions. In addition, nanomedical entities are committed to extend the "active life" of PSs once injected in patient's body by preventing premature RES-clearance and protecting them from chemical degradation, which is a crucial factor for achieving an optimal performance as phototoxic agents[225].

In recent years, several nanomedical approaches have been investigated with the aim of increasing the potential translation of PSs to the clinics. The firsts were settled on the incorporation of some of the most representative PSs (Figure 20)[226]. In this line, Li and Yan, as well as Sztandera and coworkers, collected in recent reviews different approaches to improve the activity of PSs by using nanomedicine[227,228].

Narrowing down in some specific and relevant examples, Shemesh and collaborators developed ICG-loaded liposomes and evaluated their potential against triple negative breast cancer (TNBC). Using 808 nm irradiation with a fiber-coupled laser system, a growth inhibition of tumoral and non-tumoral breast cell lines was achieved, but without *in vitro* selectivity for cancer cells[229].

Yang and collaborators also used liposomal delivery to encapsulate aggregation-induced PSs, meaning that they only turn-on ROS generation ability when the liposomes are disassembled into cancer cells. A preferential accumulation of liposomes in tumor tissues was attributed to folate-functionalization of the surface, and photoinduced reduction of tumors was achieved by using 800 nm infrared femtosecond radiation[230].

Landfester's group has gone a step forward by combining the encapsulation of cisplatin (conventional chemotherapy) and PSs + Fe_3O_4-NPs (Photodynamic Therapy), in PEGylated ovalbumin (OVA) nanocapsules (Figure 25). Although the structure of the PS was not revealed, it seems it could be related with a BODIPY dye. The irradiation was carried out with a 660 nm xenon lamp, generating promising results in normoxic and hypoxic cytotoxicity assays *in vitro*, as well as producing notably *in vivo* results in tumor growth inhibition and an improvement on survival rate[231].

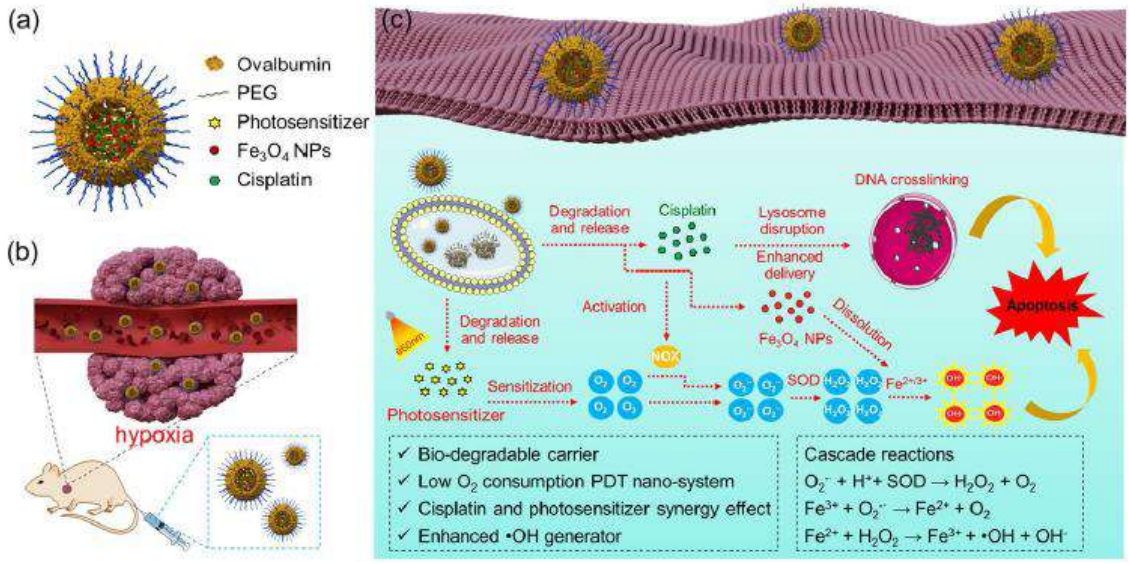

Figure 25. Illustration of OVA nanoparticles with synergistic photodynamic and chemotherapeutic effect developed by Landfester's group. Adapted with permission from reference [231].

Similarly, Yang and collaborators developed synergistic liposomes in a "cocktail therapy" for photodynamic and chemotherapeutic activity, using the liposoluble PS IR780 and hydrosoluble chemotherapeutic tirapazamine (TPZ) agent, reporting excellent results in tumor-growth inhibition, upon 808 nm irradiation, in mice bearing resistant 4T1 breast cancer cell line[232].

In a different approach, Zhang and collaborators combined PDT and photothermal therapy (PTT) to enhance the activity of chlorin e6 (Ce6), avoiding premature activity of the PS by FRET interaction with the conjugated IR780-albumin contained in the nanocarrier, which was selectively degraded by PTT, enabling the ROS generation activity of Ce6 under 660 nm laser irradiation. Using this methodology, they were able to avoid the skin photosensitization caused by a premature photoactivation of the Ce6[233].

Yang and collaborators envisioned the bioluminescence of luciferases as a powerful tool for *in situ* activation of the PSs. For this purpose, Rose Bengal was attached to PLA-PLGA nanoparticles, which were then externally conjugated through the carboxyl groups of PLGA to luciferase proteins. Then, addition D-luciferin to the nanocapsules media triggered the oxidation of this substrate and catalyzed surface-expressed luciferases to emit photons, which activated the generation of ROS by Rose Bengal[234].

One of the most sophisticated methodologies on the combination of PDT and chemotherapeutic agents was recently reported by Xu and collaborators in ACS Nano journal. It is based on a complex system that uses biodegradable copper/manganese silicate nanospheres coated with lanthanide-doped nanoparticles (Figure 26). They can visualize the nanoparticles *in vivo* with second NIR (NIR-II, region between 1000-1700 nm) irradiation, which both produces UV radiation, in combination with the nanoparticles disassembling and hypoxia-relieved ROS generation, generating O_2 from H_2O_2, triggered by photonic excitation of lanthanides (it is a type II PDT mechanism under hypoxic conditions). In parallel, they take advantage of the overexpression of GSH in tumor cells to expose Mn^{2+}/Cu^{2+} ions to intracellular media, generating ROS by conventional chemotherapy[235].

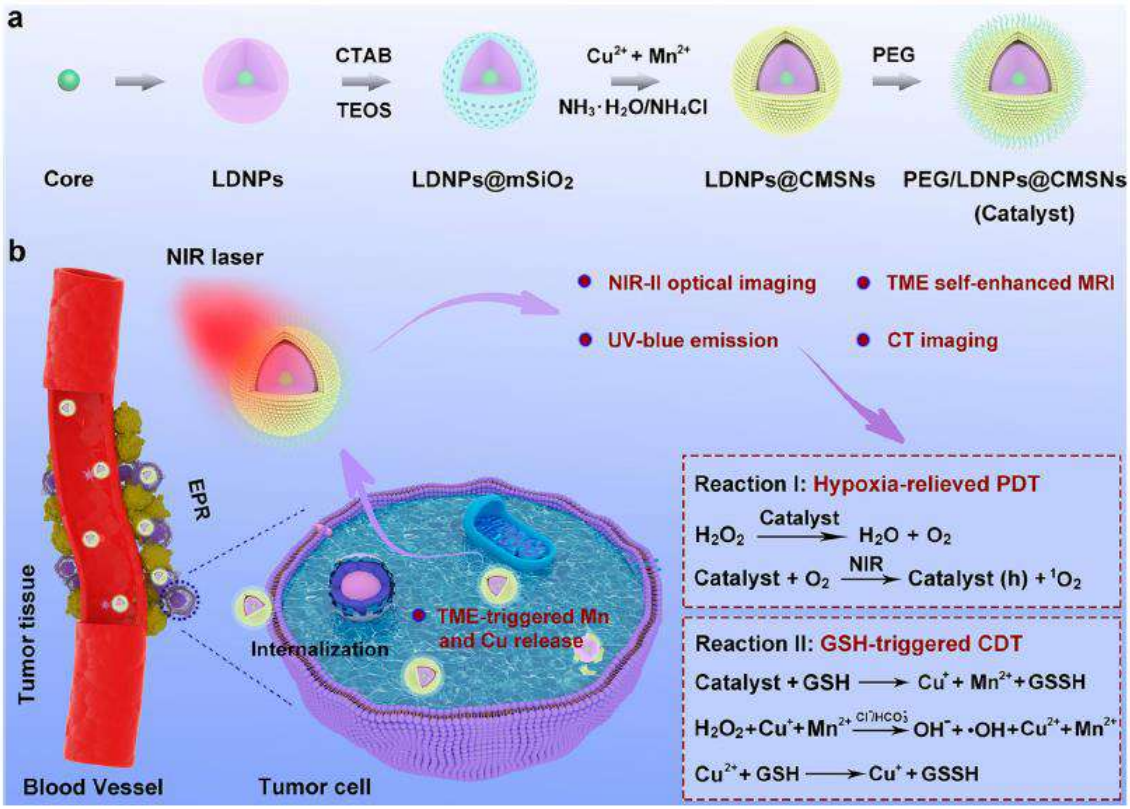

Figure 26. Mechanism of PDT and chemotherapy generated by nanomedical solutions developed by Xu and collaborators. Adapted with permission from reference [235].

3.2 Organic fluorophores in bioimaging and fluorescence-guided surgery

3.2.1 Usefulness of organic fluorophores in medical imaging

The use of non-invasive light devices for the diagnosis of different diseases is considered pivotal approach for the development of novel and biocompatible organic fluorophores.

By the end of 2008, Osamu Shimomura, Martin Chalfie and Roger Tsien were awarded the Nobel Prize in Chemistry for ‘‘the discovery and development of the green fluorescent protein, GFP’’ isolated from jellyfish, as well as for the development of fluorescent proteins, and for envisioning their tremendous applications in the field of biology and medicine[236]. Previous studies of Prof. Shimomura were focused on the development of a wide range of water-soluble, biocompatible, and high-performing fluorescent probes, extracted from biological sources[237,238].

Evidently, the obsession in the development of novel fluorescent probes for biomedical applications has always been related with reaching optimal photophysical properties in aqueous solution, thus avoiding quenching and premature degradation. Therefore, fluorescent dye candidates have been designed to be photostable and water-soluble entities, with operability in the far-red/NIR window to afford enhanced tissue penetration while minimizing issues related with light scattering and ground-noise that appear shorter wavelengths.

As it has been mentioned in previous sections, complete or partial tumor resection is the first line therapy, in those cases where it is applicable (considering the surgical accessibility or metastatic gradeless, among others), in oncological treatments. This therapeutic approach ensures the elimination of the maximum amount of cancer cells from patient’s body, being then always the first option evaluated by clinicians. Even though, surgery is currently considered a high-invasive technique. However, it leads to poor side effects and the recent technological advances have softened the impact on patients’ comfort, resulting in an increased demand on the applicability of this technique from patients [239]. In this context, organic fluorophores offer interesting possibilities for theragnosis (putting aside if they are also developed for phototherapy) in the field of Fluorescence-Guided Surgery (FGS).

FGS consists of a surgical procedure where the patient has been previously administered with a bioimaging agent which will mark out to the surgeon the area for the surgical intervention. The aim of FGS is to improve the optimal resection of damaged tissues, while avoiding unnecessary damage to normal tissues on the surrounding

margins. The monitorization of the fluorescent probe is commonly carried out by laparoscopic analysis or, in more recent advances, by non-invasive extracorporeal light irradiation. The latter approach requires the use of high-performance bioimaging agents, exhibiting low-energetic and high-penetrating light absorption spectra that can be monitorable driven by advanced technological devices in medicine.

FGS is emerging as a less-invasive technique for synergistic diagnosis and treatment of cancer[240]. In the optimal situation, the bioimaging agent can specifically tag tumor cells/tissues, *in situ* guiding the decisions of the surgeon's team and evidencing the tumor margins for an ideal tumor elimination. With the aim of increasing the efficiency of the bioimaging agent, while minimizing the body invasion, NIR fluorophores have been positioned in bull's-eye as promising therapeutic agents since they are excited with non-toxic and highly penetrating light[241], and that is why, in recent years, have been translated to several clinical solutions in oncology[242]. In fact, they must be considered not only as simple diagnostic agents, but as theragnostic ones since they play a crucial role in the surgical treatment. They are not only intended to perform a qualitative analysis of the tumor location or the grade of the disease, but they will also specifically define which damaged tissues cannot remain unremoved from patients' body, by the thorough quantitative analysis of their fluorescence intensity[243].Tumor-targeted FGS is a relatively newborn solution (Figure 27), highlighted with the approval, in 2007, of the 5'-aminolevulinic acid hydrochloride for the intraoperative visualization and resection of high-grade glioma (HGG)[244], after presenting very good results in oncological patients with a variety of tumor locations and grades[245].

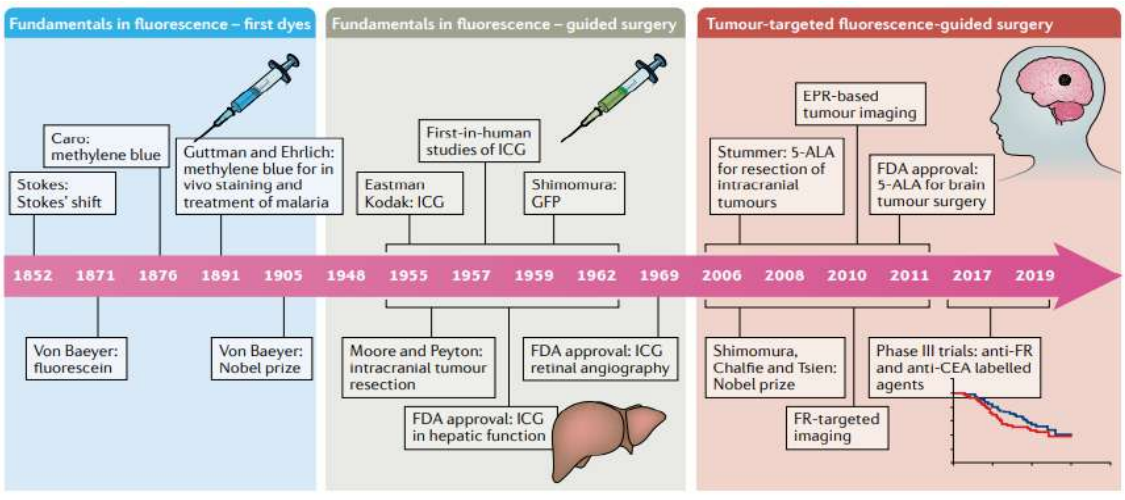

Figure 27. Timeline of tumor-targeted FGS appearance. Adapted with permission from reference [244].

A small handful of organic fluorophores, such as Indocyanine Green (ICG, IC-Green™), Fluorescein (FLUORESCITE™), Methylene Blue (PROVAYBLUE™) or the previous mentioned 5-aminolevulinic acid (5-ALA, GLIOLAN™; the only that has been

approved in oncology for intraoperative visualization in the resection of glioma), have been approved by Regulatory Bodies as fluorescent probes for non-invasive bioimaging.

3.2.2 Towards near-infrared based fluorescence-guided surgery solutions in oncology

The implementation of FGS methodology requires four essential pillars: a fluorescent probe, a suitable source of light, an imaging device and the surgeon's team or a remote-controlled resection device.

Focusing on the first pillar, 5-ALA fluorescent probe is currently used as imaging agent in the FGS processes for glioma resection as previously stated, as well as in the bioimaging and identification of malignant lesions, such as lymph node metastases[246]. The light-active specie from 5-ALA is protoporphyrin IX (PpIX), which is formed by dimerization of 5-ALA followed by subsequent metabolization in mitochondria. The resulting PpIX can be efficiently excited using the 405 nm blue laser, emitting above 600 nm[247].

Despite the great potential of 5-ALA in neurooncological application, its operational window is limited due to the appearance of cell autofluorescence at such short irradiation wavelengths. In addition, continuous irradiation over PpIX has been demonstrated to generate ROS, which can lead to undesired cell death, even under daylight irradiation[248].

By contrast NIR irradiation has been positioned as the preferred methodology for tumor tissue imaging since it reduces the light scattering and cellular photodamage. Among the above-mentioned approved fluorescent probes, ICG is the only fluorescent probe that can operate in this imaging window, while displaying efficient fluorescence quantum yield. In fact, ICG fluorescence imaging has generated a lot of interest, being employed for the NIR visualization of, for example, peritoneal carcinomatosis during surgical treatment of abdominal malignancies[249], as well as for the evaluation of the proper hepatic function, appearing some studies that support its possibilities for the monitorization of hepatocarcinoma[250]. In recent years, surgeons have evaluated ICG-guided surgery in flow-based tumor identification, sentinel lymph node mapping or lymphatic obstruction visualization[251,252].

Onda and collaborators drew the potential of free ICG as tumor tracer for specific accumulation in tumors after intravenous injection but, analyzing the results they reported, it seems far from being true. In the figure 2 of their manuscript, they show the fluorescence analysis obtained at different times after tail vein injection of ICG free. Between 2 and 10 minutes after injection, indistinctive signals can be detected through

the whole body of the mouse. From 2 hours to 8 hours after injection, clear patterns of biodistribution can be differentiated, but the signal is not specifically accumulated in tumor, since excretion organs like kidneys and small intestine show similar levels of qualitative fluorescence. But then, after 24 h of injection, the fluorescent signal, which is recognizable preferentially in tumor, becomes very poor, hampering the possibilities to translate this analysis to a more internal type of tumor (this study was carried out in a subcutaneous model of HT-29 in BALB/C nude mice, where the tumor is reproduced close to the epithelial cells of mouse dermis after its subcutaneous injection). Indeed, there is an angiogenic progression in the neighboring vessels of a tumor cells clustering, and ICG can clearly highlight these processes, but it cannot be assumed as an unequivocal way for tumor signaling[253].

3.2.3 Near-infrared operative nanomedicines: a winning combination in oncology

Nanomedical carriers incorporating ICG are among the preferred solutions for the identification of tumor cells/tissues with NIR light[254]. The biological fate of nanomedicine, thus basically biodistribution, is a key factor again in the trendy search of novel nanomedicines for theragnosis[255] (Figure 28).

One of the most important challenges that nanomedicine needs to face to incorporate ICG into the core of drug delivery systems and, consequently, to isolate it from the external aqueous media, relays on the high solubility of this compound in water. This property has difficulted the incorporation of ICG into some of the most useful methodologies based on water nanodispersions.

In an intensive review on the uses of ICG for oncological treatment, both as a fluorescent probe as well as a photosensitizer, Kaibori and collaborators thresh the most pioneering advances, including the development of ICG-loaded nanoparticles, that are formed by self-assemble of amphipathic polydepsipeptide (ICG-lactosome)[256] in blood. The PDT effect was demonstrated after five minutes of irradiation at 774 nm over malignant hepatic cells, and the penetration level of the laser in a relevant mouse model was found to be around 10-20 mm[257].

Previously, in 2012, Funayama and coworkers explored the marginal intraoperative resection of spinal metastatic tissues using similar ICG-lactosome constructions in rats challenged with CRL-1666 adenocarcinoma cell line by subcutaneous injection in the vertebral L6, developing 1 cm tumors after ten days. Both the qualitative analysis of the whole anesthetized rats as well as the further post-euthanized imaging of the lumbar spines, revealed that ICG-loaded nanoparticles selectively accumulated over tumor tissues. Nevertheless, the reason for this preferential accumulation was not elucidated[258].

Hill and collaborators reported the encapsulation of ICG in hyaluronic acid (HLA)-derived nanoparticles, where the fluorescence of ICG had been turned off. However, the specific accumulation in tumor tissues 24 hours after nanoparticles injection was described because of the ICG fluorescence reactivation, which was an indicative of nanoparticles dissasembling[259]. Souchek and collaborators incorporated different far-red and NIR dyes in the same type of nanocapsules, obtaining quite good results through conjugation of these dyes to the HLA moieties[260].

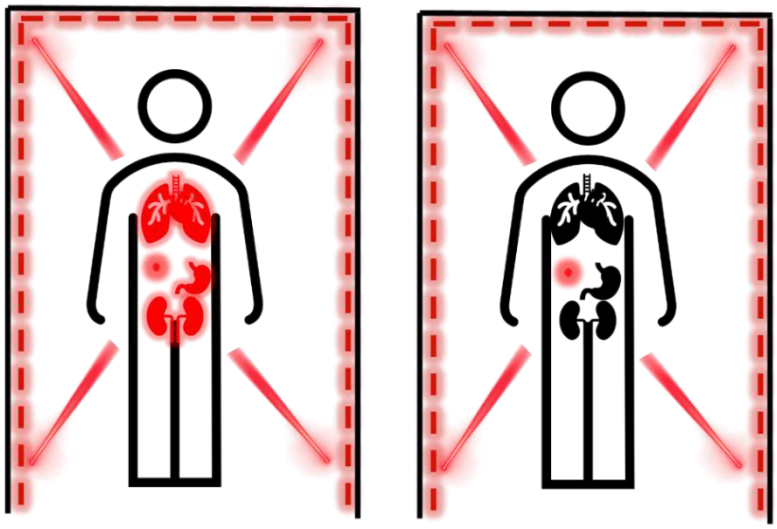

Figure 28. Non-specific fluorescence signaling of free fluorescent probes injection versus tumor signaling of a nanovehiculized fluorescent probe. In the right image tumor lesion is unequivocally signaled as a red sphere.

Evidently, none of the previous approaches were designed to actively target tumor cells/tissues. Indeed, they only take advantage of passive accumulation of nanoparticles in highly vascularized blood vessels. In contrast, other advanced approaches use the specific interaction antigen-receptor to perform an actively targeting of tumor tissues. This is the case of the PEG-coated PLGA nanoparticles, designed by Lee and Lai, which were functionalized with HER-2 antigen for the selective vehiculization of ICG to HER-2 positive breast cancers theragnosis. The study demonstrated a preferred internalization of ICG-loaded nanoparticles in HER-2 positive MDA-MB-453 breast cancer cells against the HER-2 negative MCF-7 ones, increasing the phototoxic effect in the first-mentioned cells, after irradiation at 808 nm for 5 minutes[261].

In another recent approach, excluding the use of ICG, Dong and coworkers used folic acid targeted liposomes, incorporating a superficially far-red squarene dye by click-chemistry, and tested them in SKOV-3 ovarian cancer cells expressing folate-receptors. The interest of these approach relies on the ability of using liposomes as imaging agents *per se* because they have the fluorescent probe embedded in the lipidic structure, while the core of liposome remains accessible for a drug incorporation[262].

4 Metal-based anticancer drugs

4.1 Metal complexes in conventional chemotherapy

4.1.1 Platinum-based anticancer drugs and analogues

Talking about metallodrugs in cancer therapy, it is mandatory to introduce them with platinum(II) complexes, being cisplatin (*cis*-diamminedichloridoplatinum(II)) the most important one, and the basis of current metal-based chemotherapy. Cisplatin was discovered in 1965 by Prof. Rosenberg, who described a tumor regression in sarcoma mice model[263]. Cisplatin consists of a square-planar structure of Pt(II) coordinated to two ammonia and two chloride ligands in *cis* configuration. In aqueous conditions, hydrolysis of this compound enables the formation of the active aquo species, which form stable adducts with the *N7* atoms of purine nucleobases in DNA, hampering DNA chain transcription, and finally leading to cell death[264] (Figure 29). Cisplatin performs great antitumor efficacy *in vitro* (it is commonly used as a benchmark product in biological research of new drugs), but a lack of specificity together with a poor pharmacokinetic profile make that less than 20% of intravenously administered cisplatin in solid tumor patients reach tumoral location, which requires, in most of the cases, the administration of high-toxic overdoses of the drug to achieve considerable efficacy, thereby generating serious side effects[265]. Besides the problems related with poor specificity and bioavailability, a broad range of solid tumors have developed resistance to cisplatin[266].

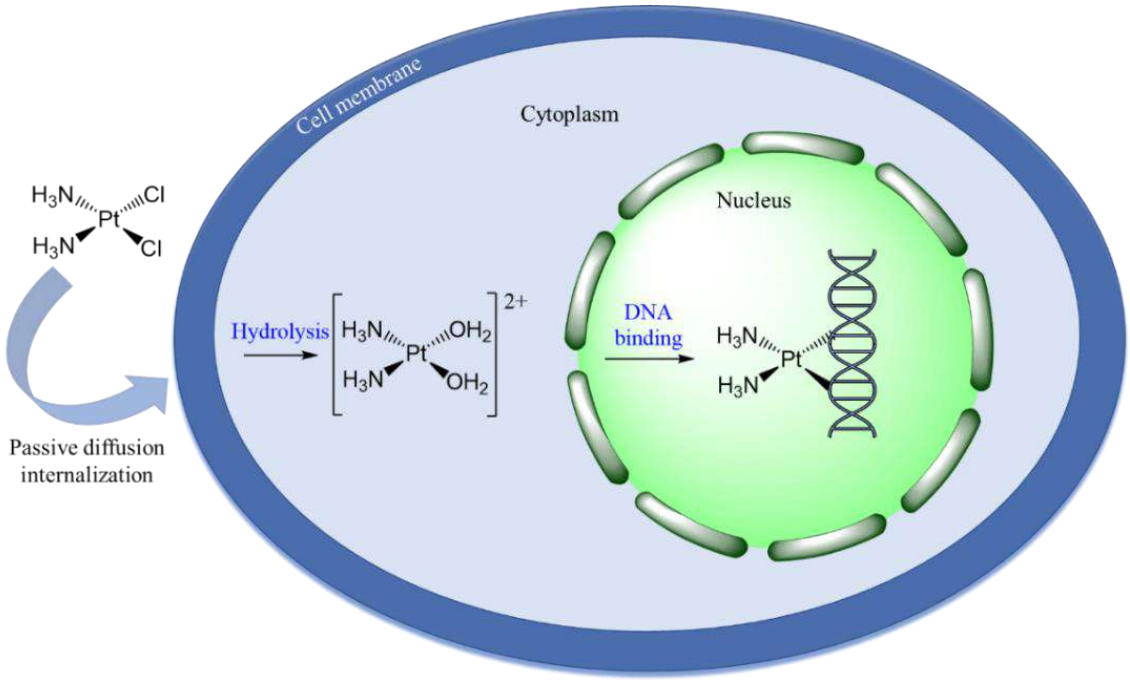

Figure 29. Simplified scheme of cisplatin mechanism of action that led to apoptosis in eukaryotic cells.

Based on cisplatin parent structure, extensive efforts were first focused on the development of a second generation of Pt(II) anticancer drugs, where ligands were modified to increase the stability of the compound in water solution, tackling bioavailability issues. Carboplatin, Oxaliplatin, Nedaplatin, Lobaplatin and Heptaplatin received the Regulatory Bodies' approval for use in cancer therapy as antineoplastic agents (Nedaplatin was only approved by the Japanese Agency and Heptaplatin by Korean one). Although such novel approaches managed to slightly reduce secondary toxicological concerns of cisplatin, they were not established as strong alternatives for cisplatin administration, owing to an unclear therapeutic effect improvement. Furthermore, with the aim of increasing the accumulation in tumor locations, synthetic efforts have been focused on the incorporation of targeting ligands into the square planar construction of Pt(II) drugs. Despite the large efforts dedicated to developing a safer therapy based on alternative Pt complexes, the most promising *in vitro* tested compounds showed a poor bioavailability and pharmacokinetics *in vivo,* failing in different stages of the preclinical and clinical phases. As a consequence, platinum(II) derivatives are the only metal-based drugs approved for cancer chemotherapy (Figure 30).

An interesting feature of metal-based anticancer drugs is that they can induce cell death through different biological pathways, decreasing the possibilities of cancer cells to develop chemoresistance[267]. In addition, they are very interesting for treating certain types of tumor lesions that are not responding to any tailor-made therapy (in the case, for example, of triple negative breast cancer, TNBC)[268]. Hence, metal complexes are considered as powerful solutions in chemotherapy since they are capable to induce a strong cytotoxic effect (platinum(II) derivatives take part as a first line treatment in more than 60% of chemotherapies) but, at the same time, the lack of specificity demands to accurately adjust the dose for each patient to avoid critical toxicities, leading to a patient stratification process which induces, in various cases, poorly clinical outcomes.

In recent years, several research groups have gone one-step forward by designing Pt(IV) prodrugs, which enable different functionalization in the "octahedral-like" hexacoordinated structure of platinum(IV) complexes and that are selectively reduced to the corresponding platinum(II) active species under glutathione overexpression inside cancer cells[269] (Figure 30). On the other hand, since the approval of platinum(II) drugs for cancer therapy, other transition metals have extensively been evaluated, in different oxidation states and coordination forms, as potential substitutes of platinum compounds, with the aim of improving therapeutic effect. Therefore, iridium, ruthenium, rhodium[270], titanium[271] or osmium[272], among others, awoke a special interest diverging from typical square planar structure of Pt(II) complexes.

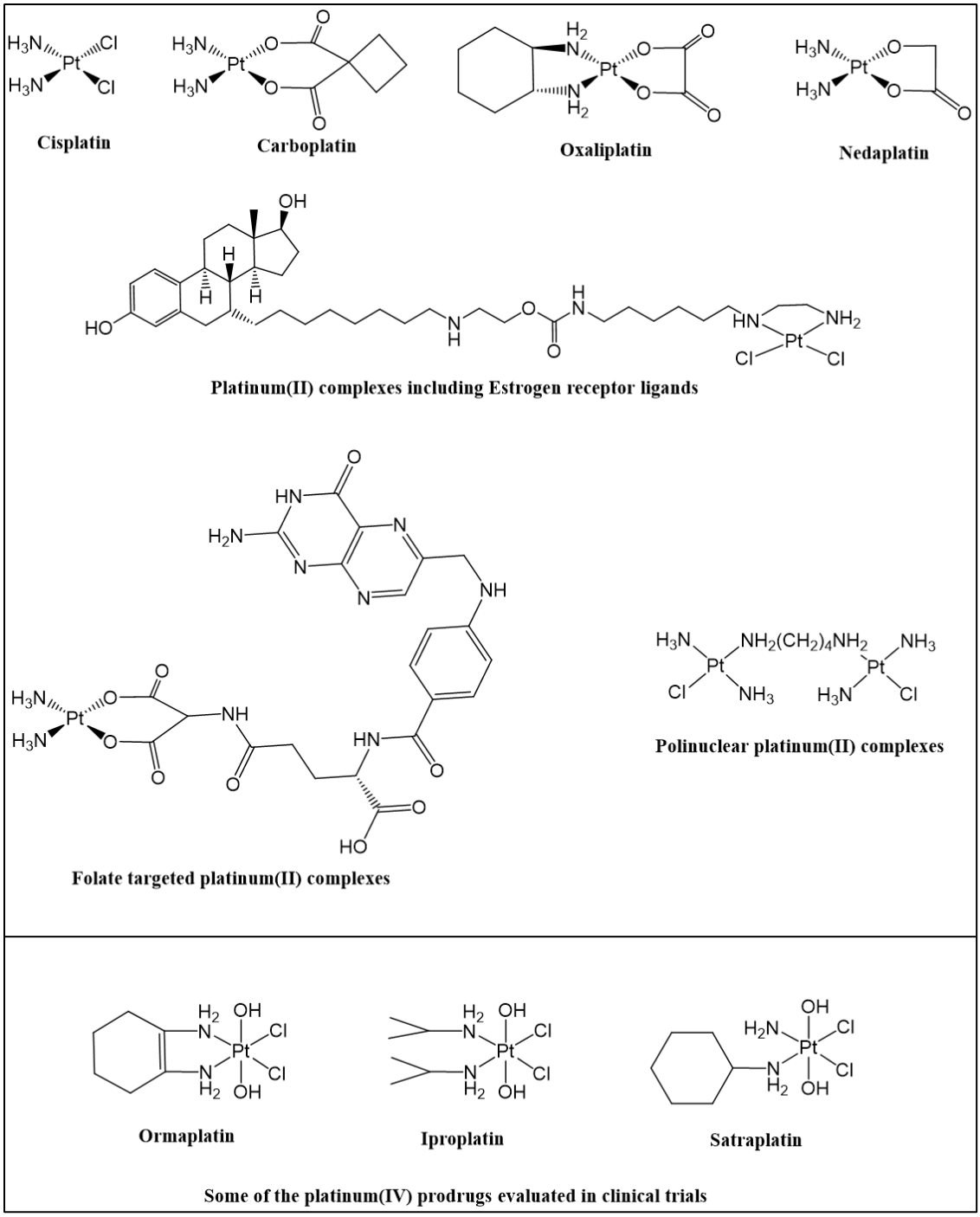

Figure 30. Platinum-based anticancer agents that have been or are being studied as chemotherapeutic agents.

4.1.2 Cyclometalated iridium(III) anticancer complexes

Even if platinum compounds are the "rockstars" in metal-based chemotherapy, other metal complexes, as previously stated, have gained a lot of interested owing to the significant cytotoxic properties they exhibit. Particularly, cyclometalated iridium(III) compounds have arisen special interest in recent years because of having a stable configuration and well-established cytotoxic properties. For example, the parent iridium bis-(phenylpyridine) dichloride (Figure 31A) substituted with a phenylimidazo-

phenantroline ligand (Figure 31B), which was found to be non-cytotoxic at all towards several cancer cell lines, was studied by Zhang and coworkers in a liposomal formulation, reporting good results in tumor weight decreasing in B16 melanoma xenograft mice models[273].

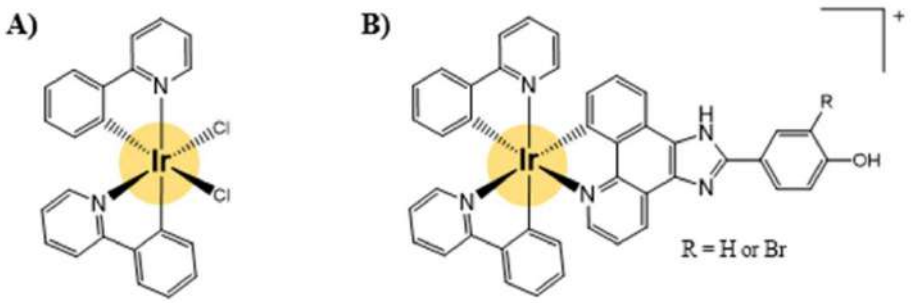

Figure 31. A) Structure of iridium bis-(phenylpyridine)dichloride complex and B) its phenylimidazo-phenantroline analogue tested by Zhang and coworkers.

The group of Prof. Ruiz and coworkers dug on the importance of cyclometalated octahedral iridium(III) compounds as new theragnostic agents or antimicrobials, revealing how the ligand substitution allows to fine-tune some of their properties (e.g., to perform selective organelle targeting, to increase DNA-binding or enhancing photo-responsive properties)[274]. In addition, the group of Prof. Ruiz has deeply explored the design of novel ligands, finding that some of the phenyl-benzimidazole phosphorescent derivatives show better cytotoxic *in vitro* activity than cisplatin. Surprisingly, the cytotoxicity of these compounds was not attributed to covalent binding to DNA (Figure 32A). Indeed, an inverse correlation between DNA binding and cytotoxicity was demonstrated for these compounds. This study suggests that the internalization of these compounds to the cellular cytosol compromises the proper endoplasmic reticulum operability. For those compounds where hydrophobicity was significantly increased, a poor cytotoxic activity was obtained, which was associated with a lack of endoplasmic reticulum accumulation[275]. Even so, other more hydrophobic compounds such as **Ir1** and **Ir2** (Figures 32B and 32C, respectively), could not be tested due to poor aqueous solubility and cellular uptake.

Based on their promising cytotoxic properties, metallodrugs are being called to be one of the most interesting compounds for exploring selective delivery into tumor locations by using nanomedical solutions. Not only the specific delivery performance, but also increasing the overall stability in aqueous dispersion and affording safely injection into the bloodstream are some of the key factors that need to be addressed by nanomedicines to improve the therapeutic use of metal-based drugs.

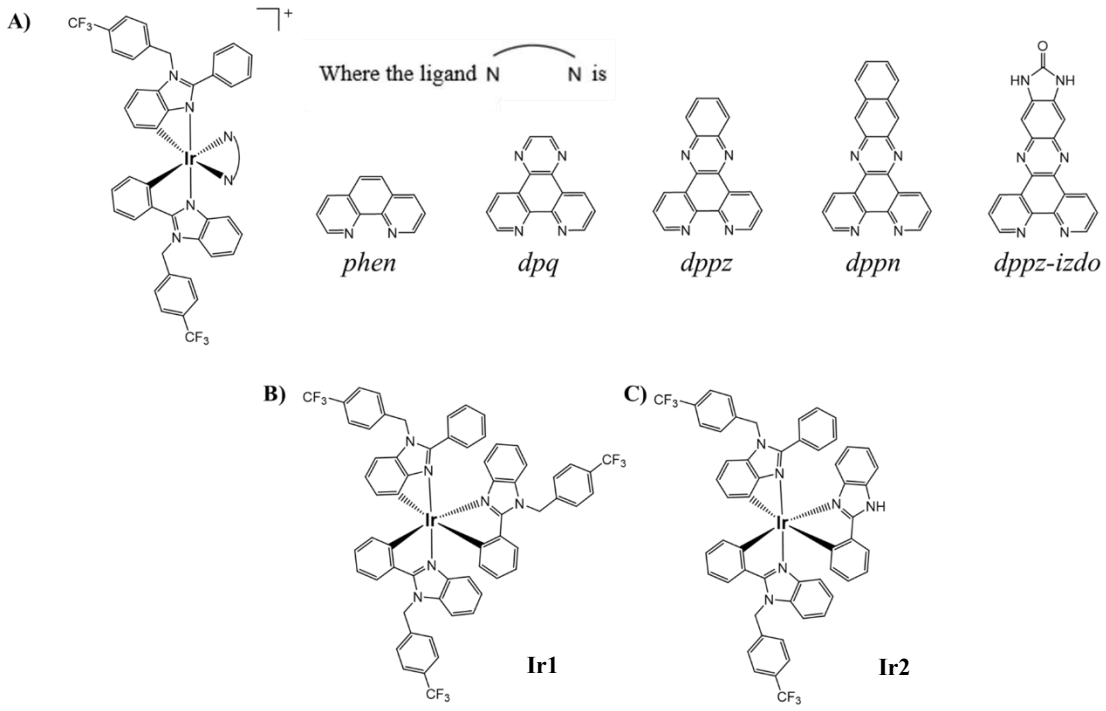

Figure 32. Examples of cyclometalated iridium(III) complexes synthesized in Prof. Ruiz's lab.

4.1.3 Current drug delivery systems for metallodrugs: the problem of loading

Not surprisingly, the nanoencapsulation or nanomedical-mediated delivery of cisplatin has been highlighted as one of the essentials of the current nanomedicine, and several formulations have been or are being purposed as efficient ways to deliver this drug into cancer cells[276]. Remarkably, the liposomal-based formulation Lipoplatin®, developed by Regulon Inc., reported successful results in clinical phases I, II and III, being now commercialized and studied worldwide[277].

A broad range of approaches have been described for metallodrug delivery in the last ten years, looking for the best compromise between platinum modification (to facilitate the incorporation into a nanostructure) and activity while avoiding toxic side effects or minimizing them[278,279]. Basically, two different ways to incorporate platinum(II) derivatives into a nanomedical structure have been described. The first one consists of the direct encapsulation of the active species, while the second one is based on the tranformation of the active species into a Pt(IV) prodrug to facilitate the encapsulation in a hydrophobic environment. Among them, the encapsulation is the one that can offer a higher amount of active platinum contained into a nanomedical structure.

Focusing on the first approach, and given that cisplatin, carboplatin and oxaliplatin are small and highly polar compounds, the direct encapsulation method must stabilize and confine a relatively hydrosoluble core, isolating it from the external dispersant aqueous

media (W/O/W approach). Liposomes are one of the first solutions that appeared owing to the capacity of the lipid bilayer to organize itself between two aqueous phases. In addition to Lipoplatin, other liposomal solutions have been evaluated and patented for clinical use[280]. Several research groups working in polymeric synthesis have also contributed to this research; for example, the group of Dr. Chen achieved the encapsulation of cisplatin into "lipid-mimicking" structures, composed by poly-L-glutamic acid polyethylene glycol copolymer, equalizing the overall response, and increasing survival rate in lung cancer mice models. Although the encapsulated cisplatin did not show better results in terms of tumor reduction compared with the injected free drug, the therapeutic efficacy was improved due to low renal toxicity associated to the encapsulated form, leading to increased survival rates[281]. In addition to liposomal formulations, polymeric nanoparticles[282], dendrimers[283] and carbohydrate-based nanoparticles[284], have also been studied for the encapsulation of cisplatin.

Regarding the second approach, based on the synthesis of platinum prodrugs, the platinum(II) atom of the cisplatin structure is commonly oxidized to platinum(IV), which allows the incorporation of ligands through the two axial positions, facilitating the introduction of interesting functionalities in the metallodrug construction. In this way, redox-labile ligands, light-responsive ligands, or biological moieties to selectively target cancer cells have been incorporated into the square planar structure of the Pt(IV) complex. Lippard and coworkers have reviewed the synthetic methods for the preparation of such platinum(IV) complexes[285]. This type of derivatization vertebrates the development of platinum-based anticancer candidates in clinical phase evaluation, like Mitaplatin and Satraplatin.

Aiming at increasing the encapsulation capacity of platinum(IV) prodrugs, Lippard's group described the incorporation of hydrophobic ligands into the axial positions, like fatty acids, through oxidation of the platinum(II) center with hydrogen peroxide and subsequent reaction with succinic anhydride and a wide range of hydrophobic isocyanates, enabling their incorporation through carbamate bonds[286] (Figure 33).

This hydrophobic modification allowed to move forward with the encapsulation technology by using an oil in water (O/W) system, where the liposoluble core of the nanostructure brings the possibility to define a stratified gradient from lipo- to hydro solubility, being able to leverage a higher volume of the nanosphere[287]. Evidently, a direct oil in water encapsulation is more efficient than a water in oil in water encapsulation process because in double emulsions processes the stabilization of the first water in oil encapsulation, where the use of low HLB surfactant is mandatory, is followed by the

emulsification of this system by a high HLB surfactant that performs the W/O/W system (Figure 17).

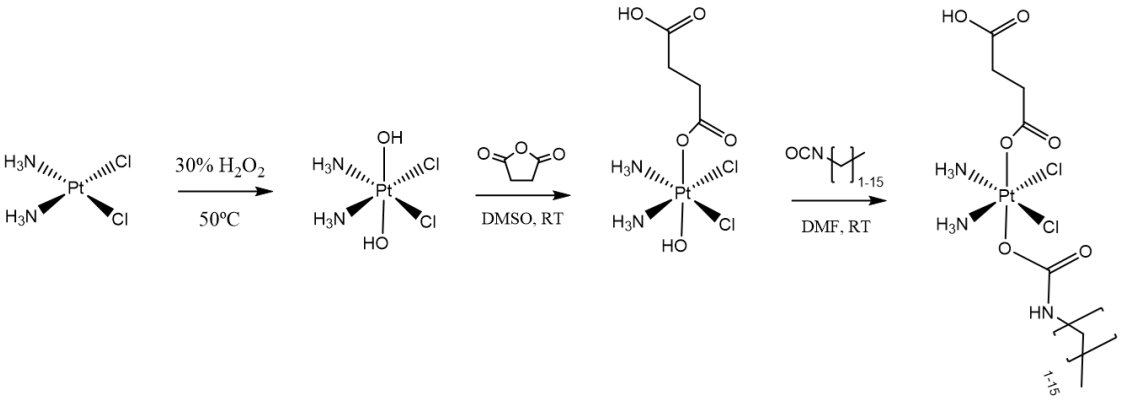

Figure 33. Hydrophobic derivatization performed by Lippard and coworkers over Pt(IV) derivatives of cisplatin.

A wide range of hydrophobic derivatives of platinum-based drugs have been studied using this nanomedical approach[288], but not only restricted to these, other metal complexes have been also tested as potential candidates in chemotherapy. In fact, a large amount of metallodrugs from other previously mentioned metals that could not be *in vivo* evaluated because of poor solubility in aqueous media, bounced back as promising candidates by means of encapsulation.

Considering the encapsulation of iridium(III) complexes, Liao and co-workers evaluated an analogue containing a bicyclo-tetraazacyclo-pentaphenanthrene (BTCP) (Figure 34A), which was cytotoxic *per se*. Notably, encapsulation in liposomal structures led to an enhancement of the antitumoral efficiency, by increasing the ROS levels, as well as the mitochondrial disfunction[289]. Following this line, Mukhopadhyay and co-workers studied the influence of terpyridyl-based ligands substitution in the parent $[Ir(ppy)_2Cl_2]$ (Figures 34B and 34C), on DNA binding capabilities through intercalative/electrostatic interactions by molecular docking studies, concluding that the most active compound (even compared with cisplatin) was the one that localizes in the cytosol of cancer cells, triggering the cell apoptosis by different mechanisms than DNA intercalation[290]. The group of Prof. Sadler published an exhaustive analysis on how the modification of the phenylpyridine ligand in half-sandwich iridium(III) complexes (Figures 34D and 34E) influences their biological activity[291]. Similarly, Wang and collaborators concluded that a coordination of α-lipoic acid-functionalized bipyridine bis-(phenyl pyridine)iridium(III) yielded better results in terms of cytotoxicity, compared to the cyclopentadiene half-sandwich α-lipoic acid-functionalized bipyridine analogue (Figures

34F and 34G), triggering cell-death through different biological pathways and relegating the role of cyclopentadiene half-sandwich iridium(III) compounds in chemotherapy[292].

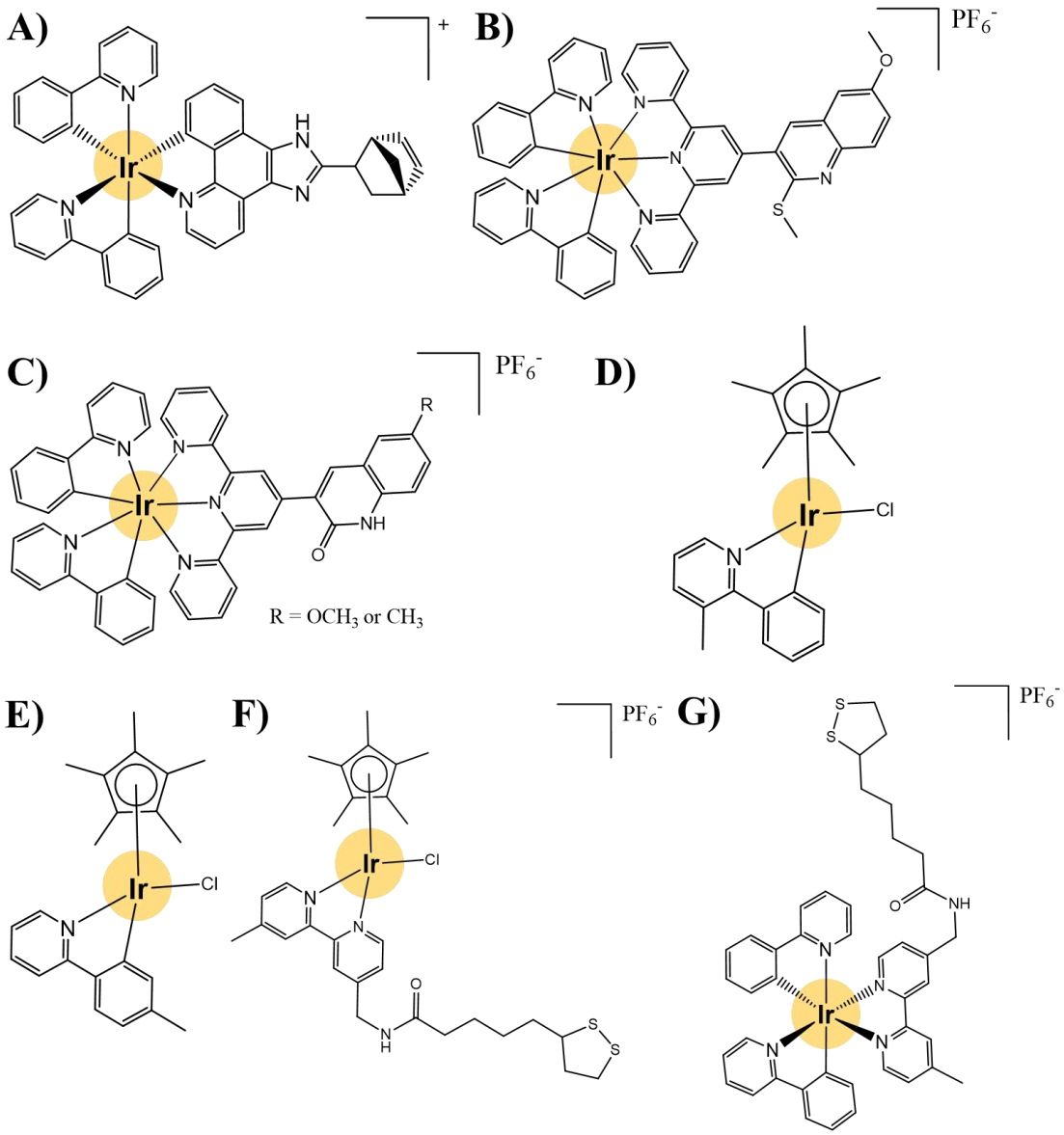

Figure 34. Some examples of iridium(III) complexes described in the literature.

4.2 Metal complexes in photodynamic therapy

4.2.1 Metal-based photosensitizers

In recent years, transition metal complexes have been positioned as promising PS agents in PDT[293]. For this reason, plenty of bioinorganic research groups have focused their attention on the development of novel PSs based on metal coordination complexes as an alternative to organic fluorophores by increasing their phototoxicity in the tumoral adverse conditions of hypoxia while being activatable within the phototherapeutic window to facilitate tissue penetration. Indeed, some of them have been approved (e.g., sulfonated aluminum phthalocyanine-based Photosens® and palladium-bacteriopheophorbide TOOKAD®) or are on their way for the approval process by different Regulatory Agencies all over the world as anticancer agents[294].

Prof. McFarland and co-workers wrote a recent review where the principles of PDT using metal complexes to treat cancer are reported. They examine the potential of some published metal complexes and what are their likelihood approval as phototherapeutic agents in oncological treatments. The review pays special attention to ruthenium(II) polypyridyl complexes analogues of the ongoing clinical phase II experimental TLD-1433 agent[295–297], which will be discussed further in this section.

4.2.2 Iridium(III)- and Ruthenium(II)-based photosensitizers

To fence the possibilities of metal complexes on PDT, and taking into account that a wide range of compounds are being evaluated as potential PSs around the world[298], iridium(III) and ruthenium(II) are currently the two hot metals in the development of novel phototherapeutic agents against cancer. Ruthenium and iridium belong to the groups VIII and IX of the 2nd and 3rd row of transition metals in the periodic table, conferring them unoccupied *d*-orbitals, and stabilizing their preferential oxidation states +2 and +3, respectively. Such stable compounds are commonly based on an hexacoordinated configuration, furnishing pure or distorted, depending on the ligand combination, octahedral complexes[299].

The group of Prof. Mao, in Guangzhou, published the firsts iridium(III) complexes intended for oncological PDT, testing a range of phenylpyridine/benzimidazolyl-carboline complexes, in A549 lung carcinoma cells, for a lysosome-targeted photodamage, obtaining high-sensitivity to light, with PI values above 800[300] (Figure 35A) In the same line, Prof. Kwon and co-workers developed different bipyridine and phenyl-pyridine cyclometalated iridium(III) complexes, inducing endoplasmic-reticulum photodamage by ROS generation under two-photon irradiation at 860 nm[301] (Figure 35B). Even Prof. Sadler's group evaluated the phototoxic activity of some of their iridium(III) compounds, in-depth analyzing the functionalization possibilities for PDT, not only

restricted to increase the phototoxicity or light selectivity, but also putting on the table how the pharmacokinetic profile of the iridium-based PSs could be improved for an effective *in vivo* performance[302].

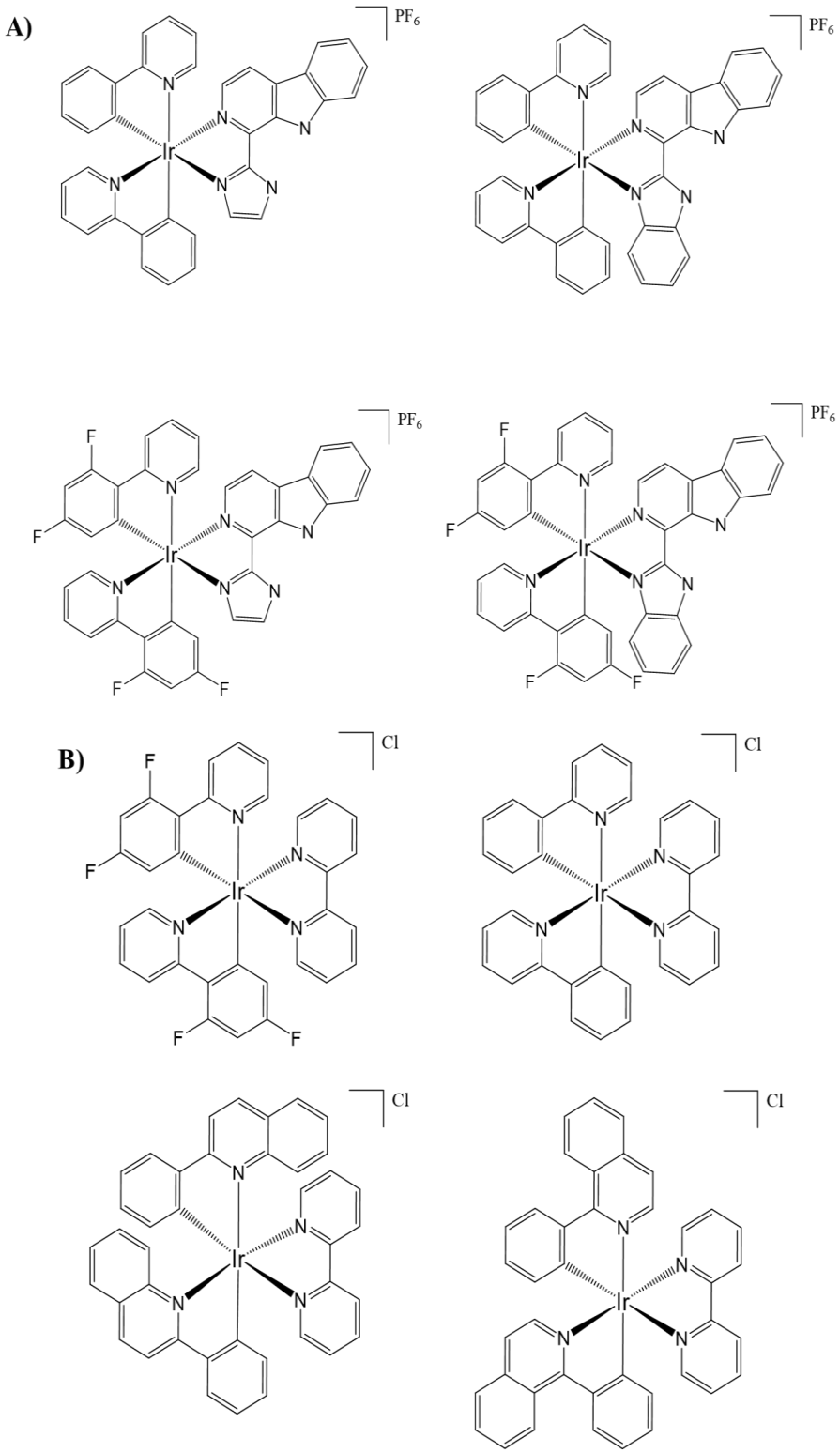

Figure 35. Structure of some cyclometalated iridium(III) complexes described as phototherapeutic agents by A) Mao and co-workers and B) Kwon and co-workers.

The groups of Ruiz and Marchán combined their expertise in the synthesis of metallodrugs and coumarin-based derivatives, respectively, to design a novel class of PSs based on the conjugation of cyclometalated iridium(III) complexes and far-red emitting COUPY coumarins, which reported interesting PI values after visible light irradiation, even under hypoxia[303].

Other relevant authors in literature, like Prof. Bryant[304] and Prof. Sun[305], have described a potent photoinduced anticancer activity in other iridium complexes. In more recent studies, the group of Prof. Chao reported the antiproliferative activity of a mitochondrion-targeted BODIPY-Ir(III) conjugate in breast adenocarcinoma cells[306].

In recent years, ruthenium(II) complexes have gained more attention in the PDT field. Prof. Glazer described a range of Phen- and Bphen-substituted polypyridyl ruthenium(II) complexes with remarkable PI values upon irradiation with visible light, around 450 nm, in HL60 and A549 tumor cell lines. Nevertheless, they were not considered as PDT agents, because their mechanism of action goes through a ligand ejection to make the uncoordinated product a potent DNA intercalating agent [307,308]. Despite these amazing properties intended for PACT, they did not evaluate the ROS generated by the compound under light irradiation.

Prof. Gasser and co-workers reported, in 2015, a perspective analysis of the different possibilities that ruthenium-based complexes offer in combination with light irradiation for PDT applications. They started from the organic-based agents approved for PDT to end up with the analogues developed by Glazer's group. Even so, they concluded that the lack of *in vivo* studies with these compounds hampered their jump into clinical phases[309]. Gasser's group intensively works on the development of ruthenium-based PSs, by combining the ability to generate ROS upon light irradiation with the good performance that some of them shown as DNA-intercalating agents[310].

The turning point arrived when the research carried out in Prof. McFarland's group led, in 2018, to the first ruthenium complex (TLD-1433) that entered in clinical trials for the intravesical photodynamic therapy of Non-Muscle Invasive Bladder Cancer (NMIBC). TLD-1433 (Figure 36A) is a thiophene-containing ruthenium(II) polypyridyl complex that is photoactivable upon green light irradiation centered at 525 nm[311]. TLD-1433 is currently going through a clinical phase II process, being evaluated in tumor bearing patients in USA.

The promising results that TLD-1433 showed in preclinical studies encouraged researchers in the lasts years to find similar solutions, using ruthenium as reference metal for PDT. McFarland's group focused its work on the development of novel PSs that are

able to produce ROS under hypoxic conditions, in order to improve the results showed by TLD-1433. Using the thiophene-modifications, they adressed the synthesis of two analogues, both with an extra thiophene ring on the ligand structure and one of them coordinated to two phenantrolines instead of bypyridines (Figure 36B and 36C, respectively). These compounds were biologically tested against some of the most common cancer cell lines and exhibited, in their own words, "inexplicable efficacy under hypoxic conditions" and high PI values (e.g., 10,000 in SK-MEL-28 cell line) under different monochromatic light irradiation, [312]. Analogues of TLD-1433 have also been synthesized in McFarland group with osmium instead of ruthenium, reporting also good values under hypoxic conditions, even when irradiating with monochromatic red light (633 nm)[313].

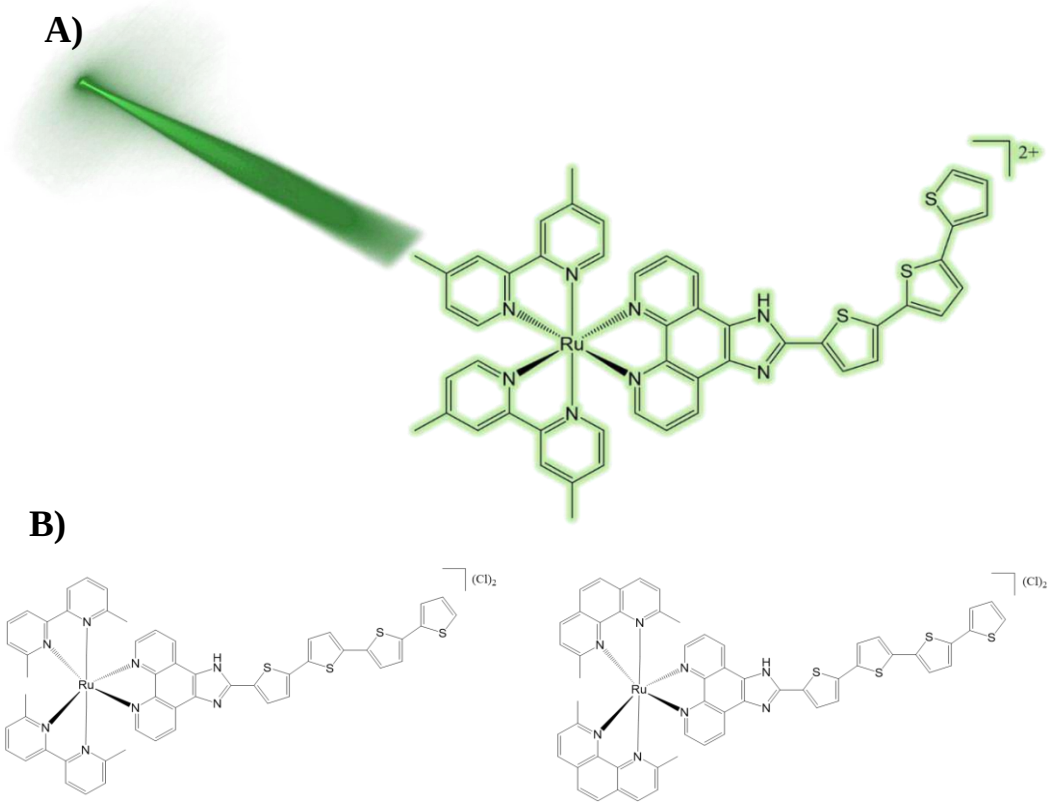

Figure 36. Thiophene-modified ruthenium (II) polypyridyl compounds developed in McFarland's lab. A) TLD-1433. B) TLD-1433 analogues that showed phototoxicity under hypoxia.

Despite these incredible advances, PDT has also a great road ahead. The selectivity that light provides is sometimes not enough when the photosensitizers are formerly designed to generate a high amount of ROS. Moreover, most PSs lack of the ability to address some *in vivo* concerns, particularly in terms of prolonged effect, poor targeting, and side-effects mitigation[314]. Here, again, nanomedicine can provide some solutions, unaffecting or even improving PSs properties and making them suitable tools for clinical translation.

In this context, in Marchán's group, a series of new far-red and NIR photoactivable ruthenium(II) polypyridyl complexes (unpublished results) have been recently synthesized and characterized for their intended use as photosensitizers in anticancer PDT. These novel complexes exhibited interesting phototoxic properties in different cancer cell lines, under both normoxic and hypoxic conditions, after far-red and NIR monochromatic irradiation with outstanding PI values (>30.000). The encapsulation of two of such Ru(II) polypyridyl complexes will be explored in this thesis (Chapter 1).

4.2.3 Nanomedical developments including metal-based photosensitizers

Since the appearance of cisplatin, metals have attracted a lot of interest in the development of novel anticancer agents due to their ability to operate as synergistic agents, deploying their activity at different subcellular levels and by different biological mechanisms. As it has been mentioned in previous sections, iridium and ruthenium compounds exhibit stunning properties that lead to cell death through different mechanisms of action, including DNA damage, protein inactivation or photoinduced ROS generation. Interestingly, some of them are also able to combine two or more of these effects, reaching an efficient cyto- and phototoxic performance (Figure 37).

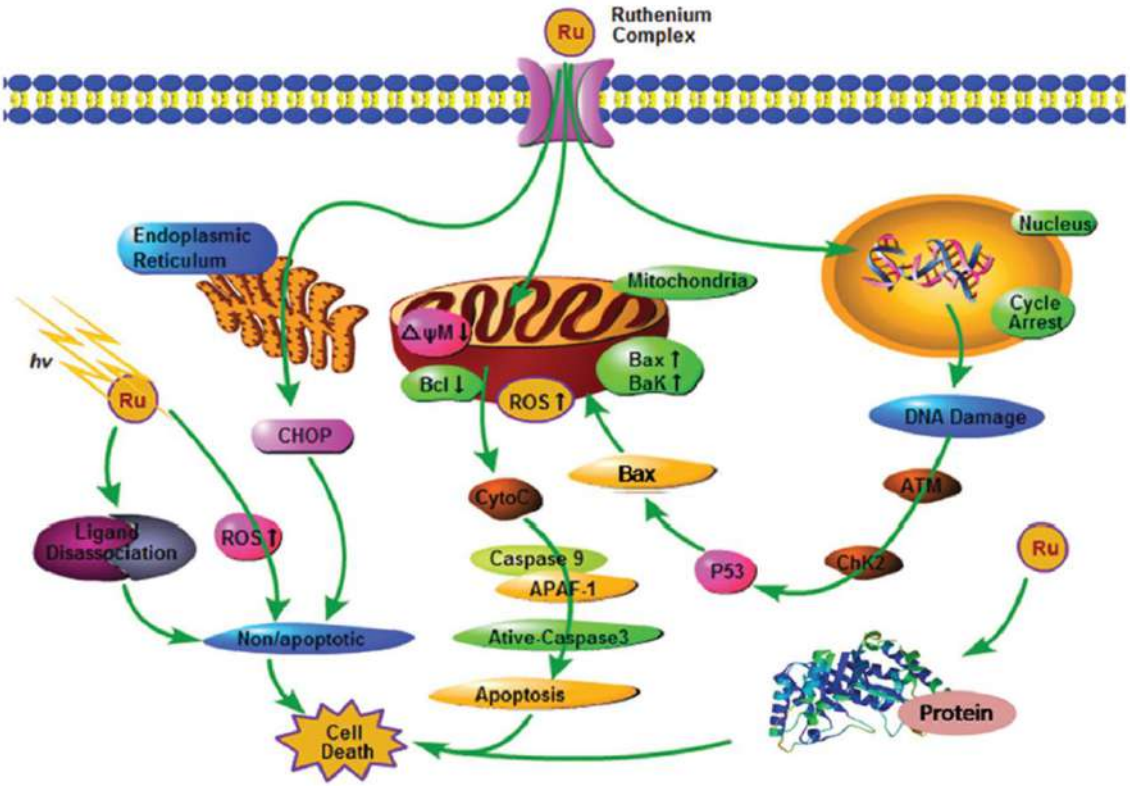

Figure 37. Illustration of different subcellular targets and mechanism of action of ruthenium compounds. Adapted with permission from reference [315].

The intracellular activity of the abovementioned compounds is more than proven, and their potential in different medical fields is beyond any doubt. However, how can the

ruthenium compounds access to their biological targets? Chen and co-workers summarized in an excellent review published in 2017, the different families of ruthenium-complexes that had been designed as anticancer agents, concluding that a poor percentage of them had been evaluated *in vivo*. In addition, they analyzed those complexes that had been incorporated into nanomedical approaches, reporting significant improvements in pharmacokinetics, solubility, toxicity and biodistribution against the free complexes[315].

Recently, Prof. Chao and co-workers reported an encapsulated iridium(III) complex that synergistically generates highly cytotoxic iridium(III) species, singlet oxygen and an alkoxy radical upon blue light irradiation (405 nm), thereby combining PDT and PACT. This compound also showed impressive activity under hypoxic conditions, in A549 lung cancer cell line, as well as significant tumor growth inhibition under two-photon irradiation (750 nm)[316].

If we set our sights on the nanoencapsulated solutions for ruthenium-based photosensitizers, particularly in those that were designed to promote accumulation in tumor locations and to potentiate the phototoxic effect of the agent, the advances achieved during lasts years have been wider compared to other metal complexes. As early as 2010, eight years before the staging of TLD-1433, Prof. Landfester and co-workers predicted the incorporation of ruthenium cyclometalated compounds into supramolecular nanostructures or into solid matrices as a promising strategy to improve their biological performance[317] (Figure 38).

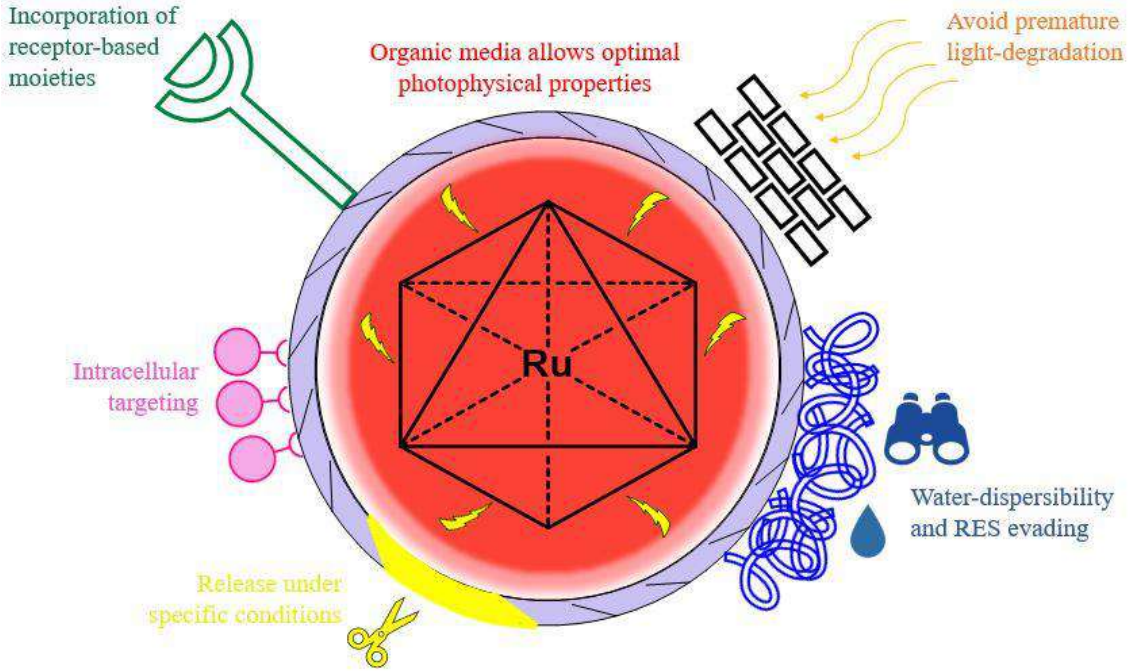

Figure 38: Nanoencapsulation potential functionalities that enhance the therapeutic effect of ruthenium PSs.

By the end of 2010's decade, Gasser's group got seriously involved into combining nanomedical carriers with photoactivable ruthenium(II) complexes. They started analyzing what were the limitations that these compounds must overcome to improve *in vivo* efficacy, while scanning the polymeric-based potential solutions described in the literature and the results they have raised[318]. This analysis crystallized in several recent studies, where different polymer therapeutic solutions have been used to improve the biological action of some ruthenium(II) polypyridyl complexes.

Starting from self-assembled nanoparticles built-up with a block-polymer of Pluronic F-127/Poloxamer-407 that allowed to achieve good phototoxic results under green light irradiation in human cervical carcinoma cell line [319], Gasser and collaborators moved one step forward using a "synthetic lipid" polymeric solution approach, reporting significant *in vivo* improvements when comparing the free compound with the nanoencapsulated form, both under green light and two-photon irradiation in A549-bearing nude mice models[320]. The system was refined by incorporating folic acid motifs on the polymeric backbone, looking for a preferential accumulation in tumor tissues overexpressing folate receptor[321], and the same strategy was also used in an approach based on mesoporous silica nanoparticles with similar ruthenium(II) polypyridyl complexes[322].

Even if other relevant authors, like Prof. Bonnet, used nanosized polymers for the delivery of ruthenium compounds[323,324], the encapsulation of ruthenium photosensitizers into polyurethane-polyurea hybrid polymeric nanocapsules has not been reported so far.

5. Objectives

The overall goal of this Thesis was to expand the scope of the applications of polyurethane-polyurea based nanocarriers in oncological developments by using the encapsulation technology developed by Ecopol Tech S.L. On the one hand, this Thesis will explore the encapsulation of photosensitizers based on organic fluorophores and on metal complexes, as a potential way to improve their light-responsive properties in the context of anticancer PDT. On the other hand, the nanoencapsulation of liposoluble metal-based anticancer drugs based on cyclometalated Ir(III) complexes as novel chemotherapeutic agents will be also evaluated. Finally, this Thesis will be focused on the development of a novel encapsulation technology based on polyurethane-polyurea hybrid nanocapsules for the isolation and stabilization of hydrosoluble bioactive agents in biological media, such as ICG.

Specifically, three main goals are proposed:

5.1 Nanoencapsulation of photosensitizers based on organic fluorophores and metal complexes for application in anticancer photodynamic therapy

As previously described in section 3.1.3 of the introduction, our research group has recently demonstrated the potential of COUPY fluorophores as non-conventional photosensitizers for anticancer PDT, particularly that of **COUPY 1** and **COUPY 2** coumarins (Figure 24, Section 3.1.3), which were identified in a SARS study[221]. Based on these antecedents, here we have addressed the synthesis and characterization of polyurethane-polyurea hybrid nanocapsules incorporating both coumarin-based PSs with the aim of investigating how encapsulation influences the biological performance of the PSs as a previous step for *in vivo* evaluation.

In addition, we have addressed the encapsulation of two promising photosensitizers based on ruthenium(II) polypyridyl complexes recently developed in our group (**Ru1** and **Ru2**) that have shown outstanding phototoxic activities, as well as that of a zinc-phthalocyanine compound (**Zn-Pc**) and its conjugate with a cyclometalated Ir(III) complex (**Ir-Zn(Pc)**)**.** The biological properties of all of the nanoencapsulated metal-based PSs were compared with those of the free compounds. It is worth noting that the structure of the compounds cannot be shown here due to confidential reasons.

The following specific objectives have been addressed within this first chapter:

5.1.1 Encapsulation of COUPY PSs: Synthesis, payload determination and physicochemical and photophysical characterization.

5.1.2 Cellular uptake of COUPY-loaded nanocapsules in HeLa cells.

5.1.3 In vitro phototoxicity evaluation of COUPY-loaded nanocapsules in cancer cells.

5.1.4 In vitro phototoxicity evaluation of COUPY-loaded nanocapsules in multicellular HeLa tumor spheroids.

5.1.5 Encapsulation of Ru(II) polypyridyl complexes: Synthesis, payload determination and physicochemical characterization.

5.1.6 Cellular uptake Ru(II)-loaded nanocapsules in HeLa cells

5.1.7 In vitro phototoxicity evaluation of Ru(II)-loaded nanocapsules in cancer and healthy cells.

5.1.8 Encapsulation of Zn(Pc) and Ir-Zn(Pc): synthesis, payload determination and physicochemical characterization.

5.1.9 Cellular uptake of Zn(Pc)- and Ir-Zn(Pc)-loaded NCs in HeLa cells.

5.1.10 In vitro phototoxicity evaluation of Zn(Pc)- and Ir-Zn(Pc)-loaded NCs in HeLa cells.

The results concerning the specific objectives 5.1.1 to 5.1.4 are discussed in the Publication I of the Chapter I (Ia) of this Thesis (*Biomacromolecules* **2022**, *23*, 2900–2913). The work related with the encapsulation of Ru(II) polypyridyl complexes **Ru1** and **Ru2** (objectives 5.1.5-5.1.7) has been gathered up as a second part of Chapter I (Ib). Finally, the work performed on the encapsulation of the zinc(phthalocyanine) derivative and the iridium-zinc(phthalocyanine) conjugate (objectives 5.1.8-5.1.10) is presented as a third part of Chapter I (Ic).

5.2 Nanoencapsulation of cyclometalated iridium(III) complexes for an improved cancer chemotherapy.

High lipophilicity and poor aqueous solubility are some of the factors that hamper the elucidation of the biological properties and preclinical evaluation of a large number of metal-based anticancer drugs. In this context, the nanoencapsulation of two liposoluble cyclometalated iridium(III) complexes, **Ir1** and **Ir2** (Figure 32, section 4.1.2), has been addressed in Chapter II of this Thesis with the aim of increasing bioavailability and to allow their *in vitro* evaluation as potential chemotherapeutic agents.

This main goal can be divided into the following specific objectives:

5.2.1 Encapsulation of Ir(III) complexes: Synthesis, payload determination and physicochemical and photophysical characterization.

5.2.2 Cellular uptake of Ir(III)-loaded nanocapsules in HeLa cells.

5.2.3 Study of cell internalization mechanisms and intracellular localization of Ir(III)-loaded nanocapsules.

5.2.4 In vitro evaluation of the chemotherapeutic potential of Ir(III)-loaded nanocapsules in cancer cells.

5.2.5 In vitro evaluation of the chemotherapeutic potential of Ir(III)-loaded nanocapsules in multicellular HeLa tumor spheroids.

5.2.6 Oxidative stress analysis caused by Ir(III)-loaded nanocapsules in HeLa cells.

The results concerning the specific objectives arisen from this work have been included in Publication II (*Inorganic Chemistry Frontiers* **2022**, 9, 2123–2138), contained in the Chapter II of this Thesis.

5.3. Development of water-in-oil-in-water polyurethane-polyurea hybrid nanocapsules for the delivery of hydrosoluble bioactive compounds: Nanoencapsulation of Indocyanine Green for *in vivo* tumor imaging.

Fluorescent probes present several limitations for *in vivo* cancer imaging because of premature degradation, aqueous solubility problems and/or lack of specific targeting over tumoral tissues. In such a context, the third main goal of this Thesis has been focused on the encapsulation of Indocyanine Green (ICG) (Figure 20 in section 3.1.2), an FDA-approved NIR fluorescent probe, to facilitate a selective vehiculation onto solid tumor lesions.

In order to achieve this goal, a new class of W/O/W double-walled polyurethane-polyurea hybrid nanocapsules had to be developed due to the hydrosoluble nature of ICG. This main goal can be divided into the following specific objectives:

5.3.1 Rational design of W/O/W double-walled polyurethane-polyurea hybrid nanocapsules.

5.3.2 Nanoencapsulation of ICG in polyurethane-polyurea based W/O/W nanocapsules: Payload determination and physicochemical characterization.

5.3.3 ICG stability analysis in W/O/W nanocapsules under different degradation conditions.

5.3.4 Cellular uptake evaluation of ICG-loaded nanocapsules in dendritic cells.

5.3.5 In vitro toxicological analysis of ICG-loaded nanocapsules

5.3.6 In vivo biodistribution analysis of ICG-loaded nanocapsules in a healthy mouse model.

5.3.7 In vivo biodistribution analysis of nanocapsules in melanoma A375 tumor challenged mouse model.

The synthetic design, nanocapsules' characterization and all *in vitro* and *in vivo* studies related with this project have been included in the Chapter III of this Thesis as a Publication III, a manuscript submitted for publication.

6. References

(1) Kaufmann, S. H. E. Immunology's Foundation - the 100-Year Anniversary of the Nobel Prize to Paul Ehrlich and Elie Metchnikoff. *Nat. Immunol.* **2008**, *9*, 705–712. https://doi.org/https://doi.org/10.1038/ni0708-705.

(2) Faraday, M. The Bakerian Lecture: Experimental Relations of Gold (and Other Metals) to Light. *Philosophical Transactions* **1857**, *147*, 145–181. https://doi.org/10.1098/rst.

(3) Elmer Kraemer, B. O.; Dexter, S. T. The Light-Scattering Capacity (Tyndall Effect) and Colloidal Behaviour of Gelatin Sols and Gels* Fellow of the National Research Council during the First Part of This Investigation. *Arisz: Proc. Acad. Sci. Amsterdam* **1910**, *12*, 21.

(4) Zsigmondy, R. Composition of Ruby Glass. US703512, July 1, 1902.

(5) European Scientific Foundation. *Nanomedicine: An ESF– European Medical Research Councils (EMRC) Forward Look*; Strasbourg, France, 2005.

(6) Harayama, T.; Riezman, H. Understanding the Diversity of Membrane Lipid Composition. *Nat Rev Mol Cell Biol* **2018**, *19*, 281–296. https://doi.org/10.1038/nrm.2017.138.

(7) Alberts, B.; Johnson, A.; Lewis, J.; Morgan, D.; Raff, M.; Roberts, K.; Walter, P. *Molecular Biology of the Cell*, 6th Edition.; W.W. Norton & Company, 2017. https://doi.org/10.1201/9781315735368.

(8) Kai, L.; Kaldenhoff, R. A Refined Model of Water and CO2 Membrane Diffusion: Effects and Contribution of Sterols and Proteins. *Sci. Rep.* **2014**, *4*. https://doi.org/10.1038/srep06665.

(9) Backes, S.; Herrmann, J. M. Protein Translocation into the Intermembrane Space and Matrix of Mitochondria: Mechanisms and Driving Forces. *Front. Mol. Biosci.* **2017**, *4*. https://doi.org/10.3389/fmolb.2017.00083.

(10) Gauthier-Coles, G.; Vennitti, J.; Zhang, Z.; Comb, W. C.; Xing, S.; Javed, K.; Bröer, A.; Bröer, S. Quantitative Modelling of Amino Acid Transport and Homeostasis in Mammalian Cells. *Nat. Commun.* **2021**, *12*. https://doi.org/10.1038/s41467-021-25563-x.

(11) Dudev, T.; Lim, C. Factors Governing the Na+ vs K+ Selectivity in Sodium Ion Channels. *J. Am. Chem. Soc.* **2010**, *132*, 2321–2332. https://doi.org/10.1021/ja909280g.

(12) Izquierdo-Useros, N.; Lorizate, M.; Contreras, F. X.; Rodriguez-Plata, M. T.; Glass, B.; Erkizia, I.; Prado, J. G.; Casas, J.; Fabriàs, G.; Kräusslich, H. G.; Martinez-Picado, J. Sialyllactose in Viral Membrane Gangliosides Is a Novel Molecular Recognition Pattern for Mature Dendritic Cell Capture of HIV-1. *PLoS Biol.* **2012**, *10*. https://doi.org/10.1371/journal.pbio.1001315.

(13) Kumari, S.; Mg, S.; Mayor, S. Endocytosis Unplugged: Multiple Ways to Enter the Cell. *Cell Res.* **2010**, *20*, 256–275. https://doi.org/10.1038/cr.2010.19.

(14) Kaksonen, M.; Roux, A. Mechanisms of Clathrin-Mediated Endocytosis. *Nat. Rev. Mol. Cell Biol.* **2018**, *19*, 313–326. https://doi.org/10.1038/nrm.2017.132.

(15) Thottacherry, J. J.; Sathe, M.; Prabhakara, C.; Mayor, S. Diverse Endocytic Pathways Function at the Cell Surface. *Annu. Rev. Cell Dev. Biol.* **2019**, *35*, 55–84. https://doi.org/10.1146/ANNUREV-CELLBIO-100617-062710.

(16) Galluzzi, L.; Senovilla, L.; Vitale, I.; Michels, J.; Martins, I.; Kepp, O.; Castedo, M.; Kroemer, G. Molecular Mechanisms of Cisplatin Resistance. *Oncogene* **2012**, *31*, 1869–1883. https://doi.org/10.1038/onc.2011.384.

(17) Peterson, E.; Kaur, P. Antibiotic Resistance Mechanisms in Bacteria: Relationships between Resistance Determinants of Antibiotic Producers, Environmental Bacteria, and Clinical Pathogens. *Front. Microbiol.* **2018**, *9*. https://doi.org/10.3389/fmicb.2018.02928.

(18) Akinc, A.; Battaglia, G. Exploiting Endocytosis for Nanomedicines. *Cold Spring Harb. Perspect. Biol.* **2013**, *5*. https://doi.org/10.1101/cshperspect.a016980.

(19) Sahay, G.; Alakhova, D. Y.; Kabanov, A. Endocytosis of Nanomedicines. *J. Control. Release* **2010**, *145*, 182–195. https://doi.org/10.1016/j.jconrel.2010.01.036.

(20) Tian, X.; Angioletti-Uberti, S.; Battaglia, G. On the Design of Precision Nanomedicines. *Sci. Adv.* **2020**, *6*. https://doi.org/10.1126/SCIADV.AAT0919/SUPPL_FILE/AAT0919_SM.PDF.

(21) Woythe, L.; Tito, N. B.; Albertazzi, L. A Quantitative View on Multivalent Nanomedicine Targeting. *Adv. Drug. Deliv. Rev.* **2021**, *169*, 1–21. https://doi.org/10.1016/j.addr.2020.11.010.

(22) Haute, D. van; Berlin, J. M. Challenges in Realizing Selectivity for Nanoparticle Biodistribution and Clearance: Lessons from Gold Nanoparticles. *Ther. Deliv.* **2017**, *8*, 763–774. https://doi.org/10.4155/tde-2017-0057.

(23) Li, T.; Shi, W.; Yao, J.; Hu, J.; Sun, Q.; Meng, J.; Wan, J.; Song, H.; Wang, H. Combinatorial Nanococktails via Self-Assembling Lipid Prodrugs for Synergistically Overcoming Drug Resistance and Effective Cancer Therapy. *Biomater. Res.* **2022**, *26*, 3. https://doi.org/10.1186/s40824-022-00249-7.

(24) Fang, T.; Dong, Y.; Zhang, X.; Xie, K.; Lin, L.; Wang, H. Integrating a Novel SN38 Prodrug into the PEGylated Liposomal System as a Robust Platform for Efficient Cancer Therapy in Solid Tumors. *Int. J. Pharm.* **2016**, *512*, 39–48. https://doi.org/10.1016/j.ijpharm.2016.08.036.

(25) Fu, X.; Shi, Y.; Qi, T.; Qiu, S.; Huang, Y.; Zhao, X.; Sun, Q.; Lin, G. Precise Design Strategies of Nanomedicine for Improving Cancer Therapeutic Efficacy Using Subcellular Targeting. *Signal Transduct. Target. Ther.* **2020**, *5*. https://doi.org/10.1038/s41392-020-00342-0.

(26) Cifuentes-Rius, A.; Desai, A.; Yuen, D.; Johnston, A. P. R.; Voelcker, N. H. Inducing Immune Tolerance with Dendritic Cell-Targeting Nanomedicines. *Nat. Nanotechnol.* **2021**, *16*, 37–46. https://doi.org/10.1038/s41565-020-00810-2.

(27) Yeh, Y. C.; Huang, T. H.; Yang, S. C.; Chen, C. C.; Fang, J. Y. Nano-Based Drug Delivery or Targeting to Eradicate Bacteria for Infection Mitigation: A Review of Recent Advances. *Front. Chem.* **2020**, *8*. https://doi.org/10.3389/fchem.2020.00286.

(28) Kim, Y. A.; Cho, D. Y.; Przytycka, T. M. Understanding Genotype-Phenotype Effects in Cancer via Network Approaches. *PLoS Comput. Biol.* **2016**, *12*. https://doi.org/10.1371/journal.pcbi.1004747.

(29) Matsumura, Y.; Maeda, H. A New Concept for Macromolecular Therapeutics in Cancer Chemotherapy: Mechanism of Tumoritropic Accumulation of Proteins and the Antitumor Agent Smancs. *Cancer Res.* **1986**, *46*, 6387–6392.

(30) Maeda, H.; Nakamura, H.; Fang, J. The EPR Effect for Macromolecular Drug Delivery to Solid Tumors: Improvement of Tumor Uptake, Lowering of Systemic

Toxicity, and Distinct Tumor Imaging in Vivo. *Adv. Drug Deliv. Rev.* **2013**, *65*, 71–79. https://doi.org/10.1016/j.addr.2012.10.002.

(31) Maeda, H. Toward a Full Understanding of the EPR Effect in Primary and Metastatic Tumors as Well as Issues Related to Its Heterogeneity. *Adv. Drug Deliv. Rev.* **2015**, *91*, 3–6. https://doi.org/10.1016/j.addr.2015.01.002.

(32) Danhier, F. To Exploit the Tumor Microenvironment: Since the EPR Effect Fails in the Clinic, What Is the Future of Nanomedicine? *J. Control. Release* **2016**, *244*, 108–121. https://doi.org/10.1016/j.jconrel.2016.11.015.

(33) Shen, Y. A.; Shyu, I. L.; Lu, M.; He, C. L.; Hsu, Y. M.; Liang, H. F.; Liu, C. P.; Liu, R. S.; Shen, B. J.; Wei, Y. H.; Chuang, C. M. Bypassing the EPR Effect with a Nanomedicine Harboring a Sustained-Release Function Allows Better Tumor Control. *Int. J. Nanomedicine* **2015**, *10*, 2485–2502. https://doi.org/10.2147/IJN.S78321.

(34) Perillo, B.; di Donato, M.; Pezone, A.; di Zazzo, E.; Giovannelli, P.; Galasso, G.; Castoria, G.; Migliaccio, A. ROS in Cancer Therapy: The Bright Side of the Moon. *Exp. Mol. Med.* **2020**, *52*, 192–203. https://doi.org/10.1038/s12276-020-0384-2.

(35) Gibellini, L.; Pinti, M.; Nasi, M.; de Biasi, S.; Roat, E.; Bertoncelli, L.; Cossarizza, A. Interfering with ROS Metabolism in Cancer Cells: The Potential Role of Quercetin. *Cancers (Basel)* **2010**, *2*, 1288–1311. https://doi.org/10.3390/cancers2021288.

(36) Traverso, N.; Ricciarelli, R.; Nitti, M.; Marengo, B.; Furfaro, A. L.; Pronzato, M. A.; Marinari, U. M.; Domenicotti, C. Role of Glutathione in Cancer Progression and Chemoresistance. *Oxid. Med. Cell Longev.* **2013**. https://doi.org/10.1155/2013/972913.

(37) Petrova, V.; Annicchiarico-Petruzzelli, M.; Melino, G.; Amelio, I. The Hypoxic Tumour Microenvironment. *Oncogenesis* **2018**, *7*. https://doi.org/10.1038/s41389-017-0011-9.

(38) Böhme, I.; Bosserhoff, A. K. Acidic Tumor Microenvironment in Human Melanoma. *Pigm. Cell Melanoma Res.* **2016**, *29*, 508–523. https://doi.org/10.1111/pcmr.12495.

(39) Yasothamani, V.; Karthikeyan, L.; Sarathy, N. P.; Vivek, R. Targeted Designing of Multimodal Tumor-Seeking Nanomedicine for Breast Cancer-Specific Triple-

Therapeutic Effects. *ACS Appl. Bio. Mater.* **2021**, *4*, 6575–6588. https://doi.org/10.1021/acsabm.1c00740.

(40) Torres-Pérez, S. A.; Torres-Pérez, C. E.; Pedraza-Escalona, M.; Pérez-Tapia, S. M.; Ramón-Gallegos, E. Glycosylated Nanoparticles for Cancer-Targeted Drug Delivery. *Front. Oncol.* **2020**, *10*. https://doi.org/10.3389/fonc.2020.605037.

(41) Koppenol, W. H.; Bounds, P. L.; Dang, C. v. Otto Warburg's Contributions to Current Concepts of Cancer Metabolism. *Nat. Rev. Cancer* **2011**, *11*, 325–337. https://doi.org/10.1038/nrc3038.

(42) Senyilmaz, D.; Teleman, A. A. Chicken or the Egg: Warburg Effect and Mitochondrial Dysfunction. *F1000Prime Rep.* **2015**, *7*. https://doi.org/10.12703/P7-41.

(43) Liu, C.; Jin, Y.; Fan, Z. The Mechanism of Warburg Effect-Induced Chemoresistance in Cancer. *Front. Oncol.* **2021**, *11*. https://doi.org/10.3389/fonc.2021.698023.

(44) Jo, Y.; Choi, N.; Kim, K.; Koo, H. J.; Choi, J.; Kim, H. N. Chemoresistance of Cancer Cells: Requirements of Tumor Microenvironment-Mimicking in Vitro Models in Anti-Cancer Drug Development. *Theranostics* **2018**, *8*, 5259–5275. https://doi.org/10.7150/thno.29098.

(45) Lin, D.; Shen, L.; Luo, M.; Zhang, K.; Li, J.; Yang, Q.; Zhu, F.; Zhou, D.; Zheng, S.; Chen, Y.; Zhou, J. Circulating Tumor Cells: Biology and Clinical Significance. *Signal Transduct. Target Ther.* **2021**, *6*. https://doi.org/10.1038/s41392-021-00817-8.

(46) Cheteh, E. H.; Augsten, M.; Rundqvist, H.; Bianchi, J.; Sarne, V.; Egevad, L.; Bykov, V. J.; Östman, A.; Wiman, K. G. Human Cancer-Associated Fibroblasts Enhance Glutathione Levels and Antagonize Drug-Induced Prostate Cancer Cell Death. *Cell Death Dis.* **2017**. https://doi.org/10.1038/cddis.2017.225.

(47) Liberti, M. v.; Locasale, J. W. The Warburg Effect: How Does It Benefit Cancer Cells? *Trends Biochem. Sci.* **2016**, *41*, 211–218. https://doi.org/10.1016/j.tibs.2015.12.001.

(48) Kennedy, L.; Sandhu, J. K.; Harper, M. E.; Cuperlovic-culf, M. Role of Glutathione in Cancer: From Mechanisms to Therapies. *Biomolecules* **2020**, *10*, 1–27. https://doi.org/10.3390/biom10101429.

(49) Nathan, A. B.; Odenwelder, D. C.; Harcum Id, S. W. High Extracellular Lactate Causes Reductive Carboxylation in Breast Tissue Cell Lines Grown under Normoxic Conditions. *PLoS One* **2019**, 1–21. https://doi.org/10.1371/journal.pone.0213419.

(50) Bertrand, N.; Wu, J.; Xu, X.; Kamaly, N.; Farokhzad, O. C. Cancer Nanotechnology: The Impact of Passive and Active Targeting in the Era of Modern Cancer Biology. *Adv. Drug Deliv. Rev.* **2014**, *66*, 2–25. https://doi.org/10.1016/j.addr.2013.11.009.

(51) Shi, J.; Kantoff, P. W.; Wooster, R.; Farokhzad, O. C. Cancer Nanomedicine: Progress, Challenges and Opportunities. *Nat. Rev. Cancer* **2017**, *17*, 20–37. https://doi.org/10.1038/nrc.2016.108.

(52) Blanco, E.; Shen, H.; Ferrari, M. Principles of Nanoparticle Design for Overcoming Biological Barriers to Drug Delivery. *Nat. Biotechnol.* **2015**, *33*, 941–951. https://doi.org/10.1038/nbt.3330.

(53) Food and Drug Administration. *Doxil Label*; 1995.

(54) Deng, S.; Gigliobianco, M. R.; Censi, R.; di Martino, P. Polymeric Nanocapsules as Nanotechnological Alternative for Drug Delivery System: Current Status, Challenges and Opportunities. *Nanomaterials* **2020**, *10*. https://doi.org/10.3390/nano10050847.

(55) Han, Z.; Liu, G. Sugar-Based Biopolymers as Novel Imaging Agents for Molecular Magnetic Resonance Imaging. *Wiley Interdiscip. Rev. Nanomed. Nanobiotechnol.* **2019**, *11*. https://doi.org/10.1002/wnan.1551.

(56) Cabral, H.; Miyata, K.; Osada, K.; Kataoka, K. Block Copolymer Micelles in Nanomedicine Applications. *Chem. Rev.* **2018**, *118*, 6844–6892. https://doi.org/10.1021/acs.chemrev.8b00199.

(57) Hunt, N. J.; Lockwood, G. P.; Kang, S. W. S.; Westwood, L. J.; Limantoro, C.; Chrzanowski, W.; McCourt, P. A. G.; Kuncic, Z.; le Couteur, D. G.; Cogger, V. C. Quantum Dot Nanomedicine Formulations Dramatically Improve Pharmacological Properties and Alter Uptake Pathways of Metformin and Nicotinamide Mononucleotide in Aging Mice. *ACS Nano* **2021**, *15*, 4710–4727. https://doi.org/10.1021/acsnano.0c09278.

(58) Oller-Salvia, B.; Sánchez-Navarro, M.; Giralt, E.; Teixidó, M. Blood-Brain Barrier Shuttle Peptides: An Emerging Paradigm for Brain Delivery. *Chem. Soc. Rev.* **2016**, *45*, 4690–4707. https://doi.org/10.1039/c6cs00076b.

(59) Lambert, J. M. Drug-Conjugated Antibodies for the Treatment of Cancer. *Br. J. Clin. Pharmacol*. **2013**, *76*, 248–262. https://doi.org/10.1111/bcp.12044.

(60) Masarapu, H.; Patel, B. K.; Chariou, P. L.; Hu, H.; Gulati, N. M.; Carpenter, B. L.; Ghiladi, R. A.; Shukla, S.; Steinmetz, N. F. Physalis Mottle Virus-Like Particles as Nanocarriers for Imaging Reagents and Drugs. *Biomacromolecules* **2017**, *18*, 4141–4153. https://doi.org/10.1021/acs.biomac.7b01196.

(61) Gradishar, W. J. Albumin-Bound Paclitaxel: A next-Generation Taxane. *Expert Opin. Pharmacother.* **2006**, *7*, 1041–1053. https://doi.org/10.1517/14656566.7.8.1041.

(62) Cortes, J.; Saura, C. Nanoparticle Albumin-Bound (Nab^{TM})-Paclitaxel: Improving Efficacy and Tolerability by Targeted Drug Delivery in Metastatic Breast Cancer. *Eur. J. Cancer, Supp.* **2010**, *8*, 1–10. https://doi.org/10.1016/S1359-6349(10)70002-1.

(63) Hirsh, V. Nab-Paclitaxel for the Management of Patients with Advanced Non-Small-Cell Lung Cancer. *Expert. Rev. Anticancer. Ther.* **2014**, *14*, 129–141. https://doi.org/10.1586/14737140.2014.881719.

(64) Gao, Y.; Nai, J.; Yang, Z.; Zhang, J.; Ma, S.; Zhao, Y.; Li, H.; Li, J.; Yang, Y.; Yang, M.; Wang, Y.; Gong, W.; Yu, F.; Gao, C.; Li, Z. I.; Mei, X. A Novel Preparative Method for Nanoparticle Albumin-Bound Paclitaxel with High Drug Loading and Its Evaluation Both in Vitro and in Vivo. *PLoS One* **2021**, 1–25. https://doi.org/10.1371/journal.pone.0250670.

(65) West, H.; McCleod, M.; Hussein, M.; Morabito, A.; Rittmeyer, A.; Conter, H. J.; Kopp, H. G.; Daniel, D.; McCune, S.; Mekhail, T.; Zer, A.; Reinmuth, N.; Sadiq, A.; Sandler, A.; Lin, W.; Ochi Lohmann, T.; Archer, V.; Wang, L.; Kowanetz, M.; Cappuzzo, F. Atezolizumab in Combination with Carboplatin plus Nab-Paclitaxel Chemotherapy Compared with Chemotherapy Alone as First-Line Treatment for Metastatic Non-Squamous Non-Small-Cell Lung Cancer (IMpower130): A Multicentre, Randomised, Open-Label, Phase 3 Trial. *Lancet Oncol.* **2019**, *20*, 924–937. https://doi.org/10.1016/S1470-2045(19)30167-6.

(66) He, H.; Liu, L.; Morin, E. E.; Liu, M.; Schwendeman, A. Survey of Clinical Translation of Cancer Nanomedicines - Lessons Learned from Successes and Failures. *Acc. Chem. Res.* **2019**, *52*, 2673–2683. https://doi.org/10.1021/acs.accounts.9b00228.

(67) Halwani, A. A. Development of Pharmaceutical Nanomedicines: From the Bench to the Market. *Pharmaceutics* **2022**, *14*. https://doi.org/10.3390/pharmaceutics14010106.

(68) Huynh, N. T.; Passirani, C.; Saulnier, P.; Benoit, J. P. Lipid Nanocapsules: A New Platform for Nanomedicine. *Int. J. Pharm.* **2009**, *379*, 201–209. https://doi.org/10.1016/j.ijpharm.2009.04.026.

(69) Hua, S.; Karl, G.; Nell, H. Orally Administered Liposomal Formulations for Colon Targeted Drug Delivery. *Front. Pharmacol.* **2014**, *5*, 1–4. https://doi.org/10.3389/fphar.2014.00138.

(70) Bozzuto, G.; Molinari, A. Liposomes as Nanomedical Devices. *Int. J. Nanomedicine* **2015**, *10*, 975–999. https://doi.org/10.2147/IJN.S68861.

(71) Grimaldi, N.; Andrade, F.; Segovia, N.; Ferrer-Tasies, L.; Sala, S.; Veciana, J.; Ventosa, N. Lipid-Based Nanovesicles for Nanomedicine. *Chem. Soc. Rev.* **2016**, *45*, 6520–6545. https://doi.org/10.1039/c6cs00409a.

(72) Egito, S.; Machado, L.; Farias, I.; Silva, G.; Oliveira, A. HLB Concept: A Way to Never Forget It. *Biomed. J. Sci. Tech. Res.* **2018**, *10*. https://doi.org/10.26717/bjstr.2018.10.001983.

(73) Gould, J. M.; Furse, S.; Wolf, B. The Role of Endogenous Lipids in the Emulsifying Properties of Cocoa. *Front. Chem.* **2016**, *4*. https://doi.org/10.3389/fchem.2016.00011.

(74) Foteini, P.; Pippa, N.; Naziris, N.; Demetzos, C. Physicochemical Study of the Protein–Liposome Interactions: Influence of Liposome Composition and Concentration on Protein Binding. *J. Liposome Res.* **2019**, *29*, 313–321. https://doi.org/10.1080/08982104.2018.1468774.

(75) Beltrán-Gracia, E.; López-Camacho, A.; Higuera-Ciapara, I.; Velázquez-Fernández, J. B.; Vallejo-Cardona, A. A. Nanomedicine Review: Clinical Developments in Liposomal Applications. *Cancer Nanotechnol.* **2019**, *10*. https://doi.org/10.1186/s12645-019-0055-y.

(76) Sercombe, L.; Veerati, T.; Moheimani, F.; Wu, S. Y.; Sood, A. K.; Hua, S. Advances and Challenges of Liposome Assisted Drug Delivery. *Front. Pharmacol.* **2015**, *6*. https://doi.org/10.3389/fphar.2015.00286.

(77) Vallet-Regí, M.; Colilla, M.; Izquierdo-Barba, I.; Manzano, M. Mesoporous Silica Nanoparticles for Drug Delivery: Current Insights. *Molecules* **2018**, *23*. https://doi.org/10.3390/molecules23010047.

(78) Gao, Y.; Gao, D.; Shen, J.; Wang, Q. A Review of Mesoporous Silica Nanoparticle Delivery Systems in Chemo-Based Combination Cancer Therapies. *Front. Chem.* **2020**, *8*. https://doi.org/10.3389/fchem.2020.598722.

(79) Chaudhary, Z.; Subramaniam, S.; Khan, G. M.; Abeer, M. M.; Qu, Z.; Janjua, T.; Kumeria, T.; Batra, J.; Popat, A. Encapsulation and Controlled Release of Resveratrol Within Functionalized Mesoporous Silica Nanoparticles for Prostate Cancer Therapy. *Front. Bioeng. Biotechnol.* **2019**, *7*. https://doi.org/10.3389/fbioe.2019.00225.

(80) Janjua, T. I.; Cao, Y.; Yu, C.; Popat, A. Clinical Translation of Silica Nanoparticles. *Nat Rev Mater* **2021**, *6*, 1072–1074. https://doi.org/10.1038/s41578-021-00385-x.

(81) Deng, Y. di; Zhang, X. D.; Yang, X. S.; Huang, Z. L.; Wei, X.; Yang, X. F.; Liao, W. Z. Subacute Toxicity of Mesoporous Silica Nanoparticles to the Intestinal Tract and the Underlying Mechanism. *J. Hazard. Mater.* **2021**, *409*. https://doi.org/10.1016/j.jhazmat.2020.124502.

(82) Antwi-Baah, R.; Wang, Y.; Chen, X.; Yu, K. Metal-Based Nanoparticle Magnetic Resonance Imaging Contrast Agents: Classifications, Issues, and Countermeasures toward Their Clinical Translation. *Adv. Mater. Interfaces* **2022**, *9*. https://doi.org/10.1002/admi.202101710.

(83) Vlcnovska, M.; Stossova, A.; Kuchynka, M.; Dillingerova, V.; Polanska, H.; Masarik, M.; Hrstka, R.; Adam, V.; Kanicky, V.; Vaculovic, T.; Vaculovicova, M. Comparison of Metal Nanoparticles (Au, Ag, Eu, Cd) Used for Immunoanalysis Using La-Icp-Ms Detection. *Molecules* **2021**, *26*. https://doi.org/10.3390/molecules26030630.

(84) Fan, J.; Cheng, Y.; Sun, M. Functionalized Gold Nanoparticles: Synthesis, Properties and Biomedical Applications. *Chem. Rec.* **2020**, *20*, 1474–1504. https://doi.org/10.1002/tcr.202000087.

(85) Valkenier, H.; Malytskyi, V.; Blond, P.; Retout, M.; Mattiuzzi, A.; Goole, J.; Raussens, V.; Jabin, I.; Bruylants, G. Controlled Functionalization of Gold Nanoparticles with Mixtures of Calix[4]Arenes Revealed by Infrared Spectroscopy. *Langmuir* **2017**, *33*, 8253–8259. https://doi.org/10.1021/acs.langmuir.7b02140.

(86) Oh, E.; Susumu, K.; Goswami, R.; Mattoussi, H. One-Phase Synthesis of Water-Soluble Gold Nanoparticles with Control over Size and Surface Functionalities. *Langmuir* **2010**, *26*, 7604–7613. https://doi.org/10.1021/la904438s.

(87) Xie, X.; Liao, J.; Shao, X.; Li, Q.; Lin, Y. The Effect of Shape on Cellular Uptake of Gold Nanoparticles in the Forms of Stars, Rods, and Triangles. *Sci. Rep.* **2017**, *7*. https://doi.org/10.1038/s41598-017-04229-z.

(88) Ma, X.; Hartmann, R.; Jimenez De Aberasturi, D.; Yang, F.; Soenen, S. J. H.; Manshian, B. B.; Franz, J.; Valdeperez, D.; Pelaz, B.; Feliu, N.; Hampp, N.; Riethmüller, C.; Vieker, H.; Frese, N.; Gölzhäuser, A.; Simonich, M.; Tanguay, R. L.; Liang, X. J.; Parak, W. J. Colloidal Gold Nanoparticles Induce Changes in Cellular and Subcellular Morphology. *ACS Nano* **2017**, *11*, 7807–7820. https://doi.org/10.1021/acsnano.7b01760.

(89) Păduraru, D. N.; Ion, D.; Niculescu, A.-G.; Mușat, F.; Andronic, O.; Grumezescu, A. M.; Bolocan, A. Recent Developments in Metallic Nanomaterials for Cancer Therapy, Diagnosing and Imaging Applications. *Pharmaceutics* **2022**, *14*, 435. https://doi.org/10.3390/pharmaceutics14020435.

(90) *NU-0129 in Treating Patients With Recurrent Glioblastoma or Gliosarcoma Undergoing Surgery - Full Text View - ClinicalTrials.gov*. https://clinicaltrials.gov/ct2/show/NCT03020017 (accessed 2022-06-06).

(91) Macdougall, I. C.; Comin-Colet, J.; Breymann, C.; Spahn, D. R.; Koutroubakis, I. E. Iron Sucrose: A Wealth of Experience in Treating Iron Deficiency. *Adv. Ther.* **2020**, *37*, 1960–2002. https://doi.org/10.6084/m9.figshare.12030552.

(92) Rajkumar, S.; Prabaharan, M. Multi-Functional Nanocarriers Based on Iron Oxide Nanoparticles Conjugated with Doxorubicin, Poly(Ethylene Glycol) and Folic Acid as Theranostics for Cancer Therapy. *Colloids Surf. B. Biointerfaces* **2018**, *170*, 529–537. https://doi.org/10.1016/j.colsurfb.2018.06.051.

(93) Nikolova, M. P.; Chavali, M. S. Metal Oxide Nanoparticles as Biomedical Materials. *Biomimetics* **2020**, *5*, 1–47. https://doi.org/10.3390/BIOMIMETICS5020027.

(94) Yaqoob, A. A.; Ahmad, H.; Parveen, T.; Ahmad, A.; Oves, M.; Ismail, I. M. I.; Qari, H. A.; Umar, K.; Mohamad Ibrahim, M. N. Recent Advances in Metal Decorated Nanomaterials and Their Various Biological Applications: A Review. *Front. Chem.* **2020**, *8*. https://doi.org/10.3389/fchem.2020.00341.

(95) van der Zande, M.; Vandebriel, R. J.; van Doren, E.; Kramer, E.; Herrera Rivera, Z.; Serrano-Rojero, C. S.; Gremmer, E. R.; Mast, J.; Peters, R. J. B.; Hollman, P. C. H.; Hendriksen, P. J. M.; Marvin, H. J. P.; Peijnenburg, A. A. C. M.; Bouwmeester, H. Distribution, Elimination, and Toxicity of Silver Nanoparticles and Silver Ions in Rats after 28-Day Oral Exposure. *ACS Nano* **2012**, *6*, 7427–7442. https://doi.org/10.1021/nn302649p.

(96) Ji, B.; Giovanelli, E.; Habert, B.; Spinicelli, P.; Nasilowski, M.; Xu, X.; Lequeux, N.; Hugonin, J. P.; Marquier, F.; Greffet, J. J.; Dubertret, B. Non-Blinking Quantum Dot with a Plasmonic Nanoshell Resonator. *Nat. Nanotechnol.* **2015**, *10*, 170–175. https://doi.org/10.1038/nnano.2014.298.

(97) Matea, C. T.; Mocan, T.; Tabaran, F.; Pop, T.; Mosteanu, O.; Puia, C.; Iancu, C.; Mocan, L. Quantum Dots in Imaging, Drug Delivery and Sensor Applications. *Int. J. Nanomedicine* **2017**, *12*, 5421–5431. https://doi.org/10.2147/IJN.S138624.

(98) Lio, H.; Gil, M.; Price, T. W.; Chelani, K.; Bouillard, J.-S. G.; Calaminus, S. D. J.; Stasiuk, G. J. NIR-Quantum Dots in Biomedical Imaging and Their Future. *iScience* **2021**, *24*, 1–26. https://doi.org/10.1016/j.isci.

(99) Chen, L. L.; Zhao, L.; Wang, Z. G.; Liu, S. L.; Pang, D. W. Near-Infrared-II Quantum Dots for In Vivo Imaging and Cancer Therapy. *Small* **2021**. https://doi.org/10.1002/smll.202104567.

(100) Efros, A. L.; Delehanty, J. B.; Huston, A. L.; Medintz, I. L.; Barbic, M.; Harris, T. D. Evaluating the Potential of Using Quantum Dots for Monitoring Electrical Signals in Neurons. *Nat. Nanotechnol.* **2018**, *13*, 278–288. https://doi.org/10.1038/s41565-018-0107-1.

(101) Chen, D.; Chen, B.; Yao, F. Doxorubicin-Loaded PEG-CdTe Quantum Dots as a Smart Drug Delivery System for Extramedullary Multiple Myeloma Treatment. *Nanoscale Res. Lett.* **2018**, *13*. https://doi.org/10.1186/s11671-018-2782-0.

(102) Zhao, C.; Song, X.; Liu, Y.; Fu, Y.; Ye, L.; Wang, N.; Wang, F.; Li, L.; Mohammadniaei, M.; Zhang, M.; Zhang, Q.; Liu, J. Synthesis of Graphene Quantum Dots and Their Applications in Drug Delivery. *J. Nanobiotechnology* **2020**, *18*. https://doi.org/10.1186/s12951-020-00698-z.

(103) Patel, V.; Rajani, C.; Paul, D.; Borisa, P.; Rajpoot, K.; Youngren-Ortiz, S. R.; Tekade, R. K. Dendrimers as Novel Drug-Delivery System and Its Applications. In *Drug Delivery Systems*; Elsevier, 2019; pp 333–392. https://doi.org/10.1016/B978-0-12-814487-9.00008-9.

(104) Kheraldine, H.; Rachid, O.; Habib, A. M.; al Moustafa, A. E.; Benter, I. F.; Akhtar, S. Emerging Innate Biological Properties of Nano-Drug Delivery Systems: A Focus on PAMAM Dendrimers and Their Clinical Potential. *Adv. Drug Deliv. Rev.* **2021**, *178*. https://doi.org/10.1016/j.addr.2021.113908.

(105) Wu, L. P.; Ficker, M.; Christensen, J. B.; Trohopoulos, P. N.; Moghimi, S. M. Dendrimers in Medicine: Therapeutic Concepts and Pharmaceutical Challenges. *Bioconjug. Chem.* **2015**, *26*, 1198–1211. https://doi.org/10.1021/acs.bioconjchem.5b00031.

(106) Ornelas, C. Brief Timelapse on Dendrimer Chemistry: Advances, Limitations, and Expectations. *Macromol. Chem. Phys.* **2016**, *217*, 149–174. https://doi.org/10.1002/macp.201500393.

(107) Caminade, A. M.; Turrin, C. O. Dendrimers for Drug Delivery. *J. Mater. Chem. B* **2014**, *2*, 4055–4066. https://doi.org/10.1039/c4tb00171k.

(108) Chauhan, A. S. Dendrimers for Drug Delivery. *Molecules* **2018**, *23*. https://doi.org/10.3390/molecules23040938.

(109) Yeon Son, H.; Rak Kim, K.; Am Hong, C.; Sung Nam, Y. Morphological Evolution of Gold Nanoparticles into Nanodendrites Using Catechol-Grafted Polymer Templates. *ACS Omega* **2018**, *3*, 6683–6691. https://doi.org/10.1021/acsomega.8b00538.

(110) Svenson, S. The Dendrimer Paradox - High Medical Expectations but Poor Clinical Translation. *Chem. Soc. Rev.* **2015**, *44*, 4131–4144. https://doi.org/10.1039/c5cs00288e.

(111) Müller, L. K.; Landfester, K. Natural Liposomes and Synthetic Polymeric Structures for Biomedical Applications. *Biochem. Biophys. Res. Commun.* **2015**, *468*, 411–418. https://doi.org/10.1016/j.bbrc.2015.08.088.

(112) Battaglia, G.; Ryan, A. J. Bilayers and Interdigitation in Block Copolymer Vesicles. *J. Am. Chem. Soc.* **2005**, *127*, 8757–8764. https://doi.org/10.1021/ja050742y.

(113) Lee, J. S.; Feijen, J. Polymersomes for Drug Delivery: Design, Formation and Characterization. *J. Control. Release* **2012**, *161*, 473–483. https://doi.org/10.1016/J.JCONREL.2011.10.005.

(114) Meerovich, I.; Dash, A. K. Polymersomes for Drug Delivery and Other Biomedical Applications. In *Materials for Biomedical Engineering*; Elsevier, 2019; Vol. Chapter 8, pp 269–309. https://doi.org/10.1016/B978-0-12-818433-2.00008-X.

(115) Simón-Gracia, L.; Hunt, H.; Scodeller, P.; Gaitzsch, J.; Kotamraju, V. R.; Sugahara, K. N.; Tammik, O.; Ruoslahti, E.; Battaglia, G.; Teesalu, T. IRGD Peptide Conjugation Potentiates Intraperitoneal Tumor Delivery of Paclitaxel with Polymersomes. *Biomaterials* **2016**, *104*, 247–257. https://doi.org/10.1016/j.biomaterials.2016.07.023.

(116) Hunter, S. J.; Armes, S. P. Pickering Emulsifiers Based on Block Copolymer Nanoparticles Prepared by Polymerization-Induced Self-Assembly. *Langmuir* **2020**, *36*, 15463–15484. https://doi.org/10.1021/acs.langmuir.0c02595.

(117) Bueno, C. Z.; Apolinário, A. C.; Duro-Castano, A.; Poma, A.; Pessoa, A.; Rangel-Yagui, C. O.; Battaglia, G. L-Asparaginase Encapsulation into Asymmetric Permeable Polymersomes. *ACS Macro Lett.* **2020**, *9*, 1471–1477. https://doi.org/10.1021/acsmacrolett.0c00619.

(118) Scarpa, E.; de Pace, C.; Joseph, A. S.; de Souza, S. C.; Poma, A.; Liatsi-Douvitsa, E.; Contini, C.; de Matteis, V.; Martí, J. S.; Battaglia, G.; Rizzello, L. Tuning Cell Behavior with Nanoparticle Shape. *PLoS One* **2020**, *15*. https://doi.org/10.1371/journal.pone.0240197.

(119) Fenaroli, F.; Robertson, J. D.; Scarpa, E.; Gouveia, V. M.; di Guglielmo, C.; de Pace, C.; Elks, P. M.; Poma, A.; Evangelopoulos, D.; Canseco, J. O.; Prajsnar, T. K.; Marriott, H. M.; Dockrell, D. H.; Foster, S. J.; McHugh, T. D.; Renshaw, S. A.; Martí, J. S.; Battaglia, G.; Rizzello, L. Polymersomes Eradicating Intracellular Bacteria. *ACS Nano* **2020**, *14*, 8287–8298. https://doi.org/10.1021/acsnano.0c01870.

(120) Joseph, A.; Contini, C.; Cecchin, D.; Nyberg, S.; Ruiz-Perez, L.; Gaitzsch, J.; Fullstone, G.; Tian, X.; Azizi, J.; Preston, J.; Volpe, G.; Battaglia, G. Chemotactic

Synthetic Vesicles: Design and Applications in Blood-Brain Barrier Crossing. *Biomed. Eng., Sci. Adv.* **2017**, *3*, 1–12.

(121) Scheerstra, J. F.; Wauters, A. C.; Tel, J.; Abdelmohsen, L. K. E. A.; van Hest, J. C. M. Polymersomes as a Potential Platform for Cancer Immunotherapy. *Mater. Today Adv.* **2022**, *13*. https://doi.org/10.1016/j.mtadv.2021.100203.

(122) Khalil, I. R.; Burns, A. T. H.; Radecka, I.; Kowalczuk, M.; Khalaf, T.; Adamus, G.; Johnston, B.; Khechara, M. P. Bacterial-Derived Polymer Poly-γ-Glutamic Acid (γ-PGA)-Based Micro/Nanoparticles as a Delivery System for Antimicrobials and Other Biomedical Applications. *Int. J. Mol. Sci.* **2017**, *18*. https://doi.org/10.3390/ijms18020313.

(123) Wang, L.; Zhao, P.; Feng, C.; Wu, Y.; Ding, Y.; Hu, A. Controlled Synthesis of Water-Dispersible Conjugated Polymeric Nanoparticles for Cellular Imaging. *Eur. Polym. J.* **2018**, *105*, 1–6. https://doi.org/10.1016/j.eurpolymj.2018.05.008.

(124) Piñón-Segundo, E.; Llera-Rojas, V. G.; Leyva-Gómez, G.; Urbán-Morlán, Z.; Mendoza-Muñoz, N.; Quintanar-Guerrero, D. The Emulsification-Diffusion Method to Obtain Polymeric Nanoparticles: Two Decades of Research. In *Nanoscale Fabrication, Optimization, Scale-up and Biological Aspects of Pharmaceutical Nanotechnology*; Elsevier, 2017; pp 51–83. https://doi.org/10.1016/B978-0-12-813629-4.00002-4.

(125) Casalini, T.; Rossi, F.; Castrovinci, A.; Perale, G. A Perspective on Polylactic Acid-Based Polymers Use for Nanoparticles Synthesis and Applications. *Front. Bioeng. Biotechnol.* **2019**, *7*. https://doi.org/10.3389/fbioe.2019.00259.

(126) Kassick, A. J.; Allen, H. N.; Yerneni, S. S.; Pary, F.; Kovaliov, M.; Cheng, C.; Pravetoni, M.; Tomycz, N. D.; Whiting, D. M.; Nelson, T. L.; Feasel, M.; Campbell, P. G.; Kolber, B.; Averick, S. Covalent Poly(Lactic Acid) Nanoparticles for the Sustained Delivery of Naloxone. *ACS Appl. Bio. Mater.* **2019**, *2*, 3418–3428. https://doi.org/10.1021/acsabm.9b00380.

(127) da Silva, J.; Jesus, S.; Bernardi, N.; Colaço, M.; Borges, O. Poly(D, L-Lactic Acid) Nanoparticle Size Reduction Increases Its Immunotoxicity. *Front. Bioeng. Biotechnol.* **2019**, *7*. https://doi.org/10.3389/fbioe.2019.00137.

(128) Ambrogio, M. W.; Toro-González, M.; Keever, T. J.; McKnight, T. E.; Davern, S. M. Poly(Lactic- Co-Glycolic Acid) Nanoparticles as Delivery Systems for the

Improved Administration of Radiotherapeutic Anticancer Agents. *ACS Appl. Nano Mater.* **2020**, *3*, 10565–10570. https://doi.org/10.1021/acsanm.0c02350.

(129) Samadi Moghaddam, M.; Heiny, M.; Shastri, V. P. Enhanced Cellular Uptake of Nanoparticles by Increasing the Hydrophobicity of Poly(Lactic Acid) through Copolymerization with Cell-Membrane-Lipid Components. *Chem. Commun.* **2015**, *51*, 14605–14608. https://doi.org/10.1039/c5cc06397c.

(130) Wu, J.; Zhao, J.; Zhang, B.; Qian, Y.; Gao, H.; Yu, Y.; Wei, Y.; Yang, Z.; Jiang, X.; Pang, Z. Polyethylene Glycol-Polylactic Acid Nanoparticles Modified with Cysteine-Arginine-Glutamic Acid-Lysine-Alanine Fibrin-Homing Peptide for Glioblastoma Therapy by Enhanced Retention Effect. *Int. J. Nanomedicine* **2014**, *9*, 5261–5271. https://doi.org/10.2147/IJN.S72649.

(131) Ghasemi, R.; Abdollahi, M.; Emamgholi Zadeh, E.; Khodabakhshi, K.; Badeli, A.; Bagheri, H.; Hosseinkhani, S. MPEG-PLA and PLA-PEG-PLA Nanoparticles as New Carriers for Delivery of Recombinant Human Growth Hormone (RhGH). *Sci. Rep.* **2018**, *8*. https://doi.org/10.1038/s41598-018-28092-8.

(132) Liang, H.; Friedman, J. M.; Nacharaju, P. Fabrication of Biodegradable PEG–PLA Nanospheres for Solubility, Stabilization, and Delivery of Curcumin. *Artif. Cells Nanomed. Biotechnol.* **2017**, *45*, 297–304. https://doi.org/10.3109/21691401.2016.1146736.

(133) Maisha, N.; Naik, N.; Okesola, M.; Coombs, T.; Zilberberg, R.; Pandala, N.; Lavik, E. Engineering PEGylated Polyester Nanoparticles to Reduce Complement-Mediated Infusion Reaction. *Bioconjug. Chem.* **2021**, *32*, 2154–2166. https://doi.org/10.1021/acs.bioconjchem.1c00339.

(134) Müller, K.; Klapper, M.; Müllen, K. Polyester Nanoparticles by Non-Aqueous Emulsion Polycondensation. *J. Polym. Sci. A. Polym. Chem.* **2007**, *45*, 1101–1108. https://doi.org/10.1002/pola.21874.

(135) Kumar, K.; Kumar, P.; Vijayalakshmi, S. Anticancer Studies of Drug Encapsulated Polyethylene Terephthalate-Co- Polylactic Acid Nanocapsules. *J. Pharm. Bioallied Sci.* **2011**, *3*, 286–293. https://doi.org/10.4103/0975-7406.80772.

(136) Crespy, D.; Landfester, K. Preparation of Nylon 6 Nanoparticles and Nanocapsules by Two Novel Miniemulsion/Solvent Displacement Hybrid Techniques. *Macromol. Chem. Phys.* **2007**, *208*, 457–466. https://doi.org/10.1002/macp.200600487.

(137) Duro-Castano, A.; Borrás, C.; Herranz-Pérez, V.; Blanco-Gandía, M. C.; Conejos-Sánchez, I.; Armiñán, A.; Mas-Bargues, C.; Inglés, M.; Miñarro, J.; Rodríguez-Arias, M.; García-Verdugo, J. M.; Viña, J.; Vicent, M. J. Targeting Alzheimer's Disease with Multimodal Polypeptide-Based Nanoconjugates. *Appl. Sci. and Eng., Sci. Rep.* **2021**, *7*.

(138) Wessel, E. M.; Tomich, J. M.; Todd, R. B. Biodegradable Drug-Delivery Peptide Nanocapsules. *ACS Omega* **2019**, *4*, 20059–20063. https://doi.org/10.1021/acsomega.9b03245.

(139) Cuesta, C. M.; Ibañez, F.; Lopez-Hidalgo, R.; Ureña, J.; Duro-Castano, A.; Armiñán, A.; Vicent, M. J.; Pascual, M.; Guerri, C. A Targeted Polypeptide-Based Nanoconjugate as a Nanotherapeutic for Alcohol-Induced Neuroinflammation. *Nanomedicine* **2021**, *34*. https://doi.org/10.1016/j.nano.2021.102376.

(140) Andrieu, J.; Kotman, N.; Maier, M.; Mailänder, V.; Strauss, W. S. L.; Weiss, C. K.; Landfester, K. Live Monitoring of Cargo Release from Peptide-Based Hybrid Nanocapsules Induced by Enzyme Cleavage. *Macromol. Rapid Commun.* **2012**, *33*, 248–253. https://doi.org/10.1002/marc.201100729.

(141) Cassano, D.; la Spina, R.; Ponti, J.; Bianchi, I.; Gilliland, D. Inorganic Species-Doped Polypropylene Nanoparticles for Multifunctional Detection. *ACS Appl. Nano Mater.* **2021**, *4*, 1551–1557. https://doi.org/10.1021/acsanm.0c03039.

(142) Schoth, A.; Landfester, K.; Muñoz-Espí, R. Surfactant-Free Polyurethane Nanocapsules via Inverse Pickering Miniemulsion. *Langmuir* **2015**, *31*, 3784–3788. https://doi.org/10.1021/acs.langmuir.5b00442.

(143) Pramanik, S. K.; Sreedharan, S.; Singh, H.; Khan, M.; Tiwari, K.; Shiras, A.; Smythe, C.; Thomas, J. A.; Das, A. Mitochondria Targeting Non-Isocyanate-Based Polyurethane Nanocapsules for Enzyme-Triggered Drug Release. *Bioconjug. Chem.* **2018**, *29*, 3532–3543. https://doi.org/10.1021/acs.bioconjchem.8b00460.

(144) Morral-Ruíz, G.; Melgar-Lesmes, P.; Solans, C.; García-Celma, M. J. Multifunctional Polyurethane-Urea Nanoparticles to Target and Arrest Inflamed Vascular Environment: A Potential Tool for Cancer Therapy and Diagnosis. *J. Control. Release* **2013**, *171*, 163–171. https://doi.org/10.1016/j.jconrel.2013.06.027.

(145) Rosenbauer, E. M.; Landfester, K.; Musyanovych, A. Surface-Active Monomer as a Stabilizer for Polyurea Nanocapsules Synthesized via Interfacial Polyaddition in

Inverse Miniemulsion. *Langmuir* **2009**, *25*, 12084–12091. https://doi.org/10.1021/la9017097.

(146) Schlegel, I.; Renz, P.; Simon, J.; Lieberwirth, I.; Pektor, S.; Bausbacher, N.; Miederer, M.; Mailänder, V.; Muñoz-Espí, R.; Crespy, D.; Landfester, K. Highly Loaded Semipermeable Nanocapsules for Magnetic Resonance Imaging. *Macromol. Biosci.* **2018**, *18*. https://doi.org/10.1002/mabi.201700387.

(147) Rossi, G.; Barnoud, J.; Monticelli, L. Polystyrene Nanoparticles Perturb Lipid Membranes. *J. Phys. Chem. Lett.* **2014**, *5*, 241–246. https://doi.org/10.1021/jz402234c.

(148) Homaeigohar, S.; Kabir, R.; Elbahri, M. Size-Tailored Physicochemical Properties of Monodisperse Polystyrene Nanoparticles and the Nanocomposites Made Thereof. *Sci. Rep.* **2020**, *10*. https://doi.org/10.1038/s41598-020-62095-8.

(149) Verma, M. L.; Dhanya, B. S.; Sukriti; Rani, V.; Thakur, M.; Jeslin, J.; Kushwaha, R. Carbohydrate and Protein Based Biopolymeric Nanoparticles: Current Status and Biotechnological Applications. *Int. J. Biol. Macromol.* **2020**, *154*, 390–412. https://doi.org/10.1016/j.ijbiomac.2020.03.105.

(150) Keliher, E. J.; Ye, Y. X.; Wojtkiewicz, G. R.; Aguirre, A. D.; Tricot, B.; Senders, M. L.; Groenen, H.; Fay, F.; Perez-Medina, C.; Calcagno, C.; Carlucci, G.; Reiner, T.; Sun, Y.; Courties, G.; Iwamoto, Y.; Kim, H. Y.; Wang, C.; Chen, J. W.; Swirski, F. K.; Wey, H. Y.; Hooker, J.; Fayad, Z. A.; Mulder, W. J. M.; Weissleder, R.; Nahrendorf, M. Polyglucose Nanoparticles with Renal Elimination and Macrophage Avidity Facilitate PET Imaging in Ischaemic Heart Disease. *Nat. Commun.* **2017**, *8*. https://doi.org/10.1038/ncomms14064.

(151) Herdiana, Y.; Wathoni, N.; Shamsuddin, S.; Muchtaridi, M. Drug Release Study of the Chitosan-Based Nanoparticles. *Heliyon* **2022**, *8*. https://doi.org/10.1016/j.heliyon.2021.e08674.

(152) Attia, M. F.; Ranasinghe, M.; Akasov, R.; Anker, J. N.; Whitehead, D. C.; Alexis, F. In Situ Preparation of Gold-Polyester Nanoparticles for Biomedical Imaging. *Biomater. Sci.* **2020**, *8*, 3032–3043. https://doi.org/10.1039/d0bm00175a.

(153) van Lysebetten, D.; Malfanti, A.; Deswarte, K.; Koynov, K.; Golba, B.; Ye, T.; Zhong, Z.; Kasmi, S.; Lamoot, A.; Chen, Y.; van Herck, S.; Lambrecht, B. N.; Sanders, N. N.; Lienenklaus, S.; David, S. A.; Vicent, M. J.; de Koker, S.; de Geest,

B. G. Lipid-Polyglutamate Nanoparticle Vaccine Platform. *ACS Appl. Mater. Interfaces* **2021**, *13*, 6011–6022. https://doi.org/10.1021/acsami.0c20607.

(154) Gregory, G. L.; Lopez-Vidal, E. M.; Buchard, A. Polymers from Sugars: Cyclic Monomer Synthesis, Ring-Opening Polymerisation, Material Properties and Applications. *Chem. Commun.* **2017**, *53*, 2198–2217. https://doi.org/10.1039/c6cc09578j.

(155) Landfester, K.; Musyanovych, A.; Mailänder, V. From Polymeric Particles to Multifunctional Nanocapsules for Biomedical Applications Using the Miniemulsion Process. *J. Polym. Sci. A Polym. Chem.* **2010**, *48*, 493–515. https://doi.org/10.1002/pola.23786.

(156) Chen, Z.; Hadjichristidis, N.; Feng, X.; Gnanou, Y. Poly(Urethane-Carbonate)s from Carbon Dioxide. *Macromolecules* **2017**, *50*, 2320–2328. https://doi.org/10.1021/acs.macromol.7b00142.

(157) Błażek, K.; Beneš, H.; Walterová, Z.; Abbrent, S.; Eceiza, A.; Calvo-Correas, T.; Datta, J. Synthesis and Structural Characterization of Bio-Based Bis(Cyclic Carbonate)s for the Preparation of Non-Isocyanate Polyurethanes. *Polym. Chem.* **2021**, *12*, 1643–1652. https://doi.org/10.1039/d0py01576h.

(158) Phoungtawee, P.; Crespy, D. Shining a New Light on the Structure of Polyurea/Polyurethane Materials. *Polym Chem* **2021**, *12*, 3893–3899. https://doi.org/10.1039/d1py00649e.

(159) Ying, H.; Cheng, J. Hydrolyzable Polyureas Bearing Hindered Urea Bonds. *J. Am. Chem. Soc.* **2014**, *136*, 16974–16977. https://doi.org/10.1021/ja5093437.

(160) Lapprand, A.; Boisson, F.; Delolme, F.; Méchin, F.; Pascault, J. P. Reactivity of Isocyanates with Urethanes: Conditions for Allophanate Formation. *Polym. Degrad. Stab.* **2005**, *90*, 363–373. https://doi.org/10.1016/J.POLYMDEGRADSTAB.2005.01.045.

(161) Burke, A.; Hasirci, N. Polyurethanes in Biomedical Applications. In *Advances in Experimental Medicine and Biology*; Springer, Boston, MA, 2004; Vol. 553, pp 83–101. https://doi.org/10.1007/978-0-306-48584-8_7.

(162) Kucinska-Lipka, J.; Gubanska, I.; Sienkiewicz, M. Thermal and Mechanical Properties of Polyurethanes Modified with L-Ascorbic Acid. *J. Therm. Anal. Calorim.* **2017**, *127*, 1631–1638. https://doi.org/10.1007/s10973-016-5743-9.

(163) Wendels, S.; Avérous, L. Biobased Polyurethanes for Biomedical Applications. *Bioact. Mater.* **2021**, *6*, 1083–1106. https://doi.org/10.1016/j.bioactmat.2020.10.002.

(164) Shi, D.; Xiao, J.; Gu, R.; Wu, G.; Liao, H. Polyurethane Conjugating TGF-β on Surface Impacts Local Inflammation and Endoplasmic Reticulum Stress in Skeletal Muscle. *J. Biomed. Mater. Res. A* **2017**, *105*, 1156–1165. https://doi.org/10.1002/jbm.a.35999.

(165) Tiarks, F.; Landfester, K.; Antonietti, M. One-Step Preparation of Polyurethane Dispersions by Miniemulsion Polyaddition. *J. Polym. Sci. A Polym. Chem.* **2001**, *39*, 2520–2524. https://doi.org/10.1002/POLA.1228.

(166) Barrè, M.; Landfester, K. High Molecular Weight Polyurethane and Polymer Hybrid Particles in Aqueous Miniemulsion. *Macromolecules* **2003**, *36*, 5119–5125. https://doi.org/10.1021/ma025981.

(167) Alkanawati, M. S.; Wurm, F. R.; Thérien-Aubin, H.; Landfester, K. Large-Scale Preparation of Polymer Nanocarriers by High-Pressure Microfluidization. *Macromol. Mater. Eng.* **2018**, *303*. https://doi.org/10.1002/mame.201700505.

(168) Uebel, F.; Thérien-Aubin, H.; Landfester, K. Glycerol-Based Polyurethane Nanoparticles Reduce Friction and Wear of Lubricant Formulations. *Macromol. Mater. Eng.* **2021**. https://doi.org/10.1002/mame.202100821.

(169) Breucker, L.; Schöttler, S.; Landfester, K.; Taden, A. Polyurethane Dispersions with Peptide Corona: Facile Synthesis of Stimuli-Responsive Dispersions and Films. *Biomacromolecules* **2015**, *16*, 2418–2426. https://doi.org/10.1021/acs.biomac.5b00672.

(170) Breucker, L.; Landfester, K.; Taden, A. Phosphonic Acid-Functionalized Polyurethane Dispersions with Improved Adhesion Properties. *ACS Appl. Mater. Inter.* **2015**, *7*, 24641–24648. https://doi.org/10.1021/acsami.5b06903.

(171) Crespy, D.; Landfester, K.; Fickert, J.; Rohwerder, M. Self-Healing for Anticorrosion Based on Encapsulated Healing Agents. *Adv. Polym. Sci.* **2016**, *273*, 219–246. https://doi.org/10.1007/12_2015_342.

(172) Busch, L.; Avlasevich, Y.; Zwicker, P.; Thiede, G.; Landfester, K.; Keck, C. M.; Meinke, M. C.; Darvin, M. E.; Kramer, A.; Müller, G.; Kerscher, M.; Lademann, J.; Patzelt, A. Release of the Model Drug SR101 from Polyurethane Nanocapsules

in Porcine Hair Follicles Triggered by LED-Derived Low Dose UVA Light. *Int. J. Pharm.* **2021**, *597*. https://doi.org/10.1016/j.ijpharm.2021.120339.

(173) Paiphansiri, U.; Dausend, J.; Musyanovych, A.; Mailänder, V.; Landfester, K. Fluorescent Polyurethane Nanocapsules Prepared via Inverse Miniemulsion: Surface Functionalization for Use as Biocarriers. *Macromol. Biosci.* **2009**, *9*, 575–584. https://doi.org/10.1002/mabi.200800293.

(174) Fan, W.; Li, J.; Yuan, L.; Chen, J.; Wang, Z.; Wang, Y.; Guo, C.; Mo, X.; Yan, Z. Intra-Articular Injection of Kartogenin-Conjugated Polyurethane Nanoparticles Attenuates the Progression of Osteoarthritis. *Drug Deliv.* **2018**, *25*, 1004–1012. https://doi.org/10.1080/10717544.2018.1461279.

(175) Borcan, F.; Chirita-Emandi, A.; Andreescu, N. I.; Borcan, L. C.; Albulescu, R. C.; Puiu, M.; Tomescu, M. C. Synthesis and Preliminary Characterization of Polyurethane Nanoparticles with Ginger Extract as a Possible Cardiovascular Protector. *Int. J. Nanomedicine* **2019**, *14*, 3691–3703. https://doi.org/10.2147/IJN.S202049.

(176) Narmani, A.; Rezvani, M.; Farhood, B.; Darkhor, P.; Mohammadnejad, J.; Amini, B.; Refahi, S.; Abdi Goushbolagh, N. Folic Acid Functionalized Nanoparticles as Pharmaceutical Carriers in Drug Delivery Systems. *Drug Dev. Res.* **2019**, *80*, 404–424. https://doi.org/10.1002/ddr.21545.

(177) Yan, H.; You, Y.; Li, X.; Liu, L.; Guo, F.; Zhang, Q.; Liu, D.; Tong, Y.; Ding, S.; Wang, J. Preparation of RGD Peptide/Folate Acid Double-Targeted Mesoporous Silica Nanoparticles and Its Application in Human Breast Cancer MCF-7 Cells. *Front. Pharmacol.* **2020**, *11*. https://doi.org/10.3389/fphar.2020.00898.

(178) Chen, M.; Hu, J.; Wang, L.; Li, Y.; Zhu, C.; Chen, C.; Shi, M.; Ju, Z.; Cao, X.; Zhang, Z. Targeted and Redox-Responsive Drug Delivery Systems Based on Carbonic Anhydrase IX-Decorated Mesoporous Silica Nanoparticles for Cancer Therapy. *Sci. Rep.* **2020**, *10*. https://doi.org/10.1038/s41598-020-71071-1.

(179) Rocas, P.; Fernández, Y.; García-Aranda, N.; Foradada, L.; Calvo, P.; Avilés, P.; Guillén, M. J.; Schwartz, S.; Rocas, J.; Albericio, F.; Abasolo, I. Improved Pharmacokinetic Profile of Lipophilic Anti-Cancer Drugs Using Aνβ3-Targeted Polyurethane-Polyurea Nanoparticles. *Nanomedicine* **2018**, *14*, 257–267. https://doi.org/10.1016/j.nano.2017.10.009.

(180) Song, N.; Ding, M.; Pan, Z.; Li, J.; Zhou, L.; Tan, H.; Fu, Q. Construction of Targeting-Clickable and Tumor-Cleavable Polyurethane Nanomicelles for Multifunctional Intracellular Drug Delivery. *Biomacromolecules* **2013**, *14*, 4407–4419. https://doi.org/10.1021/bm401342t.

(181) Rosenblum, D.; Joshi, N.; Tao, W.; Karp, J. M.; Peer, D. Progress and Challenges towards Targeted Delivery of Cancer Therapeutics. *Nat. Commun.* **2018**, *9*. https://doi.org/10.1038/s41467-018-03705-y.

(182) Qian, H.; Wang, K.; Lv, M.; Zhao, C.; Wang, H.; Wen, S.; Huang, D.; Chen, W.; Zhong, Y. Recent Advances on next Generation of Polyzwitterion-Based Nano-Vectors for Targeted Drug Delivery. *J. Control. Release* **2022**, *343*, 492–505. https://doi.org/10.1016/j.jconrel.2022.02.004.

(183) Zhang, Y.; Chen, W.; Yang, C.; Fan, Q.; Wu, W.; Jiang, X. Enhancing Tumor Penetration and Targeting Using Size-Minimized and Zwitterionic Nanomedicines. *J. Control. Release* **2016**, *237*, 115–124. https://doi.org/10.1016/j.jconrel.2016.07.011.

(184) Cuscó, C.; Garcia, J.; Nicolás, E.; Rocas, P.; Rocas, J. Multisensitive Drug-Loaded Polyurethane/Polyurea Nanocapsules with PH-Synchronized Shell Cationization and Redox-Triggered Release. *Polym. Chem.* **2016**, *7*, 6457–6466. https://doi.org/10.1039/c6py01275b.

(185) Pérez-Hernández, M.; Cuscó, C.; Benítez-García, C.; Bonelli, J.; Nuevo-Fonoll, M.; Soriano, A.; Martínez-García, D.; Arias-Betancur, A.; García-Valverde, M.; Segura, M. F.; Quesada, R.; Rocas, J.; Soto-Cerrato, V.; Pérez-Tomás, R. Multi-Smart and Scalable Bioligands-Free Nanomedical Platform for Intratumorally Targeted Tambjamine Delivery, a Difficult to Administrate Highly Cytotoxic Drug. *Biomedicines* **2021**, *9*. https://doi.org/10.3390/biomedicines9050508.

(186) Yared, J. A.; Tkaczuk, K. H. R. Update on Taxane Development: New Analogs and New Formulations. *Drug Des. Devel. Ther.* **2012**, *6*, 371–384. https://doi.org/10.2147/DDDT.S28997.

(187) Katti, A.; Diaz, B. J.; Caragine, C. M.; Sanjana, N. E.; Dow, L. E. CRISPR in Cancer Biology and Therapy. *Nat. Rev. Cancer* **2022**. https://doi.org/10.1038/s41568-022-00441-w.

(188) Herskovitz, J.; Hasan, M.; Patel, M.; Blomberg, W. R.; Cohen, J. D.; Machhi, J.; Shahjin, F.; Mosley, R. L.; McMillan, J. E.; Kevadiya, B. D.; Gendelman, H. E.

CRISPR-Cas9 Mediated Exonic Disruption for HIV-1 Elimination. *EBioMedicine* **2021**, *73*. https://doi.org/10.1016/j.ebiom.2021.103678.

(189) Duschmalé, J.; Hansen, H. F.; Duschmalé, M.; Koller, E.; Albaek, N.; Møller, M. R.; Jensen, K.; Koch, T.; Wengel, J.; Bleicher, K. In Vitro and in Vivo Properties of Therapeutic Oligonucleotides Containing Non-Chiral 3′ and 5′ Thiophosphate Linkages. *Nucleic Acids Res.* **2020**, *48*, 63–74. https://doi.org/10.1093/nar/gkz1099.

(190) Li, Q.; Li, X.; Zhao, C. Strategies to Obtain Encapsulation and Controlled Release of Small Hydrophilic Molecules. *Front. Bioeng. Biotechnol.* **2020**, *8*. https://doi.org/10.3389/fbioe.2020.00437.

(191) Lombardo, D.; Calandra, P.; Barreca, D.; Magazù, S.; Kiselev, M. A. Soft Interaction in Liposome Nanocarriers for Therapeutic Drug Delivery. *Nanomaterials* **2016**, *6*. https://doi.org/10.3390/nano6070125.

(192) Becker Peres, L.; Becker Peres, L.; de Araújo, P. H. H.; Sayer, C. Solid Lipid Nanoparticles for Encapsulation of Hydrophilic Drugs by an Organic Solvent Free Double Emulsion Technique. *Colloid Surface B* **2016**, *140*, 317–323. https://doi.org/10.1016/j.colsurfb.2015.12.033.

(193) Tenchov, R.; Bird, R.; Curtze, A. E.; Zhou, Q. Lipid Nanoparticles from Liposomes to MRNA Vaccine Delivery, a Landscape of Research Diversity and Advancement. *ACS Nano* **2021**, *15*, 16982–17015. https://doi.org/10.1021/acsnano.1c04996.

(194) Saeki, D.; Sugiura, S.; Kanamori, T.; Sato, S.; Ichikawa, S. Microfluidic Preparation of Water-in-Oil-in-Water Emulsions with an Ultra-Thin Oil Phase Layer. *Lab Chip* **2010**, *10*, 357–362. https://doi.org/10.1039/b916318b.

(195) Okushima, S.; Nisisako, T.; Torii, T.; Higuchi, T. Controlled Production of Monodisperse Double Emulsions by Two-Step Droplet Breakup in Microfluidic Devices. *Langmuir* **2004**, *20*, 9905–9908. https://doi.org/10.1021/la0480336.

(196) Cao, Z.; Wang, Z.; Herrmann, C.; Ziener, U.; Landfester, K. Narrowly Size-Distributed Cobalt Salt Containing Poly(2-Hydroxyethyl Methacrylate) Particles by Inverse Miniemulsion. *Langmuir* **2010**, *26*, 7054–7061. https://doi.org/10.1021/la904380k.

(197) Schoth, A.; Landfester, K.; Muñoz-Espí, R. Surfactant-Free Polyurethane Nanocapsules via Inverse Pickering Miniemulsion. *Langmuir* **2015**, *31*, 3784–3788. https://doi.org/10.1021/acs.langmuir.5b00442.

(198) Li, M.; Jiang, S.; Haller, A.; Wirsching, S.; Fichter, M.; Simon, J.; Wagner, M.; Mailänder, V.; Gehring, S.; Crespy, D.; Landfester, K. Encapsulation of Polyprodrugs Enables an Efficient and Controlled Release of Dexamethasone. *Nanoscale Horiz.* **2021**, *6*, 791–800. https://doi.org/10.1039/d1nh00266j.

(199) Wang, J.; Shi, A.; Agyei, D.; Wang, Q. Formulation of Water-in-Oil-in-Water (W/O/W) Emulsions Containing Trans-Resveratrol. *RSC Adv.* **2017**, *7*, 35917–35927. https://doi.org/10.1039/c7ra05945k.

(200) Qi, X.; Wang, L.; Zhu, J. Water-in-Oil-in-Water Double Emulsions: An Excellent Delivery System for Improving the Oral Bioavailability of Pidotimod in Rats. *J. Pharm. Sci.* **2011**, *100*, 2203–2211. https://doi.org/10.1002/jps.22443.

(201) Hanson, J. A.; Chang, C. B.; Graves, S. M.; Li, Z.; Mason, T. G.; Deming, T. J. Nanoscale Double Emulsions Stabilized by Single-Component Block Copolypeptides. *Nature* **2008**, *455*, 85–88. https://doi.org/10.1038/nature07197.

(202) Allison, R. R.; Moghissi, K. Photodynamic Therapy (PDT): PDT Mechanisms. *Clin. Endosc.* **2013**, *46*, 24–29. https://doi.org/10.5946/ce.2013.46.1.24.

(203) Dai, Z.; Wang, Z. Photoactivatable Platinum-Based Anticancer Drugs: Mode of Photoactivation and Mechanism of Action. *Molecules* **2020**, *25*. https://doi.org/10.3390/molecules25215167.

(204) Wan, Y.; Fu, L. H.; Li, C.; Lin, J.; Huang, P. Conquering the Hypoxia Limitation for Photodynamic Therapy. *Adv. Mater.* **2021**, *33*. https://doi.org/10.1002/adma.202103978.

(205) Alford, R.; Simpson, H. M.; Duberman, J.; Hill, G. C.; Ogawa, M.; Regino, C.; Kobayashi, H.; Choyke, P. L. Toxicity of Organic Fluorophores Used in Molecular: Literature Review. *Mol. Imaging* **2009**, *8*, 341–354. https://doi.org/10.2310/7290.2009.00031.

(206) Luz, A. F. S.; Pucelik, B.; Pereira, M. M.; Dąbrowski, J. M.; Arnaut, L. G. Translating Phototherapeutic Indices from in Vitro to in Vivo Photodynamic Therapy with Bacteriochlorins. *Lasers Surg. Med.* **2018**, *50*, 451–459. https://doi.org/10.1002/lsm.22931.

(207) Liu, M.; Li, C. Recent Advances in Activatable Organic Photosensitizers for Specific Photodynamic Therapy. *Chempluschem* **2020**, *85*, 948–957. https://doi.org/10.1002/cplu.202000203.

(208) Baskaran, R.; Lee, J.; Yang, S. G. Clinical Development of Photodynamic Agents and Therapeutic Applications. *Biomater. Res.* **2018**, *22*. https://doi.org/10.1186/s40824-018-0140-z.

(209) Sibrian-Vazquez, M.; Ortiz, J.; Nesterova, I. v.; Fernández-Lázaro, F.; Sastre-Santos, A.; Soper, S. A.; Vicente, M. G. H. Synthesis and Properties of Cell-Targeted Zn(II)-Phthalocyanine-Peptide Conjugates. *Bioconjug. Chem.* **2007**, *18*, 410–420. https://doi.org/10.1021/bc060297b.

(210) Al-Warhi, T.; Sabt, A.; Elkaeed, E. B.; Eldehna, W. M. Recent Advancements of Coumarin-Based Anticancer Agents: An up-to-Date Review. *Bioorg. Chem.* **2020**, *103*. https://doi.org/10.1016/j.bioorg.2020.104163.

(211) Stefanachi, A.; Leonetti, F.; Pisani, L.; Catto, M.; Carotti, A. Coumarin: A Natural, Privileged and Versatile Scaffold for Bioactive Compounds. *Molecules* **2018**, *23*. https://doi.org/10.3390/molecules23020250.

(212) Zou, Q.; Fang, Y.; Zhao, Y.; Zhao, H.; Wang, Y.; Gu, Y.; Wu, F. Synthesis and in Vitro Photocytotoxicity of Coumarin Derivatives for One- and Two-Photon Excited Photodynamic Therapy. *J. Med. Chem.* **2013**, *56*, 5288–5294. https://doi.org/10.1021/jm400025g.

(213) Brühlmann, C.; Ooms, F.; Carrupt, P. A.; Testa, B.; Catto, M.; Leonetti, F.; Altomare, C.; Carotti, A. Coumarins Derivatives as Dual Inhibitors of Acetylcholinesterase and Monoamine Oxidase. *J. Med. Chem.* **2001**, *44*, 3195–3198. https://doi.org/10.1021/jm010894d.

(214) Stefanachi, A.; Favia, A. D.; Nicolotti, O.; Leonetti, F.; Pisani, L.; Catto, M.; Zimmer, C.; Hartmann, R. W.; Carotti, A. Design, Synthesis, and Biological Evaluation of Imidazolyl Derivatives of 4,7-Disubstituted Coumarins as Aromatase Inhibitors Selective over 17-α-Hydroxylase/C17-20 Lyase. *J. Med. Chem.* **2011**, *54*, 1613–1625. https://doi.org/10.1021/jm101120u.

(215) Catto, M.; Pisani, L.; Leonetti, F.; Nicolotti, O.; Pesce, P.; Stefanachi, A.; Cellamare, S.; Carotti, A. Design, Synthesis and Biological Evaluation of Coumarin Alkylamines as Potent and Selective Dual Binding Site Inhibitors of

Acetylcholinesterase. *Bioorg. Med. Chem.* **2013**, *21*, 146–152. https://doi.org/10.1016/j.bmc.2012.10.045.

(216) Jung, D.; Maiti, S.; Lee, J. H.; Lee, J. H.; Kim, J. S. Rational Design of Biotin-Disulfide-Coumarin Conjugates: A Cancer Targeted Thiol Probe and Bioimaging. *Chem. Commun.* **2014**, *50*, 3044–3047. https://doi.org/10.1039/c3cc49790a.

(217) Medina, F. G.; Marrero, J. G.; Macías-Alonso, M.; González, M. C.; Córdova-Guerrero, I.; Teissier García, A. G.; Osegueda-Robles, S. Coumarin Heterocyclic Derivatives: Chemical Synthesis and Biological Activity. *Nat. Prod. Rep.* **2015**, *32*, 1472–1507. https://doi.org/10.1039/c4np00162a.

(218) Gandioso, A.; Bresolí-Obach, R.; Nin-Hill, A.; Bosch, M.; Palau, M.; Galindo, A.; Contreras, S.; Rovira, A.; Rovira, C.; Nonell, S.; Marchán, V. Redesigning the Coumarin Scaffold into Small Bright Fluorophores with Far-Red to Near-Infrared Emission and Large Stokes Shifts Useful for Cell Imaging. *J. Org. Chem.* **2018**, *83*, 1185–1195. https://doi.org/10.1021/acs.joc.7b02660.

(219) López-Corrales, M.; Rovira, A.; Gandioso, A.; Bosch, M.; Nonell, S.; Marchán, V. Transformation of COUPY Fluorophores into a Novel Class of Visible-Light-Cleavable Photolabile Protecting Groups. *Chem.-Eur. J.* **2020**, *26*, 16222–16227. https://doi.org/10.1002/chem.202002314.

(220) Rovira, A.; Pujals, M.; Gandioso, A.; López-Corrales, M.; Bosch, M.; Marchán, V. Modulating Photostability and Mitochondria Selectivity in Far-Red/NIR Emitting Coumarin Fluorophores through Replacement of Pyridinium by Pyrimidinium. *J. Org. Chem.* **2020**, *85*, 6086–6097. https://doi.org/10.1021/acs.joc.0c00570.

(221) Ortega-Forte, E.; Rovira, A.; Gandioso, A.; Bonelli, J.; Bosch, M.; Ruiz, J.; Marchán, V. COUPY Coumarins as Novel Mitochondria-Targeted Photodynamic Therapy Anticancer Agents. *J. Med. Chem.* **2021**, *64*, 17209–17220. https://doi.org/10.1021/acs.jmedchem.1c01254.

(222) Cao, D.; Liu, Z.; Verwilst, P.; Koo, S.; Jangjili, P.; Kim, J. S.; Lin, W. Coumarin-Based Small-Molecule Fluorescent Chemosensors. *Chem. Rev.* **2019**, *119*, 10403–10519. https://doi.org/10.1021/acs.chemrev.9b00145.

(223) Pisani, L.; Farina, R.; Catto, M.; Iacobazzi, R. M.; Nicolotti, O.; Cellamare, S.; Mangiatordi, G. F.; Denora, N.; Soto-Otero, R.; Siragusa, L.; Altomare, C. D.; Carotti, A. Exploring Basic Tail Modifications of Coumarin-Based Dual

Acetylcholinesterase-Monoamine Oxidase B Inhibitors: Identification of Water-Soluble, Brain-Permeant Neuroprotective Multitarget Agents. *J. Med. Chem.* **2016**, *59*, 6791–6806. https://doi.org/10.1021/acs.jmedchem.6b00562.

(224) Zhao, N.; Li, Y.; Yin, W.; Zhuang, J.; Jia, Q.; Wang, Z.; Li, N. Controllable Coumarin-Based NIR Fluorophores: Selective Subcellular Imaging, Cell Membrane Potential Indication, and Enhanced Photodynamic Therapy. *ACS Appl. Mater. Interfaces* **2020**, *12*, 2076–2086. https://doi.org/10.1021/acsami.9b18666.

(225) Huang, Y.-Y.; Sharma, S. K.; Dai, T.; Chung, H.; Yaroslavsky, A.; Garcia-Diaz, M.; Chang, J.; Chiang, L. Y.; Hamblin, M. R. Can Nanotechnology Potentiate Photodynamic Therapy? *Nanotechnol. Rev.* **2012**, *1*, 111–146.

(226) Krajczewski, J.; Rucińska, K.; Townley, H. E.; Kudelski, A. Role of Various Nanoparticles in Photodynamic Therapy and Detection Methods of Singlet Oxygen. *Photodiagnosis Photodyn Ther* **2019**, *26*, 162–178. https://doi.org/10.1016/j.pdpdt.2019.03.016.

(227) Sztandera, K.; Gorzkiewicz, M.; Klajnert-Maculewicz, B. Nanocarriers in Photodynamic Therapy—in Vitro and in Vivo Studies. *Wiley Interdiscip. Rev. Nanomed. Nanobiotechnol.* **2020**, *12*. https://doi.org/10.1002/wnan.1599.

(228) Li, T.; Yan, L. Functional Polymer Nanocarriers for Photodynamic Therapy. *Pharmaceuticals* **2018**, *11*. https://doi.org/10.3390/PH11040133.

(229) Shemesh, C. S.; Hardy, C. W.; Yu, D. S.; Fernandez, B.; Zhang, H. Indocyanine Green Loaded Liposome Nanocarriers for Photodynamic Therapy Using Human Triple Negative Breast Cancer Cells. *Photodiagnosis Photodyn. Ther.* **2014**, *11*, 193–203. https://doi.org/10.1016/j.pdpdt.2014.02.001.

(230) Yang, Y.; Wang, L.; Cao, H.; Li, Q.; Li, Y.; Han, M.; Wang, H.; Li, J. Photodynamic Therapy with Liposomes Encapsulating Photosensitizers with Aggregation-Induced Emission. *Nano Lett.* **2019**, *19*, 1821–1826. https://doi.org/10.1021/acs.nanolett.8b04875.

(231) Jiang, S.; Xiao, M.; Sun, W.; Crespy, D.; Mailänder, V.; Peng, X.; Fan, J.; Landfester, K. Synergistic Anticancer Therapy by Ovalbumin Encapsulation-Enabled Tandem Reactive Oxygen Species Generation. *Angew. Chem. – Int. Ed.* **2020**, *59*, 20008–20016. https://doi.org/10.1002/anie.202006649.

(232) Yang, Y.; Yang, X.; Li, H.; Li, C.; Ding, H.; Zhang, M.; Guo, Y.; Sun, M. Near-Infrared Light Triggered Liposomes Combining Photodynamic and Chemotherapy

for Synergistic Breast Tumor Therapy. *Colloids Surf B Biointerfaces* **2019**, *173*, 564–570. https://doi.org/10.1016/j.colsurfb.2018.10.019.

(233) Zhang, Y.; He, L.; Wu, J.; Wang, K.; Wang, J.; Dai, W.; Yuan, A.; Wu, J.; Hu, Y. Switchable PDT for Reducing Skin Photosensitization by a NIR Dye Inducing Self-Assembled and Photo-Disassembled Nanoparticles. *Biomaterials* **2016**, *107*, 23–32. https://doi.org/10.1016/j.biomaterials.2016.08.037.

(234) Yang, Y.; Hou, W.; Liu, S.; Sun, K.; Li, M.; Wu, C. Biodegradable Polymer Nanoparticles for Photodynamic Therapy by Bioluminescence Resonance Energy Transfer. *Biomacromolecules* **2018**, *19*, 201–208. https://doi.org/10.1021/acs.biomac.7b01469.

(235) Xu, J.; Shi, R.; Chen, G.; Dong, S.; Yang, P.; Zhang, Z.; Niu, N.; Gai, S.; He, F.; Fu, Y.; Lin, J. All-in-One Theranostic Nanomedicine with Ultrabright Second Near-Infrared Emission for Tumor-Modulated Bioimaging and Chemodynamic/Photodynamic Therapy. *ACS Nano* **2020**, *14*, 9613–9625. https://doi.org/10.1021/acsnano.0c00082.

(236) Zimmer, M. GFP: From Jellyfish to the Nobel Prize and Beyond. *Chem. Soc. Rev.* **2009**, *38*, 2823–2832. https://doi.org/10.1039/b904023d.

(237) Inouye, S.; Shimomura, O. The Use of Renilla Luciferase, Oplophorus Luciferase, and Apoaequorin as Bioluminescent Reporter Protein in the Presence of Coelenterazine Analogues as Substrate. *Biochem. Biophys. Res. Commun.* **1997**, *233*, 349–353. https://doi.org/10.1006/BBRC.1997.6452.

(238) Nakamura, H.; Wu, C.; Murai, A.; Inouye, S.; Shimomura, O. Efficient Bioluminescence of Bisdeoxycoelenterazine with the Luciferase of a Deep-Sea Shrimp Oplophorus. *Tetrahedron Lett.* **1997**, *38*, 6405–6406. https://doi.org/10.1016/S0040-4039(97)01438-X.

(239) Perera, S. K.; Jacob, S.; Wilson, B. E.; Ferlay, J.; Bray, F.; Sullivan, R.; Barton, M. Global Demand for Cancer Surgery and an Estimate of the Optimal Surgical and Anaesthesia Workforce between 2018 and 2040: A Population-Based Modelling Study. *Lancet Oncol.* **2021**, *22*, 182–189. https://doi.org/10.1016/S1470-2045(20)30675-6.

(240) Debie, P.; Hernot, S. Emerging Fluorescent Molecular Tracers to Guide Intra-Operative Surgical Decision-Making. *Front. Pharmacol.* **2019**, *10*. https://doi.org/10.3389/fphar.2019.00510.

(241) Gioux, S.; Choi, H. S.; Frangioni, J. v. Image-Guided Surgery Using Invisible Near-Infrared Light: Fundamentals of Clinical Translation. *Mol. Imaging* **2010**, *9*, 237–255.

(242) Xu, D.; Li, L.; Chu, C.; Zhang, X.; Liu, G. Advances and Perspectives in Near-Infrared Fluorescent Organic Probes for Surgical Oncology. *Wiley Interdiscip. Rev. Nanomed. Nanobiotechnol.* **2020**, *12*. https://doi.org/10.1002/wnan.1635.

(243) DSouza, A. v.; Lin, H.; Gunn, J. R.; Pogue, B. W. Logarithmic Intensity Compression in Fluorescence Guided Surgery Applications. *J. Biomed. Opt.* **2015**, *20*, 1. https://doi.org/10.1117/1.jbo.20.8.080504.

(244) Mieog, J. S. D.; Achterberg, F. B.; Zlitni, A.; Hutteman, M.; Burggraaf, J.; Swijnenburg, R. J.; Gioux, S.; Vahrmeijer, A. L. Fundamentals and Developments in Fluorescence-Guided Cancer Surgery. *Nat. Rev. Clin. Oncol.* **2022**, *19*, 9–22. https://doi.org/10.1038/s41571-021-00548-3.

(245) Charalampaki, P.; Proskynitopoulos, P. J.; Heimann, A.; Nakamura, M. 5-Aminolevulinic Acid Multispectral Imaging for the Fluorescence-Guided Resection of Brain Tumors: A Prospective Observational Study. *Front. Oncol.* **2020**, *10*. https://doi.org/10.3389/fonc.2020.01069.

(246) Minamikawa, T.; Matsuo, H.; Kato, Y.; Harada, Y.; Otsuji, E.; Yanagisawa, A.; Tanaka, H.; Takamatsu, T. Simplified and Optimized Multispectral Imaging for 5-ALA-Based Fluorescence Diagnosis of Malignant Lesions. *Sci. Rep.* **2016**, *6*. https://doi.org/10.1038/srep25530.

(247) Tewari, K. M.; Eggleston, I. M. Chemical Approaches for the Enhancement of 5-Aminolevulinic Acid-Based Photodynamic Therapy and Photodiagnosis. *Photochem. Photobio. Sci.* **2018**, *17*, 1553–1572. https://doi.org/10.1039/c8pp00362a.

(248) von Dobbeler, C.; Schmitz, L.; Dicke, K.; Szeimies, R. M.; Dirschka, T. PDT with PPIX Absorption Peaks Adjusted Wavelengths: Safety and Efficacy of a New Irradiation Procedure for Actinic Keratoses on the Head. *Photodiagnosis Photodyn. Ther.* **2019**, *27*, 198–202. https://doi.org/10.1016/j.pdpdt.2019.05.015.

(249) Baiocchi, G. L.; Gheza, F.; Molfino, S.; Arru, L.; Vaira, M.; Giacopuzzi, S. Indocyanine Green Fluorescence-Guided Intraoperative Detection of Peritoneal Carcinomatosis: Systematic Review. *BMC Surg.* **2020**, *20*. https://doi.org/10.1186/s12893-020-00821-9.

(250) Zheng, Y.; Yang, H.; Wang, H.; Kang, K.; Zhang, W.; Ma, G.; Du, S. Fluorescence-Guided Surgery in Cancer Treatment: Current Status and Future Perspectives. *Ann. Transl. Med.* **2019**, *7*, S6–S6. https://doi.org/10.21037/atm.2019.01.26.

(251) Woo, Y.; Chaurasiya, S.; O'Leary, M.; Han, E.; Fong, Y. Fluorescent Imaging for Cancer Therapy and Cancer Gene Therapy. *Mol. Ther. Oncolytics* **2021**, *23*, 231–238. https://doi.org/10.1016/j.omto.2021.06.007.

(252) Spinoglio, G.; Bertani, E.; Borin, S.; Piccioli, A.; Petz, W. Green Indocyanine Fluorescence in Robotic Abdominal Surgery. *Updates Surg* **2018**, *70*, 375–379. https://doi.org/10.1007/s13304-018-0585-6.

(253) Onda, N.; Kimura, M.; Yoshida, T.; Shibutani, M. Preferential Tumor Cellular Uptake and Retention of Indocyanine Green for in Vivo Tumor Imaging. *Int. J. Cancer* **2016**, *139*, 673–682. https://doi.org/10.1002/ijc.30102.

(254) Wojtynek, N. E.; Mohs, A. M. Image-Guided Tumor Surgery: The Emerging Role of Nanotechnology. *Wiley Interdiscip. Rev. Nanomed. Nanobiotechnol.* **2020**, *12*. https://doi.org/10.1002/wnan.1624.

(255) Hu, X.; Dong, X.; Lu, Y.; Qi, J.; Zhao, W.; Wu, W. Bioimaging of Nanoparticles: The Crucial Role of Discriminating Nanoparticles from Free Probes. *Drug Discov. Today* **2017**, *22*, 382–387. https://doi.org/10.1016/j.drudis.2016.10.002.

(256) Makino, A.; Kizaka-Kondoh, S.; Yamahara, R.; Hara, I.; Kanzaki, T.; Ozeki, E.; Hiraoka, M.; Kimura, S. Near-Infrared Fluorescence Tumor Imaging Using Nanocarrier Composed of Poly(l-Lactic Acid)-Block-Poly(Sarcosine) Amphiphilic Polydepsipeptide. *Biomaterials* **2009**, *30*, 5156–5160. https://doi.org/10.1016/j.biomaterials.2009.05.046.

(257) Kaibori, M.; Kosaka, H.; Matsui, K.; Ishizaki, M.; Matsushima, H.; Tsuda, T.; Hishikawa, H.; Okumura, T.; Sekimoto, M. Near-Infrared Fluorescence Imaging and Photodynamic Therapy for Liver Tumors. *Front. Oncol.* **2021**, *11*. https://doi.org/10.3389/fonc.2021.638327.

(258) Funayama, T.; Sakane, M.; Abe, T.; Hara, I.; Ozeki, E.; Ochiai, N. Intraoperative Near-Infrared Fluorescence Imaging with Novel Indocyanine Green-Loaded Nanocarrier for Spinal Metastasis: A Preliminary Animal Study. *Open Biomed. Eng. J.* **2012**, *6*, 80–84.

(259) Hill, T. K.; Abdulahad, A.; Kelkar, S. S.; Marini, F. C.; Long, T. E.; Provenzale, J. M.; Mohs, A. M. Indocyanine Green-Loaded Nanoparticles for Image-Guided Tumor Surgery. *Bioconjug. Chem.* **2015**, *26*, 294–303. https://doi.org/10.1021/bc5005679.

(260) Souchek, J. J.; Wojtynek, N. E.; Payne, W. M.; Holmes, M. B.; Dutta, S.; Qi, B.; Datta, K.; LaGrange, C. A.; Mohs, A. M. Hyaluronic Acid Formulation of near Infrared Fluorophores Optimizes Surgical Imaging in a Prostate Tumor Xenograft. *Acta Biomater.* **2018**, *75*, 323–333. https://doi.org/10.1016/j.actbio.2018.06.016.

(261) Lee, Y. H.; Lai, Y. H. Synthesis, Characterization, and Biological Evaluation of Anti-Her2 Indocyanine Green-Encapsulated Peg-Coated Plga Nanoparticles for Targeted Phototherapy of Breast Cancer Cells. *PLoS One* **2016**, *11*. https://doi.org/10.1371/journal.pone.0168192.

(262) Dong, S.; Teo, J. D. W.; Chan, L. Y.; Lee, C. L. K.; Sou, K. Far-Red Fluorescent Liposomes for Folate Receptor-Targeted Bioimaging. *ACS Appl. Nano Mater.* **2018**, *1*, 1009–1013. https://doi.org/10.1021/acsanm.8b00084.

(263) Rosenberg, B.; VanCamp, L. The Successful Regression of Large Solid Sarcoma 180 Tumors by Platinum Compounds. *Cancer Res* **1970**, *30*, 1799–1802.

(264) Dasari, S.; Bernard Tchounwou, P. Cisplatin in Cancer Therapy: Molecular Mechanisms of Action. *Eur. J. Pharmacol.* **2014**, *740*, 364–378. https://doi.org/10.1016/j.ejphar.2014.07.025.

(265) Tsang, R. Y.; Al-Fayea, T.; Au, H.-J. *Cisplatin Overdose Toxicities and Management*; Edmonton, Alberta, 2009.

(266) Chang, Q.; Ornatsky, O. I.; Siddiqui, I.; Straus, R.; Baranov, V. I.; Hedley, D. W. Biodistribution of Cisplatin Revealed by Imaging Mass Cytometry Identifies Extensive Collagen Binding in Tumor and Normal Tissues. *Sci. Rep.* **2016**, *6*. https://doi.org/10.1038/srep36641.

(267) Bijelic, A.; Aureliano, M.; Rompel, A. Polyoxometalates as Potential Next-Generation Metallodrugs in the Combat Against Cancer. *Angew. Chem.* **2019**, *131*, 3008–3029. https://doi.org/10.1002/ange.201803868.

(268) Nayeem, N.; Contel, M. Exploring the Potential of Metallodrugs as Chemotherapeutics for Triple Negative Breast Cancer. *Chem.-Eur. J.* **2021**, *27*, 8891–8917. https://doi.org/10.1002/chem.202100438.

(269) Johnstone, T. C.; Suntharalingam, K.; Lippard, S. J. The Next Generation of Platinum Drugs: Targeted Pt(II) Agents, Nanoparticle Delivery, and Pt(IV) Prodrugs. *Chem. Rev.* **2016**, *116*, 3436–3486. https://doi.org/10.1021/acs.chemrev.5b00597.

(270) Yellol, G. S.; Donaire, A.; Yellol, J. G.; Vasylyeva, V.; Janiak, C.; Ruiz, J. On the Antitumor Properties of Novel Cyclometalated Benzimidazole Ru(II), Ir(III) and Rh(III) Complexes. *Chem. Commun.* **2013**, *49*, 11533–11535. https://doi.org/10.1039/c3cc46239k.

(271) Cini, M.; Bradshaw, T. D.; Woodward, S. Using Titanium Complexes to Defeat Cancer: The View from the Shoulders of Titans. *Chem. Soc. Rev.* **2017**, *46*, 1040–1051. https://doi.org/10.1039/c6cs00860g.

(272) van Rijt, S. H.; Peacock, A. F. A.; Johnstone, R. D. L.; Parsons, S.; Sadler, P. J. Organometallic Osmium(Ii) Arene Anticancer Complexes Containing Picolinate Derivatives. *Inorg. Chem.* **2009**, *48*, 1753–1762. https://doi.org/10.1021/ic8020222.

(273) Zhang, W. Y.; Du, F.; He, M.; Bai, L.; Gu, Y. Y.; Yang, L. L.; Liu, Y. J. Studies of Anticancer Activity in Vitro and in Vivo of Iridium(III) Polypyridyl Complexes-Loaded Liposomes as Drug Delivery System. *Eur. J. Med. Chem.* **2019**, *178*, 390–400. https://doi.org/10.1016/j.ejmech.2019.06.009.

(274) Zamora, A.; Vigueras, G.; Rodríguez, V.; Santana, M. D.; Ruiz, J. Cyclometalated Iridium(III) Luminescent Complexes in Therapy and Phototherapy. *Coord. Chem. Rev.* **2018**, *360*, 34–76. https://doi.org/10.1016/j.ccr.2018.01.010.

(275) Pracharova, J.; Vigueras, G.; Novohradsky, V.; Cutillas, N.; Janiak, C.; Kostrhunova, H.; Kasparkova, J.; Ruiz, J.; Brabec, V. Exploring the Effect of Polypyridyl Ligands on the Anticancer Activity of Phosphorescent Iridium(III) Complexes: From Proteosynthesis Inhibitors to Photodynamic Therapy Agents. *Chem.-Eur. J.* **2018**, *24*, 4607–4619. https://doi.org/10.1002/chem.201705362.

(276) Farooq, M. A.; Aquib, M.; Farooq, A.; Haleem Khan, D.; Joelle Maviah, M. B.; Sied Filli, M.; Kesse, S.; Boakye-Yiadom, K. O.; Mavlyanova, R.; Parveen, A.; Wang, B. Recent Progress in Nanotechnology-Based Novel Drug Delivery Systems in Designing of Cisplatin for Cancer Therapy: An Overview. *Artif. Cells Nanomed. Biotechnol.* **2019**, *47*, 1674–1692. https://doi.org/10.1080/21691401.2019.1604535.

(277) Boulikas, T. Clinical Overview on Lipoplatin™: A Successful Liposomal Formulation of Cisplatin. *Expert Opin. Investig. Drugs* **2009**, *18*, 1197–1218. https://doi.org/10.1517/13543780903114168.

(278) Oberoi, H. S.; Nukolova, N. v.; Kabanov, A. v.; Bronich, T. K. Nanocarriers for Delivery of Platinum Anticancer Drugs. *Adv. Drug Deliv. Rev.* **2013**, *65* (13–14), 1667–1685. https://doi.org/10.1016/j.addr.2013.09.014.

(279) Dzhardimalieva, G. I.; Rabinskiy, L. N.; Kydralieva, K. A.; Uflyand, I. E. Recent Advances in Metallopolymer-Based Drug Delivery Systems. *RSC Adv.* **2019**, *9*, 37009–37051. https://doi.org/10.1039/c9ra06678k.

(280) McGhee, W. Liposomal Cisplatin Compositions For Cancer Therapy. US 10,039,716 B2, 2018.

(281) Shi, C.; Yu, H.; Sun, D.; Ma, L.; Tang, Z.; Xiao, Q.; Chen, X. Cisplatin-Loaded Polymeric Nanoparticles: Characterization and Potential Exploitation for the Treatment of Non-Small Cell Lung Carcinoma. *Acta Biomater.* **2015**, *18*, 68–76. https://doi.org/10.1016/j.actbio.2015.02.009.

(282) Shabani, R.; Ashjari, M.; Ashtari, K.; Izadyar, F.; Behnam, B.; Khoei, S.; Asghari-Jafarabadi, M.; Koruji, M. Elimination of Mouse Tumor Cells from Neonate Spermatogonial Cells Utilizing Cisplatin-Entrapped Folic Acid-Conjugated Poly(Lactic-Co-Glycolic Acid) Nanoparticles in Vitro. *Int. J. Nanomedicine* **2018**, *13*, 2943–2954. https://doi.org/10.2147/IJN.S155052.

(283) Cai, L.; Xu, G.; Shi, C.; Guo, D.; Wang, X.; Luo, J. Telodendrimer Nanocarrier for Co-Delivery of Paclitaxel and Cisplatin: A Synergistic Combination Nanotherapy for Ovarian Cancer Treatment. *Biomaterials* **2015**, *37*, 456–468. https://doi.org/10.1016/j.biomaterials.2014.10.044.

(284) Babu, A.; Amreddy, N.; Muralidharan, R.; Pathuri, G.; Gali, H.; Chen, A.; Zhao, Y. D.; Munshi, A.; Ramesh, R. Chemodrug Delivery Using Integrin-Targeted PLGA-Chitosan Nanoparticle for Lung Cancer Therapy. *Sci. Rep.* **2017**, *7*. https://doi.org/10.1038/s41598-017-15012-5.

(285) Wilson, J. J.; Lippard, S. J. Synthetic Methods for the Preparation of Platinum Anticancer Complexes. *Chem. Rev.* **2014**, *114*, 4470–4495. https://doi.org/10.1021/cr4004314.

(286) Zheng, Y. R.; Suntharalingam, K.; Johnstone, T. C.; Yoo, H.; Lin, W.; Brooks, J. G.; Lippard, S. J. Pt(IV) Prodrugs Designed to Bind Non-Covalently to Human

Serum Albumin for Drug Delivery. *J. Am. Chem. Soc.* **2014**, *136*, 8790–8798. https://doi.org/10.1021/ja5038269.

(287) Johnstone, T. C.; Lippard, S. J. The Effect of Ligand Lipophilicity on the Nanoparticle Encapsulation of Pt(IV) Prodrugs. *Inorg. Chem.* **2013**, *52*, 9915–9920. https://doi.org/10.1021/ic4010642.

(288) Zheng, Y. R.; Suntharalingam, K.; Johnstone, T. C.; Lippard, S. J. Encapsulation of Pt(IV) Prodrugs within a Pt(II) Cage for Drug Delivery. *Chem. Sci.* **2015**, *6*, 1189–1193. https://doi.org/10.1039/c4sc01892c.

(289) Liao, C.; Xu, D.; Liu, X.; Fang, Y.; Yi, J.; Li, X.; Guo, B. Iridium (III) Complex-Loaded Liposomes as a Drug Delivery System for Lung Cancer through Mitochondrial Dysfunction. *Int. J. Nanomedicine* **2018**, *13*, 4417–4431. https://doi.org/10.2147/IJN.S170035.

(290) Mukhopadhyay, S.; Singh, R. S.; Paitandi, R. P.; Sharma, G.; Koch, B.; Pandey, D. S. Influence of Substituents on DNA and Protein Binding of Cyclometalated Ir(III) Complexes and Anticancer Activity. *Dalton T.* **2017**, *46*, 8572–8585. https://doi.org/10.1039/c7dt01015j.

(291) Millett, A. J.; Habtemariam, A.; Romero-Canelón, I.; Clarkson, G. J.; Sadler, P. J. Contrasting Anticancer Activity of Half-Sandwich Iridium(III) Complexes Bearing Functionally Diverse 2-Phenylpyridine Ligands. *Organometallics* **2015**, *34*, 2683–2694. https://doi.org/10.1021/acs.organomet.5b00097.

(292) Wang, M. M.; Xue, X. L.; Sheng, X. X.; Su, Y.; Kong, Y. Q.; Qian, Y.; Bao, J. C.; Su, Z.; Liu, H. K. Unveiling the Anti-Cancer Mechanism for Half-Sandwich and Cyclometalated Ir(Iii)-Based Complexes with Functionalized α-Lipoic Acid. *RSC Adv.* **2020**, *10*, 5392–5398. https://doi.org/10.1039/c9ra10357k.

(293) McKenzie, L. K.; Bryant, H. E.; Weinstein, J. A. Transition Metal Complexes as Photosensitisers in One- and Two-Photon Photodynamic Therapy. *Coord. Chem. Rev.* **2019**, *379*, 2–29. https://doi.org/10.1016/j.ccr.2018.03.020.

(294) Karges, J. Clinical Development of Metal Complexes as Photosensitizers for Photodynamic Therapy of Cancer. *Angew. Chem. – Int. Ed.* **2022**, *61*. https://doi.org/10.1002/anie.202112236.

(295) Monro, S.; Colón, K. L.; Yin, H.; Roque, J.; Konda, P.; Gujar, S.; Thummel, R. P.; Lilge, L.; Cameron, C. G.; McFarland, S. A. Transition Metal Complexes and Photodynamic Therapy from a Tumor-Centered Approach: Challenges,

Opportunities, and Highlights from the Development of TLD1433. *Chem. Rev.* **2019**, *119*, 797–828. https://doi.org/10.1021/acs.chemrev.8b00211.

(296) Chen, Q.; Ramu, V.; Aydar, Y.; Groenewoud, A.; Zhou, X. Q.; Jager, M. J.; Cole, H.; Cameron, C. G.; McFarland, S. A.; Bonnet, S.; Snaar-Jagalska, B. E. TLD1433 Photosensitizer Inhibits Conjunctival Melanoma Cells in Zebrafish Ectopic and Orthotopic Tumour Models. *Cancers (Basel)* **2020**, *12*. https://doi.org/10.3390/cancers12030587.

(297) McFarland, S. A.; Mandel, A.; Dumoulin-White, R.; Gasser, G. Metal-Based Photosensitizers for Photodynamic Therapy: The Future of Multimodal Oncology? *Curr. Opin. Chem. Biol.* **2020**, *56*, 23–27. https://doi.org/10.1016/j.cbpa.2019.10.004.

(298) Gourdon, L.; Cariou, K.; Gasser, G. Phototherapeutic Anticancer Strategies with First-Row Transition Metal Complexes: A Critical Review. *Chem. Soc. Rev.* **2022**, *51*, 1167–1195. https://doi.org/10.1039/d1cs00609f.

(299) Jabłońska-Wawrzycka, A.; Rogala, P.; Michałkiewicz, S.; Hodorowicz, M.; Barszcz, B. Ruthenium Complexes in Different Oxidation States: Synthesis, Crystal Structure, Spectra and Redox Properties. *Dalton T.* **2013**, *42*, 6092–6101. https://doi.org/10.1039/c3dt32214a.

(300) He, L.; Li, Y.; Tan, C. P.; Ye, R. R.; Chen, M. H.; Cao, J. J.; Ji, L. N.; Mao, Z. W. Cyclometalated Iridium(III) Complexes as Lysosome-Targeted Photodynamic Anticancer and Real-Time Tracking Agents. *Chem. Sci.* **2015**, *6*, 5409–5418. https://doi.org/10.1039/c5sc01955a.

(301) Nam, J. S.; Kang, M. G.; Kang, J.; Park, S. Y.; Lee, S. J. C.; Kim, H. T.; Seo, J. K.; Kwon, O. H.; Lim, M. H.; Rhee, H. W.; Kwon, T. H. Endoplasmic Reticulum-Localized Iridium(III) Complexes as Efficient Photodynamic Therapy Agents via Protein Modifications. *J. Am. Chem. Soc.* **2016**, *138*, 10968–10977. https://doi.org/10.1021/jacs.6b05302.

(302) Huang, H.; Banerjee, S.; Sadler, P. J. Recent Advances in the Design of Targeted Iridium(III) Photosensitizers for Photodynamic Therapy. *ChemBioChem* **2018**, *19*, 1574–1589. https://doi.org/10.1002/cbic.201800182.

(303) Novohradsky, V.; Rovira, A.; Hally, C.; Galindo, A.; Vigueras, G.; Gandioso, A.; Svitelova, M.; Bresolí-Obach, R.; Kostrhunova, H.; Markova, L.; Kasparkova, J.; Nonell, S.; Ruiz, J.; Brabec, V.; Marchán, V. Towards Novel Photodynamic

Anticancer Agents Generating Superoxide Anion Radicals: A Cyclometalated Ir III Complex Conjugated to a Far-Red Emitting Coumarin. *Angew. Chem.* **2019**, *131*, 6377–6381. https://doi.org/10.1002/ange.201901268.

(304) McKenzie, L. K.; Sazanovich, I. v.; Baggaley, E.; Bonneau, M.; Guerchais, V.; Williams, J. A. G.; Weinstein, J. A.; Bryant, H. E. Metal Complexes for Two-Photon Photodynamic Therapy: A Cyclometallated Iridium Complex Induces Two-Photon Photosensitization of Cancer Cells under Near-IR Light. *Chem.-Eur. J.* **2017**, *23*, 234–238. https://doi.org/10.1002/chem.201604792.

(305) Lu, C.; Xu, W.; Shah, H.; Liu, B.; Xu, W.; Sun, L.; Qian, S. Y.; Sun, W. In Vitro Photodynamic Therapy of Mononuclear and Dinuclear Iridium(III) Bis(Terpyridine) Complexes. *ACS Appl. Bio Mater.* **2020**, *3*, 6865–6875. https://doi.org/10.1021/acsabm.0c00784.

(306) Qiao, L.; Liu, J.; Kuang, S.; Liao, X.; Kou, J.; Ji, L.; Chao, H. A Mitochondrion-TargetedBODIPY-Ir(Iii) Conjugate as a Photoinduced ROS Generator for the Oxidative Destruction of Triple-Negative Breast Cancer Cells. *Dalton T.* **2021**, *50* (40), 14332–14341. https://doi.org/10.1039/d1dt01460a.

(307) Howerton, B. S.; Heidary, D. K.; Glazer, E. C. Strained Ruthenium Complexes Are Potent Light-Activated Anticancer Agents. *J. Am. Chem. Soc.* **2012**, *134*, 8324–8327. https://doi.org/10.1021/ja3009677.

(308) Dickerson, M.; Sun, Y.; Howerton, B.; Glazer, E. C. Modifying Charge and Hydrophilicity of Simple Ru(II) Polypyridyl Complexes Radically Alters Biological Activities: Old Complexes, Surprising New Tricks. *Inorg. Chem.* **2014**, *53*, 10370–10377. https://doi.org/10.1021/ic5013796.

(309) Mari, C.; Pierroz, V.; Ferrari, S.; Gasser, G. Combination of Ru(II) Complexes and Light: New Frontiers in Cancer Therapy. *Chem. Sci.* **2015**, *6*, 2660–2686. https://doi.org/10.1039/c4sc03759f.

(310) Mari, C.; Pierroz, V.; Rubbiani, R.; Patra, M.; Hess, J.; Spingler, B.; Oehninger, L.; Schur, J.; Ott, I.; Salassa, L.; Ferrari, S.; Gasser, G. DNA Intercalating RuII Polypyridyl Complexes as Effective Photosensitizers in Photodynamic Therapy. *Chem.-Eur. J.* **2014**, *20*, 14421–14436. https://doi.org/10.1002/chem.201402796.

(311) McFarland, S. A. Metal-Based Thiophene Photodynamic Compounds and Their Use. US 9,676,806 B2, December 14, 2013. https://doi.org/10.1016/j.molstruc.2011.09.021.

(312) Cole, H. D.; Roque, J. A.; Shi, G.; Lifshits, L. M.; Ramasamy, E.; Barrett, P. C.; Hodges, R. O.; Cameron, C. G.; Mcfarland, S. A. Anticancer Agent with Inexplicable Potency in Extreme Hypoxia: Characterizing a Light-Triggered Ruthenium Ubertoxin. *J. Am. Chem. Soc.* **2021**. https://doi.org/10.1021/jacs.1c09010.

(313) Roque, J. A.; Barrett, P. C.; Cole, H. D.; Lifshits, L. M.; Shi, G.; Monro, S.; von Dohlen, D.; Kim, S.; Russo, N.; Deep, G.; Cameron, C. G.; Alberto, M. E.; McFarland, S. A. Breaking the Barrier: An Osmium Photosensitizer with Unprecedented Hypoxic Phototoxicity for Real World Photodynamic Therapy. *Chem. Sci.* **2020**, *11*, 9784–9806. https://doi.org/10.1039/d0sc03008b.

(314) Gunaydin, G.; Gedik, M. E.; Ayan, S. Photodynamic Therapy—Current Limitations and Novel Approaches. *Front. Chem.* **2021**, *9*. https://doi.org/10.3389/fchem.2021.691697.

(315) Zeng, L.; Gupta, P.; Chen, Y.; Wang, E.; Ji, L.; Chao, H.; Chen, Z. S. The Development of Anticancer Ruthenium(II) Complexes: From Single Molecule Compounds to Nanomaterials. *Chem. Soc. Rev.* **2017**, *46*, 5771–5804. https://doi.org/10.1039/c7cs00195a.

(316) Kuang, S.; Wei, F.; Karges, J.; Ke, L.; Xiong, K.; Liao, X.; Gasser, G.; Ji, L.; Chao, H. Photodecaging of a Mitochondria-Localized Iridium(III) Endoperoxide Complex for Two-Photon Photoactivated Therapy under Hypoxia. *J Am Chem Soc* **2022**, *144*, 4091–4101. https://doi.org/10.1021/jacs.1c13137.

(317) Crespy, D.; Landfester, K.; Schubert, U. S.; Schiller, A. Potential Photoactivated Metallopharmaceuticals: From Active Molecules to Supported Drugs. *Chem. Commun.* **2010**, *46*, 6651–6662. https://doi.org/10.1039/c0cc01887b.

(318) Villemin, E.; Ong, Y. C.; Thomas, C. M.; Gasser, G. Polymer Encapsulation of Ruthenium Complexes for Biological and Medicinal Applications. *Nat. Rev. Chem.* **2019**, *3*, 261–282. https://doi.org/10.1038/s41570-019-0088-0.

(319) Karges, J.; Chao, H.; Gasser, G. Synthesis, Characterization, and Biological Evaluation of the Polymeric Encapsulation of a Ruthenium(II) Polypyridine Complex with Pluronic F-127/Poloxamer-407 for Photodynamic Therapy Applications. *Eur. J. Inorg. Chem.* **2020**, *2020*, 3242–3248. https://doi.org/10.1002/EJIC.202000545.

(320) Karges, J.; Li, J.; Zeng, L.; Chao, H.; Gasser, G. Polymeric Encapsulation of a Ruthenium Polypyridine Complex for Tumor Targeted One- And Two-Photon Photodynamic Therapy. *ACS Appl. Mater. Interfaces* **2020**, *12*, 54433–54444. https://doi.org/10.1021/acsami.0c16119.

(321) Karges, J.; Tharaud, M.; Gasser, G. Polymeric Encapsulation of a Ru(II)-Based Photosensitizer for Folate-Targeted Photodynamic Therapy of Drug Resistant Cancers. *J. Med. Chem.* **2021**, *64*, 4612–4622. https://doi.org/10.1021/acs.jmedchem.0c02006.

(322) Karges, J.; Díaz-García, D.; Prashar, S.; Gómez-Ruiz, S.; Gasser, G. Ru(II) Polypyridine Complex-Functionalized Mesoporous Silica Nanoparticles as Photosensitizers for Cancer Targeted Photodynamic Therapy. *ACS Appl. Bio Mater.* **2021**, *4*, 4394–4405. https://doi.org/10.1021/acsabm.1c00151.

(323) Meijer, M. S.; Talens, V. S.; Hilbers, M. F.; Kieltyka, R. E.; Brouwer, A. M.; Natile, M. M.; Bonnet, S. NIR-Light-Driven Generation of Reactive Oxygen Species Using Ru(II)-Decorated Lipid-Encapsulated Upconverting Nanoparticles. *Langmuir* **2019**, *35*, 12079–12090. https://doi.org/10.1021/acs.langmuir.9b01318.

(324) Zhang, J.; Ramu, V.; Zhou, X. Q.; Frias, C.; Ruiz-Molina, D.; Bonnet, S.; Roscini, C.; Novio, F. Photoactivable Ruthenium-Based Coordination Polymer Nanoparticles for Light-Induced Chemotherapy. *Nanomaterials* **2021**, *11*. https://doi.org/10.3390/nano11113089.

Results and Discussion

Chapter I. Nanoencapsulation of photosensitizers based on organic fluorophores and metal complexes for application in anticancer photodynamic therapy

7. Chapter Ia. Publication I: Improving Photodynamic Therapy Anticancer Activity of a Mitochondria-Targeted Coumarin Photosensitizer Using a Polyurethane–Polyurea Hybrid Nanocarrier (*Biomacromolecules* **2022**, 23, 7, 2900–2913).

BioMACROMOLECULES

pubs.acs.org/Biomac

Article

Improving Photodynamic Therapy Anticancer Activity of a Mitochondria-Targeted Coumarin Photosensitizer Using a Polyurethane–Polyurea Hybrid Nanocarrier

Joaquín Bonelli, Enrique Ortega-Forte, Anna Rovira, Manel Bosch, Oriol Torres, Cristina Cuscó, Josep Rocas, José Ruiz,* and Vicente Marchán*

Cite This: *Biomacromolecules* 2022, 23, 2900–2913

Read Online

ACCESS | Metrics & More | Article Recommendations | Supporting Information

ABSTRACT: Integration of photosensitizers (PSs) within nanoscale delivery systems offers great potential for overcoming some of the "Achiles' heels" of photodynamic therapy (PDT). Herein, we have encapsulated a mitochondria-targeted coumarin PS into amphoteric polyurethane–polyurea hybrid nanocapsules (NCs) with the aim of developing novel nanoPDT agents. The synthesis of coumarin-loaded NCs involved the nanoemulsification of a suitable prepolymer in the presence of a PS without needing external surfactants, and the resulting small nanoparticles showed improved photostability compared with the free compound. Nanoencapsulation reduced dark cytotoxicity of the coumarin PS and significantly improved in vitro photoactivity with red light toward cancer cells, which resulted in higher phototherapeutic indexes compared to free PS. Importantly, this nanoformulation impaired tumoral growth of clinically relevant three-dimensional multicellular tumor spheroids. Mitochondrial photodamage along with reactive oxygen species (ROS) photogeneration was found to trigger autophagy and apoptotic cell death of cancer cells.

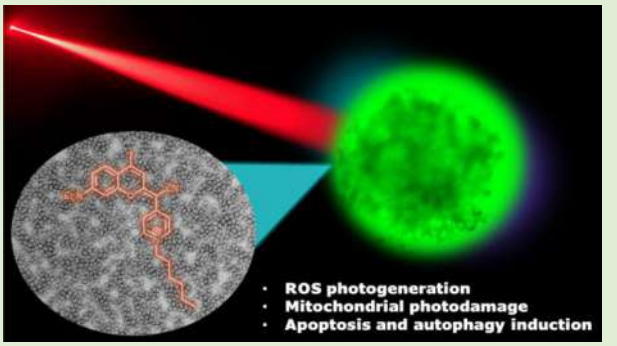

1. INTRODUCTION

Fluorophores based on small organic molecules have become powerful tools in diagnosis, prognosis, and bioimaging applications, especially those operating in the far-red to near-infrared (NIR) region of the electromagnetic spectrum because the radiation of long wavelengths is nontoxic, exhibits minimal interference from tissue autofluorescence, and penetrates deeper into biological tissues.[1] In addition, many organic fluorophores exhibit the ability to generate cytotoxic reactive oxygen species (ROS) in the presence of molecular oxygen and under certain excitation conditions, thus allowing their use as photosensitizers (PSs) in photodynamic therapy (PDT), which is an emerging clinically approved procedure for treating several cancers, including bladder, lung, skin, esophageal, brain, and ovarian cancers.[2] PDT is also a well-established modality in dermatology, ophthalmology, dentistry, and cosmetics, as well as in other nonclinical fields (e.g., eradication of viruses and other pathogens).[3] Hence, organic fluorophores exhibiting optimal physicochemical, photophysical, and photochemical properties are promising candidates for clinical phototheranostics because they provide in a single chemical entity optical imaging and photodynamic treatment of a given pathology.[4]

Despite the large number of compounds that have been described so far that can act as PSs, both porphyrinoids and nonporphyrinoids, most of them suffer from several drawbacks, and only a limited number of them have received approval for clinical use.[5] Poor aqueous solubility, aggregation, low photostability, concentration-dependent toxicity, and rapid clearance by excretion organs hamper, in most of the cases, their transition to clinical acceptance. The ability of PSs to target cancer cells while sparing healthy cells, the O_2-dependent nature of PDT, and the capacity of penetration of light required for activation in a given target tissue also determine the efficacy and clinical outcome of PDT agents, especially for combating hypoxic deep-seated tumors.[6] Therefore, many efforts have been invested by researchers to overcome some of the "Achilles' heels" of PDT by developing PSs based on alternative chemical entities with optimal physicochemical, photophysical, and photochemical properties, as well as with good biological performance. However, the difficulties associated with combining all of them in a single molecule demands to integrate known and de novo-synthesized PSs within nanoscale delivery systems. Besides

Received: March 22, 2022
Revised: May 25, 2022
Published: June 13, 2022

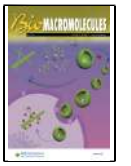

ACS Publications

© 2022 The Authors. Published by American Chemical Society

https://doi.org/10.1021/acs.biomac.2c00361
Biomacromolecules 2022, 23, 2900–2913

protecting the PS from degradation and enabling specific accumulation in different tumor tissues, nanocarriers can strongly influence its photophysical properties[7] and, consequently, there is an increased interest in the development of novel nanoPDT carriers.[8] Inorganic nanoparticles,[9] PEGylated dendrimers,[10] liposomes,[11] polymerosomes,[12] and protein[13] and polymeric nanoparticles[14] have been investigated, among others, as organic fluorophores' nanocarriers for bioimaging and PDT applications, as well as quantum dots being some of them PSs by themselves.[15]

Polyurethane-based polymers and copolymers[16] are generally considered biocompatible products for medical applications because they have been used for producing, for example, catheters[17] and stents.[18] ECOSTRATAR technology[19] has been recently introduced in nanomedical solutions to provide robust, nontoxic, and long-circulating polyurethane-polyurea hybrid nanocapsules (NCs) for the stabilization of hydrophobic compounds in aqueous media.[20] Polyurethane chemistry also facilitates the incorporation of suitable functional groups and targeting ligands on the NCs' surface for promoting preferential accumulation in specific locations.[21] Because the reduction of pH values in specific areas has been mostly associated with some types of dysfunctions or abnormal biological situations such as in the location of atheroma plaques in damaged arteries,[22] in inflamed zones of tissues micromilieu caused by immune system activation mechanisms,[23] or in the solid tumor microenvironment (TME),[24] the introduction of amphoteric groups on the NCs' surface triggers accumulation at pH media below 7.2 by selective cationization of surface amino groups.[25] This targeted encapsulation strategy opens the door to exploring the biological activity of hydrophobic drugs in different medical fields, tuning the NCs' surface to modify their biological behavior.[26] In this context, we have recently described polyurethane-polyurea hybrid NCs loaded with two cell impermeable cyclometalated Ir(III) complexes whose anticancer activity could be investigated, thanks to their nanoencapsulation.[27] Such Ir(III)-loaded nanoparticles were found to be completely stable in complete human AB serum but degradable in the presence of glutathione owing to the incorporation of disulfide bonds in the polymeric wall. Moreover, in vivo safety and biodistribution assays have been carried out using this type of NCs by system injection through the tail vein, in order to elucidate associated toxicity and preferential accumulation in ectopic and orthotopic lung cancer tumors, respectively, yielding very good results in both models.[28]

Herein, we have explored the encapsulation of a new class of coumarin-based fluorophores (COUPYs) into NCs based on ECOSTRATAR technology with the aim of developing novel phototheranostic agents for nanoPDT applications. Besides being small and amenable to structural modifications, COUPY dyes exhibit attractive photophysical properties such as absorption and emission in the far-red/NIR region, large Stokes' shifts, and brightness.[29] In addition, COUPY derivatives are cell membrane-permeable in living cells and, depending on their structure, accumulate preferentially in the mitochondria owing to the presence of the lipophilic positively charged N-alkyl pyridinium moiety.[30] Recently, we have investigated structure−activity relationships (SAR) within the COUPY scaffold and identified several PS candidates whose phototoxicity was related with ROS generation, even under hypoxia.[31] Among them, COUPY derivatives **1** and **2** (Figure 1) were able to promote cell death both by apoptosis and autophagy induction after visible light irradiation and showed good phototherapeutic indexes. In this work, we have successfully encapsulated coumarin **2** in polyurethane-polyurea hybrid NCs and demonstrated that key parameters for bioimaging applications and photostability were significantly improved. Moreover, the PDT activity of COUPY **2**-loaded NCs was investigated in two-dimensional (2D) monolayer cancer cells as well as in clinically relevant three-dimensional (3D) multicellular tumor spheroids, and their mechanism of action was studied in detail.

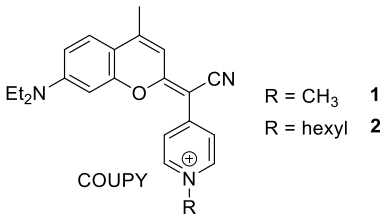

Figure 1. Structure of COUPY-based PSs investigated in this work.

2. EXPERIMENTAL SECTION

2.1. Photophysical Characterization. The ultraviolet−visible (UV−vis) absorption and emission spectra of coumarin **2** were recorded in ACN, EtOH, and H_2O. Milli-Q water suspensions were used for **COUPY 2**-loaded NCs (**NC-COUPY-2**). Absorption spectra were recorded in a Jasco V-730 spectrophotometer at room temperature. Emission spectra were registered in a Photon Technology International (PTI) fluorimeter. Fluorescence quantum yields (Φ_F) were measured using a comparative method using cresyl violet in ethanol ($\Phi_{F;\,Ref} = 0.54 \pm 0.03$) as the reference. Then, optically matched solutions of the compounds and cresyl violet were excited, and the fluorescence spectrum was recorded. The absorbance of sample and reference solutions was set below 0.1 at the excitation wavelength, and Φ_F values were calculated using the following eq 1:

$$\Phi_{F;Sample} = \frac{Area_{Sample}}{Area_{Ref}} \times \left(\frac{\eta_{Sample}}{\eta_{Ref}}\right)^2 \times \Phi_{F;ref} \quad (1)$$

where $Area_{Sample}$ and $Area_{Ref}$ are the integrated fluorescence for the sample and the reference, and η_{Sample} and η_{Ref} are the refractive index of sample and reference solutions, respectively. The uncertainty in the experimental value of Φ_F has been estimated to be approximately 10%.

Photostability of the free coumarin (**COUPY 2**) and of **COUPY 2**-loaded NCs (**NC-COUPY-2**) was investigated by monitoring fluorescence bleaching of a MilliQ water solution of the compounds at 37 °C irradiated with a high power 505 nm LED (100 mW/cm^2). Fluorescence intensity values were recorded at $t = 0$ (F_0) and after different irradiation times (F).

2.2. Singlet Oxygen Measurements. Singlet oxygen quantum yields of **COUPY 2** and **NC-COUPY-2** were determined in an air-saturated 1:1 (v/v) mixture of H_2O and EtOH (bubbled for 15 min) using 1,3-diphenylisobenzofuran (DPBF) as a chemical trap upon green light irradiation using a high-power light-emitting diode (LED) source (505 nm, 100 mW cm^{-2}) following previously reported procedures.[32] Upon reaction with singlet oxygen, the fluorescent scavenger DPBF decomposes into a colorless product.[33] The starting absorbance of DPBF in EtOH/H_2O 1:1 was adjusted around 1.0 (50 μM); then, the compounds were added to the cuvette, and their absorbance was adjusted around 0.06 at the light irradiation wavelength (505 nm). Then, the decrease in the absorbance of DPBF at 411 nm was monitored. The linear relation of the variation in the absorbance ($A_0 - A_t$) of DPBF at 411 nm against irradiation time was plotted. Singlet oxygen quantum yields were calculated by the following eq 2:

https://doi.org/10.1021/acs.biomac.2c00361
Biomacromolecules 2022, 23, 2900−2913

$$\Phi_{\Delta s} = \Phi_{\Delta r} \frac{m_s}{m_r} \frac{(1 - 10^{A\lambda r})}{(1 - 10^{A\lambda s})} \quad (2)$$

where $\Phi_{\Delta r}$ is the reference singlet oxygen quantum yield of methylene blue ($\Phi_{\Delta r}$ = 0.52 in H_2O),[34] m is the slope, and $A\lambda s$ and $A\lambda r$ are the absorbance of the compounds and of the reference (methylene blue, MB) at the irradiation wavelength, respectively. The slopes of MB, **COUPY 2**, and **NC-COUPY-2** were 0.10, 0.0040, and 0.0076, respectively.

2.3. Fluorescence Imaging by Confocal Microscopy. HeLa cells were maintained in DMEM (Dulbecco's modified Eagle medium) containing high glucose (4.5 g/L) and were supplemented with 10% fetal bovine serum (FBS), 50 U/mL penicillin−streptomycin, and 2 mM L-glutamine. For cellular uptake experiments and posterior observation under the microscope, cells were seeded on glass bottom dishes (P35G-1.5-14-C, Mattek). Twenty-four hours after cell seeding, cells were incubated at 37 °C for 30 min with free and encapsulated coumarin (1 μM) in supplemented DMEM. To determine the internalization mechanism of both compounds, low-temperature incubations were performed at 4 °C during 30 min in the same biological medium and at the same concentration (1 μM). Then, cells were washed three times with DPBS (Dulbecco's phosphate-buffered saline) to remove the excess of the compounds and kept in low glucose DMEM without phenol red supplemented with Hepes 10 mM for fluorescence imaging.

All microscopy observations were performed using a Zeiss LSM 880 confocal microscope equipped with a heating insert (P S1, Pecon). In the case of low-temperature internalization, cells were kept at RT. Cells were observed using a 63× 1.4 oil immersion objective. The compounds were excited using the 561 nm laser and detected from 570 to 670 nm. Image analysis was performed using Fiji.[35] Unless otherwise stated, images are colorized using a Fire lookup table.

2.4. Biological Studies. Human cervix adenocarcinoma cell line, HeLa, and buffalo green monkey kidney cells, BGM, were cultured in DMEM supplemented with 10% FBS, 2 mM L-glutamine, 1% penicillin−streptomycin, and 1% nonessential amino acids. Human ovarian cisplatin-resistant cancer cells, A2780cis, were maintained in RPMI-1640 cell medium supplemented with 10% FBS, 2 mM L-glutamine, and 1% penicillin−streptomycin. Cisplatin acquired resistance was maintained by adding 1 μM of water-diluted cisplatin to cell culture flasks every second passage. All the cells were cultured in humidified incubators at 310 K in a 5% CO_2 atmosphere, subcultured two or three times a week with appropriate densities, and were confirmed to be mycoplasma-free using a standard Hoechst DNA staining method.

2.4.1. Photocytotoxicity Evaluation in 2D Monolayer Cells. HeLa cells were used to determine photocytotoxicity of the tested complexes. Cells were cultured in 96-well plates at a density of 5000 cells/well in complete medium and incubated for 24 h in normoxia (21% O_2) or hypoxia (2% O_2). A detailed setup for hypoxia experiments has been previously described.[31] Serial dilutions of the compounds (final DMSO % below 0.4) or nanoparticles (water-diluted) were added at the final concentrations in the range of 0 to 200 μM in a final volume of 100 μL per well. The treatment schedule was performed as follows: 0.5 h incubation in the dark followed by 1 h incubation under irradiation conditions by placing the photoreactor EXPO-LED from LuzChem (Canada) fitted with white lamps (final light intensity applied of 3 mW/cm^2 at λ_{max} = 520 nm; 2.6 mW/cm^2 at λ_{max} = 595 nm) inside the CO_2 incubator. Alternatively, LuzChem well plate illuminator fitted with red lamps (89 mW/cm^2 at λ_{max} = 630 nm) was used for 0.5 h or 1 h. Control samples were kept in dark conditions during the phototoxic schedule in a humidified CO_2 incubator. Then, 48 h treatment-free cell recovery period was allowed; temperature throughout the experiment was maintained at 310 K. Cell medium was aspirated by suction, cells washed with saline PBS buffer, and loaded with 50 μL of MTT solution (1 mg/mL) for additional 4 h, then removed, and 50 μL of DMSO was added to solubilize the purple formazan crystals formed in active cells. The absorbance was measured at 570 nm using a microplate reader (FLUOstar Omega), and the IC_{50} values were calculated based on the inhibitory rate curves using the next eq 3:

$$I = \frac{I_{max}}{1 + \left(\frac{IC_{50}}{C}\right)^n} \quad (3)$$

where I represents the percentage inhibition of viability observed, I_{max} is the maximal inhibitory effect, IC_{50} is the concentration that inhibits 50% of maximal growth, C is the concentration of the treatment, and n is the slope of the semi-logarithmic dose−response sigmoidal curves. The nonlinear fitting was performed using SigmaPlot 14.0 software. All experiments were performed in three independent studies with triplicate points per concentration level (n = 3 biologically independent replicates).

2.4.2. Photocytotoxicity Evaluation on 3D Multicellular Spheroids. For the generation of HeLa multicellular tumor spheroids (MTCS), 96-well Corning microplates with ultralow attachment surface coating were used. Briefly, a single suspension of HeLa cells at a density of 5 × 10^3 cells/well was prepared in complete DMEM medium and dispensed into wells. The plates were covered and transferred to incubator at 310 K with 5% CO_2 atmosphere. Within 3 days, uniform 200 μm diameter MTCS were formed from cell suspension and were maintained under these conditions. At day 3, MTCS were incubated with tested agents (2 μM) for 6 h and then irradiated with red light for 0.5 h. Treatments were then replaced with fresh cell media and changed every 3 days by replacing 50% of the media. The formation, integrity, diameter, and volume of the multicellular tumor spheroids (MCTS) were monitored using a DMi1 inverted phase contrast microscope (Leica Microsystems) over a span of 9 days.

2.4.3. ROS Generation. ROS levels were determined using the 2′-7′dichlorofluorescein diacetate (DCFH-DA). HeLa cells were seeded onto 96-well plates at 2 × 10^{4}cells/well for 24 h in a humidified CO_2 incubator. Alternatively, MCTS were cultured in ULA 96-well plates and spheroids were formed within 3 days. Then, cells were stained with 10 μM of DCFH-DA for 0.5 h and washed with PBS prior treatments. Tested compounds were then administered in cell media for the allowed time, and visible light irradiation was then applied for 1 h. Cells were then washed with PBS twice and imaged using a Zeiss Axio microscope with the 40× objective using the green fluorescence channel and the intensities analyzed with ImageJ software. The assay was performed in three independent experiences (n = 3 per replicate). Alternatively, ROS generation was analyzed by flow cytometry following a similar procedure. Briefly, HeLa cells were seeded onto 12-well plate (2 × 10^5 cells/well). Treatments with tested agents for 1 h were applied. Cells were trypsinized, and pellets were resuspended in DCFH-DA staining solution for 30 min. Samples were then irradiated for 1 h and subjected to flow cytometry (FACSCAlibur BecktonDickinson; 10^4 events acquired per sample), using λ_{exc} = 488 nm and λ_{em} = 530 ± 30 nm in the FL1-H channel. Three independent experiments were performed (n = 2 replicates).

2.4.4. Mitochondrial Membrane Potential Assessment. Mitochondrial membrane potential (MMP) was evaluated with the fluorescent probe JC-1 chloride (Promocell). Briefly, HeLa cells in the density of 1.5 × 10^5 were seeded for 24 h in complete medium on 12-well plates, and then treated with indicated concentrations of tested compounds for 0.5 h. Visible light irradiation was applied for 1 h (3 mW/cm^2 at λ_{max} = 520 nm) using photoreactor EXPO-LED (Luzchem). Dark analogues were kept in the dark for 1.5 h. Untreated cells were used as a negative control, whereas CCCP (50 μM; 24 h) was used as a positive control for mitochondrial dysfunction. After drug exposure, treatment-containing media were removed, and cells were incubated with fresh media for 24 h. Then, staining JC-1 dye (1 μM) for 20 min was applied, and cells were subjected to flow cytometry (FACSCAlibur BecktonDickinson; 10^4 events acquired per sample), using λ_{exc} = 488 nm, λ_{em} = 530 ± 30 nm (green), and 585 ± 30 nm (red) parameters to discriminate green JC1 monomers (FL1-H channel) and red JC1 aggregates (FL2-H channel). Three independent experiments were performed (n = 2 replicates).

https://doi.org/10.1021/acs.biomac.2c00361
Biomacromolecules 2022, 23, 2900−2913

2.4.5. Apoptosis Induction. Cell death induction was evaluated using standard Annexin V-FITC staining. Briefly, HeLa cells were seeded in 12-well plates at a density of 1.5 × 10^5cells/well and incubated overnight. Compounds and cisplatin (20 μM) were added following the described treatment schedule (0.5 h incubation +1 h irradiation) at IC_{50}^{LIGHT} concentrations. Dark analogues were kept in the dark for 1.5 h. After 24 h of drug-free recovery period, cells were harvested by trypsinization, washed with PBS, centrifuged, and the pellets were resuspended in 200 μL of binding buffer. Then, Annexin V-FITC was added as instructed by the manufacturer (eBioscience). The resuspended cell solution was left at room temperature in the dark for 15 min prior to analysis by flow cytometry (FACSCalibur BecktonDickinson; 10^4 events acquired per sample) with λ_{exc} = 488 nm using FL1 channels. Data were analyzed using FlowingSoftware version 2.5.1. The assay was performed in three independent experiences (n = 2 replicates).

2.4.6. Autophagy Detection. Autophagic processes were detected using the fluorescent probe monodansylcadaverine (MDC; Sigma), as previously described.[36] Briefly, HeLa cells at a density of 15,000 cells/cm^2 were seeded onto confocal 8 μ-slide chambers (Ibidi) and allowed to attach and grow inside the CO_2 incubator. Cells were then treated with equitoxic concentrations (close to IC_{50}^{LIGHT}) of tested compounds, following described phototoxicity schedules. Resveratrol (50 μM, 2 h) was used as a positive control.[37] After irradiation, drug-containing media was replaced by fresh media, and a 6 h recovery period was allowed. Cells were then washed with PBS, stained with the selective autophagy marker MDC (50 μM in PBS) for 10 min at 310 K, washed again with PBS three times, and imaged under confocal microscopy (SP8 Leica systems, λ_{exc} = 405 nm). The number of MDC vesicles were counted and processed using ImageJ software.

2.4.7. Cell Metabolism Measurements. The mitochondrial OXPHOS and glycolysis function of HeLa cells was measured by determining the oxygen consumption rate (OCR) and extracellular acidification rate (ECAR) with a Seahorse XFe96 extracellular flux analyzer. In brief, HeLa cells were seeded at a density of 3 × 10^4 cells/well to the XFe96-well culture microplates (Seahorse Agilent) the day before. The sensor cartridge was hydrated through immersion on calibration buffer at 310 K in a non-CO_2 incubator overnight. Buffered DMEM (Seahorse Bioscience) was used for the assay. Cells were treated for 2 h at indicated concentrations with testing compounds. Cellular metabolism was assessed using a XF Glycolytic Rate Test Kit. OCR and ECAR measurements were monitored in real time, and respiration rates were averaged before and after the injection of a mixture of complex III electron transport chain inhibitors (Rotenone/Antimycin A, 1 μM) to impair OXPHOS and glycolysis inhibitor (2-deoxyglucose, 50 mM) to block glucose metabolism. All tests had four replicates.

2.4.8. Cell Cycle Distribution. Determination of the cell cycle distribution of HeLa cells was performed using a standard propidium iodide staining method. Briefly, HeLa cells were seeded onto 12-well plates at a density of 1.5 × 10^5cells/well and incubated overnight. Compounds and cisplatin (20 μM) were added following the described treatment schedule (0.5 h incubation +1 h irradiation) at IC_{50}^{LIGHT} concentrations. Dark analogues were kept in the dark for 1.5 h. After 24 h of the cell recovery period, cells were harvested by trypsinization and permeabilized in 70% ethanol for 1 h. Cells were then centrifuged and stained with propidium iodide for 30 min prior to analysis by flow cytometry (FACSCalibur BecktonDickinson; 10^4 events acquired per sample) with λ_{exc} = 488 nm using an FL2-A channel. Data were analyzed using FlowingSoftware version 2.5.1. The assay was performed in three independent experiences (n = 2 replicates).

2.4.9. Statistical Methods. All biological experiments were repeated at least in triplicate. Statistical analysis was performed using either analysis of variance (ANOVA) or unpaired t-test in GraphPad Prism software. P-values less than 0.05 were considered to be statistically significant.

3. RESULTS AND DISCUSSION

3.1. Synthesis and Characterization of COUPY-Loaded NCs. The synthesis of COUPY-loaded NCs involves two main processes, as described in detail in the Supporting Information: (i) the preparation of a bifunctional NH_2-terminal redox-responsive amphiphilic polyurethane−polyurea prepolymer and (ii) the fluorophore nanoencapsulation. As shown in Scheme 1, three different diol monomers (blue, yellow, and green pieces) were reacted first in the presence of an excess of isophorone diisocyanate (black pieces) (step 1) to furnish an NCO-terminated polyurethane polymer, as confirmed by Fourier transform infrared (FT-IR) analysis (step 2). Once the urethane stretching band growth reached a plateau, the product was dissolved in tetrahydrofuran (THF) and added over an excess of a hydrophobic diamine (red pieces) (step 3), which furnished the final NH_2-capped polyurethane−polyurea prepolymer (step 4).

Scheme 1. Schematic Representation of the Synthesis of the Amphiphilic Polyurethane−Polyurea Prepolymer (Steps 1−4) Followed the Nanoemulsion and Nanoencapsulation Processes (Steps 5−8)[a]

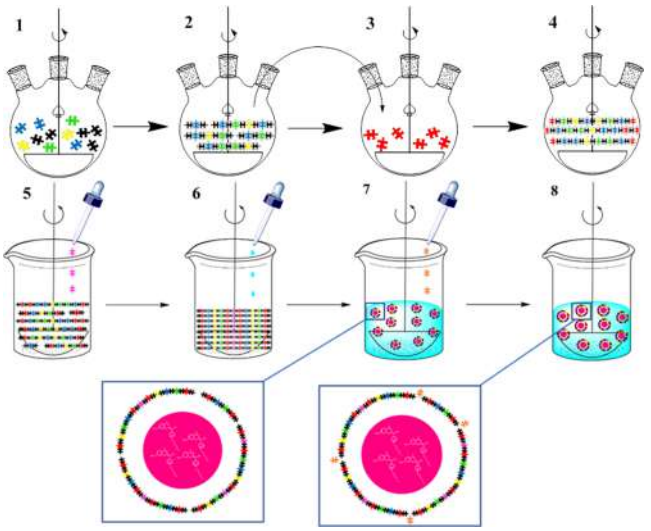

[a]Puzzle pieces codes: black for isophorone diisocyanate; blue for YMER N-120; green for *N*-(3-dimethylaminopropyl)-*N*,*N*′-diisopropanolamine; yellow for 2,2′-dihydroxyethyl disulfide; red for 1,3-diamino-*N*-octadecylpropane; pink for L-lysine, and orange for diethylenetriamine.

The amino functionalization allows the prepolymer storage, avoiding degradation of isocyanate groups by moisture. This self-emulsifiable prepolymer is the starting material for initiating the nanoencapsulation process (Scheme 1). First, the prepolymer was reactivated by the addition of an excess of isophorone diisocyanate (step not shown) and, after NCO bond appearance was confirmed by FT-IR, it was mixed with the COUPY PS (fuchsia circles in Scheme 1). Once coumarin was completely dissolved in the THF solution of the activated prepolymer, the dropwise addition of an aqueous solution of L-lysine (pink pieces) was started to extend the prepolymer chain, also furnishing an amphoteric polymer (step 5). Then, MilliQ water was added dropwise to form an inverted phase nanoemulsion (step 6), where the COUPY derivative was contained into the liposoluble core. Once oil in water nanoemulsion was defined, a polyamine (orange pieces) was

https://doi.org/10.1021/acs.biomac.2c00361
Biomacromolecules 2022, 23, 2900−2913

added as a cross-linking agent to react with terminal NCO groups (step 7), providing robustness and resulting in the final NC formation (step 8). After 24 h of dialysis purification using a molecular porous membrane tubing with a 12−14 kDa MWCO, physicochemical and encapsulation yielding parameters of the resulting coumarin-loaded NCs were evaluated.

It is worth noting that all the chemical reactions performed during the encapsulation process (see steps 5−8 in Scheme 1) are carried out at the interphase of the emulsion, furnishing a hybrid, and ordered, polyurethane−polyurea wall where the hydrophilic groups face the external aqueous phase and lipophilic ones are internally (core)-oriented. As a consequence, this synthetic methodology would allow, if required, the NCs' size, surface charge, and/or wall thickness to be easily modified by changing the ratio of monomers or the global amount of polymers because the self-emulsifiable prepolymer both drives nanodispersion stabilization and, after the final cross-linking, the generation of the NC.

As illustrated in Figure 2, the polyurethane−polyurea backbone of the NCs' shell incorporates moieties that enable

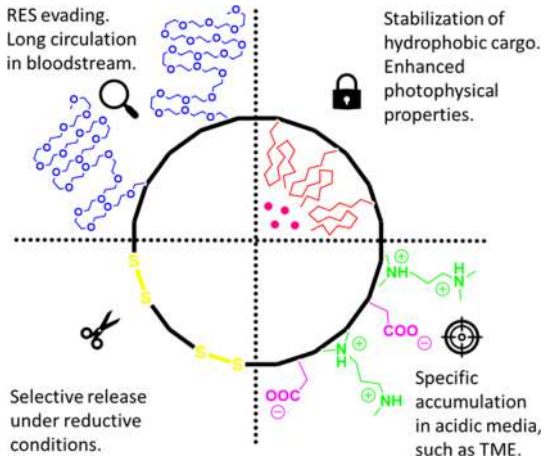

Figure 2. Schematic representation of the different moieties incorporated in the polyurethane-polyurea backbone of the NCs' shell structure.

distinctive and genuine performance, making the NCs sensitive to biological media variations. On the one hand, the incorporation of polyethylenglycol (PEG) chains ensures a long circulation lifetime in bloodstream and minimizes the clearance using the reticuloendothelial system (RES),[38] while ionomeric groups facilitate accumulation in an acidic TME. On the other hand, core-oriented hydrophobic chains are expected not only to solubilize and stabilize the lipophilic cargo but also to positively influence its photophysical properties by providing a protective and nonpolar environment. Finally, NCs might be degraded under reductive conditions owing to the incorporation of disulfide bonds in the polymer backbone, which will facilitate the release of the PS.[25]

Following the general procedure described above, the encapsulation of coumarins **1** and **2** (Figure 1) was investigated. Strikingly, water acquired a pink color during dialysis of **COUPY 1**-loaded NCs (Figure S1), which indicated that the coumarin might have been released partially from the NCs. By contrast, no color was observed in water during purification of NCs synthesized with **COUPY 2** (Figure S2). Based on these observations, the amount of coumarins **1** and **2** inside NCs was quantified by UV−vis spectroscopy. As shown in Table S2, the encapsulation efficiency was very high for coumarin **2** (ca. 91%), and a high dye loading was reached (1.16 ± 0.01 mM) for **COUPY 2**-loaded NCs (**NC-COUPY 2**) considering that no surfactants had been used during the encapsulation process. However, consistent with the observations during dialysis purification, **COUPY 1**-loaded NCs (**NC-COUPY 1**) did not contain the expected dye, which indicates that the incorporation of the hexyl group in the coumarin moiety of the COUPY scaffold is required for the retention of the compound inside the hydrophobic environment provided by the NCs.

The size and morphology of **NC-COUPY 2** was then studied by dynamic light scattering (DLS) and by transmission electron microscopy (TEM), respectively. As shown in Figure S7, the average particle size distribution was centered approximately at 14.55 ± 0.53 nm (Table S3), and TEM micrographs revealed a roughly round shape and a homogeneous particle size (Figure 3). Other TEM micrographs of **COUPY 2**-loaded NCs are shown in Figure S8. As shown in Figure S9, the morphology of the NCs was also analyzed by high-resolution TEM (HR-TEM). Although nanocarriers are usually designed to facilitate accumulation at the tumor site by the enhanced and permeability and retention effect (EPR),[39] smaller nanomedicines (e.g., 15−20 nm) are ideal for cancer therapy because of their superior tumor

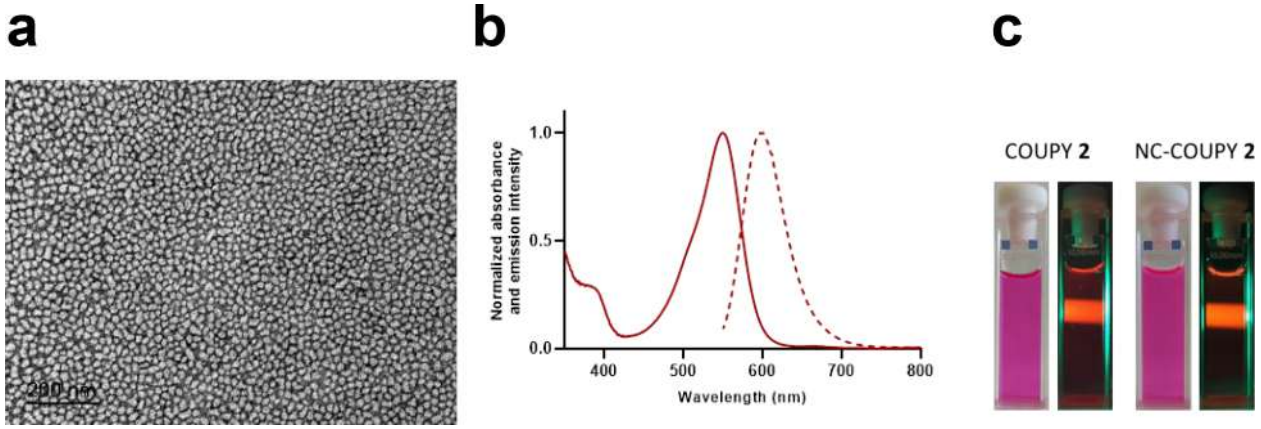

Figure 3. Characterization of **NC-COUPY-2**. (a) TEM micrograph (left). (b) UV−vis and emission spectra in water solution. (c) Photographic images of free and encapsulated **COUPY 2** in daylight and in the dark upon irradiation with a green LED source.

https://doi.org/10.1021/acs.biomac.2c00361
Biomacromolecules 2022, 23, 2900−2913

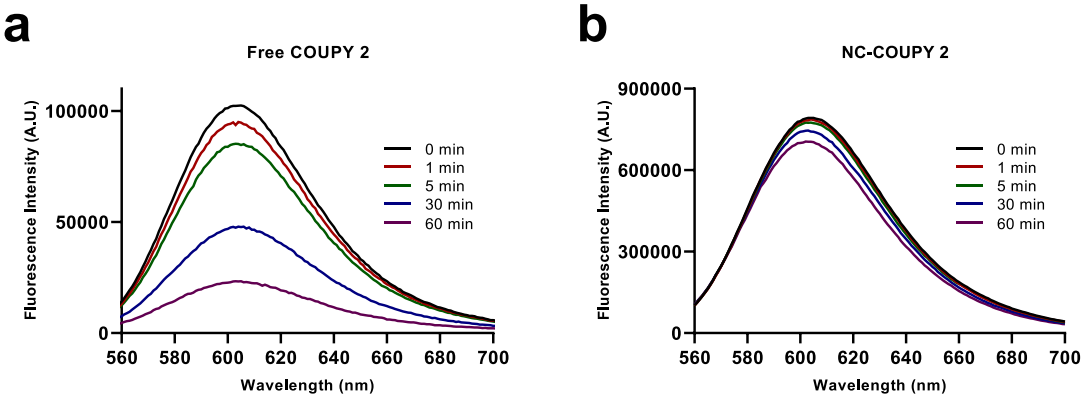

Figure 4. Emission spectra of **COUPY 2** (a) and **NC-COUPY-2** (b) after green LED irradiation at different times.

penetration.[40] In addition, the degradability of the NCs in glutathione-supplemented PBS buffer (10 mM) was also investigated with the aim of reproducing the situation in the intracellular media of cancer cells, where the concentration of the reduced form of this tripeptide is about 10 times higher than that in normal cells. As expected, the release of the coumarin PS from **NC-COUPY 2** was confirmed after incubation in PBS supplemented with glutathione for 24 and 48 h at 37 °C (Figure S10), which suggests that the degradation of the nanoparticles and release of the PS could be triggered in cancer cells through the glutathione-mediated reduction of the disulfide bonds incorporated along the polyurethane backbone of the NC wall. The results from these experiments are in good agreement with our previous observations by TEM, which demonstrated that NCs loaded with iridium(III) complexes were selectively degraded in the presence of glutathione, while they remained completely stable after incubation at 37 °C in PBS and in serum AB.[27]

The Z-potential of **NC-COUPY 2** at three pH values was also measured to evaluate the pH-dependent amphoteric properties of the polymeric shell (Figure S11). As expected, the NCs were found to be slightly anionic at physiological pH (7.4) but become cationic entities at low pH values. Based on the sub-100 nm size and the pH-dependent properties, we would expect that this novel nanoplatform will be presumably benefited from both EPR effect and acidic TME to preferentially target the tumor tissue in vivo. Regarding to its biodistribution, it is worth considering the long circulation times in the blood stream of small size nanoparticles (~12 nm) and their superior flux into tumors, which would lead to favorable toxicity profiles in vivo.[40] In addition, the intrinsic fluorescence of the COUPY cargo along with the homogenous particle size could facilitate biodistribution and pharmacokinetic studies as well as noninvasive imaging of **NC-COUPY 2** in vivo.

3.2. Photophysical and Photochemical Characterization of COUPY-Loaded NCs. Having at hand **COUPY 2**-loaded NCs, we investigated the effect of encapsulation on the spectroscopic and photophysical properties of the coumarin fluorophore (absorption and emission spectra, as well as fluorescence quantum yield (Φ_F)). Considering that the NCs are dispersed in H_2O but that the environment around the cargo is hydrophobic, the photophysical properties of the coumarin alone were also studied in three solvents of different polarities (H_2O, ethanol, and ACN) for comparison purposes. The UV−vis absorption and emission spectra are shown in Figure 3 (**NC-COUPY 2**) and S12 (COUPY **2**), and the photophysical properties are summarized in Table S4. As shown in Figure 3, aqueous solutions of **COUPY 2**-loaded NCs showed a deep pink color owing to an intense absorption band in the yellow-red region of the electromagnetic spectrum with an absorption maximum centered at 550 nm. Interestingly, the absorption maximum of the encapsulated coumarin was slightly redshifted (ca. 5 nm) with respect to that of the free compound in H_2O (λ_{abs} = 545 nm for **COUPY 2**). The fact that the absorption maximum value for **NC-COUPY 2** was similar to that of the free coumarin in ACN (λ_{abs} = 550 nm) and EtOH (λ_{abs} = 554 nm) accounts for the hydrophobic and protective environment inside the NCs. By contrast, the emission of the coumarin, which was located in the far-red to NIR region, was less sensitive to the polarity of the environment, and similar emission maxima wavelengths were obtained both for the encapsulated (λ_{em} = 600 nm) and free coumarin (λ_{em} = 602−604 nm depending on the solvent). As shown in Table S4, the fluorescence quantum yield for **NC-COUPY 2** was higher than that of the free coumarin in H_2O (Φ_F = 0.36 and 0.20, respectively), which again can be attributed to the hydrophobicity around the fluorophore inside the NCs.

The photostability of **COUPY 2**, either alone or encapsulated, was also investigated in PBS under green light irradiation. To our delight, encapsulation had a clear positive effect on the photostability of the fluorophore, which was much higher than that of the free coumarin. As shown in Figure 4 and S13, **NC-COUPY 2** were found highly photostable up to light fluences larger 400 J cm^{-2}, which are more than 20-fold higher than those used in bioimaging experiments with living cells. In summary, all these observations allowed us to conclude that the encapsulation of COUPY-based PSs in polyurethane−polyurea hybrid NCs had a positive effect in key photophysical properties for bioimaging applications because the hydrophobic environment around the organic fluorophore led to an improvement of its fluorescence emission yield and photostability, as well slightly red-shifting the maximum absorption.

Furthermore, the singlet oxygen generation by **NC-COUPY 2** was investigated by using 1,3-diphenylisobenzofuran (DPBF) as a $^1O_2$ scavenger and methylene blue (MB) as a reference in air-saturated EtOH/H_2O 1:1 (v/v) and compared with that of the free coumarin **2**. As shown in Figures S14 and S15, a gradual decrease in the absorbance of DPBF at 411 nm was observed upon irradiation with green light in the presence of the compounds, thereby confirming the generation of singlet oxygen. The fact that this process was slightly more efficient

https://doi.org/10.1021/acs.biomac.2c00361
Biomacromolecules 2022, 23, 2900−2913

when the coumarin was encapsulated (Φ_Δ = 0.04 for **NC-COUPY 2** vs Φ_Δ = 0.02 for **COUPY 2**) suggests that nanoencapsulation in a hydrophobic environment has a positive effect on type II PDT photochemical reactions, leading to the generation of singlet oxygen. This conclusion is supported by the fact that the singlet oxygen production for the free coumarin **2** was much more efficient in DCM (Φ_Δ = 0.11)[31] than in EtOH/H_2O 1:1 (v/v) (Φ_Δ = 0.02).

3.3. Fluorescence Imaging of NC-COUPY 2 in Living Cells. The cellular uptake of **COUPY 2**-loaded NCs was investigated in living HeLa cells by confocal microscopy and compared with that of the free coumarin with the aim of assessing the effect of encapsulation on the internalization of the PS. As shown in Figure 5, the fluorescence signal after

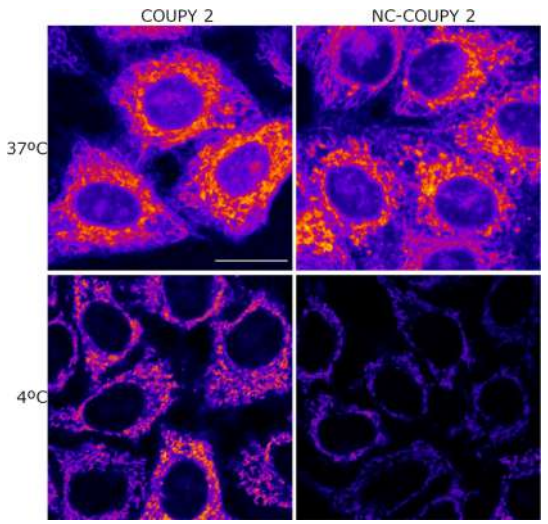

Figure 5. Cellular uptake of **COUPY 2** and **NC-COUPY 2** at 37 and 4 °C. Single confocal planes of HeLa cells incubated with the compounds at 1 μM for 30 min at 37 °C or 4 °C. Scale bar: 20 μm.

incubation with **NC-COUPY 2** (1 μM, 30 min, 37 °C) and irradiation with a yellow light laser (λ_{ex} = 561 nm) was clearly observed inside the cells, mainly in mitochondria, which suggested that the NCs were able to cross the cell membrane, even after shorter incubations times (Figure S16). Strikingly, this pattern of staining was similar to that obtained for the free coumarin (Figure 5), which might be attributed to the fact that the NCs liberate very quickly the cargo coumarin once internalized and, for this reason, accumulation in the coumarin final target organelles was observed. As previously stated, glutathione-mediated reduction of the disulfide bonds incorporated in the polymeric wall of the NCs might account for the rapid release of the coumarin cargo, which can be explained by the high concentration of this tripeptide and other reducing biomolecules in cancer cells compared with normal cells.[27,41] These observations were supported by the measurement of the mean fluorescence intensities for the mitochondria, nucleoli, and cytoplasm, which were quite similar both for the **COUPY 2**-loaded NCs and for the free coumarin (Figure S17). In addition, colocalization experiments with mitotracker green (MTG) (Figure S18) led to the same Pearson's coefficients for **COUPY 2** (0.95) and **NC-COUPY-2** (0.94), which confirmed a perfect correlation between the coumarin signal and that of MTG. Similarly, Manders' coefficients were quite high in both compounds ($M1$, $M2$ = 0.89 for **COUPY 2**; $M1$ = 0.83, $M2$ = 0.95 for **NC-COUPY-2**). As previously found with **COUPY 2** alone,[31] the mitochondria of HeLa cells after incubation with **NC-COUPY-2** showed a characteristic donut-shaped morphology after excitation with the laser beam of the microscope (Figure S19), which point out to the mitochondria stress and could be related with ROS generation upon light irradiation.[42]

To further investigate the cellular uptake of **COUPY 2**-loaded NCs, low-temperature incubation experiments were also carried out. As shown in Figure 5, the intensity of the overall fluorescence signal was clearly reduced at 4 °C in the case of **NC-COUPY 2** (Figure S20), thereby suggesting that the nanoencapsulated form requires an enabled active transport to be internalized. This result is in good agreement with previous cellular uptake studies with Ir(III)-loaded NCs by inductively coupled plasma-mass spectroscopy (ICP-MS) that demonstrated that energy-dependent mechanisms are involved in the internalization of small polyurethane-polyurea hybrid NCs.[25]

3.4. Biological Activity of NC-COUPY 2. *3.4.1. Phototoxic Activity Determination in 2D Monolayer Cells.* The efficacy of **NC-COUPY 2** as a nanoPDT agent was evaluated under irradiation with monochromatic red light (89 mW/cm^2 at λ_{max} = 630 nm) and with broadband visible light (3 mW/cm^2 at λ_{max} = 520 nm; 2.6 mW/cm^2 at λ_{max} = 595 nm). Normoxic (21% O_2) and hypoxic conditions (2% O_2) were set up to investigate photodynamic effects under challenging low-oxygen environments. The antiproliferative activity of the nanoformulation **NC-COUPY 2** in the dark (dark cytotoxicity) and under light irradiation (phototoxicity) was evaluated in cervix adenocarcinoma cells (HeLa), cisplatin-resistance ovarian cancer cells (A2780cis), and nontumorigenic renal cells (BGM), and the results were compared with those of the free compound **COUPY 2** to evaluate the effect of nanoencapsulation. The parent compound **COUPY 1** was also included for comparison.

As already reported in our previous work,[31] a dramatic increase in dark cytotoxicity was observed for coumarin **2**

Table 1. Phototoxicity of the Compounds toward Cancer and Normal Cells upon Red Light Irradiation Expressed as Mean IC_{50} Values (μM) of Three Independent Measurements[a]

	HeLa			A2780cis			BGM
	dark	light	PI[b]	dark	light	PI[b]	dark
COUPY 1	>200	16 ± 2	>12.5	>200	10.7 ± 0.9	>18.7	>200
COUPY 2	5.7 ± 0.4	0.18 ± 0.01	31.7	5.9 ± 0.9	0.75 ± 0.02	7.9	2.2 ± 0.1
NC-COUPY 2	199 ± 14	0.78 ± 0.09	255.1	20 ± 2	0.7 ± 0.1	28.6	6 ± 1

[a]Cells were treated for 1.5 h (0.5 h of incubation and 1 h of red irradiation at doses of 89 mW/cm^2), followed by 48 h of incubation in drug-free medium under normoxia (21% O_2). Dark analogues were directly kept in the dark for 1 h. [b]PI (phototoxic index) = IC_{50} (nonirradiated cells; dark)/IC_{50} (irradiated cells; red light).

https://doi.org/10.1021/acs.biomac.2c00361
Biomacromolecules 2022, 23, 2900−2913

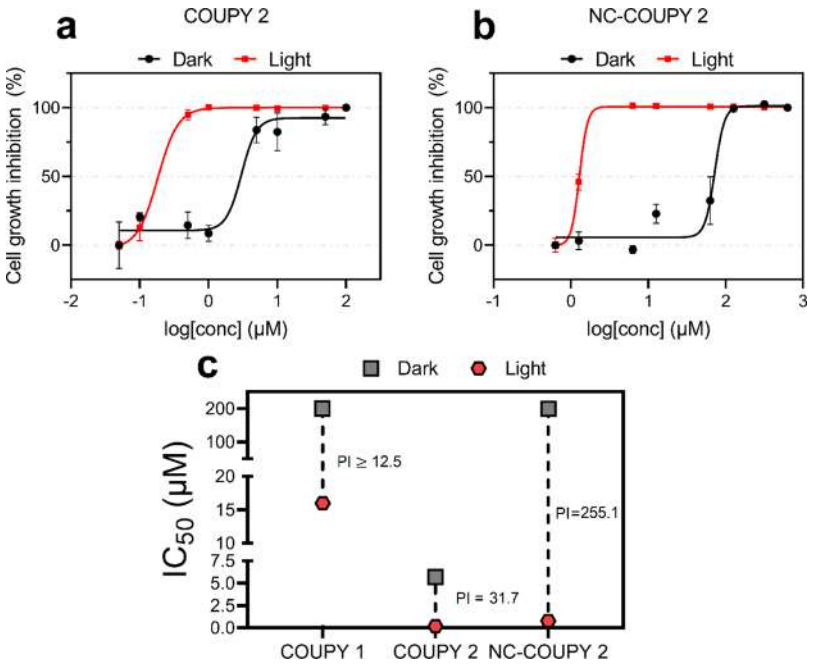

Figure 6. Dose−response curves of **COUPY 2** (a) and **NC-COUPY 2** (b) in HeLa cells. (c) Comparison of half-maximal inhibitory concentration (IC_{50}) and phototoxic index (PI) values for light-activated COUPY compounds (0.5 h in dark +1 h red light irradiation followed by 48 h drug-free recovery period) in HeLa cells.

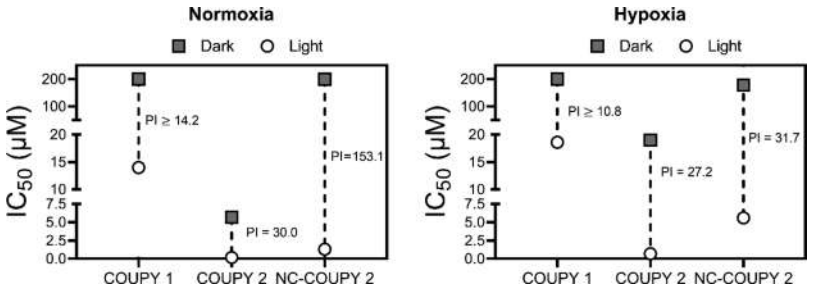

Figure 7. Comparison of half-maximal inhibitory concentration (IC_{50}) and PI values for light-activated COUPY compounds (0.5 h in dark + 1 h visible light irradiation followed by 48 h drug-free recovery period) under normoxia (21% O_2) and hypoxia (2% O_2) in HeLa cells.

treatment (IC_{50}^{DARK} = 5.7−5.9 μM) in contrast to coumarin **1** (IC_{50}^{DARK} > 200 μM), which is ascribable to the *N*-alkylation of the pyridine moiety in the COUPY scaffold with the hexyl group. Very interestingly, the dark cytotoxicity associated to **COUPY 2** was reduced between 4- and 35-fold in A2780cis and HeLa cells, respectively, when the nanoformulation **NC-COUPY 2** was administered. This might be explained by the energy-dependent internalization pathway followed by **NC-COUPY 2** in contrast to **COUPY 2**, which may achieve intracellular accumulation *via* passive diffusion (Figures 5 and S20). Upon red light irradiation, both **COUPY 2** and **NC-COUPY 2** achieved high photoactivation (IC_{50}^{LIGHT} = 0.18−0.78 μM) in cancer cells, with phototoxic indexes (PI) up to 255.1 for **NC-COUPY 2** in HeLa cells (Table 1 and Figure 6). Overall, these results indicated that nanoencapsulation of the coumarin PS resulted in decreased dark cytotoxicity and improved in vitro photoactivity with biologically compatible and highly penetrating red light. In addition, it is noteworthy that **NC-COUPY 2** also showed lower cytotoxicity than free coumarin **2** in renal BGM cell line under the dark, which suggest that encapsulation could reduce undesired toxicity on normal dividing cells.

Considering that the highest photoactivation using red light for **NC-COUPY 2** was obtained in the HeLa cell line (Figure 6), we conducted a series of experiments reducing red light exposure from 1 h to 0.5 h to evaluate the influence of time during treatments on these cells (Table S1). Compared to 1 h irradiation, slightly high IC_{50}^{LIGHT} values were obtained for both free and encapsulated **COUPY 2** when 0.5 h of light exposure was applied, suggesting that the photodynamic effects might be time-dependent. Moreover, 1 h dark cytotoxicity in HeLa cells was found to be similar to those previously obtained with 1.5 h, which led us to think that the cytotoxicity exerted by both **COUPY 2** and **NC-COUPY 2** in the dark was produced shortly after administration to monolayer cells in culture.

Because these compounds absorb light in the visible region of the electromagnetic spectrum, we decided to investigate photoactivation under broadband visible light instead of using monochromatic red light. This also allowed us to compare their phototoxicity with our previously reported family of COUPY PSs because similar protocols were used.[31] As shown in Figure 7 and Table S2, PI values for both free coumarins (**1** and **2**) and the encapsulated nanoformulation of **2** in HeLa cells under visible light were comparable to those obtained

https://doi.org/10.1021/acs.biomac.2c00361
Biomacromolecules 2022, 23, 2900−2913

with red light irradiation in normoxia, being much higher for **NC-COUPY 2** (153.1) than for **COUPY 2** (30), which again demonstrated the positive effect of nanoencapsulaton on the phototoxicity of the PS. It is worth noting that red light lamps delivered high intensity (89 mW/cm^2 at λ_{max} = 630 nm), whereas visible light irradiation was applied at a much lower intensity (close to 3 mW/cm^2 at λ_{max} = 520 nm). However, similar IC_{50}^{LIGHT} values were obtained (0.19−1.3 μM with visible light compared to 0.18−0.78 μM with red light) for free and encapsulated forms of coumarin **2**. From this, it was clear that COUPY PSs can achieve high photoactivation with low doses of visible light in the wavelength range where they absorb.

Compared to normal oxygen conditions, a reduction in the photoactivity of **NC-COUPY 2** was observed under hypoxia after visible light irradiation (Figure 7). This was probably due to impaired PDT reactions in the low-oxygen environment. Nonetheless, IC_{50}^{LIGHT} values were still in the low micromolar range (0.7−5.6 μM), suggesting that the coumarin derivative could still exhibit anticancer photoactivity under low oxygen conditions.

3.4.2. Phototoxic Activity Evaluation on 3D Multicellular Tumor Spheroids. After the evaluation of the photocytotoxicity of both **COUPY 2** and **NC-COUPY 2** on 2D monolayer cells, their photoactivity on 3D MCTS was investigated. MCTS represents a closer model to real tumors and can give information about drug penetration into tumoral tissues.[43] First, the penetration of the compound inside MCTS was examined because COUPY derivatives have demonstrated to act as fluorescent tools that exhibit rapid intracellular accumulation.[31] Fluorescence microscopy imaging revealed that **NC-COUPY 2** and **COUPY 2** penetrated efficiently into tumor spheres and emitted strong fluorescence (Figures 8 and S18). Interestingly, in contrast to **COUPY 2** fluorescence, which was found evenly distributed across MCTS, **NC-COUPY 2** fluorescence was mostly found on the outer surface of MCTS after 2 h (Figure 8). Nonetheless, increasing the incubation time up to 6 h resulted in complete penetration inside tumor spheres (Figure S21). This delay in complete drug penetration of **NC-COUPY 2** compared to free **COUPY 2** would also imply a reduction in dark cytotoxicity toward MCTS.

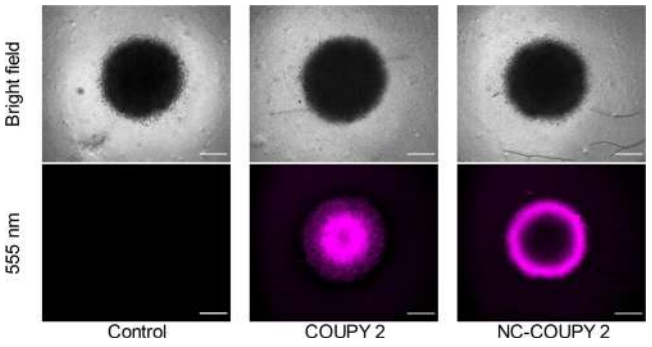

Figure 8. Fluorescence microscopy images of HeLa spheroids treated with **COUPY 2** and **NC-COUPY 2** at 2 μM for 2 h. Scale bar: 100 μm.

Following this, the tumor growth of HeLa MCTS was monitored after red light irradiation with **COUPY 2** either free or encapsulated. After the formation of the tumor spheres on day 3, the compounds were incubated for 6 h in the dark as this time was shown to be required for complete penetration into tumor spheres (Figure S21) Then, MCTS were exposed to 0.5 h of red light irradiation at doses of 89 mW/cm^2. Drug-containing medium was removed, and the volume of the MCTS was monitored over a span of 9 days. Unlike nontreated control cells, the volume of **COUPY 2** and **NC-COUPY 2**-treated MCTS was significantly reduced after light irradiation and provided shrank tumor spheres within the following days until day 9, thereby indicating a potent tumoral growth inhibition effect (Figures 9 and S22). It is noteworthy that

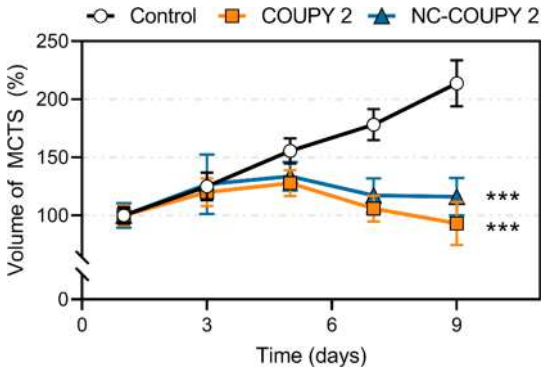

Figure 9. Normalized volume of HeLa MCTS over a span of 9 days. MCTS were treated on day 3 with **COUPY 2** or **NC-COUPY 2** (2 μM) for 6 h in the dark and then exposed to red light irradiation (630 nm, 0.5 h, 89 mW/cm^2). Data expressed as mean ± SD from three replicates. An independent unpaired *t*-test was used to define statistical differences between the values obtained on day 9 (***p < 0.001).

similar inhibitory effects on 3D MTCS were found with both free and encapsulated agent after irradiation. These results correlated with those observed in 2D monolayer cells, where similar IC_{50}^{LIGHT} were obtained. Overall, this allowed us to confirm the photoactivity of both **COUPY 2** and **NC-COUPY 2** in 3D cellular models, where hypoxia plays a more realistic role than in 2D cell cultures.

3.4.3. Photogeneration of ROS in 2D and 3D Cancer Models. To visualize intracellular ROS generation from the coumarin-based PS, either free or nanoencapsulated, HeLa cells treated with **COUPY 2** or **NC-COUPY 2** at 2 μM upon light irradiation were stained with a 2′,7′-dichlorofluorescein diacetate (DCFH-DA) probe. DCFH-DA is enzymatically converted to the green, fluorescent product DCF in the presence of ROS. Menadione was used as positive control for ROS generation.[44] The results depicted in Figure 10a proved that **NC-COUPY 2** effectively raised ROS levels in tumor cells in 2D cultures after visible light irradiation. In contrast, although still significant compared to control cells, a weaker green fluorescence was observed for **COUPY 2**-treated cells, suggesting slightly lower ROS generation efficiency in monolayer cells (Figure 10b).

This ROS generating ability was also investigated on MCTS because, as previously indicated, they simulate clinical conditions of tumors such as hypoxia and metabolic gradients to the center.[43] Treatments with both free and encapsulated agents managed to significantly raise ROS levels after visible light irradiation compared to untreated MCTS (Figure 10a). Interestingly, DCF fluorescence was observed both in the center and in the outer sphere of **COUPY 2**-phototreated MCTS, whereas images of tumorspheres treated with **NC-**

https://doi.org/10.1021/acs.biomac.2c00361
Biomacromolecules 2022, 23, 2900−2913

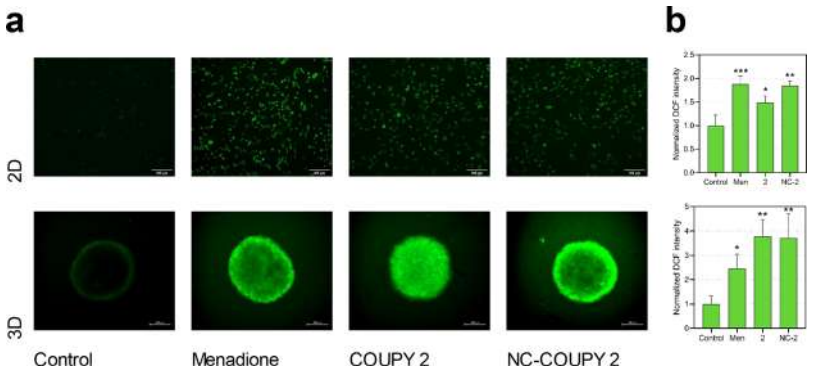

Figure 10. ROS generation in HeLa cells after light irradiation treatments with **COUPY 2** and **NC-COUPY 2** at 2 μM (1 h incubation + 1 h visible light irradiation). (a) ROS levels of HeLa cells on 2D monolayer cells or 3D MCTS stained with DCFH-DA for 0.5 h at 310 K after phototreatments and imaged on a Zeiss Axiovert inverted microscope; menadione (50 μM) being used as positive control. Scale bar: 200 μm. (b) Quantitation of oxidative stress based on DCF fluorescence after irradiation treatments. Three independent experiments were performed, and the error bars were calculated as the SD from the mean. Statistical significance control vs treatments determined *via* one-way ANOVA test (*$p < 0.05$; **$p < 0.01$ and ***$p < 0.001$).

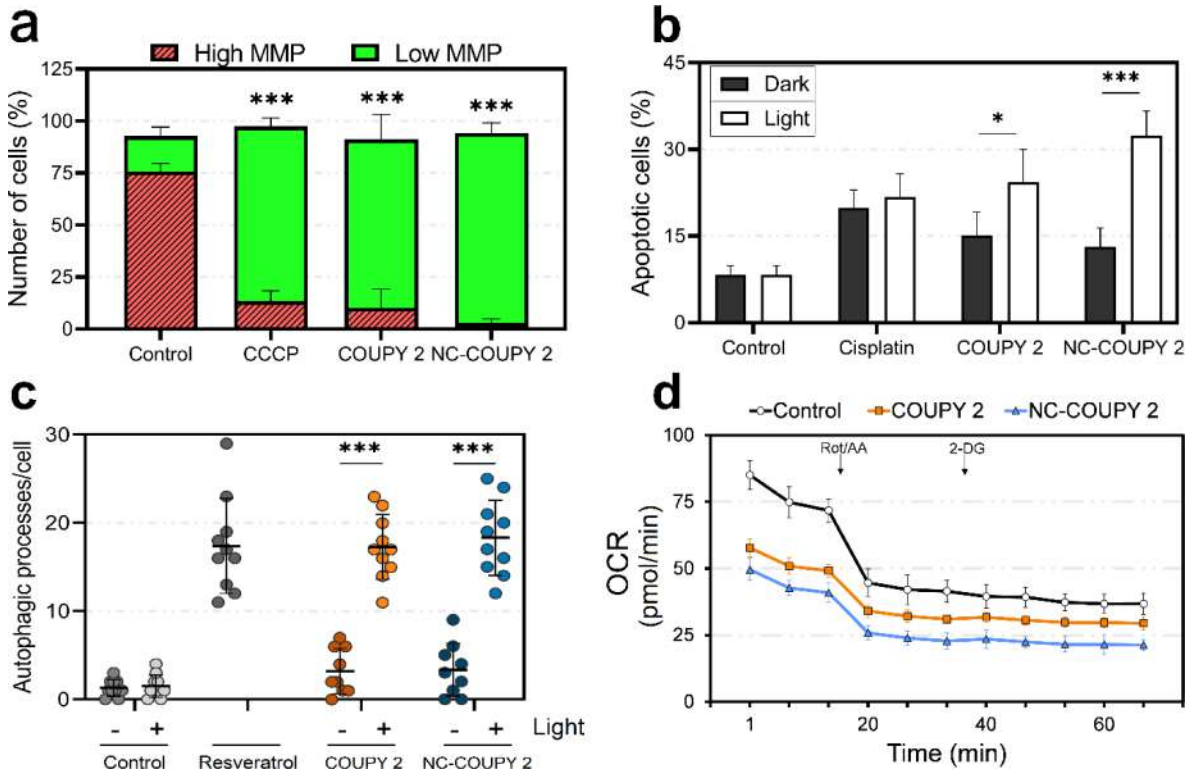

Figure 11. Phototoxic mechanism of action in HeLa cancer cells after treatments with **COUPY 2** or **NC-COUPY 2** at IC_{50}^{LIGHT} concentrations (0.5 h incubation + 1 h visible light irradiation and 24 h recovery). (a) Flow cytometry analysis of the MMP using JC-1 dye. The mitochondrial phosphorylation inhibitor carbonyl cyanide *m*-chlorophenyl hydrazone (CCCP 50 μM, 24 h) was used as a positive control for mitochondrial dysfunction. (b) Apoptosis induction upon exposure to **COUPY 2** or **NC-COUPY 2** in the dark or after visible light irradiation treatments detected by flow cytometry as Annexin V-FITC fluorescence on the FL1-H channel; cisplatin (20 μM) was used as the positive control. (c) Number of autophagic processes detected in HeLa cells as quantified by confocal microscopy imaging through monodansylcadaverine (MDC) staining from >10 cells; resveratrol (50 μM, 2 h) was used as the positive control. (d) Mitochondrial oxidative phosphorylation on the basis of the OCR after 2 h treatment with tested complexes (10 μM) in the dark using the Seahorse XFe analyzer. All data represented as mean ± SD from three independent experiments. Statistical significance was determined via two-way ANOVA tests (*$p < 0.05$; ***$p < 0.001$).

COUPY 2 showed fluorescence mainly on the outer part. This result is in agreement with the fluorescent penetration pattern observed for the compounds after 2 h (Figure 8). Strikingly, the mean DCF fluorescence intensity was found to be similar for both **COUPY 2** and **NC-COUPY 2** according to quantitative measurement analysis (Figure 10b). Whereas **NC-COUPY 2** only increased DCF fluorescence in the external part of MCTS after irradiation, the overall emission intensity was comparable to those treated with **COUPY 2**, where DCF fluorescence was found across all the tumor spheres. These observations led us to hypothesize that although ROS might not be extensively produced in the hypoxic center of MCTS, a potent ROS generation was achieved with **NC-COUPY 2** in the normoxic outer part of

https://doi.org/10.1021/acs.biomac.2c00361
Biomacromolecules 2022, 23, 2900−2913

tumor spheres. This also correlated with their phototoxic profile, which resulted in higher PI values in normoxia than under hypoxic conditions (Figures 6 and 7).

Flow cytometry assays using a DCFH-DA probe were also performed to quantitatively analyze ROS generation after phototreatments. As presented in Figure S23, both **COUPY 2** and **NC-COUPY 2** induced large populations of HeLa cells with strong DCF signals compared to control cells. These results correlate well with those previously obtained with fluorescence intensity measurements and corroborated ROS production in cancer cells as a main phototherapeutic mechanism.

3.4.4. Mechanism of Cell Death Induction after Light Irradiation. To gain insights into the cell death mechanisms produced after **NC-COUPY 2** photoactivation, a series of cell-experiments were conducted in HeLa cells. For these experiments, 1 h of visible light irradiation at low doses was applied in order to allow proper comparisons with our previous mechanistic studies with COUPY PSs.[31] The mechanism of action-related experiments with **COUPY 2** and **NC-COUPY 2** were performed at concentrations close to IC_{50}^{LIGHT} with visible light (i.e., 0.5 and 1.5 μM, respectively).

3.4.4.1. Mitochondrial Dysfunction. As shown in Figure 5, mitochondria were found to be the targeted organelle for these family of COUPY derivatives.[31] Therefore, mitochondrial dysfunction was examined after light irradiation. JC-1 dye was used to assess MMP and mitochondrial health of HeLa cells upon treatments. This dye accumulates in healthy mitochondria in a potential-dependent fashion emitting red fluorescence but exhibits green fluorescence if membrane depolarization occurs. As shown in Figures 11a and S24, both **COUPY 2** and **NC-COUPY 2** dramatically decreased red to green fluorescence ratio after light irradiation, indicating a loss of MMP.

3.4.4.2. Apoptosis Induction. Our previous studies with COUPY derivatives showed that they could act as apoptotic inducers in HeLa cells after visible light irradiation.[31] To check apoptosis-mediated cell death photoactivation by **NC-COUPY 2**, flow cytometry experiments were performed using Annexin V-FITC (fluorescein isothiocyanate) staining. As shown in Figure 11b, **COUPY 2** and **NC-COUPY 2** produced low to moderate apoptosis levels in the dark, while significant apoptosis induction occurred after irradiation. Interestingly, cell populations with high Annexin V-binding capacity were raised to a larger extent when the nanoformulated agent was applied, suggesting that encapsulation contributed to trigger apoptosis in higher levels (Figures 11b and S25). Along with the depletion of MMP, these findings pointed out an apoptosis induction *via* the mitochondrial intrinsic pathway produced by **NC-COUPY 2.**

3.4.4.3. Autophagy Initiation. To understand cell death mechanisms mediated by **NC-COUPY 2** against HeLa cells after light application, autophagy initiation was investigated. The detection of autophagic processes was performed with monodansylcadaverine(MDC), a probe that accumulates in the acidic compartments of autophagic vesicles; and resveratrol served as a chemical autophagy inducer.[37] Confocal microscopy imaging revealed that the number of MDC-labeled vesicles significantly increased upon irradiation with both **COUPY 2** and **NC-COUPY 2** (Figures 11c and S26). This is in good correlation with our previously reported results, where pretreatment with the autophagy inhibitor wortmannin was found to significantly attenuate **COUPY 2** phototoxicity.[31]

3.4.4.4. Cell Metabolic Alteration. Because cancer cells generally exhibit a distinct metabolism characterized by producing ATP from glycolysis rather than from mitochondrial oxidative phosphorylation (OXPHOS),[45] these two major metabolic pathways were studied to assess the bioenergetic state of HeLa cells in real-time using the Seahorse XF-96 flux analyzer. The OCR was used to monitor mitochondrial energetics, whereas glycolysis was evaluated by means of extracellular acidification rate (ECAR) measurements. Treatment for 2 h with both **COUPY 2** and **NC-COUPY 2** resulted in the impairment of mitochondrial respiration as evidenced by reduced OCR before and after the injection of respiratory chain inhibitors (Figure 11d). This is in agreement with MMP depolarization observed upon treatments with these agents.[31] In addition, ECAR measurements revealed a strong decline in glycolytic function in the presence of these agents, thus revealing strong abrogation of normal cell metabolism (Figure S27).

3.4.4.5. Cell Cycle Distribution. Additionally, the progression of the cell cycle of HeLa cancer cells was examined using propidium iodide staining after irradiation treatments with **NC-COUPY 2** (Figure S28). Compared to cisplatin, which produced S and G2/M phase arrest, **COUPY 2** and **NC-COUPY 2** did not alter cell cycle distribution significantly in the dark. However, light exposure triggered significant accumulation of HeLa cells in the subG1 phase, an indicative of fragmented DNA probably derived from apoptotic cell death induction.

Because both autophagy and mitochondrial dysfunction were observed after irradiation with these compounds (Figure 11), we hypothesize that mitophagy might occurr as a result of cellular photodamage. In fact, this was observed under confocal microscopy upon laser beam irradiation (Figure S19)[31] and is consistent with the depleted MMP and declined OCR observed after treatment with **COUPY 2** and **NC-COUPY 2** (Figure 11). The mitochondrial photodamage induced by this PS agent could then trigger both apoptotic cell death and mitochondrial degradation through autophagy. Altogether, these results showed that the mechanism of the action of **COUPY 2** involved a combination of autophagy and apoptosis, which may arise from ROS-generating PDT reactions. This mode of cell death was induced in a greater extent when nanoformulation **NC-COUPY 2** was applied, suggesting that the encapsulation of **COUPY 2** improved the phototherapeutic activity of the PS, probably due to the increased amount of the PS being delivered into cancer cells at a time *via* active transport.

4. CONCLUSIONS

In summary, we have demonstrated that polyurethane–polyurea hybrid NCs can be used to efficiently encapsulate low-molecular-weight PSs based on organic fluorophores for application as nanoPDT agents. As a proof-of-concept, two mitochondria-targeted PS agents based on *N*-alkylpyridinium COUPY coumarins (**1** and **2**) were selected to set up the nanoencapsulation process. Although both coumarins could be encapsulated, the *N*-methyl analogue (**1**) was lost from the NC during the dialysis purification, which indicates that higher hydrophobicity is required to generate stable COUPY-loaded NCs. By contrast, the *N*-hexyl-containing COUPY **2**-loaded NCs (**NC-COUPY 2**) showed a high cargo loading content, as determined by UV–vis spectroscopy, and a controlled particle size distribution of approximately 14 nm with a roughly round

https://doi.org/10.1021/acs.biomac.2c00361
Biomacromolecules 2022, 23, 2900−2913

shape according to DLS analysis and TEM micrographs, respectively. To our delight, the hydrophobic environment provided by the NCs around the cargo had a positive effect in some key photophysical properties for bioimaging applications. On the one hand, **COUPY 2**-loaded NCs showed a deep pink color owing to an intense absorption band centered around 555 nm, which was slightly redshifted with respect that of the free coumarin in H_2O. Similarly, the fluorescence quantum yield of **NC-COUPY 2** was higher than that of the nonencapsulated compound in H_2O. On the other hand, encapsulation had a clear positive effect on the photostability of the coumarin PS in PBS under green light irradiation. Singlet oxygen generation was slightly more efficient when the coumarin was encapsulated, thereby suggesting that nanoencapsulation in a hydrophobic environment has also a positive effect on type II PDT photochemical reactions, leading to the generation of singlet oxygen.

Confocal microscopy revealed that an enabled active transport was involved in the cellular internalization of the NCs and that the released **COUPY 2** accumulates preferentially in the mitochondria. Our in vitro evaluation analyses showed that nanoencapsulation of the coumarin PS decreased dark cytotoxicity and improved photoactivity with biologically compatible and highly penetrating red light, leading to higher PI values compared with the free compound (255 for **NC-COUPY 2** vs 30 for **COUPY 2**) in normoxia and micromolar efficacy under hypoxia. This reduction in dark cytotoxicity was also observed in normal dividing BGM cells. Importantly, a potent tumor growth inhibition effect against clinically relevant multicellular 3D tumorspheres was found upon red light irradiation. The high phototoxic profile of **NC-COUPY 2** can be explained by strong ROS photogeneration in both 2D and 3D cancer models. Along with mitochondrial photodamage, these ROS-generating PDT reactions triggered apoptotic cell death and mitochondrial degradation through autophagy. The fact that this mode of cell death was induced in a greater extent when nanoformulation **NC-COUPY 2** was applied compared with the free coumarin confirms the potential of polyurethane-polyurea hybrid NCs in the development of novel nanoPDT agents. Work is in progress in our laboratory to explore the encapsulation of NIR PSs to explore clinical applications.

■ ASSOCIATED CONTENT

Supporting Information

The Supporting Information is available free of charge at https://pubs.acs.org/doi/10.1021/acs.biomac.2c00361.

General methods and analytical techniques. Detailed procedures for the synthesis and characterization (IR, DLS, TEM, Z-potential, UV−vis and fluorescence spectroscopy, and photostability) of coumarin-loaded NCs. Additional figures and tables for their biological evaluation (confocal microscopy, antiproliferative activity in 2D monolayer cells and in 3D multicellular spheroids, mitochondrial potential assessment, apoptosis induction, autophagy detection, cell metabolism measurements, and cell cycle distribution) (PDF)

■ AUTHOR INFORMATION

Corresponding Authors

José Ruiz − *Departamento de Química Inorgánica, Universidad de Murcia, Institute for Bio-Health Research of Murcia (IMIB-Arrixaca), E-30071 Murcia, Spain;* orcid.org/0000-0002-0834-337X; Email: jruiz@um.es

Vicente Marchán − *Departament de Química Inorgànica i Orgànica, Secció de Química Orgànica, Institut de Biomedicina de la Universitat de Barcelona (IBUB), Universitat de Barcelona (UB), E-08028 Barcelona, Spain;* orcid.org/0000-0002-1905-2156; Email: vmarchan@ub.edu

Authors

Joaquín Bonelli − *Departament de Química Inorgànica i Orgànica, Secció de Química Orgànica, Institut de Biomedicina de la Universitat de Barcelona (IBUB), Universitat de Barcelona (UB), E-08028 Barcelona, Spain; Nanobiotechnological Polymers Division, Ecopol Tech, S.L., L'Arboç del Penedès 43720 Tarragona, Spain*

Enrique Ortega-Forte − *Departamento de Química Inorgánica, Universidad de Murcia, Institute for Bio-Health Research of Murcia (IMIB-Arrixaca), E-30071 Murcia, Spain*

Anna Rovira − *Departament de Química Inorgànica i Orgànica, Secció de Química Orgànica, Institut de Biomedicina de la Universitat de Barcelona (IBUB), Universitat de Barcelona (UB), E-08028 Barcelona, Spain*

Manel Bosch − *Unitat de Microscòpia Òptica Avançada, Centres Científics i Tecnològics (CCiTUB), Universitat de Barcelona (UB), E-08028 Barcelona, Spain;* orcid.org/0000-0001-5870-6346

Oriol Torres − *Nanobiotechnological Polymers Division, Ecopol Tech, S.L., L'Arboç del Penedès 43720 Tarragona, Spain*

Cristina Cuscó − *Nanobiotechnological Polymers Division, Ecopol Tech, S.L., L'Arboç del Penedès 43720 Tarragona, Spain*

Josep Rocas − *Nanobiotechnological Polymers Division, Ecopol Tech, S.L., L'Arboç del Penedès 43720 Tarragona, Spain*

Complete contact information is available at: https://pubs.acs.org/10.1021/acs.biomac.2c00361

Author Contributions

J.B., E.O.-F., J.R., J.R., and V.M. conceived the study. J.B., C.C., and O.T. synthesized and characterized NCs. J.B. and A.R. carried out photophysical and photochemical studies. J.B., A.R., and M.B. performed confocal microscopy studies. E.O.-F. designed and performed all biological experiments. J.B., E.O.-F., and V.M. wrote the manuscript, which was contributed by all authors, who have approved the submitted version of the manuscript. J.B. and E.O.-F. contributed equally to this work.

Notes

The authors declare no competing financial interest.

■ ACKNOWLEDGMENTS

This work was supported by funds from the Spanish Ministerio de Ciencia e Innovación-Agencia Estatal de Investigación (MCI/AEI/10.13039/501100011033) and FEDER funds (Projects CTQ2017-84779-R, RTI2018-096891-B-I00 and PID2020-117508RB-I00), the Generalitat de Catalunya (2017 DI 072) and Fundación Séneca-Región de Murcia (Project 20857/PI/18). E.O.-F. thanks AECC (PRDMU19003ORTE). A.R. was a recipient fellow of the University of Barcelona.

https://doi.org/10.1021/acs.biomac.2c00361
Biomacromolecules 2022, 23, 2900−2913

REFERENCES

(1) (a) Zheng, Q.; Juette, M. F.; Jockusch, S.; Wasserman, M. R.; Zhou, Z.; Altmana, R. B.; Blanchard, S. C. Ultra-stable organic fluorophores for single-molecule research. *Chem. Soc. Rev.* **2014**, *43*, 1044−1056. (b) Zheng, Q.; Lavis, L. D. Development of photostable fluorophores for molecular imaging. *Curr. Opin. Chem. Biol.* **2017**, *39*, 32−38. (c) Freidus, L. G.; Pradeep, P.; Kumar, P.; Choonara, Y. E.; Pillay, V. Alternative fluorophores designed for advanced molecular imaging. *Drug Discovery Today* **2018**, *23*, 115−133. (d) Colas, K.; Doloczki, S.; Urrutia, M. P.; Dyrager, C. Prevalent bioimaging scaffolds: Synthesis, photophysical properties and applications. *Eur. J. Org. Chem.* **2021**, 2133−2144.

(2) (a) Yun, S. H.; Kwok, S. J. J. Light in diagnosis, therapy and surgery. *Nat. Biomed. Eng.* **2017**, *1*, No. 0008. (b) Mari, C.; Pierroz, V.; Ferrari, S.; Gasser, G. Combination of Ru(II) complexes and light: new frontiers in cancer therapy. *Chem. Sci.* **2015**, *6*, 2660−2686. (c) Zhou, Z.; Song, J.; Nie, L.; Chen, X. Reactive oxygen species generating systems meeting challenges of photodynamic cancer therapy. *Chem. Soc. Rev.* **2016**, *45*, 6597−6626.

(3) Wiehe, A.; O'Brien, J. M.; Senge, M. O. Trends and targets in antiviral phototherapy. *Photochem. Photobiol. Sci.* **2019**, *18*, 2565−2612.

(4) (a) Rodriguez-Amigo, B.; Planas, O.; Bresoli-Obach, R.; Torra, J.; Ruiz-Gonzalez, R.; Nonell, S. Photosensitisers for photodynamic therapy: state of the art and perspectives. *Compr. Ser. Photochem. Photobiol. Sci.* **2016**, *15*, 25−64. (b) Abrahamse, H.; Hamblin, M. R. New photosensitizers for photodynamic therapy. *Biochem. J.* **2016**, *473*, 347−364. (c) Feng, G.; Zhang, G.-Q.; Ding, D. Design of superior phototheranostic agents guided by Jablonski diagrams. *Chem. Soc. Rev.* **2020**, *49*, 8179−8234. (d) Gao, Z.; Li, C.; Shen, J.; Dingy, D. Organic optical agents for image-guided combined cancer therapy. *Biomed. Mater.* **2021**, *16*, No. 042009.

(5) (a) Ormond, A. B.; Freeman, H. S. Dye Sensitizers for Photodynamic Therapy. *Materials* **2013**, *6*, 817−840. (b) Zhao, X.; Liu, J.; Fan, J.; Chao, H.; Peng, Z. Recent progress in photosensitizers for overcoming the challenges of photodynamic therapy: from molecular design to application. *Chem. Soc. Rev.* **2021**, *50*, 4185−4219.

(6) Li, X.; Kwon, N.; Guo, T.; Liu, Z.; Yoon, J. Innovative Strategies for Hypoxic-Tumor Photodynamic Therapy. *Angew. Chem., Int. Ed.* **2018**, *57*, 11522−11531.

(7) Chen, C.; Ou, H.; Liu, R.; Ding, D. Regulating the Photophysical Property of Organic/Polymer Optical Agents for Promoted Cancer Phototheranostics. *Adv. Mater.* **2020**, *32*, No. 1806331.

(8) (a) Navarro, J. R. G.; Lerouge, F.; Cepraga, C.; Micouin, G.; Favier, A.; Chateau, D.; Charreyre, M.-T.; Lanoe, P.-H.; Monnereau, C.; Chaput, F.; Marotte, S.; Leverrier, Y.; Marvel, J.; Kamada, K.; Andraud, C.; Baldeck, P. L.; Parola, S. Nanocarriers with ultrahigh chromophore loading for fluorescence bio-imaging and photodynamic therapy. *Biomaterials* **2013**, *34*, 8344−8351. (b) Bhaumik, J.; Mittal, A. K.; Banerjee, A.; Chisti, Y.; Banerjee, U. C. Applications of phototheranostic nanoagents in photodynamic therapy. *Nano Res.* **2015**, *8*, 1373−1394. (c) Lucky, S. S.; Soo, K. C.; Zhang, Y. Nanoparticles in Photodynamic Therapy. *Chem. Rev.* **2015**, *115*, 1990−2042. (d) Cai, Y.; Si, W.; Huang, W.; Chen, P.; Shao, J.; Dong, X. Organic dye-based nanoparticles for cancer phototheranostics. *Small* **2018**, *14*, No. 1704247. (e) Beauté, L.; McClenaghan, N.; Lecommandoux, S. Photo-triggered polymer nanomedicines: From molecular mechanisms to therapeutic applications. *Adv. Drug Delivery Rev.* **2019**, *138*, 148−166. (f) Fang, F.; Li, M.; Zhang, J.; Lee, C.-S. *ACS Mater. Lett.* **2020**, *2*, 531−549. (g) Gao, D.; Guo, X.; Zhang, X.; Chen, S.; Wang, Y.; Chen, T.; Huang, G.; Gao, Y.; Tian, Z.; Yang, Z. Multifunctional phototheranostic nanomedicine for cancer imaging and treatment. *Mater. Today Bio* **2020**, *5*, No. 100035. (h) Deng, X.; Shao, Z.; Zhao, Y. Solutions to the drawbacks of photothermal and photodynamic cancer therapy. *Adv. Sci.* **2021**, *8*, No. 2002504.

(9) Wu, Y.; Jiao, L.; Song, F.; Chen, M.; Liu, D.; Yang, W.; Sun, Y.; Hong, G.; Liu, L.; Peng, X. Achieving long-lived thermally activated delayed fluorescence in the atmospheric aqueous environment by nano-encapsulation. *Chem. Commun.* **2019**, *55*, 14522−14525.

(10) Albertazzi, L.; Brondi, M.; Pavan, G. M.; Sato, S. S.; Signore, G.; Storti, B.; Ratto, G. M.; Beltram, F. Dendrimer-Based Fluorescent Indicators: In Vitro and In Vivo Applications. *PLoS One* **2011**, *6*, No. e28450.

(11) Shemesh, C. S.; Hardy, C. W.; Yu, D. S.; Fernandez, B.; Zhang, H. Indocyanine green loaded liposome nanocarriers for photodynamic therapy using human triple negative breast cancer cells. *Photodiagn. Photodyn. Ther.* **2014**, *11*, 193−203.

(12) De Oliveira, H.; Thevenot, J.; Lecommandoux, S. Smart polymersomes for therapy and diagnosis: fast progress toward multifunctional biomimetic nanomedicines. *Nanomed. Nanobiotechnol.* **2012**, *4*, 525−546.

(13) (a) Jiang, S.; Xiao, M.; Sun, W.; Crespy, D.; Mailänder, V.; Peng, X.; Fan, J.; Landfester, K. Synergistic Anticancer Therapy by Ovalbumin Encapsulation-Enabled Tandem Reactive Oxygen Species Generation. *Angew. Chem., Int. Ed.* **2020**, *59*, 20008−20016. (b) Sun, B.; Chang, R.; Cao, S.; Yuan, C.; Zhao, L.; Yang, H.; Li, J.; Yan, X.; van Hest, J. C. M. Acid-Activatable Transmorphic Peptide-Based Nanomaterials for Photodynamic Therapy. *Angew. Chem., Int. Ed.* **2020**, *59*, 20582−20588.

(14) (a) Ding, M.; Zeng, Z.; He, X.; Li, J.; Tan, H.; Fu, Q. Cell Internalizable and Intracellularly Degradable Cationic Polyurethane Micelles as a Potential Platform for Efficient Imaging and Drug Delivery. *Biomacromolecules* **2014**, *15*, 2896−2906. (b) Li, K.; Liu, B. Polymer-encapsulated organic nanoparticles for fluorescence and photoacoustic imaging. *Chem. Soc. Rev.* **2014**, *43*, 6570−6597. (c) Conte, C.; Maiolino, S.; Pellosi, D. S.; Miro, A.; Ungaro, F.; Quaglia, F. Polymeric Nanoparticles for Cancer Photodynamic Therapy. *Top. Curr. Chem.* **2016**, *370*, 61−112. (d) Yang, Y.; Hou, W.; Liu, S.; Sun, K.; Li, M.; Wu, C. Biodegradable Polymer Nanoparticles for Photodynamic Therapy by Bioluminescence Resonance Energy Transfer. *Biomacromolecules* **2018**, *19*, 201−208.

(15) Chen, J.; Wu, W.; Zhang, F.; Zhang, J.; Liu, H.; Zheng, J.; Guo, S.; Zhang, J. Graphene quantum dots in photodynamic therapy. *Nanoscale Adv.* **2020**, *2*, 4961−4967.

(16) (a) Morral-Ruíz, G.; Melgar-Lesmes, P.; García, M. L.; Solans, C.; García-Celma, M. J. Design of biocompatible surface-modified polyurethane and polyurea nanoparticles. *Polymer* **2012**, *53*, 6072−6080. (b) Hood, M. A.; Paiphansiri, U.; Schaeffel, D.; Koynov, K.; Kappl, M.; Landfester, K.; Muñoz-Espí, R. Hybrid Poly(urethane−urea)/Silica NCs with pH-Sensitive Gateways. *Chem. Mater.* **2015**, *27*, 4311−4318. (c) Phoungtawee, P.; Crespy, D. Shining a new light on the structure of polyurea/polyurethane materials. *Polym. Chem.* **2021**, *12*, 3893−3899. (d) Rosenbauer, E.-M.; Wagner, M.; Musyanovych, A.; Landfester, K. Controlled Release from Polyurethane NCs via pH-UV-Light- or Temperature-Induced Stimuli. *Macromolecules* **2010**, *43*, 5083−5093.

(17) Teilmann, A. C.; Falkenberg, M. K.; Hau, J.; Abelson, K. S. P. Comparison of silicone and polyurethane catheters for the catheterization of small vessels in mice. *Lab. Anim.* **2014**, *43*, 397−403.

(18) Jin, L.; Yao, L.; Yuan, F.; Dai, G.; Xue, B. Evaluation of a novel biodegradable ureteral stent produced from polyurethane and magnesium alloys. *J. Biomed. Mater. Res.* **2021**, *109*, 665−672.

(19) Rocas, J.; Rocas, P. Method for the production of a microencapsulate, and corresponding reactive amphiphilic compound, microencapsulate and composition. WO2014114838A2, 2014.

(20) Flórez-Graua, G.; Rocas, P.; Cabezón, R.; España, C.; Panés, J.; Rocas, J.; Albericio, F.; Benítez-Ribas, D. Nanoencapsulated budesonide in self-stratified polyurethane-polyurea nanoparticles is highly effective in inducing human tolerogenic dendritic cells. *Int. J. Pharm.* **2016**, *511*, 785−793.

(21) Rocas, P.; Hoyos-Nogués, M.; Rocas, J.; Manero, J. M.; Gil, J.; Albericio, F.; Mas-Moruno, C. Installing Multifunctionality on Titanium with RGD Decorated Polyurethane-Polyurea Roxithromycin Loaded Nanoparticles: Toward New Osseointegrative Therapies. *Adv. Healthcare Mater.* **2015**, *4*, 1956−1960.

https://doi.org/10.1021/acs.biomac.2c00361
Biomacromolecules 2022, 23, 2900−2913

(22) Ruiz-Esparza, G. U.; Flores-Arredondo, J. H.; Segura-Ibarra, V.; Torre-Amione, G.; Ferrari, M.; Blanco, E.; Serda, R. E. The physiology of cardiovascular disease and innovative liposomal platforms for therapy. *Int. J. Nanomed.* **2013**, *8*, 629−640.
(23) Erra Díaz, F.; Dantas, E.; Geffner, J. Unravelling the Interplay between Extracellular Acidosis and Immune Cells. *Mediators Inflamm.* **2018**, No. 1218297.
(24) Damgaci, S.; Ibrahim-Hashim, A.; Enriquez-Navas, P. M.; Pilon-Thomas, S.; Guvenis, A.; Gillies, R. J. Hypoxia and acidosis: immune suppressors and therapeutic targets. *Immunology* **2018**, *154*, 354−362.
(25) Cuscó, C.; Garcia, J.; Nicolás, E.; Rocas, P.; Rocas, J. Multisensitive drug-loaded polyurethane/polyurea NCs with pH-synchronized shell cationization and redox-triggered release. *Polym. Chem.* **2016**, *7*, 6457−6466.
(26) Rocas, P.; Cuscó, C.; Rocas, J.; Albericio, F. On the importance of polyurethane and polyurea nanosystems for future drug delivery. *Curr. Drug Delivery* **2018**, *15*, 37−43.
(27) Bonelli, J.; Ortega-Forte, E.; Vigueras, G.; Bosch, M.; Cutillas, N.; Rocas, J.; Ruiz, J.; Marchán, V. Polyurethane-polyurea hybrid NCs as efficient delivery systems of anticancer Ir(III) metallodrugs. *Inorg. Chem. Front.* **2022**, *9*, 2123−2138.
(28) Pérez-Hernández, M.; Cuscó, C.; Benítez-García, C.; Bonelli, J.; Nuevo-Fonoll, M.; Soriano, A.; Martínez-García, D.; Arias-Betancur, A.; García-Valverde, M.; Segura, M. F.; Quesada, R.; Rocas, J.; Soto-Cerrato, V.; Pérez-Tomás, R. Multi-Smart and Scalable Bioligands-Free Nanomedical Platform for Intratumorally Targeted Tambjamine Delivery, a Difficult to Administrate Highly Cytotoxic Drug. *Biomedicines* **2021**, *9*, 508.
(29) (a) Gandioso, A.; Bresolí-Obach, R.; Nin-Hill, A.; Bosch, M.; Palau, M.; Galindo, A.; Contreras, S.; Rovira, A.; Rovira, C.; Nonell, S.; Marchán, V. Redesigning the Coumarin Scaffold into Small Bright Fluorophores with Far-Red to Near-Infrared Emission and Large Stokes Shifts Useful for Cell Imaging. *J. Org. Chem.* **2018**, *83*, 1185−1195. (b) Gandioso, A.; Palau, M.; Bresolí-Obach, R.; Galindo, A.; Rovira, A.; Bosch, M.; Nonell, S.; Marchán, V. High Photostability in Nonconventional Coumarins with Far-Red/NIR Emission through Azetidinyl Substitution. *J. Org. Chem.* **2018**, *83*, 11519−11531. (c) Rovira, A.; Gandioso, A.; Goñalons, M.; Galindo, A.; Massaguer, A.; Bosch, M.; Marchán, V. Solid-Phase Approaches for Labeling Targeting Peptides with Far-Red Emitting Coumarin Fluorophores. *J. Org. Chem.* **2019**, *84*, 1808−1817.
(30) (a) Rovira, A.; Pujals, M.; Gandioso, A.; López-Corrales, M.; Bosch, M.; Marchán, V. Modulating Photostability and Mitochondria Selectivity in Far-Red/NIR Emitting Coumarin Fluorophores through Replacement of Pyridinium by Pyrimidinium. *J. Org. Chem.* **2020**, *85*, 6086−6097. (b) López-Corrales, M.; Rovira, A.; Gandioso, A.; Bosch, M.; Nonell, S.; Marchán, V. Transformation of COUPY Fluorophores into a Novel Class of Visible-Light-Cleavable Photolabile Protecting Groups. *Chem. − Eur. J.* **2020**, *26*, 16222−16227.
(31) Ortega-Forte, E.; Rovira, A.; Gandioso, A.; Bonelli, J.; Bosch, M.; Ruiz, J.; Marchán, V. COUPY Coumarins as Novel Mitochondria-Targeted Photodynamic Therapy Anticancer Agents. *J. Med. Chem.* **2021**, *64*, 17209−17220.
(32) (a) Adarsh, N.; Avirah, R. R.; Ramaiah, D. Tuning photosensitized singlet oxygen generation efficiency of novel aza-BODIPY dyes. *Org. Lett.* **2010**, *12*, 5720−5723. (b) Li, W.; Li, L.; Xiao, H.; Qi, R.; Huang, Y.; Xie, Z.; Jing, X.; Zhang, H. Iodo-BODIPY: a visible-light-driven, highly efficient and photostable metal-free organic photocatalyst. *RSC Adv.* **2013**, *3*, 13417−13421. (c) Lv, Z.; Wei, H.; Li, Q.; Su, X.; Liu, S.; Zhang, K. Y.; Lv, W.; Zhao, Q.; Li, X.; Huang, W. Achieving efficient photodynamic therapy underboth normoxia and hypoxia using cyclometalated Ru(II) photosensitizer through type I photochemicalprocess. *Chem. Sci.* **2018**, *9*, 502−512.
(33) Zhang, X.; Zhang, G. Q.; Zhu, J. Methylated unsymmetric BODIPY compounds: synthesis, high fluorescence quantum yield and long fluorescence time. *J. Fluoresc.* **2019**, *29*, 407−416.
(34) (a) Wilkinson, F. Quantum Yields for the Photosensitized Formation of the Lowest Electronically Excited Singlet State of Molecular Oxygen in Solution. *J. Phys. Chem. Ref. Data* **1993**, *22*, 113. (b) Lutkus, L. V.; Rickenbach, S. S.; McCormick, T. M. Singlet oxygen quantum yields determined by oxygen consumption. *J. Photochem. Photobiol., A* **2019**, *378*, 131−135.
(35) Schindelin, J.; Arganda-Carreras, I.; Frise, E.; Kaynig, V.; Longair, M.; Pietzsch, T.; Preibisch, S.; Rueden, C.; Saalfeld, S.; Schmid, B.; Tinevez, J.-Y.; White, D. J.; Hartenstein, V.; Eliceiri, K.; Tomancak, P.; Cardona, A. Fiji: An Open-Source Platform for Biological-Image Analysis. *Nat. Methods* **2012**, *9*, 676−682.
(36) Munafó, D. B.; Colombo, M. I. A novel assay to study autophagy: regulation of autophagosome vacuole size by amino acid deprivation. *J. Cell Sci.* **2001**, *114*, 3619−3629.
(37) Park, D.; Jeong, H.; Lee, M. N.; Koh, A.; Kwon, O.; Yang, Y. R.; Noh, J.; Suh, P.-G.; Park, H.; Ryu, S. H. Resveratrol induces autophagy by directly inhibiting mTOR through ATP competition. *Sci. Rep.* **2016**, *6*, 21772.
(38) Li, S.-D.; Huang, L. Nanoparticles evading the reticuloendothelial system: Role of the supported bilayer. *Biochim. Biophys. Acta* **2009**, *1788*, 2259−2266.
(39) (a) Tessaro, A. L.; Fraix, A.; Failla, M.; Cardile, V.; Graziano, A. C. E.; Estevao, B. M.; Rescifina, A.; Sortino, S. Light-controlled simultaneous "on demand" released of cytotoxic combinations for bimodal killing of cancer cells. *Chem. − Eur. J.* **2018**, *24*, 7664−7670. (b) Wicki, A.; Witzigmann, D.; Balasubramanian, V.; Huwyler, J. Nanomedicine in cancer therapy: challenges, opportunities, and clinical applications. *J. Controlled Release* **2015**, *200*, 138−157.
(40) Chauhan, V. P.; Stylianopoulos, T.; Martin, J. D.; Popović, Z.; Chen, O.; Kamoun, W. S.; Bawendi, M. G.; Fukumura, D.; Jain, R. K. Normalization of tumour blood vessels improves the delivery of nanomedicines in a size-dependent manner. *Nat. Nanotechnol.* **2012**, *7*, 383−388.
(41) (a) Latorre, A.; Somoza, A. Glutathione-Triggered Drug Release from Nanostructures. *Curr. Top. Med. Chem.* **2014**, *14*, 2662−2671. (b) Kennedy, L.; Sandhu, J. K.; Harper, M. E.; Cuperlovic-Culf, M. Role of Glutathione in Cancer: From Mechanisms to Therapies. *Biomolecules* **2020**, *10*, 1429.
(42) Liu, X.; Hajnóczky, G. Altered Fusion Dynamics Underlie Unique Morphological Changes in Mitochondria during Hypoxia−Reoxygenation Stress. *Cell Death Differ.* **2011**, *18*, 1561−1572.
(43) Friedrich, J.; Seidel, C.; Ebner, R.; Kunz-Schughart, L. A. Spheroid-based drug screen: considerations and practical approach. *Nat. Protoc.* **2009**, *4*, 309−324.
(44) Criddle, D. N.; Gillies, S.; Baumgartner-Wilson, H. K.; Jaffar, M.; Chinje, E. C.; Passmore, S.; Chvanov, M.; Barrow, S.; Gerasimenko, O. V.; Tepikin, A. V.; Sutton, R.; Petersen, O. H. Menadione-induced Reactive Oxygen Species Generation via Redox Cycling Promotes Apoptosis of Murine Pancreatic Acinar Cells. *J. Biol. Chem.* **2006**, *281*, 40485−40492.
(45) Cairns, R. A.; Harris, I. S.; Mak, T. W. Regulation of cancer cell metabolism. *Nat. Rev. Cancer* **2011**, *11*, 85−95.

https://doi.org/10.1021/acs.biomac.2c00361
Biomacromolecules 2022, 23, 2900−2913

SUPPORTING INFORMATION

Improving PDT anticancer activity of a mitochondria-targeted coumarin photosensitizer using a polyurethane-polyurea hybrid nanocarrier

Joaquín Bonelli,[1,2,#] Enrique Ortega-Forte,[3,#] Anna Rovira,[1] Manel Bosch,[4] Oriol Torres,[2] Cristina Cuscó,[2] Josep Rocas,[2] José Ruiz,[3,*] Vicente Marchán[1,*]

[1] Departament de Química Inorgànica i Orgànica, Secció de Química Orgànica, IBUB, Universitat de Barcelona (UB), E-08028 Barcelona, Spain. Email: vmarchan@ub.edu

[2] Nanobiotechnological Polymers Division, Ecopol Tech, S.L., El Foix Business Park, Indústria 7, 43720 L'Arboç del Penedès, Tarragona, Spain

[3] Departamento de Química Inorgánica, Universidad de Murcia, and Institute for Bio-Health Research of Murcia (IMIB-Arrixaca), E-30071 Murcia, Spain. Email: jruiz@um.es

[4] Unitat de Microscòpia Òptica Avançada, Centres Científics i Tecnològics (CCiTUB), Universitat de Barcelona (UB), E-08028 Barcelona (Spain)

# These authors contributed equally

Table of contents

1. Materials

1.1. Building blocks and crosslinkers

Isophorone diisocyanate (IPDI) was purchased from Quimidroga (Barcelona, Spain), YMER N-120 was kindly supplied by Perstorp (Malmö, Sweden) and Genamin TAP 100D (1,3-diamino-*N*-octadecylpropane) was provided by Clariant (Barcelona, Spain). Jeffcat DPA (*N*-(3-dimethylaminopropyl)-*N*,*N´*-diisopropanolamine), DEDS (2-hydroxyethyl disulfide), DETA (diethylene triamine) and L-lysine hydrochloride were purchased from Sigma Aldrich (St Louis, USA).

1.2. Encapsulated coumarins

COUPY dyes **1** and **2** were synthesized as previously described.[1] Neobee 1053 (caprilyc/capric triglyceride or GTCC) was purchased from Stepan Company (Illinois, United States).

1.3. Solvents and auxiliary solutions

Milli-Q water was obtained from a Merck Millipore purification system (Madrid, Spain) and PBS, HCl 37% and NaOH in pellets were purchased from Merck (Madrid, Spain).

1.4. Biological agents, mediums, and supplements

L-Glutathione (GSH) and its oxidized derivative (GSSG) were acquired from TCI Chemicals (Tokyo, Japan). Dulbecco's Modification of Eagle's Medium (DMEM) was purchased from Corning (Arizona, USA) and DMEM with low glucose, pyruvate and without glutamine and Phenol Red were purchased from Thermo Fischer Scientific (Massachusetts, USA), as well as Fetal Bovine Serum (FBS), Horse serum, Hoescht 33342 solution, and Mytotracker Green (MTG). L-glutamine solution (200 mM), F12 (HAM) media and 100 U mL^{-1} penicillin/100 μg mL^{-1} streptomycin were acquired from Biological Industries (Cromwell, USA). Hepes buffer (1M) was purchased from Lonza (Basel, Switzerland). Insulin, Hydrocortisone and Epidermal Growth Factor (EGF) were acquired from Sigma-Aldrich (St Louis, USA). Choleric toxin was purchased from Calbiochem (San Diego, CA, USA).

2. Analytical techniques

2.1. Infrared spectroscopy (IR)

IR spectra were performed in a Smart ATR (Nicolet iS10, Thermo Scientific, Raleigh, USA) using a transmittance mode (16 scans) and OMNIC software. For the monitoring of solvent-based samples, one drop was deposited onto the diamond crystal and the solvent was left to dry by evaporation. IR spectra were recorded from a dry film of the sample for the reaction control after emulsification.

2.2. pH measurements

The pH of the emulsion was determined right after the crosslinker was added and at different time intervals until the last polyaddition reaction was complete. All the determinations were carried out in a pH-meter HI 2211 pH/ORP-Meter (HANNA Instruments, Eibar, Spain) equipped with a pH electrode Crison 5029 (Crison Instruments, Barcelona, Spain) and a temperature probe.

2.3. Dynamic light scattering (DLS)

The size distribution of the NCs was analyzed on a Zetasizer Nano-ZS90 (Malvern, Worcestershire, UK) in Milli-Q water at 25 °C at a concentration of 0.5 mg/mL.

2.4. Transmission electron microscopy (TEM)

The morphology of nanocapsules was studied on a TEM Jeol J1010 (Peabody, MA, USA) equipped with a CCD Orius camera (Gatan). A 400-mesh copper grid coated with 0.75 % FORMVAR was deposited on 6 μL of a suspension of nanocapsules in water (10 mg mL−1) for 25 min. Excess of sample was removed by oblique contact with Whatman filter paper and the grid was deposited on a drop of uranyl acetate (2 % w/w) in water for 30 s. Excess uranyl acetate was removed and the grid was air-dried for at least 3 h prior to measurement.

2.5. High resolution transmission electron microscopy (HR-TEM)

HR-TEM observations were performed in a JEOL J2100 microscope (Peabody, MA, USA), operating at an accelerating voltage of 120 kV. Images were recorded using a Gatan Orius CCD camera. A 200-mesh copper grid coated with 0.75% FORMVAR was deposited on 6 μL of a suspension of nanocapsules in water (10 mg mL−1) for 1 min. Excess of sample was removed by contact with ultrapure water for 1 min and the grid was deposited on a drop of uranyl acetate (2% w/w) in water for 1 min. Excess uranyl acetate was removed and the grid was air-dried for at least 3 h prior to measurement.

2.6. Zeta potential (Z-pot)

The Z-pot of the NCs was analyzed on a Zetasizer Nano-ZS90 (Malvern, Worcestershire, UK) in Milli-Q water at 25 °C at a concentration of 1 mg/mL, measured at different pH values.

2.7. Dialysis purification

The NCs were dialyzed against Milli-Q water for 24 h using a Spectra/Por molecular porous membrane tubing with a 12–14 kDa molecular weight cut-off (MWCO) (Spectrum Laboratories, Rancho Dominguez, USA).

2.8. Determination of cargo loading by UV-vis spectroscopy

The coumarin loading (or drug-loading, DL) of the NCs was determined by UV-Vis measurements performed in a DINKO UV-6900 spectrophotometer (Dinko Instruments, Barcelona, Spain). First, a calibration curve was developed by preparing a range of standard solutions containing the coumarin at different concentrations and analyzing their UV profile and maximum absorbance. Then, Encapsulation Efficiency EE (%) and Dye Loading DL (%) were calculated from the following equations:

$$\%\, EE = \frac{amount\ of\ COUPY\ compound\ incorporated\ in\ the\ nanocapsule}{total\ amount\ of\ COUPY\ compound\ added\ in\ the\ synthesis} * 100 \quad (1)$$

$$\%\, DL = \frac{amount\ of\ COUPY\ compound\ incorporated\ in\ the\ nanocapsule}{total\ amount\ of\ dried\ nanocapsules} * 100 \quad (2)$$

To determine the amount of coumarin incorporated in the NCs, a desired amount of dried NCs (previously dialyzed) was dissolved in an exact volume of solvent and the measurement was calculated from the calibration curve. Non-loaded NCs were used as the reference. All measurements were recorded at the desired wavelength range, depending on the maximum of absorption of the molecule under study and assayed in triplicates.

2.9. Solids concentration

NCs concentration in the aqueous dispersion was determined by triplicate leading to dryness using a Digitheat-TFT oven (J.P.Selecta, Barcelona, Spain), with a fixed temperature of 40 ºC for 48 h.

3. Synthetic procedures

3.1. Synthesis of redox-responsive amphiphilic cationic prepolymer (P1)

2,2´-Dihydroxyethyl disulfide (901.0 mg, 11.68 meq), YMER N-120 (12.04 g, 23.18 meq) and *N*-(3-dimethylaminopropyl)-*N*,*N*´-diisopropanolamine (981.3 mg, 8.99 meq) were added into a three-necked round-bottom flask equipped with mechanical stirring at room temperature and purged with N_2. When the mixture was homogeneous, isophorone diisocyanate (8.14 g, 73.24 meq) was added into the reaction vessel under gentle mechanical stirring. The polyaddition reaction was kept under these conditions until the NCO stretching band intensity did not change, monitored by IR spectroscopy. At this point, dry THF (21 mL) was added into the reaction mixture to fluidify the polymer. In parallel, 1,3-diamino-*N*-octadecylpropane (5.99 g, 35.45 meq) was dissolved with dry THF (5.23 mL) into another 100 mL three-necked round-bottom flask, which had previously been purged with N_2. The former reaction mixture was added dropwise onto the latter under half-moon 100 rpm mechanical stirring. The reaction was monitored by IR until the NCO stretching band intensity had completely disappeared.

3.2. Synthesis of COUPY 1-loaded amphoteric redox responsive NCs (NC-COUPY 1)

Isophorone diisocyanate (69.9 mg, 0.63 meq) was added into a three-necked round bottom flask equipped with mechanical stirring, purged with N_2 and protected from light. In parallel, COUPY **1** (3.1 mg, 8.06 µmol), Neobee 1053 (14.6 mg, 35.73 µmol), polymer **P1** (655.1 mg, 0.07 meq) and dry THF (0.25 mL) were mixed in a vial, added into the flask and homogenized for 10 min at 150 rpm, protected from light. At this point, an alkaline aqueous solution of L-lysine was prepared by dissolving 0.93 g L-lysine in 11.37 g of Milli-Q water and adjusting pH to 11.0 with alkaline NaOH solutions at 3 M and 1 M (total L-lysine concentration 7.56% by wt). This solution (22.84 mg of L-lysine, 0.27 meq) was added at 250 rpm and the polyaddition reaction was checked after 15 min by IR. Then, the organic phase was emulsified at 300 rpm with cold Milli-Q water (10.11 g) and finally a 10% w/w aqueous solution of diethylenetriamine (9.43 mg, 0.27 meq) was added in order to generate crosslinked NCs from the nano micelles. The stirring was reduced to 100 rpm. This polyaddition reaction was monitored by IR and pH measurements. Once the NCs were formed, THF was removed from the reactor at 35 °C under vacuum and the dialysis purification was carried out using a molecular porous membrane tubing with a 12–14 kDa MWCO. After dialyzing for 24 h, water acquired a pink color, as shown in Figure S1, which indicated that the coumarin was partially released from the NCs.

Figure S1. Photographic image of the dialysis process of **NC-COUPY 1** after 24 h.

3.3. Synthesis of COUPY 2-loaded amphoteric and redox responsive NCs (NC-COUPY 2)

Isophorone diisocyanate (71.1 mg, 0.64 meq) was added into a three-necked round-bottom flask equipped with mechanical stirring, purged with N_2 and protected from light. In parallel, COUPY **2** (5.4 mg, 10.89 μmol), Neobee 1053 (24.5 mg, 59.96 μmol), polymer **P1** (877.1 mg, 0.09 meq) and dry THF (0.5 mL) were mixed in a vial, added into the flask and homogenized for 10 min at 150 rpm, protected from light. At this point, an alkaline aqueous solution of L-lysine was prepared by dissolving 0.93 g L-lysine in 11.37 g of Milli-Q water and adjusting pH to 11.0 with alkaline NaOH solutions at 3 M and 1 M (total L-lysine concentration 7.56% by wt). This solution (23.74 mg of L-lysine, 0.28 meq) was added at 250 rpm and the polyaddition reaction was checked after 15 min by IR. Then, the organic phase was emulsified at 300 rpm with cold Milli-Q water (6.70 g) and finally a 10% w/w aqueous solution of diethylenetriamine (7.63 mg, 0.22 meq) was added in order to generate crosslinked NCs from the nano micelles. The stirring was reduced to 100 rpm. This polyaddition reaction was monitored by IR and pH measurements. Once the NCs were formed, THF was removed from the reactor at 35 °C under vacuum and the dialysis purification was carried out for 24 h using a molecular porous membrane tubing with a 12–14 kDa MWCO. As shown in Figure S2, water did not acquire any color, indicating that COUPY **2** was retained inside the NCs during the dialysis purification (compare with Figure S1).

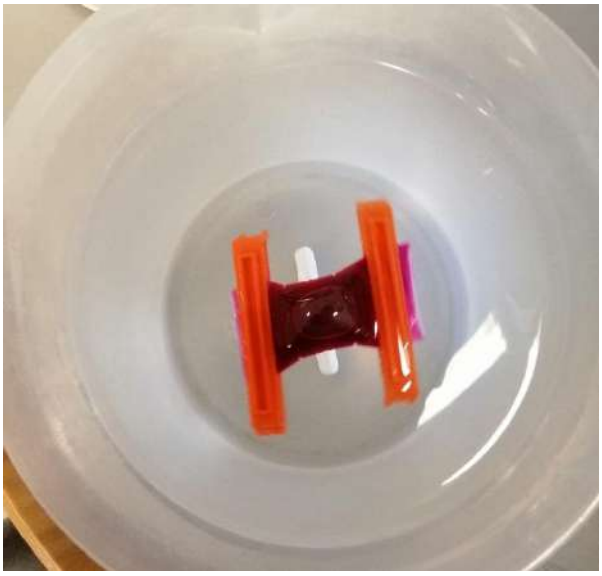

Figure S2. Photographic image of the dialysis process of **NC-COUPY2** after 24 h.

3.4. Synthesis of non-loaded amphoteric and redox responsive NCs (NC-GTCC)

The procedure was based on the one used for the synthesis of redox responsive COUPY **2**-loaded amphoteric NCs (see section 3.3) with the exception that no coumarin was added to the reaction. The exact amounts of the reagents are detailed in Table S1.

Table S1. Amounts of reagents used to prepare **NC-GTCC.**

Compound	Amount	Equivalents or mols
IPDI	69.7 mg	0.63 meq
Neobee 1053 (GTCC)	26.3 mg	56.61 □mol
Polymer (P1)	812.5 mg	0.09 meq
Dry THF	1 mL	–
L-lysine	20.9 mg	0.25 meq
Milli-Q water	5.93 g	–
DETA	7.8 mg	0.23 meq

4. Characterization of polymer P1 and NCs

4.1. Infrared Spectroscopy

The polymerization reaction was easily controlled by IR spectroscopy given that NCO group has a very clear and characteristic stretching band at 2280-2230 cm^{-1}.

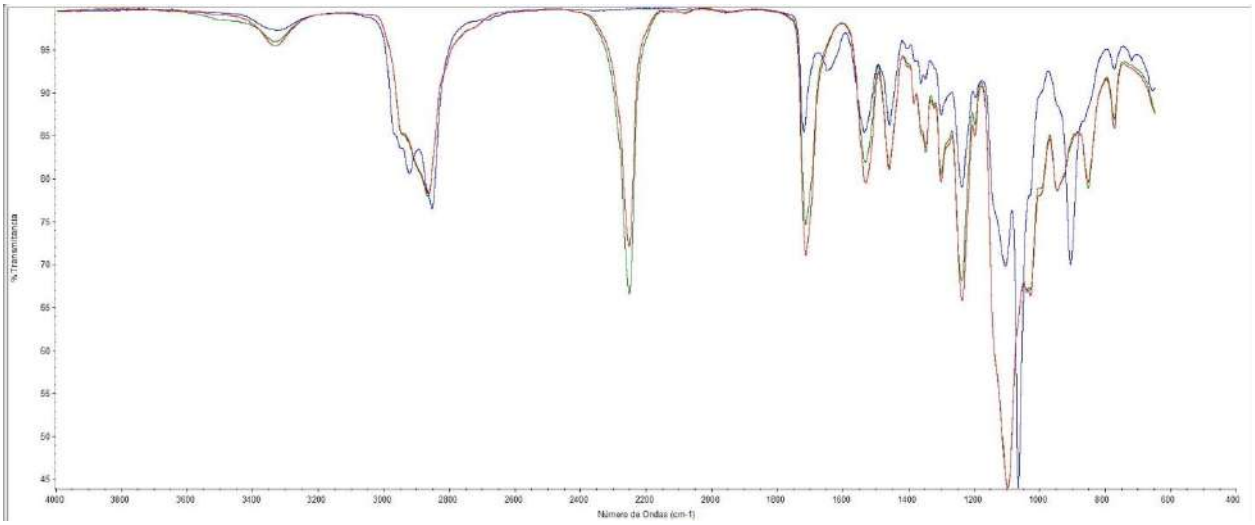

Figure S3. Consecutive IR spectra recorded during the synthesis of **P1**.

As shown in Figure S3, IR spectra of the polymer (**P1**) indicated a successful polymerization reaction between diols, the diamine and the diisocyanate, in both steps of the polymer synthesis. The green line corresponds to the first sample recorded, at the begin of the reaction. At that time, the NCO asymmetric stretching band at 2252 cm^{-1} was very sharp and intense. At the end of the first step, involving the reaction between the diols and the diisocyanate (red line), the intensity of the NCO stretching band decreased significantly. Meanwhile, the intensities of the CO stretching band at 1719 cm^{-1}, the CN stretching band at 1537 cm^{-1}, the NCOO/COC asymmetric stretching band at 1240 cm^{-1} increased. Overall, the IR spectra registered during the first step of the synthesis confirmed polyurethane bond formation along with NCO consumption. Once the diamine was added, during the second step of the polymer synthesis (blue line), the NCO stretching band at 2252 cm^{-1} disappeared instantaneously, which was explained by the high reactivity of the amines. Simultaneously, other characteristic bands appeared or changed, such as a new stretching band at 1634 cm^{-1}, which was associated to the carbonyl of urea bonds and a new wagging band at 908 cm^{-1} corresponding to the free secondary amine, which also confirmed polyurea formation.

The encapsulation process was also controlled by IR spectroscopy. As shown in Figure S4, IR spectra of the NCs (regardless their loading) indicated also a successful nanocapsule formation. The blue line in the IR spectra represents the sample 30 min after the polymer, together with the coumarin, was mixed with the diisocyanate. This initial step was the reactivation of the polymer and its conversion to an NCO-reactive entity. Afterwards, L-lysine sodium salt was added (purple line) and reacted with the activated polymer. A decrease on the intensity of the NCO stretching band at 2255 cm^{-1}, concomitantly with an increase of the carbonyl and CN stretching bands, confirmed urea formation (1642 cm^{-1} and 1532 cm^{-1}, respectively). Finally, the triamine was added (red line) and the NCO stretching band instantaneously disappeared and the urea-associated bands increased their intensity because of the rapid reaction between remaining NCO groups and this polyamine.

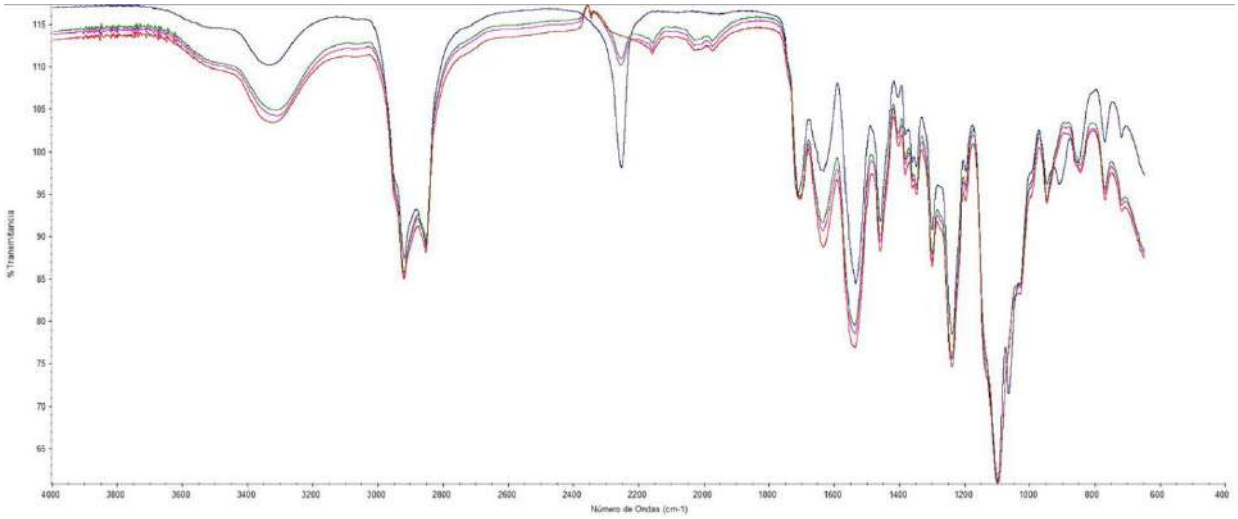

Figure S4. Consecutive IR spectra recorded during the encapsulation process with COUPY **2**.

4.2. COUPY loading

The concentration of NCs in the final emulsions (mg/mL) was quantified with a solids concentrator, as indicated in section 2.8. Dye Loading (DL) and Encapsulation Efficiency (EE) were determined by UV-Vis spectroscopy following the method described in section 2.7. The calibration plot for COUPY **2** is shown in Figure S8 and the DL and EE parameters for **NC-GTCC**, **NC-COUPY 1** and **NC-COUPY 2** are indicated in Table S3.

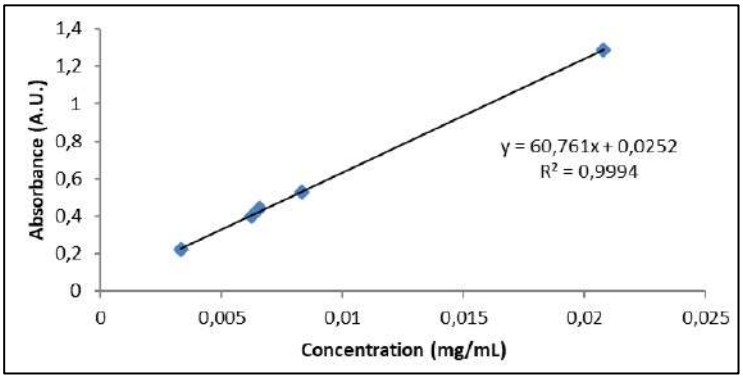

Figure S5. Calibration plot for COUPY **2**.

Table S2. DL and EE parameters for NCs.

	[NCs] (mg/mL)	**Dye Loading (DL, µM)**	**Encapsulation Efficiency (EE, %)**
NC-GTCC	34.57 ± 1.11	-	-
NC-COUPY-1	41.61 ± 3.63	Non detected	-
NC-COUPY-2	48.45 ± 1.08	1157.5 ± 14.0	91.2%

4.3. Average size of NCs by DLS

The particle size distribution of the NCs was measured by dynamic light scattering (DLS) (Figures S5 and S6 and Table S2).

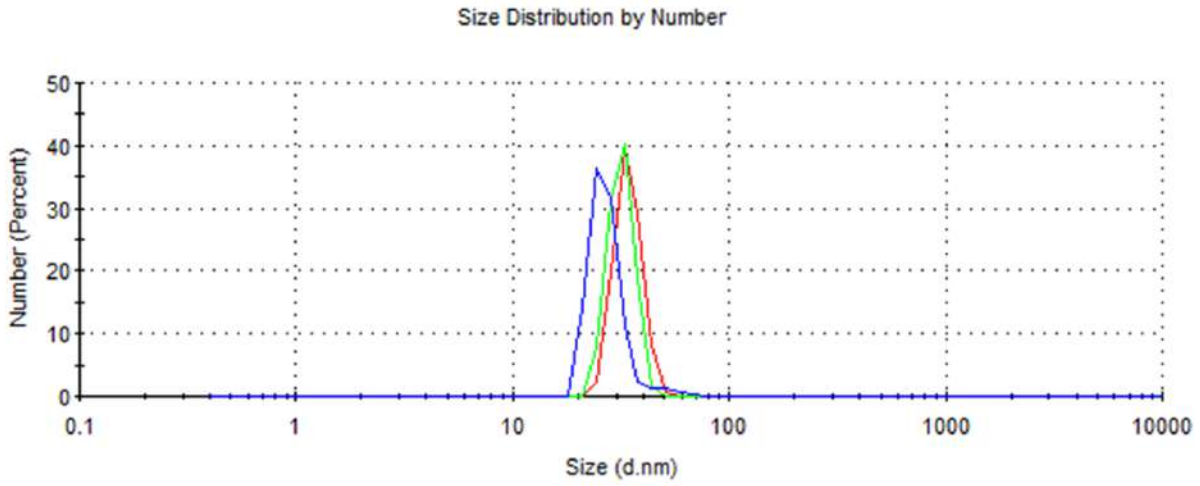

Figure S6. Hydrodynamic diameter distribution by number of **NC-COUPY 1**.

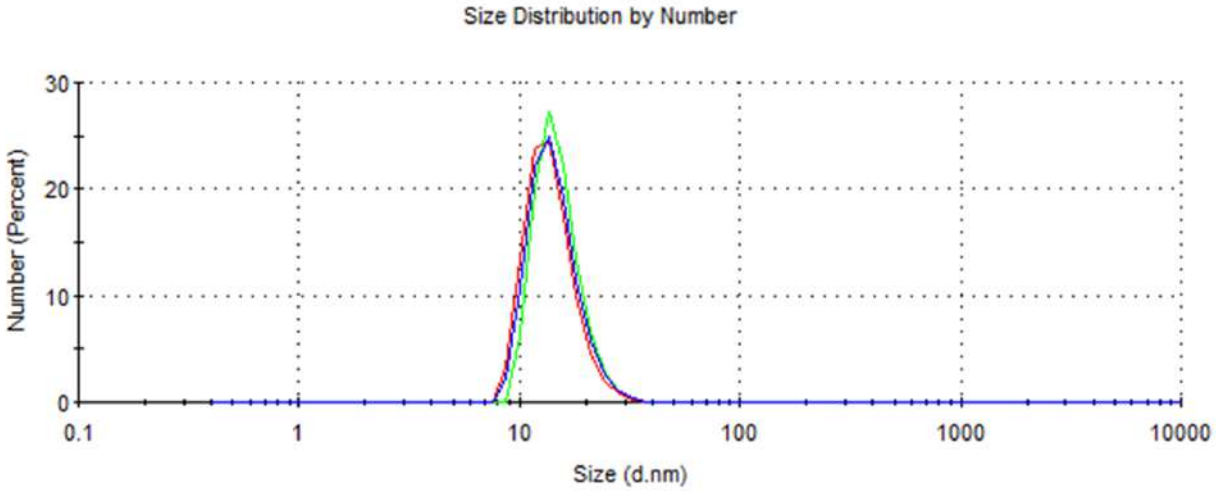

Figure S7. Hydrodynamic diameter distribution by number of **NC-COUPY 2**.

Table S3. Hydrodynamic diameter average of COUPY-loaded NCs.

	Experimental Values	Average ± SD
NC-COUPY 1	34.32 nm	31.21 ± 3.48 nm
	31.85 nm	
	27.45 nm	
NC-COUPY 2	14.04 nm	14.55 ± 0.53 nm
	15.09 nm	
	14.53 nm	

4.4. Transmission electron microscopy (TEM)

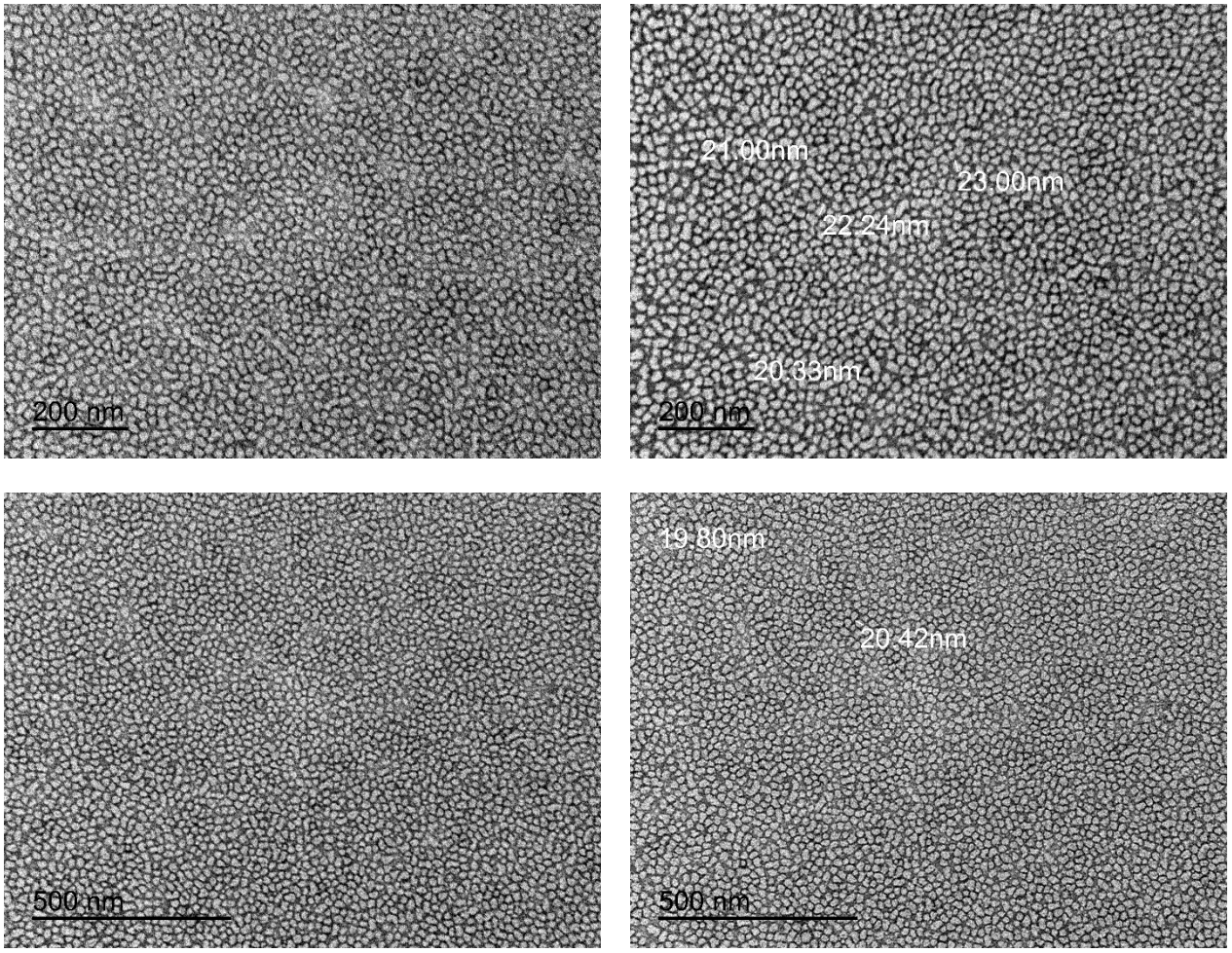

Figure S8. Selected TEM micrographs of **NC-COUPY 2** (scale bar: 200 nm and 500 nm).

4.5. High resolution transmission electron microscopy (HR-TEM)

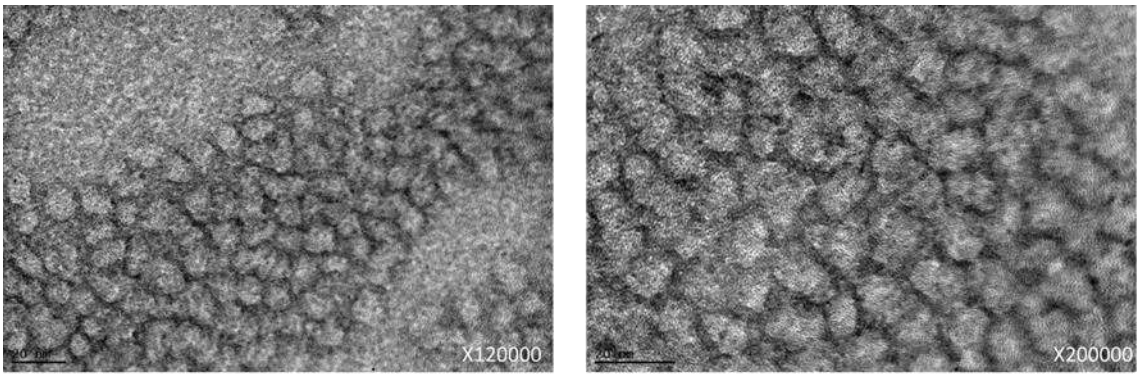

Figure S9. Selected HR-TEM images of **NC-COUPY 2** (scale bar: 20 nm) collected at x120000 and x200000 magnifications.

4.6. Stability of COUPY 2-loaded NCs under reducing conditions

The degradability of the nanocapsules in PBS supplemented with glutathione (GSH) (10 mM) was studied with the aim of reproducing the situation in the intracellular media of a cancer cell. As shown in Figure S10, incubation of **NC-COUPY 2** in GSH-supplemented PBS for 24 and 48 h at 37 ºC confirmed their degradation and the release of the coumarin PS as inferred with a dialysis methodology. Indeed, the concentration of **COUPY 2** in the dialyzed water, in the case of the PBS-incubated sample, reached a plateau after 24 h of incubation, while the concentration of the coumarin PS in the dialyzed water coming from the GSH-supplemented PBS incubation sample continued increasing over the time.

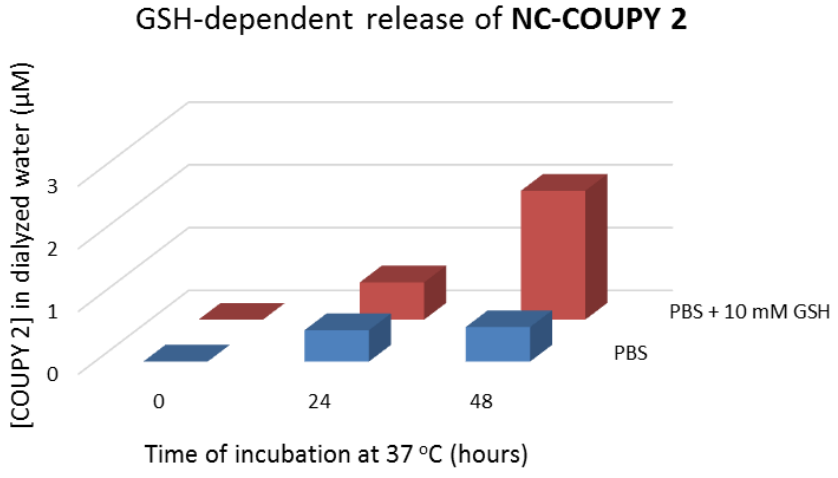

Figure S10. Concentration of **COUPY 2** in the dialyzed water of **NC-COUPY 2** in PBS and in PBS supplemented with glutathione at t = 0 and after incubation for 24 h and 48 h at 37 ºC.

4.7. Z-potential of NCs

As shown in Figure S9, the Z-potential values (surface charge) of the NCs were determined at different pH values as described in section 2.5.

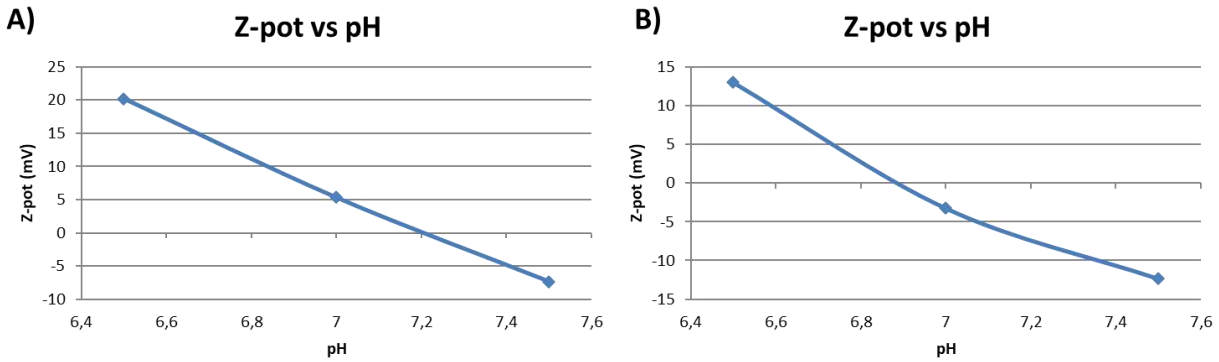

Figure S11 Z-pot analysis of A) **NCs-COUPY 1** and B) **NCs-COUPY 2** vs pH media

5. Photophysical characterization

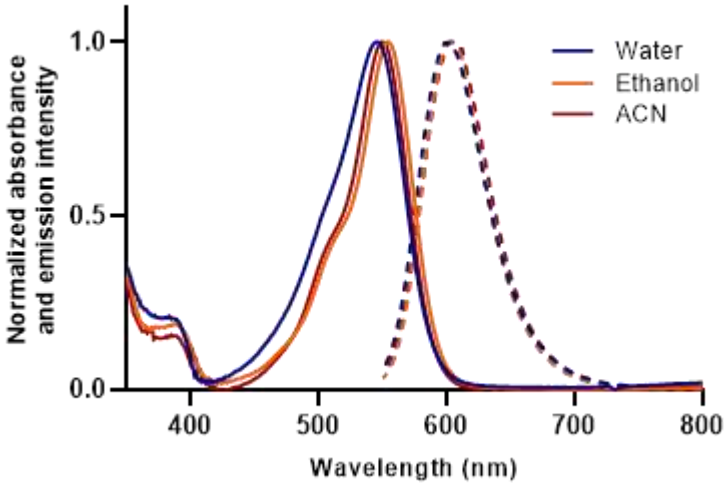

Figure S12. Comparison of the normalized absorption (solid lines) and fluorescence (dotted lines) spectra of **COUPY 2** in H_2O, ethanol and ACN.

Table S4. Photophysical data of **COUPY 2** and of **NC-COUPY-2**.

Compound	Solvent	λ_{abs} [nm][a]	λ_{em} [nm][b]	Stokes' shift [nm][c]	Φ_F[d]
COUPY 2	H_2O	545	602	57	0.20
	Ethanol	554	604	50	0.47
	ACN	550	604	54	0.33
NC-COUPY-2	H_2O	550	600	50	0.36

[a] Wavelength of the absorption maximum. [b] Wavelength of the emission maximum upon excitation at a wavelength 20 nm below λ_{abs}. [c] Stokes' shift. [d] Fluorescence quantum yields (Φ_F) were measured by a comparative method using cresyl violet in ethanol ($\Phi_{F;Ref} = 0.54$) as a reference.

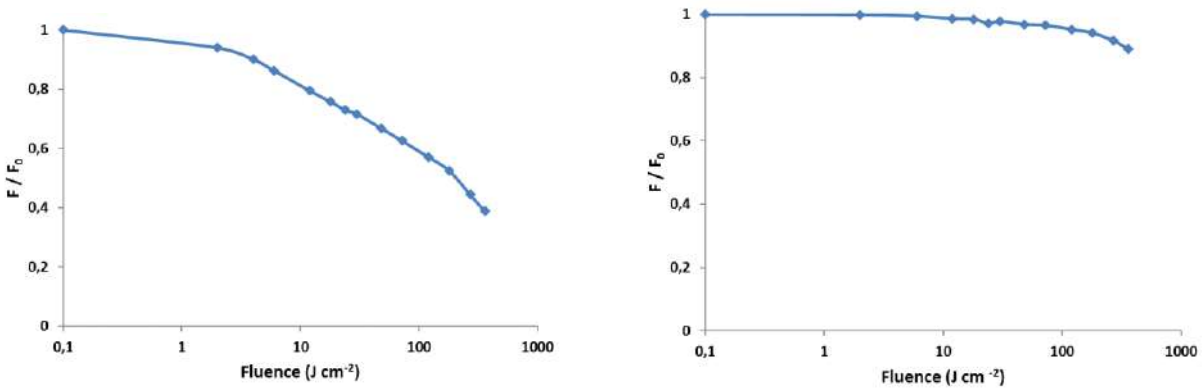

Figure S13. Photostability of **COUPY 2** (left) and **NC-COUPY 2** (right) after green LED irradiation at different times expressed as decay of fluorescence emission after subsequent irradiation times.

6- Singlet oxygen measurements

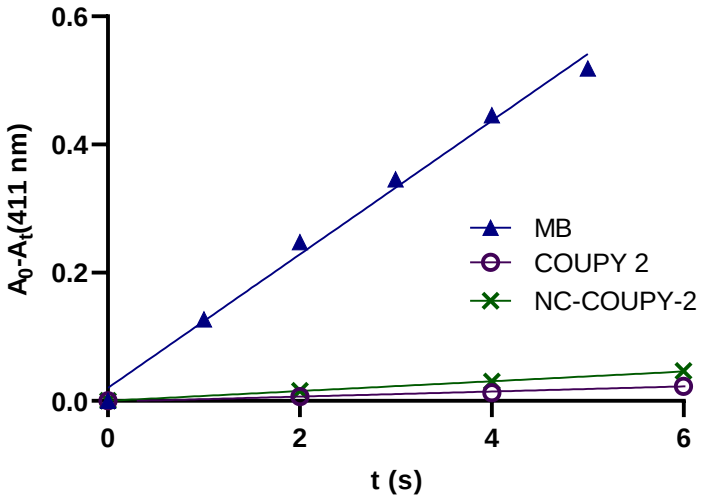

Figure S14. Plot of the changes in the absorbance (A_0-A_t) of DPBF at 411 nm against irradiation time in the presence of the standard photosensitizer methylene blue and the **COUPY 2** and **NC-COUPY 2** in aerated EtOH/H_2O 1:1 (v/v).

A) DPBF

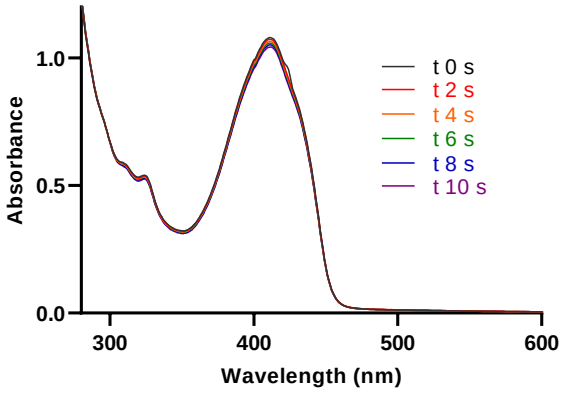

B) MB

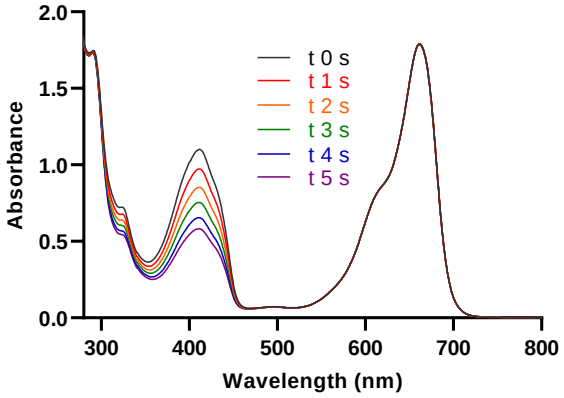

C) COUPY 2

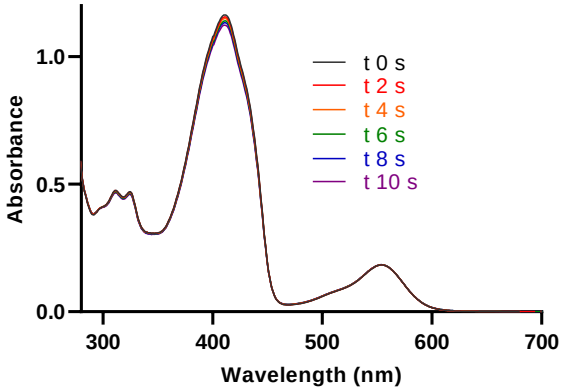

D) NC-COUPY-2

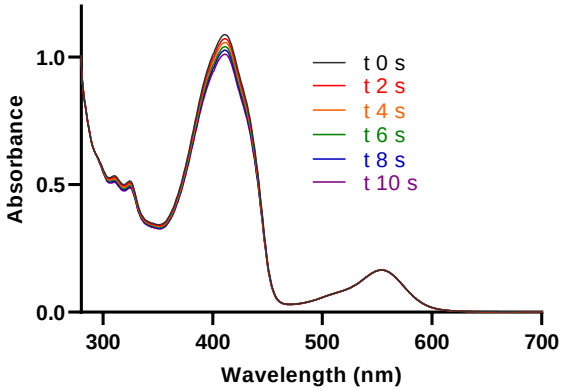

Figure S15 . Changes in the absorption spectra of DPBF resulting from the irradiation with green LED light in the absence (A) and in the presence of MB (B), **COUPY 2** (C) and **NC-COUPY 2** (D).

7. Fluorescence imaging by confocal microscopy

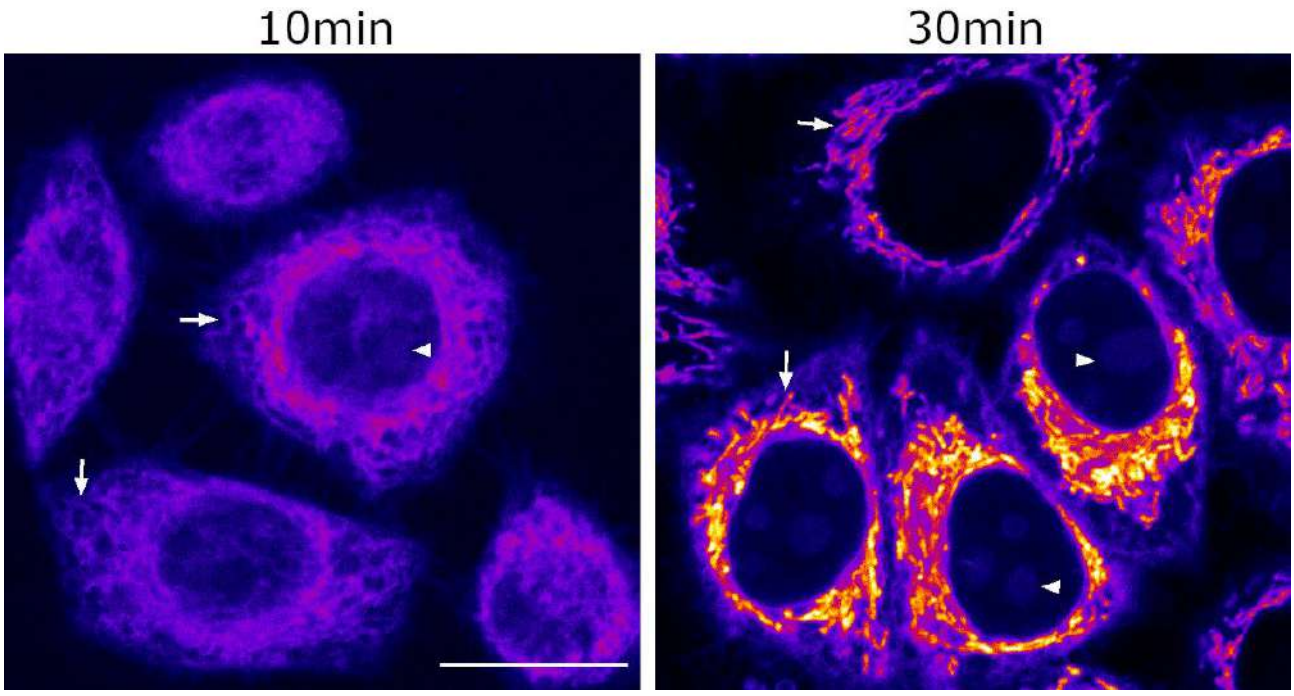

Figure S16. Cellular uptake of **NC-COUPY 2**. Single confocal planes of HeLa cells incubated with the NCs (1.0 μM, 37 °C; left. 10 min, right: 30 min). White arrows point out mitochondria and white arrowheads nucleoli staining. Scale bar: 20 μm.

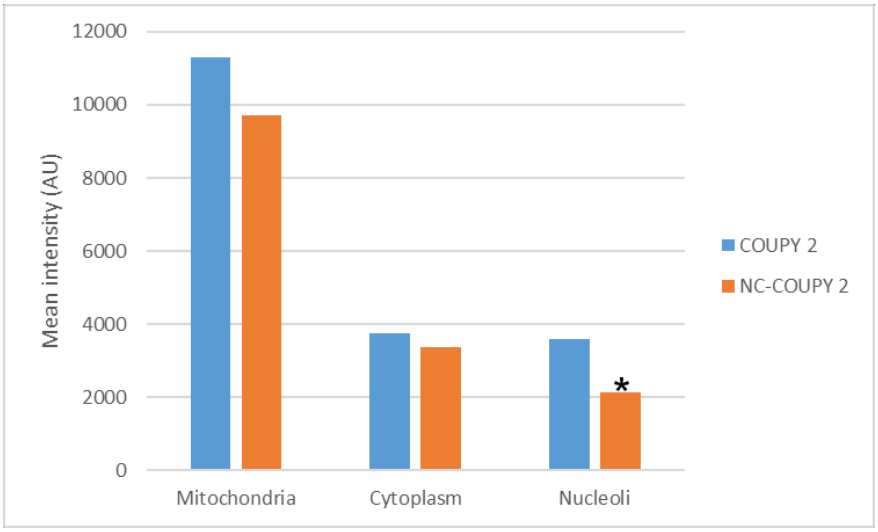

Figure S17. Mean intensity (Arbitrary Units) graph of **COUPY 2** and **NC-COUPY 2** at the mitochondria, cytoplasm and nucleoli after incubation with the compounds (1.0 μM, 37 °C, 30 min).

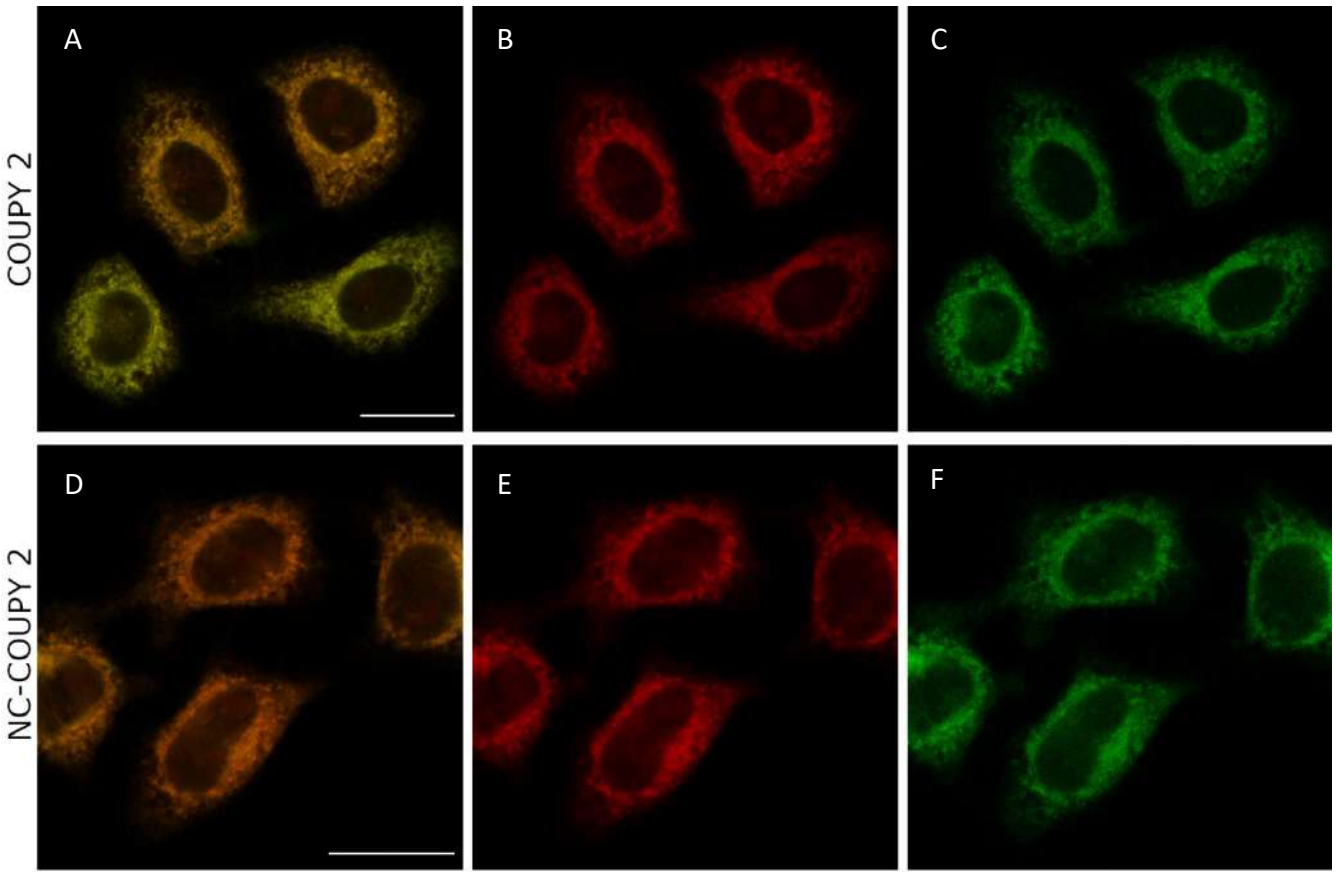

Figure S18. Co-localization studies with **COUPY 2** (top) and **NC-COUPY 2** (bottom) and Mitotracker Green FM. Single confocal plane of HeLa cells incubated with **COUPY 2** or **NC-COUPY 2** (1 μM, red) and Mitotracker Green FM (0.1 μM, green). A), D) Overlay of the two staining. B), E) **COUPY 2** and **NC-COUPY 2** signal, respectively. C), F) Mitotracker Green FM signal. Scale bar: 10 μm. All images are at the same scale as A.

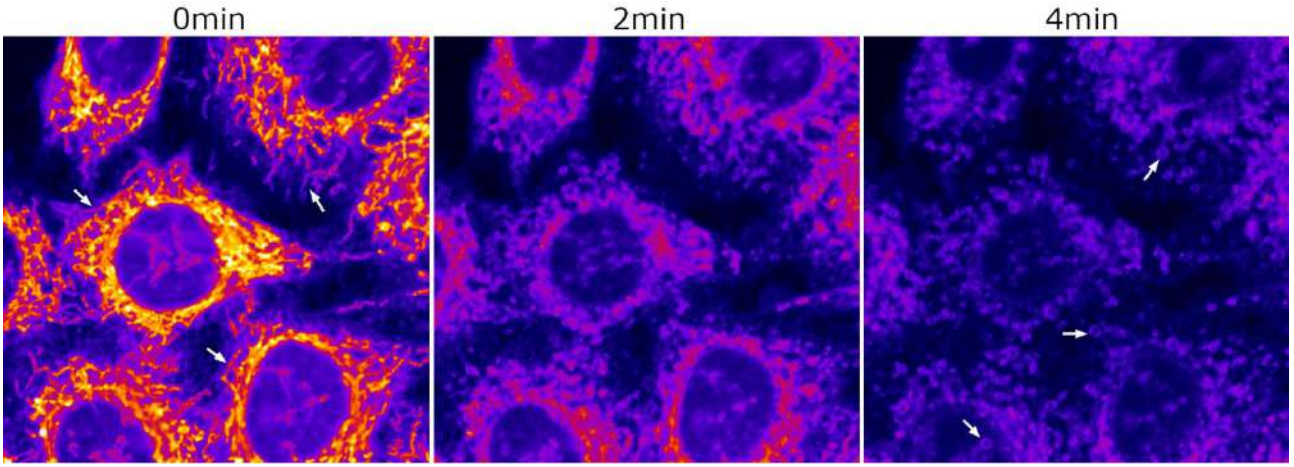

Figure S19. Cellular uptake of **NC-COUPY-2**. Single confocal planes at three different time points of image acquisition (left, t = 0; center, t = 2 min; right t = 4 min) are shown after incubation of HeLa cells with the NCs (1.0 μM) during 30 min at 37 ºC. White arrows point out mitochondria and donut-shaped mitochondria staining at t = 0 and 4 min, respectively. Scale bar: 20 μm.

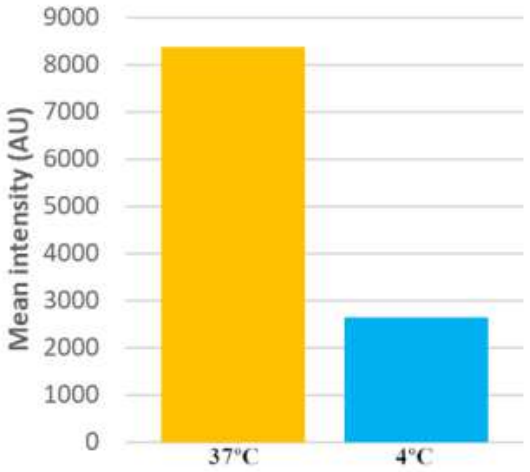

Figure S20. Mean intensity (Arbitrary Units) graph of **NC-COUPY 2** after incubation at 37 °C or 4 °C (1.0 μM, 30 min).

8. Biological studies

8.1. Photocytotoxicity evaluation in 2D monolayer cells

Table S1. Phototoxicity of the compounds towards HeLa cancer cells under normoxia upon red light irradiation expressed as mean IC_{50} values (µM) of three independent measurements.[a]

	Dark	Red light	PI [b]
COUPY 1	>200	18 ± 2	>5.5
COUPY 2	5.3 ± 0.3	0.76 ± 0.004	7.0
NC-COUPY 2	196 ± 15	1.8 ± 0.09	108.8

[a] Cells were treated for 1 h (0.5 h of incubation and 0.5 h of irradiation) followed by 48 h of incubation in drug-free medium. Dark analogues were directly kept in the dark for 1 h.

[b] PI=IC_{50} (non-irradiated cells; dark)/IC_{50} (irradiated cells; red light).

Table S2. Phototoxicity of the compounds towards HeLa cancer cells under normoxia (21% O_2) or hypoxia (2% O_2) upon visible light irradiation expressed as IC_{50} values (µM).[a]

		Dark	Light	PI [b]
COUPY 1	Normoxia	>200	14 ± 2	>14.2
	Hypoxia	>200	18.6 ± 0.9	>10.8
COUPY 2	Normoxia	5.7 ± 0.4	0.19 ± 0.03	30.0
	Hypoxia	19 ± 3	0.7 ± 0.1	27.2
NC-COUPY 2	Normoxia	199 ± 14	1.3 ± 0.4	153.1
	Hypoxia	178 ± 23	5.6 ± 0.9	31.7

[a] Cells were treated for 1.5 h (0.5 h of incubation and 1 h of visible irradiation with withe lamps) followed by 48 h of incubation in drug-free medium under normoxic or hypoxic conditions. Dark analogues were directly kept in the dark for 1.5 h.

[b] PI=IC_{50} (dark-non-irradiated cells)/IC_{50} (irradiated cells; white light).

8.2. Photocytotoxicity evaluation on 3D multicellular spheroids.

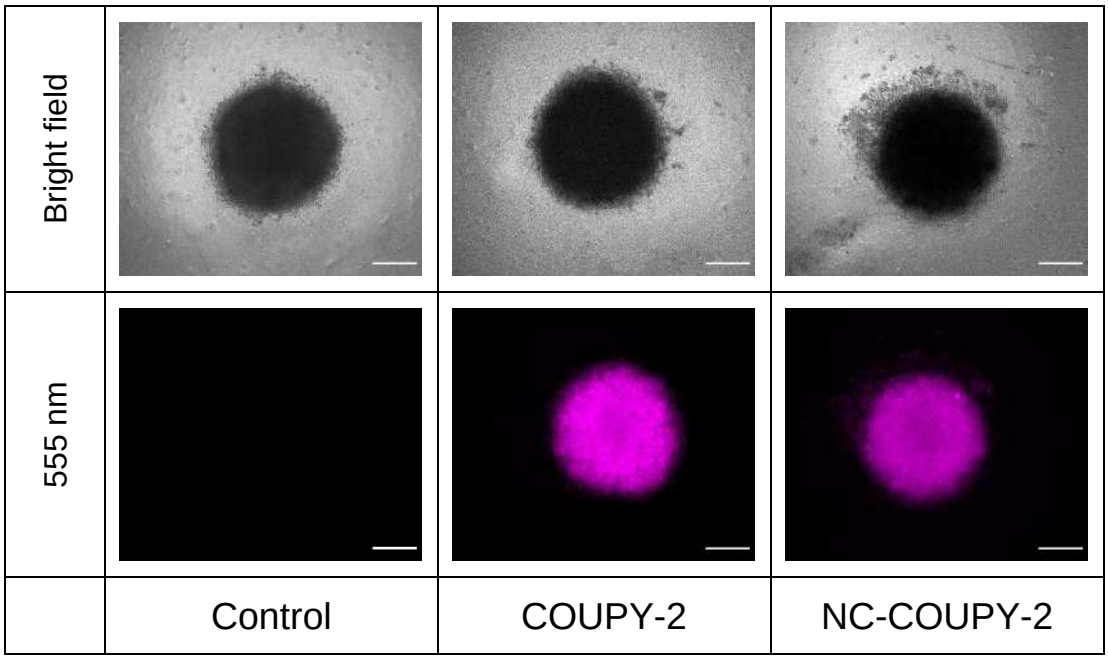

Figure S21. Fluorescence microscopy images of HeLa spheroids treated with **COUPY 2** and **NC-COUPY 2** at 2 μM for 6 h. Scale bar: 100 μm.

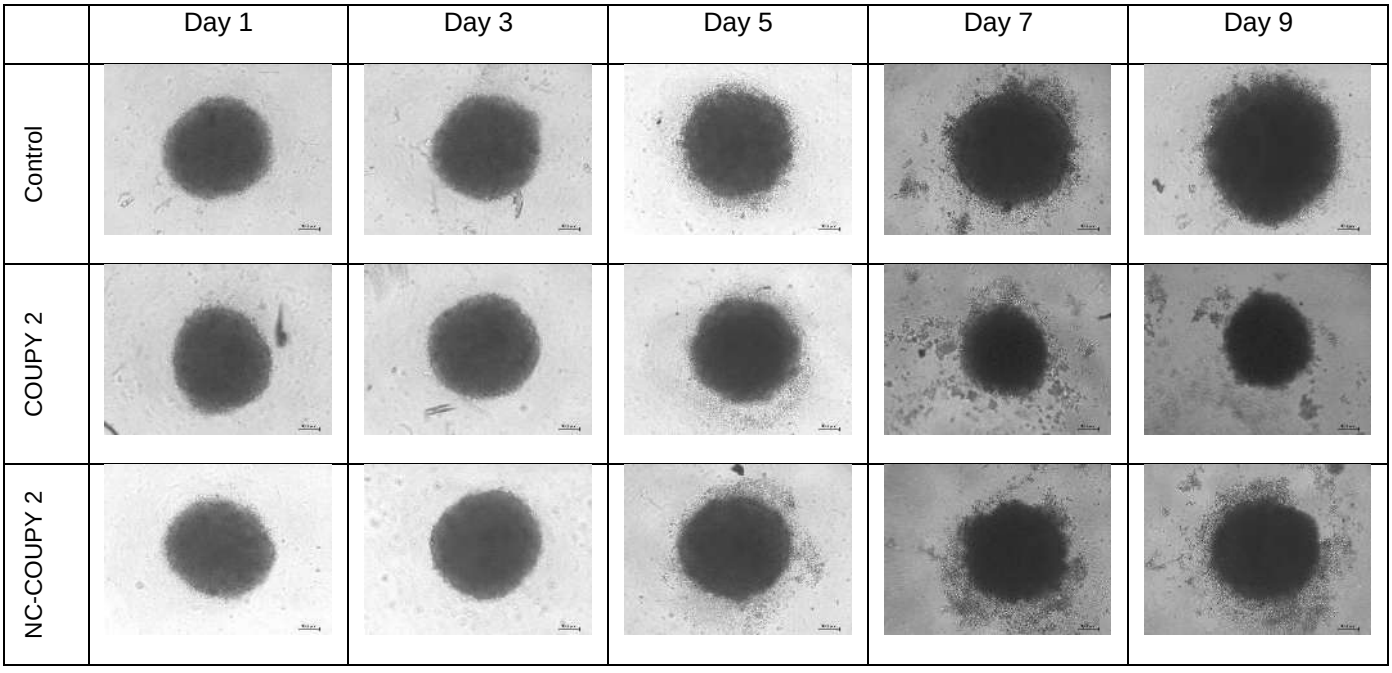

Figure S22. Representative microscopy images of HeLa spheroids after treatment with **COUPY 2** and **NC-COUPY 2** at 2 μM (6 h incubation + 0.5 h red light irradiation) on day 3. Scale bar: 100 μm.

8.3. Reactive oxygen species generation

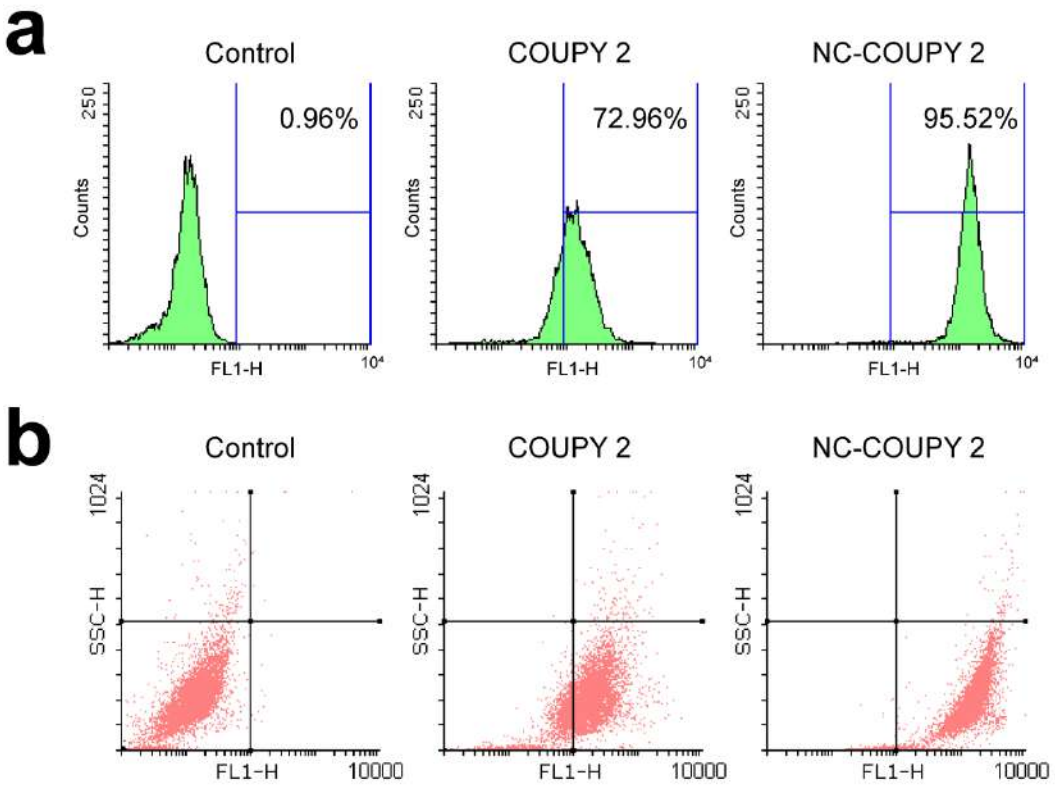

Figure S23. Flow cytometry analysis of ROS generation after phototreatments in HeLa cells. (**a**) Representative histograms of ROS generation as measured by DCF intensity (FL1-H) upon treatment with **COUPY 2** and **NC-COUPY 2** at 2 µM after irradiation (gated region corresponding to DCF+ cells). (**b**) Cell internal complexity (SSC-H) vs. DCF fluorescence (FL1-H) analysis of HeLa cells after phototreatment with **COUPY 2** and **NC-COUPY 2** at 2 µM.

8.4. Mitochondrial membrane potential assessment

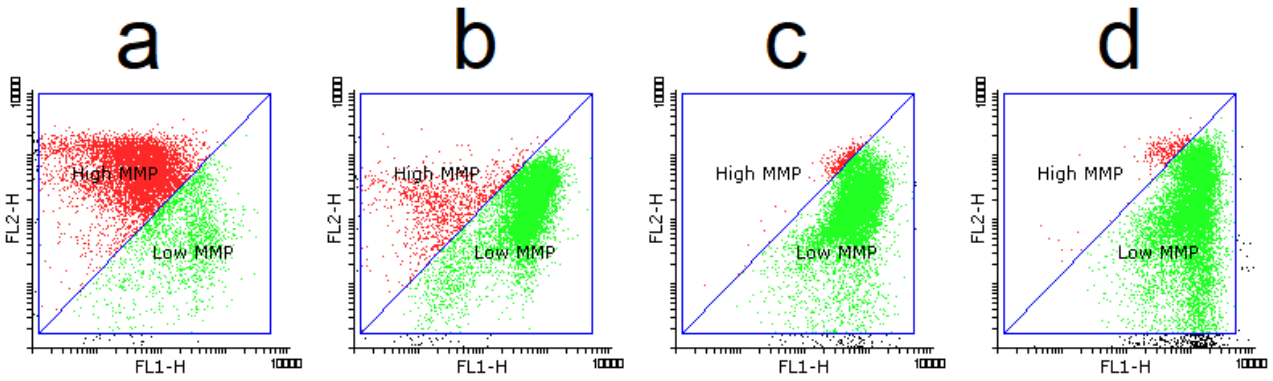

Figure S24. Evaluation of mitochondrial membrane potential (MMP). Representative flow cytometry dot plots of HeLa cells stained with JC-1 dye after visible light irradiation treatments with **COUPY 2** (c) or **NC-COUPY 2** (d) at IC_{50} concentrations. Control cells (a) served as negative control, whereas 50 µM CCCP (b) was used as positive control. Green JC-1 monomers (low MMP) detected in FL1-H channel and red JC-1 aggregates (high MMP) in FL2-H ($\lambda_{exc}/\lambda_{em}$ = 488/530 and 620 nm respectively).

8.5. Apoptosis induction

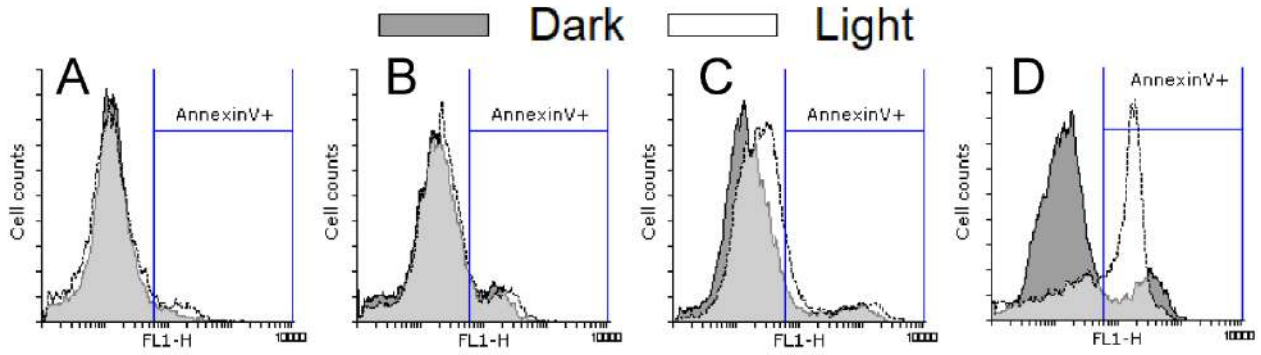

Figure S25. Representative flow cytometry histograms of HeLa cells stained with Annexin V-FITC after irradiation treatments with after visible light irradiation treatments with **COUPY 2** (C) or **NC-COUPY 2** (D) at IC_{50} concentrations. Control cells (A) served as negative control, whereas 20 µM cisplatin (B) was used as positive control. Annexin V+ populations detected in FL1-H ($\lambda_{exc}/\lambda_{em}$ = 488/530 nm).

8.6. Autophagy detection

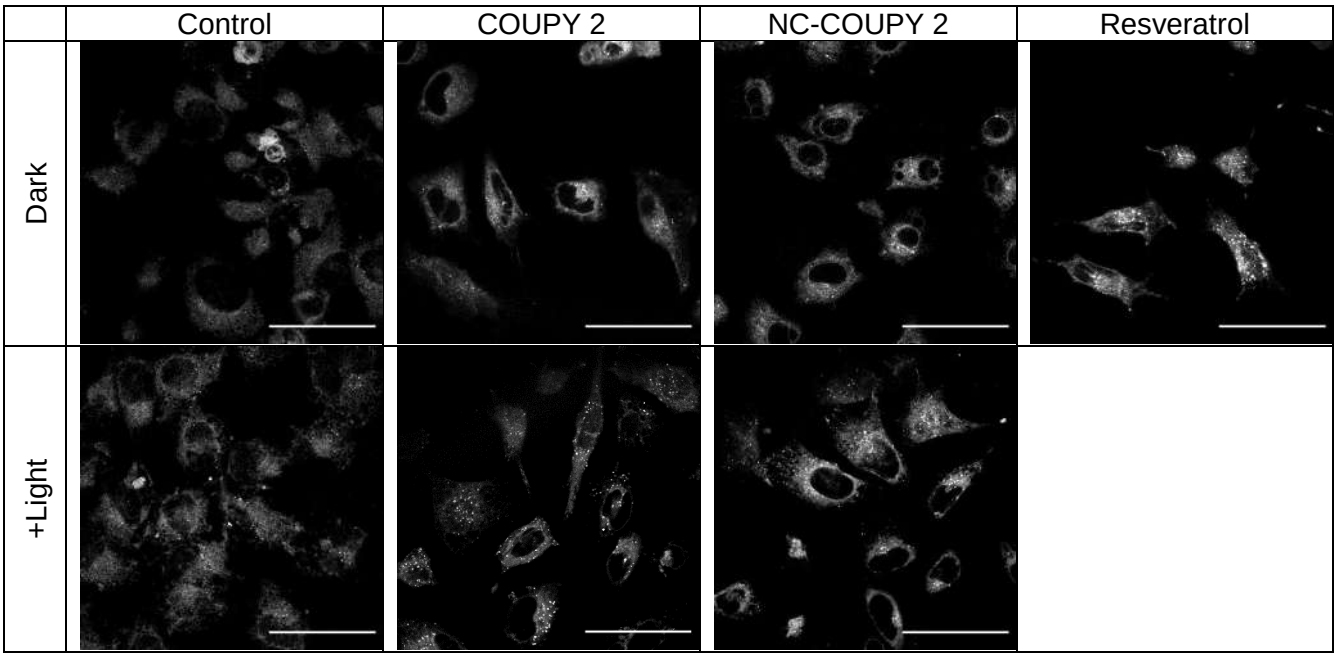

Figure S26. Autophagy detection in HeLa cells by confocal microscopy using monodansylcadaverine (MDC) staining after visible light irradiation treatments with **COUPY** 2 and **NC-COUPY 2** at IC_{50} concentrations. Resveratrol (50 µM) was used as a positive control. Scale bar: 50 µm.

8.7. Cell metabolism measurements.

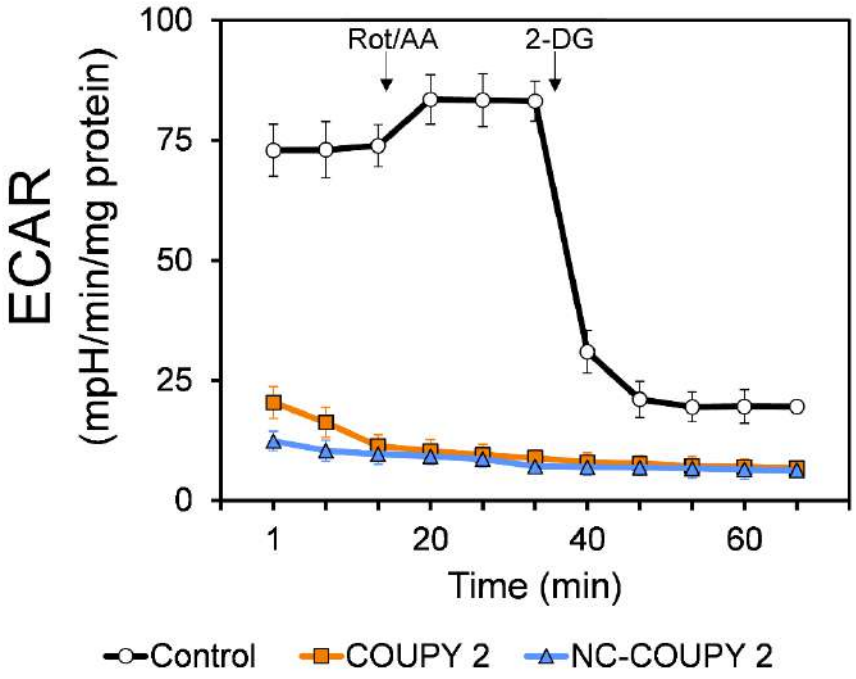

Figure S27. Glycolysis of HeLa cells as measured by extracellular acidification rate (ECAR) after 2 h treatment with tested compounds (10 µM). Data obtained with Seahorse XFe analyzer and represented as mean ± SEM (n= 4 replicates).

8.8. Cell cycle distribution

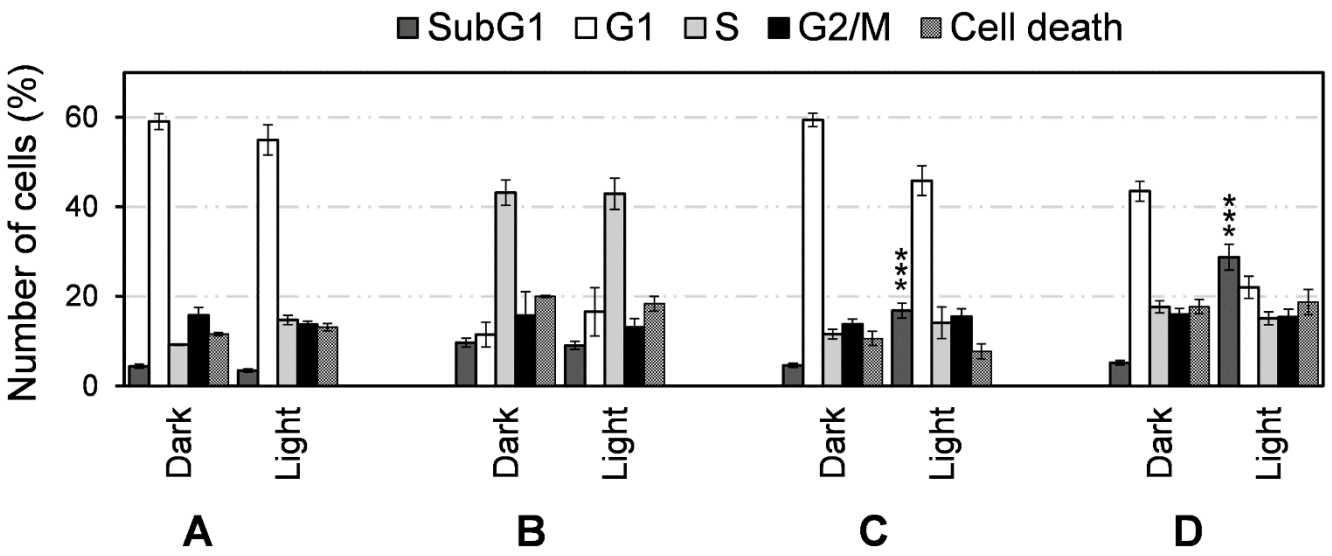

Figure S28. Cell cycle distribution analysis of HeLa cells as detected by propidium iodide staining after visible light irradiation treatments with **COUPY 2** (C) or **NC-COUPY 2** (D) at IC_{50} concentrations. Control cells (A) served as negative control, whereas 20 µM cisplatin (B) was used as positive control. Data expressed as mean ± SD from three independent experiments. Statistical significant dark vs light from unpaired t-test (***$p<0.001$).

9. References

1.- a) A. Gandioso, R. Bresolí-Obach, A. Nin-Hill, M. Bosch, M. Palau, A Galindo, S Contreras, A Rovira, C Rovira, S Nonell, V Marchán. Redesigning the Coumarin Scaffold into Small Bright Fluorophores with Far-Red to Near-Infrared Emission and Large Stokes Shifts Useful for Cell Imaging. *J. Org. Chem*. **2018**, *83*, 1185–1195. b) E. Ortega-Forte, A. Rovira, A. Gandioso, J. Bonelli, M. Bosch, J. Ruiz, V. Marchán. COUPY Coumarins as Novel Mitochondria-Targeted Photodynamic Therapy Anticancer Agents. *J. Med. Chem*. **2021**, *64*, 17209–17220.

8. **Chapter Ib.** Nanoencapsulation and biological evaluation of Ru(II)-based photosensitizers

Framework

The research work reported in this section aims to support the potential of polyurethane-polyurea hybrid nanocapsules in the context of anticancer PDT. This project was carried out in collaboration with Dr. Albert Gandioso and Prof. Gilles Gasser of Chimie Paris Tech, in France, where I carried out an academic stay for 2 months (November-December 2021).

Objectives

As it has been mentioned in the introduction of this Thesis (section 4.2.2), ruthenium(II) complexes have attracted enormous interest in recent years as promising PSs in anticancer PDT. As reported in a perspective in 2015 by Gasser and coworkers, ruthenium(II) complexes have been positioned as a corner stone in the development of metal-based PSs[1]. The ability of ruthenium(II) to stabilize hexacoordinated complexes has been exploited by different research groups by synthesizing a wide range compounds that generate high ROS levels after light irradiation. Although different ligands have been used to assemble metal-based PSs, ruthenium(II) polypyridyl complexes have been established as the most interesting scaffolds for PDT applications. Indeed, Glazer and McFarland groups, among others, are representative examples of pioneering groups working on the development of efficient ruthenium(II) polypyridyl complexes. This field of research crystallized on the appearance of TLD-1433, a PS agent described by McFarland and collaborators that is actually one of the reference compounds in PDT for bladder cancer treatment.

Despite the incredible potential of Ru(II) polypyridyl complexes as light-responsive anticancer agents, selective vehiculation into tumor locations *in vivo* and, in some cases, *in vitro* intracellular internalization remain a challenge. In this context, the main goal of this research project was focused on the encapsulation of two promising photosensitizers based on Ru(II) polypyridyl complexes recently developed in our research group by Sergi Chumillas, **Ru1** and **Ru2**, with the aim of evaluating the biological activity of the nanoencapsulated formulations. Both ruthenium-based photosensitizers are highly phototoxic under far-red and NIR monochromatic light irradiation, both under normoxia and hypoxia conditions, lacking of toxicity under dark conditions, thus leading to outstanding PI values. Although nanoformulation is expected to enhance the stability of the PSs in biological media, as well as to improve *in vivo* biodistribution, the biological evaluation included in this thesis will only comprise *in vitro* phototoxicity in cancer cells. Phototoxicity results of encapsulated **Ru1** and **Ru2** are discussed in comparison with those of the free complexes. As previously stated, the structure of the Ru(II) complexes cannot be shown here because of confidentiality reasons.

Analytical techniques

Infrared spectroscopy (IR)

IR spectra were registered in a Smart ATR (Nicolet iS10, Thermo Scientific, Raleigh, USA) using a transmittance mode (16 scans) and OMNIC software. For the monitoring of solvent-based samples, one drop was deposited onto the diamond crystal and the solvent was left to dry by evaporation. IR spectra were recorded from a dry film of the sample for the reaction control after emulsification.

pH measurements

The pH of the emulsion was determined right after the crosslinker was added and at different time intervals until the last polyaddition reaction was complete. All the determinations were carried out in a pH-meter HI 2211 pH/ORP-Meter (HANNA Instruments, Eibar, Spain) equipped with a pH electrode Crison 5029 (Crison Instruments, Barcelona, Spain) and a temperature probe.

Dynamic light scattering (DLS)

The size distribution of the NCs was analyzed on a Zetasizer Nano-ZS90 (Malvern, Worcestershire, UK) in Milli-Q water at 25 °C at a concentration of 0.5 mg/mL.

Transmission electron microscopy (TEM)

The morphology of the nanocapsules was studied on a TEM Jeol J1010 (Peabody, MA, USA) equipped with a CCD Orius camera (Gatan). A 400-mesh copper grid coated with 0.75 % FORMVAR was deposited on 6 μL of a suspension of nanocapsules in water (10 mg mL^{-1}) for 25 min. Excess of sample was removed by oblique contact with a Whatman filter paper and the grid was deposited on a drop of uranyl acetate (2 % w/w) in water for 30 s. Excess uranyl acetate was removed and the grid was air-dried for at least 3 h prior to measurement.

Zeta potential (Z-pot)

The Z-pot of the NCs was analyzed on a Zetasizer Nano-ZS90 (Malvern, Worcestershire, UK) in Milli-Q water at 25 °C at a concentration of 1 mg/mL, measured at different pH values.

Dialysis purification

The NCs were dialyzed against Milli-Q water for 24 h using a Spectra/Por molecular porous membrane tubing with a 12–14 kDa molecular weight cut-off (MWCO) (Spectrum Laboratories, Rancho Dominguez, USA).

Determination of Ru cargo loading by ICP-MS

To determine the amount of ruthenium-based PS incorporated in the NCs, a fixed volume of 20 μL of NCs emulsion (previously dialyzed) was diluted with 500 μL of concentrated 72 % (v/v) nitric acid into wheaton v-vials (Sigma-Aldrich) and heated in an oven at 100 ºC for 18 h. The vials were then allowed to cool, and each sample solution was transferred into a volumetric tube and combined with Milli-Q water washings (1.5 mL). Digested samples were diluted 5 times with Milli-Q to obtain a final HNO_3 concentration of approximately 3.6 % (v/v). Ruthenium content was analyzed on a Nexion350D Perkin Elmer instrument at the Centres Científics i Tecnològics of the Universitat de Barcelona. The solvent used for all ICP-MS experiments was Milli-Q water with 1 % HNO_3. The ruthenium standard (High-Purity Standards, 1000 μg/mL ± 5 μg/mL in 5 % HNO_3) was diluted with 1 % HNO_3 to 10 ppb. Ruthenium standards were freshly prepared in Milli-Q water with 1 % HNO_3 before each experiment. The concentrations used for the calibration curve were in all cases 0, 0.2, 0.4, 1, and 2 ppb. The isotope detected was ^{102}Ru and readings were made in triplicate for each sample. Rhodium was added as an internal standard at a concentration of 10 ppb in all samples.

The following equations (1 and 2) were respectively used to calculate Encapsulation Efficiency EE (%) and Drug Loading DL (%):

$$\%\, EE = \frac{amount\ of\ Ru\ complex\ incorporated\ in\ the\ nanocapsule}{total\ amount\ of\ Ru\ complex\ added\ in\ the\ aq.dispersion} * 100 \quad \textbf{(1)}$$

$$\%\, DL = \frac{amount\ of\ Ru\ complex\ incorporated\ in\ the\ nanocapsule}{total\ amount\ of\ dried\ nanocapsules} * 100 \quad \textbf{(2)}$$

Solids concentration

NCs concentration in the aqueous dispersion was determined by triplicate leading to dryness using a Digitheat-TFT oven (J.P.Selecta, Barcelona, Spain), with a fixed temperature of 40 ºC for 48 h.

Experimental section:

Synthetic procedures

Synthesis of redox-responsive amphiphilic cationic prepolymer (P1)

2,2´-Dihydroxyethyl disulfide (901.0 mg, 11.68 meq), YMER N-120 (12.04 g, 23.18 meq) and *N*-(3-dimethylaminopropyl)-*N*,*N*´-diisopropanolamine (981.3 mg, 8.99 meq) were added into a three-necked round-bottom flask equipped with mechanical stirring at room temperature and purged with N_2. When the mixture was homogeneous, isophorone diisocyanate (8.14 g, 73.24 meq) was added into the reaction vessel under gentle mechanical stirring. The polyaddition reaction was kept under these conditions until the NCO stretching band intensity did not change, monitored by IR spectroscopy. At this point, dry THF (21 mL) was added into the reaction mixture to fluidify the polymer. In parallel, 1,3-diamino-*N*-octadecylpropane (5.99 g, 35.45 meq) was dissolved in dry THF (5.23 mL) in another 100 mL three-necked round-bottom flask, which had previously been purged with N_2. The former reaction mixture was added dropwise onto the latter under half-moon 100 rpm mechanical stirring. The evolution of the reaction was monitored by IR spectroscopy until the NCO stretching band intensity had completely disappeared.

Synthesis of Ru(II)-loaded amphoteric redox responsive NCs (Ru1-NCs and Ru2-NCs)

Isophorone diisocyanate (69.9 mg, 0.63 meq) was added into a three-necked round bottom flask equipped with mechanical stirring, purged with N_2 and protected from light. In parallel, **Ru1** or **Ru2** (9.7 mg and 13.1 mg, respectively), Neobee 1053 (14.6 mg, 35.73 µmol), polymer **P1** (655.1 mg, 0.07 meq) and dry THF (0.25 mL) were mixed in a vial, added into the first flask, and homogenized for 10 min at 150 rpm while protected from light. At this point, an alkaline aqueous solution of L-lysine was prepared by dissolving 0.93 g L-lysine in 11.37 g of Milli-Q water and adjusting pH to 11.0 by using 3 M and 1 M NaOH solutions (total L-lysine concentration 7.56% by wt). The resulting solution (22.84 mg of L-lysine, 0.27 meq) was added at 250 rpm to the reaction flask and the polyaddition reaction was checked after 15 min by IR spectroscopy. Then, the organic phase was emulsified at 300 rpm with cold Milli-Q water (10.11 g) and finally a 10 % (w/w) aqueous solution of diethylenetriamine (9.43 mg, 0.27 meq) was added in order to generate crosslinked NCs from the nanomicelles. The stirring was reduced to 100 rpm. The exact amounts of the reagents are detailed in Table 1. The polyaddition reaction was

monitored by IR spectroscopy and pH measurements. Once the NCs were formed, THF was removed from the reactor by heating at 35 °C under vacuum and the dialysis purification was carried out using a molecular porous membrane tubing with a 12–14 kDa MWCO.

Table 1. Amount of reagents used to prepare Ru(II)-loaded NCs.

Compound	Amount	Equivalents or mols
IPDI	69.7 mg	0.63 meq
Ru1 or Ru2	9.7mg Ru1 or 13.1mg Ru2	10.69 μmol Ru1 or 13.30 μmol Ru2
Neobee 1053 (GTCC)	26.3 mg	56.61 μmol
Polymer (P1)	812.5 mg	0.09 meq
Dry THF	1 mL	–
L-lysine	20.9 mg	0.25 meq
Milli-Q water	5.93 g	–
DETA	7.8 mg	0.23 meq

Synthesis of non-loaded amphoteric and redox responsive NCs (NC-GTCC)

The procedure was based on the one used for the synthesis of redox responsive **Ru1** and **Ru2**-loaded amphoteric NCs with the exception that no ruthenium photosensitizer was added to the reaction.

Characterization of polymer P1 and NCs

Infrared Spectroscopy

The polymerization reaction was easily controlled by IR spectroscopy given that NCO group has a very clear and characteristic stretching band at 2280-2230 cm^{-1}.

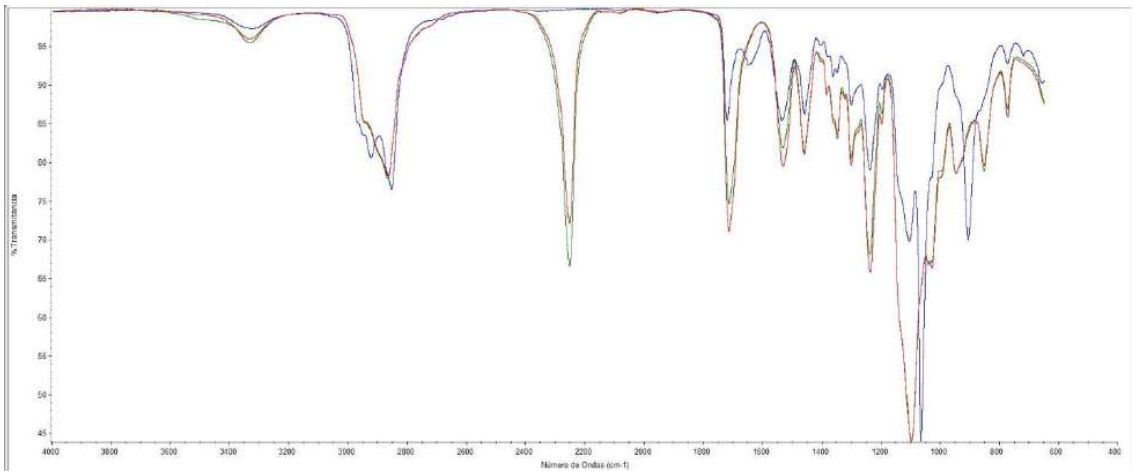

Figure 1. Consecutive IR spectra recorded during the synthesis of **P1**.

As shown in Figure 1, IR spectra of the polymer (**P1**) confirmed a successful polymerization reaction between diols, the diamine and the diisocyanate, in both steps of the polymer synthesis. The green line corresponds to the first sample recorded, at the beginning of the reaction. At that time, the NCO asymmetric stretching band at 2252 cm^{-1} was very sharp and intense. At the end of the first step, involving the reaction between the diols and the diisocyanate (red line), the intensity of the NCO stretching band decreased significantly. Meanwhile, the intensities of the CO stretching band at 1719 cm^{-1}, the CN stretching band at 1537 cm^{-1}, the NCOO/COC asymmetric stretching band at 1240 cm^{-1} increased. Overall, the IR spectra registered during the first step of the synthesis confirmed polyurethane bond formation along with NCO consumption. Once the diamine was added, during the second step of the polymer synthesis (blue line), the NCO stretching band at 2252 cm^{-1} disappeared instantaneously, which can be explained due to the high reactivity of the amines. Simultaneously, other characteristic bands appeared or changed, such as a new stretching band at 1634 cm^{-1}, which was associated to the carbonyl of urea bonds and a new wagging band at 908 cm^{-1} corresponding to the free secondary amine, which also confirmed polyurea formation.

The encapsulation process was also controlled by IR spectroscopy. As shown in Figure 2, IR spectra of the NCs (regardless their loading) confirmed a successful nanocapsule formation. The red line in the IR spectra represents the sample 30 min after addition of the polymer, together with the Ru(II) complexes, which was mixed with the diisocyanate. This initial step consisted of the reactivation of the polymer and its conversion to an NCO-reactive entity. Afterwards, L-lysine sodium salt was added (green line) and reacted with the activated polymer. A decrease on the intensity of the NCO stretching band at 2255 cm^{-1}, concomitantly with an increase of the carbonyl and CN stretching bands, confirmed urea bond formation (1642 cm^{-1} and 1532 cm^{-1}, respectively). Finally, the NCO stretching band instantaneously disappeared upon addition of the triamine (blue line) and the urea-associated bands increased their intensity because of the rapid reaction between remaining NCO groups and this polyamine.

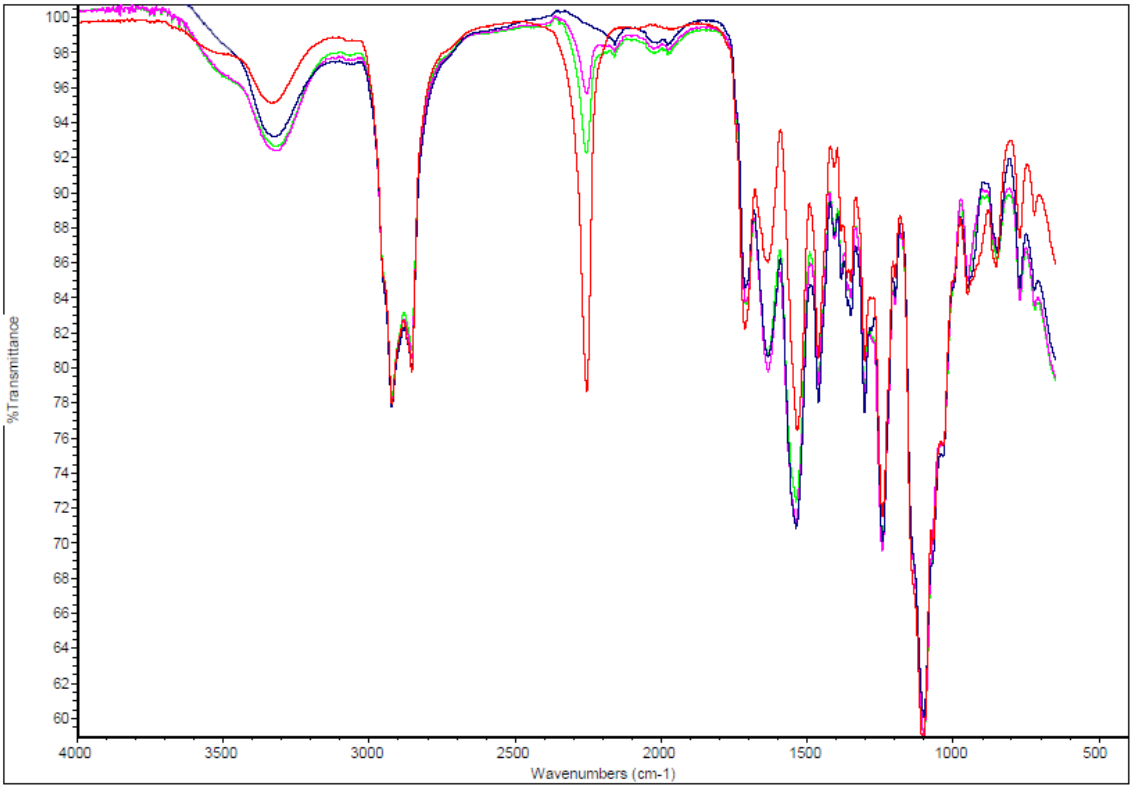

Figure 2. Consecutive IR spectra recorded during the encapsulation process with **Ru2**.

NCs concentration, Ru(II) complex loading and encapsulation efficiency

The concentration of NCs in the final emulsions (mg/mL) was quantified with a solids concentrator, as indicated in the previous section. PSs loading (DL) and Encapsulation Efficiency (EE) were determined by ICP-MS analysis following the method described in the previous section. The DL and EE parameters for non-loaded NCs (**GTCC-NCs**), **Ru1-NCs** and **Ru2-NCs** are indicated in Table 2.

Table 2. DL and EE parameters for control and Ru-loaded NCs.

	[NCs] (mg/mL)	**PS Loading (DL, μM)**	**Encapsulation Efficiency (EE)**
NC-GTCC	42.9 ± 1.6	-	-
Ru1-NCs	57.2 ± 0.7	1005.3 ± 32.9	83.9 %
Ru2-NCs	42.7 ± 1.4	439.7 ± 27.6	38.0 %

Average size of Ru(II)-loaded NCs

The particle size distribution of the NCs was measured by dynamic light scattering (DLS), and the results are shown in Table 3.

Table 3. Hydrodynamic diameter average of control and Ru(II)-loaded NCs.

	Experimental Values	Average ± SD
NC-GTCC	17.07 nm	17.0 ± 1.0 nm
	15.86 nm	
	17.91 nm	
Ru1-NCs	16.21 nm	17.0 ± 0.7 nm
	17.55 nm	
	17.34 nm	
Ru2-NCs	17.44 nm	17.5 ± 0.4 nm
	17.95 nm	
	17.24 nm	

The size distribution by number of the NCs is graphically displayed in Figures 3-5.

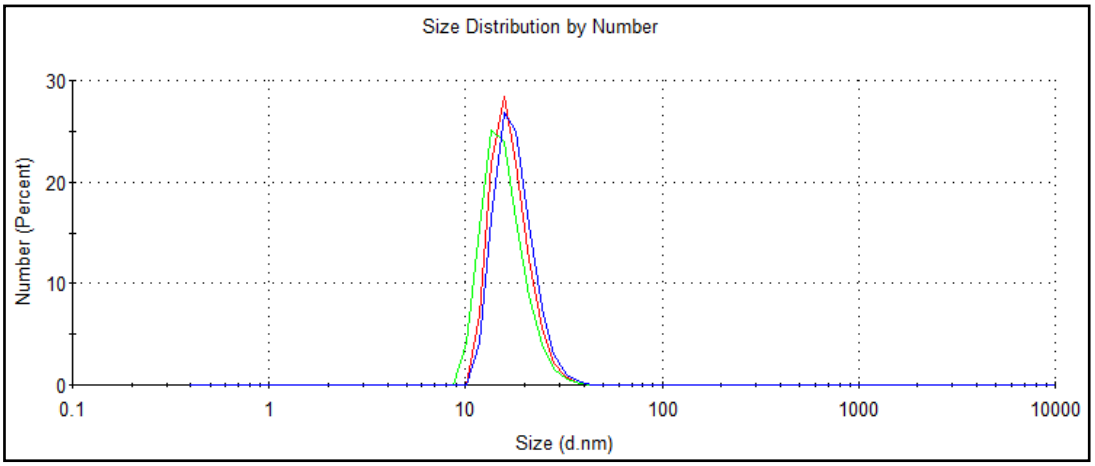

Figure 3. Distribution size by number of control non-loaded **GTCC-NCs**.

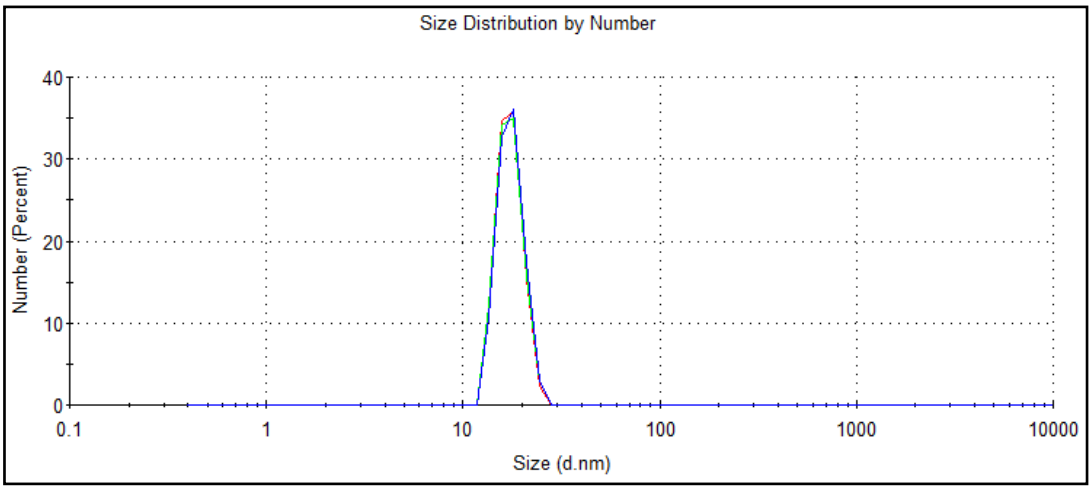

Figure 4. Distribution size by number of **Ru1-NCs**.

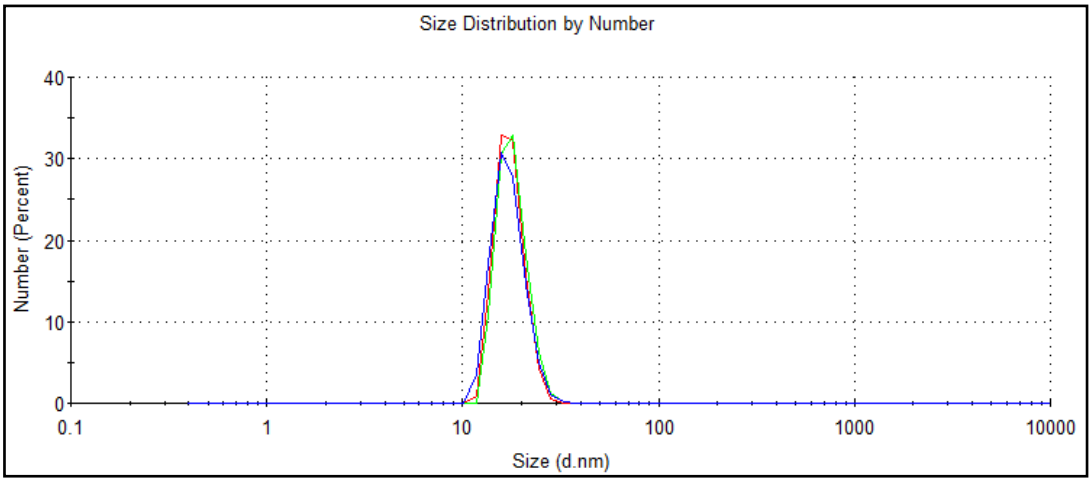

Figure 5. Distribution size by number of **Ru2-NCs**.

Z-potential of NCs

As shown in following Figures 6-8, the Z-potential values (surface charge) of the NCs were determined at different pH values as described in the Analytical Techniques section.

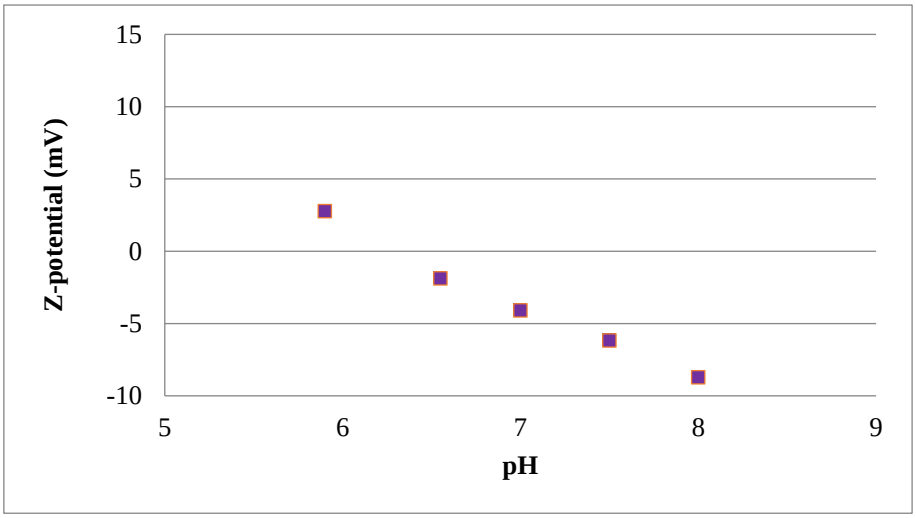

Figure 6. Z-potential values of **GTCC-NCs** *versus* pH.

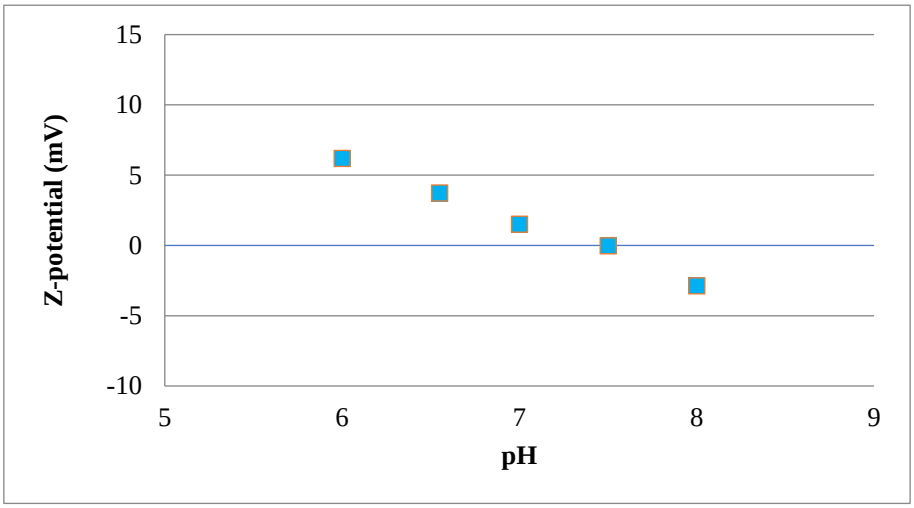

Figure 7. Z-potential values of **Ru1-NCs** *versus* pH.

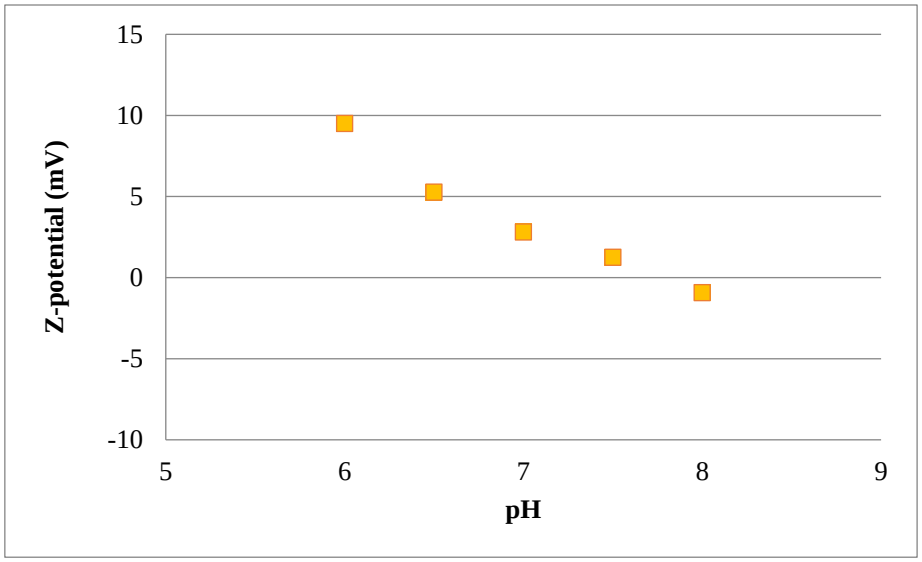

Figure 8. Z-potential values of **Ru2-NCs** *versus* pH.

Photobleaching experiments

The photostability of free and encapsulated Ru(II) complexes under the irradiation conditions used in phototoxicity experiments was investigated. Stock solutions of free Ru(II) complexes in DMSO and aqueous dispersions of Ru(II)-loaded nanocapsules were diluted in phenol-red free Agilent Seahorse XF Media (20 μM final concentration of ruthenium complex). The samples were introduced in 96-well plates and exposed to 645 nm (spectral half-width: 32 nm, 2.50 mW cm^{-2}, 9.0 J cm^{-2}) or 740 nm (spectral half-width: 32 nm, 3.50 mW cm^{-2}, 12.6 J cm^{-2}) light for 1 h using an Atlas Photonics LUMOS BIO irradiator. The absorbance signal of the 96-well plates was measured in an Infinite 200 PRO microplate Reader from TECAN.

Biological evaluation

Cell culture

The CT-26 and HeLa cell lines were cultured in DMEM media (Gibco) supplemented with 10 % fetal calf serum (Gibco) and 1% Penicillin-Streptomycin antibiotic (Gibco). The RPE-1 cell line was cultured in DMEM/F-12 media (Gibco) supplemented with 10 % fetal calf serum and 1% Penicillin-Streptomycin antibiotic (Gibco). The HEK-293 cell line was cultured in DMEM media (Gibco) supplemented with 10 % fetal calf serum and 1 % Penicillin-Streptomycin antibiotic (Gibco). The MRC-5 cell line was cultured in DMEM/F-12 media (Gibco) supplemented with 10 % fetal calf serum and 1 % Penicillin-Streptomycin antibiotic (Gibco). Cell lines were maintained in a humidified atmosphere at 37 °C with 5 % CO_2.

Confocal microscopy analysis

The cellular uptake of ruthenium(II)-loaded NCs was investigated in HeLa cells by confocal microscopy. First, cells were seeded on glass bottom dishes (P35G-1.5-14-C, Mattek). 24 h after cell seeding, cells were incubated at 37 ºC for 30 min with **Ru1-NCs** and **Ru2-NCs** (10 μM) in supplemented DMEM. Then, cells were washed three times with DPBS (Dulbecco's Phosphate-Buffered Saline) to remove the excess of the compounds and kept in low glucose DMEM without phenol red supplemented with Hepes 10 mM for fluorescence imaging.

All microscopy observations were performed using a Zeiss LSM 880 confocal microscope equipped with a heating insert (P S1, Pecon). In the case of low temperature internalization cells were kept at RT. Cells were observed using a 63X 1.4 oil immersion objective. The compounds were excited using the 405 nm laser. Image analysis was performed using Fiji[2]. Unless otherwise stated images are colorized using Fire lookup table.

Phototoxicity evaluation in cancer cells

The phototoxicity of the tested compounds under normoxia (21% O_2) was assessed by a fluorometric cell viability assay using Resazurin (Acros Organics). Briefly, cells were seeded in triplicate in 96-well plates at a density of 4×10^3 cells/well in a final volume of 100 μL per well. After 24 h, cells were treated with increasing concentrations of the metal complexes and control compounds. Serial dilutions of the tested compounds with cell media from 10 mM or 25 mM stock solutions in DMSO were added at the final concentrations in the range of 0.001 to 250 μM in a final volume of 100 μL per well. The cells were incubated with the samples in the dark for 4 h and, after this time, the medium was refreshed. To study the phototoxic effect of the tested compounds, the cells were exposed to 540 nm (spectral half-width: 32 nm, 40 min, 3.75 mW cm^{-2}, 9.0 J cm^{-2}), 645 nm (spectral half-width: 32 nm, 60 min, 2.50 mW cm^{-2}, 9.0 J cm^{-2}) and 740 nm (spectral half-width: 32 nm, 60 min, 3.50 mW cm^{-2}, 12.6 J cm^{-2}) light using an Atlas Photonics LUMOS BIO irradiator. To study the dark cytotoxicity of the samples, the cells were not irradiated. Then, 44 h treatment-free cell recovery period was allowed while maintaining the temperature throughout the experiment at 37 °C. After 44 h of incubation, the medium was removed by suction, and 100 μL of complete medium containing Resazurin (0.2 mg/mL final concentration) were added. After 4 h of incubation at 37 °C, the fluorescence signal of the Resorufin product was measured (λ_{ex} = 540 nm, λ_{em} = 590 nm) using an Infinite 200 PRO Microplate Reader from TECAN. IC_{50} values were then calculated based on the inhibitory rate curves using the following equation (3):

$$I = \frac{I_{max}}{1 + \left(\frac{IC_{50}}{C}\right)^{n}} \quad (\mathbf{3})$$

where I represent the percentage inhibition of viability observed, I_{max} is the maximal inhibitory effect, IC_{50} is the concentration that inhibits 50% of maximal growth, C is the concentration of the treatment and n is the slope of the semi-logarithmic dose-response sigmoidal curves. The non-linear fitting was performed using GraphPad Prism software. PI values were calculated as the ratio between $IC_{50\ dark}/IC_{50\ light}$. All experiments were performed in three independent studies with triplicate points per concentration level (n=3 biologically independent replicates).

Results and Discussion

Synthesis and characterization of Ru(II)-loaded NCs

Ru(II)-loaded nanocapsules (**Ru1-NCs** and **Ru2-NCs**) have been prepared following the methodology described for the encapsulation of liposoluble COUPY PSs in chapter Ia (*Biomacromolecules* **2022**, *23*, 2900–2913). The encapsulation of the compounds was carried out using an amphiphilic-amphoteric polyurethane-polyurea polymeric wall, that has been previously described as a TME-targeting nanocarrier that can be degraded under reducing conditions (e.g., by overexpressed GSH in cancer cells).

The DLS and Z-potential values (Tables 3 and 4, respectively) were found in good concordance with the expected ones for the ratio of dispersible phase and self-emulsifiable polymer. The hydrodynamic diameter in dispersion for both Ru(II)-loaded and blank nanocapsules (*ca* 17 nm) coincide with the values that were previously described as optimal for an efficient *in vivo* biodistribution[3]. On the other hand, TEM analyses confirmed the spherical morphology and the diameter of dried nanocapsules (Figure 9).

Table 4. Z-potential values of the control and ruthenium(II)-loaded nanocapsules.

	Z-Pot ± SD (mV)				
Sample	pH=6.0	pH=6.5	pH=7.0	pH=7.5	pH=8.0
GTCC-NCs	2.8 ± 0.5	-1.9 ± 0.1	-4.1 ± 0.6	-6.2 ± 0.2	-8.7 ± 0.1
Ru1-NCs	6.2 ± 0.7	3.7 ± 0.3	1.5 ± 0.3	-0.03 ± 0.13	-2.9 ± 0.3
Ru2-NCs	9.5 ± 0.4	5.3 ± 0.6	2.8 ± 0.1	1.3 ± 0.1	-0.9 ± 0.6

As shown in Table 4 and Figures 6-8, Z-potential determination under different pH values support the amphoteric behavior of the nanocapsules' surface. Indeed, when the pH of the media was decreased to slightly acidic, which simulates the conditions described for TME, accessible amines on the surface were protonated, thereby shifting the surface charge of the nanocapsules from neutral to positively charged. As discussed in previous sections, this fact is intended to promote the selective accumulation of the nanocapsules in tumor tissues.

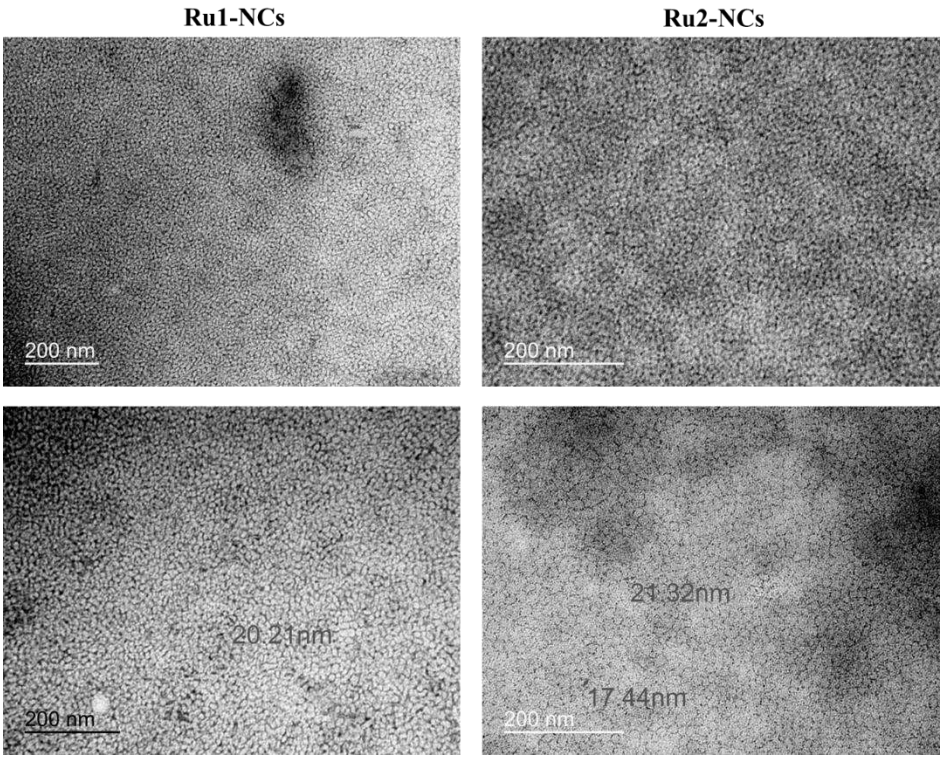

Figure 9. Selected TEM micrographs of **Ru1-NCs and Ru2-NCs** (scale bar: 200 nm).

ICP-MS analysis of the nanocapsules emulsions allowed to easily quantify the ruthenium content in the samples, facilitating the cargo determination after purification by dialysis, as well as the assessment of the encapsulation efficacy (Table 2). Although both ruthenium(II) complexes have been properly encapsulated in the same liposoluble core of polyurethane-polyurea hybrid NCs, the differences in the encapsulation efficacy (84 % for **Ru1-NCs** and 38 % for **Ru2-NCs**) are probably related to their chemical structure and, consequently, will not be discussed in this work.

Photostability of Ru(II) complexes

As shown in Figures 10 and 11, photobleaching experiments confirmed that encapsulation enhances the stability of the compounds upon visible and NIR light irradiation in biological media, which is in good agreement with the results previously found with COUPY-based PSs (see Chapter Ia). In both cases, after 1 h of irradiation with 645 nm monochromatic red light, a decrease in the absorption maxima was observed both in the encapsulated and in the free forms. However, the overall reduction in the absorbance of the encapsulated complexes was much lower compared with the free complexes, which suggests that the ability of the encapsulated compounds to generate ROS might be prolonged over time. In the case of photobleaching experiments under irradiation with 740 nm monochromatic light, none of the complexes, either free or encapsulated, showed a significant decrease in their absorption spectra, which could be attributed to their reduced absorptivity in this region.

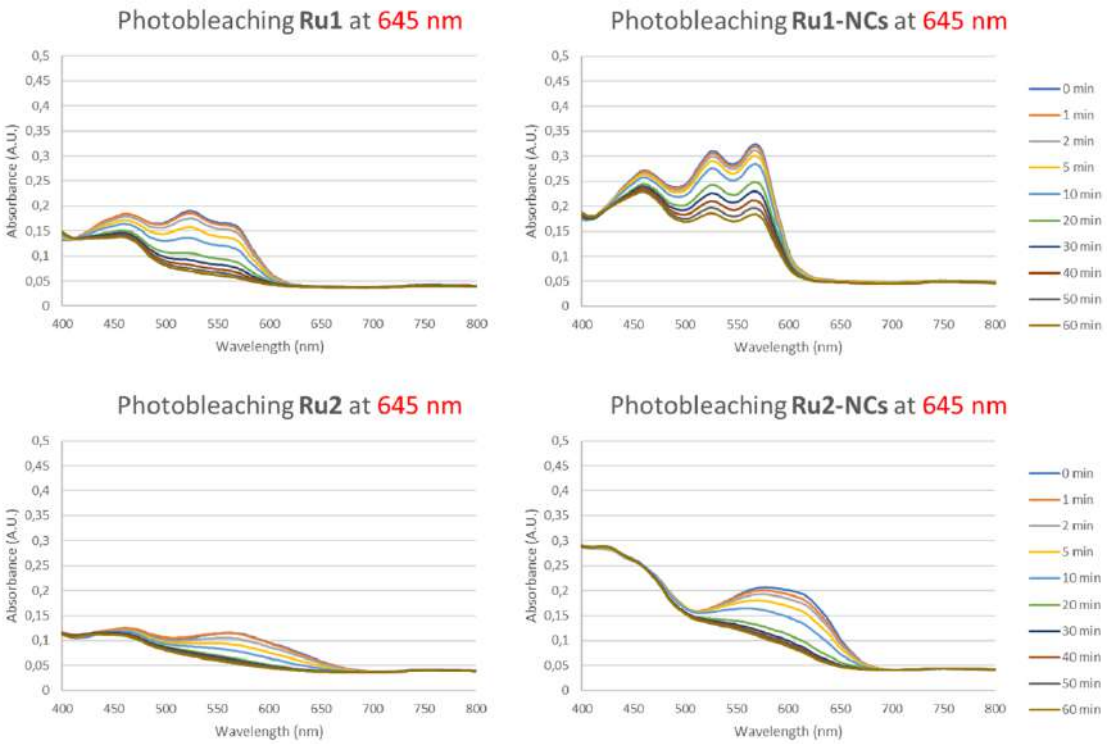

Figure 10. Comparison of the photostability of free **Ru1** and **Ru2** complexes *versus* the corresponding encapsulated nanoformulations under 645 nm irradiation.

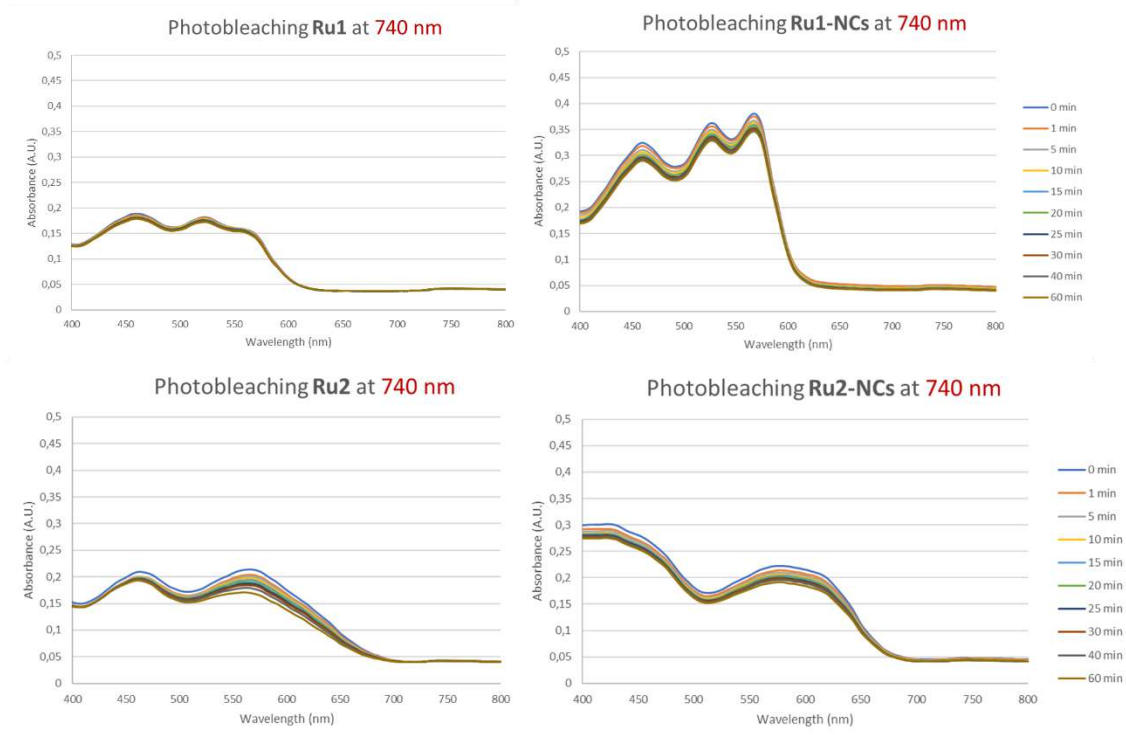

Figure 11. Comparison of the photostability of free **Ru1** and **Ru2** complexes *versus* the corresponding encapsulated nanoformulations under 740 nm irradiation.

Cellular uptake evaluation

The *in vitro* evaluation of **Ru1-NCs** and **Ru2-NCs** had two main objectives: the first one was to qualitatively investigate the cellular uptake of both nanoformulations in cancer cells by confocal microscopy by taking advantage of the luminescent properties of the Ru(II) polypyridyl complexes; the second one was to evaluate the influence of nanoencapsulation on the photoactivity of the complexes in comparison with the free forms.

As shown in Figure 12, confocal microscopy studies revealed that both encapsulated compounds were efficiently internalized by HeLa cells after 30 min of incubation (10 μM concentration). Compounds could be easily monitored under irradiation with visible light. Even if colocalization analysis using organelle biomarkers has not been carried out yet, in the case of **Ru1-NCs** the "spheric-worm shaped" staining suggests mitochondria accumulation. By contrast, the pattern of staining of **Ru2-NCs** suggests vesicle accumulation in addition to mitochondria, probably lysosomes. Further confocal microscopy studies, particularly, colocalization studies, will be required to confirm the accumulation of the encapsulated compounds.

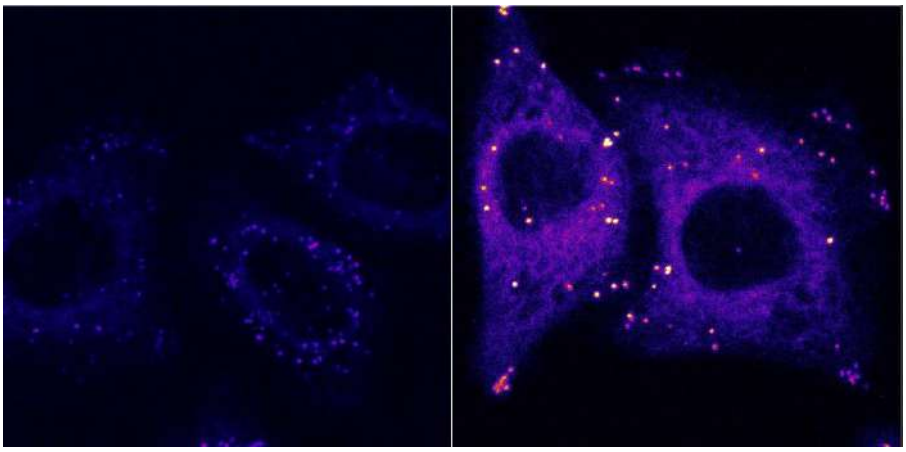

Figure 12. Confocal microscopy images for **Ru1-NCs (left)** and **Ru2-NCs (right)**.

It is worth noting that previous studies had indicated that the non-encapsulated Ru(II) complexes **Ru1** and **Ru2** exhibit a similar subcellular localization than the one described here for the encapsulated forms. Overall, these results demonstrate the proper invagination of Ru(II)-loaded nanocapsules after 30 min of incubation and suggest an immediate release of the cargo PSs from the nanocapsules once internalized, thereby confirming the results discussed in the Chapter Ia for the rapid degradation of polyurethane-polyurea hybrid nanocapsules upon HeLa cells internalization.

Phototoxicity evaluation

Phototoxicity experiments were carried out by defining a 4 h-incubation time before irradiation, followed by a wash-up process to remove the excess of non-internalized compounds. Then, after 1 h of irradiation (experiments in dark conditions were not irradiated), a 43 h recovery time was allowed.

As previously described in objectives' section of this Chapter Ib, **Ru1** and **Ru2** complexes had been confirmed as non-toxic in the dark both in healthy cells and in the CT-26 cancer cell line. On the contrary, the phototoxic activity they exhibited under green and red-light irradiation was located on the nanomolar range (e.g., IC_{50} = 8.2 nM for **Ru1** at 540 nm, and IC_{50} = 7.4 nM for **Ru2** at 645 nm). Very interestingly, **Ru2** was also found highly phototoxic under NIR irradiation. Owing to the high differences between dark and light cytotoxicities, both compounds yielded outstanding PI values under 540 nm (above 30000 for **Ru1** and above 10000 for **Ru2**) and 645 nm (above 5000 for **Ru1** and above 33000 for **Ru2**) light irradiation (Table 5), which are in agreement with the absorptivity they display under the mentioned wavelengths (Figures 10 and 11).

Moving to the comparison between free and polyurethane-polyurea encapsulated photosensitizers, **Ru1** was also found highly phototoxic in its encapsulated form upon 540 nm and 645 nm irradiation (Table 5), whereas no toxicity was observed in the dark. In the same line, no cytotoxicity was observed under 740 nm irradiation as a consequence of a the lack of absorbance in this region of the electromagnetic spectrum. Indeed, IC_{50} values under green-light irradiation were found slightly lower for **Ru1-NCs** compared with the free **Ru1** form, enhancing the PI value for **Ru1-NCs** above 55000. To our delight, the compound also showed an extraordinary performance under red-light irradiation, with similar IC_{50} and PI values for both **Ru1** and **Ru1-NCs**, positioning its phototoxic activity in an interesting operative-window for PDT.

In the case of **Ru2**, the results are even more interesting: while this compound was also highly phototoxic under green and red-light irradiation, it was still found active under NIR-irradiation at 740 nm both in the free and in the encapsulated forms. The latter is in good concordance with its UV-Vis spectrum, which shows an absorption maximum around 650 nm and a tail that penetrates in the NIR region (it should be noted that the spectral half-width is 32 nm for the 740 nm LED used in phototoxicity experiments). Nevertheless, it is worth noting that **Ru2-NCs** showed controversial results when comparing phototoxicity data under visible and NIR light: while **Ru2-NCs** displayed a reduced photoactivity under 645 nm irradiation compared with **Ru2** (PI >19231 *vs* 33700, respectively), this situation is reversed when phototoxicity of each form is compared under green (PI >32895 *vs* 10000, respectively) and NIR irradiation (926 *vs* 328,

respectively). Based on these results, the optimal irradiation procedure for this compound, the ones that produces the highest phototoxicity, should be carried out using green or red light. However, the extraordinary phototoxic values reported under 740 nm irradiation for **Ru2-NCs** opens the door to the design of an irradiation regime using highly penetrating NIR light, which is very attractive for *in vivo* PDT treatments.

The photoactivities of **Ru1** and **Ru2** complexes are incredibly encouraging when compared to other ruthenium(II) polypyridyl compounds reported in the literature. As mentioned in the objectives' section of Chapter Ib, Glazer and coworkers reported a first generation of light-responsive active ruthenium(II) polypyridyl compounds intended for use as PDT agents with PI values around 200 under 450 nm blue light irradiation[4]. Later, they were able to reach PI values of 1889 under similar blue-light irradiation through synthetic modifications over the first generation of the Ru(II) polypyridyl complexes[5].

Table 5: Cyto- and phototoxicity of **Ru1-NCs** and **Ru2-NCs** *versus* their corresponding free complexes in dark conditions as well as under different irradiation conditions towards CT-26 murine colorectal carcinoma cell line expressed as IC_{50} values (μM). Phototoxic index (PI) = IC_{50} (dark-non-irradiated cells)/IC_{50} (irradiated cells).

	CT-26			
	Ru1-NCs		**Ru1**	
	IC_{50}	*PI*	*IC_{50}*	*PI*
Dark	>250	-	>250	-
540 nm	0.0045 ± 0.0005	>55000	0.0082 ± 0.0006	>30487
645 nm	0.059 ± 0.005	>4237	0.048 ± 0.003	>5208
740 nm	>100	----	31.3 ± 6.1	>3
	Ru2-NCs		**Ru2**	
	IC_{50}	*PI*	*IC_{50}*	*PI*
Dark	>250	-	>250	-
540 nm	0.0076 ± 0.0007	>32895	0.025 ± 0.002	>10000
645 nm	0.013 ± 0.001	>19231	0.0074 ± 0.0006	>33780
740 nm	0.27 ± 0.03	>926	0.76 ± 0.06	>328

Prof. McFarland discloses in the patent that describes TLD-1433 and its first analogues, PI values up to 1500 under 633 nm red-light irradiation[6], which have been considerably increased in some recent publications with second generation of thiophene-substituted Ru(II) polypyridyl complexes. Indeed, McFarland and collaborators have reported PI values over 100000 under blue-light irradiation, up to 10000 under green-light irradiation and less than 10 under red-light irradiation[7].

Even though our compounds **Ru1** and **Ru2** exhibit extraordinary results under red-light irradiation (645 nm,) the performance of **Ru2** and **Ru2-NCs** under NIR-light irradiation (740 nm) is particularly appealing and highlight the enormous potential of this new class of Ru(II) polypyridyl complexes developed in our group as novel photosensitizers in anticancer PDT. Indeed, both green-light and red-light PI values for **Ru1** and **Ru2** and for their encapsulated forms are above the standard Ru(II)-polypyridyl complexes, including those described by McFarland and coworkers based on TLD-1433 technology, supposing a clear advantage for their introduction in preclinical studies.

Based on these results, we next focused on investigating the phototoxicity of **Ru2-NCs** and free **Ru2** in different cell lines under NIR light irradiation since it could be a potential candidate for *in vivo* studies. Whereas murine colorectal carcinoma cell line CT-26 was chosen as reference for the phototoxicity assays in tumorigenic cell lines, the evaluation of the photoactivity of the compounds in different healthy cell lines was carried out to assess the selectivity of the treatment towards cancer cells. As shown in Table 6, the free form of **Ru2** produces a similar phototoxicity levels in healthy RPE-1 or MRC-5 cell lines compared with the tumorigenic CT-26. In contrast, to our delight, **Ru2-NCs** have a clear tendency to produce higher phototoxicity in CT-26 cancer cell line than in healthy cells.

Table 6: Cyto- and phototoxicity of **Ru2** and **Ru2-NCs** in dark conditions and under 740 nm monochromatic light irradiation, in different tumorigenic and healthy cell lines, expressed as IC_{50} values (μM). Phototoxic index (PI) = IC_{50} (dark-non-irradiated cells)/IC_{50} (irradiated cells).

	Ru2-NCs			**Ru2**		
	Dark	**740nm**	*PI*	***Dark***	**740nm**	*PI*
CT-26	>100	0.27 ± 0.03	>370	>100	0.76 ± 0.06	>131
RPE-1	>100	3.84 ± 0.04	>26	>100	0.80 ± 0.18	>125
HEK293	>100	2.94 ± 0.70	>34	>100	3.33 ± 0.90	>30
MRC-5	>100	0.64 ± 0.11	>156	>100	0.49 ± 0.03	>205

Although further studies will be needed to elucidate the mechanism by which nanocapsules are increasing the selectivity towards cancer cells (e.g., cellular uptake quantification by ICP-MS and ROS determination), a plausible explanation could be related with an enhanced release of **Ru2** from the **Ru2**-loaded nanocapsules in CT-26 cell line due to the overexpression of the reduced-form of glutathione tripeptide which would mediate the degradation of the polymeric wall.

In a recent review, Gasser and collaborators thresh the possibilities of using polymers as nanovehicles for ruthenium-based photosensitizers[8]. Among the different methodologies contemplated by them, there are some interesting approaches that use 740 nm NIR-light as a source for PS activation, qualitatively reporting photodamage over C6

glioma cells[9]. Glazer and coworkers have also reported the encapsulation of some Ru(II) polypyridyl complexes in crosslinked polymers, intending to combine PDT and PACT, but reaching poor PI values after 5 min of blue light irradiation[10].

Gasser and coworkers have recently released two interesting articles where the potential of Ru(II) polypyridyl complexes incorporated in mesoporous silica nanoparticles (MSNs) and in a DSPE-PEG_{2000}-biotin block-co-polymer emulsion was investigated. The resulting Ru(II)-loaded MSNs were evaluated in both healthy and tumorigenic lung cell lines upon irradiation with blue (480 nm) and green (540 nm) light. Furthermore, the incorporation of folic acid at the surface of MSNs was found to enhance the phototoxicity over cancer cells compared to healthy ones, reporting PI values up to 10-12[11].

On the other side, Gasser and collaborators have also published an exhaustive *in vivo* analysis for the DSPE-PEG_{2000}-biotin block-co-polymer nano-assembled in A549-bearing nude mice. These nanostructures presented an extraordinary *in vivo* efficacy upon 800 nm irradiation, being able to completely inhibit tumor growth in a 15-days treatment[12]. The biological procedures described by Gasser and coworkers are an excellent guidebook for the future *in vivo* assays with **Ru2-NCs**.

Conclusions and outlook

Phototoxicity studies in the murine colorectal carcinoma cell line CT-26 showed that encapsulated **Ru1** and **Ru2** complexes can generate similar levels of cell death, compared with their free analogues, under three types of monochromatic light irradiation sources (green, red, and NIR), being all of them completely non-toxic under dark conditions. **Ru1** complex generated high phototoxicity under green- (540 nm) and red-light (645 nm) irradiation, but no significant phototoxicity under NIR irradiation was induced. In the case of **Ru2** complex, a high phototoxicity was induced to CT-26 cells under visible light irradiation, especially with red light with impressive PI values, being also active under NIR monochromatic light irradiation. These results clearly improve the photoactivity of TLD-1433 analogues reported by McFarland and coworkers.

Moreover, to our delight, the encapsulated **Ru2** complex was found less phototoxic in healthy cells, especially against the epithelial RPE-1 cell line. These differences became less significant for MRC-5 lung fibroblasts and for HEK-293 kidney epithelial cell lines, where both encapsulated and free forms exhibited similar PI values.

Further phototoxicity studies under hypoxic conditions in 2D and 3D cell culture models will be carried out in the near future to determine the activity of ruthenium(II)-loaded nanocapsules in an hypoxic TME-mimicking in vitro model. In addition, we plan to elucidate if the reduced photoactivity of the nanoformulations in healthy cell lines might be associated to a reduced PS internalization or to other biological features of normal cell lines compared with cancer cells. These experiments will be carried out both under normoxic and hypoxic conditions. Quantitative analyses of Ru(II)-complexes NCs' internalization will be also carried out by ICP-MS in cancer and healthy cells. In parallel, ROS generation under light irradiation will be studied both for free and nanoencapsulated Ru(II) complexes. Finally, *in vivo* evaluation of the efficacy of **Ru2-NCs** in a tumor-challenged mice model might be carried out in the near future using extracorporeal NIR irradiation.

References

(1) Mari, C.; Pierroz, V.; Ferrari, S.; Gasser, G. Combination of Ru(II) Complexes and Light: New Frontiers in Cancer Therapy. *Chem. Sci.* **2015**, *6* (5), 2660–2686. https://doi.org/10.1039/c4sc03759f.

(2) Schindelin, J.; Arganda-Carreras, I.; Frise, E.; Kaynig, V.; Longair, M.; Pietzsch, T.; Preibisch, S.; Rueden, C.; Saalfeld, S.; Schmid, B.; Tinevez, J. Y.; White, D. J.; Hartenstein, V.; Eliceiri, K.; Tomancak, P.; Cardona, A. Fiji: An Open-Source Platform for Biological-Image Analysis. *Nat. Methods* **2012**, *9* (7), 676–682. https://doi.org/10.1038/nmeth.2019.

(3) Pérez-Hernández, M.; Cuscó, C.; Benítez-García, C.; Bonelli, J.; Nuevo-Fonoll, M.; Soriano, A.; Martínez-García, D.; Arias-Betancur, A.; García-Valverde, M.; Segura, M. F.; Quesada, R.; Rocas, J.; Soto-Cerrato, V.; Pérez-Tomás, R. Multi-Smart and Scalable Bioligands-Free Nanomedical Platform for Intratumorally Targeted Tambjamine Delivery, a Difficult to Administrate Highly Cytotoxic Drug. *Biomedicines* **2021**, *9* (5). https://doi.org/10.3390/biomedicines9050508.

(4) Howerton, B. S.; Heidary, D. K.; Glazer, E. C. Strained Ruthenium Complexes Are Potent Light-Activated Anticancer Agents. *J. Am. Chem. Soc.* **2012**, *134* (20), 8324–8327. https://doi.org/10.1021/ja3009677.

(5) Hidayatullah, A. N.; Wachter, E.; Heidary, D. K.; Parkin, S.; Glazer, E. C. Photoactive Ru(II) Complexes with Dioxinophenanthroline Ligands Are Potent Cytotoxic Agents. *Inorg. Chem.* **2014**, *53* (19), 10030–10032. https://doi.org/10.1021/ic5017164.

(6) McFarland, S. A. Metal-Based Thiophene Photodynamic Compounds and Their Use. US 9,676,806 B2, December 14, 2013. https://doi.org/10.1016/j.molstruc.2011.09.021.

(7) Cole, H. D.; Roque, J. A.; Shi, G.; Lifshits, L. M.; Ramasamy, E.; Barrett, P. C.; Hodges, R. O.; Cameron, C. G.; Mcfarland, S. A. Anticancer Agent with Inexplicable Potency in Extreme Hypoxia: Characterizing a Light-Triggered Ruthenium Ubertoxin. *J. Am. Chem. Soc.* **2021**. https://doi.org/10.1021/jacs.1c09010.

(8) Villemin, E.; Ong, Y. C.; Thomas, C. M.; Gasser, G. Polymer Encapsulation of Ruthenium Complexes for Biological and Medicinal Applications. *Nat. Rev. Chem.* **2019**, *3* (4), 261–282. https://doi.org/10.1038/s41570-019-0088-0.

(9) Boeuf, G.; v. Roullin, G.; Moreau, J.; van Gulick, L.; Zambrano Pineda, N.; Terryn, C.; Ploton, D.; Christine Andry, M.; Chuburu, F.; Dukic, S.; Molinari, M.; Lemercier, G. Encapsulated Ruthenium(II) Complexes in Biocompatible Poly(d,l-Lactide-Co- Glycolide) Nanoparticles for Application in Photodynamic Therapy. *Chempluschem* **2014**, *79* (1), 171–180. https://doi.org/10.1002/cplu.201300242.

(10) Dickerson, M.; Howerton, B.; Bae, Y.; C. Glazer, E. Light-Sensitive Ruthenium Complex-Loaded Cross-Linked Polymeric Nanoassemblies for the Treatment of Cancer. *J. Mater. Chem. B* **2016**, *4* (3), 394–408. https://doi.org/10.1039/c5tb01613d.

(11) Karges, J.; Díaz-García, D.; Prashar, S.; Gómez-Ruiz, S.; Gasser, G. Ru(II) Polypyridine Complex-Functionalized Mesoporous Silica Nanoparticles as Photosensitizers for Cancer Targeted Photodynamic Therapy. *ACS Appl. Bio. Mater.* **2021**, *4* (5), 4394–4405. https://doi.org/10.1021/acsabm.1c00151.

(12) Karges, J.; Li, J.; Zeng, L.; Chao, H.; Gasser, G. Polymeric Encapsulation of a Ruthenium Polypyridine Complex for Tumor Targeted One- And Two-Photon Photodynamic Therapy. *ACS Appl. Mater. Interfaces* **2020**, *12* (49), 54433–54444. https://doi.org/10.1021/acsami.0c16119.

9. Chapter Ic. Encapsulation and biological evaluation of a Zn(phthalocyanine) derivative and the corresponding Ir-Zn(phthalocyanine) conjugate

Framework

This project has been carried out in collaboration with the group of Prof. Ángela Sastre (Universidad Miguel Hernández) where the Zn(phthalocyanine) derivative and the corresponding Ir-Zn(phthalocyanine) conjugate were synthesized by Dr. Jorge Follana, and the group of Prof. José Ruiz (Universidad de Murcia), where the synthesis of the cyclometalated Ir(III) complex and preliminary *in vitro* phototoxicity evaluation were performed by Dr. Gloria Vigueras and Enrique Ortega-Forte, respectively.

Objectives

The main goal of this project was to evaluate the *in vitro* phototoxic activity of a zinc-phthalocyanine derivative (**Zn(Pc)**) and its corresponding conjugate with a cyclometalated iridium(III) complex (**Ir-Zn(Pc)**). As it has been described in the introduction (section 4.2.2), the conjugation of a COUPY derivative to a cyclometalated iridium(III) complex led to an improvement of the phototoxic activity under blue and green light irradiation when compared with both unconjugated moieties, i.e. the Ir(III) complex and the COUPY fluorophore. This phenomenon was attributed both to an enhanced cellular uptake in tumor cells as well as to a synergistic effect between the metal complex and the coumarin derivative, which triggered the generation of a specific type I ROS (superoxide radical)[1].

Inspired on the good results reported with the Ir(III)-COUPY conjugate, the groups of Prof. Ángela Sastre and Prof. José Ruiz envisioned that conjugation of the same cyclometalated iridium(III) complex to a zinc-phthalocyanine derivative could be exploited to achieve higher phototoxicity under visible light irradiation. The selection of a phthalocyanine derivative is not random since phthalocyanines have been widely described as promising PDT agents owing to a strong absorption in the phototherapeutic window[2], being their conjugation to metal complexes highly attractive for the synthesis of novel PSs[3,4]. In this context, it is worth noting that different drug delivery systems have also been recently explored as plausible vehicles to guarantee an efficient delivery of liposoluble phthalocyanines since they exhibit, in general, poor aqueous solubility[5].

Owing to the poor solubility of both **Zn(Pc)** and **Ir-Zn(Pc)** compounds in aqueous media, encapsulation using ECOSTRATAR technology was proposed as a plausible solution to facilitate the evaluation of their biological activity. Therefore, the encapsulation of **Zn(Pc)** and **Ir-Zn(Pc)** within a liposoluble core polyurethane-polyurea hybrid nanocapsules was the first objective of this project, which subsequently allowed the evaluation of the *in vitro* biological performance in terms of promoted internalization mediated by nanoencapsulation, as well as the phototoxic profile in HeLa cells.

Analytical techniques

Unless otherwise indicated, the methodologies for the following analytical techniques have been carried out as stated in the same section of Chapter Ib.

Infrared spectroscopy (IR)

pH measurements

Dynamic light scattering (DLS)

Transmission electron microscopy (TEM)

Zeta potential (Z-pot)

Dialysis purification

Solids concentration and UV-visible spectroscopy

Determination of cargo loading by ICP-MS

To determine the amount of **Zn(Pc)** and **Ir-Zn(Pc)** compounds incorporated in the NCs, iridium and zinc were quantified by ICP-MS according to the following procedure. First, a fixed volume of NCs' emulsion (previously dialyzed) was diluted in 500 μL of concentrated 72% (v/v) nitric acid into wheaton v-vials (Sigma-Aldrich) and heated in an oven at 373 K for 18 h. The vials were then allowed to cool, and each sample solution was transferred into a volumetric tube and combined with Milli-Q water washings (1.5 mL). Digested samples were diluted 4 times with Milli-Q to obtain a final HNO_3 concentration of approximately 18 % (v/v). Iridium and zinc contents were analyzed on an Nexion350D Perkin Elmer instrument at the Centres Científics i Tecnològics of the Universitat de Barcelona. The solvent used for all ICP-MS experiments was Milli-Q water with 1 % HNO_3. Iridium and zinc standards were freshly prepared in Milli-Q water with 1 % HNO_3 before each experiment. The concentrations used for the calibration curve were in all cases 0, 0.2, 0.4, 1, and 2 ppb. Isotopes detected were ^{193}Ir and ^{66}Zn. Readings were made in triplicate for each sample. Rhodium was added as an internal standard at a concentration of 10 ppb in all samples.

The following equations (1) and (2) were used to calculate Encapsulation Efficiency EE (%) and Drug Loading DL (%):

$$\%\, EE = \frac{amount\ of\ photosensitizer\ incorporated\ in\ the\ nanocapsule}{total\ amount\ of\ photosensitizer\ added\ in\ the\ aq.dispersion} * 100 \quad \textbf{(1)}$$

$$\%\, DL = \frac{amount\ of\ photosensitizer\ incorporated\ in\ the\ nanocapsule}{total\ amount\ of\ dried\ nanocapsules} * 100 \quad \textbf{(2)}$$

Experimental section:

Synthetic procedures

Synthesis of redox-responsive amphiphilic cationic prepolymer (P1)

The synthesis of prepolymer **P1** was carried out as stated in the Experimental Section of Chapter Ib.

Synthesis of Zn(Pc) and Ir-Zn(Pc)-loaded amphoteric redox responsive NCs (Zn(Pc)-NCs and Ir-Zn(Pc)-NCs)

Isophorone diisocyanate (69.9 mg, 0.63 meq) was added into a three-necked round bottom flask equipped with mechanical stirring, purged with N_2 and protected from light. In parallel, **Zn(Pc)** or **Ir-Zn(Pc)** (6.8 mg and 6.9 mg, respectively), Neobee 1053 (14.6 mg, 35.73 μmol), polymer **P1** (655.1 mg, 0.07 meq) and dry THF (0.25 mL) were mixed in a vial, and subsequently added into the flask and homogenized for 10 min at 150 rpm, while protected from light. At this point, an alkaline aqueous solution of L-lysine was prepared by dissolving 0.93 g L-lysine in 11.37 g of Milli-Q water and adjusting pH to 11.0 by using 3 M and 1 M NaOH solutions (total L-lysine concentration 7.56% by wt). The resulting solution (22.84 mg of L-lysine, 0.27 meq) was added at 250 rpm to the reaction mixture and the polyaddition reaction was checked after 15 min by IR spectroscopy. Then, the organic phase was emulsified at 300 rpm with cold Milli-Q water (10.11 g) and finally a 10% w/w aqueous solution of diethylenetriamine (9.43 mg, 0.27 meq) was added in order to generate crosslinked NCs from the nano micelles. The stirring was reduced to 100 rpm. The exact amounts of the reagents are detailed in Table 1. The polyaddition reaction was monitored by IR spectroscopy and pH measurements. Once the NCs were formed, THF was removed from the reactor at 35 °C under vacuum and the dialysis purification was carried out using a molecular porous membrane tubing with a 12–14 kDa MWCO.

Table 1. Amount of reagents used to prepare **Zn(Pc)-NCs** and **Ir-Zn(Pc)-NCs**.

Compound	Amount	Equivalents or mols
IPDI	69.7 mg	0.63 meq
Zn(Pc) or Ir-Zn(Pc)	6.8 mg Zn(Pc) or 6.9 mg Ir-Zn(Pc)	7.73 μmol Zn(Pc) or 4.09 μmol Ir-Zn(Pc)
Neobee 1053 (GTCC)	26.3 mg	56.61 μmol

Polymer (P1)	812.5 mg	0.09 meq
Dry THF	1 mL	–
L-lysine	20.9 mg	0.25 meq
Milli-Q water	5.93 g	–
DETA	7.8 mg	0.23 meq

Synthesis of non-loaded amphoteric and redox responsive NCs (NC-GTCC)

The procedure was based on the one used for the synthesis of redox responsive amphoteric **Zn(Pc)-NCs** and **Ir-Zn(Pc)-NCs** with the exception that no cargo compounds were added to the reaction.

Characterization of polymer P1 and NCs

Infrared Spectroscopy

The polymerization reaction for the synthesis of **P1** as well as for the nanoencapsulation process were monitored by IR spectroscopy, as described in the Experimental Section of Chapter Ib. On the one hand, consecutive IR spectra for **P1** synthesis are represented in Figure 1, in which the green line corresponds to the first sample recorded at the beginning of the reaction, the red line corresponds to the end of the first step (after reaction of diols with isocyanate groups), and blue line represents the spectrum once the reaction between NCO groups and the diamine was completed.

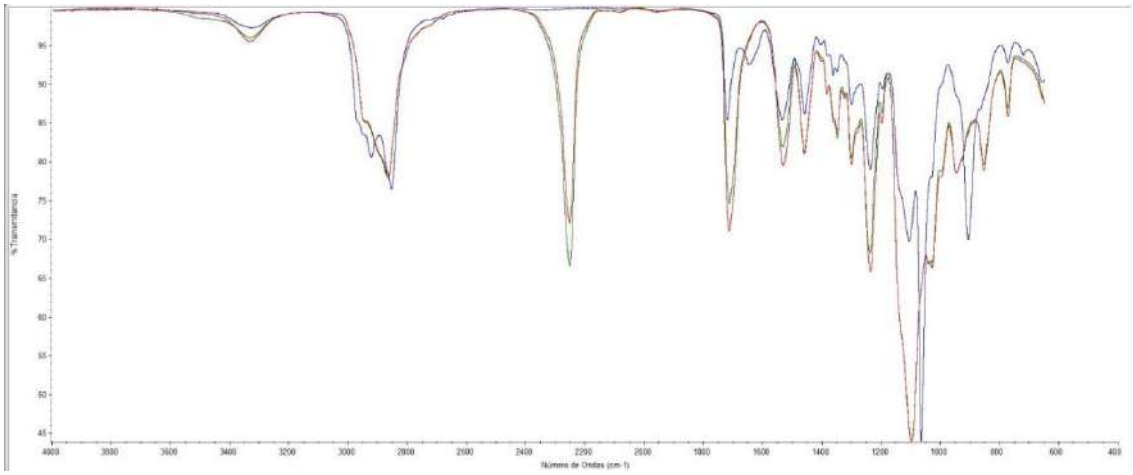

Figure 1. Consecutive IR spectra recorded during the synthesis of **P1**.

On the other hand, Figure 2 shows the consecutive IR spectra during the synthesis of **Ir-Zn(Pc)-NCs**, where the cyan line represents the sample 30 min after mixing the **P1** prepolymer with the cargo and the diisocyanate, the green line corresponds to the step in which L-lysine sodium salt was added, and the red line corresponds to the complete crosslinking of NCO-groups after addition of the triamine.

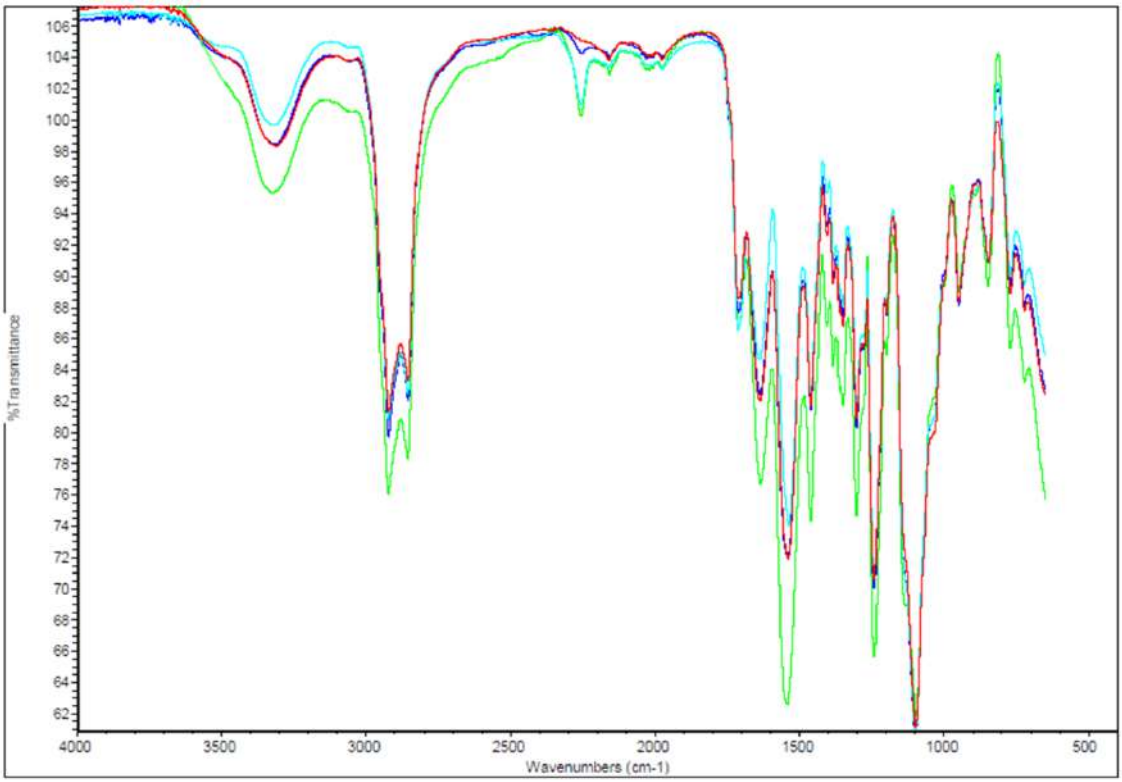

Figure 2. Consecutive IR spectra recorded during the encapsulation process of **Ir-Zn(Pc)**.

NCs concentration, Zn(Pc) and Ir-Zn(Pc) loading and encapsulation efficiency

The concentration of NCs in the final emulsions (mg/mL) was quantified with a solids concentrator, as indicated in Analytical Techniques section of the Chapter Ib. PSs loading (DL) and Encapsulation Efficiency (EE) were determined by ICP-MS analysis following the method described in Analytical Techniques section of this Chapter Ic. The DL and EE parameters for **GTCC-NCs**, **Zn(Pc)-NCs** and **Ir-Zn(Pc)-NCs** are indicated in Table 2.

Table 2. DL and EE parameters for **Zn(Pc)-** and **Ir-Zn(Pc)-**loaded NCs.

	[NCs] (mg/mL)	**PS Loading (DL, μM)**	**Encapsulation Efficiency (EE, %)**
NC-GTCC	42.9 ± 1.6	-	-
Zn(Pc)-NCs	30.2 ± 0.1	621.7 ± 93.0 μM	64.3 %
Ir-Zn(Pc)-NCs	62.4 ± 1.1	256.5 ± 20.5 μM	50.2%

Average size of NCs

The particle size distribution of the NCs was measured by dynamic light scattering (DLS). The experimental values and the number average are displayed in Table 3 and the size distribution by number of the NCs is graphically displayed in Figures 3 and 4.

Table 3. Hydrodynamic diameter average of **Zn(Pc)-** and **Ir-Zn(Pc)-**loaded NCs.

	Experimental values (nm)	Average ± SD (nm)
Zn(Pc)-NCs	12.29	11.4 ± 1.1
	11.74	
	10.19	
Ir-Zn(Pc)-NCs	13.44	15.2 ± 1.6
	16.50	
	15.55	

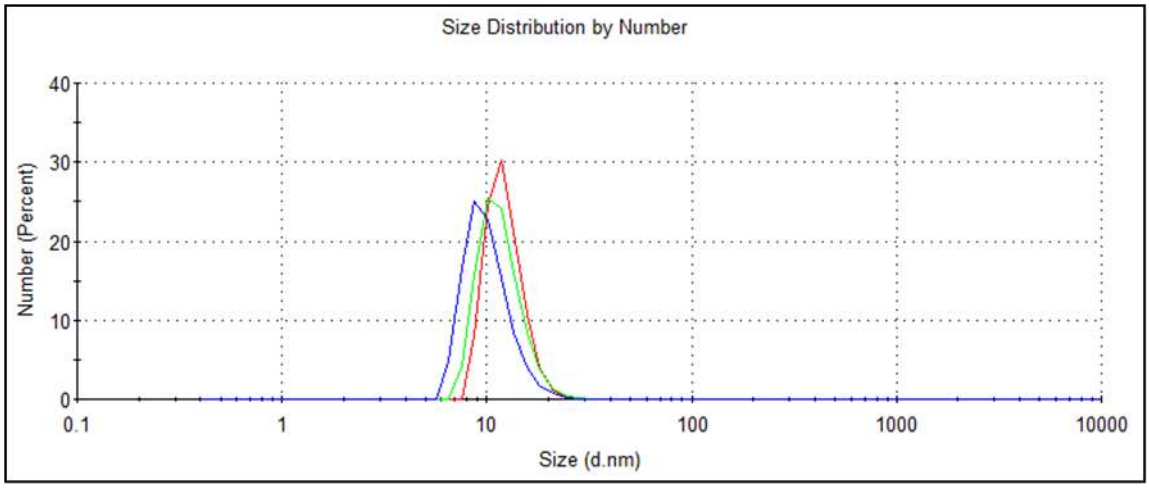

Figure 3. Average size of **Zn(Pc)-NCs**.

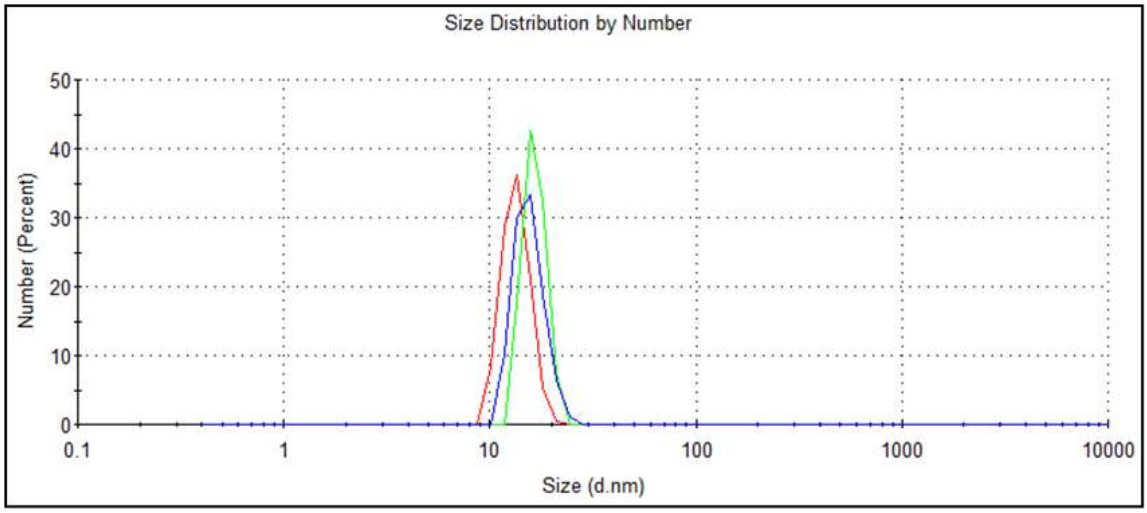

Figure 4. Average size of **Ir-Zn(Pc)-NCs**.

UV-visible spectra Zn(Pc)-NCs and Ir-Zn(Pc)-NCs

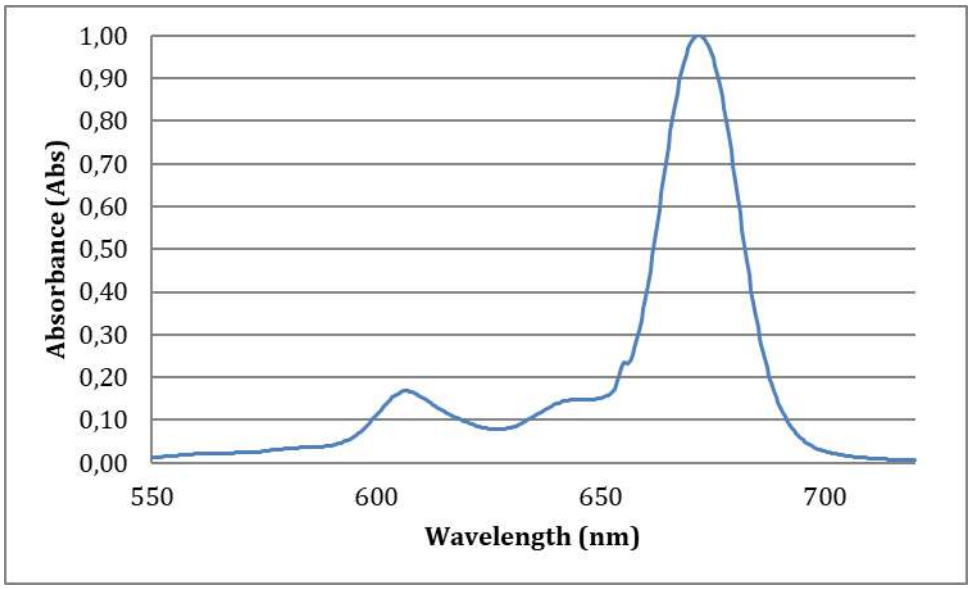

Figure 5. UV-visible spectrum of dried **Zn(Pc)-NCs** in THF.

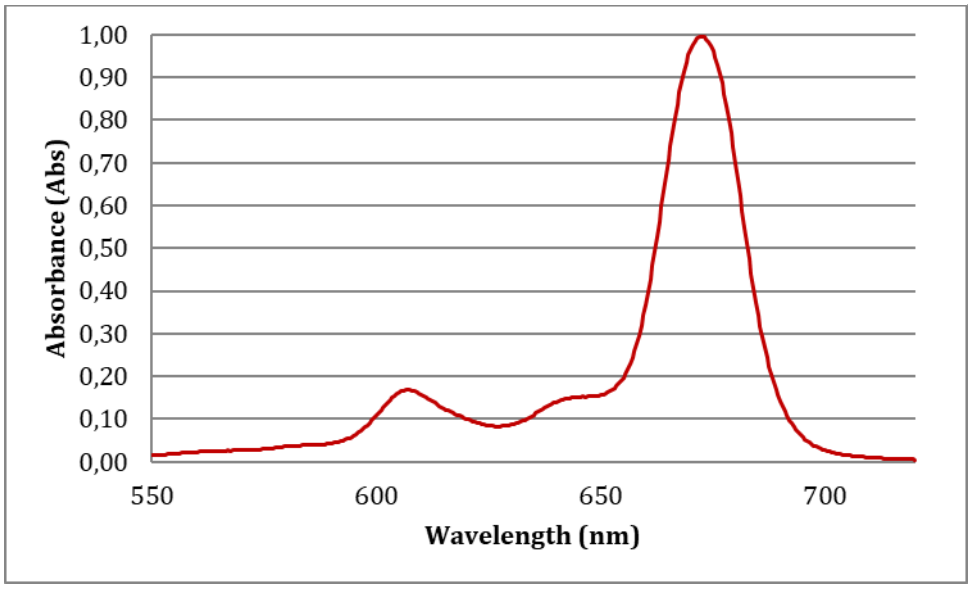

Figure 6. UV-visible spectrum of dried **Ir-Zn(Pc)-NCs** in THF.

Z-potential of Zn(Pc)-NCs and Ir-Zn(Pc)-NCs

As shown in Figures 7 and 8, the Z-potential values (surface charge) of the NCs were determined at different pH values as described in the Analytical Techniques section of Chapter Ib. Results of Z-potential analyses have been summarized in Table 5 of the Results and Discussion section.

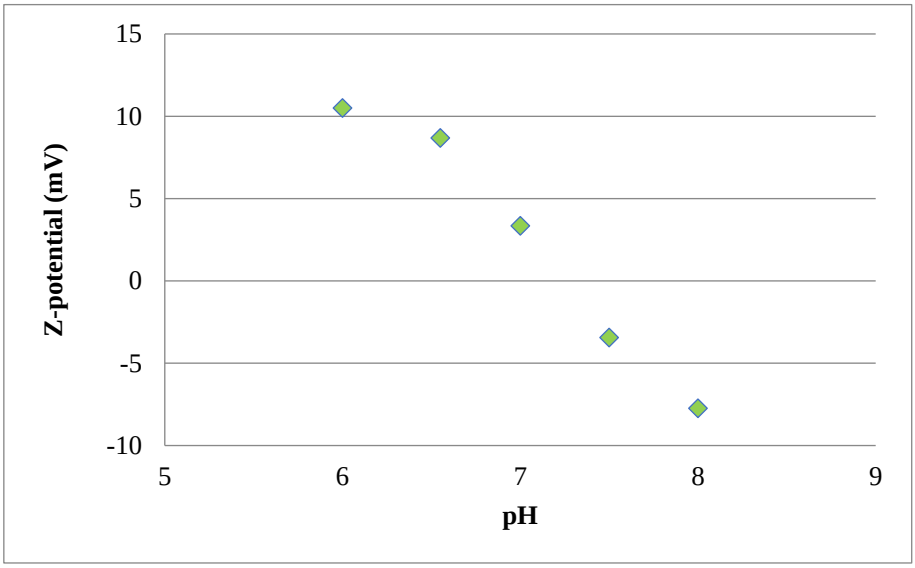

Figure 7. Z-potential values of **Zn(Pc)-NCs** *versus* pH.

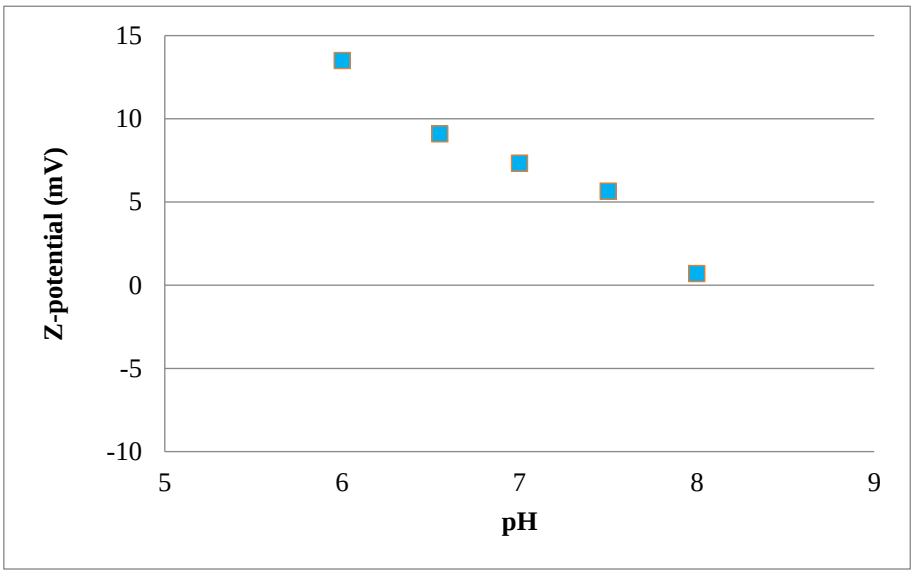

Figure 8. Z-potential values of **Ir-Zn(Pc)-NCs** *versus* pH.

Biological evaluation

Cell culture

HeLa cells were cultured in DMEM media (Gibco, Life Technologies, USA) supplemented with 10% of fetal bovine or calf serum (Gibco). Cell line was complemented with 100 $U \cdot mL^{-1}$ penicillin–streptomycin mixture (Gibco) and maintained in a humidified atmosphere at 37 °C and 5 % of CO_2.

Confocal Microscopy

HeLa cells were maintained in DMEM and supplemented with 10% fetal calf serum, 50 U/mL penicillin-streptomycin and 2 mM L-glutamine. For cellular uptake experiments and posterior observation under the microscope, cells were seeded on glass bottom dishes (P35G-1.5-14-C, Mattek). 24 h after cell seeding, cells were incubated at 37 ºC for 30 min with free and encapsulated **Zn(Pc)** and **Ir-Zn(Pc)** compounds (10 µM) in supplemented DMEM. Then, cells were washed three times with DPBS (Dulbecco's Phosphate-Buffered Saline) to remove the excess of the compounds and kept in DMEM without phenol red for fluorescence imaging.

All microscopy observations were performed using a Zeiss LSM 880 confocal microscope equipped with a 561 nm and a 633 nm laser. The microscope was also equipped with a full enclosure imaging chamber (XLmulti S1, Pecon) connected to a 37 ºC heater and a 5% CO_2 providing system. Cells were observed using a 63X 1.2 multi immersion objective. The compounds were excited using the 561 nm laser and detected from 570 to 670 nm, as well excited with the 633 nm laser and detected from 650 to 670 nm. Image analysis was performed using Fiji[6]. Unless otherwise stated images are colorized using Fire lookup table.

Colocalization images using Lysotracker Green (LTG) were acquired sequentially using 488 nm laser line and emission detected in the 500-550 nm range. Simultaneously, bright field transmitted light images were acquired. Colocalization analysis was performed using Fiji (ImageJ version 1.53f51)[6]. Images were filtered by Median and Gauss filters with a radius of 1 in both cases. Then background was subtracted using a Rolling Ball of 10. Finally, colocalization was analyzed using the JaCoP plugin[7]. Results obtained from the colocalization analyses have been summarized in Table 4.

Table 4. Pearson, Manders 1 and Manders 2 colocalization coefficients extracted from the analysis of **Zn(Pc)-NCs** images under yellow and red-light excitation.

Zn(Pc)-NCs	**561 nm**	**633 nm**
Number of cells	12	14
Pearson	0.656	0.519
Manders 1	0.737	0.677
Manders 2	0.346	0.295

Phototoxicity evaluation in cancer cells

HeLa were cultured in 96-well plates at a density of $5 \cdot 10^3$ cells/well in complete medium and incubated for 24 h at 37 ºC and 5 % CO_2 in a humidified incubator. Cell medium was removed by suction and serial dilutions of tested compounds in cell culture media were added at final concentrations in the range of 0 to 100 μM in a final volume of 100 μL/well (% v/v DMSO below 0.4%). Alternatively, water solutions of the encapsulated compounds were further diluted in cell culture media and added directly to cell plates. After 1 h incubation with the compounds, light irradiation was applied using Red Well Plate illuminator photoreactor (Luzchem; Canada) fitter with LED lamps centred at 620 nm (final intensity 89 mW/cm^2) for 1 h. Dark control analogues were directly kept in the dark for 2 h. Cells were then washed with PBS and fresh media was added for a drug-free cell recovery period of 48 h. Cell media was then removed and wells were loaded with 50 μL of MTT solution (1 mg/mL) for additional 4 h, then removed and 50 μL DMSO was added to solubilize the purple formazan crystals formed in active cells. The absorbance was measured at 570 nm using a microplate reader (FLUOstar Omega) and the IC_{50} values were calculated based on the inhibitory rate curves using the next the equation (3):

$$I = \frac{I_{max}}{1+\left(\frac{IC_{50}}{C}\right)^n} \quad \textbf{(3)}$$

Where I represent the percentage inhibition of viability observed, I_{max} is the maximal inhibitory effect, IC_{50} is the concentration that inhibits 50% of maximal growth, C is the concentration of the treatment and n is the slope of the semi-logarithmic dose-response sigmoidal curves. The non-linear fitting was performed using SigmaPlot 14.0 software. Two independent experiments were performed with triplicate points per concentration level (n=3).

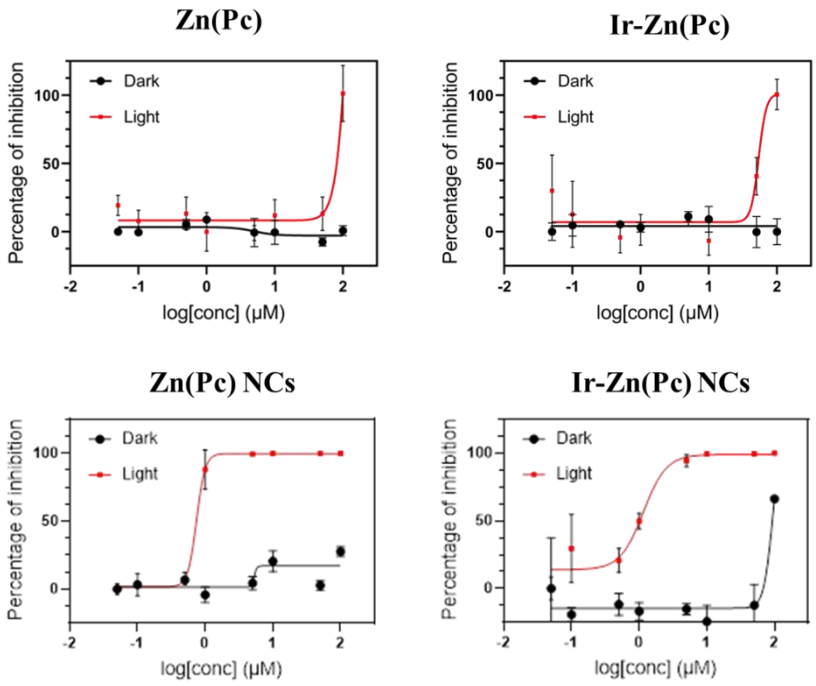

Figure 9. Cell viability curves in the dark and after red light irradiation for free and encapsulated compounds.

Results and Discussion

Synthesis and characterization of Zn(Pc)- and Ir-Zn(Pc)-loaded NCs

Zn(Pc)-NCs and **Ir-Zn(Pc)-NCs** have been prepared following the methodology previously used for the encapsulation of liposoluble compounds described in chapters Ia and Ib. ICP-MS analysis of the nanocapsules' emulsions allowed the quantification of zinc and iridium content in the samples, thereby facilitating the cargo determination after purification of the nanocapsules by dialysis, as well as to determine the encapsulation efficacy of the methodology for these compounds. Photosensitizer loading and EE value for **Zn(Pc)-NCs** have been calculated from the experimental ICP-MS analysis of the zinc content, while the iridium content was used to determine the PS-loading and EE value in the case of **Ir-Zn(Pc)-NCs**. Although the structures of both compounds are not disclosed due to confidentiality reasons, it is worth noting that encapsulation efficacy results, 64.3% for **Zn(Pc)-NCs** and 50.2% for **Ir-Zn(Pc)-NCs,** are in good concordance with the lipophilicity of both structures. Nevertheless, it is worth noting that encapsulation efficacy could be foreseeable increased by modifying the HLB of the polymer.

Table 5. Z-potential values of the samples against pH variation.

Sample	Z-Pot ± SD (mV) at pH=6.0	Z-Pot ± SD (mV) at pH=6.5	Z-Pot ± SD (mV) at pH=7.0	Z-Pot ± SD (mV) at pH=7.5	Z-Pot ± SD (mV) at pH=8.0
Zn(Pc)-NCs	10.5 ± 0.5	8.7 ± 1.0	3.4 ± 0.6	-3.4 ± 0.4	-7.7 ± 0.3
Ir-Zn(Pc)-NCs	13.5 ± 3.6	9.1 ± 1.5	7.2 ± 0.7	5.7 ± 0.5	0.7 ± 0.3

The DLS and Z-potential values for **Zn(Pc)**- and **Ir-Zn(Pc)**-loaded nanocapsules are in good agreement with the expected ones for the ratio of dispersible phase and self-emulsifiable polymer. Using similar polymer/hydrophobic-phase ratios for all of the compounds encapsulated in Chapter I (COUPY-based PSs, Ru(II)-polypyridyl complexes and phthalocyanine derivatives), slight but not significant differences can be observed in terms of nanocapsules' size. The molecular weight, the aggregation events or, specially, the intrinsic hydrophobicity of the encapsulated molecules, have been defined as crucial parameters for a proper encapsulation in a liposoluble core of polyurethane-polyurea hybrid nanocapsules. On the other hand, while a direct comparison of EE values with the different compounds that have been encapsulated in Chapter I is difficult due to the different amounts we used for each synthesis, we can, at least, confirm that aqueous solubility of the compounds significantly affects the encapsulation efficacy. Indeed, poor solubility in aqueous media drives the positioning of the cargo PS (e.g., compare **COUPY-1** and **COUPY-2** in chapter Ia) into the organic core of nanocapsule, thus

increasing the EE of the synthetic process. Finally, TEM analyses confirmed, as shown in Figure 10, the spherical morphology and the diameter of dried **Zn(Pc)-NCs** and **Ir-Zn(Pc)-NCs**.

As shown in Table 5, surface charge of **Zn(Pc)-** and **Ir-Zn(Pc)-**loaded nanocapsules has been demonstrated to be dependent of the pH of the media. These results were expected and parallel those obtained with COUPY- and Ru(II)-loaded nanocapsules. Indeed, amphoteric functionalization of the nanocapsules' surface allows protonation under acidic pH. As observed in COUPY- and Ru(II)-loaded NCs prepared using the same system, Z-potential values are only related to the degree of ionomeric moieties incorporated at the surface of the nanocapsules, masking the charge that could be contributed by the encapsulated molecule.

The size and surface charge results obtained in this chapter have also been corroborated in the Chapter II of this Thesis.

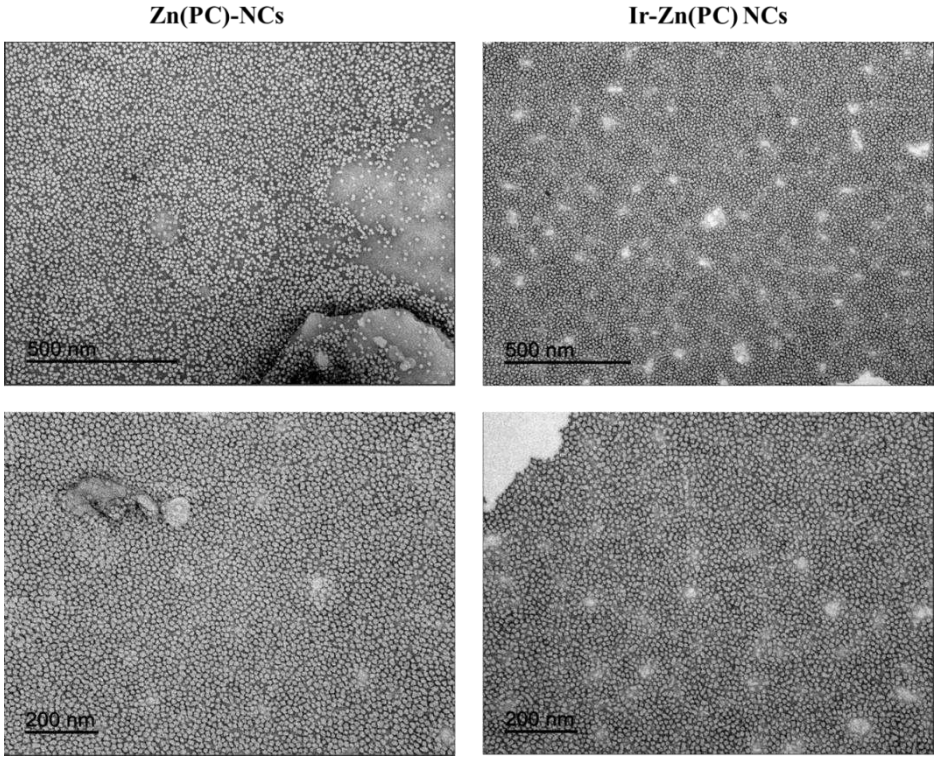

Figure 10. TEM micrographs of **Zn(Pc)-NCs** and **Ir-Zn(Pc)-NCs**.

To end up with the analysis of the physicochemical characterization, it is important to highlight that no significant differences between the UV-visible spectra of free (data not shown) and encapsulated **Zn(Pc)** and **Ir-Zn(Pc)** compounds have been observed (Figures 5 and 6), thereby indicating that the encapsulation process in polyurethane-polyurea hybrid nanocapsules do not compromise the chemical integrity of the photosensitizers.

Cellular uptake by confocal microscopy

Internalization of **Zn(Pc)** and **Ir-Zn(Pc)** using the polyurethane-polyurea NCs' formulation has been a crucial milestone in this project since allowed the evaluation of their biological activity. Indeed, previous studies with the free forms of both PSs carried out in the group of Prof. Ruiz reported a null internalization, presumably because of the poor aqueous solubility of the compounds, which caused precipitation in the biological media of cell cultures. By contrast, as shown in Figure 11, confocal microscopy studies with **Zn(Pc)-NCs** and **Ir-Zn(Pc)-NCs** confirmed the internalization of the encapsulated compounds after 30 min of incubation in HeLa cells, suggesting a vesicular intracellular distribution pattern. As previously found by Prof. Ruiz group, the non-encapsulated compounds remained within the extracellular media, adhered to the outer part of the cellular membrane forming aggregates (Figure 11), although a major part of them was removed after washing cycles.

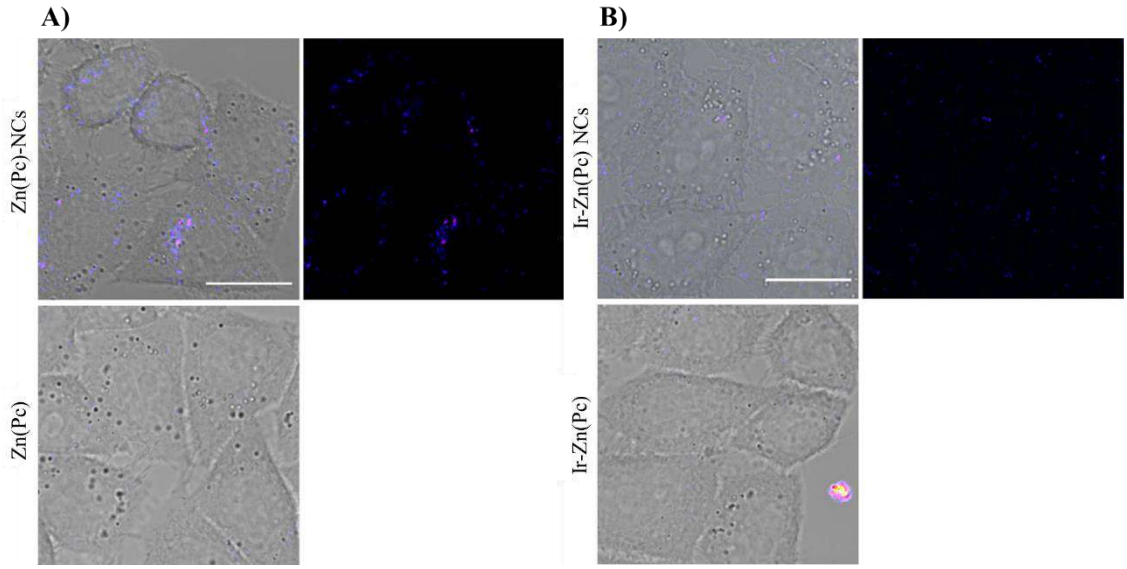

Figure 11. Cell internalization of encapsulated and free forms of compounds in HeLa cells. In both A, B panels: left shows the merge of brightfield and compound images and right the compound images alone. A) **Zn(Pc)-NCs** (encapsulated, top) and **Zn(Pc)** (free, bottom). B) **Ir-Zn(Pc)-NCs** (encapsulated, top) and **Ir-Zn(Pc)** (free, bottom). Images acquired irradiating with 561 nm yellow light. Scale bar: 20μm.

Colocalization studies with LysoTracker Green (LTG) confirmed that most of the internalized Zn(Pc)-NCs compounds were located in lysosomal constructions inside HeLa cells (Figure 12). Pearson and Manders coefficients were calculated at both excitation wavelengths (561 nm and 633 nm; n=12 and 14 cells, respectively) to quantify the lysosomal colocalization in HeLa cells. As shown in Table 4 in the experimental section, the high M1 coefficients (0.737 for the 561 excitation and 0.677 for the 633 excitation) clearly indicate that a high percentage of the fluorescence signal coming from the **Zn(Pc)-NCs** compound is overlapping the lysosomes' signal from LTG staining. It is worth noting that the poor fluorescence signal produced by **Ir-Zn(Pc)NCs** hampered the possibility of calculating these coefficients under these conditions.

Zn(Pc)-NCs have a clear tendency to accumulate in lysosomes after 30 min of incubation in HeLa cells, as it can be observable in Figure 12. Further studies will reveal if the lysosome-localized signal can be attributed to the integral nanocapsules or to the PS that has been intracellularly released from nanocapsules and subsequently accumulated in lysosomes. Nevertheless, a quick release of the cargo from nanocapsules can be foreseen considering previous results with COUPY-NCs and Ru(II)-NCs in HeLa cells. It is worth noting that the same intracellular fate occurred with Ir(III)-loaded nanocapsules described in the Chapter II of this Thesis.

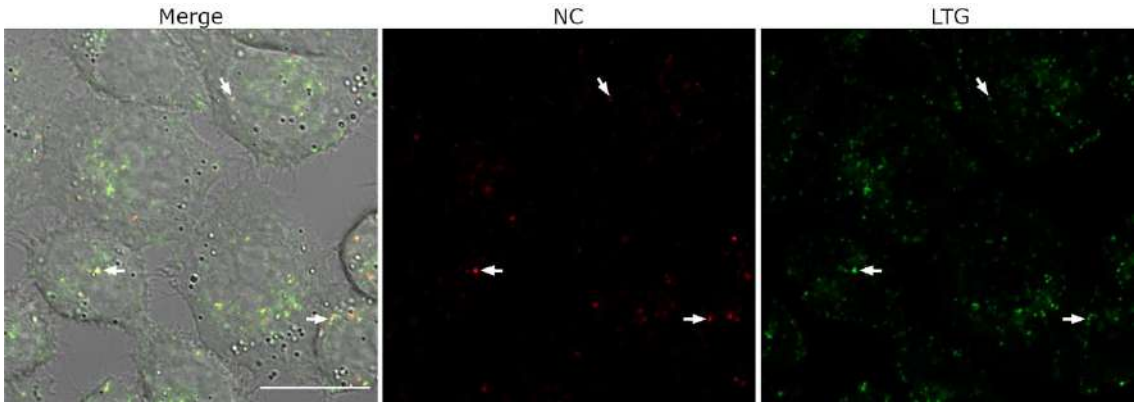

Figure 12. Colocalization studies of **Zn(Pc)-NCs** in HeLa cells. Confocal plane of HeLa cells cultured with **Zn(Pc)-NCs** (red, 10 μM) and LTG (green, 200 nM). Left: merge of brightfield, **Zn(Pc)-NCs** and LTG images; Center: **Zn(Pc)-NCs** image; Right: LTG image. White arrows point out positive colocalization of **Zn(Pc)-NCs** with LTG. Scale bar: 20 μm

Phototoxicity evaluation

In the same way that confocal microscopy did, the results from phototoxicity studies confirmed indirectly that the nanoencapsulated compounds were properly internalized in HeLa cells when compared with the non-encapsulated ones. Indeed, **Zn(Pc)** and **Ir-Zn(Pc)** did not induce any type of cellular photodamage upon red-light irradiation, while their encapsulated forms, **Zn(Pc)-NCs** and **Ir-Zn(Pc)-NCs**, generated a strong phototoxic effect under the same experimental conditions. Moreover, the analysis of cytotoxicity in dark conditions verified that no-toxicity was created by **Zn(Pc)-NCs** and **Ir-Zn(Pc)-NCs** in the absence of any external irradiation. The strong phototoxic effect of the encapsulated compounds combined with a lack of dark toxicity led to high PI values for both **Zn(Pc)-NCs** and **Ir-Zn(Pc)-NCs** (>138.9 and >83.9, respectively; see Table 6).

Table 6. Cyto- and phototoxicity of **Zn(Pc)-NCs** and **Ir-Zn(Pc)-NCs** *versus* their corresponding free compounds in dark conditions as well as under red-light irradiation (620 nm) towards HeLa cells expressed as IC_{50} values (μM). Phototoxic index (PI) = IC_{50} (dark-non-irradiated cells)/IC_{50} (irradiated cells).

	HeLa			
	Zn(Pc)-NCs		**Zn(Pc)**	
	IC_{50}	*PI*	*IC_{50}*	*PI*
Dark	>100	-	>100	-
620 nm	0.72 ± 0.2	>138.9	56 ± 4	1.8
	Ir-Zn(Pc)-NCs		**Ir-Zn(Pc)**	
	IC_{50}	*PI*	*IC_{50}*	*PI*
Dark	>100	-	>100	-
620 nm	1.2 ± 0.2	>83.3	95 ± 8	1.0

As shown in Table 6, the phototoxic activities of **Zn(Pc)-NCs** and **Ir-Zn(Pc)-NCs** were comparable, with IC_{50} values comprised in the low micromolar scale. However, further biological studies will be required (e.g., ROS determination, photostability, phototoxicity under hypoxia, etc.) to elucidate the effect of conjugating the cyclometalated Ir(III) complex to the Zn(phthalocyanine) derivative on the photoactivity of the resulting conjugate.

Finally, it is worth noting that phototoxicity data reported in the literature for zinc(II)-phthalocyanine-based PSs are in good agreement with the results obtained in this work, being the problem of aggregation/precipitation in biological media more than evident, as highlighted in several publications[8]. Indeed, some authors have performed modifications on the Zn(Pc) compounds with the aim of stabilizing them in aqueous media as well as red-shifting the absorption maximum[9]. Remarkably, encapsulation techniques together with other drug delivery systems appear to be the optimal methodologies to construct PDT agents based on Zn(Pc) compounds, since the modifications to obtain liposoluble compounds have been suggested to diminished the activity[10]. For example, Mehraban and coworkers have reported an increased phototoxic activity for a modified zinc-phthalocyanine photosensitizer when encapsulated in PLGA-b-PEG nanoparticles, being able to inhibit 50% of cell viability with a 24-hours treatment at 80 nM concentration of the zinc-phthalocyanine containing nanoparticles, under 650 nm red-light irradiation[11]. Overall, all these data endorse the nanoencapsulation as a

useful technique to increase the cell availability of zinc-phthalocyanine based photosensitizers.

Conclusions and outlook

In summary, the encapsulation of **Zn(Pc)** and **Ir-Zn(Pc)** into polyurethane-polyurea hybrid nanocapsules allowed to evaluate the potential of these new photosensitizers in the context of anticancer PDT. The strong absorbance in the far red and NIR region of the electromagnetic spectrum makes them interesting compounds to be further evaluated as potential photosensitizers in cancer treatment. To our delight, both **Zn(Pc)-NCs** and **Ir-Zn(Pc)-NCs** showed phototoxic activities in the micromolar range under red-light irradiation, leading to PI values above 80.

Subsequent studies to elucidate fluorescence half-life times and photostability of both free and encapsulated compounds are being launched. In addition, the study of ROS generation will be carried out both in solution and *in vitro* to investigate the effect of conjugating the cyclometalated Ir(III) complex to the Zn-phthalocyanine derivative. Evidently, quantification of cellular uptake for **Zn(Pc)-NCs** and **Ir-Zn(Pc) NCs** by ICP-MS needs to be addressed.

This work is still in a premature stage to consider **Zn(Pc)-NCs** and **Ir-Zn(Pc) NCs** as good candidates for *in vivo* testing. Nevertheless, phototoxicity analyses in 3D cell line models together with hypoxia experiments will provide valuable information on the potential of the compounds as new PSs for anticancer PDT.

References

(1) Novohradsky, V.; Rovira, A.; Hally, C.; Galindo, A.; Vigueras, G.; Gandioso, A.; Svitelova, M.; Bresolí-Obach, R.; Kostrhunova, H.; Markova, L.; Kasparkova, J.; Nonell, S.; Ruiz, J.; Brabec, V.; Marchán, V. Towards Novel Photodynamic Anticancer Agents Generating Superoxide Anion Radicals: A Cyclometalated Ir III Complex Conjugated to a Far-Red Emitting Coumarin. *Angew Chem In. Ed* **2019**, *131* (19), 6377–6381. https://doi.org/10.1002/ange.201901268.

(2) Li, X.; Peng, X. H.; Zheng, B. de; Tang, J.; Zhao, Y.; Zheng, B. Y.; Ke, M. R.; Huang, J. D. New Application of Phthalocyanine Molecules: From Photodynamic Therapy to Photothermal Therapy by Means of Structural Regulation Rather than Formation of Aggregates. *Chem Sci* **2018**, *9* (8), 2098–2104. https://doi.org/10.1039/c7sc05115h.

(3) Martins, T. J.; Negri, L. B.; Pernomian, L.; Faial, K. do C. F.; Xue, C.; Akhimie, R. N.; Hamblin, M. R.; Turro, C.; da Silva, R. S. The Influence of Some Axial Ligands on Ruthenium–Phthalocyanine Complexes: Chemical, Photochemical, and Photobiological Properties. *Front Mol Biosci* **2021**, *7*. https://doi.org/10.3389/fmolb.2020.595830.

(4) Prabhu C. P., K.; Nemakal, M.; Managa, M.; Nyokong, T.; Koodlur Sannegowda, L. Symmetrically Substituted Zn and Al Phthalocyanines and Polymers for Photodynamic Therapy Application. *Front Chem* **2021**, *9*. https://doi.org/10.3389/fchem.2021.647331.

(5) Rak, J.; Pouckova, P.; Benes, J.; Vetvicka, D. Drug Delivery Systems for Phthalocyanines for Photodynamic Therapy. *Anticancer Res* **2019**, *39* (7), 3323–3339. https://doi.org/10.21873/anticanres.13475.

(6) Schindelin, J.; Arganda-Carreras, I.; Frise, E.; Kaynig, V.; Longair, M.; Pietzsch, T.; Preibisch, S.; Rueden, C.; Saalfeld, S.; Schmid, B.; Tinevez, J. Y.; White, D. J.; Hartenstein, V.; Eliceiri, K.; Tomancak, P.; Cardona, A. Fiji: An Open-Source Platform for Biological-Image Analysis. *Nat Methods* **2012**, *9* (7), 676–682. https://doi.org/10.1038/nmeth.2019.

(7) Bolte, S.; Cordelières, F. P. A Guided Tour into Subcellular Colocalization Analysis in Light Microscopy. *J Microsc* **2006**, *224*, 213–232.

(8) Roguin, L. P.; Chiarante, N.; García Vior, M. C.; Marino, J. Zinc(II) Phthalocyanines as Photosensitizers for Antitumor Photodynamic Therapy. *Int J Biochem Cell Biol* **2019**, *114*. https://doi.org/10.1016/j.biocel.2019.105575.

(9) Çakir, D.; Göksel, M.; Çakir, V.; Durmuş, M.; Biyiklioglu, Z.; Kantekin, H. Amphiphilic Zinc Phthalocyanine Photosensitizers: Synthesis, Photophysicochemical Properties and in Vitro Studies for Photodynamic Therapy. *Dalton T* **2015**, *44* (20), 9646–9658. https://doi.org/10.1039/c5dt00747j.

(10) Ezquerra Riega, S. D.; Chiarante, N.; Valli, F.; Marino, J.; Roguin, L. P.; Awruch, J.; García Vior, M. C. Novel Hydro- and Lipo-Philic Selenium Zinc(II) Phthalocyanines: Synthesis, Photophysical Properties and Photodynamic Effects on CT26 Colon Carcinoma Cells. *Dyes Pigments* **2018**, *156*, 133–139. https://doi.org/10.1016/j.dyepig.2018.03.067.

(11) Mehraban, N.; Musich, P. R.; Freeman, H. S. Synthesis and Encapsulation of a New Zinc Phthalocyanine Photosensitizer into Polymeric Nanoparticles to Enhance Cell Uptake and Phototoxicity. *Appl Sci (Switzerland)* **2019**, *9* (3). https://doi.org/10.3390/app9030401.

Chapter II. Nanoencapsulation of cyclometalated iridium(III) complexes for an improved cancer chemotherapy

10. Publication II. Polyurethane–polyurea hybrid nanocapsules as efficient delivery systems of anticancer Ir(III) metallodrugs (*Inorganic Chemistry Frontiers*, **2022**, 9, 2123-2138).

Volume 9 | Number 10 | 21 May 2022

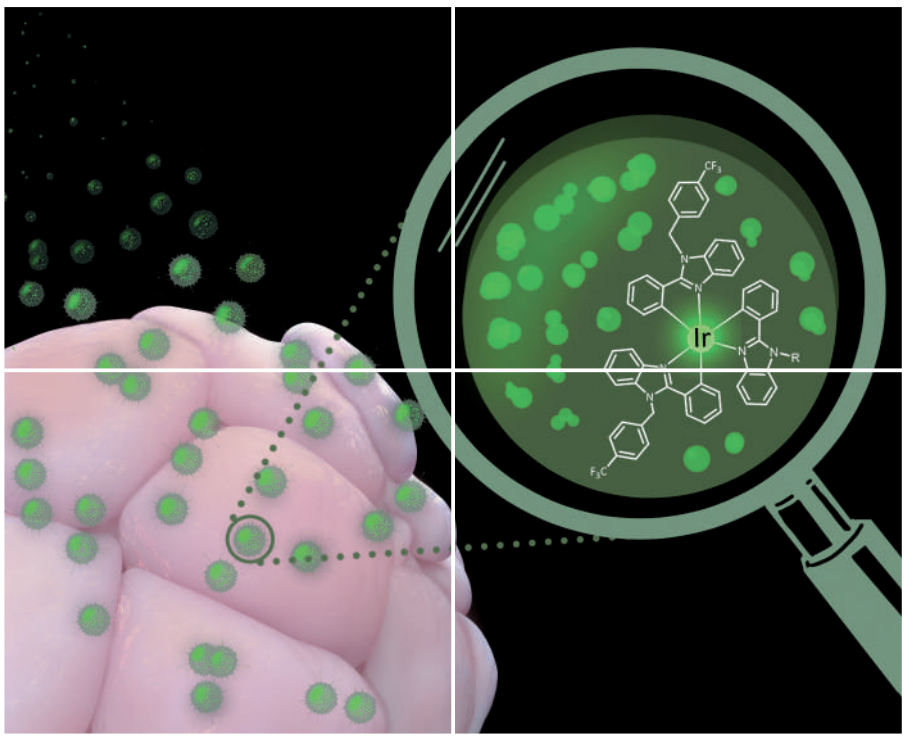

INORGANIC CHEMISTRY

FRONTIERS

CCS 中国化学会 CHINESE CHEMICAL SOCIETY
PEKING UNIVERSITY 1898
ROYAL SOCIETY OF CHEMISTRY
rsc.li/frontiers-inorganic

INORGANIC CHEMISTRY
FRONTIERS

RESEARCH ARTICLE

View Article Online
View Journal | View Issue

Check for updates

Cite this: *Inorg. Chem. Front.*, 2022, **9**, 2123

Polyurethane–polyurea hybrid nanocapsules as efficient delivery systems of anticancer Ir(III) metallodrugs†

Joaquín Bonelli, ‡[a,b] Enrique Ortega-Forte, ‡[c] Gloria Vigueras, ‡[c] Manel Bosch, [d] Natalia Cutillas, [c] Josep Rocas,[b] José Ruiz *[c] and Vicente Marchán *[a]

Cyclometalated Ir(III) complexes hold great promise as an alternative to platinum metallodrugs for the therapy and diagnosis of cancer. However, their low aqueous solubility and poor cell membrane permeability are obstacles for *in vivo* applications. Here we have encapsulated for the first time, using polyurethane–polyurea hybrid nanocapsules (NCs), two phosphorescent tris-cyclometalated Ir(III) complexes incorporating deprotonated 2-arylbenzimidazole ligands, **Ir1** and **Ir2**. Ir(III)-Loaded nanocapsules (**NC-Ir1** and **NC-Ir2**) showed a roughly round shape and controlled particle size distribution around 18 nm. The photophysical properties of aqueous solutions of NCs were similar to those of the free complexes in CH_2Cl_2, which accounts for the hydrophobic and protective environment generated by the nanoparticles around the cargo. Nanoencapsulation had also a positive effect on the cellular uptake of the metallodrugs and NCs were found to be highly cytotoxic towards several cancer cell lines, whereas Ir(III) complexes alone were found to be inactive. A strong tumor growth inhibition effect was also found in 3D tumorsphere cancer models owing to the high penetration capacity of small NCs. Finally, the mode of cell death of the NCs was found to be related to oncosis, and the mitochondrial dysfunction and generation of extensive oxidative stress appeared to be also involved in the mechanism of action of these novel nanomedicines.

Received 10th December 2021,
Accepted 1st March 2022

DOI: 10.1039/d1qi01542g

rsc.li/frontiers-inorganic

1. Introduction

Metal complexes have shown impressive properties in different medical fields, especially in oncology, where platinum(II)-based drugs such as cisplatin and its second and third generation analogues are prescribed in most of the first line anticancer treatments in clinics.[1] Nevertheless, these compounds exhibit several serious drawbacks, including systemic toxicity in patients due to poor tumor specificity, and premature degradation/inactivation in the blood stream, which become crucial issues to be considered when developing a safe metallodrug-based antitumor therapy.[2] Hence, controlled accumulation and release of metal-based anticancer drugs have aroused enormous interest in the last decades with the aim of improving their therapeutic efficacy.[3] In this context, nanosystems have been postulated as efficient carriers for enhancing metallodrugs' concentration in tumor cells.[3,4] Indeed, most of the common nanomedical approaches, such as metal–organic frameworks (MOFs),[5] liposomes,[6] micelles[7] or polymeric nanoparticles[8] and nanocapsules,[9] have been explored as potential candidates for the targeted delivery of metallodrugs. In the case of liposoluble compounds, the effect of the nanocarrier should not only be restricted to enhance their accumulation in target tissues, but also to improve selective internalization in cancer cells, which really triggers their cytotoxic effect.

Polyurethanes have gained interest in different biomedical applications, from stents[10] or catheter implants[11] to "polymeric director" groups[12] and nanocapsules,[13] since they exhibit reasonable toxicity and biocompatibility, together with

[a]*Departament de Química Inorgànica i Orgànica, Secció de Química Orgànica, IBUB, Universitat de Barcelona, E-08028 Barcelona, Spain. E-mail: vmarchan@ub.edu*
[b]*Nanobiotechnological Polymers Division, Ecopol Tech, S.L., El Foix Business Park, Indústria 7, 43720 L'Arboç del Penedès, Tarragona, Spain*
[c]*Departamento de Química Inorgánica, Universidad de Murcia, and Institute for Bio-Health Research of Murcia (IMIB-Arrixaca), E-30071 Murcia, Spain. E-mail: jruiz@um.es*
[d]*Unitat de Microscòpia Òptica Avançada, Centres Científics i Tecnològics, Universitat de Barcelona, Av. Diagonal 643, E-08028 Barcelona, Spain*

†Electronic supplementary information (ESI) available: General methods and analytical techniques. Additional figures for the synthesis and characterization of Ir(III) complexes (NMR, MS) and of the corresponding Ir(III)-loaded nanocapsules (IR, DLS, TEM, *Z*-potential, ICP-MS), and for their biological evaluation (confocal microscopy, antiproliferative activity, morphological analysis of cells, cell membrane integrity test, mitochondrial potential assessment, aerobic respiration and glycolytic rate evaluation and oxidative stress induction). See DOI: 10.1039/d1qi01542g

‡These authors contributed equally.

accessible and feasible synthetic procedures. Polyurethane–polyurea hybrid nanocapsules (NCs) have been previously reported by some of the authors as promising tools for different nanomedical solutions,[14] for example, in the fields of immunotherapy[15] and regenerative medicine.[16] This approach takes advantage of the versatility provided by polyurethane chemistry to furnish water-dispersible, with no external surfactants needed, and industrial-scalable drug-loaded nanocapsules.[17] In addition, the combination of amphiphilic groups and the ability of modifying their external surface charge under extracellular tumor microenvironment (TME) conditions, increasing their positive surface charge in acidic media, results in a higher accumulation in tumor locations compared with healthy tissues, and increased uptake by tumor cells.[17]

On the other hand, the use of Ir(III) complexes in therapy as an alternative to platinum metallodrugs has increased in the last years.[18] This is mainly because Ir(III) compounds possess several advantages over platinum complexes such as easier preparation and purification, air and moisture stability and remarkable tunability of their photophysical properties. In addition, the combination of both anticancer activity and luminescence in octahedral cyclometalated Ir(III) complexes has allowed the development of new theranostic agents which offer both therapeutic promise and potential for diagnosis.[19] Hitherto, neutral Ir(III) complexes have been the most studied phosphorescent materials[20] since they exhibit excellent properties, including stability of the octahedral geometry in both reduced and oxidized states and long emission lifetimes, high quantum yields and tunable emission color.[20a] However, highly luminescent tris-cyclometalated iridium(III) complexes have been used to a much smaller extent in living systems than cationic bis-cyclometalated compounds. One of the reasons may be that they are generally electronic-neutral molecules and thus have very low water solubility. Therefore, the structures of complexes have been modified with cationic peptides,[21] groups that increase water solubility,[22] or groups that are pH sensitive.[23] Another strategy consists of using nanocarriers that transport the complexes inside the cells.[24] Thus, Ir(III) complexes incorporated in nanometric drug delivery systems could improve their biological performance, especially in terms of cellular uptake, solubility and biocompatibility.[25]

Herein, we present the encapsulation, using polyurethane–polyurea hybrid nanocapsules, of two new phosphorescent, hydrophobic and neutral homo- or hetero-tris-cyclometalated Ir(III) complexes of the type [Ir(C^N)$_3$] (**Ir1**) and [Ir(C^N)$_2$(C′^N′)] (**Ir2**) (Fig. 1), with the aim of exploring their photophysical, cellular uptake and biological properties. The C^N ligands in both complexes have in common the benzimidazole core which has been shown to be a widely used pharmacophore[26] and has exhibited good biological performance in previous studies of some of the authors.[27] The Ir(III)-loaded nanocapsules were efficiently internalized in living HeLa cells compared to free complexes, and their photophysical properties resembled those of the compounds dissolved in an organic solvent owing to the hydrophobic and protective environment provided by the nanocapsules around the compounds. Besides studying the antiproliferative activity of the Ir(III)-loaded NCs in 2D monolayer cancer cells and in 3D tumorsphere cancer models, the mode of cell death was investigated in detail.

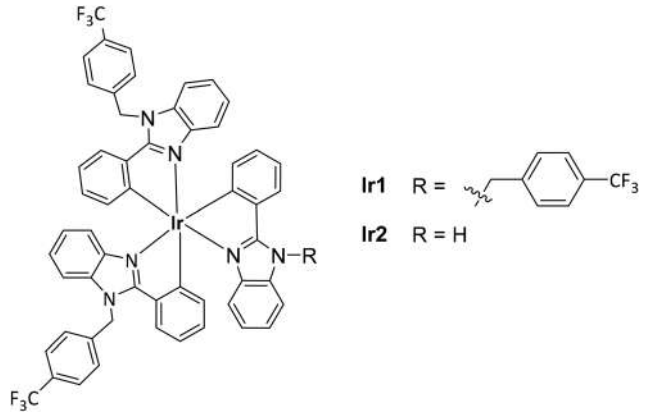

Fig. 1 Structure of tris-cyclometalated Ir(III) complexes, **Ir1** and **Ir2**, investigated in this work.

2. Experimental section

2.1. Synthesis and characterization of Ir(III) complexes

The first step for both complexes was the synthesis of the dimer complex [(Ir(μ-Cl)(C^N)$_2$]$_2$, which was carried out following a previously reported procedure.[28] 2-Phenyl-1-[4-(trifluoromethyl)benzyl]-1*H*-benzo[*d*]imidazole (2.2 mmol) and iridium (III) chloride (1 mmol) were dissolved in 2-ethoxyethanol/deionized H_2O (3 : 1) in a Schlenk flask. The mixture was stirred at 110 °C for 24 h under a nitrogen atmosphere. The mixture was cooled to room temperature, and the resultant solid was collected by filtration. The yellow solid was washed with water and ethanol and used without further purification.

2.1.1. Synthesis and characterization of Ir1. The homoleptic complex **Ir1** was synthesized using an adaptation of a previously reported method.[29] A solution of the cyclometalated iridium(III) chloro-bridged dimer (0.081 mmol), 2-phenyl-1-[4-(trifluoromethyl)benzyl]-1*H*-benzo[*d*]imidazole (0.59 mmol), and silver triflate (0.16 mmol) in 2-ethoxyethanol (2 mL) was heated at 95 °C overnight under a nitrogen atmosphere. The solvent was concentrated under reduced pressure, and the product was re-suspended in dichloromethane. The suspension was filtered with Celite to remove the white AgCl precipitate, and the filtrate was solvent-stripped to dryness. Then, the obtained solid was washed with ethyl acetate to obtain a bright yellow product.

Ir1. Bright yellow solid. Isolated yield: 65%. ^{1}H-NMR (300 MHz, [D$_2$] methylene chloride): δ (ppm) 7.55 (d, J = 8.1 Hz, 2H), 7.46 (m, 1H), 7.29 (m, 4H), 6.87 (t, J = 7.2 Hz, 1H), 6.72 (m, 3H), 6.50 (d, J = 8.1 Hz, 1H), 5.97 (m, 2H). ^{13}C-NMR (75.4 MHz, [D$_2$] methylene chloride): δ (ppm) 163.7, 142.9, 141.0, 138.4, 136.9, 135.8, 131.1, 130.7, 130.1, 127.4, 127.0, 127.0, 125.3, 124.3, 123.8, 120.7, 117.1, 110.8, 48.8. ESI-MS

This journal is © the Partner Organisations 2022

(pos. ion mode, CH_2Cl_2): m/z = 1247.3001 $[M + H]^+$, calcd m/z 1247.3035. Anal. Calcd for $C_{63}H_{42}F_{12}IrN_6$: C, 60.72; H, 3.40; N, 6.74. Found: C, 60.66; H, 3.41; N, 6.62 (%).

2.1.2. Synthesis and characterization of Ir2. The heteroleptic complex **Ir2** was synthesized using an adaptation of a previously reported method.[30] The iridium(III) dimer (1 mmol), 2-phenyl-1*H*-benzo[*d*]imidazole (10 mmol), and Na_2CO_3 (2 mmol) were all suspended in 2 mL of 2-ethoxyethanol. The mixture was refluxed for 3 h and the solid was filtered after cooling in the fridge for 2 hours. The crude was purified by column chromatography on silica gel elution with dichloromethane.

Ir2. Yellow solid. Isolated yield: 31%. ^{1}H-NMR (300 MHz, [D_2] methylene chloride): δ (ppm) 9.65 (s, 1H), 7.50 (m, 7H), 7.29 (m, 5H), 7.17 (m, 3H), 6.83 (m, 4H), 6.71 (m, 6H), 6.46 (d, J = 7.8 Hz, 1H), 6.40 (d, J = 8.4 Hz, 1H), 6.32 (d, J = 7.5 Hz, 1H), 6.07 (s br, 1H), 6.01 (s br, 1H), 5.93 (d, J = 5.8 Hz, 1H), 5.71 (d, J = 6.2 Hz, 1H). ^{13}C-NMR (75.4 MHz, [D_2] methylene chloride): δ (ppm) 174.5, 164.1, 163.2, 163.7, 143.5, 142.9, 142.8, 141.0, 138.5, 138.3, 137.8, 136.8, 135.7, 135.5, 134.1, 134.0, 131.1, 130.7, 130.5, 127.4, 127.0, 126.9, 125.4, 125.3, 124.5, 124.3, 123.9, 123.7, 123.7, 120.5, 120.4, 120.3, 117.1, 116.6, 112.6, 110.7, 110.6, 48.8. HR ESI-MS (pos ion mode, DMSO): m/z = 1089.2669 $[M + H]^+$, calcd m/z 1089.2691. Anal. Calcd for $C_{55}H_{37}F_6IrN_6$. C, 60.71; H, 3.43; N, 7.72. Found: C, 60.82; H, 3.43; N, 7.60 (%).

2.2. Synthesis of Ir(III)-loaded nanocapsules

2.2.1. Synthesis of the amphiphilic cationic polymer (P1). 2,2′-Dihydroxyethyl disulfide (DEDS) (901.0 mg, 5.84 mmol, 11.68 meq), YMER N120 (12.04 g, 11.59 mmol, 23.18 meq) and *N*-(3-dimethylaminopropyl)-*N*,*N*′-diisopropanolamine (Jeffcat DPA) (981.3 mg, 4.50 mmol, 8.99 meq) were added into a three-necked round-bottom flask equipped with mechanical stirring at room temperature and purged with N_2. When the mixture was homogeneous, isophorone diisocyanate (IPDI) (8.14 g, 36.63 mmol, 73.24 meq) was added into the reaction vessel under gentle mechanical stirring. The polyaddition reaction was subjected to these conditions until the NCO stretching band intensity did not change, when monitored by IR spectroscopy. At this point, dry THF (21 mL) was added into the reaction mixture in order to fluidify the polymer. In parallel, 1,3-diamino-*N*-octadecylpropane (Genamin TAP 100D) (5.99 g, 17.73 mmol, 35.45 meq) was dissolved with dry THF (5.23 mL) into another 100 mL three-necked round-bottom flask, which had previously been purged with N_2. The former reaction mixture was added dropwise onto the latter under half-moon 100 rpm mechanical stirring. The reaction was monitored by IR until the NCO stretching band intensity had completely disappeared.

2.2.2. Synthesis of Ir1-loaded amphoteric NCs (NC-Ir1). IPDI (70.1 mg, 0.32 mmol, 0.63 meq) was added into a three-necked round-bottom flask equipped with mechanical stirring, precooled at 4 °C, purged with N_2 and protected from light. In parallel, **Ir1** (6.1 mg, 4.89 μmol), Neobee 1053 (26.0 mg, 55.96 μmol), polymer P1 (813.7 mg, 0.09 meq) and dry THF (1 mL) were mixed in a vial, added into the flask and homogenized for 10 min at 150 rpm, and protected from light. At this point, an alkaline aqueous solution of L-lysine was prepared by dissolving 0.93 g of L-lysine in 12.31 g of Milli-Q water and adjusting pH to 11.0 with 3 M and 1 M NaOH solutions (total L-lysine concentration 7.56% by wt). This solution (24.6 mg of L-lysine, 0.15 mmol, 0.29 meq) was added at 250 rpm and the polyaddition reaction was checked after 15 min by IR. Then, the organic phase was emulsified at 300 rpm with cold Milli-Q water (7.12 g) and finally a 10% w/w aqueous solution of diethylenetriamine (DETA) (7.94 mg of DETA, 0.08 mmol, 0.23 meq) was added in order to generate cross-linked NCs from the nano micelles. The stirring was reduced to 100 rpm. This polyaddition reaction was monitored by IR and pH measurements. Once the NCs were formed, THF was removed from the reactor at 35 °C under vacuum and dialysis purification was carried out.

2.2.3. Synthesis of Ir2-loaded amphoteric NCs (NC-Ir2). Encapsulation of complex **Ir2** was carried out following the procedure used for the synthesis of **Ir1**-loaded amphoteric NCs. The exact amounts of the reagents used are detailed in Table S1.†

2.2.4. Synthesis of non-loaded amphoteric NCs (NC-GTCC). The procedure was based on the one used for the synthesis of **Ir1**-loaded amphoteric NCs with the exception that no iridium complex was added to the reaction. The exact amounts of the reagents are detailed in Table S2.†

2.3. Biological studies

2.3.1. Cell culture. HeLa cervical cancer cells and BGM primate kidney cells were cultured in Dulbecco's modified Eagle's medium (1 g L^{-1} glucose) and supplemented with fetal bovine serum (10% v/v) and 1 mM L-glutamine in a CO_2 incubator at 310 K. Sensitive and resistant A2780 and A2780cis ovarian cancer cells were cultured in RPMI-1640 cell media, supplemented with 10% fetal bovine serum and 1 mM L-glutamine. Cell culture was maintained with a subculture routine of 2–3 times a week with an appropriate density for each cell line. To maintain the resistance to cisplatin of A2780cis, cisplatin (1 μM) was added to culture media every second passage. Cells were confirmed to be mycoplasma-free using a standard Hoechst staining method.[31]

For cell treatments, both compounds and nanoparticles were prepared in serial dilutions using Eppendorf tubes. For compounds **Ir1** and **Ir2**, serial dilutions with sterile DMSO as a solvent were prepared to obtain stock solutions that were 250× concentrated. Then, cell media were used to further dilute the samples until 10×. By dispensing 10% of the volume per well into the cell plates, a final 1× concentration was achieved with final 0.4% DMSO (v/v). For nanoparticles **NC-Ir1** and **NC-Ir2**, stock water-dissolved solutions were directly diluted in cell media and were used for treatments thereafter.

2.3.2. Cellular accumulation by ICP-MS. Cellular accumulation from iridium complexes (**Ir1** and **Ir2**) and from iridium-containing nanocapsules (**NC-Ir1** and **NC-Ir2**) was measured in HeLa cells. The cells were seeded in 6-well plates at a density

of 6×10^5 cells per well in 1.8 mL of complete growth medium and incubated for 48 h prior treatment. Cells were then treated with 5 μM of the iridium complexes or nanocapsules for 2 h at 37 °C and 4 °C. After trypsinization, cells were counted and the pellets were digested using Suprapur® nitric acid 30% for 1 h. The amount of iridium was determined using inductively coupled plasma mass spectrometry (ICP-MS). Three independent measurements were conducted (n = 2 replicate).

2.3.3. Cellular uptake by confocal microscopy. HeLa cells were maintained in DMEM (Dulbecco's modified Eagle's medium) Corning Glutagro™ (10-101-CV) containing high glucose (4.5 g L^{-1}) and supplemented with 10% FBS (fetal bovine serum (FBS) and 50 U mL^{-1} penicillin–streptomycin. For cellular uptake experiments and posterior observation under the microscope, cells were seeded on glass bottom dishes (P35G-1.5-14-C, Mattek). 24 h after cell seeding, cells were incubated at 37 °C for 30 min with free (**Ir1** and **Ir2**) and encapsulated iridium compounds (**NC-Ir1** and **NC-Ir2**) (5 μM) in supplemented DMEM. Then, cells were washed three times with DPBS (Dulbecco's phosphate-buffered saline) to remove the excess compounds and kept in low glucose (1 g L^{-1}) DMEM without phenol red for fluorescence imaging.

All microscopy observations were performed using a Zeiss LSM 880 confocal microscope equipped with 405 and 488 nm lasers. The microscope was also equipped with a full enclosure imaging chamber (XLmulti S1, Pecon) connected to a 37 °C heater and a 5% CO_2 providing system. Cells were observed using a 63× 1.4 oil immersion objective. The Ir(III) complexes were excited using the 405 nm laser and detected from 423 to 547 nm whereas iridium-containing nanocapsules were excited at 488 nm and detected from 497 to 597 nm. Image analysis was performed using Fiji.[32] Unless otherwise stated images are colorized using Fire lookup table.

2.3.4. Antiproliferative activity. A2780, A2780cis and HeLa cells were cultured in 96-well plates at a density of 5000 cells per well in complete medium and incubated for 24 h in a humidified CO_2 incubator at 37 °C. Serial dilutions of NC particles were added at final concentrations in the range of 0 to 30 mg mL^{-1} in a final volume of 100 μL per well for the indicated periods of time. After this incubation period, treatment-containing medium was aspirated by suction, cells were washed with saline PBS buffer and loaded with 50 μL of MTT solution (1 mg mL^{-1}) for additional 4 h, then removed and 50 μL of DMSO was added to solubilize the purple formazan crystals formed in active cells. The absorbance was measured at 570 nm using a microplate reader (FLUOstar Omega) and the IC_{50} values were calculated based on the inhibitory rate curves using the next the equation:

$$I = \frac{I_{max}}{1 + \left(\frac{IC_{50}}{C}\right)^{n}}$$

where I represents the percentage inhibition of viability observed, I_{max} is the maximal inhibitory effect, IC_{50} is the concentration that inhibits 50% of maximal growth, C is the concentration of the treatment and n is the slope of the semi-logarithmic dose–response sigmoidal curves. The non-linear fitting was performed using SigmaPlot 14.0 software. All experiments were performed in at least two independent studies with triplicate points per concentration level (n = 3).

For the generation of multicellular tumor spheroids (MTCS), 96-well Corning® microplates with ultra-low attachment surface coating were used. Briefly, a single suspension of HeLa cells at a density of 5×10^3 cells per well was prepared in complete DMEM medium and dispensed into wells. The plates were covered and transferred to an incubator at 37 °C with 5% CO_2 atmosphere. Within 3–4 days, uniform 200 μm-diameter MTCS were formed from cell suspension and were maintained under these conditions. The cell culture medium was replaced every 3 days and treated with **NC-Ir1** and **NC-Ir2** (6 μM) by replacing 50% of the media. The formation, integrity, diameter, and volume of the MCTS were monitored by a DMi1 inverted phase contrast microscope (Leica Microsystems). The volumes were calculated using the equation $V = 4/3\pi r^3$.

2.3.5. Cell death induction assays. Cell death induction of the nanocapsules on HeLa cells was determined by the dual FITC-Annexin V/propidium iodide (PI) labelling method *via* flow cytometry. Briefly, HeLa cells were seeded in 12-well plates at a density of 1.5×10^5 cells per well and incubated overnight. Testing treatments were added at indicated concentrations for 24 h and cisplatin was used as a positive control for apoptosis induction. After treatment, cells were harvested by trypsinization, washed with binding buffer, centrifuged and the pellets were resuspended in 185 μL of binding buffer (Roche). Then, 5 μL of Annexin-V-FLUOS and 10 μL of PI were added and the resuspended cell solution was left at room temperature in the dark for 15 min. Cells were analyzed by flow cytometry (Beckton Dickinson FACSCalibur), 10^4 events were acquired in each sample by registering at 620 and 525 nm for PI and Annexin V, respectively, λ_{exc} = 488 nm. Data were analyzed using FlowingSoftware version 2.5.1. The assay was performed in three independent experiments (n = 2 per replicate) yielding similar results.

2.3.6. Morphological analysis of cells. The cell morphology of HeLa cells upon treatment was determined by flow cytometry. Briefly, HeLa cells were seeded in 12-well plates at a density of 1.5×10^5 cells per well and incubated overnight. Testing treatments were added at indicated concentrations for 24 h and cisplatin was used as a positive control for the induction of apoptotic changes. After treatment, cells were harvested by trypsinization, washed with binding buffer, centrifuged and the pellets were resuspended in PBS. Samples were then subjected to flow cytometry (Beckton Dickinson FACSCalibur), where 10^4 events were acquired per sample by plotting FSC-H (cell size) *vs.* SSC-H (cell complexity). Data were analyzed using FlowingSoftware version 2.5.1. The assay was performed in two independent experiments (n = 2 per replicate) yielding similar results.

2.3.7. Cell membrane integrity test. HeLa cells were seeded in 12-well plates at a density of 1.5×10^5 cells per well. After overnight incubation, treatments were added at indicated concentrations for 24 h. Then, cells were harvested by trypsiniza-

 This journal is © the Partner Organisations 2022

tion and the pellets were resuspended in propidium iodide solution (20 μg mL^{-1}) for 15 min. Samples where then subjected to flow cytometry (Beckton Dickinson FACSCalibur). 10^4 events were acquired per sample in the FL2-H channel. Data were analyzed using FlowingSoftware version 2.5.1. The assay was performed in three independent experiments (n = 2 replicates).

2.3.8. Mitochondrial potential assessment. The mitochondrial membrane potential was evaluated with the fluorescent probe JC-1 chloride (Promocell). HeLa cells with the density of 1.5×10^5 were seeded for 24 h in complete medium on 12-well plates, and then treated with indicated concentrations of tested compounds for 24 h. Untreated cells contained the maximal concentration of DMSO used in the treatment (0.4%) and were used as a negative control, whereas Antimycin A (50 μM) was used as a positive control for mitochondrial dysfunction. After drug exposure, the cells were incubated with JC-1 dye (1 μM) for 20 min and subjected to flow cytometry (FACSCAlibur BecktonDickinson; 10^4 events acquired per sample), using λ_{exc} = 488 nm and registering emission in the range 430–600 nm to discriminate green JC1 monomers (FL1-H channel) and red JC1 aggregates (FL2-H channel). Three independent experiments were performed (n = 2 replicates).

2.3.9. Aerobic respiration and glycolytic rate evaluation. The mitochondrial OXPHOS and glycolysis function of HeLA cells were measured by determining the oxygen consumption rate (OCR) and extracellular acidification rate (ECAR) in real-time with a Seahorse XFe96 extracellular flux analyzer. HeLA cells were seeded at a density of 3×10^4 cells per well to the XFe96-well culture microplates (Seahorse Agilent) the day before. The sensor cartridge was hydrated through immersion on calibration buffer at 310 K in a non-CO_2 incubator overnight. Buffered DMEM (Seahorse Bioscience) was used for the glycolysis test prior to the assay. Cells were treated for 24 h at indicated concentrations with testing compounds. Then the cell metabolism was assessed using the XF glycolytic rate test kit. Different parameters were calculated by subtracting average respiration rates before and after the injection of a mixture of complex III electron transport chain inhibitors (Rotenone/Antimycin A, 1 μM) and glycolysis inhibitor (2-deoxyglucose, 50 mM). Each test had four replicates.

2.3.10. Oxidative stress induction. Briefly, HeLa cells were seeded in 12-well plates at 1.5×10^5 cells per well and treated for 24 h with nanoparticles at indicated concentrations; cisplatin (20 μM) was used as the positive control for DNA damage induction. Cells were then collected by trypsinization, fixed in 400 μL of 0.2% paraformaldehyde for 5 min and permeabilized with Triton X 0.5%. After fixation and permeabilization, a 3% FBS solution containing 0.6 μg mL^{-1} anti-pH2AX (ser139) FITC-conjugated monoclonal antibody (CR55T33, eBioscience™) was added and incubated for 1 h at room temperature avoiding direct light. Cells were then analyzed using a Beckton Dickinson FACSCalibur flow cytometer with 10^4 acquisitions per sample in the FL1-H channel, λ_{exc} = 488 nm. Three independent experiments with n = 3 were performed.

3. Results and discussion

3.1. Synthesis of Ir(III) complexes

Ir(III) complexes **Ir1** and **Ir2** were synthesized in the thermodynamically favored *fac*-configuration. The first step consisted of the synthesis of the dimer, $[Ir(C\hat{}N)_2(\mu\text{-}Cl)_2]$, by the reaction of $IrCl_3 \cdot H_2O$ with 2-phenyl-1-[4-(trifluoromethyl)benzyl]-1*H*-benzo[*d*]imidazole (Scheme S1†), which was previously synthesized.[28] Homoleptic complex **Ir1** was synthesized in a good yield (65%) by the reaction of $[Ir(C\hat{}N)_2(\mu\text{-}Cl)_2]$ with an excess of the ligand, using a high boiling point solvent (2-ethoxyethanol) and silver triflate to extract the chlorides (Scheme S2†).[29] On the other hand, heteroleptic complex **Ir2** was synthesized by reaction of the dimer with commercially available 2-phenyl-1*H*-benzo[*d*]imidazole in reflux of 2-ethoxyethanol for 3 hours using sodium carbonate (Scheme S3†).[30] The product of this reaction was a mixture of the three possible neutral compounds: the previously synthesized $[Ir(C\hat{}N)_3]$ **Ir1**, $[Ir(C\hat{}N)_2(C'\hat{}N')]$ **Ir2** and $[Ir(C\hat{}N)(C'\hat{}N')_2]$ (Scheme S4†), **Ir2** being the main component of the mixture. A similar behaviour was previously described.[33] Pure heteroleptic complex **Ir2** was isolated by silica column chromatography as the retention factor (R_f) depending on the number of NH groups of the complexes. **Ir2** was eluted in the second place (31%), preceded by complex **Ir1** (9%) and finally, the most retained product $[Ir(C\hat{}N)(C'\hat{}N')_2]$ (13%) (Scheme S4†).

All investigated complexes were fully characterized by ^1H and ^{13}C NMR spectroscopy (Fig. S1 and S3†), positive-ion ESI-HRMS (Fig. S2 and S4†) and elemental analysis. The *fac-mer* configuration of the complexes was assigned using ^1H-NMR. In *fac*-tris-cyclometalated homoleptic **Ir1**, the three C^N ligands surrounding the central atom are magnetically equivalent due to the *C*3 symmetry of the compounds. This makes the total number of resonances equal to the number of resonances of a single C^N ligand.[34] The signals in the ^1H-NMR spectrum of **Ir1** (Fig. S1†) correspond to 14 protons of three equivalent benzimidazole-based ligands. Recently, *fac* isomerism has been assigned to Ir(III) heteroleptic complexes with phenylpyridine ligands based on the synthesis temperature (~135 °C) and the simplicity of their ^1H-NMR spectra.[35] In our case, given the impossibility of obtaining valid monocrystals of **Ir2** for X-ray diffraction, the *fac* configuration was assigned for these complexes based on the ^1H-NMR spectrum (Fig. S3†) and the temperature of the synthesis. In both cases, the positive-ion ESI mass spectra exhibited the expected molecular ion (Fig. S2 and S4†).

3.2. Synthesis and characterization of Ir(III)-loaded nanocapsules

The synthesis of Ir(III) complex-loaded nanocapsules involved two main processes, as shown in Scheme 1: the preparation of an amphiphilic polyurethane–polyurea amino terminal-reactive prepolymer (steps 1–3) and the metallodrug nanoencapsulation (steps 4–7). First, polymerization between the diol and the diisocyanate monomers afforded a reactive NCO-terminated pre-polymer (step 1). When the theoretical % of isocya-

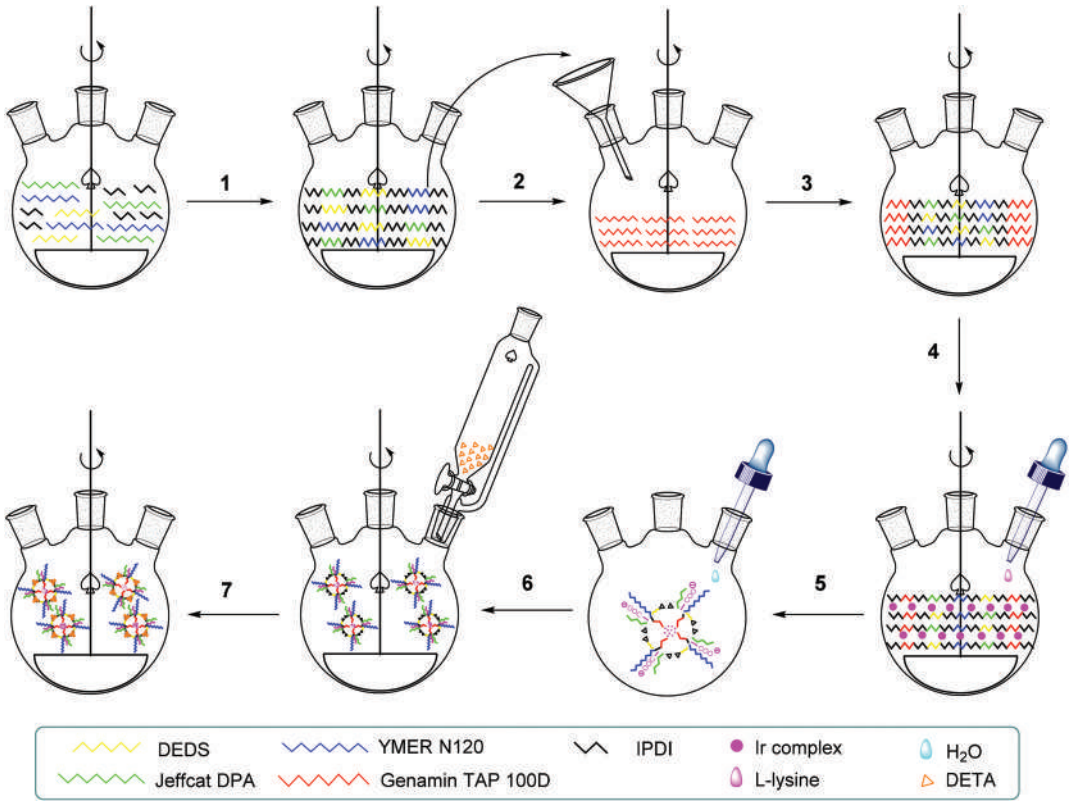

Scheme 1 Schematic representation of the preparation of the amphiphilic prepolymer (steps 1–3) and of the nanoencapsulation process (steps 4–7). Abbreviations: 2,2′-dihydroxyethyl disulfide (DEDS), *N*-(3-dimethylaminopropyl)-*N*,*N*′-diisopropanolamine (DPA), isophorone diisocyanate (IPDI), 1,3-diamino-*N*-octadecylpropane (Genamin TAP 100D), diethylenetriamine (DETA).

nate groups was reached, the polymer was dissolved in THF and added dropwise over a slightly excess of an hydrophobic diamine solution (step 2) to end-cap it with primary amines (step 3), which allows the storage of this intermediate avoiding moisture-promoted degradation due to NCO water sensitivity. This reaction was monitored by FT-IR until the complete disappearance of the NCO stretching band around 2250 cm^{-1} (Fig. S5†). For the nanoencapsulation process, the NH_2-terminal polymer was reactivated with an excess of a diisocyanate derivative in THF and the Ir(III) complexes (**Ir1** or **Ir2**) were added to this organic solution (step 4). After confirming the presence of isocyanate groups by FT-IR (Fig. S6†), a basic solution of L-lysine was added dropwise under mechanical stirring, forming a water-in-oil nanoemulsion (step 5). Then, the phase inversion was triggered by the addition of a fixed amount of water (step 6) followed by the addition of diethylenetriamine, which rapidly resulted in crosslinked cyclometalated Ir(III) complex-loaded polyurethane–polyurea hybrid nanocapsules (**NC-Ir1** and **NC-Ir2**) (step 7). Both Ir(III)-containing nanocapsules as well as control nanocapsules lacking the metallodrug cargo (**NC-GTCC**) were purified by dialysis using a molecular porous membrane tubing with a 12–14 kDa MWCO. As shown in Fig. 2, the introduction of both PEGylated and ionomeric groups, together with core-oriented lipophilic tails for solubilizing and stabilizing the metallodrug through hydrophobic interactions, defines the stratification of the shell. This structure provides a stable aqueous suspension of the nanocapsules exhibiting distinctive biological performance, such as long-circulation in blood stream and specific accumulation in the acidic TME.[17,36] In addition, the incorporation of disulphide bonds in the polymer backbone allows the specific biodegradation of the system under reductive conditions, which would facilitate the release of the Ir(III) metallodrugs.[17]

The size of the Ir(III) complex-loaded nanocapsules (**NC-Ir1** and **NC-Ir2**) was studied by dynamic light scattering (DLS) and compared with that of the non-loaded NCs (**NC-GTCC**). As shown in Fig. 2 and S7–S9,† the average particle size distribution was centered approximately at 18 nm for **NC-Ir1/Ir2**, which was of the same order than that of non-loaded NCs (22 nm). In all cases, the standard deviation (SD) was very low (Table S3†). The morphology of **NC-Ir1** and **NC-Ir2** was also studied by transmission electron microscopy (TEM), and a roughly round shape and homogeneous particle size were revealed by TEM micrographs (Fig. 2 and S10, S11†). Although nanocarriers with a size around 100 nm are usually designed to facilitate accumulation at the tumor site by the enhanced and permeability and retention effect (EPR),[37] smaller nanomedicines (*e.g.* 15–20 nm) such as Ir(III)-loaded NCs might be preferred for cancer therapy due to their higher tumor penetration.[38]

 This journal is © the Partner Organisations 2022

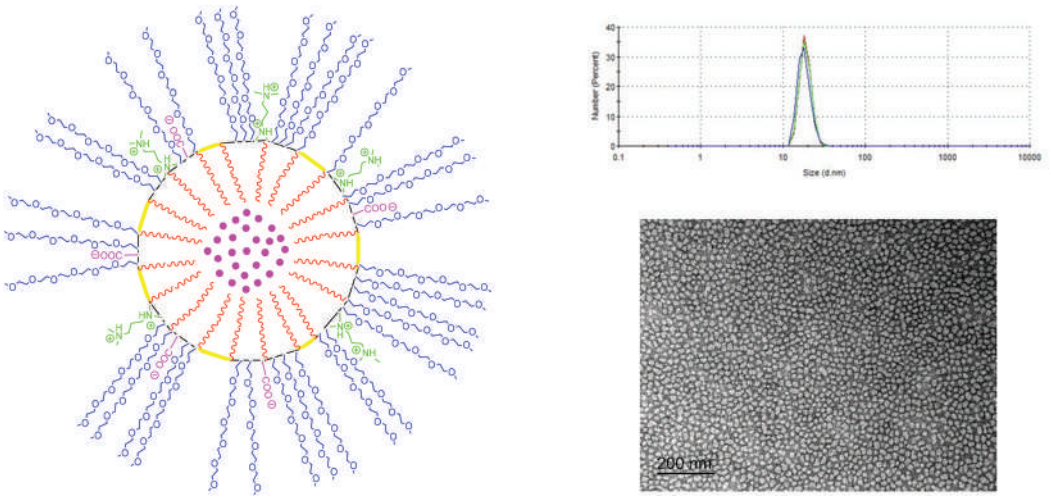

Fig. 2 Left: Schematic representation of the structure of a metallodrug-loaded nanocapsule, showing the orientation of the hydrophilic and hydrophobic tails of the prepolymer in a simplified way. It is expected to have multilayers self-stratified at the interface metallodrug/water in a gradient from inside to outside the nanocapsule wall driven mainly by hydrophobic interactions. Right: Particle size distribution measured by DLS (top) and TEM micrograph (bottom; scale bar: 200 nm) of **NC-Ir1**.

The Z-potential of the nanocapsules at different pH values (6.5, 7.0 and 7.5) was also measured to evaluate the pH-dependent amphoteric properties of the polymeric shell. As shown in Table S4 and Fig. S12,† the nanocapsules are slightly anionic under physiological conditions (pH = 7.4), particularly those containing heteroleptic complex **Ir2**, but become cationic at low pH values. This is an important property since it ensures a long circulation half-life in the blood stream, thereby allowing slow accumulation into abnormally vascularized tumor tissues where the relatively acidic environment (pH = 5.8–6.9) triggers NCs to become cationic entities and, consequently, with high internalization ability *via* association with negatively charged cell receptors.[39]

The amount of Ir complexes (**Ir1** and **Ir2**) inside the NCs was determined by ICP-MS analysis. As shown in Table S5,† the encapsulation efficiency was relatively high in both cases (*ca.* 40%) considering that no external surfactants were used, and the high loading of both hydrophobic Ir(III) complexes was obtained (*e.g.*, 130 ± 16 μM in **NC-Ir1** and 206 ± 17 μM in **NC-Ir2**).

After confirming that the Ir(III)-loaded NCs exhibited an adequate size and a relatively high Ir(III) complex loading, we focused on investigating their ability to specifically release the metallodrug cargo into cancer cells under reductive conditions as well as their stability. The latter is particularly important to avoid premature degradation and unspecific leakage of the metallodrug in the blood stream. It is well-known that the ratio of the reduced form of glutathione (GSH) *versus* the oxidized form (GSSG) is considerably higher in solid tumors cells than in healthy ones, the intracellular concentration of GSH in the cytosol (2–10 mM) being much higher than that in the blood or in the extracellular matrix (2–20 μM).[40] This upregulation in cancer cells derives from the overproduction of this antioxidant tripeptide, on account of different biological mechanisms,[41] to mitigate the oxidative stress which they are exposed to, allowing proliferation and, in most cases, enabling multidrug resistance (MDR).[42] The enhanced level of reduced glutathione is not exclusively, but thoroughly observed in solid tumor cells. For this reason, many nanomedical devices have taken advantage of this fact to selectively release anticancer drugs in the tumor microenvironment.[43] In our case, disulfide bonds were incorporated in the polymeric wall to trigger the degradation of the NCs by reductive enzymes and peptides overexpressed in the cytosolic environment of tumor cells and, consequently, the release of the metallodrug cargo.

The disruption of the polymeric wall *via* GSH-mediated disulfide bond reduction was investigated by TEM analysis after the incubation of **NC-Ir2** for 2, 24 and 48 h at 37 °C in GSH-supplemented PBS (10 mM).[44] As shown in Fig. S13,† Ir(III)-loaded NCs maintained their morphology when they were incubated in PBS and the analyzed fields remained homogeneous, with no variations in terms of morphology or distribution along the screening. However, the amount of NCs clearly diminished over time, at the same magnification analysis, when incubation was carried out in GSH-containing buffer, which suggests that **NC-Ir2** suffers from degradation through the reduction of disulfide bonds incorporated along the polyurethane backbone of the NC wall. It is also worth noting that **NC-Ir2** modified their morphology after incubation for 48 h in GSH-supplemented PBS, with the 20–25 nm spherical structures mostly disappearing and forming non-defined aggregations (Fig. S14†), which can be associated with clusters of polymer and precipitation of the free **Ir2** complex after being released.

Additionally, the stability of the NCs was also evaluated in PBS containing BSA, which is one of the most abundant proteins in plasma, as well as in complete human AB serum. As shown in Fig. S15,† **NC-Ir2** showed a clear spherical mor-

phology and proper distribution after incubation for 48 h both in BSA-containing PBS and in human AB serum, confirming the high stability of polyurethane, polyurea and disulfide bonds under common medical vehicles and human bloodstream medium, making them a suitable tool for intravenous administration.

3.3. Photophysical properties

The UV/Vis absorption and emission spectra were recorded in CH_2Cl_2 and DMSO for Ir(III) complexes (Fig. S16†) whereas water solutions were used for the nanocapsules (Fig. 3). **Ir1** and **Ir2** exhibit characteristic absorptions of tris-cyclometalated iridium complexes.[45] The luminescence lifetimes and emission quantum yields are summarized in Table S6.† The luminescence lifetimes of **Ir1** and **Ir2** go from being nanoseconds in an aerated solution to microseconds in a degassed solution (Table S6 and Fig. S17†). These long-lived excited states compare well with the respective values for other phosphorescent Ir(III) compounds, which supports the triplet nature of the emission state.[45a,b] Likewise, the luminescence lifetimes of **NC-Ir1** and **NC-Ir2** increased from ~70–90 ns in air equilibrated solutions to ~1.5 μs, in degassed solutions (Table S6 and Fig. S18†), as it happened with the free complexes in CH_2Cl_2.

This fact together with their similar spectra to that registered for **Ir1** and **Ir2** in CH_2Cl_2, is a good indicative of the hydrophobic environment generated by the nanocapsules. On the other hand, both complexes and nanocapsules exhibited high emission quantum yields in solution. Unlike free complexes, which were easily quenched by oxygen, the oxygen quenching of the emission was less efficient when the complexes were encapsulated within the nanoparticles. While the emission quantum yields of **Ir1** and **Ir2** in an air-equilibrated solvent ($\Phi_{air} \approx 3\%$) have a 30-fold reduction in luminescence features with respect to degassed solutions ($\Phi \approx 78\%$), **NC-Ir1** and **NC-Ir2** showed a smaller difference between aerated ($\Phi_{air} \approx 20\%$) and degassed ($\Phi \approx 40\%$) solutions. Interestingly, the nanocapsules displayed quantum yields of 12–20% in aerated aqueous solution, which indicated that these nanostructures can be used in the presence of dissolved oxygen and still exhibit a high quantum yield.

3.4. Biological activity of NC-Ir1 and NC-Ir2

3.4.1 Cellular uptake in cancer cells. The cellular uptake of Ir(III) complexes either alone or loaded into NCs was investigated in cervical cancer cells (HeLa) using inductively coupled plasma mass spectrometry (ICP-MS). As shown in Fig. 4, after 2 h incubation the iridium content inside cancer cells treated with **Ir1** and **Ir2** at 6 μM was much lower than that found with Ir(III) complex-loaded nanocapsules at the same concentration, especially in the case of the homoleptic complex. Indeed, Ir accumulation from **NC-Ir1** and **NC-Ir2** was 6- to 14-fold higher than those found in HeLa cells treated with the free complexes **Ir1** and **Ir2**, respectively, thus indicating that encapsulation in polyurethane–polyurea hybrid NCs allowed neutral Ir compounds to be rapidly internalized in the cells. Once attached to the cell surface, these nanoparticles might passively diffuse to cells through the lipid membrane or translocate *via* endocytosis-mediated transport. Whereas at 37 °C both passive and active transport across the membrane would be operative, at 4 °C energy-dependent transport processes are generally unable to function, and only passive diffusion or cell membrane adhesion will be operational. Since decreasing the temp-

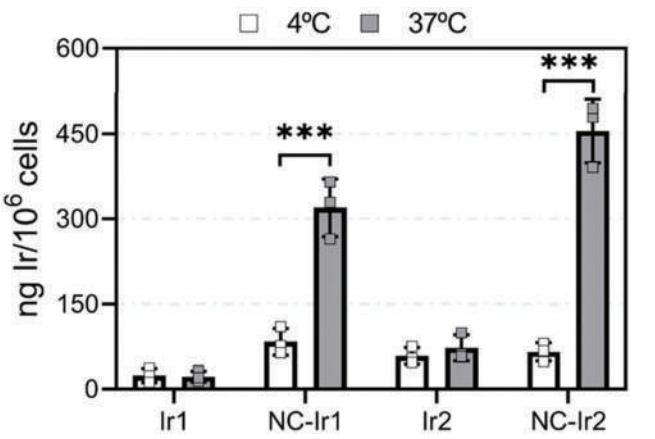

Fig. 4 Intracellular accumulation of Ir after 2 h with free or encapsulated compounds (6 μM) determined by ICP-MS in HeLa cells. Data expressed as mean ± SD of three independent measurements (***p < 0.001; unpaired t-test).

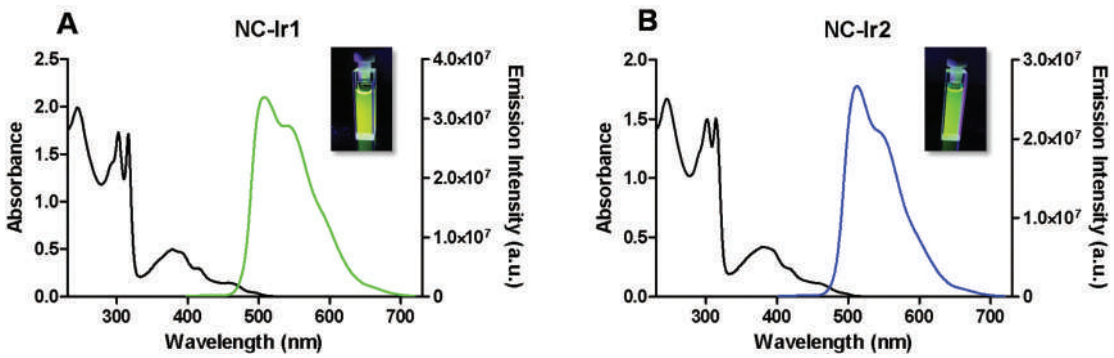

Fig. 3 UV/Vis and emission spectra in aerated water solutions of (A) **NC-Ir1** (λ_{exc} = 378 nm) and (B) **NC-Ir2** (λ_{exc} = 382 nm).

This journal is © the Partner Organisations 2022

erature from 37 °C to 4 °C significantly reduced the cellular uptake of Ir(III)-loaded NCs after 2 h (Fig. 4), energy-dependent transport could be partially responsible for the increased accumulation at the physiological temperature of **NC-Ir1** and **NC-Ir2**.

Confocal microscopy in living HeLa cells was also used to investigate the cellular uptake of the compounds. As shown in Fig. S19,† luminescent aggregates of **Ir1** and **Ir2** were observed outside the cells due to the low solubility in water of the compounds. This fact is in good agreement with the ICP-MS results and confirms the poor cellular uptake of the free iridium complexes. By contrast, intracellular staining was observed after incubation with **NC-Ir1** and **NC-Ir2** (Fig. S20†), thereby confirming an excellent cellular uptake of the Ir(III)-loaded NCs.

3.4.2. Antiproliferative activity in 2D and 3D cell culture models. The cytotoxic activities of Ir(III) complexes alone or when encapsulated into polyurethane–polyurea hybrid NCs were tested against three 2D monolayer cancer cells by means of MTT-based assays (cervical cancer cells (HeLa) and ovarian cancer sensitive (A2780)) and resistant to the clinical drug cisplatin (A2780cis), as well as in non-tumorigenic normal renal cells (BGM). **Ir1** and **Ir2** compounds were found to be inactive against cells up to 100 μM (data not shown), which is in good agreement with ICP-MS studies that showed a very low intracellular uptake of these compounds. In contrast, treatment with **NC-Ir1** and **NC-Ir2** resulted in high antiproliferative activity against cancer cells while cells treated with non-loaded NCs did not (Tables 1 and S7†). This indicated that the cytotoxic action of the iridium(III) compounds greatly improved upon encapsulation. Overall, the viability of HeLa cells was affected by **NC-Ir1** and **NC-Ir2** treatment after 2 h and was further decreased after 24 h and 48 h, which could be attributed to a higher release of the Ir(III) complex cargo over time, as suggested by TEM analysis (Fig. S13 and S14†). The NCs were also active against ovarian cancer cells, showing remarkable antiproliferative activities in both cisplatin sensitive and resistant cell lines after 24 h, whereas the absence of cytotoxicity was observed in BGM, thus indicating the ability of NC-loaded agents to preferentially eliminate cancer cells over normal dividing cells.

The tumor growth inhibition effects of the complexes were also tested in multicellular HeLa tumor spheroids (MCTS). Three-dimensional MCTS models provide an *in vitro* cell culture system which mimics the *in vivo* features of solid tumors and represent a simplified approximation of the tumor microenvironment,[46] thereby allowing a more realistic evaluation of the antitumor activities of the nanoparticles. **NC-Ir1** and **NC-Ir2** were incubated with MCTS after their formation and either fresh media or treatment-containing media were replaced every 3 days. Over a span of 15 days, the period, shape, diameter and volume of the MCTS were monitored. In contrast to the control, the size of the spheroids did not increase in treated groups, indicating the ability to impair tumor growth in these 3D models (Fig. 5 and Fig. S21†). This effect was maintained after 15 days of treatment, with shrank and disaggregated MCTS, demonstrating a strong tumor growth inhibition effect.

3.4.3. Morphological alterations of the cells. In order to determine the mechanisms responsible for the cytotoxic effects of the Ir(III)-loaded nanoparticles, confocal microscopy and flow cytometry techniques were first applied to observe the morphological alterations in HeLa cells. HeLa cells in culture appear as flattened epithelioid cells well-adhered to the surface. However, examination of these cancer cells after incubation with **NC-Ir1** and **NC-Ir2** revealed swollen cells that became rounded in shape and detached from the substrate shortly after treatment, *i.e.* ~12 h (Fig. 6). This effect, which might indicate cell death being induced, was prolonged after 24 h (Fig. S22†). Some of the cells also started to produce blebs in their cell membrane (Fig. S23†), which allowed us to rule out paraptosis as the main cell death mode since neither swelling nor blebbing are associated with paraptosis.[47] Flow cytometry experiments using forward and side scatter plots (FSC and SSC) to discriminate cell size and cell complexity respectively were performed (Fig. S24†). In contrast to cisplatin-treated cells, which showed a decrease in FSC and a concomitant increase in SSC parameters corresponding to apoptotic populations, cells treated with **NC-Ir1** and **NC-Ir2** revealed a main population of cells with increased size, which would confirm the cell swelling, and a second population of small cell particles defined by low FSC/SSC ratios corresponding to dead cells.

3.4.4. Cell death induction by NC-Ir1 and NC-Ir2. To elucidate the mode of cell death induced by NCs loaded with Ir(III) compounds, flow cytometry experiments using a Annexin

Table 1 Cytotoxicity [IC_{50} mean values (μM)][a] obtained for nanoparticles in cancer and normal cells based on the loaded metal concentration (Ir for **NC-Ir1** and **NC-Ir2**; Pt for cisplatin)

	HeLa			A2780	A2780cis	BGM
	2 h	24 h	48 h	24 h		
NC-Ir1	23 ± 1	2.9 ± 0.2	1.77 ± 0.06	3.7 ± 0.9	10 ± 1	>85
NC-Ir2	47 ± 6	3.6 ± 0.2	2.9 ± 0.1	2.5 ± 0.6	9.8± 0.9	>85
Cisplatin	—	—	33 ± 6	1.4 ± 0.2	16 ± 1	16.6 ± 0.2

[a] The results are expressed as mean values ± SD from at least two independent experiments (n = 4). The terms >85 indicate that no IC_{50} reached up to that concentration.

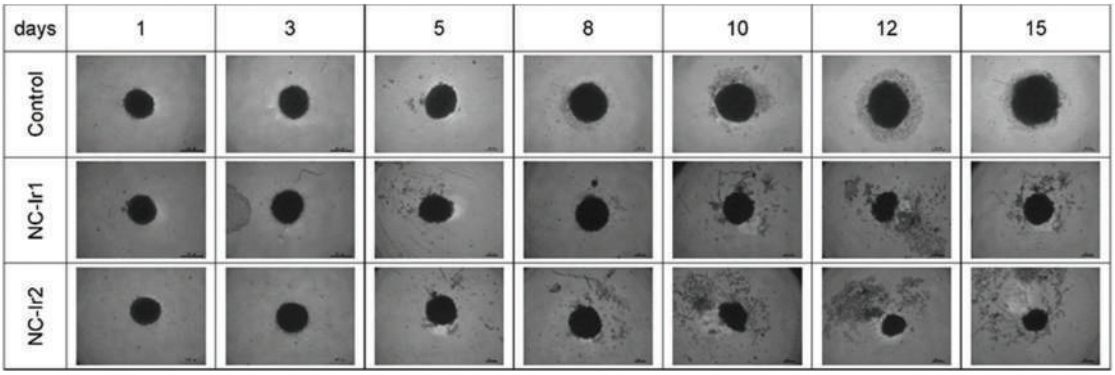

Fig. 5 Changes in relative volume in MCTS over a span of 15 days. MCTS were treated with **NC-Ir1** and **NC-Ir2** at 6 μM. Scale bar: 200 μm.

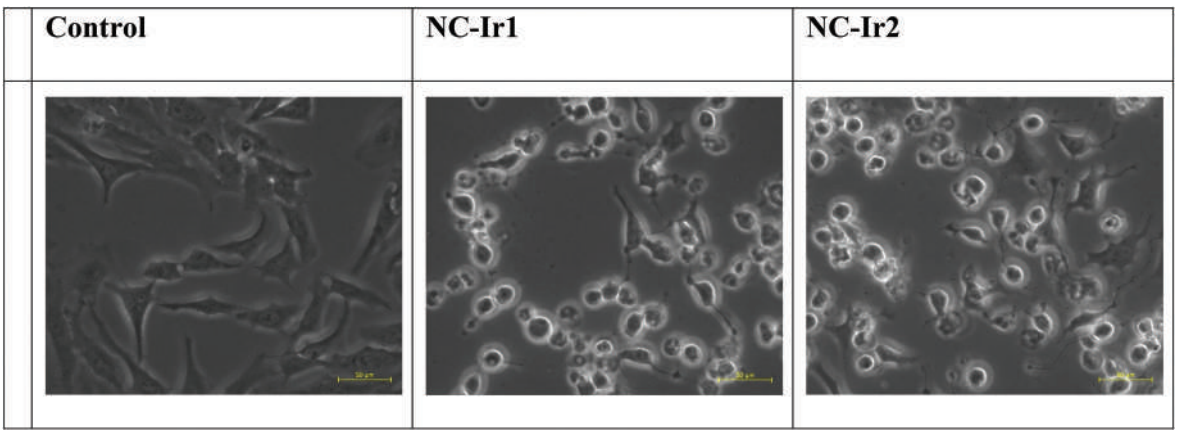

Fig. 6 Detection of cell swelling in HeLa cells after 12 h treatment with nanoparticles at equitoxic concentrations (2 × IC_{50}; *i.e.* 6 μM). Scale bar: 50 μm.

V/propidium iodide (PI) labelling method were performed. This dual-staining allowed the detection of four different populations: live cells, necrotic cells and early- and late-stage apoptosis. Although apoptosis is characterized by changes in the phospholipid membrane symmetry, the disruption of the cell membrane integrity allows the detection of necrotic cells as they become permeable to PI. In the case of HeLa cells exposed to 20 μM of cisplatin, which served as a positive control, PI^+ and double Annexin V^+/PI^+ populations were induced, revealing apoptosis and necrosis induction after 24 h (Fig. 7). Treatment with **NC-Ir1** and **NC-Ir2** also increased both Annexin V^+ and PI^+ populations; the latter being significantly produced. Overall, these results suggested that necrotic events in HeLa cells may be induced upon treatment.

Cells with compromised plasma membrane would allow PI to permeate into the cytoplasm and intercalate to DNA. Therefore, the detection of PI fluorescence by flow cytometry would allow the evaluation of cancer cell membrane integrity upon low-dose treatments with the nanoparticles (Fig. S25 and 26†). **NC-Ir1** and **NC-Ir2** for 12 h was sufficiently enough to affect membrane permeability and thereby induce loss of plasma membrane integrity. This was confirmed by confocal microscopy after staining with PI (Fig. 8). The observed changes in the cell morphology (cell swelling, blebbing and disruption of membrane integrity) were coherent with those

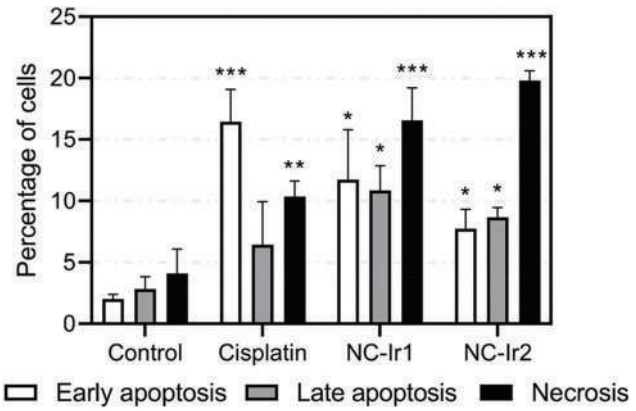

Fig. 7 Cell death induction in HeLa cells after 24 h treatment with **NC-Ir1** and **NC-Ir2** (6 μM) or cisplatin (20 μM). Data expressed as mean ± SD from three independent experiments (*$p < 0.05$, **$p < 0.01$, ***$p < 0.001$; unpaired *t*-test).

 This journal is © the Partner Organisations 2022

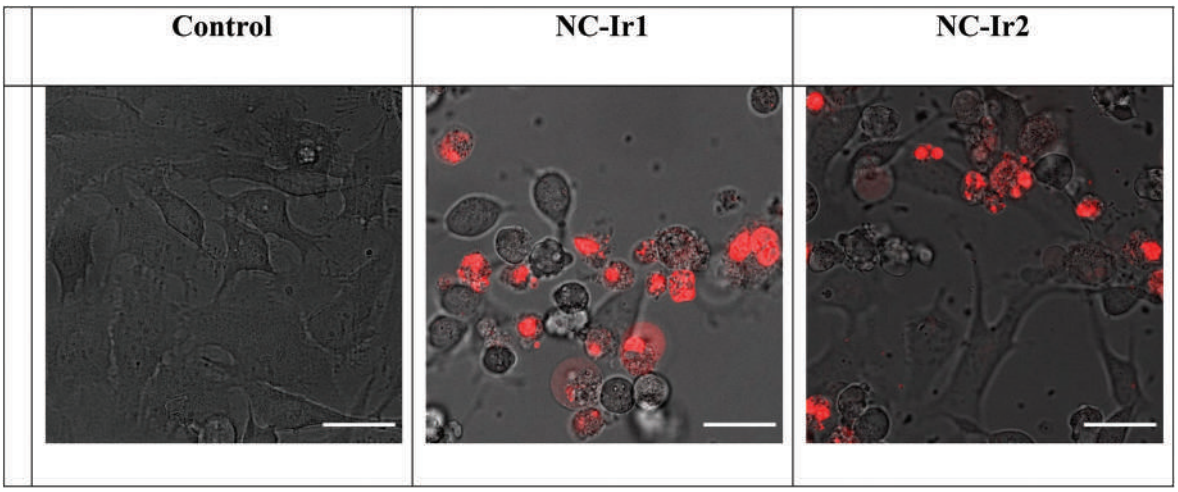

Fig. 8 Microscopy images of HeLa cells with membrane rupture stained with propidium iodide (red) after treatment with **NC-Ir1** and **NC-Ir2** at equitoxic concentrations (2 × IC_{50}; *i.e.* 6 μM) for 12 h. Scale bar = 15 μm.

found on FSC-SSC analysis, characterized by a reduction of cell size and complexity (Fig. S22†). Altogether, the onset of morphological events appeared to be consistent with oncosis or oncotic necrosis.[48]

3.4.5. Mitochondrial dysfunction. Since mitochondria play an important role in biological processes of cancer cells, including redox homeostasis and ATP production,[49] a series of experiments were performed to investigate the impact of the present encapsulated agents on mitochondrial dysfunction. First, the effects on the mitochondrial membrane potential (MMP) were evaluated after 24 h treatment with Ir(III)-loaded NCs using JC-1 staining. JC-1 dye exhibits a bright red fluorescence signal upon potential-dependent accumulation in healthy mitochondria, whereas a shift to green fluorescence is observed if dissipation of MMP occurs. Similar to the electron transport chain inhibitor antimycin A, treatment with **NC-Ir1** and **NC-Ir2** completely depleted the MMP of HeLa cells after 24 h (Fig. 9 and S27†).

To further understand how mitochondrial bioenergetics were affected, extracellular acidification (ECAR) and oxygen consumption rates (OCR) were measured in real-time using a Seahorse XF-96 flux analyzer. As depicted in Fig. S28,† the administration of **NC-Ir1** and **NC-Ir2** (6 μM) resulted in evident suppression of the glycolytic rate and mitochondrial respiration. On the one hand, HeLa cells incubated with Ir(III)-loaded NCs led to a suppression on OCR compared to **Ir1** and **Ir2**-treatments, which increased mitochondrial oxidative phosphorylation, thus showing the ability of the encapsulated agents to impair mitochondrial function (Fig. S28a†). On the other hand, it is generally accepted that cancer cell metabolism is commonly shifted from mitochondrial respiration to aerobic glycolysis in what is known as the Warburg effect.[50] Ir(III)-Loaded NCs abolished the glycolytic rate of HeLa cells, both basal glycolysis and compensatory glycolysis, as evidenced by reduced ECAR under basal conditions and after injection of mitochondrial respiratory chain inhibitors Rotenone/Antimycin A (Fig. S28b–d†). Different from them, no influences on acidification rates were found when treated with **Ir1**, **Ir2** or cisplatin under the same conditions. Overall, these results suggest that treatments with **NC-Ir1** and **NC-Ir2** altered cancer cell metabolism by suppressing glycolysis and decreasing mitochondrial oxidative phosphorylation activity. Taking into account that iridium barely entered into cancer cells when administered as free compounds compared to encapsulated administration (see Fig. 4 and S19, S20†), such differences in the biological effects could be attributed to the lower internalization of the free Ir(III) complexes rather than different intracellular distribution.

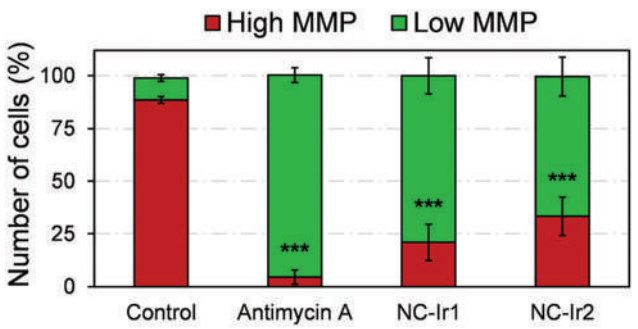

Fig. 9 Mitochondrial membrane potential (MMP) of HeLa cells after treatment with antimycin A (50 μM) **NC-Ir1** and **NC-Ir2** (6 μM) for 24 h (*p < 0.05, **p < 0.01, ***p < 0.001; unpaired t-test).

3.4.6. Oxidative stress. Mitochondria are the major cellular source of reactive oxygen species (ROS) within cells. Since mitochondrial dysfunction can result in an elevation of ROS levels,[51] we decided to assay the effect of canonical ROS on DNA damage as a marker of oxidative stress in cancer cells. Extensive ROS production can generate double-strand breaks in DNA that can be detected by using fluorescently labeled anti-γH2AX antibody specifically targeted to phosphorylated

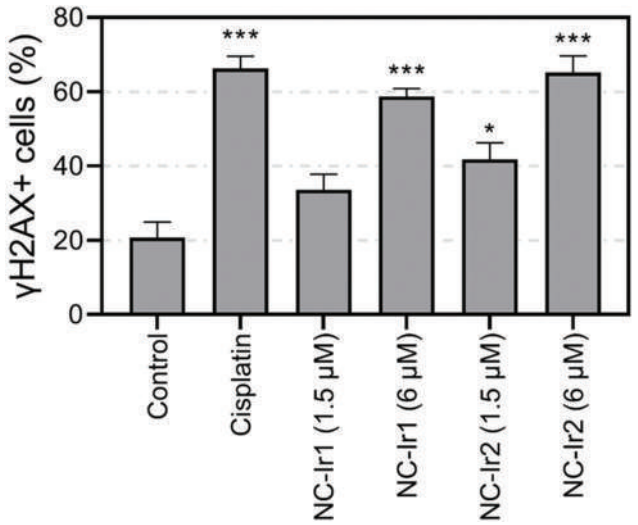

Fig. 10 Effect of **NC-Ir1** and **NC-Ir2** (1 mg ml^{-1}) on oxidative stress of HeLa cells as measured by DNA damage detected as changes in γH2AX phosphorylation in the FL1-H channel after 24 h treatment. Cisplatin (20 μM) was used as a positive control for DNA damage induction. Data from three independent experiments (n = 3 replicates).

Ser139 of the variant of histone H2A. Our results showed that DNA damage was slightly induced by low-dose treatment (0.5 × IC_{50}; *i.e.* 1.5 μM) with **NC-Ir1** and **NC-Ir2**, and more broadly at 2 × IC_{50} concentrations after 24 h (Fig. 10 and Fig. S29†). Strikingly, treatment with these concentrations significantly raised γH2AX populations as it did the well-known damaging agent cisplatin. This led us to think that oxidative stress might contribute to the mechanism of action of the present Ir(III)-loaded nanoparticles, probably as a result of mitochondrial dysfunction.

To further confirm that ROS generation was a main contributor of the nanoformulation cytotoxicity, the influence of an exogenously-added antioxidant was studied. As presented in Fig. S30,† pretreatment of HeLa cells for 1 h with the cell permeable superoxide dismutase mimetic, MnTBAP, attenuated the nanoparticle-induced cytotoxicity at 2 × IC_{50} concentrations for 24 h. The compensatory effects on cell viability exerted by this antioxidant supports the idea of extensive ROS generation being produced by these Ir-loaded nanocapsules.

4. Conclusions

In summary, we have demonstrated for the first time that polyurethane–polyurea hybrid nanocapsules can be used to efficiently encapsulate hydrophobic metallodrugs under aqueous conditions, which opens the way to the development of novel metal-based anticancer nanomedicines. As a proof of concept, we have encapsulated two neutral phosphorescent tris-cyclometalated Ir(III) complexes incorporating deprotonated 2-arylbenzimidazole ligands, **Ir1** and **Ir2**, and investigated their photophysical, cellular uptake and biological properties. A prepolymer was first designed and synthesized to facilitate the nanoencapsulation of the desired hydrophobic compounds without needing surfactants and under mild conditions given its self-emulsifying nature. This prepolymer incorporates suitable functional groups that dictate the pH-dependent amphoteric properties of the polymeric shell of the nanocapsules, as well as disulphide bonds to confer them degradability under reductive conditions. Both Ir(III) complex-loaded nanocapsules (**NC-Ir1** and **NC-Ir2**) showed a controlled particle size distribution of approximately 18 nm and a roughly round shape according to TEM micrographs, and a high drug loading content, as determined by ICP-MS. The UV/Vis absorption and emission spectra of aqueous solutions of NCs were similar to those of the free complexes in CH_2Cl_2, which accounts for the hydrophobic environment generated by the nanoparticles around the cargo. The fact that the oxygen quenching of the emission was less efficient when the complexes were encapsulated also supports the protective effect provided by the nanocapsules.

Very importantly, we demonstrated by ICP-MS experiments that nanoencapsulation had a positive effect on the cellular uptake of the complexes since Ir accumulation from **NC-Ir1** and **NC-Ir2** after 2 h incubation in HeLa cells was 6 to 14-fold higher than those treated with the free complexes **Ir1** and **Ir2**, respectively, and that energy-dependent mechanisms were involved in the cellular uptake of the NCs. The Ir(III)-loaded nanocapsules **NC-Ir1** and **NC-Ir2** were found to be highly cytotoxic against cancer cells, including cisplatin sensitive and resistant ovarian cancer cells. By contrast, the free complexes **Ir1** and **Ir2** were found to be inactive against cells up to 100 μM which is in good agreement with their poor intracellular uptake. Importantly, cells treated with non-loaded NCs did not show antiproliferative activity and an absence of cytotoxicity was also observed in normal dividing cells (BGM), which indicates that Ir(III)-loaded agents may exhibit a preference for cancer cells. Besides showing high antiproliferative activities in 2D monolayer cancer cells, a strong tumor growth inhibition effect was also found in 3D tumorsphere cancer models after treatment with **NC-Ir1** and **NC-Ir2**, which can be attributed to the high penetration capacity of the small NCs. Finally, we explored the mode of cell death induced by these agents and found that oncosis or oncotic necrosis matched with the array of phenomena observed. Shortly after treatment, *i.e.* ~12 h, **NC-Ir1** and **NC-Ir2** produced cell swelling, blebbing and disruption of membrane permeability, which are features of oncotic cell death. Together with the plasma membrane leakage, mitochondrial dysfunction induced after 24 h and the generation of extensive oxidative stress appeared to be also involved in the mechanism of action of these Ir(III)-loaded nanoparticles.

Author contributions

J. B., E. O.-F., G. V., M. B., N. C., J. R., J. R. and V. M. conceived the study. J. B. synthesized and characterized nanocapsules. G. V. synthesized and characterized Ir(III) complexes and per-

 This journal is © the Partner Organisations 2022

formed photophysical studies. J. B. and M. B. performed confocal microscopy studies. E. O.-F. designed and performed all biological experiments. J. B., E. O.-F., G. V. and V. M. wrote the manuscript, also contributed by all authors, who have approved the submitted version of the manuscript.

Conflicts of interest

There are no conflicts to declare.

Acknowledgements

This work was supported by funds from the Spanish Ministerio de Ciencia e Innovación-Agencia Estatal de Investigación (MCI/AEI/10.13039/501100011033) and European Regional Development Fund (FEDER) (projects CTQ2017-84779-R, RTI2018-096891-B-I00, PID2020-117508RB-I00 and RED2018-102471-T), the Generalitat de Catalunya (2017 DI 072) and Fundación Séneca-Región de Murcia (project 20857/PI/18). E. O.-F. thanks AECC (PRDMU19003ORTE). G. V. thanks the University of Murcia for a grant (R-1034/2016).

Notes and references

1 S. Ghosh, Cisplatin: The first metal based anticancer drug, *Bioorg. Chem.*, 2019, **88**, 102925.
2 (*a*) D. M. Cheff and M. D. Hall, A Drug of Such Damned Nature. Challenges and Opportunities in Translational Platinum Drug Research, *J. Med. Chem.*, 2017, **60**, 4517–4532; (*b*) R. Oun, Y. E. Moussa and N. J. Wheate, The side effects of platinum-based chemotherapy drugs: a review for chemists, *Dalton Trans.*, 2018, **47**, 6645–6653; (*c*) T. C. Johnstone, K. Suntharalingam and S. J. Lippard, The Next Generation of Platinum Drugs: Targeted Pt(II) Agents, Nanoparticle Delivery, and Pt(IV) Prodrugs, *Chem. Rev.*, 2016, **116**, 3436–3486.
3 (*a*) N. P. Barry and P. J. Sadler, Challenges for Metals in Medicine: How Nanotechnology May Help To Shape the Future, *ACS Nano*, 2013, **7**, 5654–5659; (*b*) T. C. Johnstone, K. Suntharalingam and S. J. Lippard, The Next Generation of Platinum Drugs: Targeted Pt(II) Agents, Nanoparticle Delivery, and Pt(IV) Prodrugs, *Chem. Rev.*, 2016, **116**, 3436–3486; (*c*) X. Wang, X. Wang, S. Jin, N. Muhammad and Z. Guo, Stimuli-Responsive Therapeutic Metallodrugs, *Chem. Rev.*, 2019, **119**, 1138–1192.
4 (*a*) L. Zeng, P. Gupta, Y. Chen, E. Wang, L. Ji, H. Chao and Z.-S. Chen, The development of anticancer ruthenium(II) complexes: from single molecule compounds to nanomaterials, *Chem. Soc. Rev.*, 2017, **46**, 5771–5804; (*b*) M. Poursharifi, M. T. Wlodarczyk and A. J. Mieszawska, Nano-Based Systems and Biomacromolecules as Carriers for Metallodrugs in Anticancer Therapy, *Inorganics*, 2019, **7**, 2; (*c*) P. Farinha, J. O. Pinho, M. Matias and M. M. Gaspar, Nanomedicines in the treatment of colon cancer: a focus on metallodrugs, *Drug Delivery Transl. Res.*, 2022, **12**, 49–66; (*d*) M. He, F. Chen, D. Shao, P. Weis, Z. Wei and W. Sun, Photoresponsive metallopolymer nanoparticles for cancer theranostics, *Biomaterials*, 2021, **275**, 120915.
5 Y. Zhang, H. Fu, S. Chen, B. Liu, W. Sun and H. Gao, Construction of an iridium(III)-complex-loaded MOF nanoplatform mediated with a dual-responsive polycationic polymer for photodynamic therapy and cell imaging, *Chem. Commun.*, 2020, **56**, 762–765.
6 F. Ledezma-Gallegos, R. Jurado, R. Mir, L. A. Medina, L. Mondragon-Fuentes and P. García-López, Liposomes Co-Encapsulating Cisplatin/Mifepristone Improve the Effect on Cervical Cancer: In Vitro and In Vivo Assessment, *Pharmaceutics*, 2020, **12**, 897.
7 H. Xiang, H. Chen, H. P. Tham, S. Z. F. Phua, J.-G. Liu and Y. Zhao, Cyclometalated Iridium(III)-Complex-Based Micelles for Glutathione-Responsive Targeted Chemotherapy and Photodynamic Therapy, *ACS Appl. Mater. Interfaces*, 2017, **9**, 27553–27562.
8 S. Dhar, N. Kolishetti, S. J. Lippard and O. C. Farokhzad, Targeted delivery of a cisplatin prodrug for safer and more effective prostate cancer therapy in vivo, *Proc. Natl. Acad. Sci. U. S. A.*, 2011, **108**, 1850–1855.
9 J. Karges, J. Li, L. Zeng, H. Chao and G. Gasser, Polymeric Encapsulation of a Ruthenium Polypyridine Complex for Tumor Targeted One- and Two-Photon Photodynamic Therapy, *ACS Appl. Mater. Interfaces*, 2020, **12**, 54433–54444.
10 N. Gadzhiev, D. Gorelov, V. Malkhasyan, G. Akopyan, R. Harchelava, D. Mazurenko, C. Kosmala, Z. Okhunov and S. Petrov, Comparison of silicone versus polyurethane ureteral stents: a prospective controlled study, *BMC Urol.*, 2020, **20**, 10.
11 Y. Liu, Y. Zou, J. Wang, S. Wang and X. Liu, A novel cationic waterborne polyurethane coating modified by chitosan biguanide hydrochloride with application potential in medical catheters, *J. Appl. Polym. Sci.*, 2021, **138**, e50290.
12 L. Zhou, D. Liang, X. He, J. Li, H. Tan, J. Li, Q. Fu and Q. Gu, The degradation and biocompatibility of pH-sensitive biodegradable polyurethanes for intracellular multifunctional antitumor drug delivery, *Biomaterials*, 2012, **33**, 2734–2745.
13 A. Schoth, K. Landfester and R. Muñoz-Espí, Surfactant-Free Polyurethane Nanocapsules via Inverse Pickering Miniemulsion, *Langmuir*, 2015, **31**, 3784–3788.
14 P. Rocas, C. Cusco, J. Rocas and F. Albericio, On the Importance of Polyurethane and Polyurea Nanosystems for Future Drug Delivery, *Curr. Drug Delivery*, 2018, **15**, 37–43.
15 G. Flórez-Graua, P. Rocas, R. Cabezón, C. España, J. Panés, J. Rocas, F. Albericio and D. Benítez-Ribas, Nanoencapsulated budesonide in self-stratified polyurethane-polyurea nanoparticles is highly effective in inducing human tolerogenic dendritic cells, *Int. J. Pharm.*, 2016, **511**, 785–793.
16 P. Rocas, M. Hoyos-Nogués, J. Rocas, J. M. Manero, J. Gil, F. Albericio and C. Mas-Moruno, Installing Multifunctionality on Titanium with RGD Decorated

Polyurethane-Polyurea Roxithromycin Loaded Nanoparticles: Toward New Osseointegrative Therapies, *Adv. Healthcare Mater.*, 2015, **4**, 1956–1960.

17 C. Cuscó, J. Garcia, E. Nicolás, P. Rocas and J. Rocas, Multisensitive drug-loaded polyurethane/polyurea nanocapsules with pH-synchronized shell cationization and redox-triggered release, *Polym. Chem.*, 2016, **7**, 6457–6466.

18 (*a*) A. Zamora, G. Vigueras, V. Rodríguez, M. D. Santana and J. Ruiz, Cyclometalated iridium(III) luminescent complexes in therapy and phototherapy, *Coord. Chem. Rev.*, 2018, **360**, 34–76; (*b*) D.-L. Ma, D. S.-H. Chan and C.-H. Leung, Group 9 Organometallic Compounds for Therapeutic and Bioanalytical Applications, *Acc. Chem. Res.*, 2014, **47**, 3614–3631.

19 (*a*) P.-Y. Ho, C.-L. Ho and W.-Y. Wong, Recent advances of iridium(III) metallophosphors for health-related applications, *Coord. Chem. Rev.*, 2020, **413**, 213267; (*b*) C.-P. Tan, Y.-M. Zhong, L.-N. Jia and Z.-W. Mao, Phosphorescent metal complexes as theranostic anticancer agents: combining imaging and therapy in a single molecule, *Chem. Sci.*, 2021, **12**, 2357–2367.

20 (*a*) A. R. Bin Mohd Yusoff, A. J. Huckaba and M. K. Nazeeruddin, Phosphorescent Neutral Iridium(III) Complexes for Organic Light-Emitting Diodes, *Top. Curr. Chem. (Z)*, 2017, **375**, 39; (*b*) E. Longhia and L. De Cola, Iridium(III) Complexes for OLED Application, in *Iridium(III) in Optoelectronic and Photonics Applications*, John Wiley & Sons, Ltd, 2017, pp. 205–274.

21 (*a*) K. Yokoi, Y. Hisamatsu, K. Naito and S. Aoki, Design, Synthesis, and Anticancer Activities of Cyclometalated Tris(2-phenylpyridine)iridium(III) Complexes with Cationic Peptides at the 4′-Position of the 2-Phenylpyridine Ligand, *Eur. J. Inorg. Chem.*, 2017, **44**, 5295–5309; (*b*) K. Yokoi, C. Balachandran, M. Umezawa, K. Tsuchiya, A. Mitrić and S. Aoki, Amphiphilic Cationic Triscyclometalated Iridium(III) Complex–Peptide Hybrids Induce Paraptosis-like Cell Death of Cancer Cells via an Intracellular Ca^{2+}-Dependent Pathway, *ACS Omega*, 2020, **5**, 6983–7001.

22 (*a*) K. Qiu, H. Huang, B. Liu, Y. Liu, Z. Huang, Y. Chen, L. Ji and H. Chao, Long-Term Lysosomes Tracking with a Water-Soluble Two-Photon Phosphorescent Iridium(III) Complex, *ACS Appl. Mater. Interfaces*, 2016, **8**, 12702–12710; (*b*) B. Liu, S. Monro, M. A. Jabed, C. G. Cameron, K. L. Colón, W. Xu, S. Kilina, S. A. McFarland and W. Sun, Neutral iridium(III) complexes bearing BODIPY-substituted N-heterocyclic carbene (NHC) ligands: synthesis, photophysics, in vitro theranostic photodynamic therapy, and antimicrobial activity, *Photochem. Photobiol. Sci.*, 2019, **18**, 2381–2396.

23 (*a*) A. Sansee, S. Meksawangwong, K. Chainok, K. J. Franz, M. Gál, L.-O. Pålsson, W. Puniyan, R. Traiphol, R. Pal and F. Kielar, Novel aminoalkyl tris-cyclometalated iridium complexes as cellular stains, *Dalton Trans.*, 2016, **45**, 17420–17430; (*b*) A. Nakagawa, Y. Hisamatsu, S. Moromizato, M. Kohno and S. Aoki, Synthesis and Photochemical Properties of pH Responsive Tris-Cyclometalated Iridium(III) Complexes That Contain a Pyridine Ring on the 2-Phenylpyridine Ligand, *Inorg. Chem.*, 2014, **53**, 409–422.

24 Z. Feng, P. Tao, L. Zou, P. Gao, Y. Liu, X. Liu, H. Wang, S. Liu, Q. Dong, J. Li, B. Xu, W. Huang, W.-Y. Wong and Q. Zhao, Hyperbranched Phosphorescent Conjugated Polymer Dots with Iridium(III) Complex as the Core for Hypoxia Imaging and Photodynamic Therapy, *ACS Appl. Mater. Interfaces*, 2017, **9**, 28319–28330.

25 (*a*) Y. Fan, C. Li, F. Li and D. Chen, pH-activated size reduction of large compound nanoparticles for in vivo nucleus-targeted drug delivery, *Biomaterials*, 2016, **85**, 30–39; (*b*) S. C. Larnaudie, J. C. Brendel, I. Romero-Canelón, C. Sanchez-Cano, S. Catrouillet, J. Sanchis, J. P. C. Coverdale, J.-I. Song, A. Habtemariam, P. J. Sadler, K. A. Jolliffe and S. Perrier, Cyclic Peptide–Polymer Nanotubes as Efficient and Highly Potent Drug Delivery Systems for Organometallic Anticancer Complexes, *Biomacromolecules*, 2018, **19**, 239–247; (*c*) C. Liao, D. Xu, X. Liu, Y. Fang, J. Yi, X. Li and B. Guo, Iridium(III) complex-loaded liposomes as a drug delivery system for lung cancer through mitochondrial dysfunction, *Int. J. Nanomed.*, 2018, **13**, 4417–4431; (*d*) W.-Y. Zhang, F. Du, M. He, L. Bai, Y.-Y. Gu, L.-L. Yang and Y.-J. Liu, Studies of anticancer activity in vitro and in vivo of iridium(III) polypyridyl complexes-loaded liposomes as drug delivery system, *Eur. J. Med. Chem.*, 2019, **178**, 390–400.

26 (*a*) P. Singla, V. Luxami and K. Paul, Benzimidazole-biologically attractive scaffold for protein kinase inhibitors, *RSC Adv.*, 2014, **4**, 12422–12440; (*b*) Y. Bansal and O. Silakari, The therapeutic journey of benzimidazoles: a review, *Bioorg. Med. Chem.*, 2012, **20**, 6208–6236.

27 (*a*) J. Pracharova, G. Vigueras, V. Novohradsky, N. Cutillas, C. Janiak, H. Kostrhunova, J. Kasparkova, J. Ruiz and V. Brabec, Exploring the Effect of Polypyridyl Ligands on the Anticancer Activity of Phosphorescent Iridium(III) Complexes: From Proteosynthesis Inhibitors to Photodynamic Therapy Agents, *Chem. – Eur. J.*, 2018, **24**, 4607–4619; (*b*) V. Novohradsky, G. Vigueras, J. Pracharova, N. Cutillas, C. Janiak, H. Kostrhunova, V. Brabec, J. Ruiz and J. Kasparkova, Molecular superoxide radical photogeneration in cancer cells by dipyridophenazine iridium(III) complexes, *Inorg. Chem. Front.*, 2019, **6**, 2500–2513; (*c*) V. Novohradsky, A. Rovira, C. Hally, A. Galindo, G. Vigueras, A. Gandioso, M. Svitelova, R. Bresolí-Obach, H. Kostrhunova, L. Markova, J. Kasparkova, S. Nonell, J. Ruiz, V. Brabec and V. Marchán, Towards Novel Photodynamic Anticancer Agents Generating Superoxide Anion Radicals: A Cyclometalated Ir^{III} Complex Conjugated to a Far–Red Emitting Coumarin, *Angew. Chem., Int. Ed.*, 2019, **58**, 6311–6315; (*d*) V. Novohradsky, L. Markova, H. Kostrhunova, J. Kasparkova, J. Ruiz, V. Marchán and V. Brabec, A Cyclometalated IrIII Complex Conjugated to a Coumarin Derivative Is a Potent Photodynamic Agent against Prostate Differentiated and Tumorigenic Cancer Stem Cells, *Chem. – Eur. J.*, 2021, **27**, 8547–8556.

 This journal is © the Partner Organisations 2022

28 J. Yellol, S. A. Pérez, G. Yellol, J. Zajac, A. Donaire, G. Vigueras, V. Novohradsky, C. Janiak, V. Brabec and J. Ruiz, Highly potent extranuclear-targeted luminescent iridium(III) antitumor agents containing benzimidazole-based ligands with a handle for functionalization, *Chem. Commun.*, 2016, **52**, 14165–14168.
29 M. C. DeRosa, D. J. Hodgson, G. D. Enright, B. Dawson, C. E. B. Evans and R. J. Crutchley, Iridium Luminophore Complexes for Unimolecular Oxygen Sensors, *J. Am. Chem. Soc.*, 2004, **126**, 7619–7626.
30 H. J. Lee and Y. Ha, Heteroleptic Orange Light-Emitting Iridium Complexes Containing Phenylbenzothiazolate Ligands, *Polym. Bull.*, 2016, **73**, 2501–2509.
31 T. R. Chen, Microscopic demonstration of mycoplasma contamination in cell cultures and cell culture media, *TCA Manual*, 1975, **1**, 229–232.
32 J. Schindelin, I. Arganda-Carreras, E. Frise, V. Kaynig, M. Longair, T. Pietzsch, S. Preibisch, C. Rueden, S. Saalfeld, B. Schmid, J.-Y. Tinevez, D. J. White, V. Hartenstein, K. Eliceiri, P. Tomancak and A. Cardona, Fiji: An Open-Source Platform for Biological-Image Analysis, *Nat. Methods*, 2012, **9**, 676–682.
33 K. Dedeian, J. Shi, N. Shepherd, E. Forsythe and D. C. Morton, Photophysical and Electrochemical Properties of Heteroleptic Tris-Cyclometalated Iridium(III) Complexes, *Inorg. Chem.*, 2005, **44**, 4445–4447.
34 A. Tsuboyama, H. Iwawaki, M. Furugori, T. Mukaide, J. Kamatani, S. Igawa, T. Moriyama, S. Miura, T. Takiguchi, S. Okada, M. Hoshino and K. Ueno, Homoleptic Cyclometalated Iridium Complexes with Highly Efficient Red Phosphorescence and Application to Organic Light-Emitting Diode, *J. Am. Chem. Soc.*, 2003, **125**, 12971–12979.
35 Z. Li, Synthesis, Photophysics, and Reverse Saturable Absorption of 7-(Benzothiazol-2-Yl)-9,9-Di(2-Ethylhexyl)-9H-Fluoren-2-Yl Tethered $[Ir(Bpy)(Ppy)_2]PF_6$ and $Ir(Ppy)_3$ Complexes (Bpy = 2,2′-Bipyridine, Ppy = 2-Phenylpyridine), *RSC Adv.*, 2016, **6**, 41214–41228.
36 M. Pérez-Hernández, C. Cuscó, C. Benítez-García, J. Bonelli, M. Nuevo-Fonoll, A. Soriano, D. Martínez-García, A. Arias-Betancur, M. García-Valverde, M. F. Segura, R. Quesada, J. Rocas, V. Soto-Cerrato and R. Pérez-Tomás, Multi-Smart and Scalable Bioligands-Free Nanomedical Platform for Intratumorally Targeted Tambjamine Delivery, a Difficult to Administrate Highly Cytotoxic Drug, *Biomedicines*, 2021, **9**, 508.
37 (*a*) A. L. Tessaro, A. Fraix, M. Failla, V. Cardile, A. C. E. Graziano, B. M. Estevao, A. Rescifina and S. Sortino, Light-controlled simultaneous "on demand" released of cytotoxic combinations for bimodal killing of cancer cells, *Chem. – Eur. J.*, 2018, **24**, 7664–7670; (*b*) A. Wicki, D. Witzigmann, V. Balasubramanian and J. Huwyler, Nanomedicine in cancer therapy: challenges, opportunities, and clinical applications, *J. Controlled Release*, 2015, **200**, 138–157.
38 V. P. Chauhan, T. Stylianopoulos, J. D. Martin, Z. Popović, O. Chen, W. S. Kamoun, M. G. Bawendi, D. Fukumura and R. K. Jain, Normalization of tumour blood vessels improves the delivery of nanomedicines in a size-dependent manner, *Nat. Nanotechnol.*, 2012, **7**, 383–388.
39 (*a*) F. Danhier, O. Feron and V. Préa, To exploit the tumor microenvironment: Passive and active tumor targeting of nanocarriers for anti-cancer drug delivery, *J. Controlled Release*, 2010, **148**, 135–146; (*b*) M. Wang, A. D. Miller and M. Thanou, *J. Drug Targeting*, 2013, **21**, 684–692; (*c*) A. Verma and F. Stellacci, *Small*, 2010, **6**, 12–21.
40 A. Latorre and A. Somoza, Glutathione-Triggered Drug Release from Nanostructures, *Curr. Top. Med. Chem.*, 2014, **14**, 2662–2671.
41 A. Bansal and M. C. Simon, Glutathione metabolism in cancer progression and treatment resistance, *J. Cell Biol.*, 2018, **217**, 2291–2298.
42 (*a*) J. Carretero, E. Obrador, M. J. Anasagasti, J. J. Martin, F. Vidal-Vanaclocha and J. M. Estrela, Growth-associated changes in glutathione content correlate with liver metastatic activity of B16 melanoma cells, *Clin. Exp. Metastasis*, 1999, **17**, 567; (*b*) D. Yoo, E. Jung, J. Noh, H. Hyun, S. Seon, S. Hong, D. Kim and D. Lee, Glutathione-Depleting Pro-Oxidant as a Selective Anticancer Therapeutic Agent, *ACS Omega*, 2019, **4**, 10070–10077.
43 (*a*) P. Laskar, S. Somani, S. J. Campbell, M. Mullin, P. Keating, R. J. Tate, C. Irving, H. Y. Leung and C. Dufès, Camptothecin-based dendrimersomes for gene delivery and redox-responsive drug delivery to cancer cells, *Nanoscale*, 2019, **11**, 20058–20071; (*b*) X. Jia, J. He, L. Shen, J. Chen, Z. Wei, X. Qin, D. Niu, Y. Li and J. Shi, Gradient Redox-Responsive and Two-Stage Rocket-Mimetic Drug Delivery System for Improved Tumor Accumulation and Safe Chemotherapy, *Nano Lett.*, 2019, **19**, 8690–8700; (*c*) Y. Nie, Y. Xu, Y. Gao, J. He, L. Sun, J. Chen, Y. Cui, H. Ge and X. Ning, A glutathione-triggered precision explosive system for improving tumor chemosensitivity, *Nano Res.*, 2021, **14**, 2372–2382.
44 L. Kennedy, J. K. Sandhu, M. E. Harper and M. Cuperlovic-Culf, Role of Glutathione in Cancer: From Mechanisms to Therapies, *Biomolecules*, 2020, **10**, 1429.
45 (*a*) Q. Mei, R. Sheng, W. Cheng, J. Zhang, P. Wang, Q. Mei, P. Chen and B. Tong, High stability and luminance efficiency thieno[2,3-d]pyridazine-based iridium complexes and their applications in high-performance yellow OLEDs, *Dalton Trans.*, 2020, **49**, 13797–13804; (*b*) S. Meksawangwong, B. Gohil, W. Punyain, R. Pal and F. Kielar, Development of tris-cyclometalated iridium complexes for cellular imaging through structural modification, *Inorg. Chim. Acta*, 2020, **508**, 119609; (*c*) T. Giridhar, J.-H. Lee, W. Cho, H. Yoo, C.-K. Moon, J.-J. Kim and S.-H. Jin, Highly efficient bluish green phosphorescent organic light-emitting diodes based on heteroleptic iridium(III) complexes with phenylpyridine main skeleton, *Org. Electron.*, 2014, **15**, 1687–1694; (*d*) J. C. Deaton, R. H. Young, J. R. Lenhard, M. Rajeswaran and S. Hu, Photophysical Properties of the Series fac- and mer-(1-Phenylisoquinolinato-N∧C2′)x(2-phenylpyridinato-N∧C2′)

3−x Iridium(III) (x = 1–3), *Inorg. Chem.*, 2010, **49**, 9151–9161.
46 H. Lu and M. H. Stenzel, Multicellular Tumor Spheroids (MCTS) as a 3D In Vitro Evaluation Tool of Nanoparticles, *Small*, 2018, **14**, 1702858.
47 S. Sperandio, I. de Belle and D. E. Bredesen, An alternative, nonapoptotic form of programmed cell death, *Proc. Natl. Acad. Sci. U. S. A.*, 2000, **97**, 14376–14381.
48 P. Weerasinghe and L. M. Buja, Oncosis: an important non-apoptotic mode of cell death, *Exp. Mol. Pathol.*, 2012, **93**, 302–308.
49 (*a*) R. S. Whelan, K. Konstantinidis, A.-C. Wei, Y. Chen, D. E. Reyna, S. Jha, Y. Yang, J. W. Calvert, T. Lindsten, C. B. Thompson, M. T. Crow, E. Gavathiotis, G. W. Dorn II, B. O'Rourke and R. N. Kitsis, Bax regulates primary necrosis through mitochondrial dynamics, *Proc. Natl. Acad. Sci. U. S. A.*, 2012, **109**, 6566–6571; (*b*) P. Golstein and G. Kroemer, Cell death by necrosis: towards a molecular definition, *Trends Biochem. Sci.*, 2007, **32**, 37–43.
50 M. G. Vander Heiden, L. C. Cantley and C. B. Thompson, Understanding the Warburg effect: the metabolic requirements of cell proliferation, *Science*, 2009, **324**, 1029–1033.
51 S. W. Ryter, H. P. Kim, A. Hoetzel, J. W. Park, K. Nakahira, X. Wang and A. M. K. Cho, Mechanisms of Cell Death in Oxidative Stress, *Antioxid. Redox Signal.*, 2007, **9**, 49–89.

 This journal is © the Partner Organisations 2022

Electronic Supplementary Material (ESI) for Inorganic Chemistry Frontiers.
This journal is © the Partner Organisations 2022

SUPPORTING INFORMATION

Polyurethane-polyurea hybrid nanocapsules as efficient delivery systems of anticancer Ir(III) metallodrugs

Joaquín Bonelli,[1,2,#] Enrique Ortega-Forte,[3,#] Gloria Vigueras,[3,#] Manel Bosch,[4] Natalia Cutillas,[3] Josep Rocas,[2] José Ruiz,[3,*] Vicente Marchán[1,*]

[1] Departament de Química Inorgànica i Orgànica, Secció de Química Orgànica, IBUB, Universitat de Barcelona, E-08028 Barcelona, Spain. Email: vmarchan@ub.edu

[2] Nanobiotechnological Polymers Division, Ecopol Tech, S.L., El Foix Business Park, Indústria 7, 43720 L'Arboç del Penedès, Tarragona, Spain

[3] Departamento de Química Inorgánica, Universidad de Murcia, and Institute for Bio-Health Research of Murcia (IMIB-Arrixaca), E-30071 Murcia, Spain. Email: jruiz@um.es

[4] Unitat de Microscòpia Òptica Avançada, Centres Científics i Tecnològics, Universitat de Barcelona, Av. Diagonal 643, E- 08028 Barcelona (Spain)

# These authors contributed equally

Table of contents

1. Materials

1.1. Building blocks and crosslinkers

Isophorone diisocyanate (IPDI) was purchased from Quimidroga (Barcelona, Spain), YMER N-120 was kindly supplied by Perstorp (Malmö, Sweden) and Genamin TAP 100D was provided by Clariant (Barcelona, Spain). Jeffcat DPA, DEDS, DETA and L-lysine hydrochloride were purchased from Sigma Aldrich (St Louis, USA).

1.2. Encapsulated compounds

Complexes **Ir1** and **Ir2** were synthesized as indicated in sections 3.1 and 3.2. $IrCl_3 \bullet H_2O$ (Johnson Matthey) was used as received. The commercial cyclometalating pro-ligand 2-phenyl-1H-benzo [d]imidazole was obtained from Sigma-Aldrich (Spain). Neobee 1053 (Caprilyc/capric triglyceride or GTCC) was purchased from Stepan Company (Illinois, United States).

1.3. Solvents and auxiliary solutions

Milli-Q water was obtained from a Merck Millipore purification system (Madrid, Spain) and PBS, HCl 37% (by wt) and NaOH in pellets were purchased from Merck (Madrid, Spain). HNO_3 72% (v/v) was purchased from Sigma Aldrich (St Louis, USA).

1.4. Biological agents, mediums and supplements

Dulbecco's Modification of Eagle's Medium (DMEM) was purchased from Corning (Arizona, USA) and DMEM with low glucose, pyruvate and without glutamine and Phenol Red was purchased from Thermo Fischer Scientific (Massachusetts, USA), as well as Fetal Bovine Serum (FBS), Lysotracker Green, Mytotracker Green and Mytotracker Orange. L-glutamine solution (200 mM) was acquired from Biological Industries (Cromwell, USA). Hepes buffer (1M) was purchased from Lonza (Basel, Switzerland). Thiazolyl-blue tetrazolium bromide (MTT)-reagent was purchased from Sigma-Aldrich. Apoptosis/necrosis FITC-Annexin V/Propidium Iodide (PI) detection kit and Phospho-Histone H2A.X (Ser139) Alexa Fluor 488-conjugated monoclonal antibody CR55T33 were purchased from eBioscience™ (Thermofisher Scientific). JC-1 dye was purchased from Promocell. Glycolytic rate test kit acquired from Seahorse Agilent Technologies. Cisplatin and antimycin A were acquired from Merck KGaA. Bovine Serum Albumin (BSA) was purchased from Sigma Aldrich (St Louis, USA) and L-glutathione (GSH) from TCI Chemicals (Tokyo, Japan). Complete Human AB Serum was purchased from Thermo Fischer Scientific (Massachusetts, USA).

2. Analytical techniques

2.1. NMR spectroscopy

The ^{1}H and ^{13}C spectra were recorded on a Bruker AC 300E, Bruker AV 400, or Bruker AV 600 NMR spectrometer and chemical shifts are cited relative to $SiMe_4$ (^{1}H and ^{13}C, external).

2.2. High resolution mass spectrometry and elemental analysis

ESI mass (positive mode) analyses were carried out on a hybrid mass spectrometer type Agilent QTOF 6550. The C, H, and N analyses were performed with a Carlo Erba model EA 1108 microanalyzer.

2.3 Infrared spectroscopy (IR)

IR spectra were acquired in a Smart ATR (Nicolet iS10, Thermo Scientific, Raleigh, USA) using a transmittance mode (16 scans) and OMNIC software. For the monitoring of solvent-based samples, one drop was deposited onto the diamond crystal and the solvent was left to dry by evaporation. IR spectra were recorded from a dry film of the sample for the reaction control after emulsification.

2.4. pH measurements

The pH of the emulsion was determined right after the crosslinker was added and at different time intervals until the last polyaddition reaction was complete. All the determinations were carried out in a pH-meter HI 2211 pH/ORP-Meter (HANNA Instruments, Eibar, Spain) equipped with a pH electrode Crison 5029 (Crison Instruments, Barcelona, Spain) and a temperature probe.

2.5. Dynamic light scattering (DLS)

The size distribution of the NCs was analyzed on a Zetasizer Nano-ZS90 (Malvern, Worcestershire, UK) in Milli-Q water at 25 °C at a concentration of 0.5 mg/mL.

2.6. Transmission electron microscopy (TEM)

The morphology of nanocapsules was studied on a TEM Jeol J1010 (Peabody, MA, USA) equipped with a CCD Orius camera (Gatan). A 400-mesh copper grid coated with 0.75 % FORMVAR was deposited on 6 μL of a suspension of nanocapsules in water (10 mg mL−1) for 25 min. Excess of sample was removed by oblique contact with Whatman filter paper and the grid was deposited on a drop of uranyl acetate (2 % w/w) in water for 30 s. Excess uranyl acetate was removed and the grid was air-dried for at least 3 h prior to measurement.

2.7. Zeta potential (Z-pot)

The Z-pot of the NCs was analyzed on a Zetasizer Nano-ZS90 (Malvern, Worcestershire, UK) in Milli-Q water at 25 °C at a concentration of 1 mg/mL, measured at different pH values.

2.8. Solids concentration

NCs concentration in the aqueous dispersion was determined by triplicate leading to dryness using an Digitheat-TFT oven (J.P.Selecta, Barcelona, Spain), with a fixed temperature of 40 ºC for 48 h.

2.9. Dialysis purification

The NCs were dialyzed against Milli-Q water for 24 h using a Spectra/Por molecular porous membrane tubing with a 12–14 kDa molecular MWCO (Spectrum Laboratories, Rancho Dominguez, USA).

2.10. ICP-MS analysis of the emulsion

To determine the amount of Ir complex incorporated in the NCs, a fixed volume of NCs emulsion (previously dialyzed) was diluted in 500 μL of concentrated 72% (v/v) nitric acid into wheaton v-vials (Sigma-Aldrich) and heated in an oven at 373 K for 18 h. The vials were then allowed to cool, and each sample solution was transferred into a volumetric tube and combined with Milli-Q water washings (1.5 mL). Digested samples were diluted 5 times with Milli-Q to obtain a final HNO_3 concentration of approximately 3.6% v/v. Iridium content was analyzed on an ICP-MS Perkin Elmer Elan 6000 series instrument at the Centres Científics i Tecnològics of the Universitat de Barcelona. The solvent used for all ICP-MS experiments was Milli-Q water with 1% HNO_3. The iridium standard (High-Purity Standards, 1000 μg/mL ± 5 μg/mL in 5% HNO_3) was diluted with 1% HNO_3 to 10 ppb. Iridium standards were freshly prepared in Milli-Q water with 1% HNO_3 before each experiment. The concentrations used for the calibration curve were in all cases 0, 0.2, 0.4, 1, and 2 ppb. The isotope detected was ^{193}Ir and readings were made in triplicate for each sample. Rhodium was added as an internal standard at a concentration of 10 ppb in all samples.

The following equations were used to calculate Encapsulation Efficiency EE (%) and Drug Loading DL (%):

$$\%\, EE = \frac{amount\ of\ Ir\ complex\ incorporated\ in\ the\ nanocapsule}{total\ amount\ of\ Ir\ complex\ added\ in\ the\ aqueous\ dispersion} * 100$$

$$\%\, DL = \frac{amount\ of\ Ir\ complex\ incorporated\ in\ the\ nanocapsule}{total\ amount\ of\ dried\ nanocapsules} * 100$$

2.11. Photophysical characterization

The UV/Vis absorption and emission spectra were recorded in CH_2Cl_2 and DMSO solutions for Ir(III) complexes and water solutions for the nanocapsules. UV/Vis spectroscopy was carried out on a PerkinElmer Lambda 750 S spectrometer with operating software, and emission spectra were obtained with a Horiba Jobin Yvon Fluorolog 3−22 modular spectrofluorimeter with a 450 W xenon lamp. Measurements were performed in a right angle configuration using 10 mm quartz fluorescence cells for solutions at 298 K. Emission lifetimes (τ) were measured using an IBH FluoroHub TCSPC controller and a NanoLED pulse diode excitation source (τ < 10 μs); the estimated uncertainty is ±10% or better. Emission quantum yields (Φ) were measured using a Hamamatsu C11347 Absolute PL Quantum Yield Spectrometer; the estimated uncertainty is ±5% or better. CH_2Cl_2, DMSO and water solutions of the samples were previously degassed by bubbling argon for 20 min.

3. Synthetic procedures

3.1. Synthesis and characterization of Ir(III) complexes

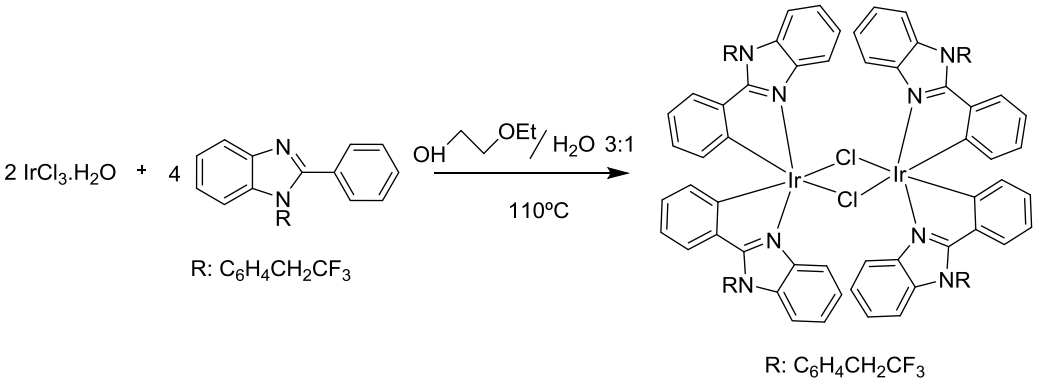

Scheme S1. Synthesis of starting dimeric iridium complex.

3.1.1. Synthesis and characterization of Ir1

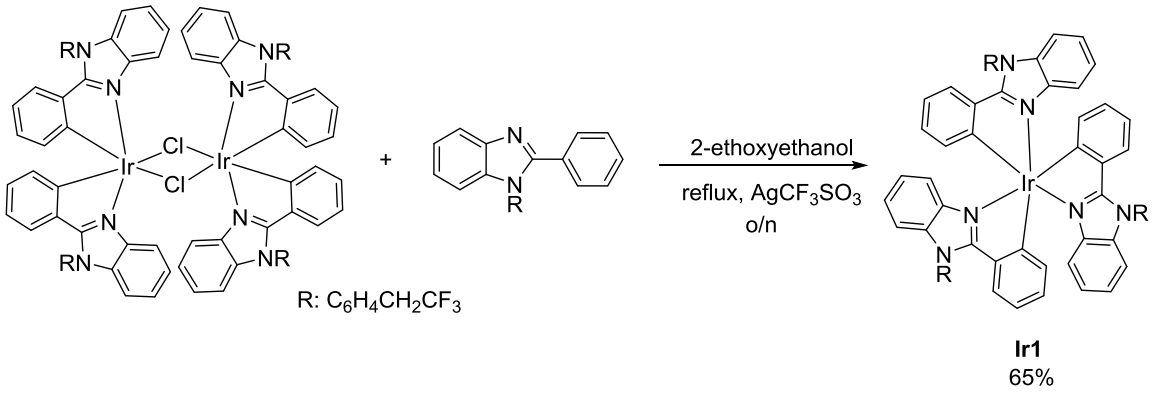

Scheme S2. Synthesis of **Ir1**.

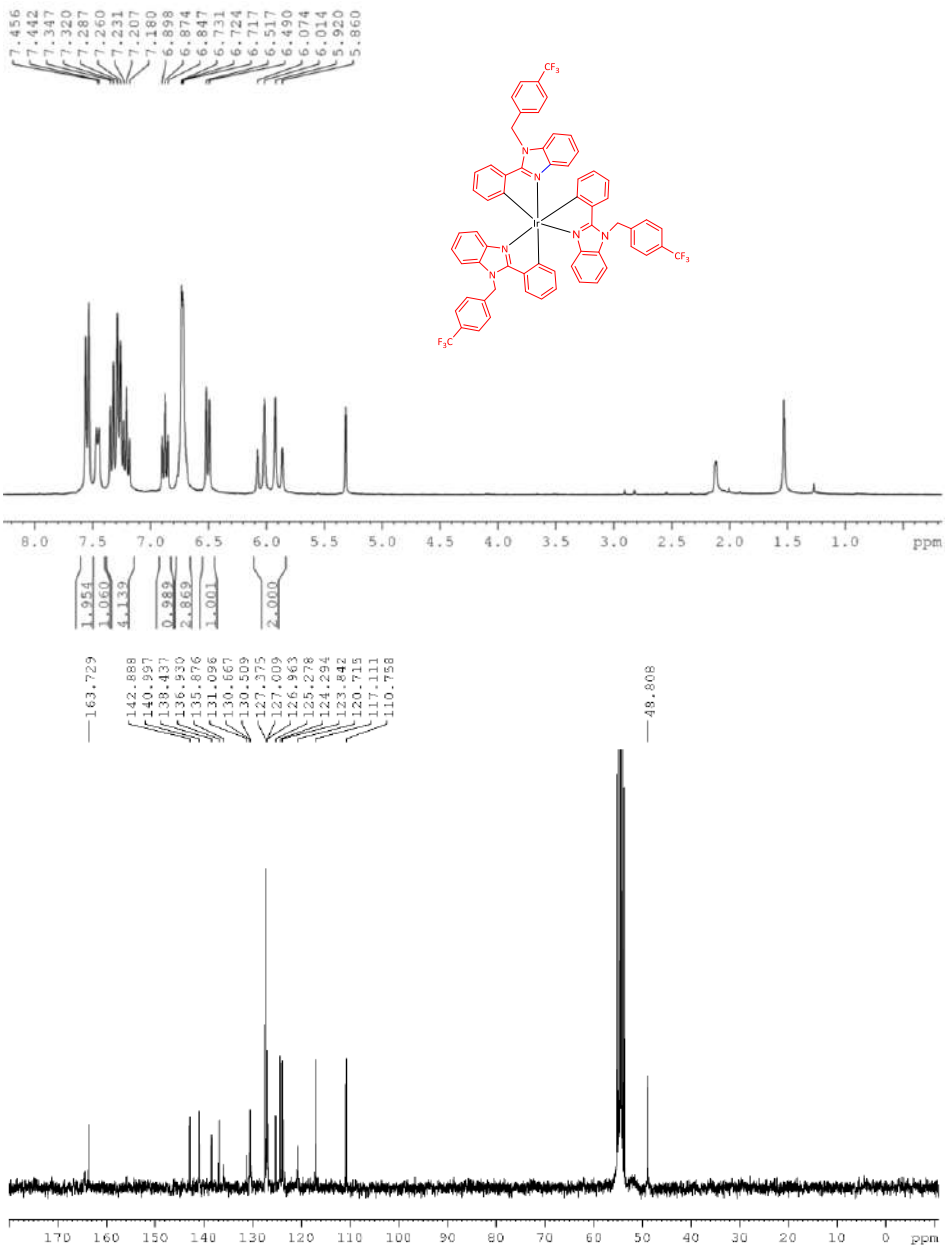

Figure S1. ^{1}H and ^{13}C NMR spectra of **Ir1** in CD_2Cl_2.

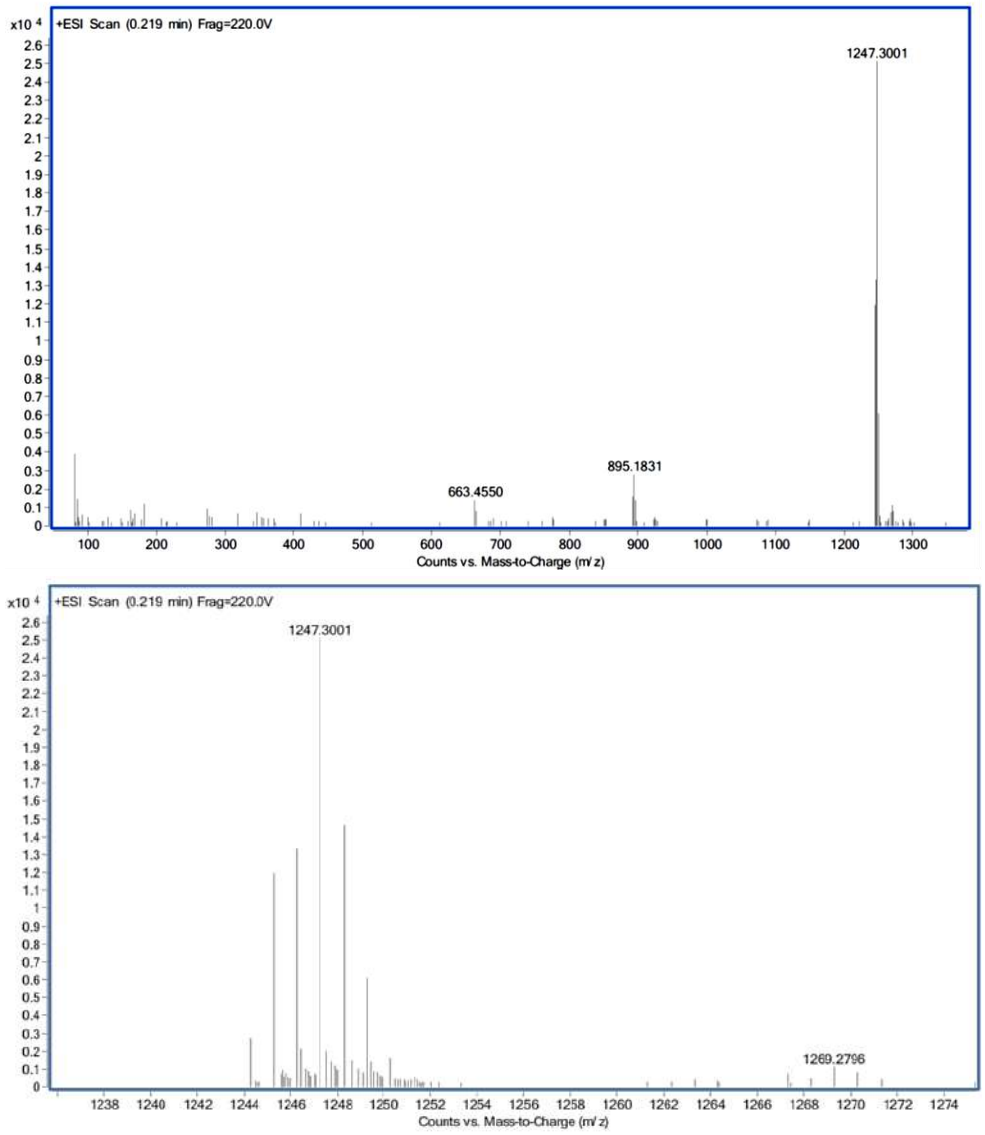

Figure S2. HR ESI-MS spectrum of **Ir1**.

3.1.2. Synthesis and characterization of Ir2

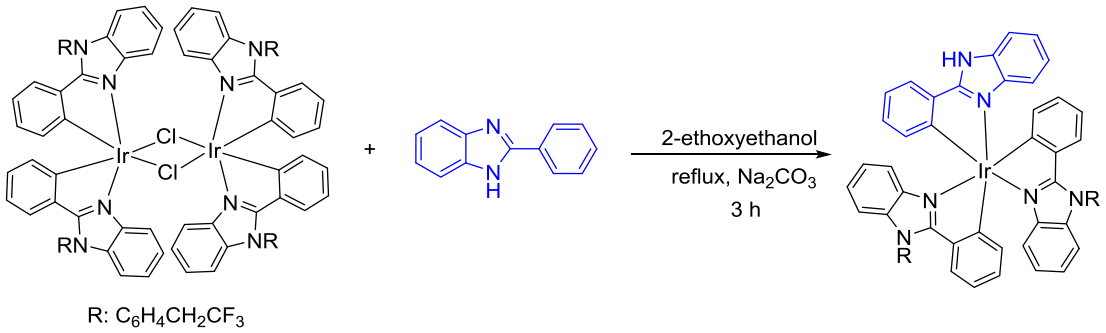

Scheme S3. Synthesis of **Ir2**.

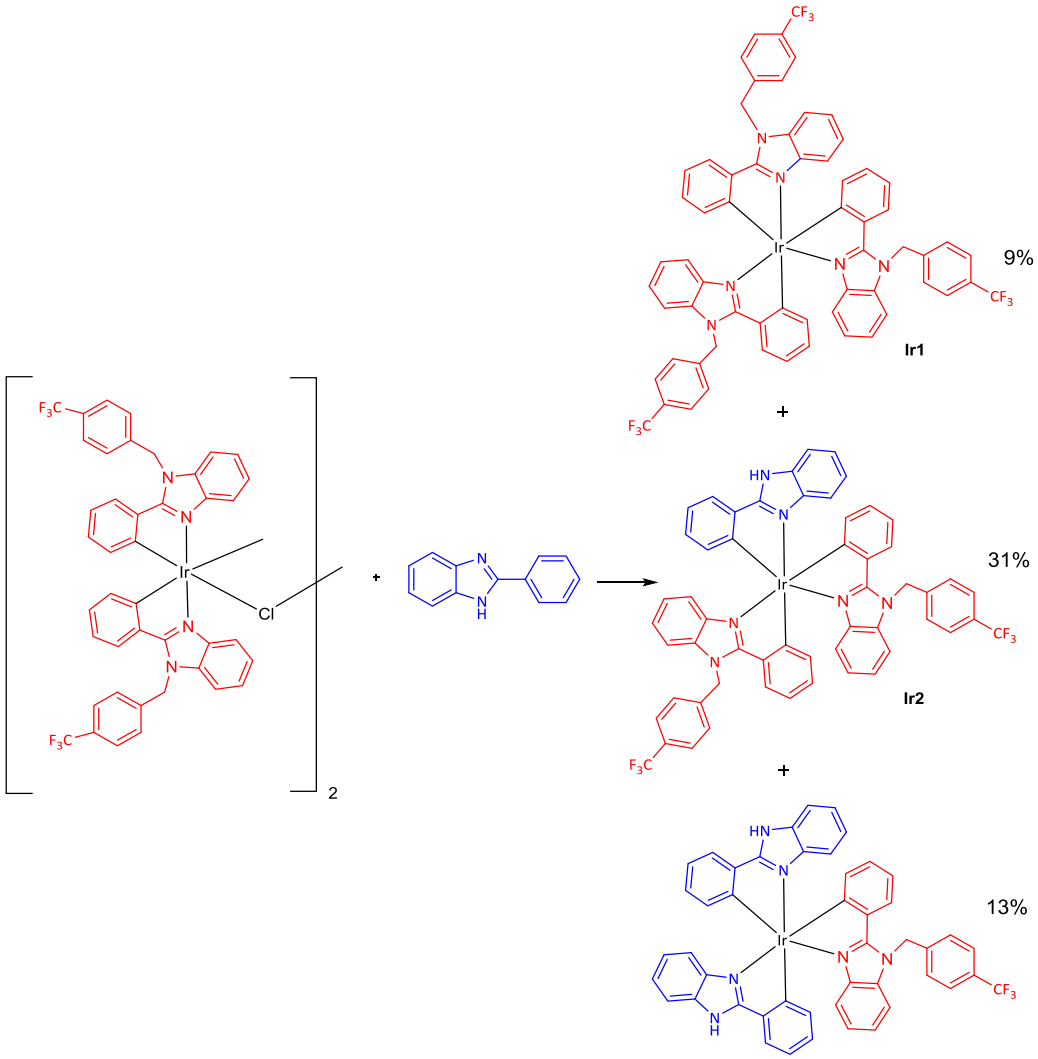

Scheme S4. Mixture of the three neutral compounds obtained in the synthesis of heteroleptic complex **Ir2**.

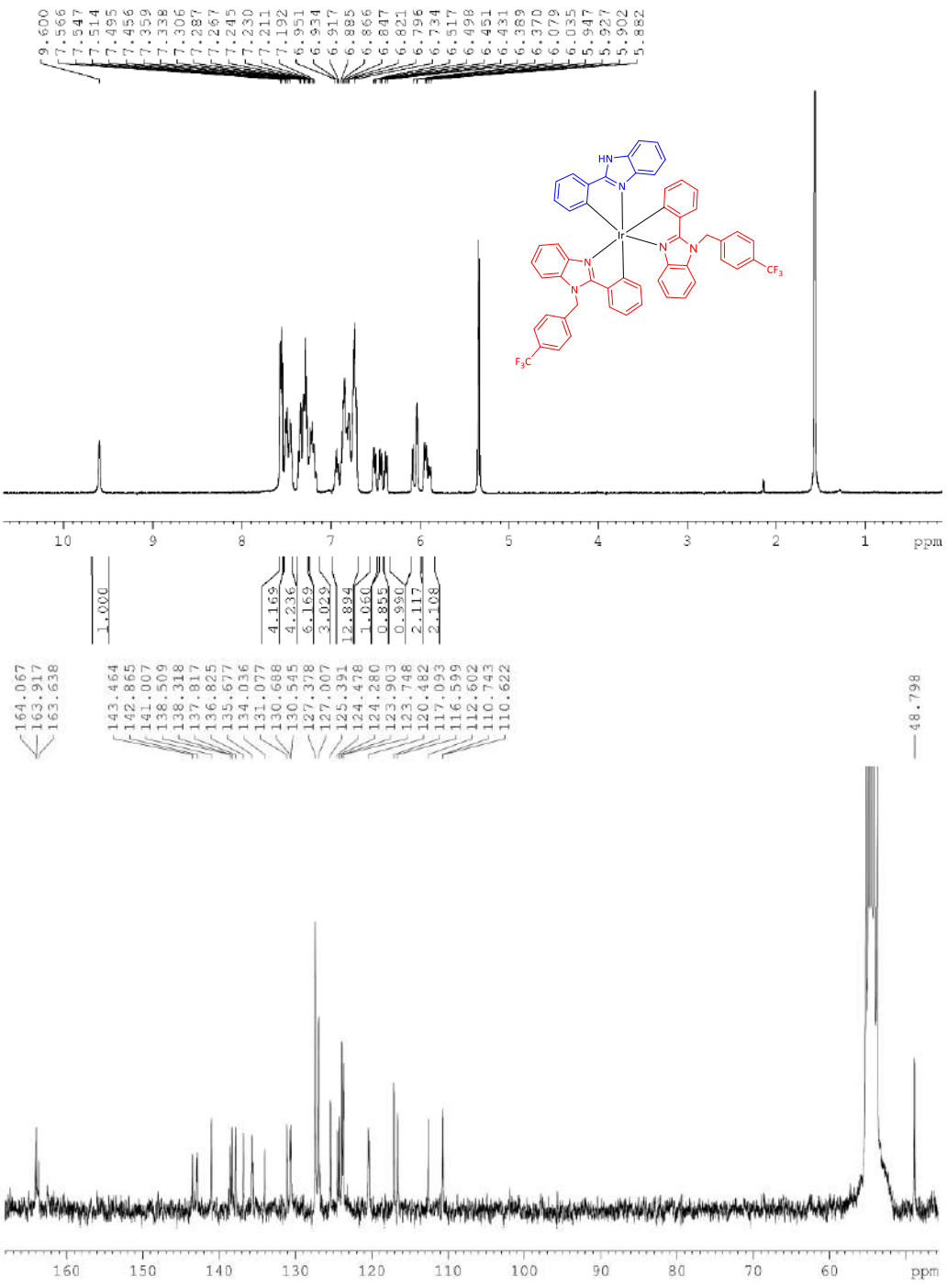

Figure S3. ^{1}H and ^{13}C NMR spectra of **Ir2** in CD_2Cl_2.

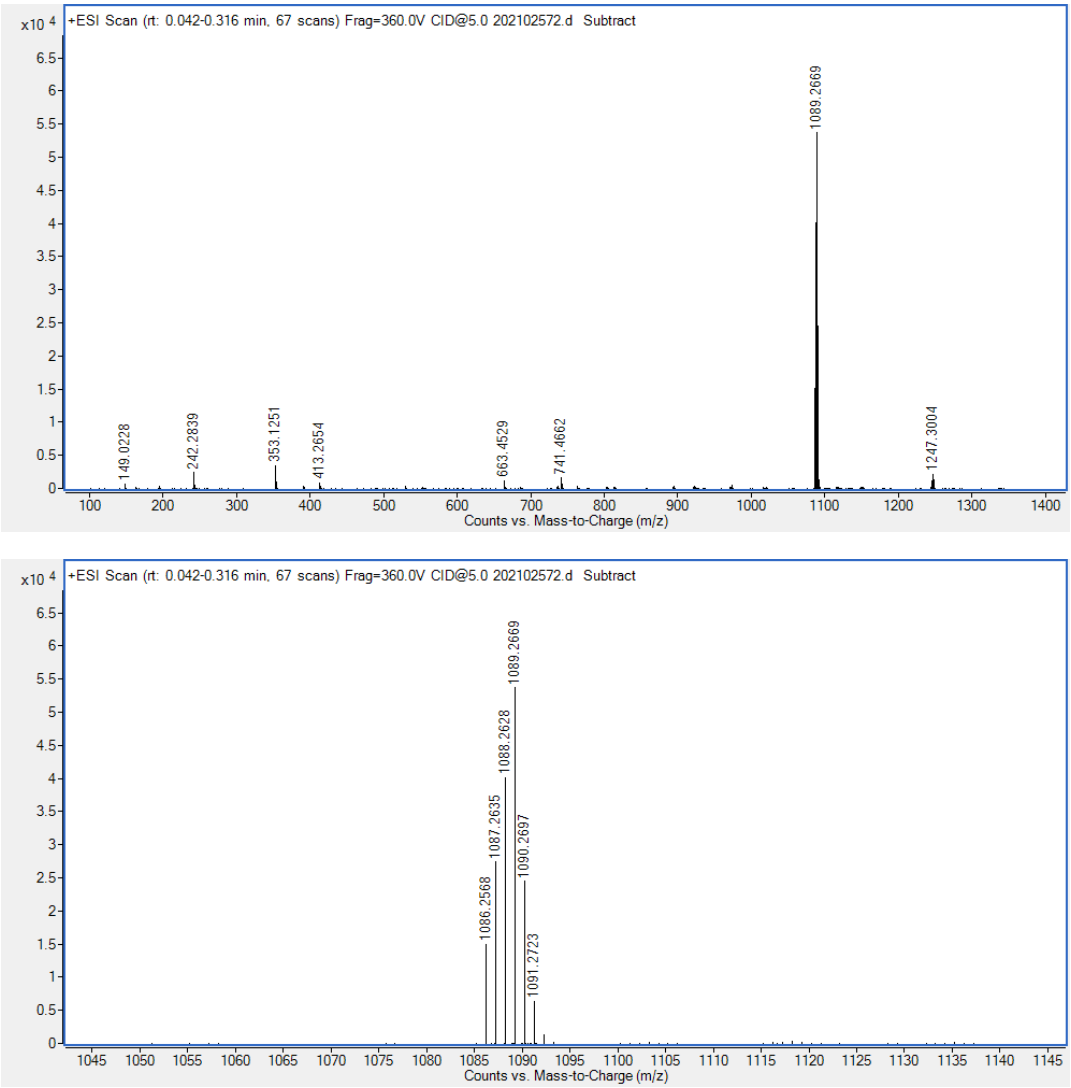

Figure S4. HR ESI-MS spectrum of **Ir2**.

3.2. Synthesis of Ir2-loaded amphoteric NCs (NC-Ir2)

Table S1. Amounts of reagents used to prepare **NC-Ir2**

Substance	Amount	Mols and equivalents
IPDI	70.4 mg	0.32 mmol / 0.63 meq
Ir2	6.0 mg	5.51 μmol
Neobee 1053 (GTCC)	26.7 mg	57.46 μmol
Polymer (P1)	816.9 mg	0.09 meq
Dry THF	1 mL	–
L-lysine	24.6 mg	0.15 mmol / 0.29 meq
Milli-Q water	5.40 g	–
DETA	7.8 mg	0.08 mmol / 0.23 meq

3.3. Synthesis of non-loaded amphoteric NCs (NC-GTCC)

Table S2. Amounts of reagents used to prepare **NC-GTCC**

Substance	Amount	Equivalents or mols
IPDI	69.7 mg	0.32 mmol / 0.63 meq
Neobee 1053 (GTCC)	26.3 mg	56.61 μmol
Polymer (P1)	812.5 mg	0.09 meq
Dry THF	1 mL	–
L-lysine	24.6 mg	0.15 mmol / 0.29 meq
Milli-Q water	5.93 g	–
DETA	7.8 mg	0.08 mmol / 0.23 meq

4. Characterization of Ir(III)-loaded NCs

4.1. Infrared Spectroscopy

The polymerization reaction progress for amphiphilic cationic polymer (P1) synthesis was controlled by IR spectroscopy using the procedure detailed in section 2.1., given that NCO has a very clear and characteristic stretching band at 2280–2230 cm^{-1}.

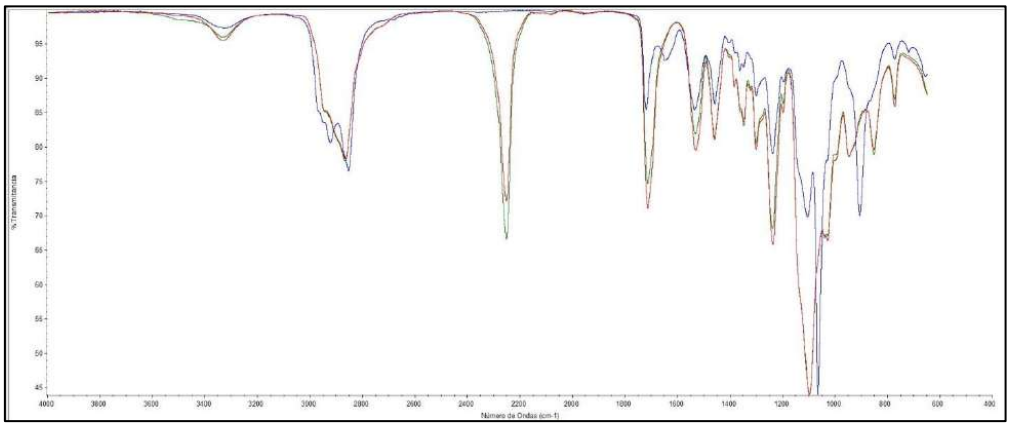

Figure S5. IR spectra of amphiphilic cationic polymer (P1).

As shown in Figure S5, IR spectra of the polymer (P1) indicated that the polymerization reaction between diols, the diamine and the diisocyanate was successful, in both steps of the polymer synthesis. The green line corresponds to the first sample recorded, at the beginning of the reaction. At that time, the NCO asymmetric stretching band at 2252 cm^{-1} was very sharp and intense. At the end of the first step, involving the reaction between the diols and the diisocyanate (red line), the intensity of the NCO stretching band decreased significantly. Meanwhile, the intensities of the CO stretching band at 1719 cm^{-1}, the CN stretching band at 1537 cm^{-1}, the NCOO/COC asymmetric stretching band at 1240 cm^{-1} increased. Overall, the IR spectra performed during the first step of the synthesis confirmed polyurethane bond formation along with NCO consumption. Once the diamine was added during the second step of the polymer synthesis (blue line), the NCO stretching band at 2252 cm^{-1} disappeared immediately, which was explained by the high reactivity of the amines. Simultaneously, other characteristic bands appeared or changed, such as a new stretching band at 1634 cm^{-1}, which was associated to the carbonyl of urea bonds and a new wagging band at 908 cm^{-1} corresponding to the free secondary amine, which also confirmed polyurea formation.

The encapsulation reaction was also controlled by IR spectroscopy. As shown in Figure S6, IR spectra of the NCs (regardless of their loading) indicated that the formation of the nanocapsule was also successful. The green line in the IR spectra represents the sample 30 min after the polymer, together with the cargo, was mixed with the diisocyanate. This initial step was the reactivation of the polymer and its conversion to an NCO-reactive entity. Afterwards, L-lysine sodium salt was added (red line) and reacted with the activated polymer. A decrease on the intensity of the NCO stretching band at 2255 cm^{-1}, concomitantly with an increase of the carbonyl and CN stretching bands, confirmed urea formation (1642 cm^{-1} and 1532 cm^{-1}, respectively). Finally, the triamine was added (purple line) and the NCO stretching band instantaneously disappeared and the urea-associated bands increased their intensity as a result of the rapid reaction between remaining NCO groups and this polyamine.

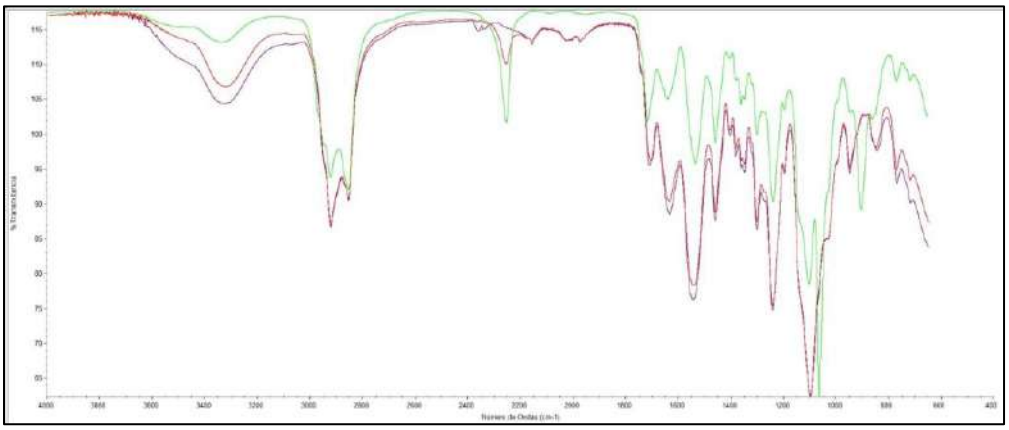

Figure S6. IR spectra of the encapsulation reaction.

4.2. Average size of NCs by DLS

The particle size distribution of the NCs was measured by dynamic light scattering (DLS) (Figures S7-S9 and Table S3).

Table S3. Average particle size of NCs

Sample	Diameter ± SD (nm)
NC-GTCC	22.48 ± 3.95
NC-Ir1	18.61 ± 0.39
NC-Ir2	18.45 ± 0.39

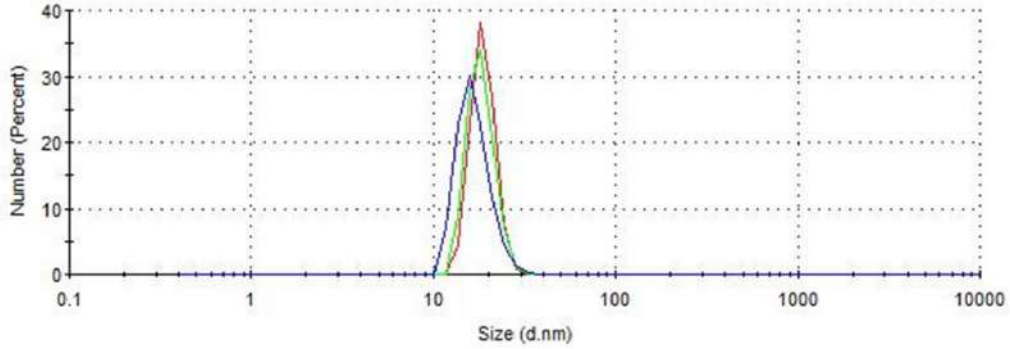

Figure S7. Particle size distribution of non-loaded NCs measured by DLS.

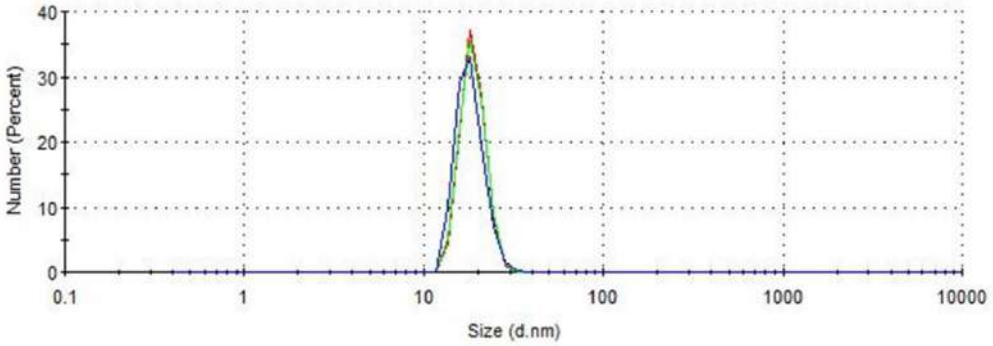

Figure S8. Particle size distribution of **Ir1**-loaded NCs measured by DLS.

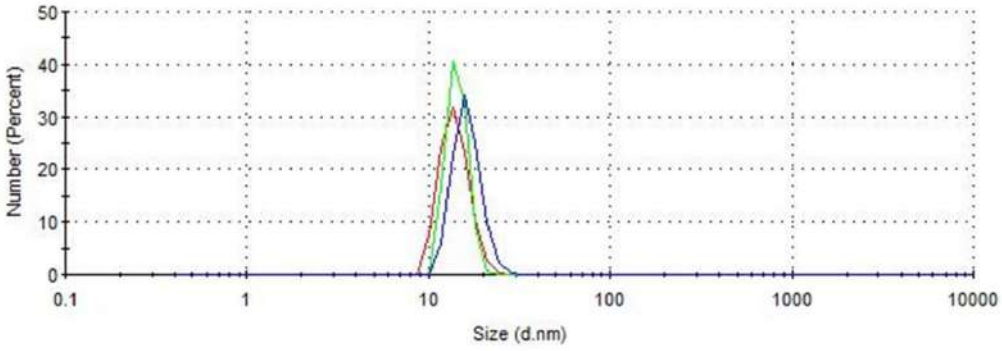

Figure S9. Particle size distribution of **Ir2**-loaded NCs measured by DLS.

4.3. Transmission electron microscopy (TEM)

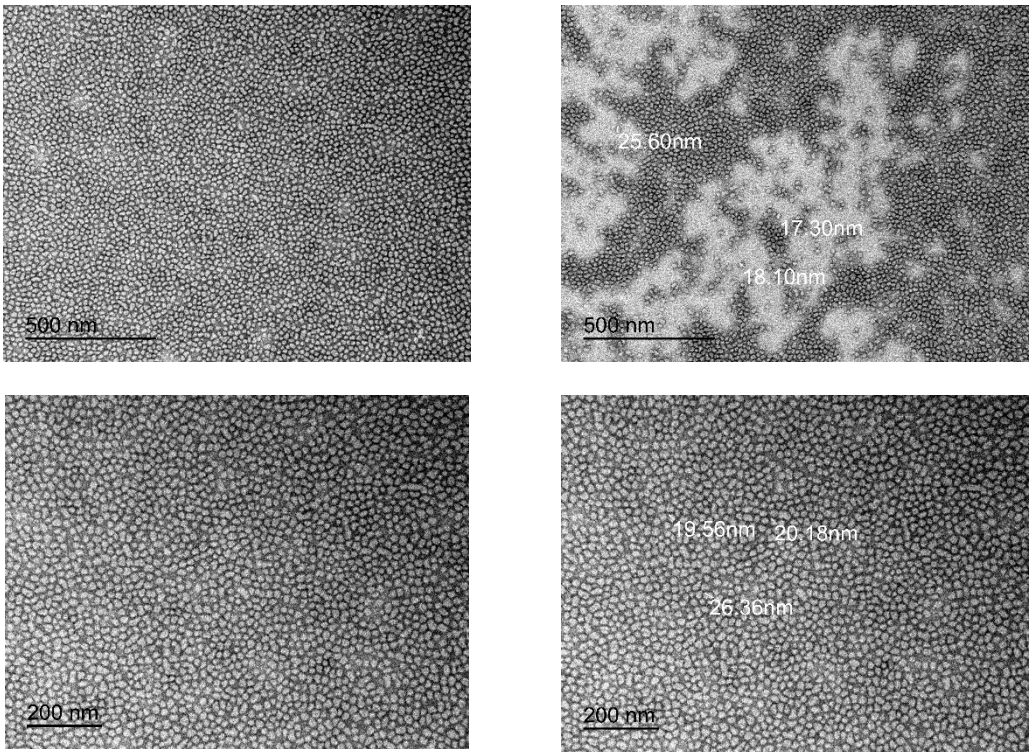

Figure S10. Selected TEM micrographs of **NC-Ir1** (scale bar: 200 nm and 500 nm).

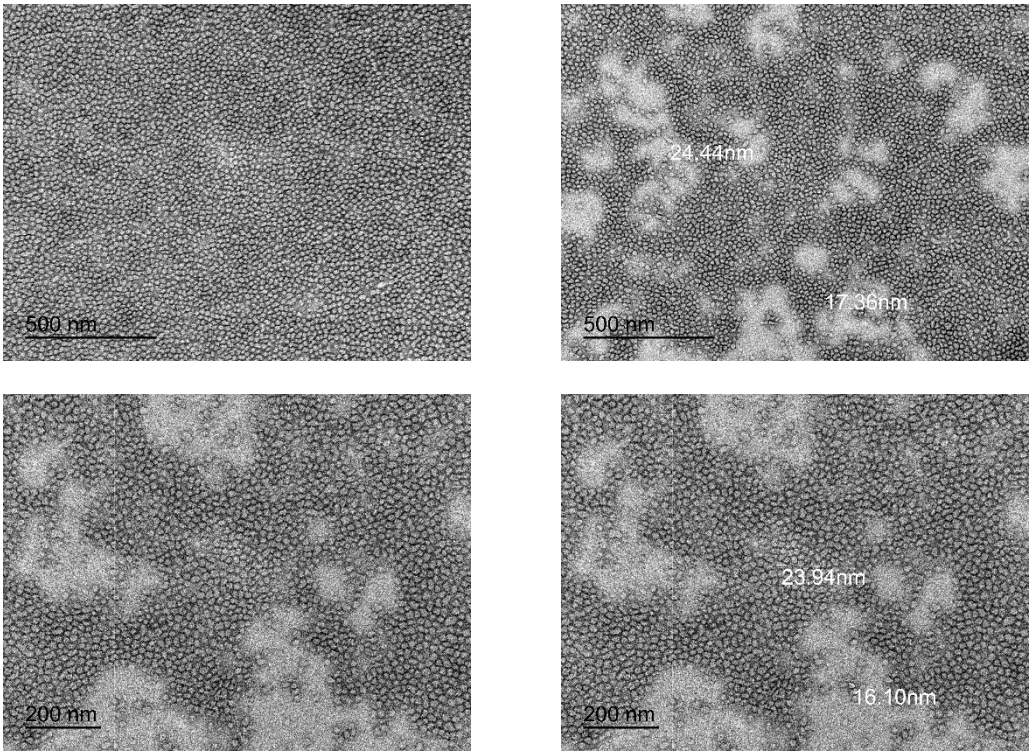

Figure S11. Selected TEM micrographs of **NC-Ir2** (scale bar: 200 nm and 500 nm).

4.4. Z-potential of NCs

As shown in Table S4 and Figure S10, the ζ-potential values (surface charge) of the NCs were determined at different pH values.

Table S4. Z-potential values of the samples at different pH values.

Sample	ζ-Pot ± SD (mV) at pH=6.5	ζ-Pot ± SD (mV) at pH=7.0	ζ-Pot ± SD (mV) at pH=7.5
NC-GTCC	1.97 ± 0.03	2.50 ± 0.26	-6.96 ± 0.47
NC-Ir1	5.95 ± 0.43	0.956 ± 0.316	-9.08 ± 0.62
NC-Ir2	5.07 ± 0.80	-6.34 ± 0.07	-26.2 ± 6.78

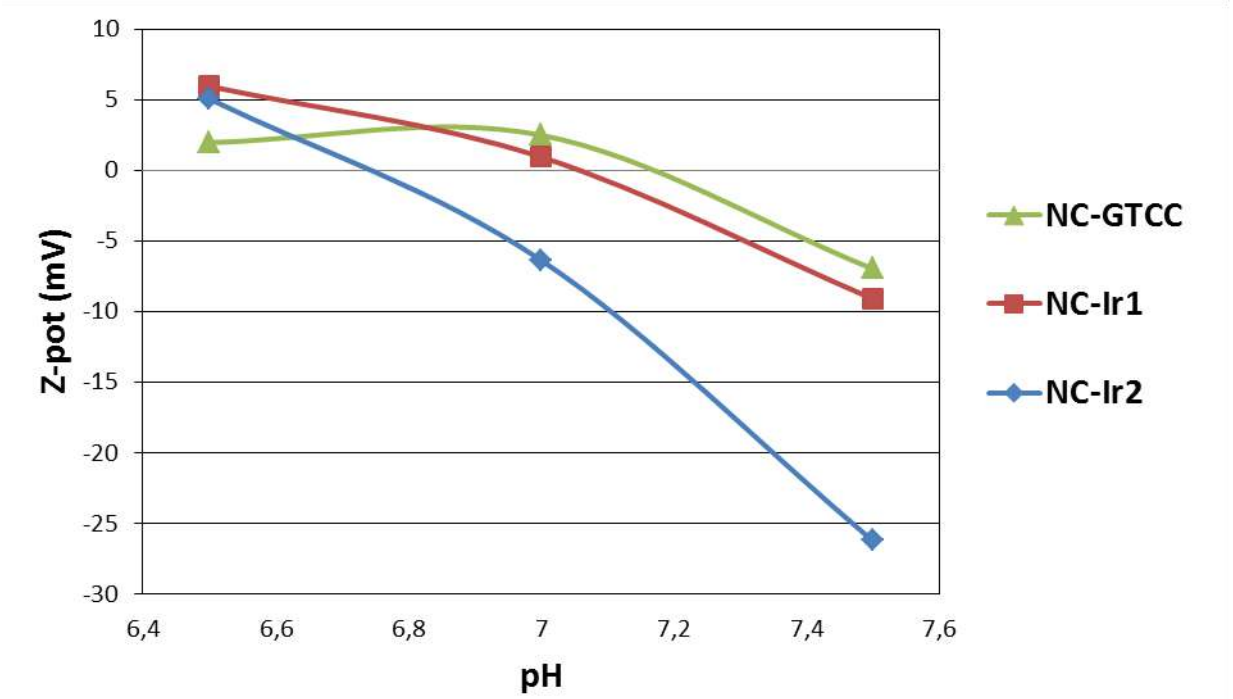

Figure S12. Z-potential measurements under different pH conditions of non-loaded NCs and **Ir1**- and **Ir2**-loaded NCs.

4.5. Ir complex loading

The concentration of NCs in the final emulsions (mg/mL) was quantified with a solids concentrator, as indicated in section 2.5. In addition, the amount of Ir complexes (**Ir1** and **Ir2**) inside the NCs was determined by ICP-MS analysis following the method described in section 2.7. Drug Loading (DL) and Encapsulation Efficiency (EE) were calculated as indicated in section 2.7.

Table S5. DL and EE parameters for **NC-Ir1** and **NC-Ir2**.

	[NCs] (mg/mL)	**Drug Loading (DL, µM)**	**Encapsulation Efficiency (EE, %)**
NC-GTCC	64.8 ± 0.5	-	-
NC-Ir1	45.4 ± 3.1	130.5 ± 16.2	41.4 %
NC-Ir2	64.8 ± 0.5	206.2 ± 16.8	40.0%

4.6. Stability studies of Ir(III)-loaded NCs

The stability of the Ir(III)-loaded NCs under different biological mediums was investigated by Transmission Electron Microscopy (TEM). On the one hand, PBS buffer, a 40 mg/mL solution of BSA in PBS buffer and complete Human AB Serum were selected to investigate the stability of the NCs in common medical vehicles. On the other hand, the degradability of the NCs was also investigated in PBS supplemented with GSH (10 mM) with the aim of reproducing the situation in the intracellular media of a solid-tumor cell, where the concentration of the reduced-form of glutathione is about 10-times higher than in healthy cells. PBS supplemented with GSH was buffered to physiological pH (pH=7.4).

As shown in Figures S13-S15, **NC-Ir2** were incubated for 2 h, 24 h and 48 h at 37ºC in the above-mentioned mediums and TEM samples were prepared as described in Section 2.6.

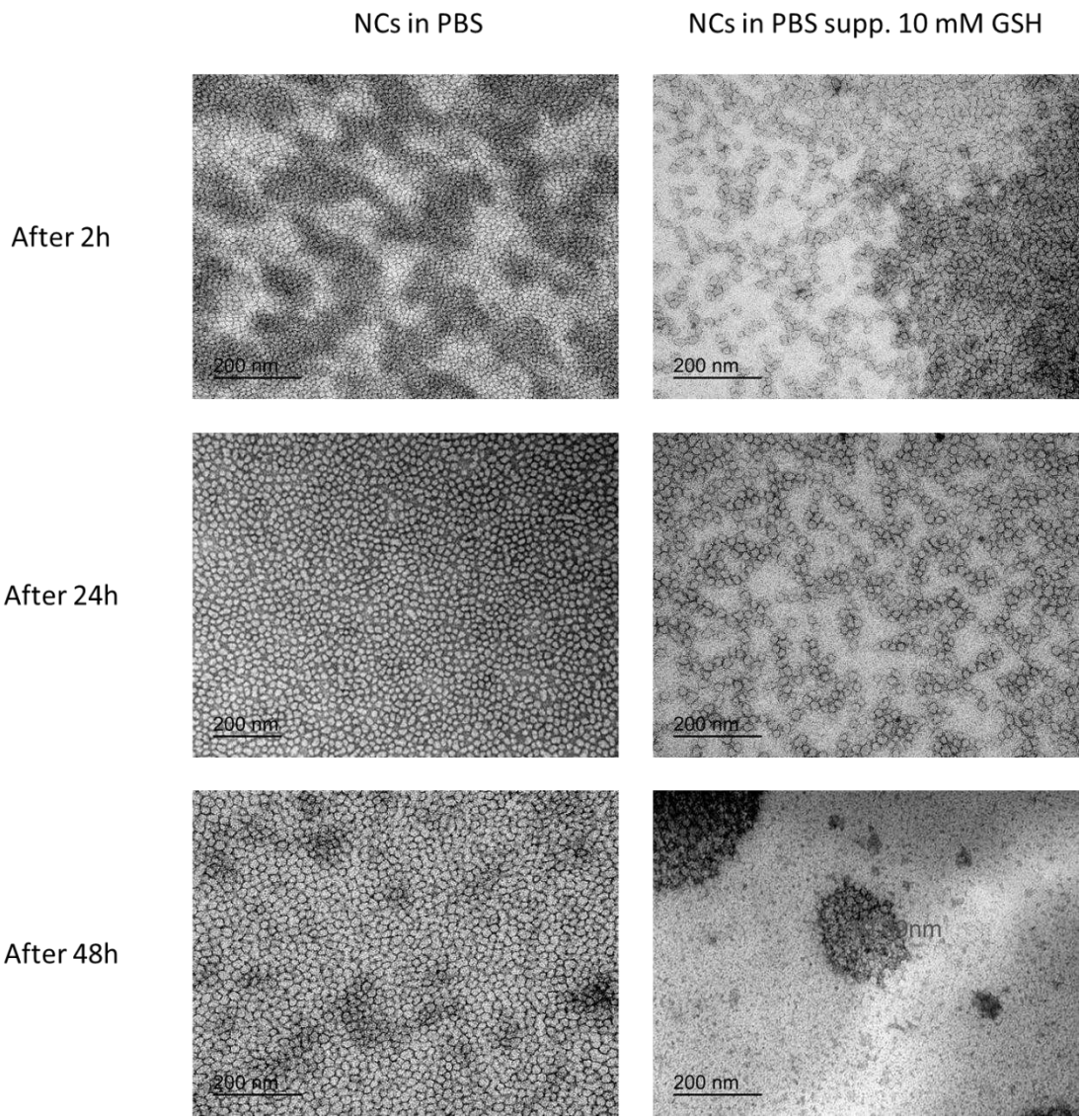

Figure S13. Selected TEM micrographs of **NC-Ir2** incubated at 16 mg/mL in PBS (left) and in 10 mM L-GSH-supplemented PBS (right) for 2 h, 24 h and 48 h at 37ºC.

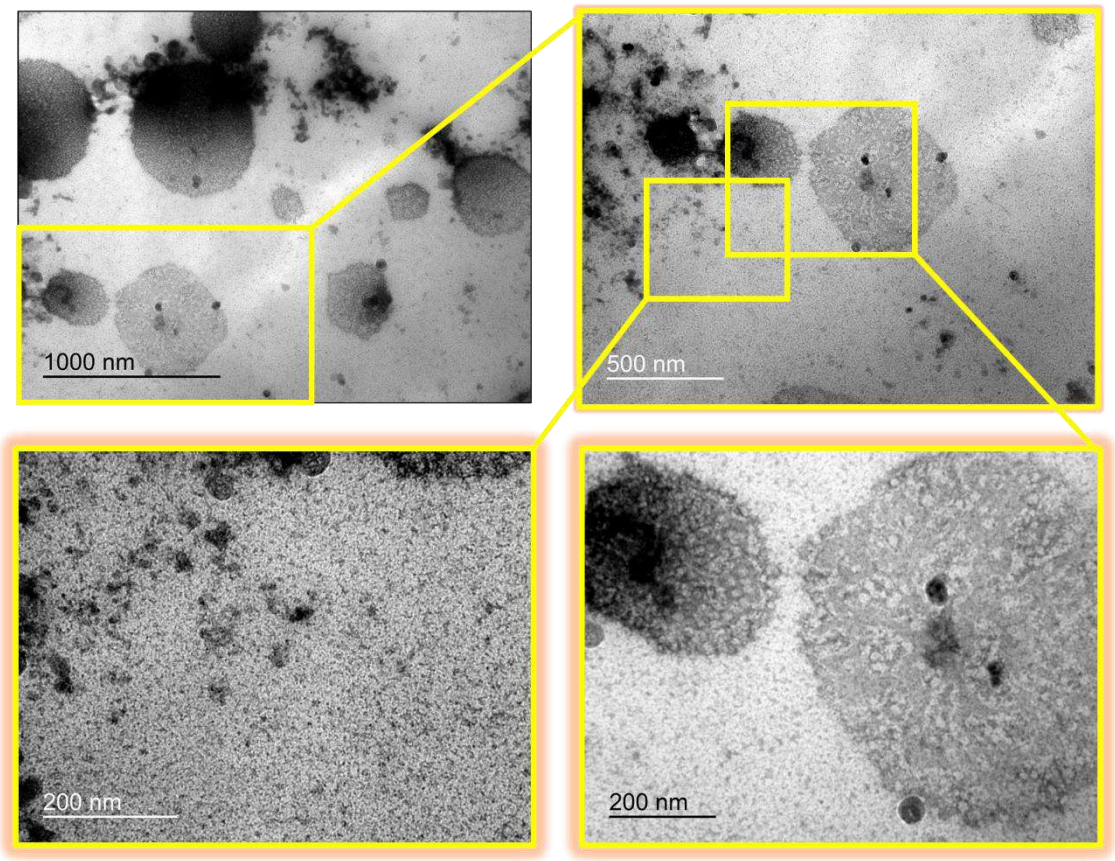

Figure S14. Magnification of TEM micrographs of **NC-Ir2** incubated at 16 mg/mL in 10 mM L-GSH-supplemented PBS for 48 h at 37ºC.

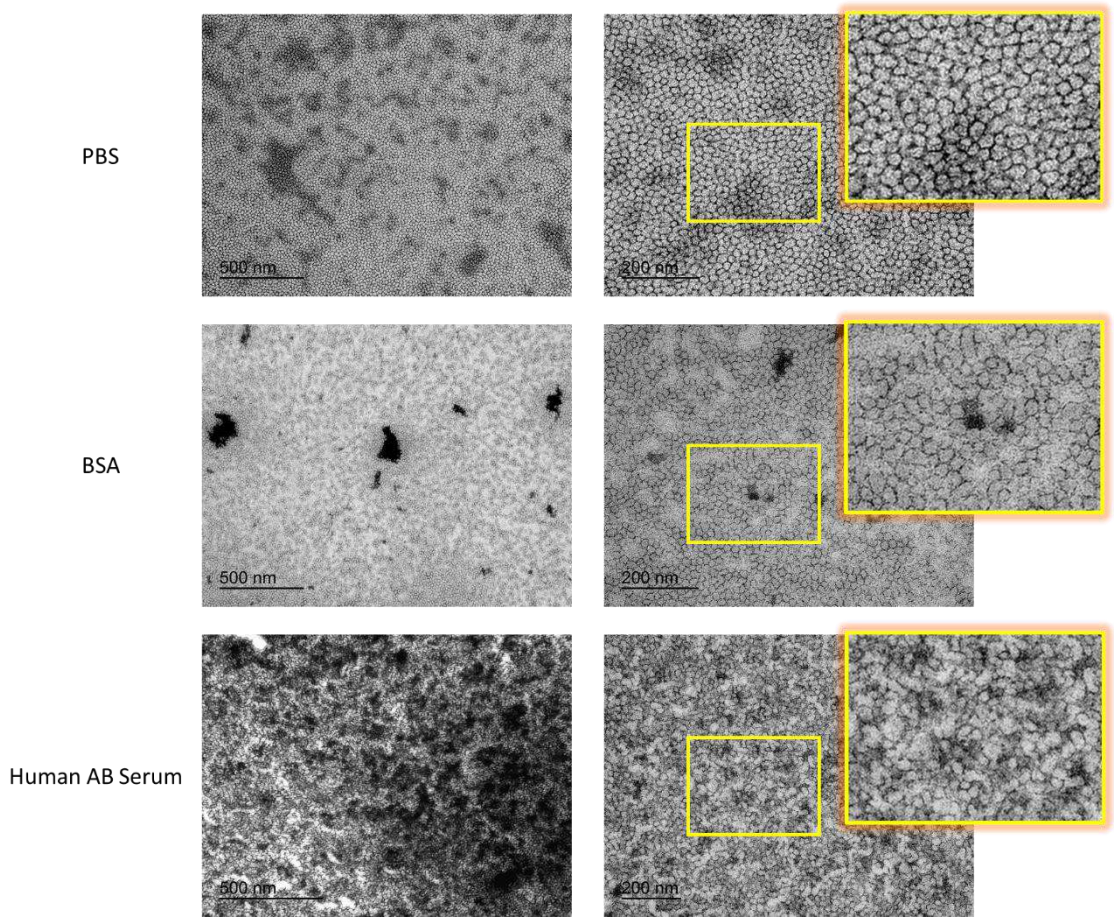

Figure S15. Stability of **NC-Ir2** in different biological mediums after incubation for 48 h at 37ºC. From top to bottom: 16 mg/mL of **NC-Ir2** in PBS, BSA-containing PBS and 32 mg/mL of **NC-Ir2** in complete Human AB Serum. Magnification on the right of the yellowish marked fields.

5. Photophysical characterization of the compounds

Table S6. Absorption (λ_{abs}) and emission (λ_{em}) maxima, emission lifetimes (τ_{em}), and quantum yields (Φ_{em}) of **Ir1** and **Ir2** in DCM and DMSO and of **NC-Ir1** and **NC-Ir2** in water.

Compound	**Solvent**	**λ_{abs}, nm**	**λ_{em}, nm**	aerated		degassed	
				τ_{em}, ns[a]	**Φ_{em}[a]**	**τ_{em}, ns[b]**	**Φ_{em}[b]**
Ir1	CH_2Cl_2	375	509	35.6 (7%) 47.9 (93%)	0.026	764 (53%) 1295 (47%)	0.784
	DMSO	380	512	171 (99.7%) 47.8 (0.3%)	0.086	1230 (100%)	0.810
Ir2	CH_2Cl_2	380	511	46.7 (98%) 139 (2%)	0.025	596 (37%) 777 (63%)	0.655
	DMSO	385	517	171 (100%)	0.094	1286 (100%)	0.799
NC-Ir1	H_2O	378	507	22.3 (8%) 75.6 (92%)	0.197	417 (6%) 1623 (94%)	0.411
NC-Ir2	H_2O	382	511	19.5 (21%) 95.1 (79%)	0.124	282 (6%) 1537 (94%)	0.198

[a] Air equilibrated solution [b] deaerated solution (20 min under argon).

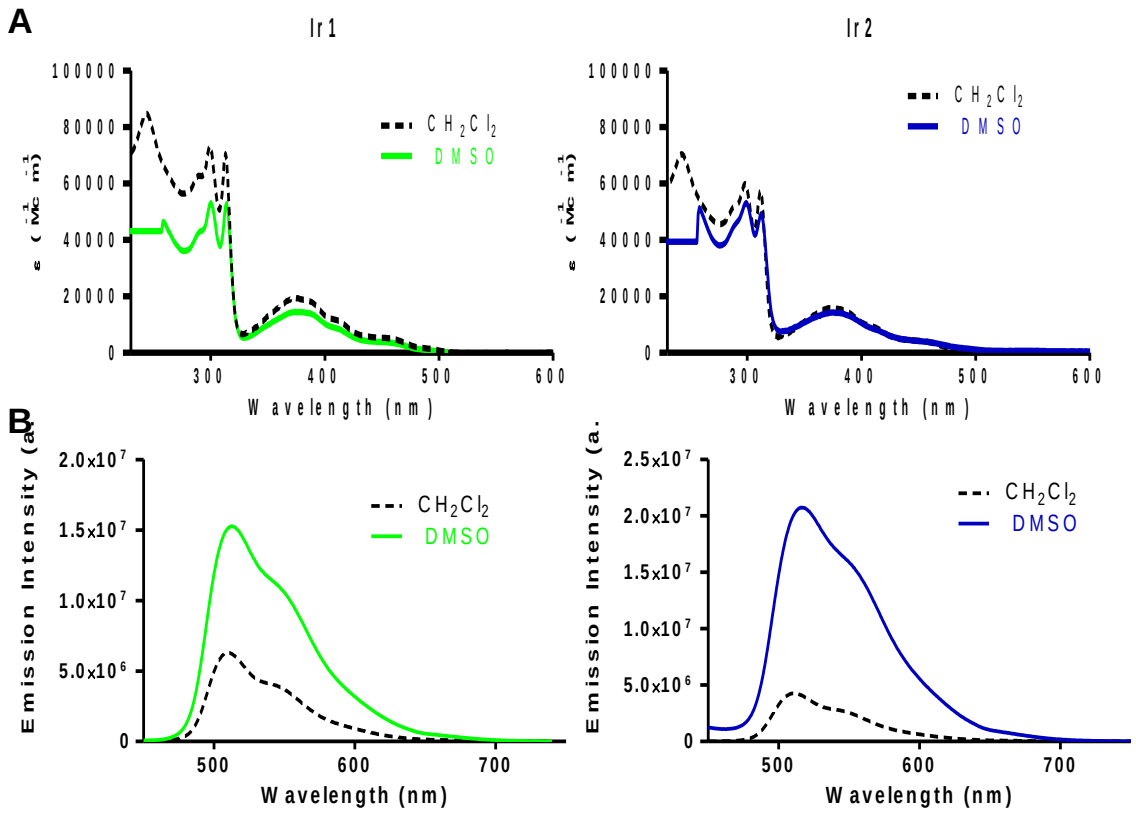

Figure S16. A) UV/Vis and B) emission spectra of Ir(III) complexes in aerated solutions of CH_2Cl_2 and DMSO.

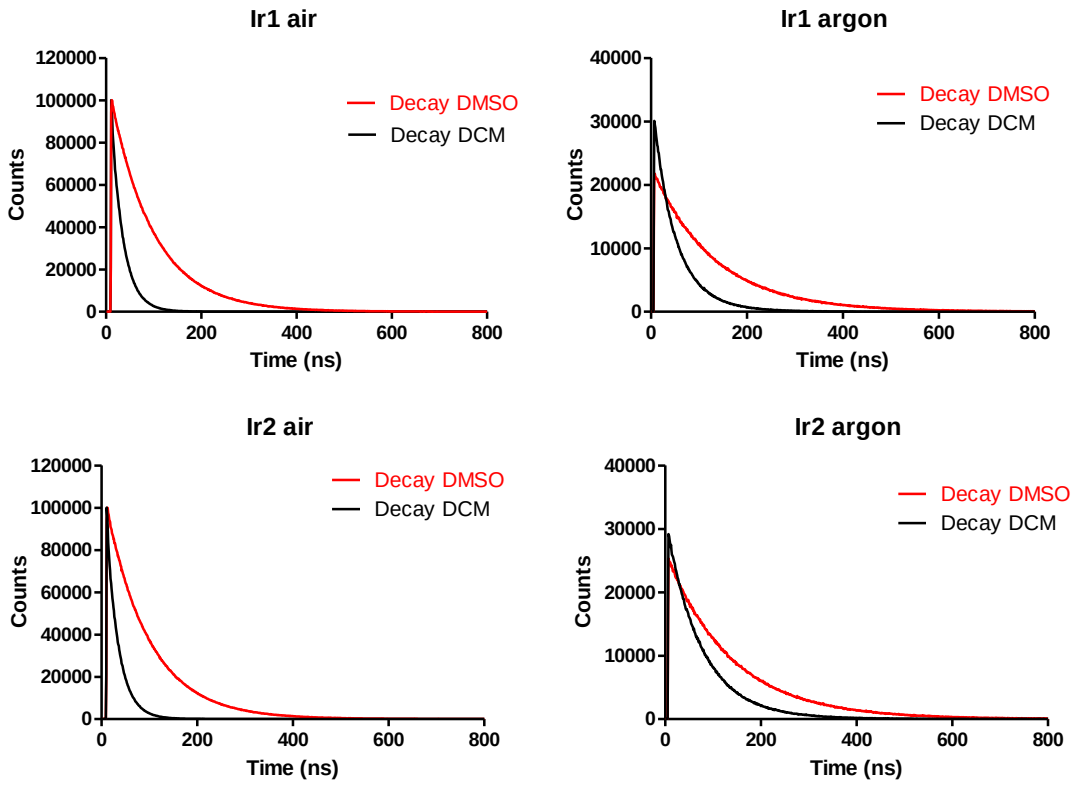

Figure S17. Fluorescence emission decay kinetics of **Ir1** and **Ir2** in CH_2Cl_2 and DMSO in aerated and degassed solutions.

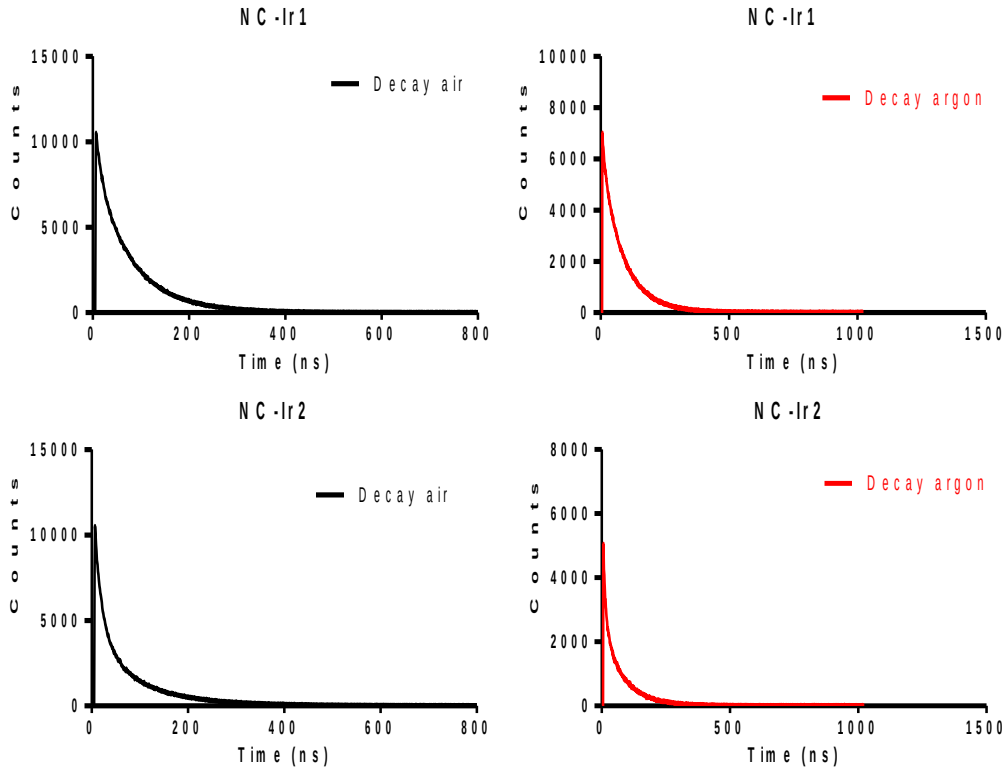

Figure S18. Fluorescence emission decay kinetics of Ir(III)-loaded nanocapsules in water.

6. Biological studies

6.1. Cellular uptake by confocal microscopy

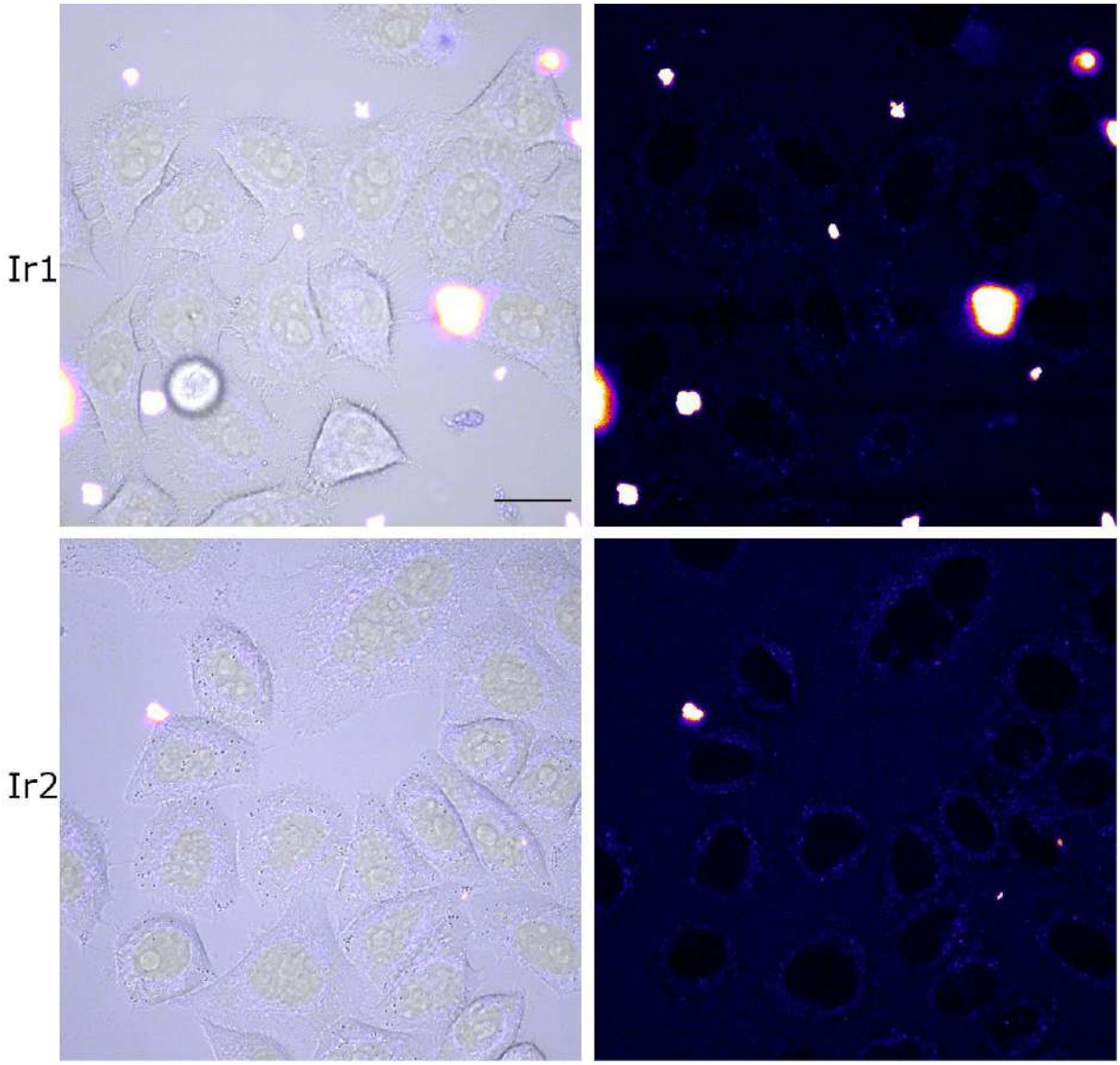

Figure S19. Cellular uptake of **Ir1** and **Ir2** complexes. Single confocal planes of HeLa cells incubated with the compounds for 30 min at 37 ^{o}C. The complexes were excited at 405 nm and emission detected from 423 to 547 nm. Left images show the merge between transmitted light and compound fluorescence images. Compound images are colour coded using the Fire lookup table from Fiji.Scale bar: 20 μm.

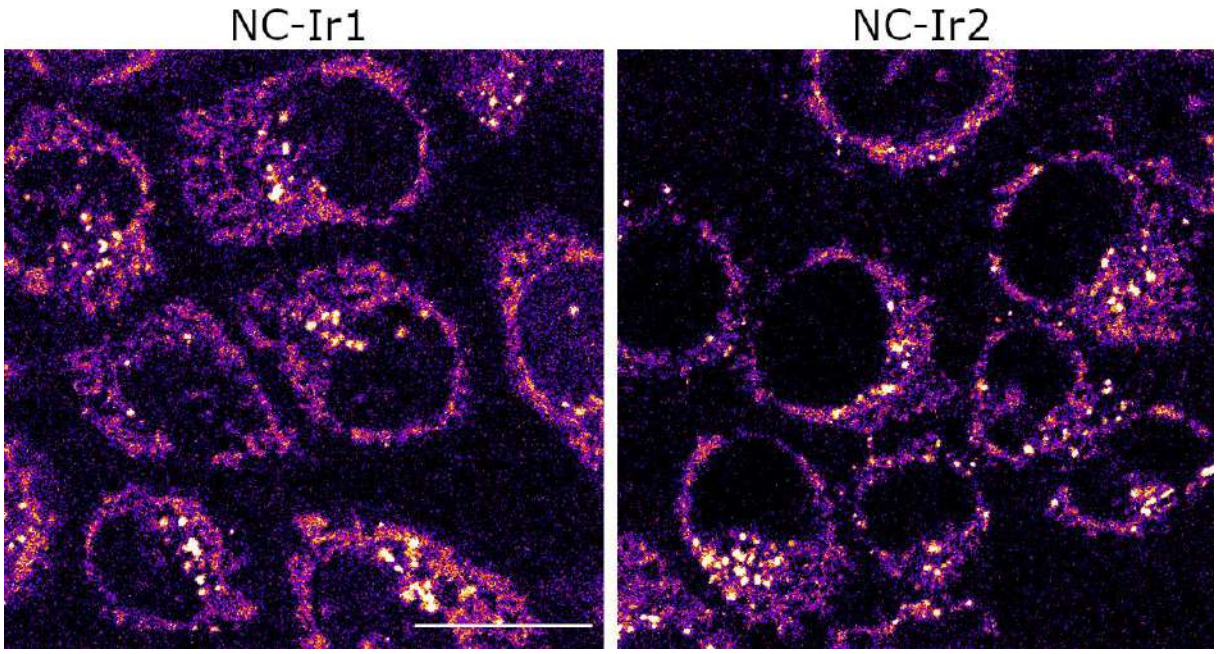

Figure S20. Cellular uptake of Ir(III)-loaded nanocapsules. Single confocal planes of HeLa cells incubated with **NC-Ir1** (left) and **NC-Ir1** (right) for 30 min at 37 ^{o}C. The compounds were excited at 488 nm and emission detected from 497 to 597 nm. All images are colour coded using the Fire lookup table from Fiji. Scale bar: 20 μm.

6.2. Antiproliferative activity.

Table S7. Cytotoxicity [IC_{50} mean values (mg/mL)] obtained for nanoparticles in cancer and normal cells.[a]

		HeLa		A2780	A2780cis	BGM
	2 h	24 h	48 h		48 h	
NC	>30	>30	>30	>30	>30	>30
NC-Ir1	8.2 ± 0.4	1.01 ± 0.07	0.62 ± 0.02	1.3 ± 0.3	3.4 ± 0.4	>30
NC-Ir2	15 ± 2	1.12 ± 0.06	0.92 ± 0.04	0.8 ± 0.2	3.1 ± 0.3	>30

[a] The results are expressed as mean values ± SD from at least two independent experiments (n=4). The terms >30 indicate that no IC_{50} was reached up to that concentration.

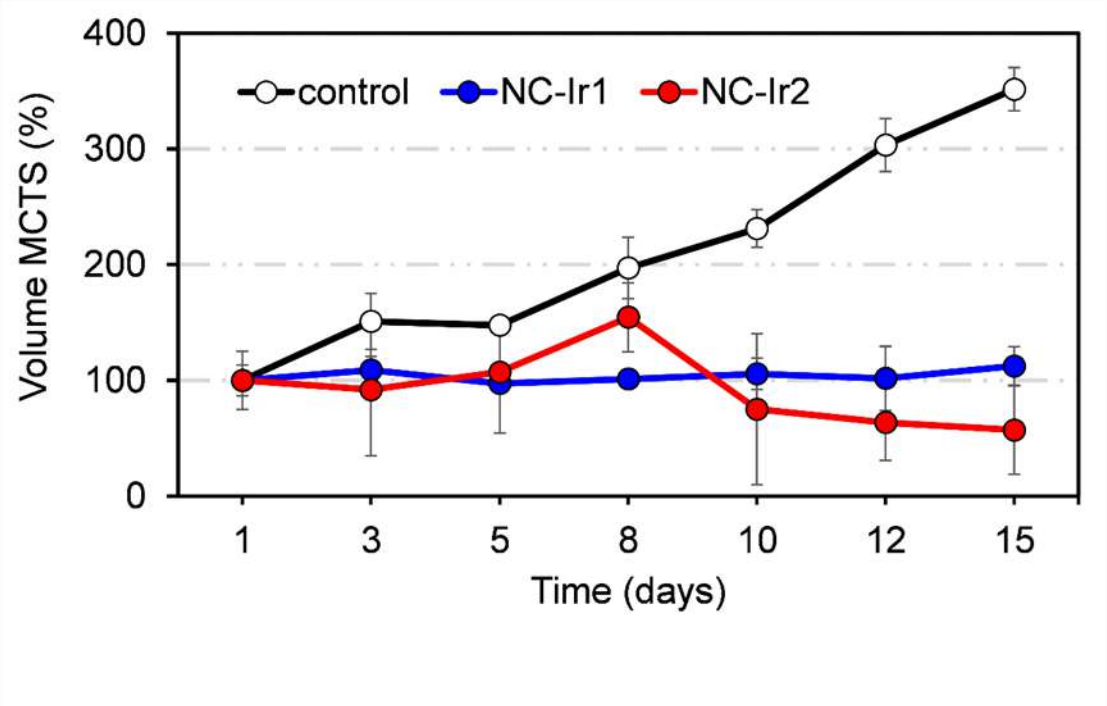

Figure S21. Changes in relative diameter in MCTS over a span of 15 days. MCTS were treated with **NC-Ir1** and **NC-Ir2** at 6 μM. Error bars correspond to standard deviation of three replicates.

6.3. Morphological analysis of cells

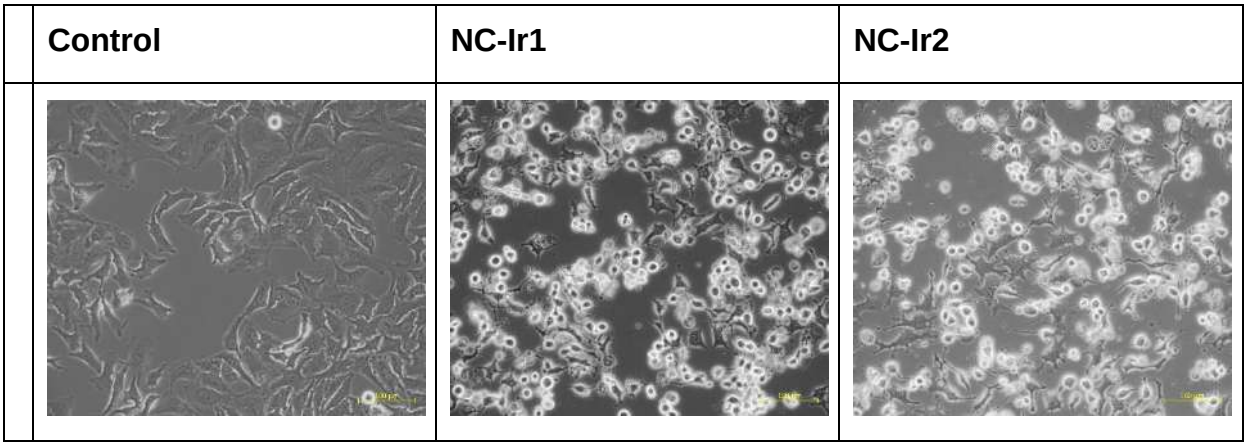

Figure S22. Microscopy images of HeLa cells swelling after treatment with **NC-Ir1** and **NC-Ir2** at equitoxic concentrations ($2\times IC_{50}$; *i.e.* 6 μM) for 24 h. Scale bar = 100 μm.

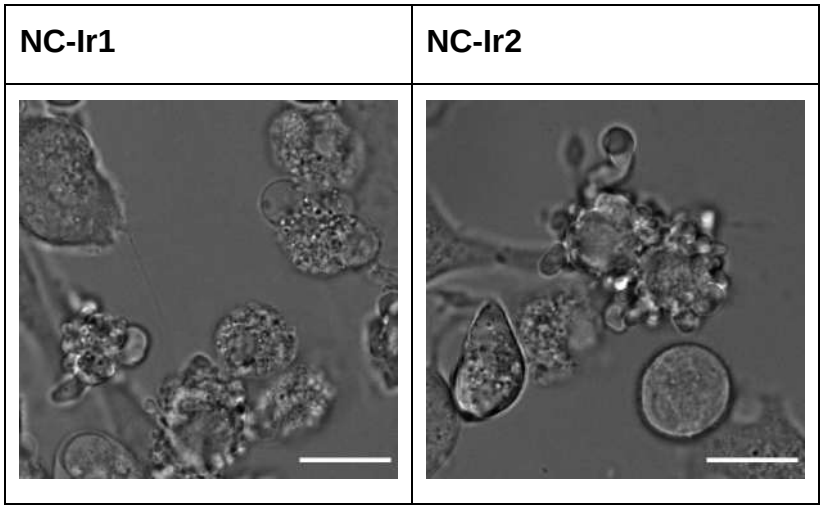

Figure S23. Microscopy images of HeLa cells blebbing after treatment with **NC-Ir1** and **NC-Ir2** at equitoxic concentrations ($2\times IC_{50}$; *i.e.* 6 μM) for 24 h. Scale bar = 15 μm.

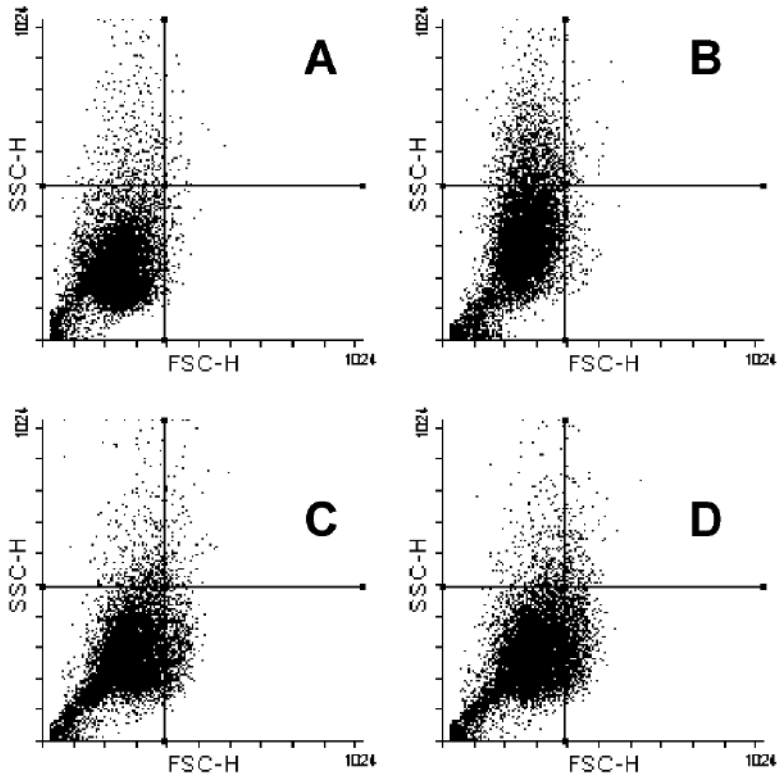

Figure S24. FSC-H (cell size) vs. SSC-H (cell complexity) flow cytometry dot plots of HeLA cells upon treatment with nanocapsules (6 μM) for 24 h. Cisplatin (20 μM) was used for comparative purposes. A) Untreated cells, B) Cisplatin, C) **NC-Ir1**, D) **NC-Ir2**.

6.4. Cell membrane integrity test

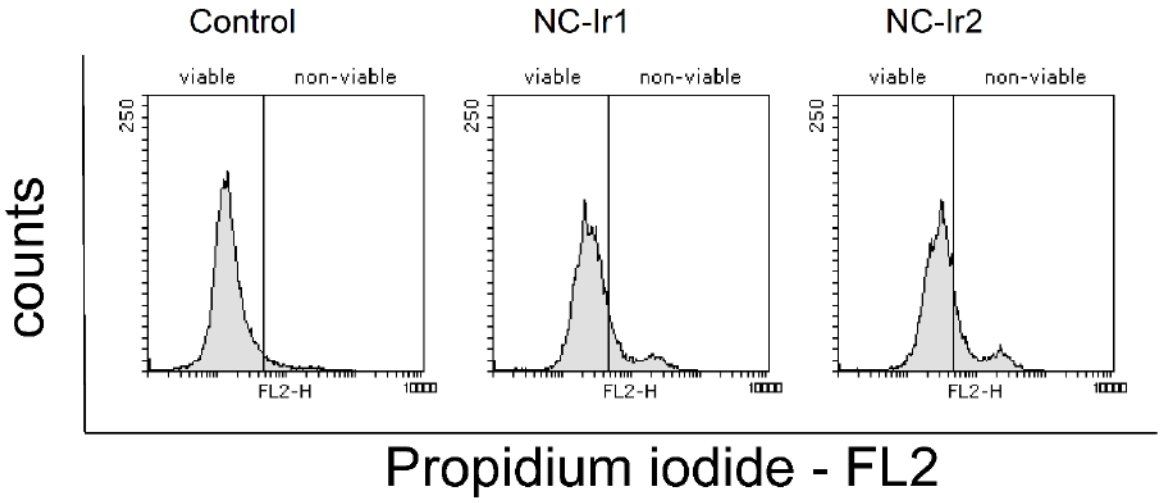

Figure S25. Membrane integrity assessment of HeLa cells after 24 h treatment determined by staining with propidium iodide in FL2 channel. Data were gated as red (viable membrane, FL2-) and green (non-viable membrane, FL2+) and processed using FowingSoftware 2.5.1. Left histogram: control, middle histogram: **NC-Ir1** (1.5 μM), right histogram: **NC-Ir2** (1.5 μM).

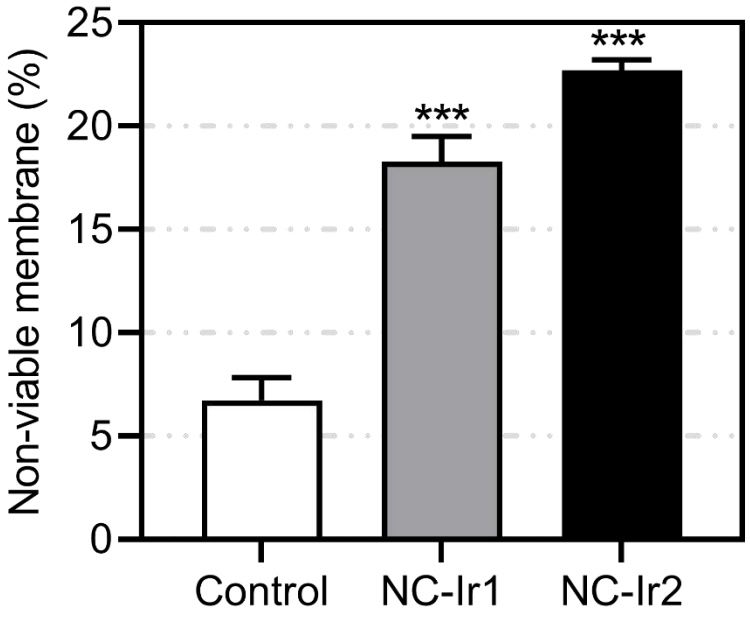

Figure S26. Membrane integrity of HeLa cells determined by staining with propidium iodide by flow cytometry after 24 h treatment with **NC-Ir1** and **NC-Ir2** (1.5 μM). Statistical analysis was carried out using unpaired t-test assuming unequal variances (***$p<0.001$).

6.5. Mitochondrial potential assessment

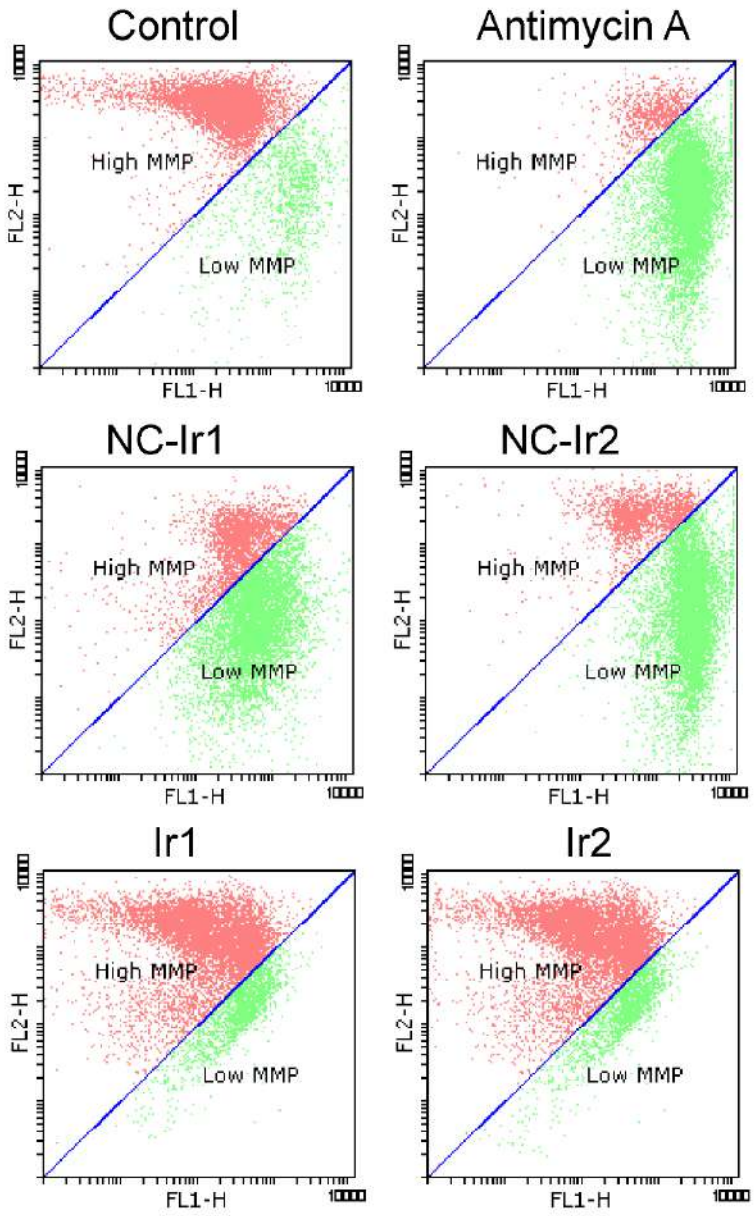

Figure S27. Representative flow cytometry dot plots of JC-1 stained HeLa cells after 24 h treatment with **Ir1**, **Ir2**, **NC-Ir1** or **NC-Ir2** (6 μM). Antimycin A (50 μM) was used as a positive control. Low mitochondrial membrane potential (MMP) measured in FL1-H channel as JC-1 monomers (green fluorescence) and high MMP values detected in the FL2-H channel as JC-1 aggregates (red fluorescence). λ_{exc}= 488 nm, λ_{em} = 530 ± 30 nm (green) and 585 ± 30 nm (red).

6.6 Aerobic respiration and glycolytic rate evaluation

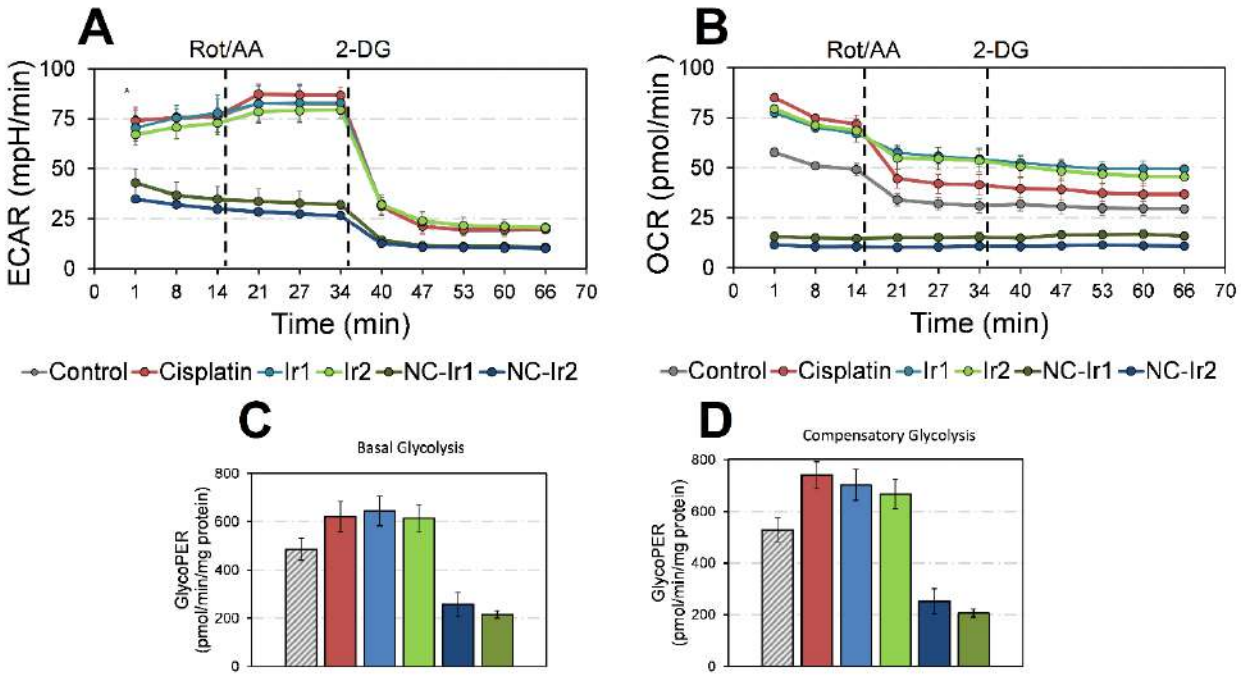

Figure S28. A) Glycolysis of HeLa cells as measured by extracellular acidification rate (ECAR), B) mitochondrial oxidative phosphorylation on the basis of the oxygen consumption rate (OCR) and C) basal glycolysis and D) compensatory glycolysis profiles as represented by the rate of protons extruded into the extracellular medium during glycolysis (glycoPER) after treatment with free complexes (10 μM), NCs (6 μM) or cisplatin (20 μM) for 24 h. Data obtained with Seahorse XFe analyzer and represented as mean ± SEM (n= 4 replicates).

6.7. Oxidative stress induction

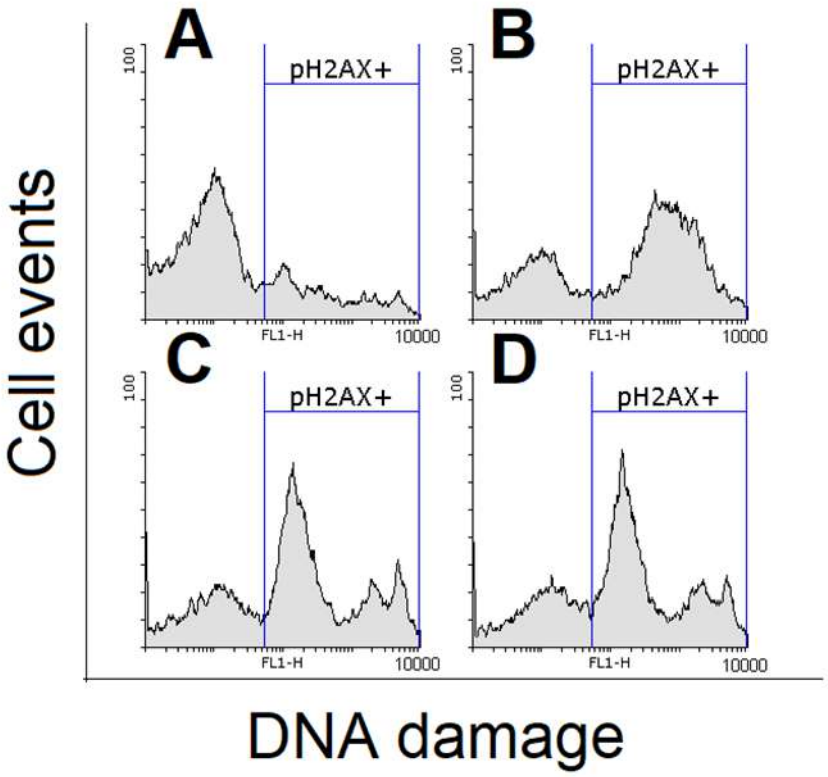

Figure S29. Representative flow cytometry histograms of γH2AX phosphorylation in HeLa cells detected in FL1-H channel after 24 h treatment **NC-Ir1** or **NC-Ir2** (6 μM).

6.8. Antioxidant influence on cell viability.

$5 \cdot 10^3$ HeLa cells/well cells were seeded in 96-well plates. After 24 h, cells were pre-treated for 1 h with superoxide dismutase mimetic MnTBAP (50 µM) and then treated with nanoparticles at indicated concentrations for further 24 h. Non-pretreated cells were directly treated with nanoparticles for 24 h. After this period, MTT analysis was performed to measure cell viability as already described at section 2.3.4 in the manuscript. Two independent experiments were performed with n=4 replicates per concentration level.

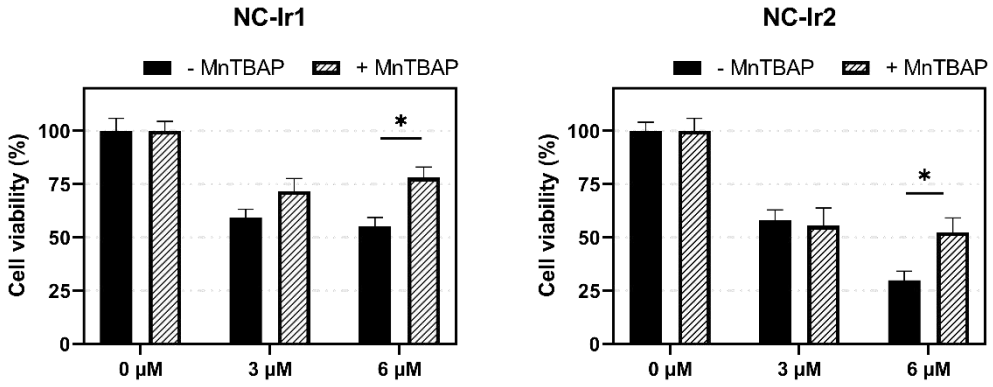

Figure S30. Impact of antioxidant MnTBAP addition in the cytotoxicity of **NC-Ir1** and **NC-Ir2** in HeLa cells. Data represented as cell viability (mean ± SD) after treatment with nanocapsules at indicated concentrations for 24 h directly or following a pretreatment with 50 µM MnTBAP for 1 h. Statistical significance *$p<0.05$ from two-way ANOVA test."

Chapter III. Development of water-in-oil-in-water polyurethane-polyurea hybrid nanocapsules for the delivery of hydrosoluble bioactive compounds: Nanoencapsulation of Indocyanine Green for in vivo tumor imaging

11. Publication III. Novel tumor-targeted self-nanostructured and compartmentalized water-in-oil-in-water polyurethane-polyurea nanocapsules for cancer theragnosis (manuscript submitted for publication)

Novel tumor-targeted self-nanostructured and compartmentalized water-in-oil-in-water polyurethane-polyurea nanocapsules for cancer theragnosis

Joaquín Bonelli,[a,b] María Velasco-de Andrés,[c] Neus Isidro,[b] Cristina Bayó,[d] Sergi Chumillas,[a] Laura Carrillo-Serradell,[c] Sergi Casadó-Llombart,[c] Cheryl Mok,[d] Daniel Benítez-Ribas,[d,e] Francisco Lozano,[c,e,f] Josep Rocas,[b] Vicente Marchán*[a]

[a] Departament de Química Inorgànica i Orgànica, Secció de Química Orgànica, Institut de Biomedicina de la Universitat de Barcelona (IBUB), Universitat de Barcelona (UB), Martí i Franquès 1-11, E-08028 Barcelona, Spain. E-mail: vmarchan@ub.edu

[b] Nanobiotechnological Polymers Division Ecopol Tech, S.L., El Foix Business Park, Indústria 7, E-43720 L'Arboç del Penedès, Tarragona, Spain

[c] Immunoreceptors del Sistema Innat i Adaptatiu, Institut d'Investigacions Biomèdiques August Pi i Sunyer (IDIBAPS), Universitat de Barcelona (UB), Villarroel 170, E-08036 Barcelona, Spain

[d] Department of Immunology, Hospital Clinic, August Pi i Sunyer Biomedical Research Institute (IDIBAPS), Universitat de Barcelona (UB), Villarroel 170, E-08036 Barcelona, Spain

[e] Servei d'Immunologia, Centre de Diagnòstic Biomèdic, Hospital Clínic de Barcelona Villarroel 170, E-08036 Barcelona, Spain

[f] Departament de Biomedicina, Universitat de Barcelona (UB), Villarroel 170, E-08036 Barcelona, Spain

ABSTRACT

Encapsulation of water-soluble bioactive compounds for enabling specific accumulation in tumor locations, while avoiding premature clearance and/or degradation in bloodstream, is one of the main hallmarks in nanomedicine, especially that of NIR fluorescent probes for cancer theragnosis. The herein reported technology furnishes water-dispersible double-walled polyurethane-polyurea hybrid nanocapsules (NCs) loaded with indocyanine green (ICG-NCs), using a versatile and highly efficient one-pot and industrially scalable synthetic process based on the use of two different prepolymers to set up the NCs walls. Flow cytometry and confocal microscopy confirmed that both ICG-loaded NCs internalized in monocyte-derived dendritic cells (moDCs). The *in vivo* analysis of xenograft A375 mouse melanoma model revealed that amphoteric functionalization of NCs' surface promotes the selective accumulation of ICG-NCs in tumor tissues, making them promising agents for a less-invasive theragnosis of cancer.

GRAPHICAL ABSTRACT

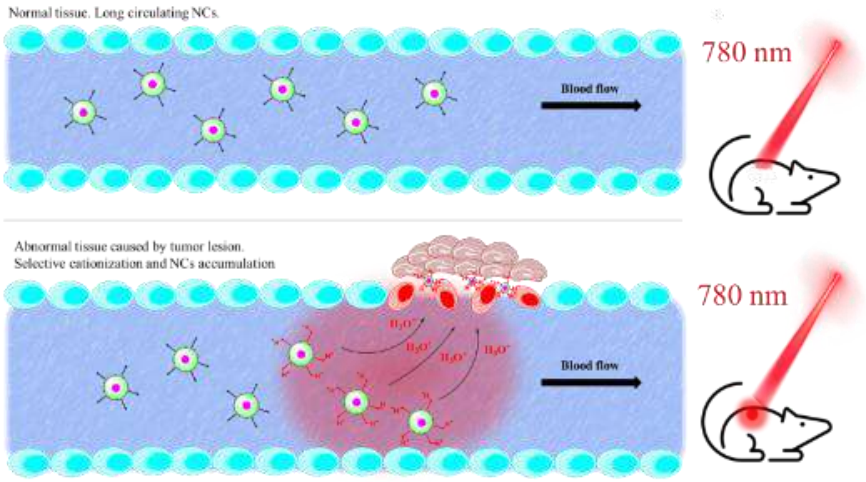

KEYWORDS

Nanoencapsulation, polyurethane-polyurea nanoparticles, tumor-targeting, drug delivery, bioimaging

1. INTRODUCTION

Polymeric nanocapsules have emerged in recent years in nanomedicine as promising delivery systems of bioactive molecules.[1] Besides preventing degradation of the cargo molecules in bloodstream, the multiple functionalization possibilities they offer through on-demand synthesis position this class of polymeric constructions as powerful chemical tools in different medical fields,[2] being diagnosis and cancer treatment two of the most studied.[3]

Among polymeric nanocarriers, polyurethane-based nanocapsules (NCs) have demonstrated in recent years great biological performance and exceptional biocompatibility. By using the isocyanate-chemistry, unique structures exhibiting privileged properties can be designed and easily synthesized for applications in nanomedicine, as well as in other medical areas.[4,5] A broad spectrum of polyurethane-based nanomedical preparations have been described so far to address several biological challenges, like increased dispersibility in aqueous media,[6-8] selective cell or tissue drug vehiculization,[9] promoted intracellular accumulation,[10] and specific release under different external or internal stimuli.[11,12]

Given the limitations that the enhanced permeability and retention (EPR) effect exhibits, mostly related to the variability of vessels extravasation in different types of solid tumors,[13] a promising approach for targeting cancer consists of promoting the selective accumulation of drug nanocarriers into solid tumor acidic locations, which are generated by an aerobic glycolysis mechanism, known as Warburg's effect. This process relays on the ability of cancer cells to generate energy, both under normoxic and hypoxic conditions, via a glycolytic pathway rather than through oxidative phosphorylation (OXPHOS), which is the common way that cells use to obtain energy from O_2 in mitochondria. The lactate generated during aerobic glycolysis inside cancer cells is afterwards released to the external media, generating a pH depletion near to the solid tumor clustering.[14] This well-described phenomenon leads to pH values below 7, thereby opening the door to the design of nanocarriers that accumulate preferentially in acidic regions within the solid tumor microenvironment (TME). In a previous work, we have described a synthetic methodology for the one-pot production of completely crosslinked and long-circulating polyurethane-polyurea hybrid NCs, incorporating different liposoluble cargo molecules, which promote the selective accumulation in tumor locations by selective cationization of the nanocapsules' surface when they

reach the acidic TME. In addition, release of the cargo can be triggered under reductive conditions (e.g., in cancer cells where the reduced form of glutathione peptide is highly overexpressed).[15] Besides preventing the premature degradation and reticuloendothelial system (RES) evading[16] of the cargo, polyurethane-polyurea hybrid NCs have been described to increase the biological activity of a range of bioactive compounds (e.g., anticancer Ir(III)-based metallodrugs, immunosuppressors and coumarin-based photosensitizers for photodynamic therapy) by mediating intracellular vehiculization.[17-19] However, the nanomedical applications of polyurethane-based NCs are currently restricted to the encapsulation of liposoluble compounds, since stabilization in aqueous media takes advantage of the stratification of the polymeric wall in a hydrophobic-hydrophilic gradient (from the core to outwards of the nanocapsule, respectively).

The encapsulation and stabilization of hydrosoluble compounds in aqueous media embrace a lot of interest within the nanomedical community since it opens the door to the selective delivery both of small molecules and of therapeutically relevant biomolecules, such as proteins and oligonucleotides, among others. However, only a handful of nanostructures can actually fill this gap.[20] Liposomes have been positioned in recent years as a benchmark solution, owing to their high biocompatibility and synthesis feasibility. Unfortunately, liposomes exhibit several drawbacks to be considered as ideal nanocarriers, as they are poor crosslinked entities, which might lead to premature release of the cargo. The lack of reactive points also difficult liposome functionalization which hampers using them in targeted therapy approaches.[21]

Fluorophore-loaded nanocapsules, that can be externally monitorable (Bioimaging) or activatable (Phototherapy) with non-toxic and highly penetrating near infrared (NIR) light, have also gained broad interest recently for the development of novel non-invasive anticancer theragnostic devices.[22,23] However, only a limited number of examples of nanomedicines exploiting vehiculization of fluorescent probes in current medical use have been described so far.[24] Hence, readdressing the biological target of FDA-approved organic fluorophores, such as Indocyanine Green (ICG, IC-Green™), Fluorescein (FLUORESCITE™), Methylene Blue (PROVAYBLUE™) or 5-aminolevulinic acid (Gliolan™; the only that has been approved in oncology for intraoperative visualization in the resection of glioma)[25] would expand considerably their medical applications for cancer theragnosis.[26,27] In this context, this study describes a groundbreaking one-pot and

industrially scalable methodology to produce biocompatible, bioligand-free, and completely crosslinked Water-in-Oil-in-Water (WOW) double-walled polyurethane-polyurea hybrid nanocarriers for tumor-targeting. As far as we know, this is the first system that allows the use of self-stratified polyurethane-based NCs for the encapsulation of hydrosoluble bioactive molecules.

As a proof of concept for encapsulation system validation, as well as for cancer targeting, the encapsulation of ICG has been addressed with the aim of producing new fluorescent probes for selective bioimaging.[28] The choice of ICG as a cargo molecule is especially interesting since it was one of the firsts NIR fluorescent probes approved by FDA for human clinical applications including cancer diagnosis. In addition, ICG-loaded nanocapsules can be easily monitorable by using a non-toxic/deep-penetrating multi-photon laser with chances for a streaming *in vivo* non-invasive tracking in animal models once injected. IVIS® technology acknowledge the use of ICG, with a maximum of absorption centered around 790 nm, for non-invasive longitudinal *in vivo* live imaging.[29] This is not the case of the other above-mentioned FDA-approved fluorescent probes that cannot be excited above 750 nm. Besides providing cancer targeting capacity, ICG encapsulation in stable and robust nanocapsules intends to avoid the well-described premature degradation of the fluorophore in plasmatic conditions,[30] extending its fluorescence ability in time.

2. EXPERIMENTAL SECTION

2.1. Synthetic procedures.

2.1.1. Synthesis of redox-responsive amphiphilic low HLB prepolymer (P1).

2,2´-Dihydroxyethyl disulfide (DEDS) (2.86 g, 37.08 meq) and YMER N-120 (3.64 g, 7.01 meq) were added into a three-necked round-bottom flask equipped with mechanical stirring at room temperature (rt) and purged with N_2. When the mixture was homogeneous, isophorone diisocyanate IPDI (8.83 g, 79.40 meq) was added into the reaction vessel under gentle mechanical stirring, checking the initial NCO stretching band intensity by FTIR. The polyaddition reaction was kept under these conditions until the NCO stretching band reach stabilization. At this point, dry acetone (18.2 mL) was added into the reaction mixture to fluidify the polymer. In parallel, 1,3-diamino-*N*-octadecylpropane (Genamin TAP 100D) (9.25 g, 56.72 meq) was dissolved in dry acetone (8.1 mL) into another 100 mL three-necked round-bottom flask, which had previously been purged with N_2. The former reaction mixture was added dropwise onto the latter under half-moon 100 rpm mechanical stirring. The reaction was monitored by IR until the NCO stretching band intensity had completely disappeared.

2.1.2. Synthesis of redox responsive amphiphilic cationic prepolymer (P2).

2,2´-Dihydroxyethyl disulfide (DEDS) (901.0 mg, 11.68 meq), YMER N-120 (12.04 g, 23.18 meq) and *N*-(3-dimethylaminopropyl)-*N*,*N*´-diisopropanolamine (Jeffcat DPA) (981.3 mg, 8.99 meq) were added into a three-necked round-bottom flask equipped with mechanical stirring at room temperature (rt) and purged with N_2. When the mixture was homogeneous, IPDI (8.14 g, 73.24 meq) was added into the reaction vessel under gentle mechanical stirring. The polyaddition reaction was kept under these conditions until the NCO stretching band intensity did not change, monitored by IR spectroscopy. At this point, dry THF (21 mL) was added into the reaction mixture to fluidify the polymer. In parallel, 1,3-diamino-*N*-octadecylpropane (Genamin TAP 100D) (5.99 g, 35.45 meq) was dissolved with dry THF (5.23 mL) into another 100 mL three-necked round-bottom flask, which had previously been purged with N_2. The former reaction mixture was added dropwise onto the latter under half-moon 100 rpm mechanical stirring. The reaction was monitored by IR until the NCO stretching band intensity had completely disappeared.

2.1.3. Synthesis of dye-loaded cationic redox responsive water-in-oil-in-water NCs (cationic dye-NCs).

The organic dye (ICG or COUPY) (5 mg), Milli-Q water (100 mg), diethylenetriamine (DETA) (4.5 mg, 0.13 meq) and prepolymer P1 (635.2 mg, 0.09 meq) were mixed in a 3 mL vial provided with magnetic stirring and protected from the light. Then, 1.28 mL of cyclohexane were dropwise added to generate the water-in-oil emulsion. Afterwards, IPDI (40 mg, 0.36 meq) was used to crosslink the polymeric entity to furnish the first water-in-oil encapsulation (ENCAP 1), leaving most of NCO groups in the surface of NCs to be reacted in further steps.

To start the second encapsulation, the ENCAP 1 was added over a P2 solution (5.87 g, 0.61 meq) and it was properly mixed under magnetic stirring to consume the previous unreacted NCO groups. IPDI (225.0 mg, 2.02 meq) was then added into a three-neck round bottom flask, and provided with mechanical stirring, purged with N_2, as well as protected from light. The mixture containing ENCAP 1 and P2 was then dropwise added over the IPDI at 100 rpm, checking the reappearance of NCO stretching band by FTIR. The resulting viscous organic phase was then emulsified at 450 rpm with cold Milli-Q water (12.0 g) and, after double-checking the presence of NCO stretching band by FTIR, a 10% (w/w) aqueous solution of DETA (36.12 mg, 1.05 meq) was finally added to generate completely crosslinked double-walled NCs from the nano micelles, consuming the NCO moieties. The stirring was then reduced to 100 rpm. Once the NCs were formed, THF, cyclohexane and acetone were removed from the reactor at 35 °C under vacuum and the dialysis purification was carried out using a molecular porous membrane tubing with a 12–14 kDa MWCO for 48 h against Milli-Q water.

2.1.4. Synthesis of dye-loaded amphoteric redox responsive water-in-oil-in-water NCs (amphoteric dye-NCs).

The organic dye (ICG or COUPY) (5 mg), Milli-Q water (100 mg), DETA (4.5 mg, 0.13 meq) and prepolymer P1 (635.2 mg, 0.09 meq) were mixed in a 3 mL vial provided with magnetic stirring and protected from the light. Then, 1.28 mL of cyclohexane were dropwise added to generate the water-in-oil emulsion. Afterwards, IPDI (40 mg, 0.36 meq) was used to crosslink the polymeric entity to furnish the first water-in-oil encapsulation (ENCAP 1), leaving most of NCO groups in the surface of NCs to be reacted in further steps.

To start the second encapsulation, the ENCAP 1 was added over a P2 solution (5.87 g, 0.61 meq) and it was properly mixed under magnetic stirring to consume the previous unreacted NCO groups. IPDI (225.0 mg, 2.02 meq) was then added, in a three-neck round bottom flask, and provided with mechanical stirring, purged with N_2, as well as protected from light. The mixture containing ENCAP 1 and P2 was then dropwise added over the IPDI at 100 rpm, checking the reappearance of NCO stretching band by FTIR. At this point, an alkaline aqueous solution of L-lysine was prepared by dissolving 0.93 g of L-lysine in 11.37 g of Milli-Q water and adjusting pH to 11.0 with NaOH solutions of 3 M and 1 M (total l-lysine concentration 7.66% by wt). Then, 0.85 g of this solution (65.20 mg of L-lysine, 0.78 meq) were added at 350 rpm and the polyaddition reaction was checked immediately by FTIR. This viscous organic phase was then emulsified at 450 rpm with cold Milli-Q water (12.00 g) and, after double-checking the presence of NCO stretching band by FTIR, a 10% w/w aqueous solution of DETA (9.43 mg, 0.27 meq) was finally added to generate completely crosslinked double-walled NCs from the nano micelles, consuming the NCO moieties. The stirring was then reduced to 100 rpm. Once the NCs were formed, THF, cyclohexane and acetone were removed from the reactor at 35 °C under vacuum and the dialysis purification was carried out using a molecular porous membrane tubing with a 12–14 kDa MWCO for 48 h against Milli-Q water.

2.2. Biological studies

2.2.1. Monocyte-derived Dendritic Cells (moDCs) generation

Buffy coats from healthy patients were obtained from the *Banc de Sang i Teixits* (Barcelona, Spain). Peripheral blood mononuclear cells (PBMCs) were isolated by gradient centrifugation on ficoll lymphoprep^{TM} (STEMCELL technologies, Grenoble, France). PBMCs were suspended in 15 mL of X-VIVO medium (BioWhittaker, Lonza, Belgium) in t75 cm^2 culture flasks and incubated for 2 h at 37 ºC in a 5 % CO_2 atmosphere to promote monocyte adherence. Non-adherent cells were discarded and 12 mL of X-VIVO medium plus 2 % human AB serum (HS), IL-4 (300 U/mL) and GM-CSF (450 U/mL) (Miltenyi Biotec, Madrid, Spain) were added to the flasks for further 72 h-incubation at 37 ºC and in 5% CO_2. Media was renewed on day 3 (12 mL X-VIVO plus HS, IL-4 and GM-CSF) and cells were recovered 72 h later (day 6), when fully derived into immature moDCs (i-moDCs).

2.2.2. Fluorescence imaging by confocal microscopy

i-moDCs were generated as previously described and separated into 4 different conditions in 8 well µslide chambers (ibidi, Gräfelfing, Germany), at a concentration of 50.000 moDCs/800 µL X-VIVO-15 medium plus 2% HS, where nanocapsules were added at 2 µM of each cationic or amphoteric ICG-NCs. Cells were incubated with nanocapsules for 2 h at 37 ºC and 5% CO_2 to promote internalization and cell adherence. Multiphoton irradiation at 790 nm and detection centered at 810 nm conditions were set up for the internalization analysis.

For colocalization experiments, all conditions were stained with Lysotracker green and Hoechst as a nuclei counterstain, following the supplier's instructions. After staining, wells were washed twice by carefully removing media without touching the well's bottom and adding room temperature phosphate buffered saline (PBS) through the side. Finally, 800 µL of PBS was added to all wells and cells were observed under a Leica TCS SP5 laser scanning confocal microscope (Leica Microsystems Heidelberg GmbH, Manheim, Germany) equipped with a DMI6000 inverted microscope, diode 405 nm, Argon Laser, HeNe 633 nm laser and 63x oil immersion objective lens (NA 1.4) and an incubation system with temperature, humidity and CO_2 control was used. i-moDCs growing on 8 well micro slide ibidi chambers were labelled with Indocyanine Green and Lysotracker Green (Thermofisher).

Lysotracker Green and ICG images were acquired sequentially using 488 and 633 laser lines, AOBS (Acoustic Optical Beam Splitter) as beam splitter and emission detection ranges 500-550 nm, 660-795 nm respectively and the confocal pinhole set at 1 Airy unit. Simultaneously, bright field transmitted light images were acquired. Images were acquired at 400 Hz in a 1024 x 1024 pixels format, and pixel size of 118 x 118 nm. Colocalization analysis was performed using JACOP plugin (Bolte and Cordelieres, 2006), a colocalization analysis tool from ImageJ (rsb.info.nih.gov/ij). Manders and Pearson coefficients were calculated for every set of images.

2.2.3. Internalization evaluation by Flow Cytometry

i-moDCs were cultured in 6 well plates in 3 mL X-VIVO 15 2% HS ($0.5x10^6$ moDCs/mL) and incubated with different concentrations of either cationic COUPY-NCs, or amphoteric COUPY-NCs together with a blank (non-loaded Nanocapsules) in parallel at 37 ºC and 4 ºC for 6 and 24 h to observe whether internalization was conducted through active phagocytosis. Concentrations for cationic COUPY-NCs (experimental polymer value of 174.35 ±0.26 mg/mL) were: A) 0.619

µL/mL, B) 1.55 µL/mL, C) 3.1 µL/mL, D) 6.19 µL/mL and E) a blank of 3.29 µL/mL non-loaded NCs. Concentrations for amphoteric COUPY-NCs (experimental polymer value of 87 ± 5 mg/mL) were: A) 1.24 µL/mL, B) 3.105 µL/mL, C) 6.21 µL/mL, D) 12.42 µL/mL and E) a blank of 1.61 µL/mL non-loaded NCs. After incubations, cells were detached and analyzed by flow cytometry (Attune NXT) to determine fluorescence on the green laser excitation (COUPY emission at 561 nm), with no other fluorochromes added.

2.2.4. In vivo safety assay of amphoteric and cationic control NCs

All research procedures carried out in the user center were evaluated by the Ethics Committee for Animal Experimentation of the University of Barcelona and Generalitat de Catalunya (code 176/18). Healthy mice were administered with three different concentrations (single intravenous injection) of cationic and amphoteric control NCs to confirm the lack of toxicity associated to the carrier. Hematological parameters in blood and biological parameters in plasma were evaluated after 7-days of single injection, in healthy B57BL/6 mice, and compared with those obtained from the control group.

2.2.5. In vivo fluorescence imaging biodistribution in subcutaneous tumor mice models.

Female NSG mice (9 weeks old, Charles River) were challenged by s.c. injection of A375 (1×106) cells on the right flank with a 23-gauge needle. Amphoteric ICG-NCs and cationic ICG-NCs were administered i.v. at day 14 post-tumor challenge. PBS and ICG free were injected to control groups. Fluorescence was monitoring by *in vivo* imaging system (IVIS; Perkin Elmer, Waltham, MA, USA,) using excitation/emission wavelengths of 780 nm/845 nm.

3. RESULTS AND DISCUSSION

3.1. Design and synthesis of WOW double walled polyurethane-polyurea hybrid NCs.

Inspired on the idea to reproduce liposomal arrangement, two different reactive prepolymers (P1 and P2) were first synthesized, with contrary properties in terms of Hydrophilic-Lipophilic Balance (HLB). Polyaddition reactions between a poly-isocyanate and polyalcohols or polyamines furnished the amino-capped hybrid polyurethane-polyurea hybrid structures. While both prepolymers include redox-responsive moieties to promote the polymer degradation under reductive conditions, P2 was also extra-functionalized with pH-responsive side-amines (Figures 1A and 1B). The creation of a first crosslinked water-in-oil nanocapsule was brought about using the self-emulsifying power of the low-HLB prepolymer P1, where a hydrosoluble molecule can be confined. This polymeric construction, which contains an increased ratio of lipophilic groups (C18-saturated side tails in red in Figure 1A) versus hydrophilic ones (PEGylated chains in blue in Figure 1A) generates a hydrophobicity gradient where the core-oriented PEGylated moieties settle the central aqueous phase surrounded by the first polymeric backbone, which exposes the lipophilic tails, stabilizing this water-core in an organic media (Figure 2A). The water-in-oil emulsion process is carried out as depicted in the first seven steps shown in Figure 2A. Immediately after polymer synthesis, an aqueous solution containing the hydrosoluble bioactive cargo molecules (Figure 2A; step 4) and a solution of 10% of DETA (Figure 2A; step 5) were added to the reaction flask and mixed with prepolymer P1. Dropwise addition of cyclohexane generates the W/O emulsion (Figure 2A; step 6), where the polymeric backbone of P1 is properly ordered at the interphase of the micelles. Then, the terminal secondary amino reactive functions contained in the polymer backbone, as well as the amino groups from the added DETA, were crosslinked by using a diisocyanate derivative (IPDI, Figure 2A; step 7) leading to the assembly, via the formation of stable urea bonds, of the internal water-in-oil nanocapsule construction (nanocapsule magnification in Figure 2A; step 7).

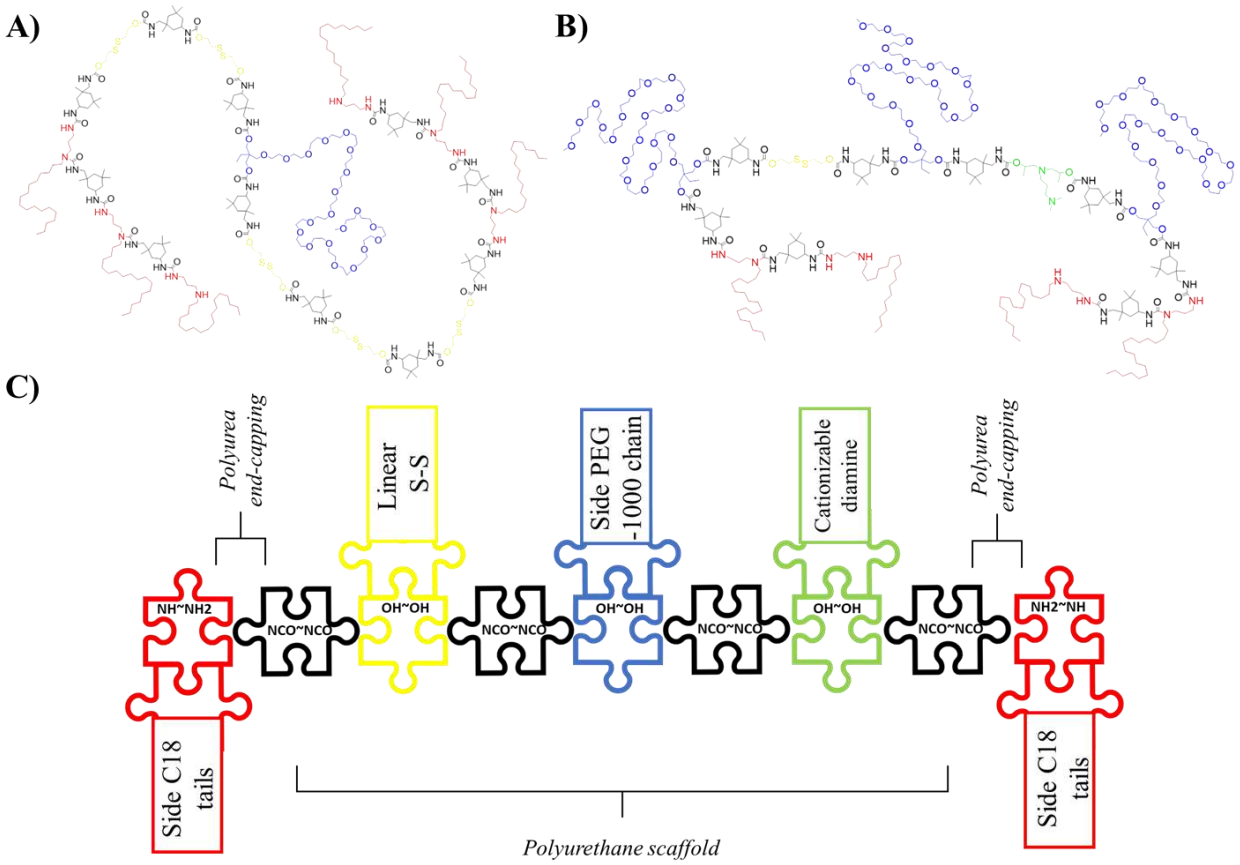

Figure 1: Chemical structure of polyurethane-polyurea hybrid prepolymers P1 (A) and P2 (B), and schematization of P2 synthesis (C), where the polyurethane backbone was initially designed to be afterwards end-capped with the amino groups from a hydrophobic diamine, furnishing the hybrid polyurethane-polyurea prepolymer.

Next, the first crosslinked nanocapsule was dispersed in an organic media and mixed with the amino-capped high-HLB P2 prepolymer (Figure 2A; step 8). After the activation of P2 with an excess of diisocyanate (IPDI), which was confirmed by the appearance of the NCO stretching band according to FTIR analysis, the *in situ* reaction with the amino groups of L-lysine (Figure 2A; step 9) allowed to extend the hybrid polyurethane-polyurea chain, as well as to provide the system with pH-responsive capabilities owing to the incorporation of the α-carboxyl group of the basic amino acid. L-lysine addition step was only required for the synthesis of amphoteric nanocapsules, not for the formation of pure cationic ones. The system was then emulsified in water, leading to a "(water in oil) in water" system (Figure 2A; step 10), where an excess of reactive isocyanate was still present in the external interface of the emulsion. At this moment the hydrophobic tails were

oriented to the core while PEGylated moieties stabilized the nanocapsule in aqueous dispersant phase. Upon addition of a polyamine (Figure 2A; step 11) and reaction with NCO groups, the crosslinking of the second polymeric backbone was achieved through the formation of urea bonds, producing the final WOW structure (Figure 2A; step 12 and corresponding magnification), where both original prepolymers P1 and P2 are defining the first and the second wall, respectively, without the need to use any external emulsifiers. Polyurethane-based prepolymers P1 and P2 were rationally designed to arrange their lateral groups in a water-in-oil interface, placing the polyurethane backbone in the appropriate location for an interfacial-promoted polyaddition with different reactants. This way to dispose stabilized reactive groups not only increases the crosslinking ability, but it would also facilitate the *in-situ* functionalization of the nanocapsules.[31] As shown in Figure 2A, the "sandwich" attachment in the final product created by the interaction between hydrophobic tails of both polymers reminds the bilayer arrangement of lipidic and amphiphilic precursors in liposomal structures. However, it is important to note that in this case the confined water-based core remains completely isolated from the aqueous external medium by means of the two crosslinked polymers.

3.2. Synthesis and characterization of ICG-loaded NCs.

Once set up the synthetic methodology for the preparation of WOW polyurethane-polyurea hybrid nanocapsules, the encapsulation of ICG was addressed. Water-dispersed ICG-loaded nanocapsules (ICG-NCs) were efficiently prepared following the abovementioned methodology with two different surface functionalities: cationic and amphoteric ICG-NCs. The fluorophore concentration in the nanocapsules was determined by UV-vis spectroscopy, showing good results for both encapsulation efficacy and dye-loading values (Table S4). The hydrodynamic diameter of ICG-loaded NCs was measured by Dynamic Light Scattering (DLS) (cationic; 55.22 ± 10.42 nm / amphoteric; 29.37 ± 5.25 nm) (Figure 2B) and then double-checked by Transmission Electron Microscopy (TEM) analysis (Figure 2C) and High-Resolution Transmission Electron Microscopy (HR-TEM) (Figure 2D).

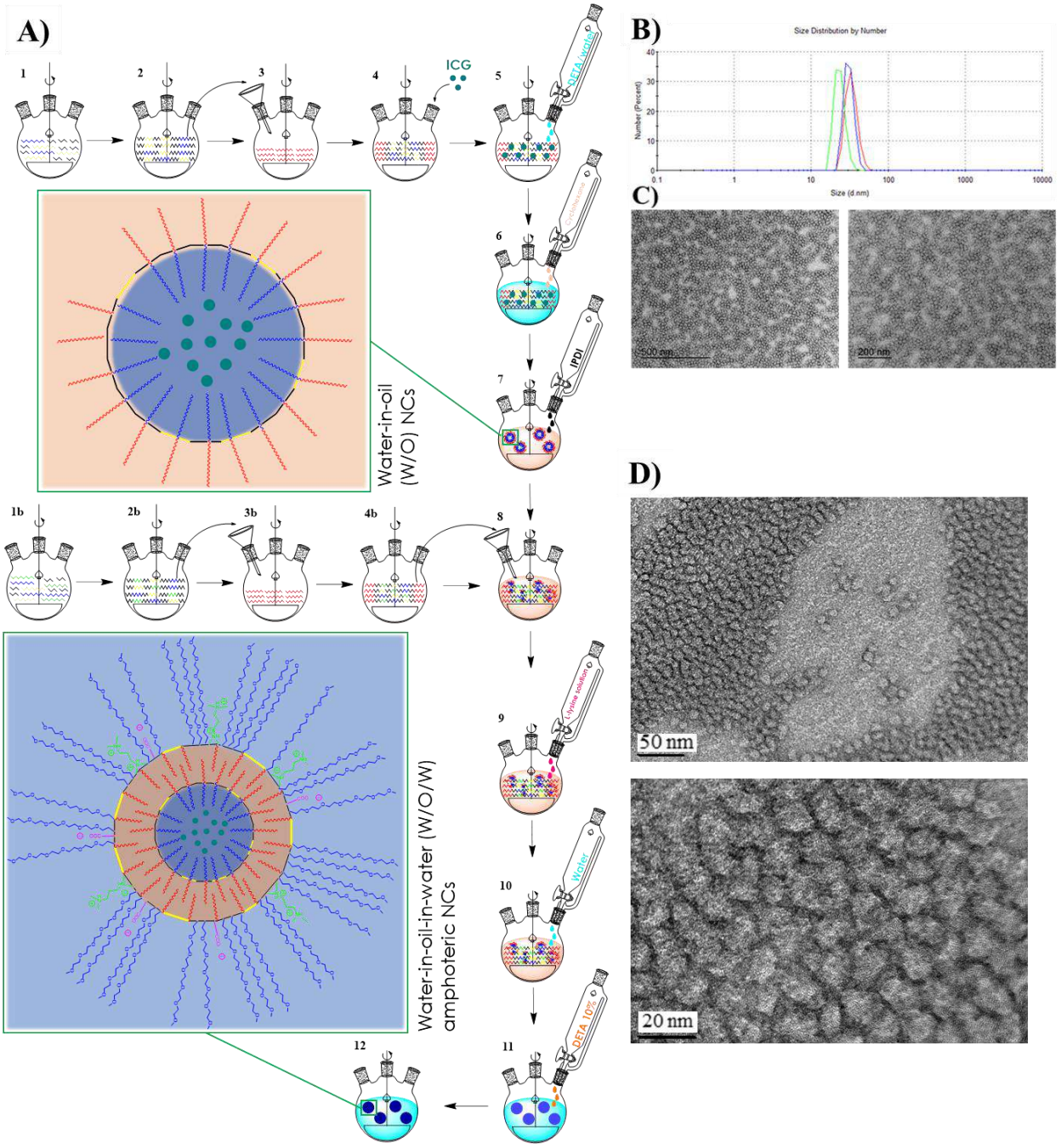

Figure 2: A) Schematic synthesis of ICG-loaded amphoteric double-walled polyurethane nanocapsules. Steps 1 to 4 and 1b to 4b refer to the synthesis of both reactive polymers. Steps from 5-7 describe the synthesis of ICG-loaded W/O nanocapsules, while the following steps 8-12 exemplify the synthesis of final W/O/W ICG-loaded amphoteric nanocapsules. Magnifications of NCs structure after each crosslinking reactions are shown in step 7 and in step 12. B) Particle size distribution by DLS of amphoteric ICG-loaded NCs C) TEM micrographs of amphoteric ICG-loaded NCs and D) the corresponding HR-TEM micrographs.

In good agreement with the expected results, amphoteric ICG-NCs were found slightly smaller than the cationic ones, owing to the incorporation of the anionic group provided by L-lysine which acts as an ionomeric surfactant. Surface charge determination versus pH variations was conducted by ξ-potential measurements, showing that cationic nanocapsules slightly modified their surface charge on pH depletion whereas a more significant change occurred in the case of amphoteric nanocapsules, which start from neutral charge at physiological pH and gradually become cationic after acidification to pH=6 (Figure S14). The stability of amphoteric ICG-NCs was also investigated under different conditions and compared with that of the free form. As shown in Figure S17, the stability of the fluorescent probe was clearly improved upon nanoencapsulation, thus allowing to extend its imaging properties over the time.

3.3. *In vitro* cellular uptake evaluation of the NCs.

A combination of Confocal Microscopy (Figure S18, S19, S20 and S21) and Flow Cytometry (Figure S22, S23, S24 and S25) studies were used to elucidate the mechanism of internalization for both cationic and amphoteric nanocapsules, as well as intracellular accumulation in Monocyte-derived Dendritic Cells (moDCs). Previously, cytotoxicity assays in moDCs had confirmed the absence of toxicity associated to ICG-loaded nanocapsules (data not shown). On one hand, cell internalization percentage was quantified by Flow Cytometry at 37 ^{o}C and 4 ^{o}C to determine the amount of nanocapsules crossing the cell membrane and to investigate the involvement of energy-dependent mechanisms. As ICG-loaded NCs require near infrared excitation, we decided to encapsulate a coumarin-based COUPY fluorophore with operability in the visible region of the electromagnetic spectrum to allow the use of a standard flow cytometer.[32,33] After 24 h incubation, both COUPY-loaded cationic and amphoteric nanocapsules reached high levels of internalization in moDCs, and energy-dependent pathways were demonstrated to be involved in the cellular uptake. As expected, cationic COUPY-loaded NCs were more rapidly internalized due to their enhanced penetrating properties. By contrast, the increasing internalization of amphoteric nanocapsules was more sustained in time compared with the cationic analogues since they deal with surface charge equilibria (Figure S23). On the other hand, the internalization of cationic and amphoteric ICG-loaded NCs in moDCs and in HeLa cells (data not shown) was investigated by confocal microscopy using multiphoton irradiation at 790 nm (detection at 810 nm). As shown in Figures S20 and S21, the fluorescence signal after incubation with both ICG-loaded NCs (2 μM,

30 min, 37 ºC) was clearly observed inside the cells, mainly in the form of vesicles, indicating an excellent cell membrane permeability, even after shorter incubations times. Colocalization experiments with Lysotracker green (LTG) confirmed that most of the fluorescent vesicles were lysosomes (Figure 3).

3.4. *In vivo* fluorescence imaging biodistribution in healthy mice.

Once demonstrated the good performance of ICG-loaded NCs upon multiphoton laser irradiation, we focused on validating the use of this methodology for cancer bioimaging in a complex live organism. For this purpose, a range of multiphoton *in vivo* live imaging experiments in different mice models using IVIS™ technology was designed.

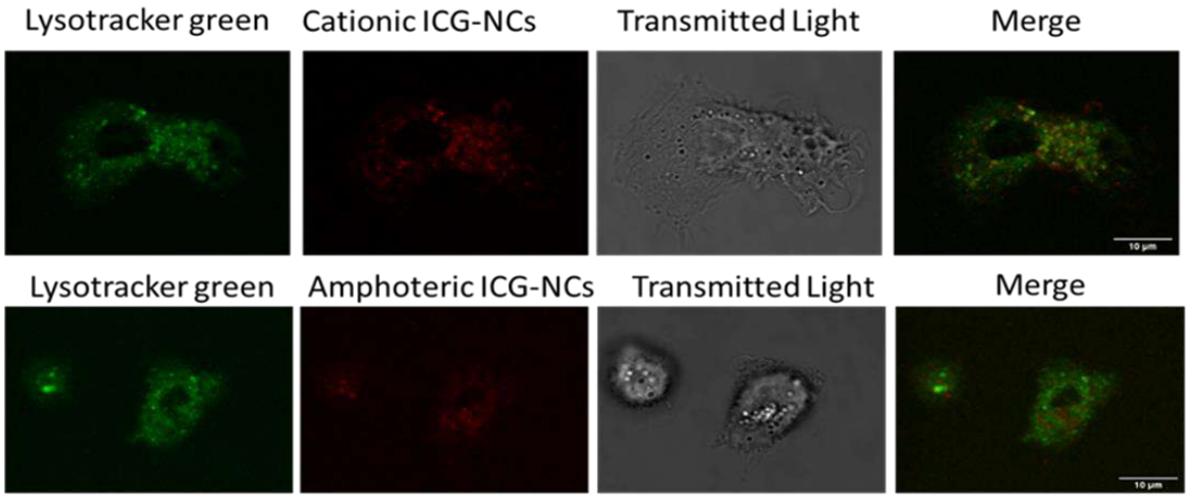

Figure 3: Cellular uptake by confocal microscopy of cationic and amphoteric ICG-loaded NCs in moDCs using multiphoton excitation. Both nanocapsules were incubated at 2 µM ICG concentration for 2 h at 37 ºC

In a zero stage of *in vivo* experimentation, the toxicity associated to the nanocarrier was first evaluated by single intravenous injection (tail vein) at three different concentrations in healthy mice for the subsequent evaluation, after one week, of the hematological parameters in blood and the biological parameters in plasma. Once demonstrated the absence of any side-toxicity associated to the nanocapsules (Tables S5 and S6), we focused on investigating the biodistribution of amphoteric and cationic ICG-loaded NCs in mice models (Figures S6-S30). First, C57BL/6 mice received a testing concentration of cationic ICG-NCs in order to ensure the imaging viability. However, due to the dark hair color this mouse strain has, we were unable to properly detect fluorescent signal

by IVIS and, consequently, we decided to euthanize mice to extract organs for ICG-loaded NC detection. Spleen, kidney and, specially, liver showed quite high accumulation (Figure S27). Based on these results, mouse strain selection was then shifted to a BALB/c albino strain to facilitate the *in vivo* ICG-mediated monitorization. Cationic and amphoteric ICG-loaded NCs were intravenously injected in a healthy BALB/c mouse, checking their biodistribution profile against free ICG for 48 h. All the mice (n=4 and 2 controls per group) received the same concentration of ICG, in either free or the nanoencapsulated form. A clear improvement in the biodistribution performance of the ICG-loaded NCs was observed compared with the free fluorophore. Indeed, the fluorescence signal of the free ICG form was turned off before 24 h-after injection (Figure S28), presumably because of a rapid clearance from mice body and/or degradation of the fluorescent probe. By contrast, while ICG-NCs were monitorable for more than 48 h-after intravenous administration, being heterogeneously distributed along the animal's body. These observations confirm that polyurethane-polyurea hybrid nanocapsules increase the circulating time of ICG, preventing degradation, opsonization and/or RES-removal (Figure S29 and S30).

3.5. *In vivo* fluorescence imaging biodistribution in subcutaneous tumor mice model.

Finally, both ICG-loaded NCs were tested for selective accumulation in tumor locations in a melanoma xenograft model, implanting A375 cells in immunosuppressed NSG mice. This human tumor model was subcutaneously implanted on the right flank of the animals (red dashed circles tag tumor cells locations in Figure S31 and Figure 4), and it was allowed to grow for 14-days before ICG free or ICG-loaded NCs administration. Remarkably, for the same dose via intravenous administration, the ICG free signal disappeared on the second visualization day, 48 h after injection (Figure 4A), while both cationic and amphoteric ICG-loaded nanocapsules could be trackable for more than 216 h after injection (n=3 per group; control group is shown on Figure S31A).

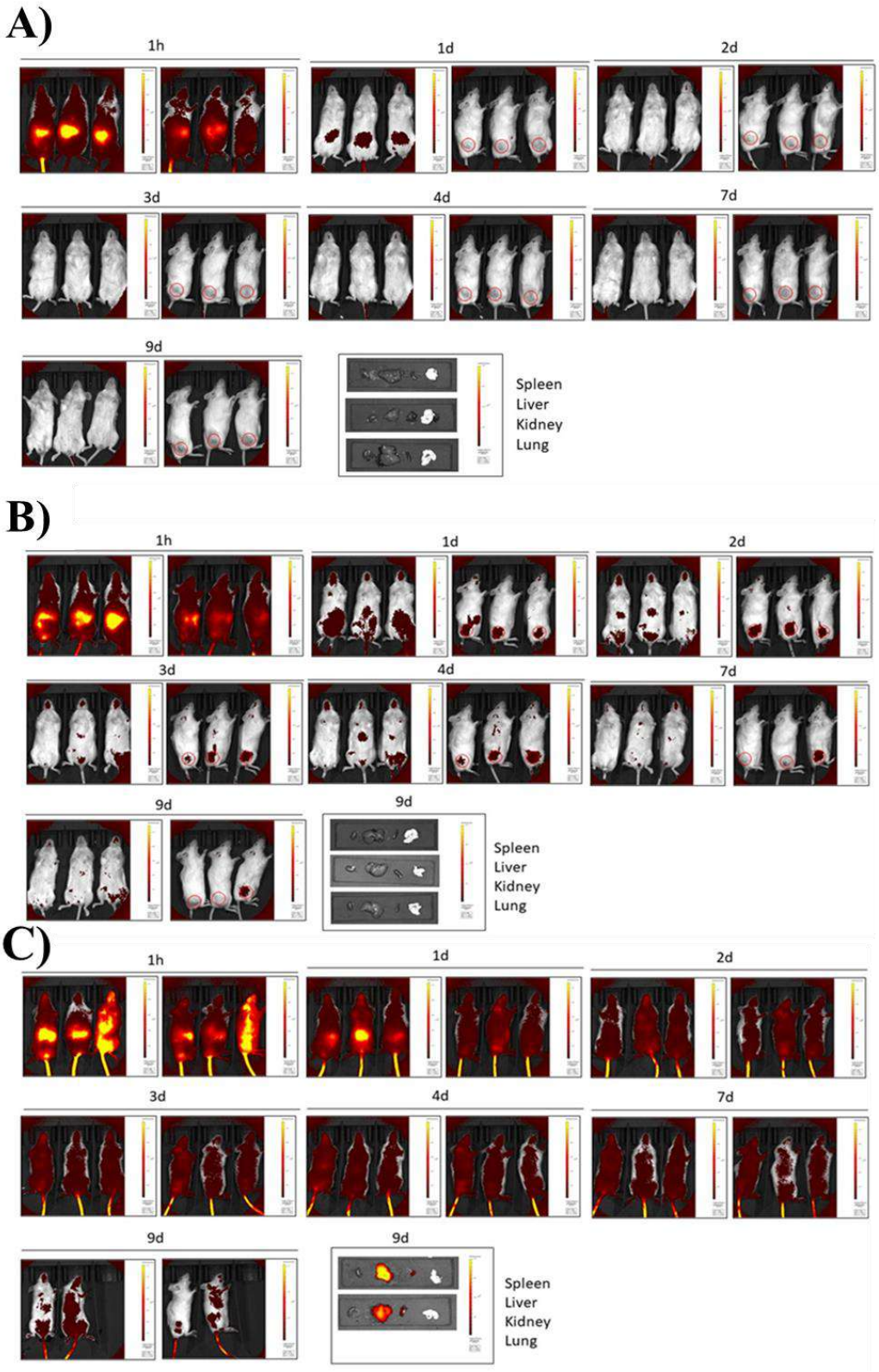

Figure 4: *In vivo* fluorescence imaging biodistribution in subcutaneous tumor mice models. 9-days biodistribution pattern of A) A375 challenged NSG mice treated with a 40 µM solution of ICG

(n=3/group), B) A375 challenged NSG mice treated with amphoteric ICG-NCs (n=3/group) at 40 µM ICG, and C) A375 challenged NSG mice treated with cationic ICG-NCs (n=3/group) at 40 µM ICG. Locations for tumor cells injections have been indicated with a red circle.

In addition to these results, it is worth noting that amphoteric ICG-NCs operate as realistic tumor tag probes, clearly promoting the accumulation of ICG onto tumor locations (Figure 4B). By contrast, cationic ICG-NCs show higher signaling but decreased selectivity for tumor tissues (Figure 4C). The evaluation of the amount of fluorescence signal over liver, kidneys, spleen and lungs supported these conclusions since the dye was absent in the case of amphoteric ICG-NCs group 9-days after injection, whereas a larger amount of fluorescence signal was found in excretion organs of the cationic ICG-NCs-administered group. In the case of well-boding amphoteric functionalized ones, accumulation in excretion organs, as a significant factor which could lead to side-toxicity inconveniences in the future, was not detectable at all.

Overall, these results are in good agreement with those previously obtained for liposoluble-drug loaded amphoteric polyurethane-polyurea hybrid NCs, where tumor accumulation was confirmed by post-euthanized fluorescence analysis of organs/tissues,[15] unmasking the importance of the amphoteric surface functionalization of polymeric nanocapsules as a promising way to target solid tumor microenvironment.

4. CONCLUSION

In summary, we have developed and validated in a biologically relevant tumor xenograft model, a novel, versatile and highly efficient one-pot and industrially scalable synthetic process for the preparation of double-walled polyurethane-based nanocapsules as selective nanocarriers of water-soluble bioactive compounds. As a proof of concept, the FDA-approved fluorescent probe ICG has been incorporated in the aqueous core of the nanocapsules, with both cationic and amphoteric surface properties, confirming their exceptional properties for bioimaging as well as for tumor targeted delivery. Furthermore, polyurethane-based control nanocapsules have been verified as non-toxic at all, both *in vitro* and *in vivo*, which position them as a powerful tool for tumor resection by fluorescence-guided surgery.

AUTHOR CONTRIBUTIONS

J.B, J.R. and V.M. conceived the study. J.B. and N.I. synthesized and characterized the nanocapsules. S.C. synthesized and characterized the COUPY fluorophore. J.B. N.I. and C.B. performed confocal microscopy studies. J.B., M.V-dA., N.I., C.B., D.B-R. and F.L. designed the biological experiments. C.B. and C.M. performed *in vitro* biological experiments. M.V-dA., L.C-S. and S.C-L. performed *in vivo* biological experiments. J.B. and V.M. wrote the manuscript, which was contributed by all authors, who have approved the submitted version of the manuscript.

DECLARATION OF COMPETING INTEREST

J.B. and J.R. participate as inventors in a patent application involving the methodology for the synthesis of the double-walled polyurethane nanocapsules reported in this manuscript.

ACKNOWLEDGEMENTS

This work was supported by funds from the Spanish Ministerio de Ciencia e Innovación-Agencia Estatal de Investigación (MCI/AEI/10.13039/501100011033) and FEDER funds (Projects CTQ2017-84779-R, PID2020-117508RB-I00) and the Generalitat de Catalunya (Projects RD17-1-0079 and 2017 DI 072). L.C-S. was a recipient of a fellowship from the Spanish MINECO (PRE2020-093993). The authors acknowledge helpful assistance of Dra. Maria Calvo Adamuz (Confocal Microscopy analysis) from CCiTUB.

Appendix A. Supplementary data

Supplementary data to this article can be found online at https://doi.org...

Data availability

The raw data required to reproduce these findings will be made available upon request.

ABBREVIATIONS

DEDS, 2,2´-Dihydroxyethyl disulfide; DETA, diethylenetriamine; DLS, Dynamic Light Scattering; EPR, enhanced permeability and retention; HLB, Hydrophilic-Lipophilic Balance; HR-TEM, High-Resolution Transmission Electron Microscopy; ICG, Indocyanine Green; IPDI, isophorone diisocyanate; LTG, Lysotracker green; moDCs, monocyte-derived dendritic cells; NCs, nanocapsules; OXPHOS, oxidative phosphorylation; PBMCs, Peripheral blood mononuclear cells; PBS, phosphate buffered saline; RES, reticuloendothelial system; TEM, Transmission Electron Microscopy; THF, tetrahydrofuran; TME, tumor microenvironment; WOW, Water-in-Oil-in-Water.

REFERENCES

1 B. L. Banik, P. Fattahi, J. L. Brown, *Nanomed. Nanobiotechnol*. **2016**, *8*, 271–299.

2 F. Alexis, E. Pridgen, L. K. Molnar, O. C. Farokhzad, *Mol. Pharmaceutics* **2008**, *5*, 505–515.

3 W. Wu, Y. Pu, J. Shi, *J. Nanobiotechnol*. **2022**, *20*, 4.

4 J. P.Santerre, K. Woodhouse, G. Laroche, R. S. Labow, *Biomaterials* **2005**, *26*, 7457–7470.

5 L. C. Rusu, L. C. Ardelean, A. A. Jitariu, C. A. Miu, C. G. Streian, *Polymers* **2020**, *12*, 1197.

6 Y. Wang, L. Zhu, Y. Wang, L. Li, Y. Lu, L. Shen, L. W. Zhang, *ACS Appl. Mater. Interfaces* **2016**, *8*, 35106–35113.

7 E. M. Rosenbauer, K. Landfester, A. Musyanovych, *Langmuir* **2009**, *25*, 12084–12091.

8 A. Schoth, K. Landfester, R. Muñoz-Espí, *Langmuir* **2015**, *31*, 3784–3788.

9 G. Morral-Ruíz, P. Melgar-Lesmes, C. Solans, M. J. García-Celma, *J. Controlled Release* **2013**, *171*, 163–171.

10 S. K. Pramanik, S. Sreedharan, H. Singh, M. Khan, K. Tiwari, A. Shiras, C. Smythe, J. A. Thomas, A. Das, *Bioconjugate Chem.* **2018**, *29*, 3532–3543.

11 E. M. Rosenbauer, M. Wagner, A. Musyanovych, K. Landfester, *Macromolecules* **2010**, *43*, 5083–5093.

12 D. Huang, Y. Zhou, Y. Xiang, M. Shu, H. Chen, B. Yang, X. Liao, *Polymer International* **2018**, *67*, 1186–1193.

13 Y. Tsvetkova, N. Beztsinna, M. Baues, D. Klein, A. Rix, S. K. Golombek, W. al Rawashdeh, F. Gremse, M. Barz, K. Koynov, S. Banala, W. Lederle, T. Lammers, F. Kiessling, *Nano Lett.* **2017**, *17*, 4665–4674.

14 B. Jiang. *Genes Dis.* **2017**, *4*, 25-27

15 M. Pérez-Hernández, C. Cuscó, C. Benítez-García, J. Bonelli, M. Nuevo-Fonoll, A. Soriano, D. Martínez-García, A. Arias-Betancur, M. García-Valverde, M. F. Segura, R. Quesada, J. Rocas, V. Soto-Cerrato, R. Pérez-Tomás, *Biomedicines* **2021**, *9*, 508.

16 P. Rocas, Y. Fernández, S. Schwartz, I. Abasolo, J. Rocas, F. Albericio, *J. Mater. Chem. B* **2015**, *3*, 7604–7613.

17 J. Bonelli, E. Ortega-Forte, G. Vigueras, M. Bosch, N. Cutillas, J. Rocas, J. Ruiz, V. Marchán, *Inorg. Chem. Front.* **2022**, *9*, 2123-2138.

18 G. Flórez-Grau, P. Rocas, R. Cabezón, C. España, J. Panés, J. Rocas, F. Albericio, D. Benítez-Ribas, *Int. J. Pharm.* **2016**, *511*, 785–793.

19 J. Bonelli, E. Ortega-Forte, A. Rovira, M. Bosch, O. Torres, C. Cuscó, J. Rocas, J. Ruiz, V. Marchán, *Biomacromolecules* **2022**, *23*, 2900-2913.

20 Q. Li, X. Li, C. Zhao, *Front. Bioeng. Biotechnol.* **2020**, *8*. 437.

21 L. M. Russell, M. Hultz, P. C. Searson, *J. Controlled Release* **2018**, *269*, 171–176.

[22] L. Luo, Q. Zhang, Y. Luo, Z. He, X. Tian, G. Battaglia, *J. Controlled Release* **2019**, *298*, 99–109.

23 S. Kunjachan, F. Gremse, B. Theek, P. Koczera, R. Pola, M. Pechar, T. Etrych, K. Ulbrich, G. Storm, F. Kiessling, T. Lammers, *ACS Nano* **2013**, *7*, 252–262.

24 T. K. Hill, A. Abdulahad, S. S. Kelkar, F. C. Marini, T. E. Long, J. M. Provenzale, A. M. Mohs, *Bioconjugate Chem.* **2015**, *26*, 294–303.

25 P. Charalampaki, P. J. Proskynitopoulos, A. Heimann, M. Nakamura, *Front. Oncol.* **2020**, *10*, 1069.

26 R. R. Zhang, A. B. Schroeder, J. J. Grudzinski, E. L. Rosenthal, J, M. Warram, A. N. Pinchuk, K. W. Eliceiri, J. S. Kuo, J. P. Weichert, *Nat. Rev. Clin. Oncol.* **2017**, *14*, 347–364.

27 B. Theek, L. Y. Rizzo, J. Ehling, F. Kiessling, T. Lammers, *Clin Transl Imaging* **2014**, *2*, 67–76.

28 L. Boni, G. David, A. Mangano, G. Dionigi, S. Rausei, S. Spampatti, E. Cassinotti, A. Fingerhut, *Surgical Endoscopy* **2015**, *29*, 2046–2055.

29 V. Sabapathy, J. Mentam, P. M. Jacob, S. Kumar, *Stem Cells Int.* **2015**, 606415.

30 S. Mindt, I. Karampinis, M. John, M. Neumaier, K. Nowak, *Photochem. Photobiol. Sci.* **2018**, *17*, 1189–1196.

31 P. Rocas, M. Hoyos-Nogués, J. Rocas, J. M. Manero, J. Gil, F. Albericio, C. Mas-Moruno, *Adv. Healthcare Mater.* **2015**, *4*, 1956–1960.

32 A. Gandioso, R. Bresolí-Obach, A. Nin-Hill, M. Bosch, M. Palau, A. Galindo, S. Contreras, A. Rovira, C. Rovira, S. Nonell, V. Marchán, *J. Org. Chem.* **2018**, *83*, 1185–1195.

33 A. Rovira, M. Pujals, A. Gandioso, M. López-Corrales, M. Bosch, V. Marchán, *J. Org. Chem.* **2020**, *85*, 6086–6097.

SUPPORTING INFORMATION

Novel tumor-targeted self-nanostructured and compartmentalized water-in-oil-in-water polyurethane-polyurea nanocapsules for cancer theragnosis

Joaquín Bonelli,[a,b] María Velasco-de Andrés,[c] Neus Isidro,[b] Cristina Bayó,[d] Sergi Chumillas,[a] Laura Carrillo-Serradell,[c] Sergi Casadó-Llombart,[c] Cheryl Mok,[d] Daniel Benítez-Ribas,[d,e] Francisco Lozano,[c,e,f] Josep Rocas,[b] Vicente Marchán[a],*

[a] Departament de Química Inorgànica i Orgànica, Secció de Química Orgànica, Institut de Biomedicina de la Universitat de Barcelona (IBUB), Universitat de Barcelona (UB), Martí i Franquès 1-11, E-08028 Barcelona, Spain. Email: vmarchan@ub.edu

[b] Nanobiotechnological Polymers Division, Ecopol Tech, S.L., El Foix Business Park, Indústria 7, E-43720 L'Arboç del Penedès, Tarragona, Spain

[c] Immunoreceptors del Sistema Innat i Adaptatiu, Institut d'Investigacions Biomèdiques August Pi i Sunyer (IDIBAPS), Universitat de Barcelona (UB), Villarroel 170, E-08036 Barcelona, Spain.

[d] Department of Immunology, Hospital Clinic, August Pi i Sunyer Biomedical Research Institute (IDIBAPS), Universitat de Barcelona (UB), Villarroel 170, E-08036 Barcelona, Spain.

[e] Servei d'Immunologia, Centre de Diagnòstic Biomèdic, Hospital Clínic de Barcelona, Villarroel 170, E-08036 Barcelona, Spain.

[f] Departament de Biomedicina, Universitat de Barcelona (UB), Villarroel 170, E-08036 Barcelona, Spain.

Table of contents

1. Materials

1.1. Building blocks and crosslinkers

Isophorone diisocyanate IPDI was purchased from Quimidroga (Barcelona, Spain), YMER N-120 was kindly supplied by Perstorp (Malmö, Sweden) and Genamin TAP 100D was provided by Clariant (Barcelona, Spain). Jeffcat DPA, DEDS (2-hydroxyethyl disulfide), DETA (diethylenetriamine) and L-lysine hydrochloride were purchased from Sigma Aldrich (St Louis, USA).

1.2. Encapsulated molecules

Indocyanine Green (ICG) was purchased from TCI Chemicals (Tokyo, Japan) whereas COUPY dye was synthesized as indicated in section 1.2.1.

1.2.1. Synthesis of 3-(4-(cyano(7-(*N,N*-diethylamino)-4-methyl-2H-chromen-2-ylidene)methyl)pyridin-1-ium-1-yl)propane-1-sulfonate (COUPY dye)

To a solution of 105 mg (0.32 mmol) of 2-(cyano(4-pyridine)methylene)-7-(*N,N*-diethylamino)-4-methyl-coumarin in ACN (30 mL), 1,3-propane-sultone (1.12 mL, 12.67 mmol) was added under an Ar atmosphere and the resulting mixture was stirred overnight at 90 ºC and protected from light. After evaporation to dryness and purification by column chromatography (silica gel, 0-20% MeOH in DCM), 83 mg of a red solid were obtained (yield: 58%). Characterization: TLC: Rf (DCM/MeOH 9:1) 0.3; ^{1}H NMR (DMSO-d_6, 400 MHz): δ (ppm) 8.69 (2H, d, J = 7.2 Hz), 8.22 (2H, d, J = 7.2 Hz), 7.75 (1H, d, J = 9.2 Hz), 7.01 (1H, s), 6.96 (1H, dd, J = 6.8 Hz), 6.91 (1H, d, J = 6.8 Hz), 4.55 (2H, t, J = 7.2 Hz), 3.55 (4H, q, J = 7.2 Hz), 2,51 (3H, s), 2.43 (4H, t, J = 7.2 Hz), 2.18 (2H, m), 1.18 (6H, t, J= 6.8 Hz); LRMS (ESI): m/z 454.11 calc. for $[C_{24}H_{27}N_3O_4S+H]^+$ = 454.18.

1.3. Solvents and auxiliary solutions

Milli-Q water was obtained from a Merck Millipore purification system (Madrid, Spain) and PBS, HCl 37% and NaOH in pellets were purchased from Merck (Madrid, Spain). Cyclohexane was purchased from Panreac AppliChem (Barcelona, Spain).

1.4. Biological agents, mediums, and supplements

Dulbecco's Modification of Eagle's Medium (DMEM) was purchased from Corning (Arizona, USA) and DMEM with low glucose, pyruvate and without glutamine and Phenol Red were purchased from Thermo Fischer Scientific (Massachusetts, USA), as well as Fetal Bovine Serum (FBS), Dulbecco′s Phosphate Buffered Saline (DPBS), Horse serum, Hoescht 33342 solution, Lysotracker Green (LGT) and Mytotracker Green (MTG). L-glutamine solution (200 mM), F12 (HAM) media and 100 U mL^{-1}

penicillin/100 μg mL^{-1} streptomycin were acquired from Biological Industries (Cromwell, USA). Hepes buffer (1M) was purchased from Lonza (Basel, Switzerland), as well as X-VIVO15 medium. Insulin, Hydrocortisone, Human Serum AB (HS) and Epidermal Growth Factor (EGF) were acquired from Sigma-Aldrich (St Louis, USA). Choleric toxin was purchased from Calbiochem (San Diego, CA, USA). The cytokines IL-4 and Granulocyte-Monocyte-Colony Stimulation Factor (GM-CSF) were purchased from Miltenyi Biotec (Bergisch Gladbach, North Rhine-Westphalia, Germany).

2. Analytical techniques

2.1. Infrared spectroscopy (IR)

IR spectra were performed in a Smart ATR (Nicolet iS10, Thermo Scientific, Raleigh, USA) using a transmittance mode (16 scans) and OMNIC software. For the monitoring of solvent-based samples, one drop was deposited onto the diamond crystal and the solvent was left to dry by evaporation. IR spectra were recorded from a dry film of the sample for the reaction control after emulsification.

2.2. pH measurements

The pH of the emulsion was determined right after the crosslinker was added and at different time intervals until the last polyaddition reaction was complete. All the determinations were carried out in a pH-meter HI 2211 pH/ORP-Meter (HANNA Instruments, Eibar, Spain) equipped with a pH electrode Crison 5029 (Crison Instruments, Barcelona, Spain) and a temperature probe.

2.3. Dynamic light scattering (DLS)

The size distribution of the NCs was analyzed on a Zetasizer Nano-ZS90 (Malvern, Worcestershire, UK) in Milli-Q water at 25 °C at a concentration of 0.5 mg/mL.

2.4. Zeta potential (Z-pot)

The Z-pot of the NCs was analyzed on a Zetasizer Nano-ZS90 (Malvern, Worcestershire, UK) in Milli-Q water at 25 °C at a concentration of 1 mg/mL, measured at different pH values.

2.5. Dialysis purification

The NCs were dialyzed against Milli-Q water for 24 h using a Spectra/Por molecular porous membrane tubing with a 12–14 kDa molecular weight cut-off (MWCO) (Spectrum Laboratories, Rancho Dominguez, USA).

2.6. Determination of cargo loading by UV-Vis spectroscopy

The coumarin and ICG loading (or dye-loading, DL) of the NCs was determined by UV-Vis measurements performed in a DINKO UV-6900 spectrophotometer (Dinko Instruments, Barcelona, Spain). First, a calibration curve was developed by preparing a range of standard solutions containing the coumarin at different concentrations and analyzing their UV profile and maximum absorbance (see Figure S14). Then, Encapsulation Efficiency EE (%) and Dye Loading DL (%) were calculated from the following equations:

$$\%\, EE = \frac{amount\ of\ dye\ incorporated\ in\ the\ nanocapsule}{total\ amount\ of\ dye\ added\ in\ the\ synthesis} * 100$$

$$\% DL = \frac{amount\ of\ dye\ incorporated\ in\ the\ nanocapsule}{total\ amount\ of\ dried\ nanocapsules} * 100$$

To determine the amount of coumarin incorporated in the NCs, a desired amount of dried NCs (previously dialyzed) was dissolved in an exact volume of solvent and the measurement was calculated from the calibration curve of free coumarin in the same organic solvent. To determine the amount of ICG incorporated in the NCs, a desired amount of suspended NCs (previously dialyzed) was diluted in an exact volume of water and the measurement was calculated from the calibration curve of free ICG in water. Non-loaded NCs were used as the reference. All measurements were recorded at the desired wavelength range, depending on the maximum of absorption of the molecule under study and assayed in triplicates.

2.7. Solids concentration

NCs concentration in the aqueous dispersion was determined by triplicate leading to dryness using a Digitheat-TFT oven (J.P.Selecta, Barcelona, Spain), with a fixed temperature of 40 ºC for 48 h.

2.8. Transmission electron microscopy (TEM)

The morphology of nanocapsules was studied on a Jeol JEM 1010 (Peabody, MA, USA). A 200-mesh copper grid coated with 0.75% FORMVAR was deposited on 6 μL of a suspension of nanocapsules in water (10 mg mL^{-1}) for 1 min. Excess of sample was removed by contact with ultrapure water for 1 min and the grid was deposited on a drop of uranyl acetate (2% w/w) in water for 1 min. Excess uranyl acetate was removed and the grid was air-dried for at least 3 h prior to measurement.

2.9 High-resolution transmission electron microscopy (HR-TEM)

HR-TEM observation was performed in a JEOL J2100 microscope (Peabody, MA, USA), operated at an accelerating voltage of 120 kV. Images were recorded using a Gatan Orius CCD camera. A 200-mesh copper grid coated with 0.75% FORMVAR was deposited on 6 μL of a suspension of nanocapsules in water (10 mg mL−1) for 1 min. Excess of sample was removed by contact with ultrapure water for 1 min and the grid was deposited on a drop of uranyl acetate (2% w/w) in water for 1 min. Excess uranyl acetate was removed and the grid was air-dried for at least 3 h prior to measurement.

3. Synthetic procedures

3.1. Synthesis of redox-responsive amphiphilic low HLB prepolymer (P1)

2,2′-Dihydroxyethyl disulfide (DEDS; yellow moieties) (2.86 g, 37.08 meq) and YMER N-120 (blue moieties) (3.64 g, 7.01 meq) were added into a three-necked round-bottom flask equipped with mechanical stirring at room temperature (rt) and purged with N_2. When the mixture was homogeneous, isophorone diisocyanate IPDI (black moieties) (8.83 g, 79.40 meq) was added into the reaction vessel under gentle mechanical stirring, checking the initial NCO stretching band intensity by FTIR. The polyaddition reaction was kept under these conditions until the NCO stretching band reach stabilization. At this point, dry acetone (18.2 mL) was added into the reaction mixture to fluidify the polymer. In parallel, 1,3-diamino-*N*-octadecylpropane (Genamin TAP 100D; red moieties) (9.25 g, 56.72 meq) was dissolved in dry acetone (8.1 mL) into another 100 mL three-necked round-bottom flask, which had previously been purged with N_2. The former reaction mixture was added dropwise onto the latter under half-moon 100 rpm mechanical stirring. The reaction was monitored by IR until the NCO stretching band intensity had completely disappeared.

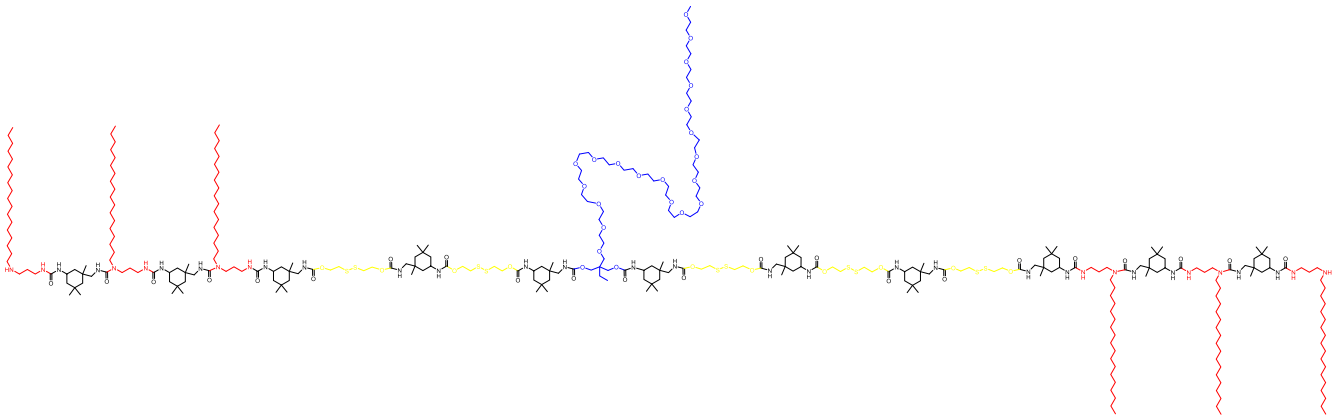

Figure S1: Structure of a representative amino-capped **P1** prepolymer.

3.2. Synthesis of redox responsive amphiphilic cationic prepolymer (P2)

2,2′-Dihydroxyethyl disulfide (DEDS; yellow moieties) (901.0 mg, 11.68 meq), YMER N-120 (blue moieties) (12.04 g, 23.18 meq) and *N*-(3-dimethylaminopropyl)-*N*,*N*′-diisopropanolamine (Jeffcat DPA; green moieties) (981.3 mg, 8.99 meq) were added into a three-necked round-bottom flask equipped with mechanical stirring at room temperature (rt) and purged with N_2. When the mixture was homogeneous, isophorone diisocyanate IPDI (black moieties) (8.14 g, 73.24 meq) was added into the reaction vessel under gentle mechanical stirring. The polyaddition reaction was kept under these conditions until the NCO stretching band intensity did not change, monitored by IR spectroscopy. At this point, dry THF (21 mL) was added into the reaction mixture to fluidify the polymer. In parallel, 1,3-diamino-*N*-octadecylpropane (Genamin TAP 100D; red moieties)) (5.99 g, 35.45 meq) was dissolved with dry THF (5.23 mL) into another 100 mL three-necked round-bottom flask, which had previously been purged with N_2. The former reaction mixture was added dropwise onto the latter under half-moon 100 rpm mechanical stirring. The reaction was monitored by IR until the NCO stretching band intensity had completely disappeared.

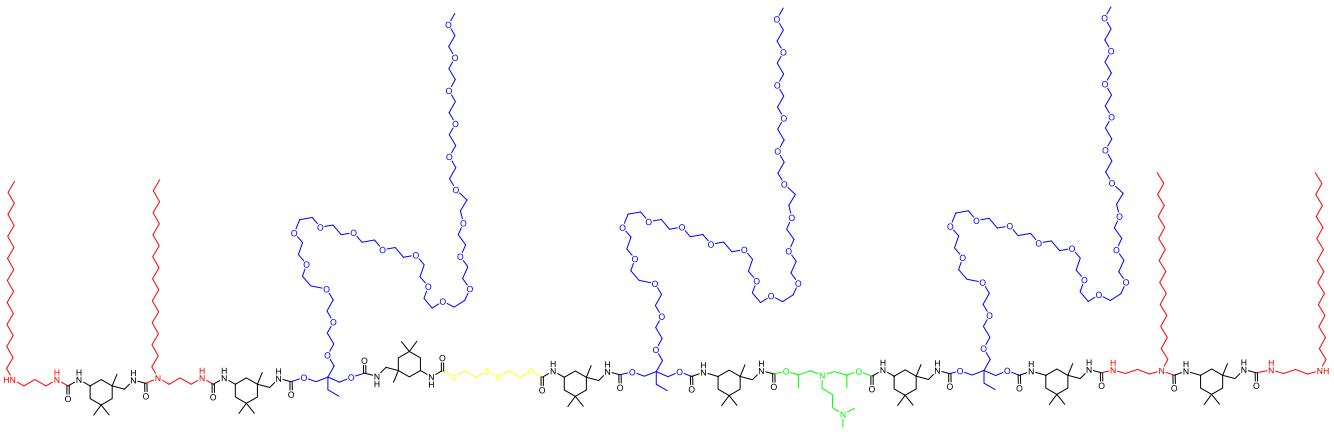

Figure S2: Structure of a representative amino-capped **P2** prepolymer.

3.3. Synthesis of dye-loaded cationic redox responsive water-in-oil-in-water NCs (cationic dye-NCs)

Table S1. Amounts of reagents used to prepare **cationic dye-loaded NCs.**

Substance	Amount	Equivalents or mols
Dye	5 mg	10.35 µmol COUPY or 6.35 µmol ICG
IPDI	265.0 mg	2.38 meq
Cyclohexane	1.28 mL	-
Polymer in acetone (P1)	635.2 mg	0.09 meq
Polymer in THF (P2)	5.87 g	0.61 meq
Milli-Q water	12.10 g	–
DETA	40.62 mg	1.18 meq

3.4. Synthesis of dye-loaded amphoteric redox responsive water-in-oil-in-water NCs (amphoteric dye-NCs)

Table S2. Amounts of reagents used to prepare **amphoteric dye-loaded NCs.**

Substance	Amount	Equivalents or mols
Dye	5 mg	10.35 μmol COUPY or 6.35 μmol ICG
IPDI	265.0 mg	2.38 meq
Cyclohexane	1.28 mL	-
Polymer in acetone (P1)	635.2 mg	0.09 meq
Polymer in THF (P2)	5.87 g	0.61 meq
L-lysine	0.65 mg	0.78 meq
Milli-Q water	12.88 g	–
DETA	13.93 mg	0.40 meq

3.5. Synthesis of non-loaded cationic and amphoteric redox responsive water-in-oil-in-water NCs (cationic and amphoteric control NCs)

Both cationic and amphoteric control nanocapsules were synthesized following the methodology described for dye-loaded ones, but without the initial addition of ICG or COUPY-derivate. Hence, the core of control nanocapsules only contains water.

3.6. Comparison of the structure of cationic and amphoteric ICG-loaded NCs

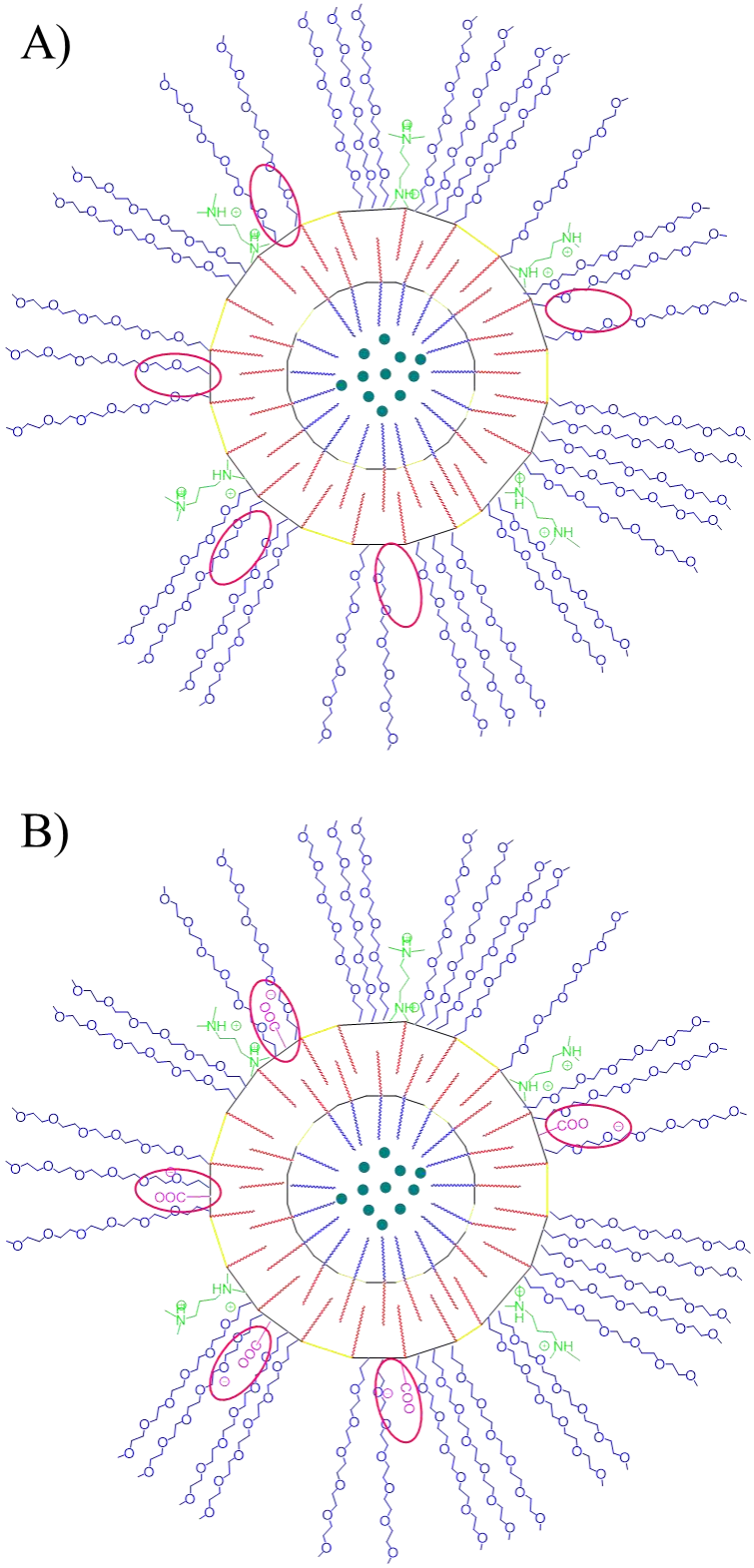

Figure S3. Comparison of the structure of A) cationic ICG-loaded NCs and B) amphoteric ICG-loaded NCs.

4. Characterization of polymers (P1 and P2) and NCs

4.1. Infrared Spectroscopy

The polymerization reaction was easily controlled by IR spectroscopy using the procedure detailed in section 2.1. given that NCO group has a very clear and characteristic stretching band at 2280-2230 cm^{-1}.

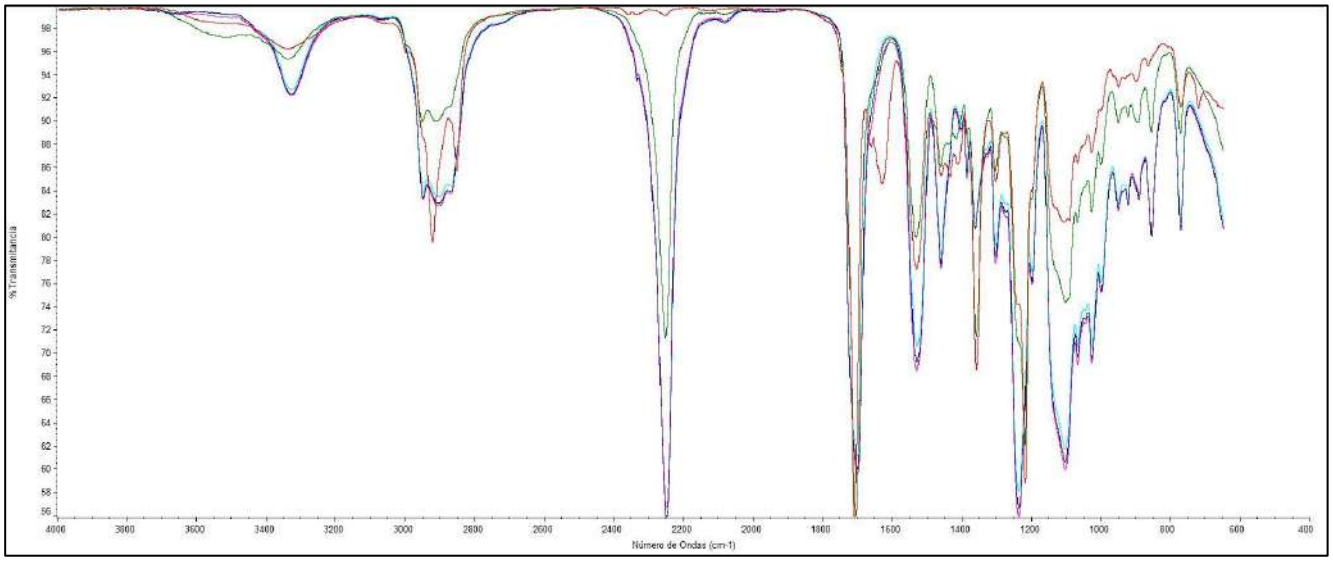

Figure S4. Consecutive IR spectra recorded during the synthesis of **P1**.

As shown in Figure S4, IR spectra of the polymer (**P1**) indicated a successful polymerization reaction between diols, the diamine and the diisocyanate, in both steps of the polymer synthesis. The purple line corresponds to the first sample recorded, at the begin of the reaction. At initial step of the reaction, the NCO asymmetric stretching band at 2252 cm^{-1} was very sharp and intense. After reacting with the diols, at the end of the first step (green line), the intensity of the NCO stretching band decreased significantly. Meanwhile, the intensities of the CO stretching band at 1719 cm^{-1}, the CN stretching band at 1537 cm^{-1} and the NCOO/COC asymmetric stretching band at 1240 cm^{-1} increased. Overall, the IR spectra registered during the first step of the synthesis confirmed polyurethane bond formation along with NCO consumption. Once the diamine was added during the second step of the polymer synthesis (red line), the NCO stretching band at 2252 cm^{-1} disappeared instantaneously, which was explained by the high reactivity of the amines. Simultaneously, other characteristic bands appeared or changed, such as a new stretching band at 1634 cm^{-1}, which was associated to the carbonyl of urea bonds and a new wagging band at 908 cm^{-1} corresponding to the free secondary amine, which also confirmed polyurea formation. Similar results were obtained during the synthesis of polymer **P2** (Figure S5).

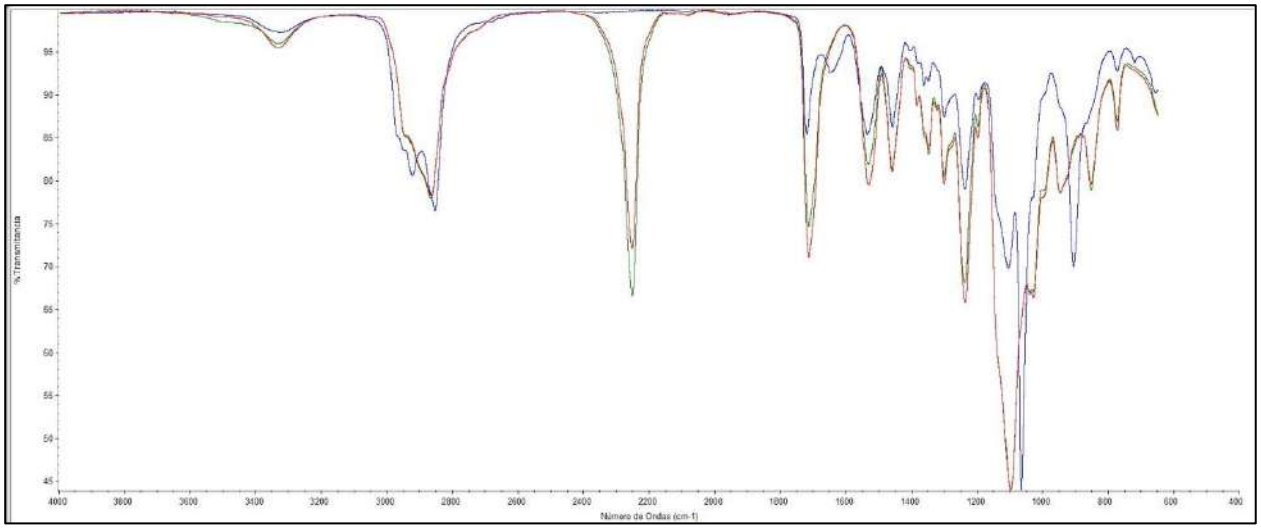

Figure S5. Consecutive IR spectra recorded during the synthesis of **P2**.

The encapsulation process was also controlled by IR spectroscopy. As shown in Figure S6, IR spectra of the water-in-oil encapsulation (regardless their loading) indicated also a successful nanocapsule formation, presenting small amount of free-NCO. In the next spectra (Figure S7) we can track the water-in-oil-in-water encapsulation process. The purple line corresponds to ENCAP 1 and P2 mixture, followed by the reactivation of the polymer with isocyanate and its conversion to an NCO-reactive entity (yellow line). Afterwards, L-lysine sodium salt was added (blue line), reacting with the activated polymer. A decrease on the intensity of the NCO stretching band at 2255 cm^{-1}, concomitantly with an increase of the carbonyl and CN stretching bands, confirmed urea formation (1642 cm^{-1} and 1532 cm^{-1}, respectively). The green line corresponds to a double-check of NCO presence after emulsion and, finally, the triamine was added (red line) and the NCO stretching band instantaneously disappeared by the same time that the urea-associated bands increased their intensity because of the rapid reaction between remaining NCO groups and this polyamine.

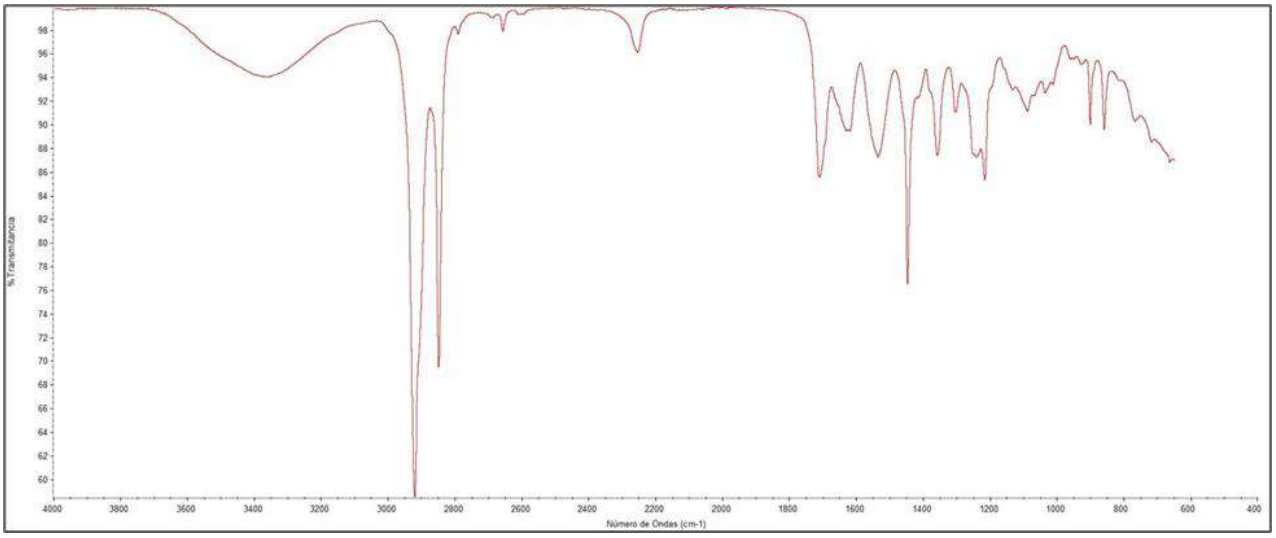

Figure S6. IR Spectrum of the W/O encapsulation reaction.

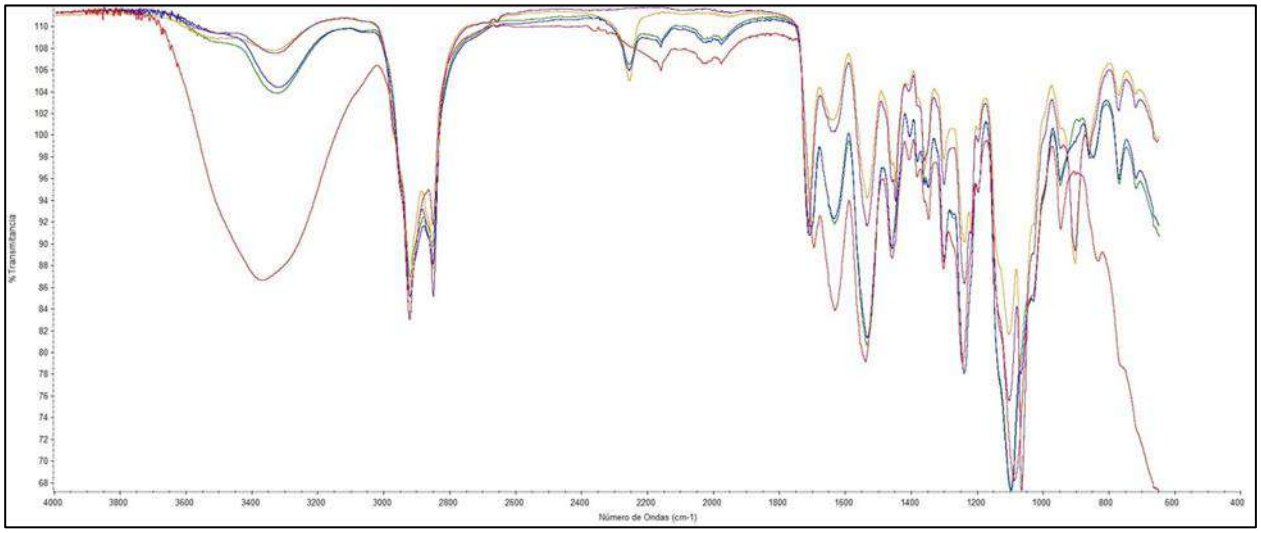

Figure S7. Consecutive IR spectra of the W/O/W encapsulation process.

4.2.Average size of NCs by Dynamic Light Scattering

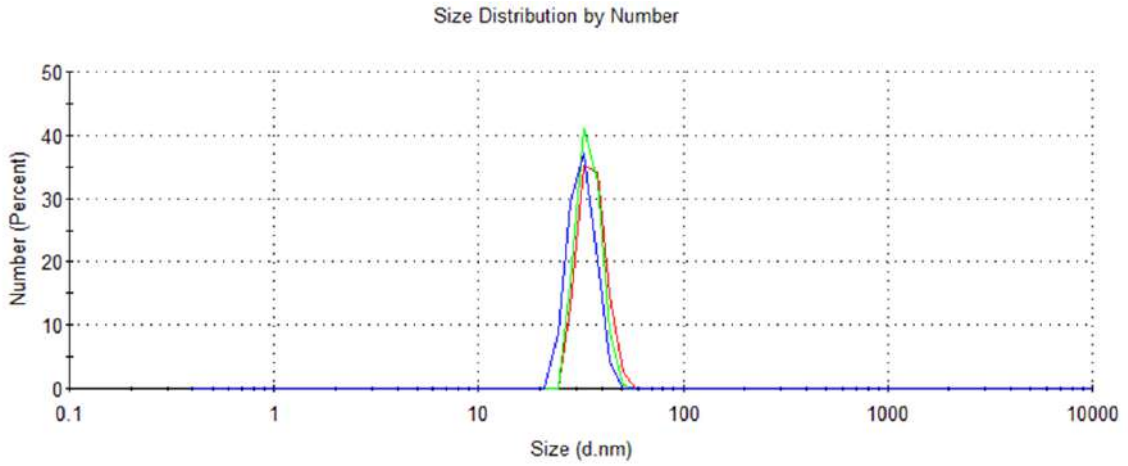

Figure S8. Hydrodynamic diameter distribution by number of cationic control NCs

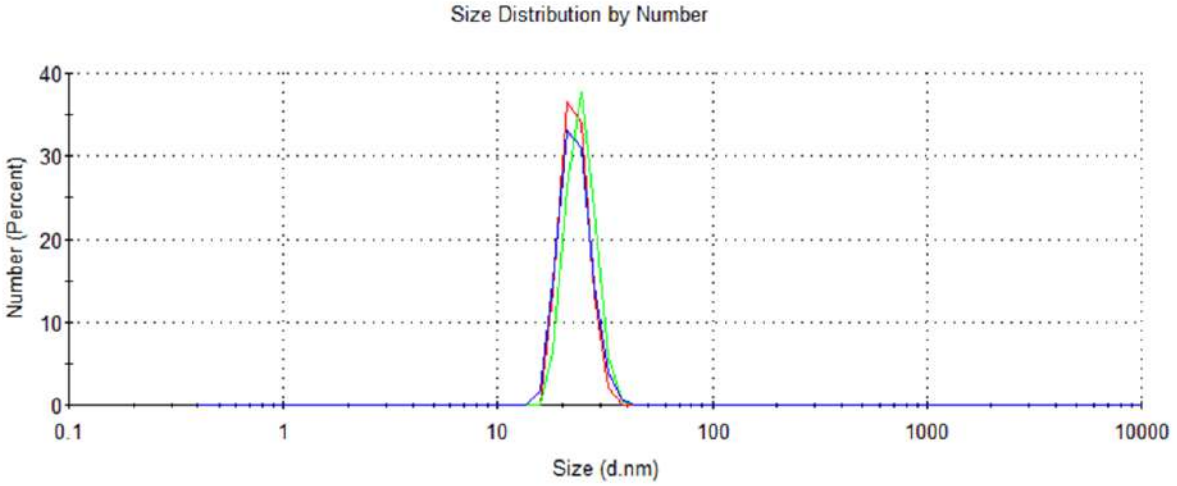

Figure S9. Hydrodynamic diameter distribution by number of amphoteric control NCs

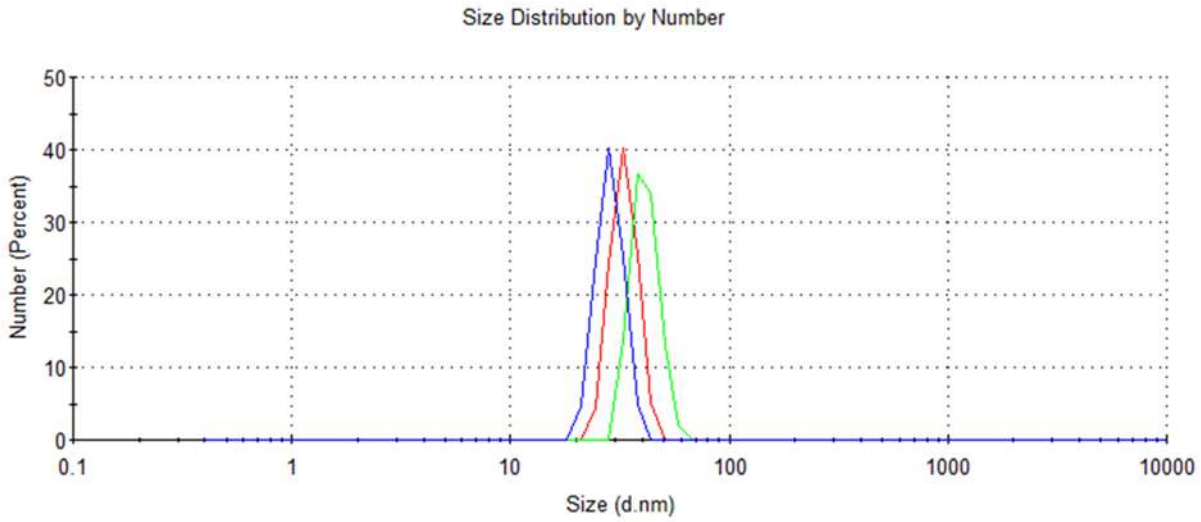

Figure S10. Hydrodynamic diameter distribution by number of cationic COUPY-NCs

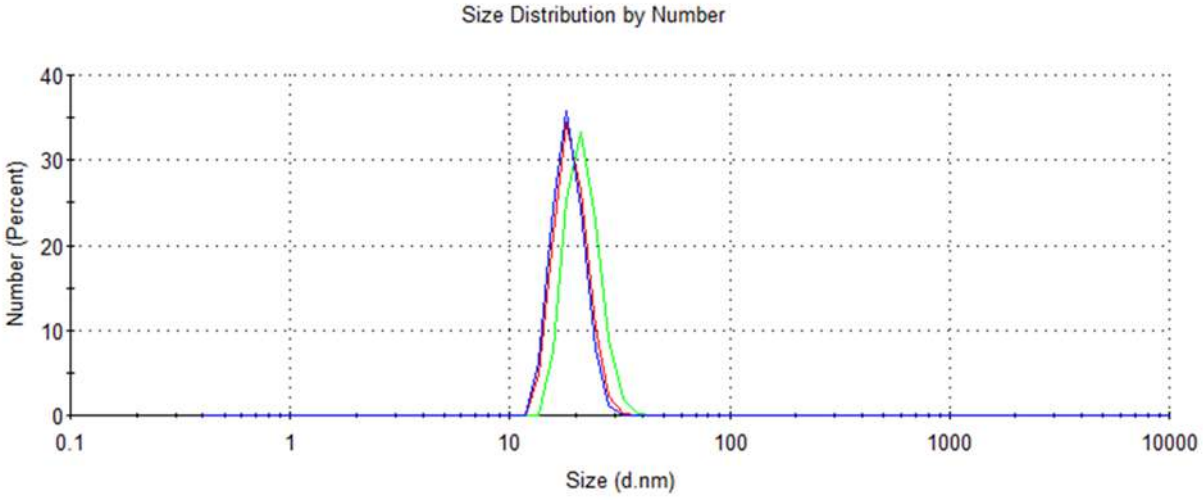

Figure S11. Hydrodynamic diameter distribution by number of amphoteric COUPY-NCs

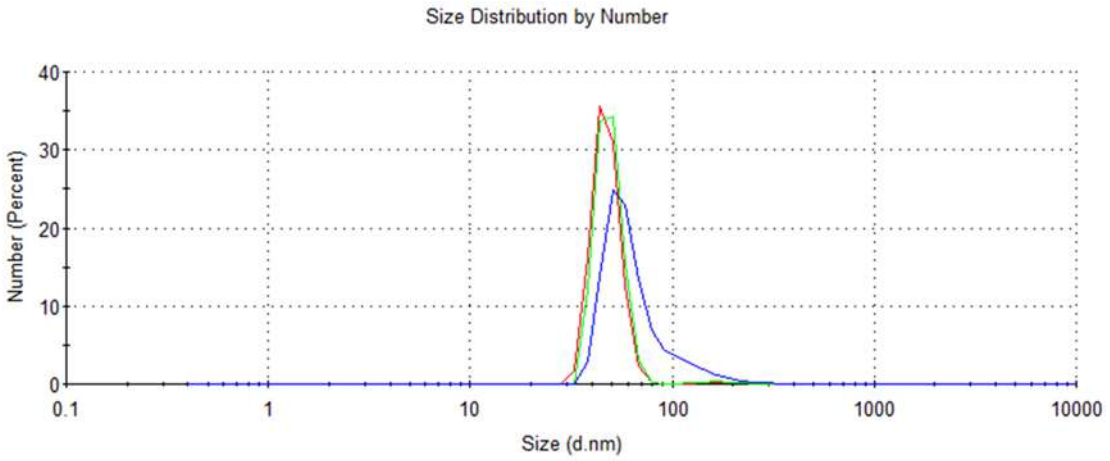

Figure S12. Hydrodynamic diameter distribution by number of cationic ICG-NCs

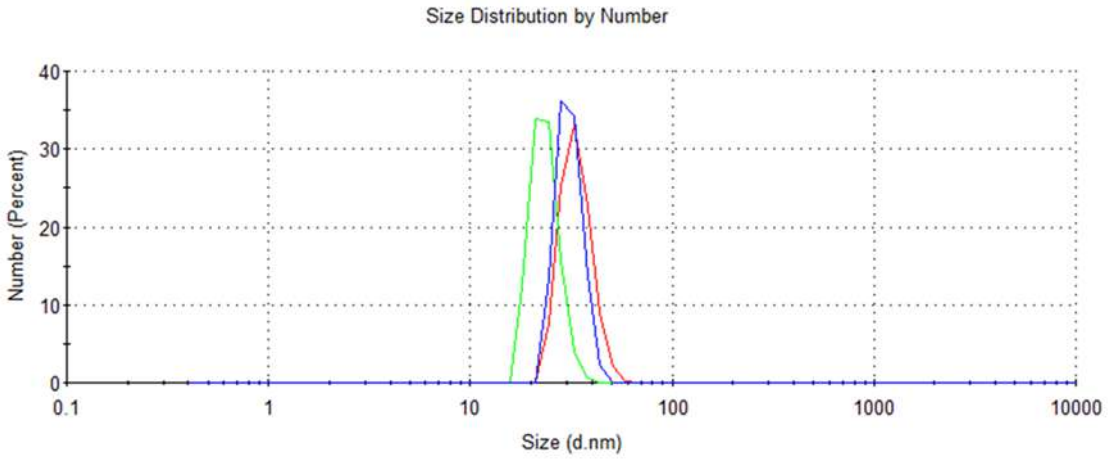

Figure S13. Hydrodynamic diameter distribution by number of amphoteric ICG-NCs

Table S3. DLS values obtained for the different types of NCs.

	Experimental Values	Average ± SD
Cationic-Control-NCs	36.36nm	34.55 ± 2.03 nm
	34.94 nm	
	32.36 nm	
Amphoteric-Control-NCs	23.03 nm	23.61 ± 0.82 nm
	24.55 nm	
	23.26 nm	
Cationic-COUPY-NCs	33.33 nm	34.59 ± 6.60 nm
	41.73 nm	
	28.71 nm	
Amphoteric-COUPY-NCs	19.09 nm	19.74 ± 1.61 nm
	21.58nm	
	18.56 nm	
Cationic-ICG-NCs	48.28 nm	55.22 ± 10.42 nm
	50.17 nm	
	67.20 nm	
Amphoteric-ICG-NCs	33.63 nm	29.37 ± 5.25 nm
	23.50 nm	
	30.98 nm	

4.3 ζ -potential of non-loaded NCs

ζ -potential (mV)	Experimental values			
	pH = 6.5	**pH = 7.0**	**pH = 7.5**	**pH = 8.0**
Cationic non-loaded NCs	50.2	47.9	36.0	32.9
	48.6	47.9	34.1	31.3
	48.3	48.2	34.5	33.8
Amphoteric non-loaded NCs	25.8	18.1	12.2	4.2
	26.2	18.2	12.0	4.33
	27.1	19.1	12.2	4.05

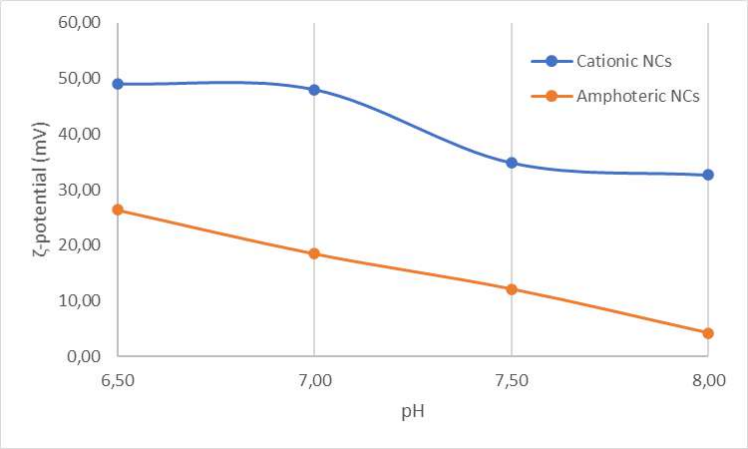

Figure S14. Plot of ζ-potential mean values of both cationic and amphiphilic non-loaded NCs vs pH

4.4. ICG and COUPY payload determination in NCs

The concentration of NCs in the final emulsions (mg/mL) was quantified with a solids concentrator, as indicated in section 2.7. Dye Loading (DL) and Encapsulation Efficiency (EE) were determined by UV-Visible spectroscopy following the method described in section 2.6. The calibration plot for COUPY and ICG, determined at 567 nm and at 794 nm, respectively, is shown in Figure S14. DL and EE parameters for NC-COUPY and NC-ICG are provided in Table S4.

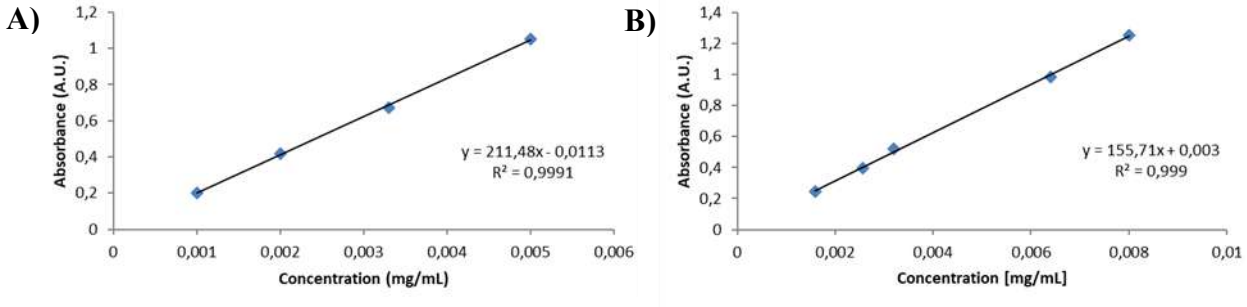

Figure S15. Calibration plot for A) COUPY and B) ICG.

Table S4. NCs concentration, DL and EE parameters for NCs.

	[NCs] (mg/mL)	Dye Loading (DL, µM)	Encapsulation Efficiency (EE, %)
Non-loaded cationic NCs	137.21 ± 1.31	-	-
Non-loaded amphoteric NCs	150.00 ± 2.00	-	-
Cationic COUPY-NCs	173.46 ± 1.16	482.99 ± 1.25	42.24%
Amphoteric COUPY-NCs	154.92 ± 2.09	470.46 ± 0.96	44.62%
Cationic ICG-NCs	199.03 ± 2.00	215.49 ± 2.58	53.91%
Amphoteric ICG-NCs	134.75 ± 0.67	237.42 ± 3.50	61.91%

4.5. TEM analysis

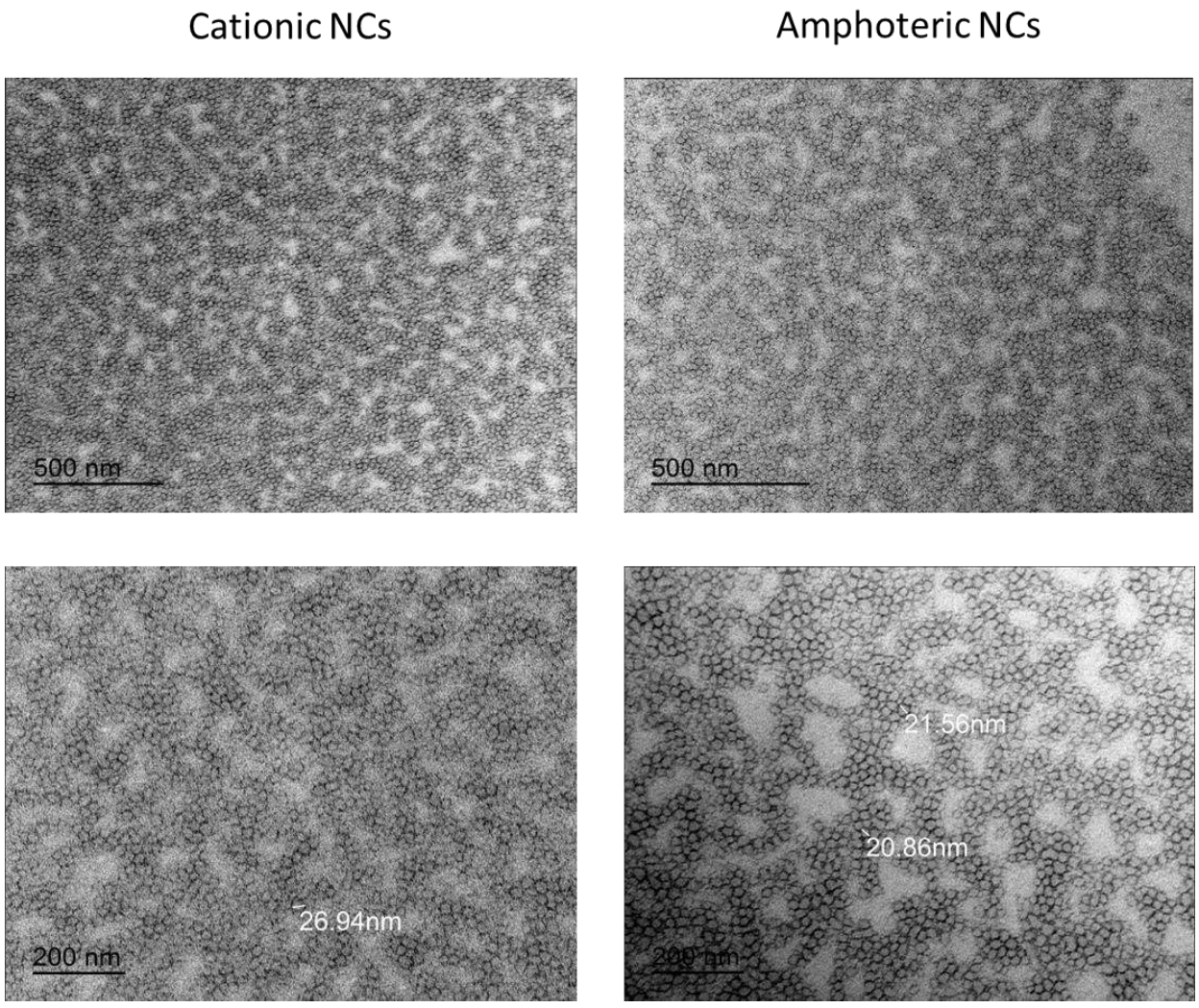

Figure S16. TEM micrographs of cationic and amphoteric control NCs

4.6 Stability of amphoteric ICG-loaded NCs under different conditions

The stability of the fluorescent probe, either free or nanoencapsulated, was evaluated in PBS buffer by UV-vis spectroscopy after subjected to three different experimental conditions during 1 week: 1) fridge storage at 4 ºC in the darkness, 2) room temperature (RT) storage under ambient light, and 3) oven incubation at 37 ºC in the darkness. The absorbance of each sample has been normalized against the maximum absorbance at the starting point of the experiment.

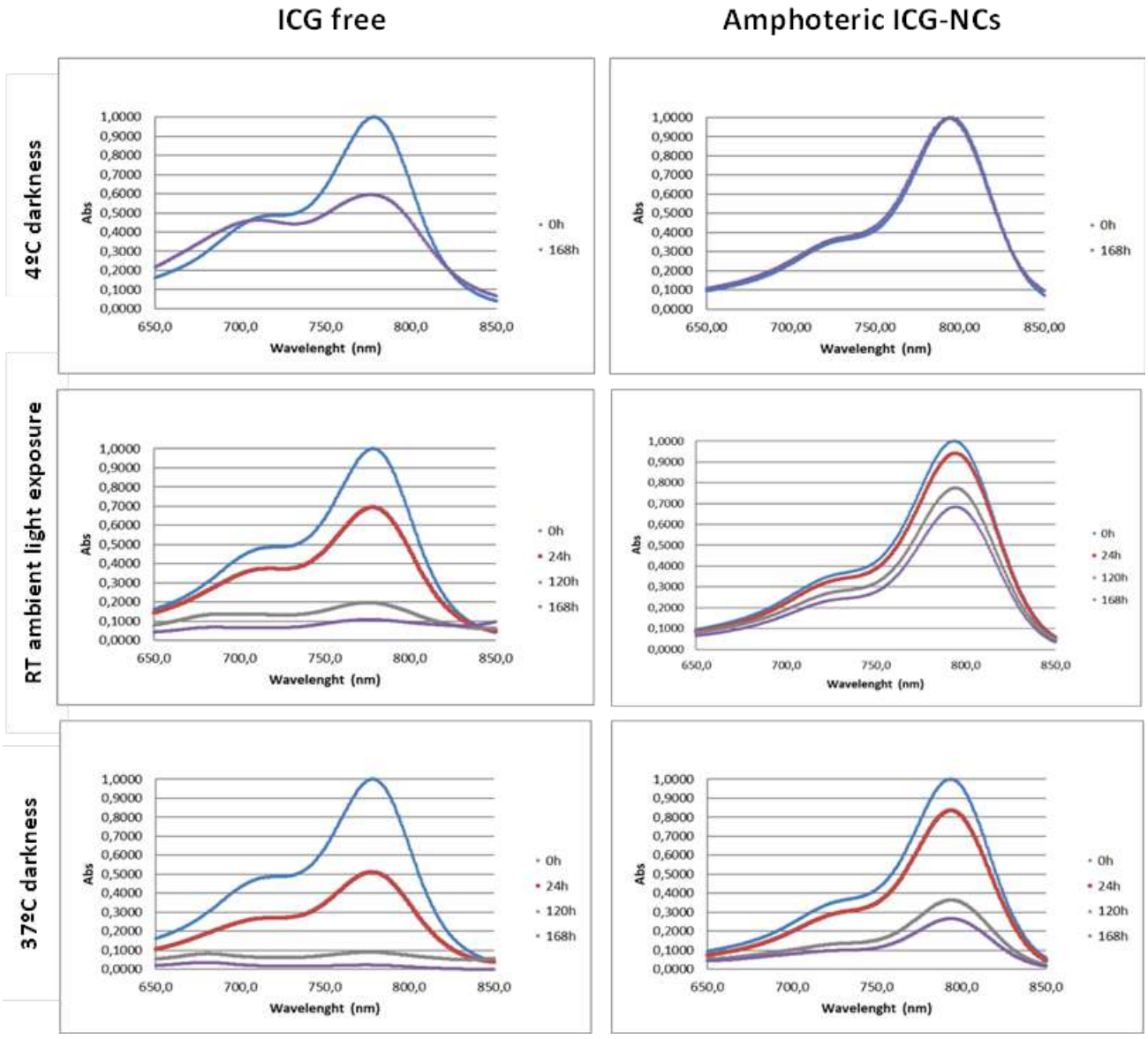

Figure S17. Normalized UV-visible absorption spectra of ICG free and amphoteric ICG-loaded NCs after 1 week (168 h) under different experimental conditions: 1) Fridge storage at 4 ºC in the darkness, 2) Room temperature (RT) storage at ambient light exposure and 3) incubation at 37 ºC in the darkness.

5. Biological studies

5.1. Internalization evaluation of ICG-loaded NCs in human monocyte derived dendritic cells (moDCs) by confocal microscopy

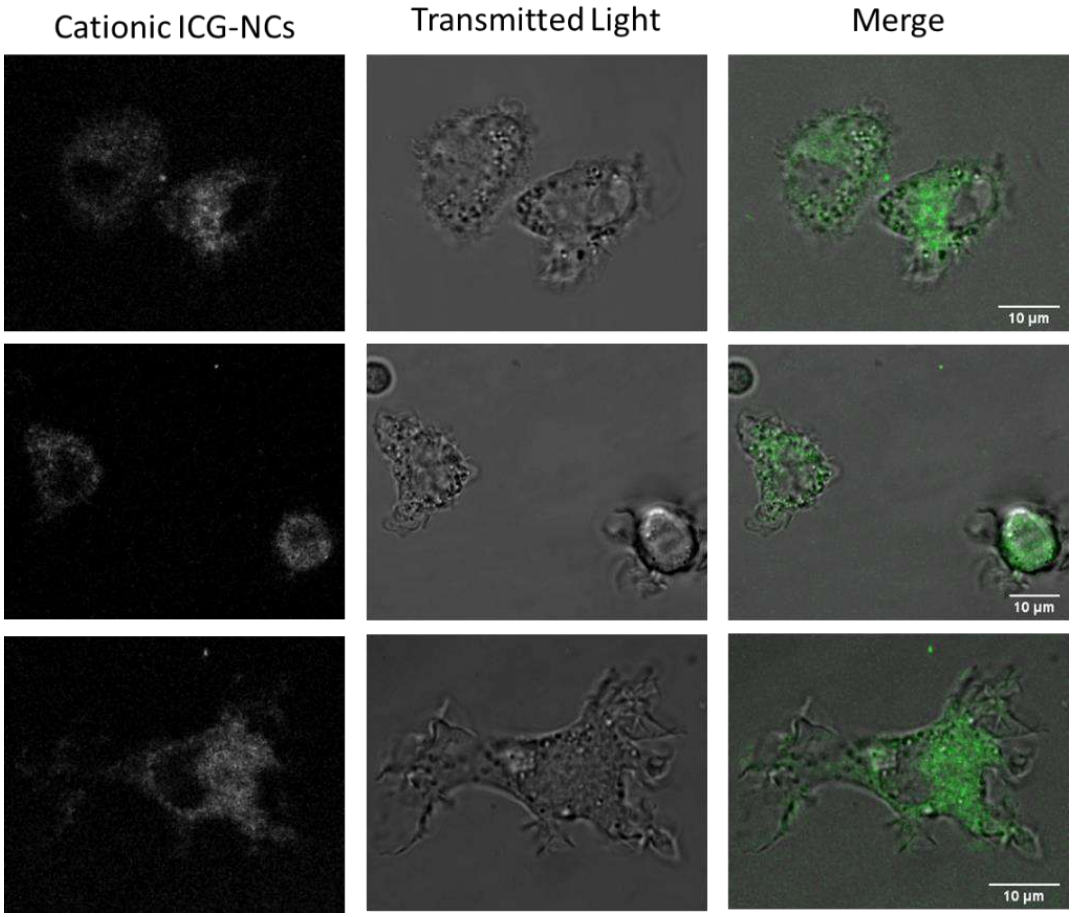

Figure S18. Internalization pattern for cationic NCs-ICG at 2 µM of ICG in moDCs for 2 h incubation at 37 ºC. Scale bar represents 10 µm.

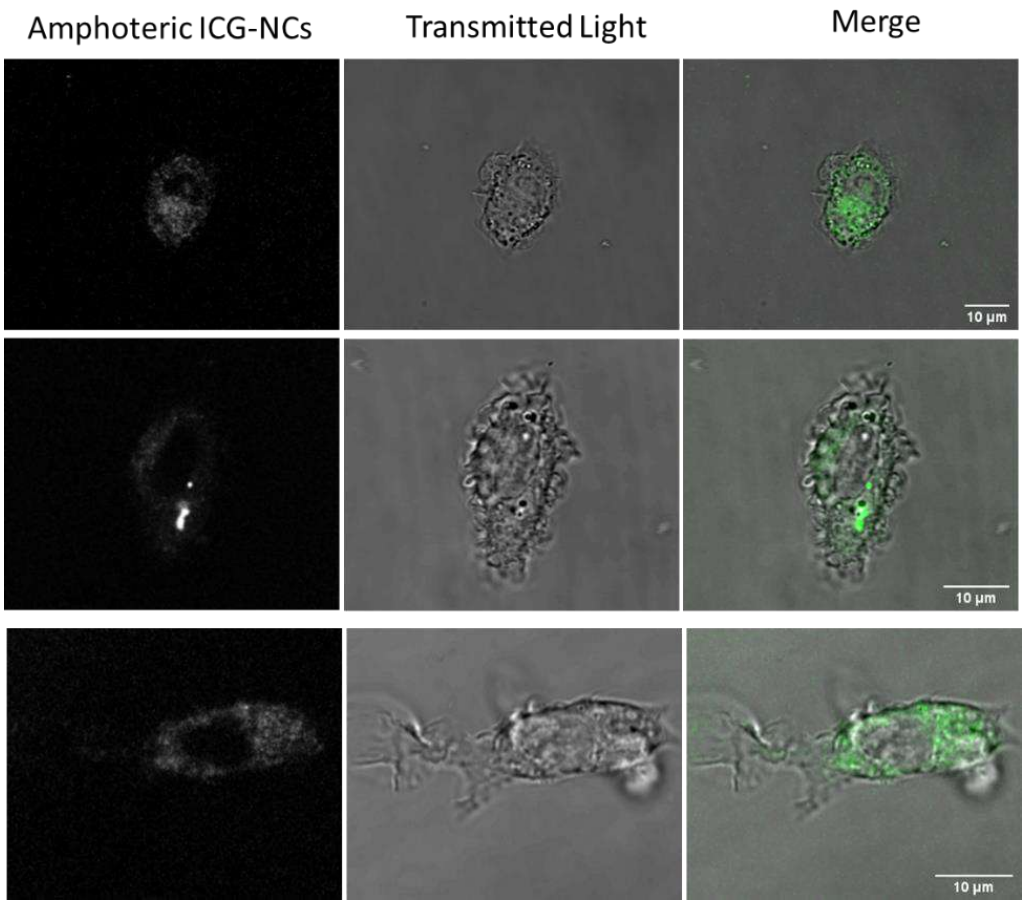

Figure S19. Internalization pattern for amphoteric NCs-ICG at 2 µM of ICG in moDCs for 2 h incubations at 37 ºC. Scale bar represents 10 µm.

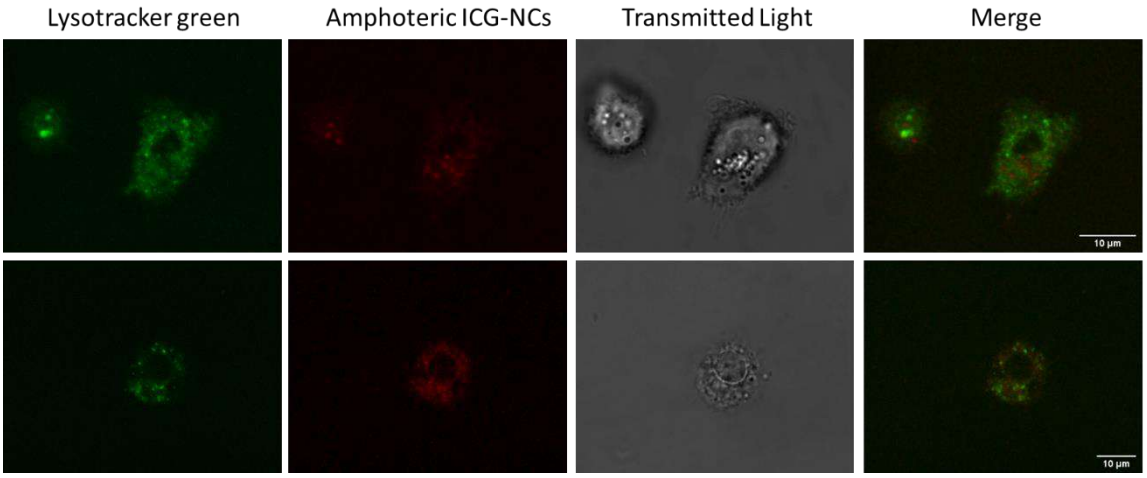

Figure S20. Colocalization pattern of amphoteric ICG-NCs and Lysotracker Green in moDCs. Incubation for 2 h at 37 ºC.

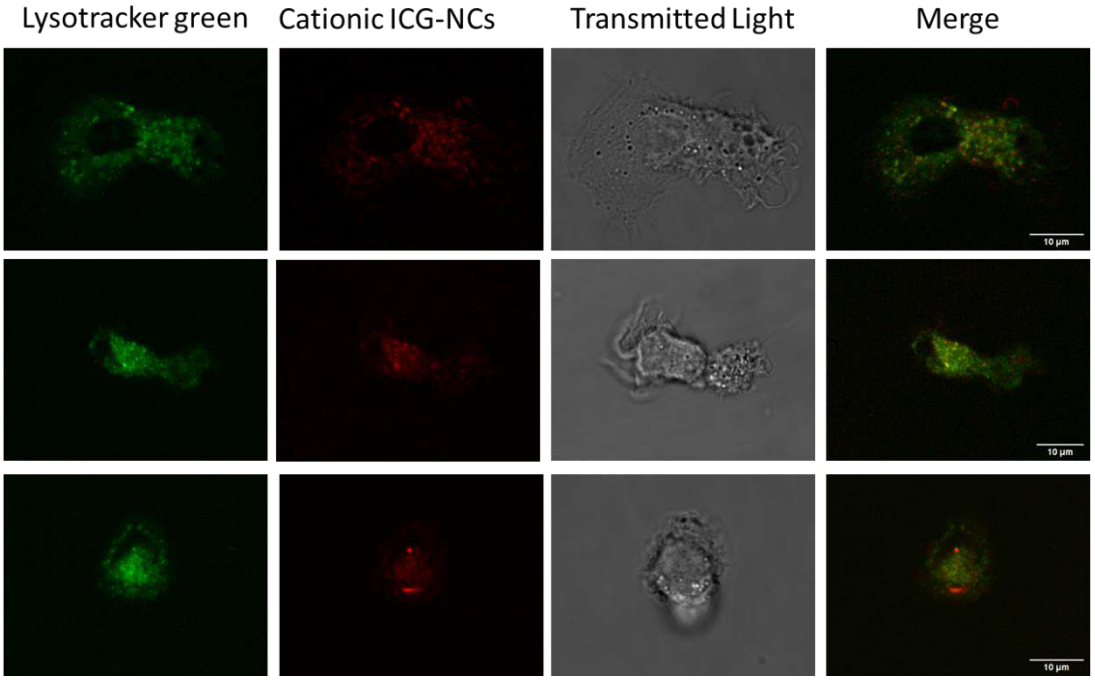

Figure S21. Colocalization pattern of cationic ICG-NCs and Lysotracker Green in moDCs. Incubation for 2 h at 37 ºC.

5.2. *In vitro* Internalization studies in human monocyte derived immature DCs by Flow Cytometry

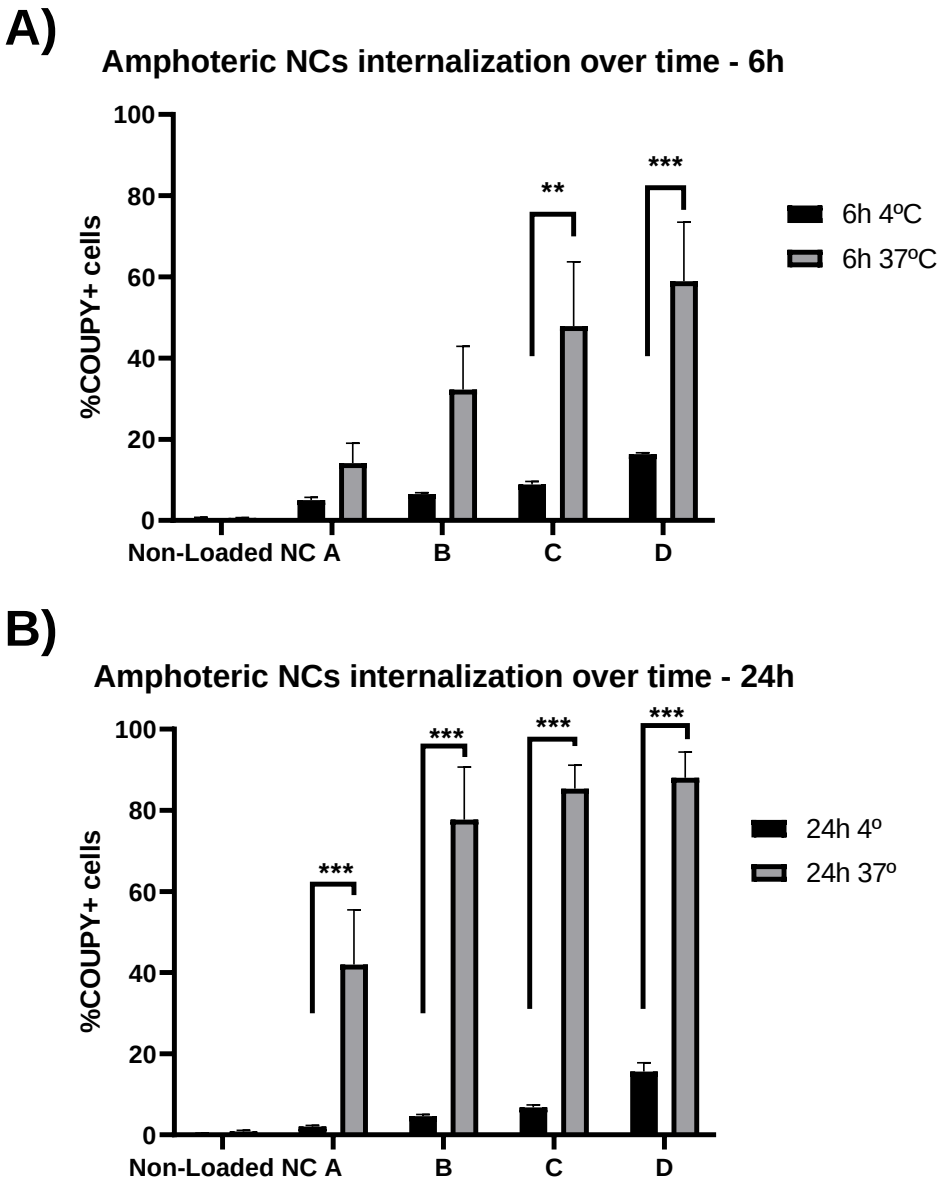

Figure S22. COUPY-loaded amphoteric nanoparticles internalization over time: A) 6h incubations and B) 24 h incubations. Conditions A-D correspond to NC concentrations of: A) 1.24 µL/mL, B) 3.105 µL/mL, C) 6.21 µL/mL, D) 12.42 µL/mL and Non-loaded NC) 1.,61 µL/mL. The graphic depicts percentages of COUPY-positive DCs from n=3 independent experiments. Significance was determined by unpaired T-tests assuming an equal scatter amongst samples using the Holm-Sidak method. p value outputs are in APA style (.12(ns), .33(*), .002(**), <.001(***)). Two-way ANOVA tests and Sidak's multiple comparisons test with a single pooled variance determined no statistical significance among 4ºC samples, and for 37 ºC samples a p=.002(**) between conditions A-D (A), a p=.002(**) between conditions A-B and A-C (B) and a p=<.001(***) between conditions A-D (B).

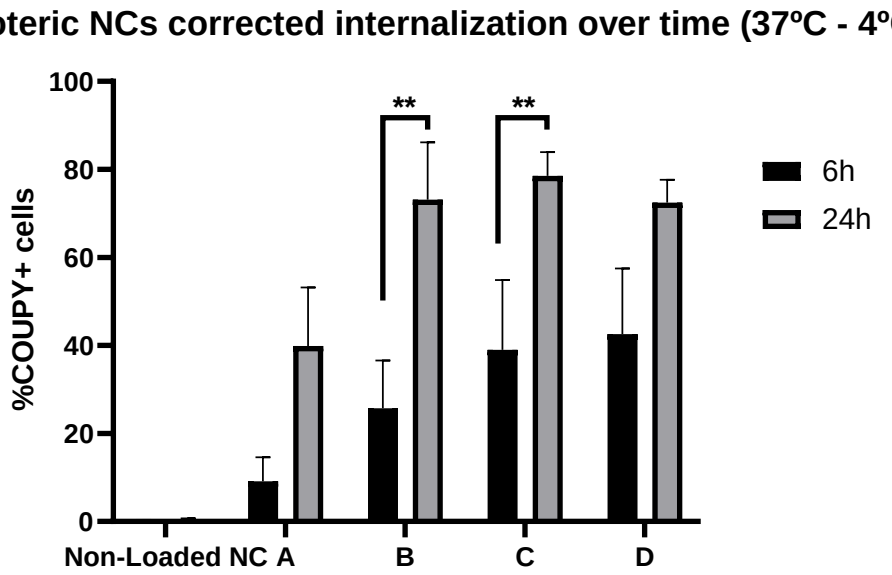

Figure S23. COUPY-loaded amphoteric NCs corrected internalization. 6 h versus 24 h incubations. 4 ºC positive percentages have been subtracted from 37 ºC ones to correct for membrane bound NCs. Conditions A-D correspond to NC concentrations of: A) 1.24 µL/mL, B) 3.105 µL/mL, C) 6.21 µL/mL, D) 12.42 µL/mL and Non-loaded NC) 1.61 µL/mL. Graphic depicts n=3 experiments. Significance was determined by unpaired T-tests assuming an equal scatter amongst samples using the Holm-Sidak method. p value outputs are in APA style (.12(ns), .33(*), .002(**), <.001(***)).

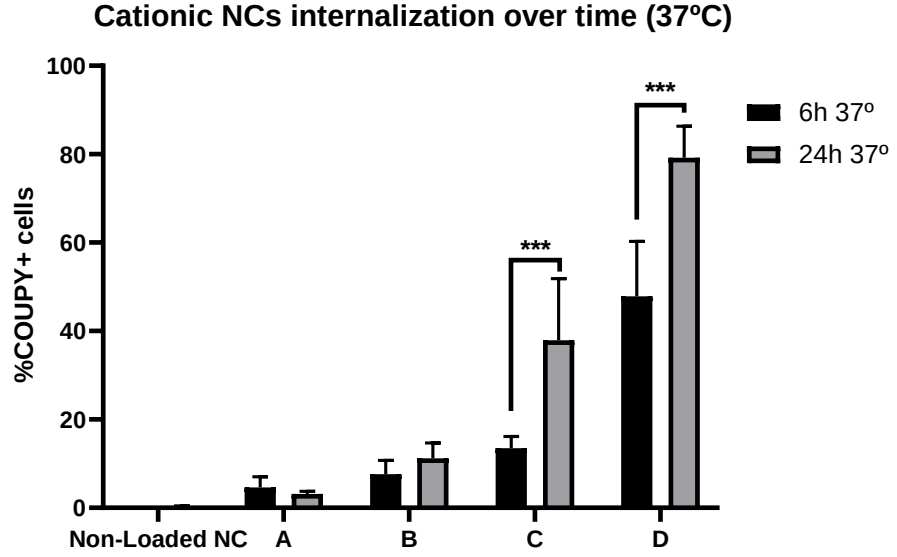

Figure S24. COUPY-loaded cationic NCs internalization over time. 6 h versus 24 h incubations at 37ºC. Conditions A-D correspond to NC concentrations of: A) 0.619 µL/mL, B) 1.55 µL/mL, C) 3.1 µL/mL, D) 6.19 µL/mL and Non-loaded NC) 3.29 µL/mL. Graphic depicts n=4 independent experiments. Significance was determined by unpaired T-tests assuming an equal scatter amongst samples using the Holm-Sidak method. p value outputs are in APA style (.12(ns), .33(*), .002(**), <.001(***)).

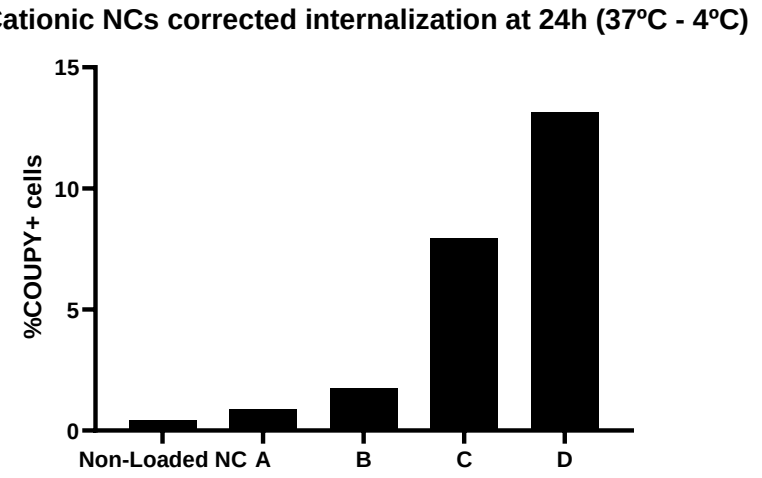

Figure S25. COUPY-loaded cationic NCs internalization at 24 h incubations. 4º positive percentages have been subtracted from 37ºC ones to correct for membrane bound NCs. Conditions A-D correspond to NC concentrations of: A) 0.619 µL/mL, B) 1.55 µL/mL, C) 3.1 µL/mL, D) 6.19 µL/mL and Non-loaded NC) 3.29 µL/mL. Graphic depicts n=1 independent experiments.

5.3 *In vivo* safety assay of amphoteric and cationic control NCs

Table S5. Hematological parameters in blood (Mean ± SD)

Indexes	*Control*	*Cationic control NCs*			*Amphoteric control NCs*		
Concentration		low	medium	high	low	medium	high
WBC (10^3/uL)	3,31±0,02	3,12±0,51	4,14±1,09	2,49±0,18	3,63±0,87	3,57±1,15	2,79±0,29
RBC (10^6/uL)	10,76±0,48	10,43±0,05	10,5±0,45	11,22±0,08	10,45±0,04	10,63±0,11	10,82±0,09
HGB (g/dL)	16,2±1,27	15,9±0	15,86±0,81	17,06±0,32	15,85±0,21	16,03±0,2	16,43±0,05
HCT (%)	47±2,54	45,76±0,25	46,2±2,42	49,1±0,75	45,7±0,14	46,7±0,52	47,66±0,15
MCV (fL)	43,7±0,42	43,9±0,36	44±0,55	43,76±0,4	43,75±0,35	43,93±0,23	44,06±0,45
MCH (pg)	15,05±0,49	15,23±0,05	15,06±0,23	15,2±0,17	15,2±0,28	15,1±0,09	15,16±0,15
MCHC (g/dL)	34,4±0,84	34,73±0,15	34,33±0,15	34,76±0,3	34,65±0,35	34,33±0,05	34,46±0,05
PLT (10^3/uL)	880,5±137,9	876,3±54,6	652,7±399,2	1005,3±102	798,5±217,1	962,7±293,9	784,3±224,1
LYMPH (%)	79±1,27	68,43±9,06	59,43±1,96	53,93±10,05	63,85±6,15	59,73±6,65	31,2±25,63
MONO (%)	1,65±0,21	1,1±0,6	1,63±0,23	2±0,55	1,15±0,63	0,96±0,6	1,9±0,43
NEUT (%)	17,25±2,33	27,73±8,97	30,7±1,44	38,16±6,29	28,75±0,35	29,36±3,49	56,5±18,55
EO (%)	2,1±0,84	2,73±1,01	8,16±3,32	5,9±4,24	6,1±6,92	9,93±6,83	10,4±8,11
BASO (%)	0±0	0±0	0,06±0,11	0±0	0,15±0,21	0±0	0±0

Table S6. Biochemical parameters in serum (Mean ± SD)

Indexes	*Control*	*Cationic control NCs*			*Amphoteric control NCs*		
Concentration		low	medium	high	low	medium	high
Body weight	1,35±1,17	0,69±1,2	0,81±1,41	0,5±0,87	1,5±2,6	1,15±1,23	1,85±1,66
Albumin (g/dL)	2,87±0,06	2,59±0,24	2,49±0,09	3,31±1,09	2,51±0,17	2,61±0,28	2,44±0,71
ALT (U/L)	61,06±22,81	61,73±30,69	42,3±12,47	87,33±81,12	60,05±47,2	42,4±24,97	42,45±12,51
AST (U/L)	930±132,8	785,13±305	915,2±123,2	1103,46±702	577±172,5	792,16±92,6	600,76±295
TBIL (mg/dL)	<0.02	<0.02	<0.02	<0.02	<0.02	<0.02	<0.02
CREA (mg/dL)	0,18±0,06	0,22±0,06	0,27±0,03	0,17±0,03	0,2±0,03	0,21±0,03	0,5±0,46
GGT (U/L)	< 1	< 1	< 1	< 1	< 1	< 1	< 1
Potassium (mmo/L)	7,37±0,3	5,36±0,23	6,17±0,84	9,64±3,67	9,61±4,16	6,81±1,38	6,25±1,48
Total proteins (g/dL)	5,04±0,48	4,38±0,49	4,29±0,22	5,54±1,47	4,51±0,31	4,56±0,38	4,35±1,27
Sodium (mmol/L)	151,2±0,6	147,6±2,26	143,56±2,05	145,26±5,97	141,36±4,8	143,36±3,09	154,03±5,68
Urea (mg/dL)	41,17±6,8	37,93±4,96	33,99±4,66	38,69±6,24	32,69±0,57	30,98±1,44	169,48±236

5.4. Biodistribution of amphoteric and cationic ICG-loaded NCs in mice models.

5.4.1 *In vivo* fluorescence imaging biodistribution in healthy mice.

5.4.1.1 Intravenous administration in C57BL/6 mice.

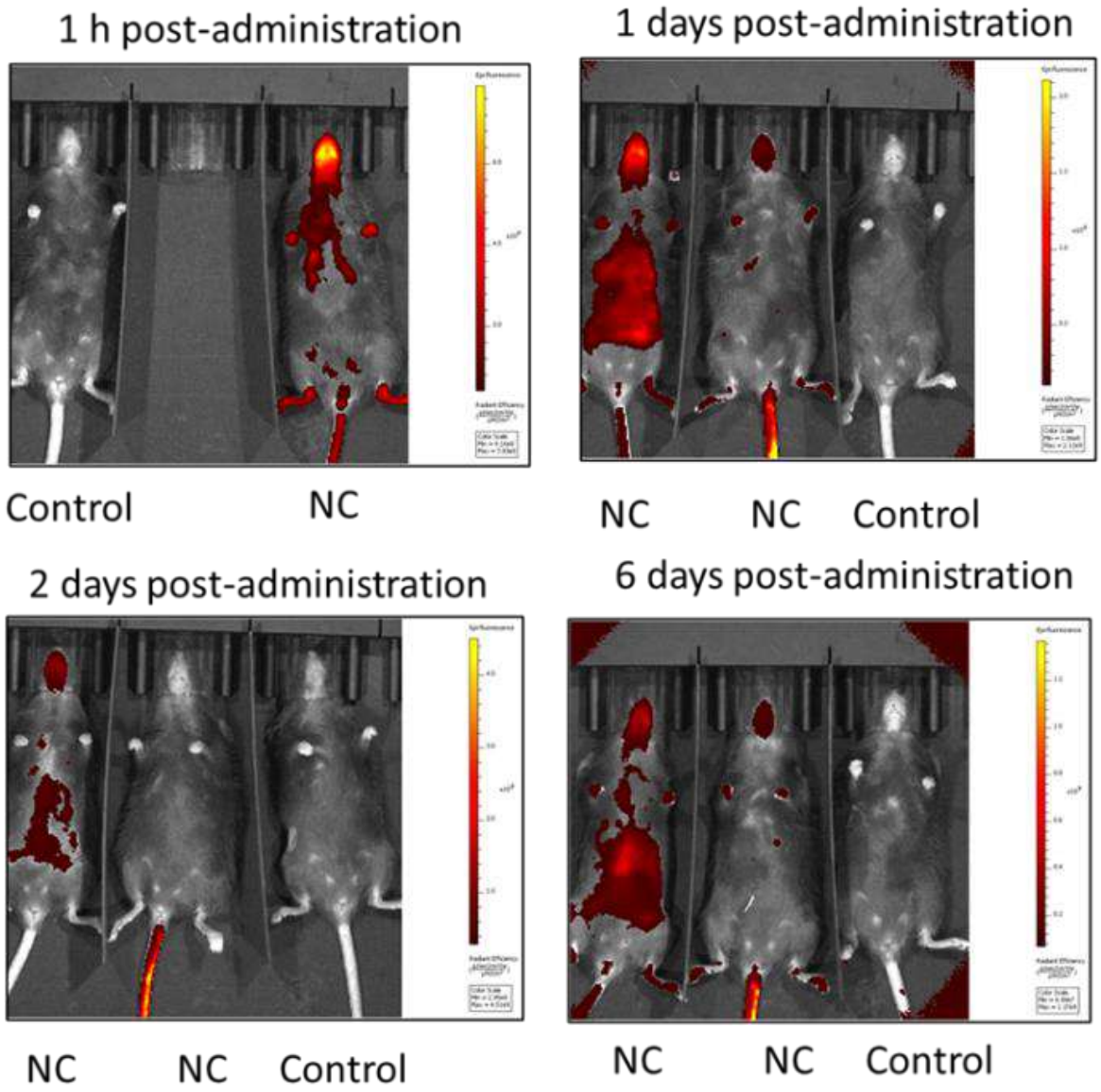

Figure S26. Cationic ICG-NCs (200 µL, 40 µM ICG) were intravenously administrated to female C57BL/6 mice (n=2). Fluorescence was monitoring by *in vivo* imaging system (IVIS; Perkin Elmer, Waltham, MA, USA,) using excitation/emission wavelengths of 780 nm/845 nm

5.4.1.2 Comparison on excretion organs NCs signal between different administrations in C57BL/6 mice model

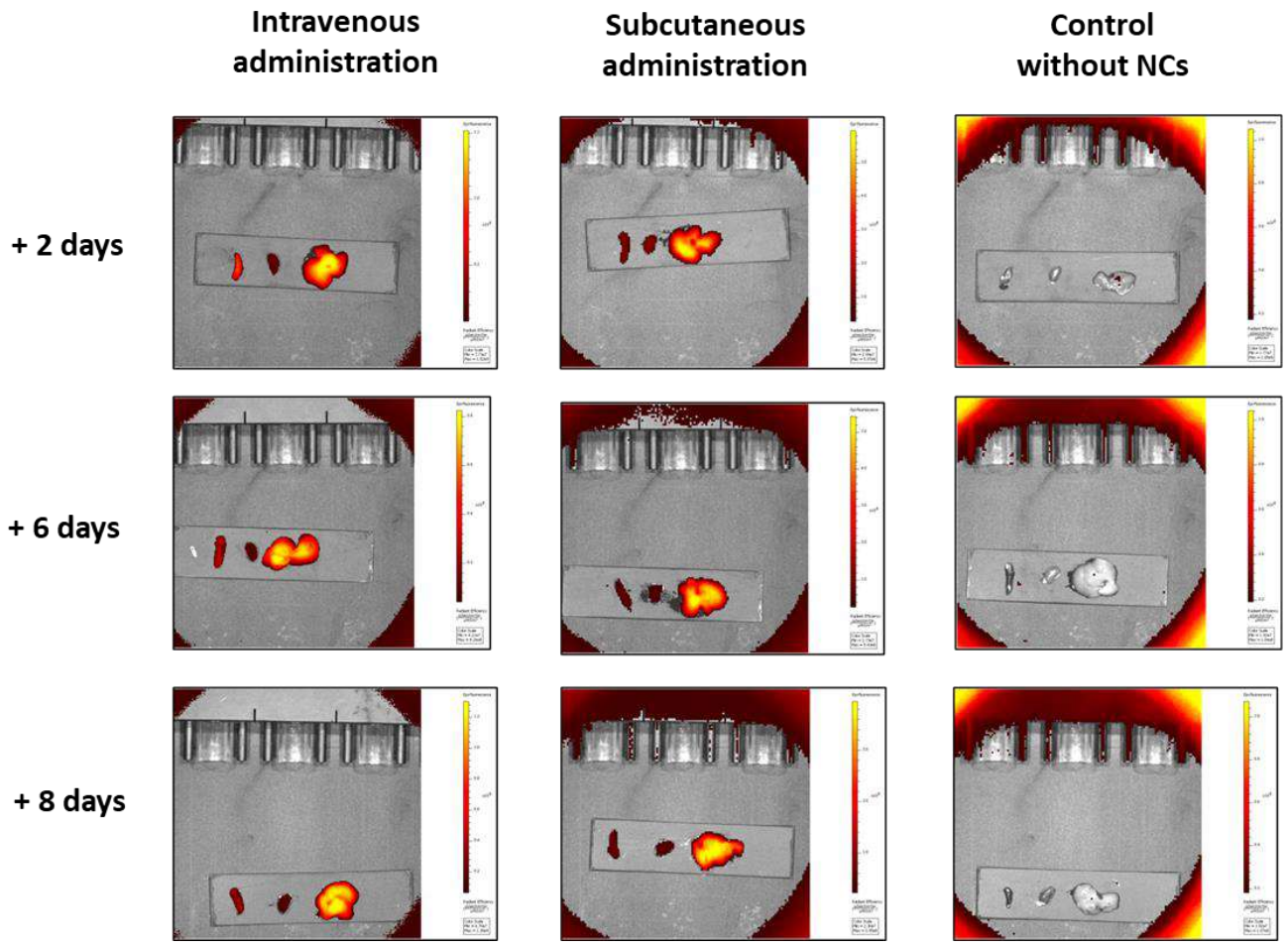

Figure S27. Cationic ICG-NCs (200 µL, 40 µM of ICG) were intravenously or subcutaneously administrated to female C57BL/6 mice (n=2/group). At indicated time points mice were euthanized and spleen (left), kidney (middle) and liver (right) were obtained for fluorescence monitoring by *in vivo* imaging system (IVIS; Perkin Elmer, Waltham, MA, USA,) using excitation/emission wavelengths of 780 nm/845 nm.

5.4.1.3 Intravenous administration biodistribution comparison between ICG, amphoteric ICG-NCs and cationic ICG-NCs at 1 h, 24 h and 48 h in healthy BALB/C mice model

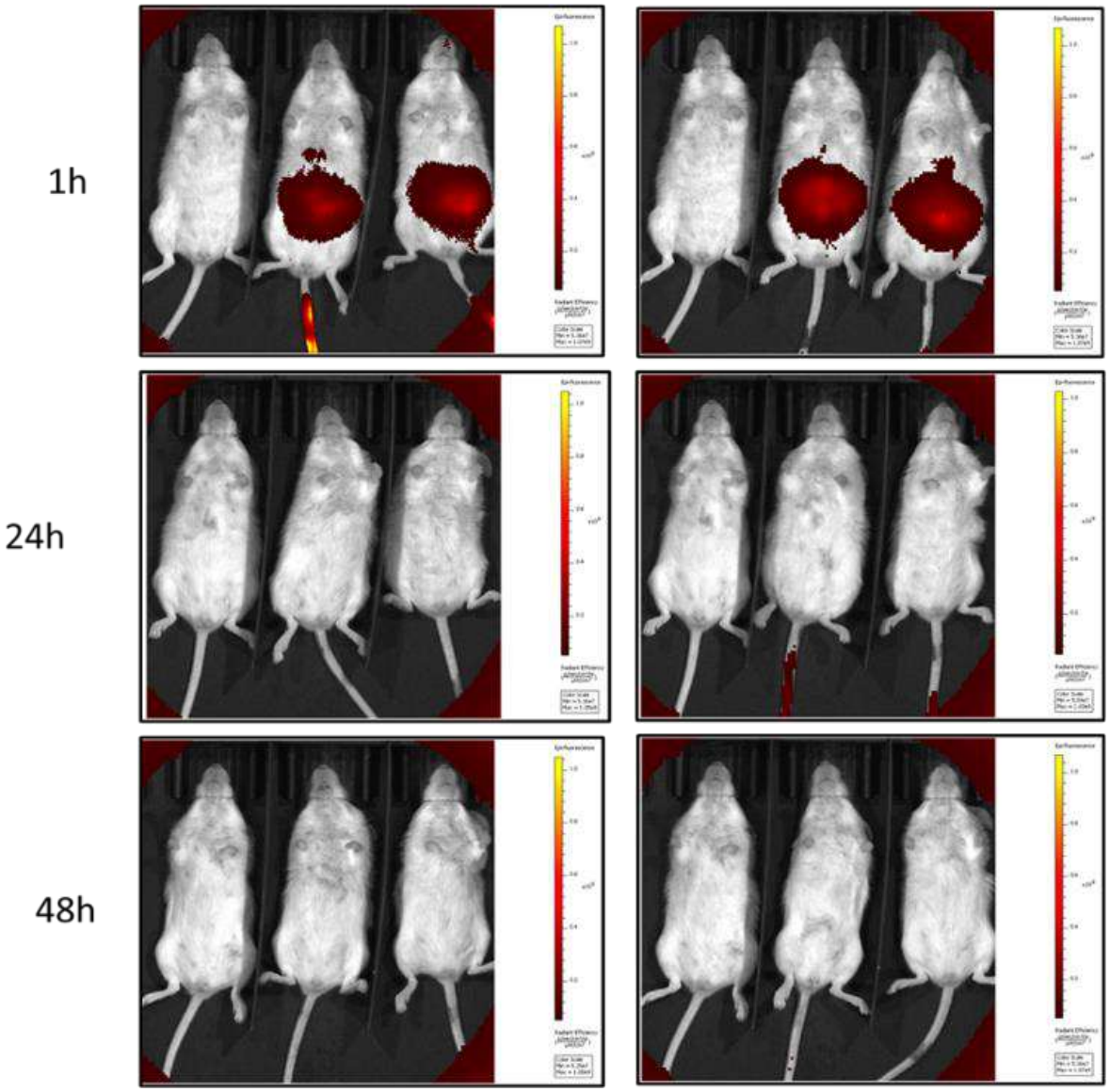

Figure S28. Intravenous administration of 160 µl, 40 µM of free **ICG**, on BALB/C mice group (n=4 mouse. Control mouse located in the left-side of each image.

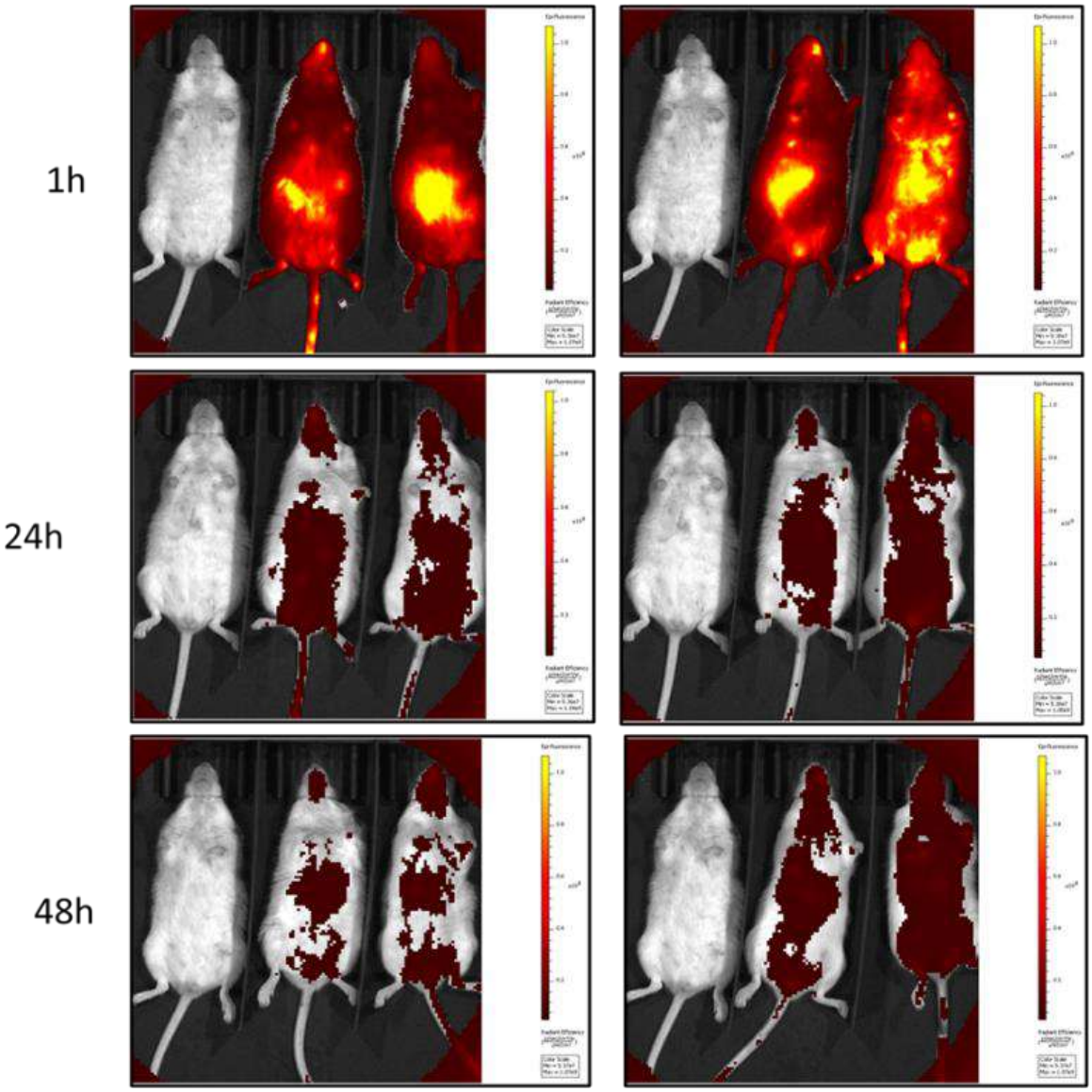

Figure S29. Intravenous administration of 160 µl, 40 µM of ICG in 30 mg/mL of cationic ICG-NCs, on BALB/C mice group (n=4 mouse). Control mouse located in the left-side of each image.

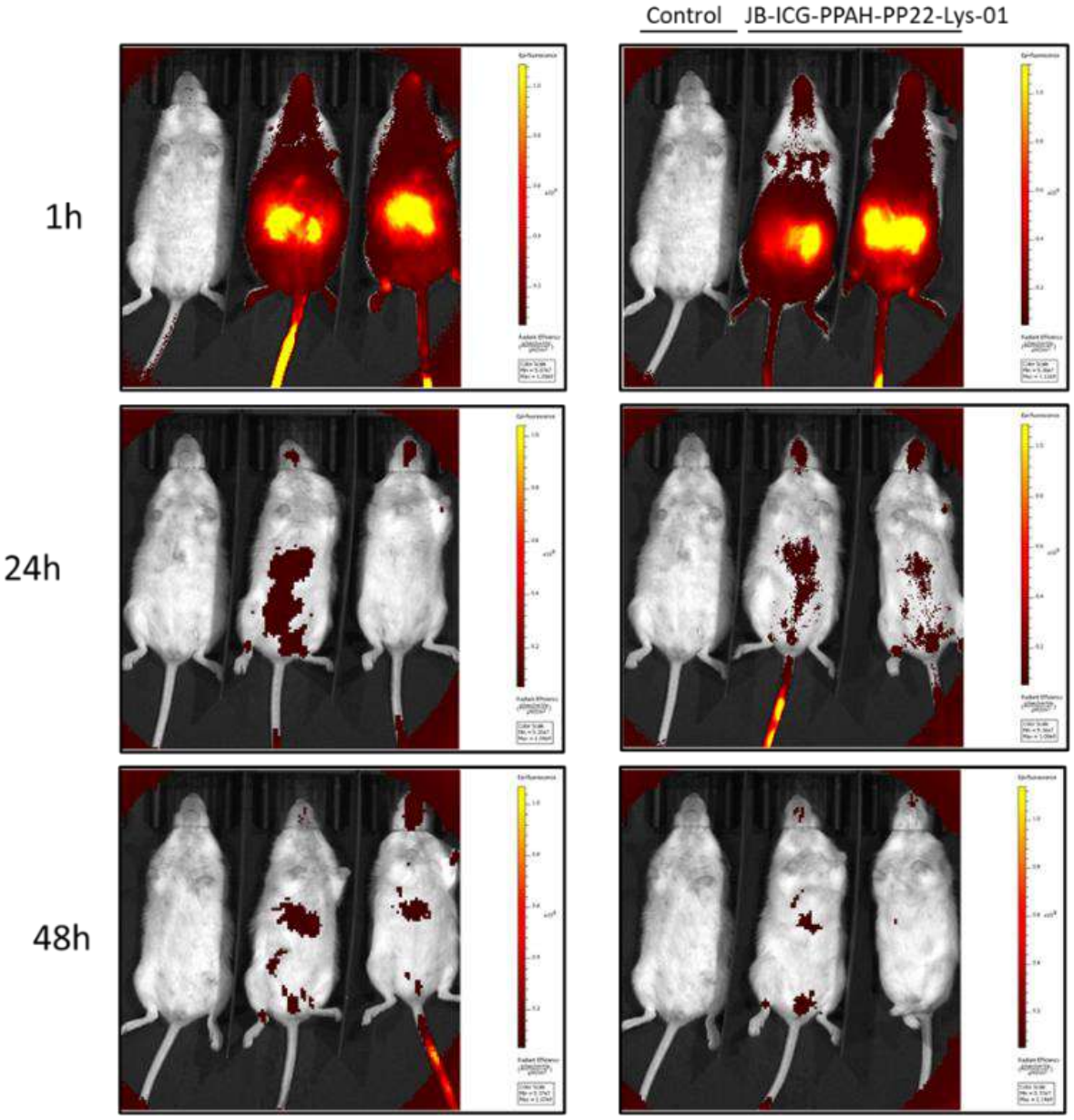

Figure S30. Intravenous administration of 160 µl, 40 µM of ICG in 30 mg/mL of amphoteric ICG-NCs, on BALB/C mice group (n=4 mouse). Control mouse located in the left-side of each image.

5.4.2 *In vivo* fluorescence imaging biodistribution in subcutaneous tumor mice models.

Female NSG mice (9 weeks old, Charles River) were challenged by s.c. injection of A375 (1×106) cells on the right flank with a 23-gauge needle. Amphoteric ICG-NCs and cationic ICG-NCs were administered i.v. at day 14 post-tumor challenge. PBS and ICG free were injected to control groups. Fluorescence was monitoring by *in vivo* imaging system (IVIS; Perkin Elmer, Waltham, MA, USA,) using excitation/emission wavelengths of 780 nm/845 nm.

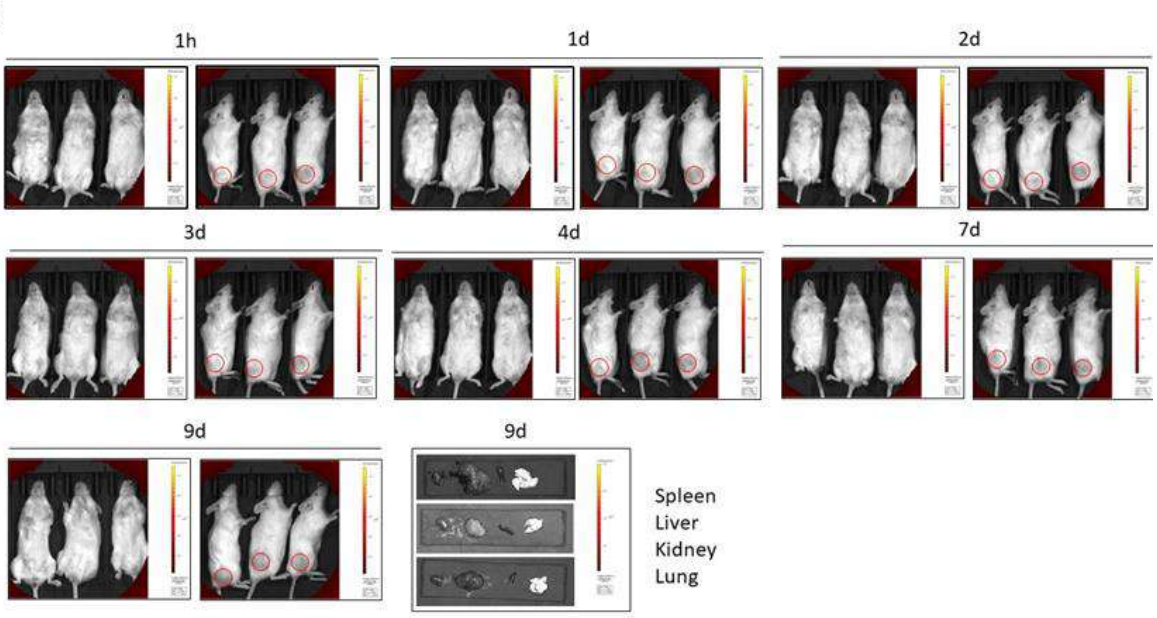

Figure S31. *In vivo* imaging of systemic biodistribution of ICG loaded nanocapsules in NSG mice. A375 challenged NSG mice were treated with vehicle (PBS) (n=3/group). Locations for tumor cells injections have been indicated with a red circle.

Conclusions

12. Conclusions

This Thesis aimed to contribute to the development of novel polyurethane-polyurea hybrid nanocapsules as potential nanomedical solutions in cancer theragnosis. Basically, this Thesis lays the groundwork for the biomedical use of such nanoentities i) to improve the delivery and enhance the phototoxic activity of different photosensitizers in anticancer PDT, including COUPY-based organic fluorophores, ruthenium(II) polypyridyl complexes and zinc-phthalocyanine derivatives; ii) to promote the bioavailability of liposoluble cyclometalated iridium(III) anticancer complexes; and iii) to encapsulate hydrosoluble bioactive molecules such as Indocyanine Green by using a novel technology that furnishes double-walled water-in-oil-in-water polyurethane-polyurea hybrid nanocapsules that preferentially accumulate in TME.

According to the previously proposed objectives and to the results presented throughout this Thesis, the main conclusions of this work are the following ones:

Chapter I

- The encapsulation of a liposoluble coumarin-based photosensitizer (**COUPY 2**) in polyurethane-polyurea hybrid nanocapsules was accomplished with high efficacy.
- Photostability and fluorescence quantum yield in aqueous media of **COUPY 2** were improved through the encapsulation.
- A strong ROS generation under green to red broad band light irradiation has been assessed for both free and encapsulated forms of **COUPY 2** photosensitizer, in both 2D and 3D relevant *in vitro* models of cancer cells.
- Apoptosis was identified as the principal cell-death mechanism induced by **NC-COUPY-2** after light irradiation.
- The encapsulation of liposoluble ruthenium(II) polypyridyl complexes (**Ru1** and **Ru2**) was properly accomplished, which allowed to enhance their biological properties as novel far-red/NIR-operating PDT agents.
- Biological studies in several cancer and healthy cell lines confirmed the potential application of **Ru1-NCs** and **Ru2-NCs** in PDT, exhibiting extraordinary phototoxicities against CT-26 cancer cells, even under NIR irradiation in the case of **Ru2-NCs**, leading to substantially increased PI values compared with the non-encapsulated compounds.
- A mitigated toxicity in healthy cell lines was also identified for Ru(II)-loaded nanocapsules, thus increasing the selectivity factor against cancer cells, in comparison to the non-encapsulated compounds.

- The encapsulation of **Zn(Pc)** and **Ir-Zn(Pc)** photosensitizers in polyurethane-polyurea hybrid nanocapsules was accomplished with moderate efficacy.
- *In vitro* vehiculation of **Zn(Pc)** and **Ir-Zn(Pc)** in cancer cells was achieved owing to the nanoencapsulation, which allowed to confirm a high photoactivity for both nanoencapsulated compounds under red light irradiation.

Chapter II

- The encapsulation of homoleptic and heteroleptic liposoluble cyclometalated iridium(III) anticancer complexes (**Ir1** and **Ir2**) was accomplished with high efficacy, maintaining their spectroscopic properties in water-based dispersion.
- An efficient cellular uptake in HeLa cells was confirmed for both **NC-Ir1** and **NC-Ir2** by ICP-MS and confocal microscopy.
- A strong cytotoxic activity for both nanoformulations was confirmed by *in vitro* resazurin-based assays.
- Cell death pathways promoted by **NC-Ir1** and **NC-Ir2** were associated with late-apoptotic and necrotic events.
- DNA-damage and cell respiration disfunction were also found to be increased by **NC-Ir1** and **NC-Ir2** cells treatment.

Chapter III

- A novel synthetic methodology for encapsulating hydrosoluble bioactive compounds using double-walled polyurethane-polyurea hybrid nanocapsules was successfully developed by employing a water-in-oil-in-water double emulsion system.
- Encapsulation of the FDA-approved NIR fluorescent probe Indocyanine Green (ICG) was successfully accomplished with high yield.
- The extracorporeal *in vivo* monitorization of the nanostructured probe was validated using IVIS® technology.
- Amphoteric functionalization on ICG-loaded nanocapsules was revealed to be an important starting point for the development of *in vivo* selective TME accumulation of nanomedicines in a melanoma-challenged mouse model.
- The intravenous administration of amphoteric ICG-NCs did not lead, after a 9-days treatment, to unspecific accumulation in the principal excretion organs.

- Besides the bioimaging application, the promoted *in vivo* accumulation in TME of amphoteric ICG-loaded nanocapsules underpins their plausible use for TME-targeted delivery of hydrosoluble anticancer agents.

Summaries

Resúmenes de resultados y discusión

Breve introducción a la nanomedicina y su uso en oncología

La nanomedicina engloba todas aquellas técnicas y/o aplicaciones en las que se empleen o modifiquen entidades menores de 1 μm para un fin terapéutico o diagnóstico en alguno de los campos de la medicina. Dentro de esta definición tan general, los sistemas nanométricos de liberación controlada de fármacos (DDS, por sus siglas en inglés) son unos de los métodos más de moda en oncología, debido a la capacidad adaptativa que presentan para acumular y liberar, de manera selectiva y eficaz, fármacos con potencial antitumoral.

Dada la particular biología del cáncer, en especial aquella derivada de la agrupación en clústeres de células tumorales sobre tejidos epiteliales que acaba originando tumores sólidos, diferentes aproximaciones nanomédicas se han focalizado en diseñar nanovehículos que, por sus características físicas, químicas o biológicas, sean capaces de incrementar el índice terapéutico de diferentes familias de compuestos antitumorales.

En este contexto, diferentes nanoestructuras han ido surgiendo en las últimas décadas con el objetivo tanto de aislar y estabilizar fármacos en el torrente sanguíneo, como de modificar el comportamiento farmacocinético de los mismos e incrementar su concentración en las células o tejidos tumorales tras su administración al paciente.

En esta línea, se deben mencionar las estructuras basadas en liposomas, siendo Doxil® el primer nanovehículo terapéutico aprobado en 1995 para su uso en pacientes oncológicos. Basándose en una estructura de bicapa lipídica con un núcleo hidrofílico que contenía hidrocloruro de doxorrubicina, Doxil arrojó resultados muy positivos en pacientes con cáncer de ovario, mieloma múltiple y sarcoma de Kaposi asociado a infección por VIH[1]. Sin embargo, esta solución nanomédica no ofrecía una vehiculización dirigida del fármaco a localizaciones tumorales, sino que más bien se restringía a aumentar la biodisponibilidad de doxorrubicina en sangre durante más tiempo.

Es a partir del diseño racional de los liposomas, imitando los compartimentos subcelulares vesiculares, y de su ensamblaje a través de interacciones intermoleculares, dónde se inicia el desarrollo de nuevas estructuras que buscan implementar mejoras en el diseño liposomal, permitiendo un mayor aislamiento del fármaco cargado, una biodistribución determinada o la implementación de sistemas sinérgicos, entre otros objetivos (Figura 1)[2]. Los dendrímeros, las nanopartículas de sílice, los polimerosomas, las nanopartículas imitadoras de virus o las nanopartículas poliméricas son algunos de los ejemplos más comunes de sistemas de nanovehiculización[3].

Dentro de este rango de nanoestructuras, Ecopol Tech viene trabajando desde el 2008 en el desarrollo de nanocápsulas híbridas de poliuretano-poliurea con capacidad para acumularse selectivamente en el microentorno tumoral (TME, por sus siglas en inglés) generado en las proximidades de un tumor sólido, mediante la funcionalización superficial de las nanocápsulas con grupos sensibles a variaciones de pH de manera que, al toparse con un entorno ligeramente ácido en el organismo, en comparación con el pH fisiológico del torrente sanguíneo, queden retenidas. En el caso concreto del TME, la disminución del pH en vasos adyacentes a la lesión tumoral es producida debido a la expulsión al medio extracelular de lactato por parte de las células tumorales en un proceso conocido como Efecto de Warburg[4].

Además del exceso de lactato y también como consecuencia del agrupamiento y crecimiento desmesurado de las células tumorales que provoca una respiración celular disfuncional, los niveles del tripéptido reductor glutatión (GSH) en el medio intracelular tumoral se encuentran descompensados al alza, en comparación con los descritos para células sanas.

Tomando ventaja de esta segunda disfunción, en la estrategia diseñada por Ecopol Tech se planteó la incorporación de grupos disulfuro en el esqueleto del polímero que forma la pared de las nanocápsulas. De este modo, se consigue que la degradación de las nanocápsulas se produzca preferentemente en medios biológicos reductores, como es el caso del medio intracelular de muchas células tumorales[5].

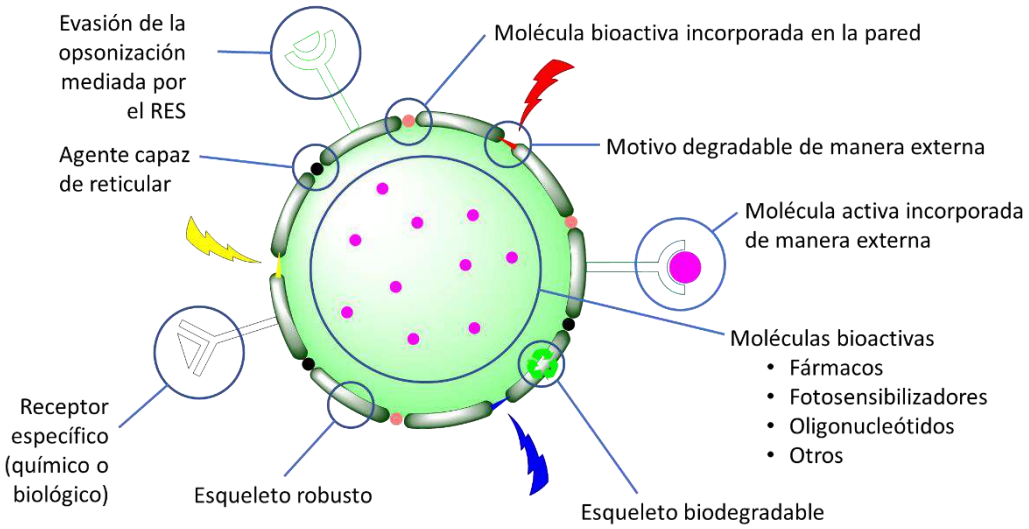

Figura 1: Posibilidades de funcionalización que ofrece el diseño de un nanovehículo.

Resumen del Capítulo I

Introducción y objetivos

El uso de la luz como herramienta de alta selectividad y baja toxicidad está siendo incorporado con cada vez más asiduidad en terapias de diferentes ámbitos de la medicina. En concreto, la terapia fotodinámica (PDT, por sus siglas en inglés) emplea la luz como fuente de activación de un fármaco, llamado comúnmente fotosensibilizador (PS, por sus siglas en inglés), que es capaz, una vez internalizado a nivel celular y como consecuencia de la absorción de fotones, de generar especies reactivas de oxígeno (ROS, por sus siglas en inglés) a una concentración suficiente como para inducir procesos de muerte celular. Esta técnica resulta particularmente atractiva en el desarrollo de nuevas terapias oncológicas, en las que se pretende una muerte selectiva de las células tumorales, manteniendo intactas aquellas sanas.

El proceso mediante el cual un fotosensibilizador es capaz de generar ROS tras absorción de luz se puede explicar mediante el denominado diagrama de Jablonski (Figura 2). Inmediatamente después de la absorción de un fotón, el PS es excitado a un estado singlete y, desde dicho estado, retorna a su estado basal a través de diferentes procesos y en diferentes tiempos. Si la molécula retorna al estado fundamental mediante un proceso de fluorescencia, el fotón absorbido es emitido en tiempos cortos (normalmente nanosegundos o picosegundos), liberando una energía que nunca puede ser superior a la absorbida inicialmente ($0 < \Phi_{fluorescencia} < 1$).

En el caso de que la molécula experimente, a través de un entrecruzamiento entre sistemas, la relajación parcial a un estado excitado triplete, se puede activar tanto la generación de ROS como el proceso de relajación completa hasta el estado molecular fundamental a través de la emisión de fosforescencia, conllevando tiempos de vida más largos que en el caso de la fluorescencia (normalmente de segundos en adelante).

La generación de ROS desde el estado triplete se puede producir mediante dos tipos de transferencia: electrónica o energética. En un sistema de transferencia electrónica, el fotosensibilizador transfiere un electrón a una molécula de agua o de oxígeno, lo que conlleva la generación de radicales citotóxicos. A este tipo de mecanismo de generación de ROS se le denomina PDT de tipo I.

Por otro lado, cuando desde el estado excitado triplete se produce una transferencia de energía a una molécula de oxígeno molecular se genera oxígeno singlete, también altamente citotóxico. A esta vía para la generación de ROS se le denomina PDT de tipo II.

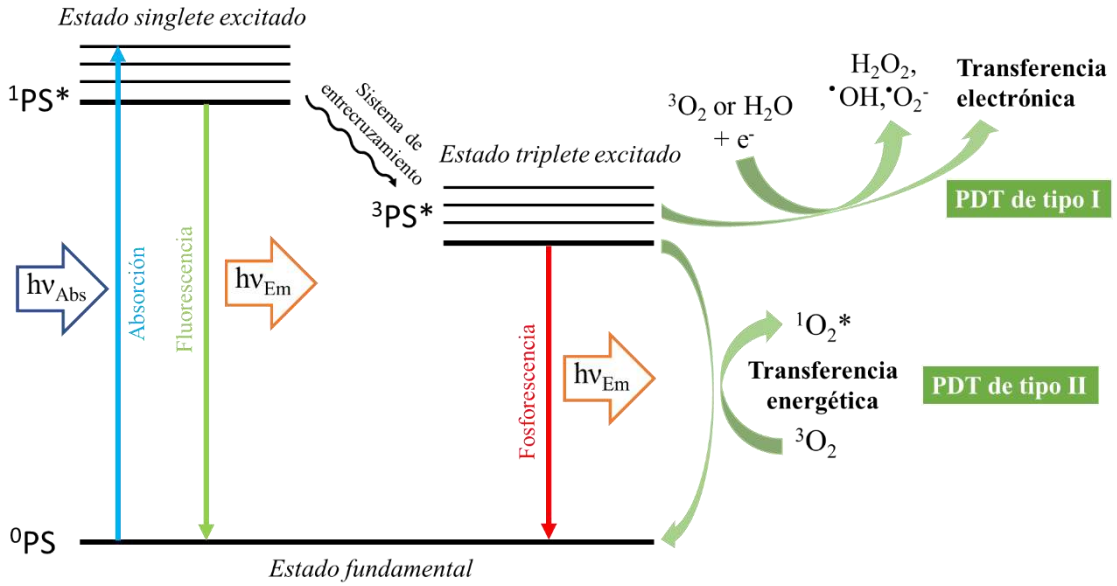

Figura 2: Diagrama de Jablonski representando los dos tipos de PDT.

El camino a través del cual un fotosensibilizador genera ROS viene determinado por muchos factores, entre los que obviamente destaca su estructura molecular[6], si bien uno de los más relevantes es el entorno físico o biológico en el que se encuentra al ser irradiado. Así, un medio biológico en condiciones de hipoxia en el que hay escasez de oxígeno, como el descrito en microambientes tumorales (TME) de diversos carcinomas o sarcomas, dificulta la generación de ROS vía PDT de tipo II.

Otro punto relevante a tener en cuenta en PDT es el tipo de luz a utilizar. Teniendo en cuenta que las radiaciones de bajas longitudes de onda (cercanas al azul o UV) son muy energéticas y generan toxicidad a través de modificaciones no deseadas en las hebras de ADN, un fotosensibilizador ideal debería presentar una buena absorción en la llamada ventana fototerapéutica, comprendida entre las zonas entre el rojo lejano y el infrarrojo cercano (NIR, según las siglas en inglés). Además de no generar toxicidad, la luz de elevadas longitudes de onda posee una mayor penetrabilidad en tejidos orgánicos, siendo apta para su empleo de manera extracorporal, permitiendo alcanzar localizaciones biológicas inaccesibles. Por lo tanto, este tipo de radiación ostenta una doble virtud para su aplicación en medicina.

Por último, un fotosensibilizador debe mostrar una elevada selectividad por la luz. Esto quiere decir que, siendo capaz de generar elevados niveles de ROS bajo irradiación, debe ser totalmente inocuo en condiciones de oscuridad. La ratio entre la citotoxicidad,

expresada en IC_{50}, en la oscuridad y la fototoxicidad generada bajo condiciones de irradiación, se define como índice fototóxico (PI, por sus siglas en inglés). Evidentemente, a mayor índice fototóxico, más eficaz es un fotosensibilizador.

Así pues, un fotosensibilizador ideal para aplicaciones anticancerígenas es aquel que cumple los siguientes requisitos:

- Posee una elevada absorción a las longitudes de onda comprendidas en la ventana fototerapéutica (650-800 nm).
- Es capaz de internalizar en el medio intracelular de una célula eucariota.
- Exhibe un elevado índice fototóxico, incluso en condiciones de hipoxia.
- Presenta una acumulación e internalización preferencial en células tumorales y/o en localizaciones tumorales.

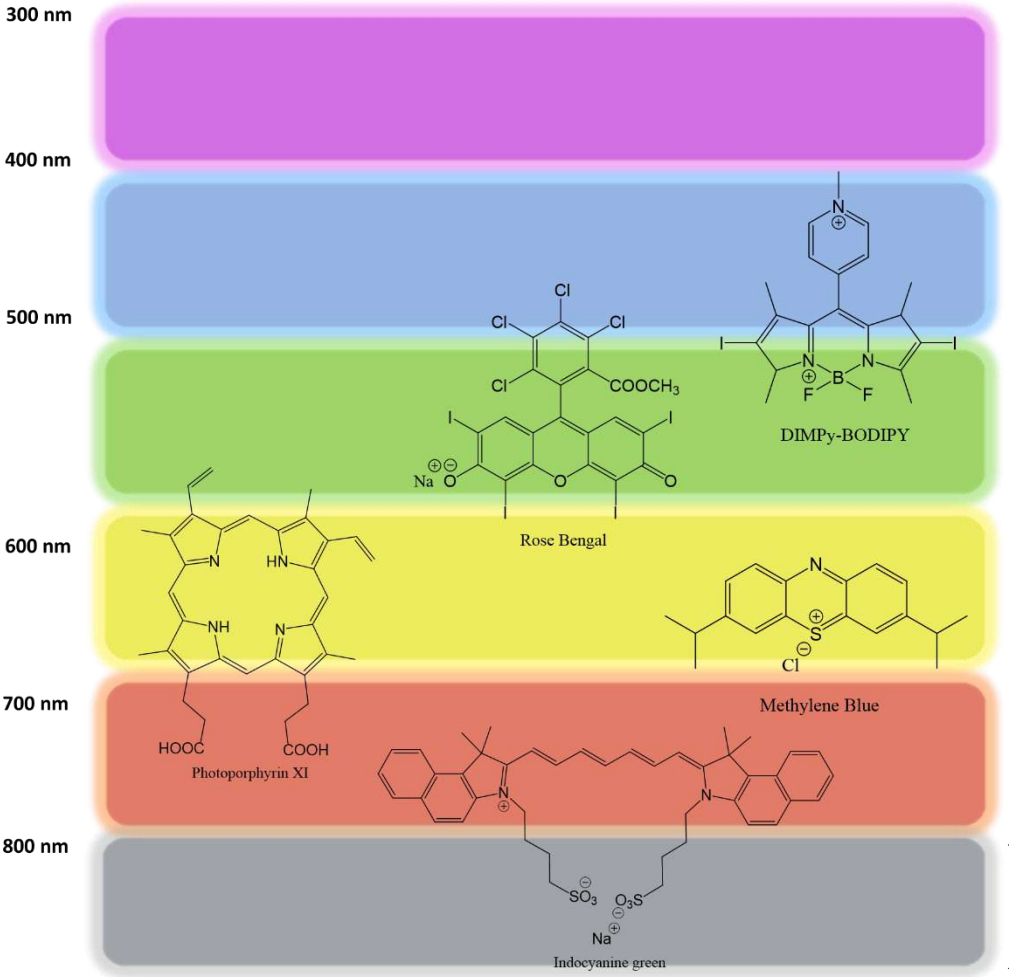

Figura 3: Algunos de los primeros fotosensibilizadores orgánicos descritos en la literatura.

En base a estos criterios, diferentes grupos de investigación dedicaron grandes esfuerzos al desarrollo de una primera generación de fotosensibilizadores orgánicos que abrieron el camino al uso de este tipo de moléculas en PDT[7](Figura 3). Así pues, toda una gama de compuestos basados en estructuras porfirínicas han sido aprobados por las

principales agencias regulatorias como agentes fotosensibilizadores para uso en fotomedicina como, por ejemplo, Foscan®, Photofrin®, Visudyne® o Laserphyrin®.

Dentro de la amplia gama de fluoróforos orgánicos con propiedades fotofísicas y biológicas interesantes, nuestro grupo de investigación en la Universidad de Barcelona se ha centrado en los últimos años en la síntesis y caracterización de nuevos fotosensibilizadores con estructura cumarínica, denominados COUPY, capaces de operar a longitudes de onda elevadas[8]. En el contexto de este proyecto, recientemente se han obtenido resultados especialmente interesantes con los compuestos denominados **COUPY 1** y **COUPY 2** (Figura 4), los cuales muestran una actividad fototóxica muy atractiva para ser usados como posibles agentes en PDT[9].

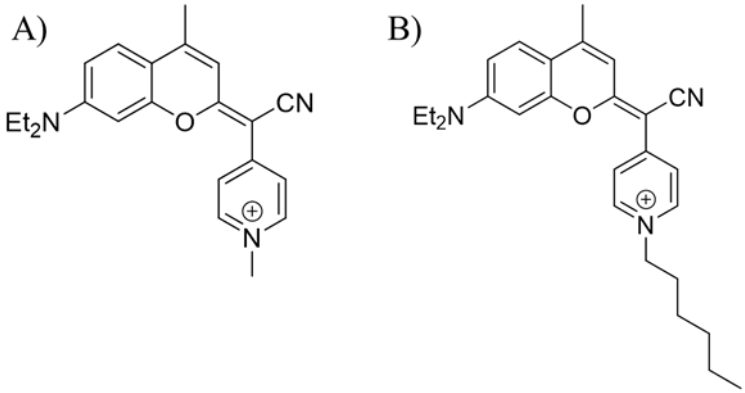

Figura 4: Estructura de los derivados A) **COUPY 1** y B) **COUPY 2**.

Además del uso de fluoróforos orgánicos en PDT, los compuestos de coordinación también han sido ampliamente estudiados por su potencial como fotosensibilizadores. En este grupo caben destacar los compuestos de platino[10], paladio[11], iridio[12] y rutenio[13], alcanzando estos últimos su auge recientemente con la introducción en fase clínica de TLD-1433 para indicaciones en PDT intravesicular contra cáncer de vejiga sin invasión muscular (NMIBC, por sus siglas en inglés), un fotosensibilizador con estructura de complejo de Ru(II) de tipo polipiridilo que incorpora un sistema de 3 tiofenos a través de uno de sus ligandos, desarrollado por el grupo de la Dra. Sherri McFarland en la Universidad de Texas, USA[14].

A partir de las estructuras de los derivados COUPY, y con la intención de mejorar sus propiedades fototerapéuticas, recientemente nuestro grupo de investigación abordó, en colaboración con el grupo del Dr. José Ruiz de la Universidad de Murcia, la síntesis de un conjugado entre **COUPY 1** y un compuesto ciclometalado de iridio(III), con la intención de desplazar el máximo de absorción del PS resultante hacia la zona roja del espectro electromagnético y posicionarlo así como un prometedor agente teragnóstico. Sorprendentemente, este compuesto reportó una muy buena acción biológica, incluso en condiciones de hipoxia[15].

Ya se había reportado anteriormente la conjugación a compuestos de coordinación de moléculas orgánicas con gran capacidad de absorción a altas longitudes de onda, como una estrategia ventajosa para la obtención de nuevos fotosensibilizadores de interés. En este contexto, los ligandos que incorporan estructuras derivadas de ftalocianina han sido y siguen siendo de los más estudiados en el campo[16]. Los compuestos de coordinación con ligandos conjugados a estructuras tipo ftalocianina son, además, de particular interés por la capacidad de la estructura ftalocianina para estabilizar un átomo metálico, por ejemplo, zinc, lo que permite incrementar la estabilidad del estado excitado triplete, mejorando así las propiedades del compuesto como fotosensibilizador[17].

Así pues, se conoce una amplia gama de moléculas que pueden ser usadas como fotosensibilizadores en PDT. Sin embargo, la obtención de una buena actividad biológica por parte de un fotosensibilizador a nivel celular no implica una traducción directa de los resultados a un modelo biológico *in vivo*. Existen una serie de parámetros que dificultan enormemente la actividad de los compuestos mencionados anteriormente en un organismo biológico relevante, entre los que destacan 1) la degradación prematura del fotosensibilizador, que impide la absorción de luz en la zona deseada del espectro electromagnético, 2) la extinción de la generación de ROS, normalmente producida por un descenso del rendimiento cuántico de activación de ROS causado por la solvatación en sistemas acuosos, y 3) una deficiente farmacocinética en la etapa posterior a la administración del fotosensibilizador, y antes de la irradiación, que conlleva una acumulación no deseado o una eliminación precoz del mismo a través de los principales órganos excretores.

Resultados y discusión

Para mitigar algunos de los problemas relacionados con el empleo de fotosensibilizadores en PDT, en este capítulo se describe como se abordó la encapsulación de diferentes fotosensibilizadores, tanto basados en fluoróforos orgánicos como en complejos metálicos, en nanocápsulas híbridas de poliuretano-poliurea, como una aproximación nanomédica para optimizar su actividad biológica en sistemas celulares.

Publicación Ia: Bonelli, J.; Ortega-Forte, E.; Rovira, A.; Bosch, M.; Torres, O.; Cuscó, C.; Rocas, J.; Ruiz, J.; Marchán, V. Improving Photodynamic Therapy Anticancer Activity of a Mitochondria-Targeted Coumarin Photosensitizer Using a Polyurethane–Polyurea Hybrid Nanocarrier. *Biomacromolecules* **2022**, *23*, 2900-2913.

En primer lugar, se llevó a cabo la **encapsulación de los derivados COUPY 1 y COUPY 2** (Figura 4) en nanocápsulas de poliuretano-poliurea (NCs) que incorporasen lateralmente en superficie motivos direccionadores a TME y que, además, contuvieran grupos químicamente degradables en ambientes reductores.

Síntesis de las COUPY-NCs

La síntesis de estas nanoestructuras se basa en la capacidad de auto-emulsionabilidad y auto-estratificación de un polímero anfifílico diseñado a través de la química del isocianato. Primero, se hace reaccionar un exceso de diisocianato de isoforona (IPDI), a unos ratios determinados, con diferentes intermedios dioles, en concreto: un diol que incorpora una cadena lateral PEG_{1000} (de nombre comercial YMER N-120), un diol-diamina en el que los dos grupos amina no son nucleófilos debido a su estructura terciaria (*N*-(3-dimetilaminopropil)-*N*,*N*-diisopropanolamina; de nombre comercial Jeffcat DPA) y un diol de cadena corta que incorpora de manera lineal un enlace disulfuro (2,2′-ditiodietanol: de nombre comercial DEDS). Esta polimerización se lleva a cabo sin necesidad de calentar el matraz de reacción ni de añadir disolvente.

Una vez finalizada la reacción de polimerización mediante la comprobación por FTIR de la desaparición de la banda de isocianato (sobre unos 2250 cm^{-1}) y la aparición de la banda de uretano (alrededor de 1530 cm^{-1}), se procede a la adición de THF como disolvente debido a la elevada viscosidad de la muestra. En un matraz a parte se prepara una disolución en THF del reactivo 1,3-diamino-N-octadecilpropano (de nombre comercial Genamin TAP 100D) en exceso respecto a los equivalentes libres de isocianato presentes en el poliuretano anteriormente preparado. En el paso final, se añade lentamente

la disolución en THF del poliuretano sobre el exceso en equivalentes de la diamina grasa, generando la aparición de enlaces urea (dando lugar a la aparición de la correspondiente banda de carbonilo de la urea sobre 1630 cm^{-1}) por la reacción entre los grupos amina e isocianato, consumiéndose este último en su totalidad y conduciendo a la **formación del prepolímero P1** de estructura híbrida poliuretano-poliurea (Figura 5).

Inmediatamente después de la síntesis de este prepolímero, se procede a la dispersión y posterior encapsulación de los activos **COUPY 1** y **COUPY 2** en nanocápsulas basadas en sistemas de dispersión aceite en agua (O/W, por sus siglas en inglés).

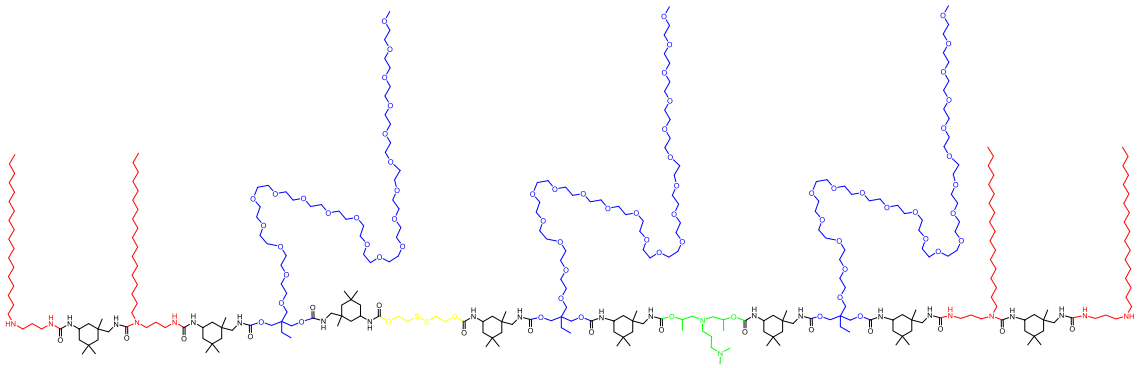

Figura 5: Estructura del esqueleto de peso molecular medio del prepolímero **P1**, dónde los tramos negros comprenden la estructura del IPDI, los tramos azules la estructura del YMER N-120, el tramo verde la estructura del Jeffcat DPA, el tramo amarillo la estructura del DEDS y los tramos rojos la estructura de la Genamin TAP 100D

A continuación, se prepara una disolución del activo a encapsular en un aceite inocuo de bajo HLB y se mezcla con el prepolímero **P1** que contiene THF. Se agita hasta disolución total en un vial provisto de un núcleo magnético, aplicando, en caso de ser necesario, ciclos cortos de ultrasonidos. Esta disolución se carga en un matraz de 3 bocas, donde previamente se ha pesado una cantidad determinada de IPDI libre. Este IPDI contenido en el balón se encuentra en exceso de equivalentes en relación con los equivalentes libres de amina presentes en **P1**, convirtiendo pues, todos los grupos funcionales amina del prepolímero en grupos isocianato funcionales.

Una vez activado **P1** (se comprueba la presencia de los grupos isocianato por FTIR), se procede a adicionar gota a gota una disolución de L-lisina en agua básica. Esta adición, además de generar una polimerización a través de la formación de grupos urea entre los grupos amina de la lisina y los grupos isocianato del prepolímero previamente activado, produce una primera etapa de dispersión en la que se forma una emulsión donde el agua es la fase dispersa y los componentes orgánicos de la muestra, la fase dispersante (emulsión W/O, por sus siglas en inglés). Inmediatamente después, previa comprobación de la disminución de la banda NCO según análisis por FTIR debido a la reacción con las aminas, se procede a la adición controlada de agua con la que se consigue llegar a la situación de inversión de fase, donde el agua pasa a ser la fase dispersante y los

componentes orgánicos la fase dispersada, la deseada emulsión O/W, en la que el carácter anfifílico del polímero que hemos ido formando *in situ* hace que este se localice en la interfase aceite/agua de esta emulsión, orientando los grupos de bajo HLB hacia su núcleo y los de alto HLB, por contra, hacia el medio acuoso externo. Gracias a esta localización racional del polímero, la adición de un agente "reticulante", en este caso la dietilentriamina o DETA, produce una reacción de polimerización ramificada instantánea en esta interfase, consumiendo todos los equivalentes presentes de isocianato y generando la estructura de la pared de la nanocápsula, que aísla completamente el núcleo liposoluble de la misma del medio acuoso (Figura 6). Finalmente, se realiza un proceso de purificación de las nanocápsulas por diálisis.

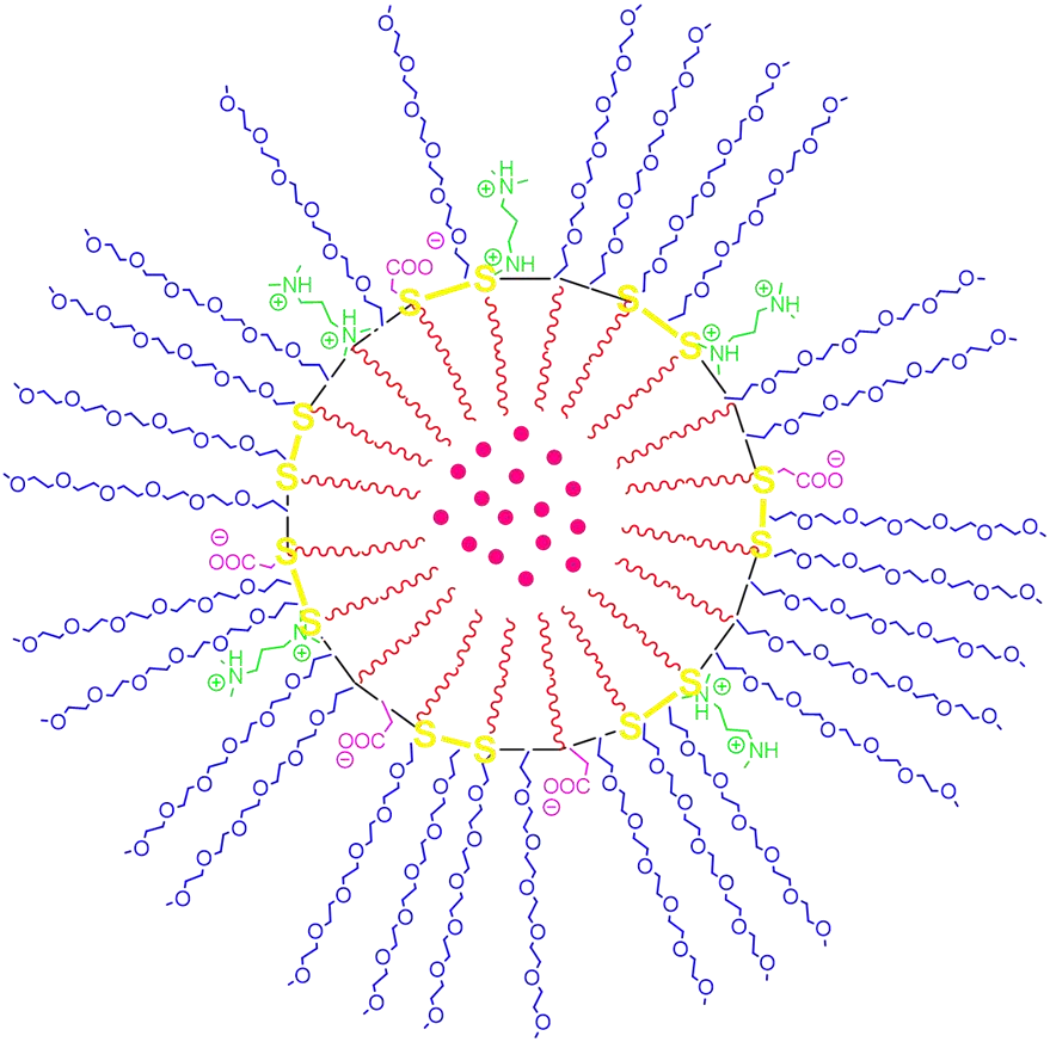

Figura 6: Esquematización de la estructura de una nanocápsula O/W híbrida de poliuretano-poliurea en la que, además de los grupos descritos en la Figura 5 pertenecientes al prepolímero **P1** inicial, se pueden apreciar los grupos carboxilato en superficie derivados de la extensión de la cadena con la lisina. Los fotosensibilizadores COUPY encapsulados son representados como esferas de color fucsia en el núcleo de la nanocápsula.

Diferentes técnicas de caracterización nos permiten evaluar la correcta formación de las nanocápsulas. Así, su diámetro se determinó tanto en medio hidrodinámico como en medio sólido mediante análisis por DLS y TEM, respectivamente, corroborando unos valores de alrededor de 20 nm para las COUPY-NCs, resultados que fueron posteriormente refrendados por análisis HR-TEM. En el caso de la carga superficial, ésta es evaluada mediante el análisis del potencial Z de las nanocápsulas. Dado que la protonación superficial de las cápsulas en medio ácido está descrita como un fenómeno crucial para permitir su acumulación en el TME, las medidas de potencial Z se llevan a cabo en un rango de pH 6-8 aproximadamente, que permita dilucidar si la carga superficial se ve alterada debido a las variaciones de pH. Tanto las nanocápsulas que incorporaban los derivados de cumarina (**NC-COUPY 1** y **NC-COUPY 2**) como las que se utilizaron como control negativo en los experimentos biológicos (**NC-GTCC**), modificaban su carga superficial hacia valores positivos al acidificar el medio de análisis.

En la evaluación de la cantidad de fotosensibilizador encapsulado, llevada a cabo mediante análisis por espectroscopía UV-visible, se concluyó que **COUPY 1** no había quedado significativamente retenida en el núcleo de las nanocápsulas. Por el contrario, **COUPY 2 mostró unos valores de carga efectiva (DL, por sus siglas en inglés) y eficacia de encapsulación (EE, %) muy prometedores: 1,16 ± 0.01 mM y 91%, respectivamente).** Estos resultados revelan que la funcionalización con el grupo hexilo sobre el anillo de piridina resulta clave para aumentar el carácter liposoluble del compuesto y así contener de manera eficaz la estructura cumarínica en la fase orgánica durante el proceso de encapsulación, quedando posteriormente retenida en el núcleo de las nanocápsulas.

Con el objetivo de cuantificar la capacidad de descarga de las nanocápsulas en un medio reductor y compararlo frente a un medio no reductor, se incubó una concentración conocida de nanocápsulas en PBS y en PBS suplementado con 10 mM del tripéptido GSH durante 24 y 48 h. Tras un proceso de diálisis, la cantidad de cumarina liberada de las muestras incubadas fue cuantificada mediante el análisis por HPLC-UV del medio de diálisis. Estos resultados confirmaron una descarga mucho más rápida en el caso de las nanocápsulas incubadas en PBS suplementado con GSH, frente a aquellas incubadas únicamente en PBS.

Caracterización fotofísica de las COUPY-NCs

En primer lugar, se comprobó que el espectro UV-visible de las **NC-COUPY 2** coincidía con el espectro de **COUPY 2** libre en diferentes solventes, confirmando que el fotosensibilizador no había sufrido degradación alguna durante el proceso de encapsulación. Con el fin de evaluar la mejora de las propiedades fotofísicas y

fotoquímicas del compuesto encapsulado respecto al producto libre, se llevaron a cabo las mediciones experimentales para determinar el rendimiento cuántico de fluorescencia en agua y la capacidad de generación de oxígeno singlete.

Para nuestro deleite, **el rendimiento cuántico de fluorescencia de las NC-COUPY 2 en agua aumentó significativamente con respecto al obtenido para COUPY 2 en el mismo medio** (0,36 y 0,20, respectivamente), fenómeno atribuible al entorno hidrofóbico en el que se encuentra el fotosensibilizador en el núcleo de las nanocápsulas que minimiza posibles fenómenos de agregación. Por otro lado, los rendimientos de generación de oxígeno singlete, medidos por valoración indirecta, resultaron muy bajos para los dos productos.

Evaluación de las propiedades biológicas de **NC-COUPY 2**

La microscopia confocal nos permitió confirmar la correcta internalización de las **NC-COUPY 2**, así como dilucidar su mecanismo de invaginación celular mediante un transporte activo, dependiente de energía. A su vez, la comparación directa con los resultados obtenidos para **COUPY 2** libre sugieren **una liberación relativamente rápida del contenido, una vez internalizado a través de la membrana celular**. Es de destacar que en los mismos experimentos ya se observó cierta toxicidad asociada a la irradiación del fotosensibilizador afectando, de manera particular, a la morfología de la mitocondria celular (Figura 7). La acumulación selectiva en mitocondria se confirmó posteriormente mediante experimentos de colocalización con MytoTracker Green (MTG).

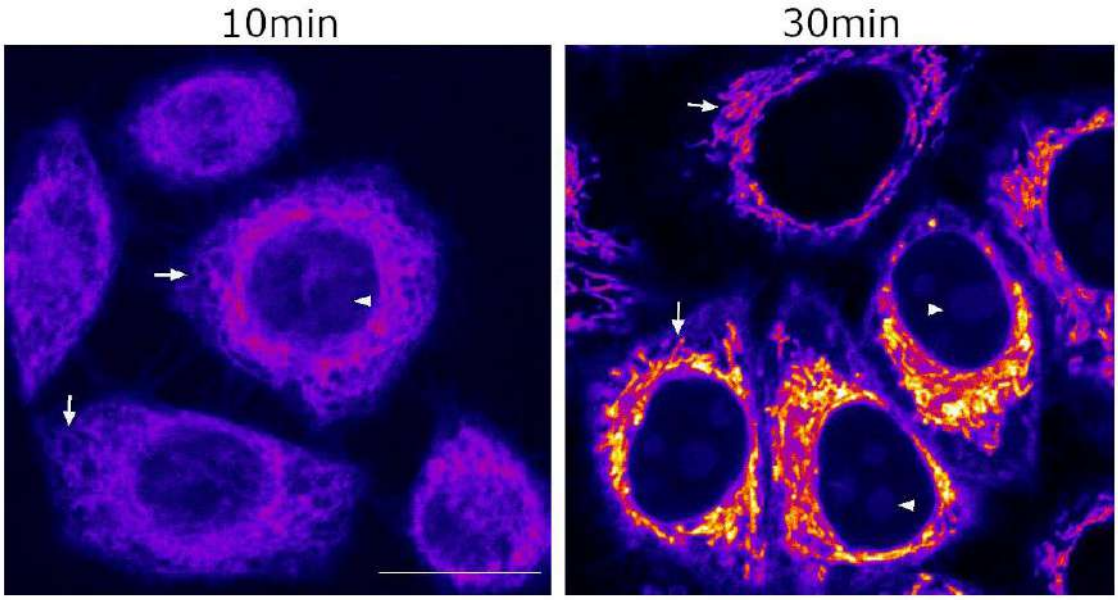

Figura 7: Imágenes de internalización celular de **NC-COUPY 2** en celulas HeLa. Las flechas blancas señalan localizaciones mitocondriales, que ya están siendo degeneradas tras la irradiación. Los triángulos blancos señalan nucleolo, otro de los puntos de acumulación preferencial de **COUPY 2** en su forma libre. Escala de la barra: 20 μm.

Centrándonos en la evaluación y cuantificación de la fototoxicidad generada por **NC-COUPY 2**, la incubación y posterior irradiación con luz roja en células HeLa se llevó a cabo para determinar y comparar los niveles de muerte celular que exhiben las **NC-COUPY 2** frente al compuesto libre y a **COUPY 1**.

Es de destacar que la forma encapsulada incrementó, de manera notable, el índice fototóxico en comparación al compuesto libre. Si bien los valores de muerte celular tras irradiación son muy parecidos, las nanocápsulas con capaces de disminuir totalmente la toxicidad que genera el fotosensibilizador libre en la oscuridad, lo que conduce a un incremento notable del valor de PI (desde 7.0 a 108.8, respectivamente, Tabla 1). El protocolo seguido para la evaluación de la fototoxicidad de los compuestos fue el siguiente: 30 minutos de incubación a 37 ºC y 21 % concentración de oxígeno, seguido de 30 minutos más de incubación bajo irradiación con luz roja, para terminar con 48 h de recuperación celular bajo las condiciones iniciales de incubación.

Tabla 1: Fototoxicidad, expresada en μM, de **COUPY 1**, **COUPY 2** y **NC-COUPY 2** en condiciones de normoxia bajo irradiación de luz roja en células HeLa y sus correspondientes valores de índice fototóxico.

	Oscuridad	**Luz roja**	**PI** [b]
COUPY 1	>200	18 ± 2	>5.5
COUPY 2	5.3 ± 0.3	0.76 ± 0.004	7.0
NC-COUPY 2	196 ± 15	1.8 ± 0.09	108.8

Viendo estas interesantes mejoras promovidas por la encapsulación, el siguiente paso fue tratar de recrear de manera más significativa *in vitro* el entorno celular tumoral. En primer lugar, se llevaron a cabo experimentos de evaluación de la fototoxicidad de los compuestos bajo condiciones de hipoxia en la línea celular HeLa. Para ello, se utilizó el mismo tipo de tratamiento descrito anteriormente, pero en cámaras de incubación de bajo nivel de oxígeno (2 %), e irradiando con un LED de luz blanca de amplio espectro. Los resultados de este experimento se resumen en la siguiente Tabla 2, donde se puede apreciar que los valores de PI de las **NC-COUPY 2** siguen siendo sustancialmente mejores que los de **COUPY 1** y **COUPY 2** en condiciones normóxicas, mientras que, en el caso de los valores de hipoxia, aún siendo mejores que en los otros dos casos anteriores, no se observa un aumento tan significativo del PI. Esto puede ser debido a diversos factores que serán estudiados en experimentos futuros.

Tabla 2: Fototoxicidad generada en células HeLa, bajo diferentes niveles de oxígeno, en condiciones de oscuridad y tras irradiación con luz blanca. Las concentraciones de citotoxicidad están expresadas en μM.

		Oscuridad	**Luz**	**PI**
COUPY 1	Normoxia	>200	14 ± 2	>14.2
	Hipoxia	>200	18.6 ± 0.9	>10.8
COUPY 2	Normoxia	5.7 ± 0.4	0.19 ± 0.03	30.0
	Hipoxia	19 ± 3	0.7 ± 0.1	27.2
NC-COUPY 2	Normoxia	199 ± 14	1.3 ± 0.4	153.1
	Hipoxia	178 ± 23	5.6 ± 0.9	31.7

En segundo lugar, se evaluó el potencial fototóxico de **COUPY 2** y **NC-COUPY 2** en modelos 3D de microesferas tumorales (MCTS, por sus siglas en ingles), generados a partir de células HeLa. En este modelo se intenta recrear el agrupamiento de células tumorales que se puede desencadenar en la aparición de un tumor sólido para mimetizar el entorno *in vivo* en el que, posteriormente, se evaluará el fotosensibilizador. Se analiza pues la capacidad de desintegración de estas microesferas mediante PDT. En este caso, se observaron, aunque no se cuantificaron, unos niveles de perturbación similares en la estructura del esferoide para los tratamientos con **COUPY 2** y **NC-COUPY 2**, después de 9 días, tras haber irradiado con luz amarilla de 555 nm.

Singularmente, experimentos de microscopia confocal confirmaron que, mientras que el compuesto libre distorsiona la estructura del esferoide desde una localización interna, las nanocápsulas quedan retenidas en la parte exterior y van destruyendo la estructura desde afuera hacia adentro (Figura 8).

Para confirmar que la desnaturalización de estas estructuras tridimensionales se producía debido a la acción del fotosensibilizador, se diseñaron experimentos para evaluar la generación de ROS, tanto en los modelos celulares 3D como en los 2D, utilizando menadiona como control positivo. Los resultados de este experimento, que se muestran de manera gráfica en la Figura 9, revelaron que la irradiación con luz visible genera, de manera significativa, un elevado nivel de ROS por parte del fotosensibilizador.

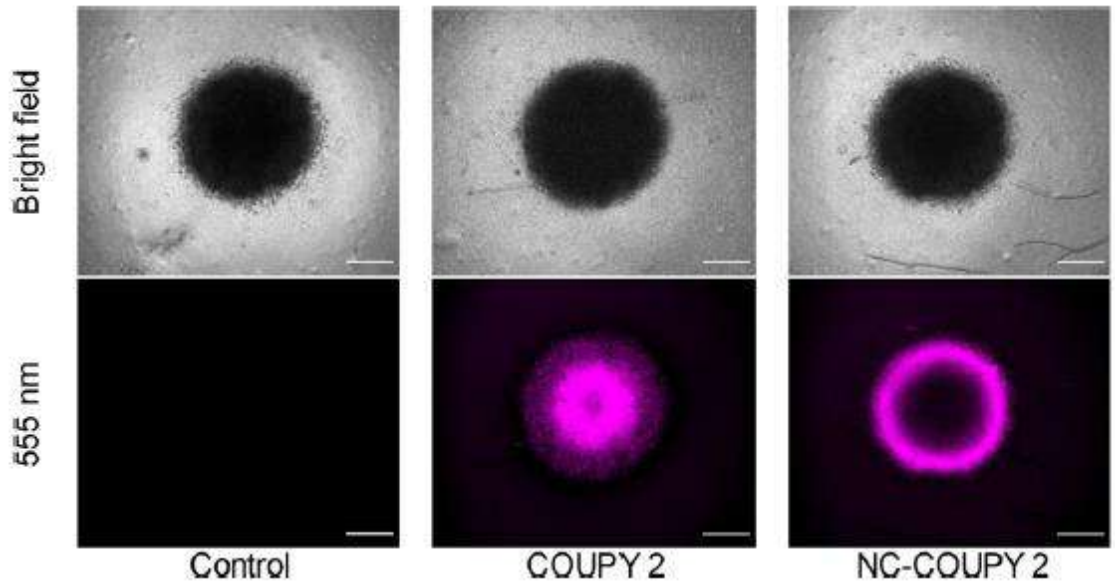

Figura 8: Análisis mediante microscopia confocal para dilucidar la localización de los compuestos testados en las estructuras esferoides de células HeLa.

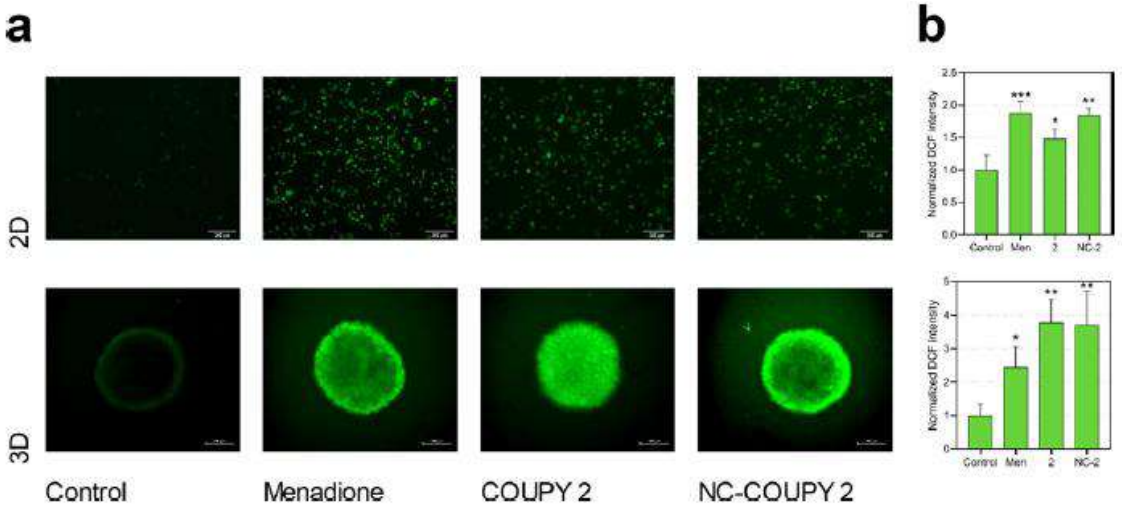

Figura 9: Generación de ROS en modelos 2D y 3D de células HeLa después de un tratamiento de 1 h de incubación más 1 h de irradiación con luz visible a una concentración de 2 μM de **COUPY 2** o de **NC-COUPY 2**. a) Imágenes de fluorescencia representando los niveles de ROS en los cultivos 2D y 3D. b) Cuantificación de la intensidad de fluorescencia relacionada directamente con los niveles de ROS.

Para concluir con la evaluación biológica de la acción de las **NC-COUPY 2**, se llevaron a cabo diversos estudios para estudiar los mecanismos de muerte celular provocados por el fotosensibilizador **COUPY 2** (tanto en su forma nanoencapsulada como libre). En primer lugar, se evaluó la funcionalidad de la membrana mitocondrial de las células HeLa mediante la medición del potencial de membrana mitocondrial (MMP, por sus siglas en inglés), observándose una reducción drástica del mismo tras irradiación con luz visible en presencia de ambos productos, **COUPY 2** y **NC-COUPY 2**.

Por otro lado, la inducción de apoptosis también se investigó bajo irradiación con luz visible mediante el uso de un marcador fluorescente de procesos apoptóticos (Annexin V-FITC), lo cual permitió revelar que las **NC-COUPY 2** mostraban un aumento de las células pro-apoptóticas significativamente mayor que **COUPY 2** y que el control positivo de cisplatino. Procesos autofágicos y el compromiso del metabolismo celular, mediante el análisis de los niveles de la oxidación fosforilativa, también se identificaron como procesos que conducen a la muerte celular como consecuencia de la irradiación con luz blanca en presencia del fotosensibilizador **COUPY 2**, tanto en su forma libre y nanoencapsulada.

Capítulo Ib (resultados no publicados): Bonelli, J. *et al*. Nanoencapsulation and biological evaluation of Ru(II)-based photosensitizers.

En la misma línea de encapsulación de fotosensibilizadores para su aplicación en PDT, en nuestro grupo de investigación en la Universidad de Barcelona surgió la idea de aplicar una aproximación similar a la que se llevó a cabo en el Capítulo Ia de esta Tesis para estabilizar y vehiculizar de manera selectiva dos compuestos de coordinación basados en un centro metálico de rutenio(II), **Ru1** y **Ru2**, de los cuales no se muestran las estructuras debido a que se han iniciado los trámites para patentarlos.

Los buenos resultados de fototoxicidad observados previamente con los compuestos libres tras irradiación tanto con luz roja como del NIR, sumado a la necesidad de elaborar y llevar a cabo una amplia gama de estudios biológicos, tanto con los compuestos libres como con los encapsulados, abrió una vía de colaboración con el grupo del Prof. Gilles Gasser de la Universidad Sorbonne de Paris, en concreto de la Facultad Chimie Paris Tech, en el que realicé una estancia académica de 2 meses en el marco de esta investigación.

Síntesis de las **Ru1-NCs** y de las **Ru2-NCs**

Sendas encapsulaciones en nanocápsulas híbridas de poliuretano-poliurea se llevaron a cabo mediante el método descrito en el caso de la publicación Ia. En términos de caracterización del producto final, el análisis por DLS de **Ru1-NCs** y **Ru2-NCs** reveló una morfología del mismo orden, pero ligeramente más pequeña que la observada para **NC-COUPY 2**, en ese caso de unos 17 nm. Estos resultados también fueron posteriormente confirmados por TEM, tal y como se puede apreciar en la Figura 10.

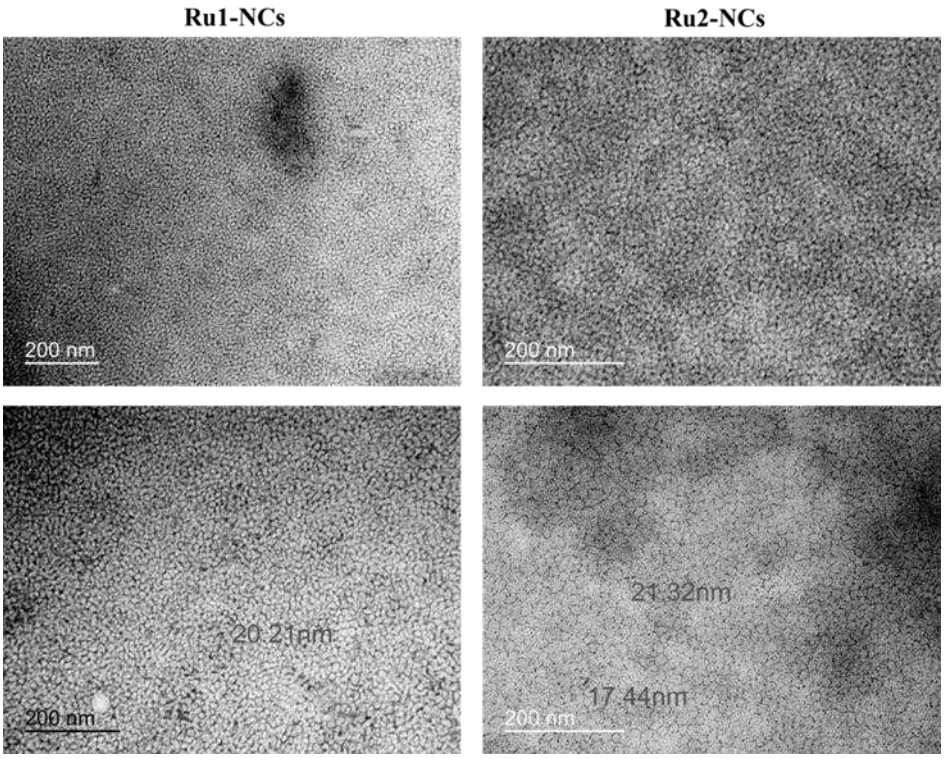

Figura 10: Imágenes TEM de **Ru1-NCs** y **Ru2-NCs**. La escala de la barra representa 200 nm.

Los análisis de la carga superficial mediante medidas de potencial Z también revelaron un comportamiento dependiente de pH, incrementándose la carga positivade las nanocápsulas al acidificar el medio de análisis.

Es de destacar que la inclusión de un fotosensibilizador con núcleo metálico nos permitía evaluar la carga efectiva y la eficacia de encapsulación mediante una técnica analítica de cuantificación mucho más sensible como es la inducción de plasma acoplado (ICP, por sus siglas en inglés): ICP-OES o ICP-MS, según la detección sea óptica o por espectrometría de masas. Para medir la concentración de rutenio en emulsión se digirieron directamente 20 μL del producto encapsulado para ambos compuestos, **Ru1** y **Ru2**, en un volumen determinado de ácido nítrico al 72% v/v durante 18 h. Al analizar las diluciones seriadas de ambas muestras se observó **que la carga efectiva y la eficacia de encapsulación utilizando el compuesto Ru1 fueron significativamente mayores que las obtenidas para el mismo proceso de encapsulación empleando el compuesto Ru2** (una concentración de 1005.3 ± 32.9 μM y un 83.9 % de EE para Ru1-NCs, frente a una concentración de 439.7 ± 27.6 μM y un 38.0 % de EE para **Ru2-NCs**). Este hecho es probablemente atribuible a las diferencias estructurales entre los dos compuestos que podrían modificar su coeficiente de partición octanol/agua (o log P) e incrementar la afinidad del compuesto **Ru2** por la fase acuosa en el momento de la emulsión O/W.

Experimentos de fotoestabilidad

Con el objetivo de cerciorar la correcta encapsulación de los compuestos **Ru1** y **Ru2** y, a la vez, elucidar si esta metodología de nanovehiculización permite incrementar los ciclos y/o el tiempo de irradiación al que puede ser sometido el fotosensibilizador, optimizando así un potencial tratamiento de PDT en organismos complejos, se prepararon soluciones en medio biológico de **Ru1**, **Ru2**, **Ru1-NCs** y **Ru2-NCs** a las mismas concentraciones y se midió su espectro de UV-visible. De inicio ya se pudo apreciar que los productos encapsulados presentan unos máximos de absorción más elevados que los compuestos libres en medio acuoso, fenómeno atribuible al entorno hidrofóbico del núcleo de las cápsulas en el que se encuentran. A partir de ahí, se realizaron ciclos de irradiación de diferente duración, hasta un máximo acumulado de 1 h, y se midió, a diferentes intervalos, la disminución de los máximos de absorción producida por la degradación del fotosensibilizador como consecuencia de la irradiación continua con luz, fenómeno comúnmente conocido como *photobleaching* en inglés.

Estos experimentos se llevaron a cabo tanto mediante irradiación con luz roja (645 nm) como NIR (740 nm), y permitieron concluir que **la encapsulación mitiga los efectos de la fotodegradación provocada por la irradiación con luz en comparación a los compuestos no encapsulados**, en los que sus bandas de absorción decrecieron a una mayor velocidad.

Evaluación de las propiedades biológicas de **Ru1-NCs** y **Ru2-NCs**

Siguiendo los pasos lógicos, en primer lugar, se evaluó cualitativamente la internalización de **Ru1-NCs** y **Ru2-NCs** en células HeLa mediante microscopia confocal. En la Figura 11 se puede observar claramente la correcta internalización de ambos compuestos encapsulados, sugiriendo el patrón de acumulación una localización vesicular.

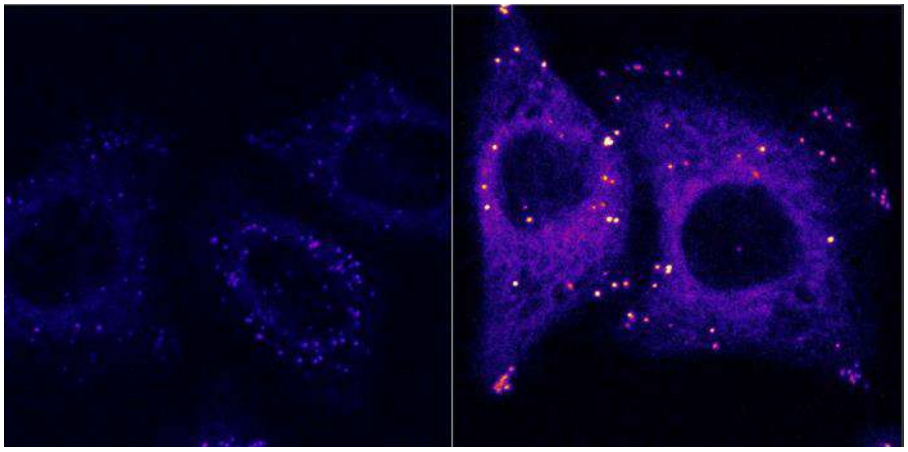

Figura 11: Imágenes de microscopia confocal de la internalización de **Ru1-NCs** (izquierda) y de **Ru2-NCs** (derecha) en células HeLa.

Una vez confirmada la correcta internalización en células cancerígenas, se abordó la evaluación de **Ru1-NCs** y **Ru2-NCs** como agentes fototóxicos. En primer lugar, se midió la actividad fototóxica de los compuestos encapsulados en la línea celular de cáncer de colon, CT-26, extraída de modelos de roedores a tres longitudes de onda diferentes (540 nm, 645 nm y 740 nm) con el objetivo de realizar una comparación directa frente a los valores obtenidos con los compuestos libres. El tratamiento constó de 4 h de incubación de los compuestos, tanto libres como encapsulados, a 37 ºC, seguido de irradiaciones de 1 hora de duración (sólo en el caso de los experimentos con luz) y finalizando con 44 h más de incubación en las condiciones descritas inicialmente.

Tabla 3: Valores de IC_{50} para **Ru1-NCs**, **Ru1**, **Ru2-NCs** y **Ru2** mostrados en μM para tratamientos en oscuridad o bajo irradiación con luz verde, roja y NIR en células CT-26. Se muestran los índices fototóxicos (PI) correspondientes para cada producto bajo las diferentes condiciones.

CT-26				
	Ru1-NCs		**Ru1**	
	IC_{50}	*PI*	*IC_{50}*	*PI*
Oscuridad	>250	-	>250	-
540 nm	0.0045 ± 0.0005	>55000	0.0082 ± 0.0006	>30487
645 nm	0.059 ± 0.005	>4237	0.048 ± 0.003	>5208
740 nm	>100	----	31.3 ± 6.1	>3
	Ru2-NCs		**Ru2**	
	IC_{50}	*PI*	*IC_{50}*	*PI*
Oscuridad	>250	-	>250	-
540 nm	0.0076 ± 0.0007	>32895	0.025 ± 0.002	>10000
645 nm	0.013 ± 0.001	>19231	0.0074 ± 0.0006	>33780
740 nm	0.27 ± 0.03	>926	0.76 ± 0.06	>328

Tal y como se muestra en la Tabla 3, ninguno de los compuestos evaluados **mostraron toxicidad alguna en condiciones de oscuridad**, hecho que ya aporta una gran ventaja frente a otros fotosensibilizadores. Analizando el detalle de los experimentos con **Ru1, encapsulado y libre**, vemos que ninguno de los dos son activos bajo radiación NIR, lo cual está en concordancia con su falta de absorción en esta zona del espectro electromagnético. Por otro lado, sí que presentan un **extraordinario índice fototóxico en el tratamiento con luz verde, así como un excelente valor en el tratamiento con luz roja** (del orden de decenas de miles en el primer caso y de miles en el segundo).

En el caso de **Ru2-NCs y Ru2 libre**, los resultados son aún más espectaculares: mientras que en ambos casos se siguen alcanzando unos **valores elevadísimos de PI tanto con luz verde como con luz roja (ambos del orden de decenas de miles)**, también presentan notables índices fototóxicos bajo radiación NIR (del orden de centenares). En este caso, **la encapsulación de Ru2 genera una mejora sustancial del PI respecto al compuesto libre, llegando casi a reducir a un tercio el valor de IC_{50} bajo radiación a 740 nm** (0.27 μM en el caso de **Ru2-NCs** y 0.76 μM para **Ru2**).

Dado que, como se ha comentado en anteriores secciones, uno de los parámetros más valorados en el desarrollo de nuevos fotosensibilizadores es su operabilidad a altas longitudes de onda, se evaluó la actividad fototóxica de **Ru2** y **Ru2-NCs** en diferentes líneas celulares, sanas y tumorales, con tratamientos de irradiación a 740 nm. En la Tabla 4 se muestran los resultados obtenidos para estos experimentos y se puede observar que, a diferencia de los valores obtenidos para el compuesto libre, la forma encapsulada muestra cierta selectividad hacia células tumorales, afectando en menor medida a las células sanas evaluadas bajo el mismo tratamiento.

Tabla 4: Valores de cito- y fototoxicidad, y sus correspondientes PI obtenidos para **Ru2-NCs** y **Ru2** en las líneas celulares CT-26 (tumoral), RPE-1, HEK293 y MRC-5 (sanas) para tratamientos con radiación NIR.

	Ru2-NCs			**Ru2**		
	Oscuridad	**740 nm**	*PI*	***Oscuridad***	**740 nm**	*PI*
CT-26	>100	0.27 ± 0.03	>370	>100	0.76 ± 0.06	>131
RPE-1	>100	3.84 ± 0.04	>26	>100	0.80 ± 0.18	>125
HEK293	>100	2.94 ± 0.70	>34	>100	3.33 ± 0.90	>30
MRC-5	>100	0.64 ± 0.11	>156	>100	0.49 ± 0.03	>205

Capítulo Ic (resultados no publicados): Bonelli, J. *et al*. Encapsulation and biological evaluation of a Zn(phthalocyanine) derivative and the corresponding Ir-Zn(phthalocyanine) conjugate.

Cerrando el trabajo de encapsulación de fotosensibilizadores de esta Tesis, nos propusimos la nanoencapsulación de dos fotosensibilizadores desarrollados en la Universidad Miguel Hernández de Elche, en el grupo de la Dra. Ángela Sastre. El primero de ellos es un derivado de ftalocianina que incorpora un átomo de zinc(II) coordinado al sistema aromático, **Zn(Pc)**. El segundo fotosensibilizador consiste en un conjugado entre dicho derivado de ftalocianina y un complejo ciclometalado de iridio(III) desarrollado en el grupo del Prof. José Ruiz en la Universidad de Murcia, **Ir-Zn(Pc)**.

La problemática de estos compuestos radicaba en su nula capacidad de internalización celular, probablemente asociada a su escasa solubilidad en agua. Es por ello que se propuso su vehiculización utilizando nanosistemas híbridos de poliuretano-poliurea que permitiera evaluar su actividad biológica. La evaluación biológica de ambos compuestos se llevó a cabo en la Universidad de Murcia.

Síntesis de **Zn(Pc)-NCs** y **Ir-Zn(Pc)-NCs**

Viendo los buenos resultados que ofrecía el sistema híbrido de poliuretano-poliurea para la estabilización y la mejora de las propiedades biológicas de diferentes fotosensibilizadores, la síntesis de estas nanocápsulas se abordó siguiendo la aproximación descrita en las secciones anteriores de este capítulo.

En este caso, los valores de tamaño de las nanocápsulas obtenidos por DLS fueron ligeramente inferiores a los obtenidos con las formulaciones que incorporan los derivados COUPY y los complejos de Ru(II). Esto podría atribuirse a diferencias en la liposolubilidad de los compuestos que obviamente afectan a la conformación de la interfase en el momento de la emulsión lo que, por tanto, puede modificar el radio de las micelas. Ahora bien, en este caso, parece estar más asociado a la cantidad de activo introducido en cada preparación. **Zn(Pc)-NCs** e **Ir-Zn(Pc)-NCs** rondan un tamaño sobre los 11-15 nm, extraídos del análisis por DLS en medio hidrodinámico y confirmado por TEM en un medio seco.

Si nos fijamos en los valores de carga superficial, medidos a través del potencial Z (Tabla 5) en disolución vemos que, de nuevo, la carga global de ambas nanopartículas se supedita al pH del medio de medición, aumentando positivamente al disminuir el pH del medio. Además de confirmar su comportamiento anfotérico, se observa también que los valores adquiridos para los diferentes pH son muy similares a los obtenidos para las cápsulas de los apartados Ia y Ib.

Tabla 5: Valores de potencial Z para las muestras **Zn(Pc)-NCs** e **Ir-Zn(Pc)-NCs** a diferentes pH.

Muestra	Pot-Z ± DS (mV) a pH=6,0	Pot-Z ± DS (mV) a pH=6,5	Pot-Z ± DS (mV) a pH=7,0	Pot-Z ± DS (mV) a pH=7,5	Pot-Z ± DS (mV) a pH=8,0
Zn(Pc)-NCs	10.5 ± 0.5	8.7 ± 1.0	3.4 ± 0.6	-3.4 ± 0.4	-7.7 ± 0.3
Ir-Zn(Pc)-NCs	13.5 ± 3.6	9.1 ± 1.5	7.2 ± 0.7	5.7 ± 0.5	0.7 ± 0.3

La determinación de la carga efectiva (DL) y la eficacia de encapsulación (EE) de ambas muestras se llevó a cabo de nuevo por ICP-OES e ICP-MS, tomando ventaja de la presencia de metales en ambos fotosensibilizadores. Los valores de la Tabla 6 muestran diferencias significativas entre los valores de DL y EE para ambas encapsulaciones.

Tabla 6: Valores de carga efectiva de fotosensibilizador y eficacia de encapsulación para cada uno de los productos.

	[NCs] (mg/mL)	Carga de PS (DL, µM)	Eficacia de encapsulación (EE, %)
NC-GTCC	42.9 ± 1,6	-	-
Zn(Pc)-NCs	30.2 ± 0,1	621.7 ± 93.0	64.3 %
Ir-Zn(Pc)-NCs	62.4 ± 1.1	256,5 ± 20.5	50.2%

Los valores de carga efectiva en micromolaridad son esperables debido a las diferencias entre los pesos moleculares del fotosensibilizador de zinc-ftalocianina y su conjugado al complejo de iridio(III) y teniendo en cuenta que se partió de una masa idéntica de compuesto en ambas síntesis. Aunque los valores de eficacia de encapsulación son bastante similares, sugieren que el compuesto **Zn(Pc)** se concentra en el núcleo de la emulsión O/W en mayor medida que su conjugado, debido probablemente a la diferencia de polaridad entre ellos. Por otro lado, los espectros UV-visible de **Zn(Pc)-NCs** e **Ir-Zn(Pc)-NCs** confirmaron que ambos compuestos se mantuvieron estables durante el proceso de encapsulación.

Evaluación de las propiedades biológicas de **Zn(Pc)-NCs** e **Ir-Zn(Pc)-NCs**

Los experimentos de microscopia confocal fueron cruciales para elucidar si se había logrado uno de los principales objetivos de este proyecto: la correcta internalización de los fotosensibilizadores en células eucariotas. No sólo se analizó la internalización de estos, sino también su localización intracelular.

Los resultados de microscopía confocal en células HeLa confirmaron que los compuestos **Zn(Pc)** e **Ir-Zn(Pc**) no son capaces de atravesar la membrana celular tras 30 min de incubación a 37ºC, mientras que las formas encapsuladas sí que permitían identificar la señal fluorescente proveniente de los respectivos fotosensibilizadores tras excitación con luz amarilla y luz roja.

Seguidamente se realizaron experimentos de colocalización de **Zn(Pc)-NCs** utilizando LysoTracker Green (LTG) como marcador de lisosoma. La Figura 12 muestra el destino intracelular de estos compuestos, exhibiendo una preferente acumulación en lisosomas, tal y como confirmaron los coeficientes de Pearson y de Manders.

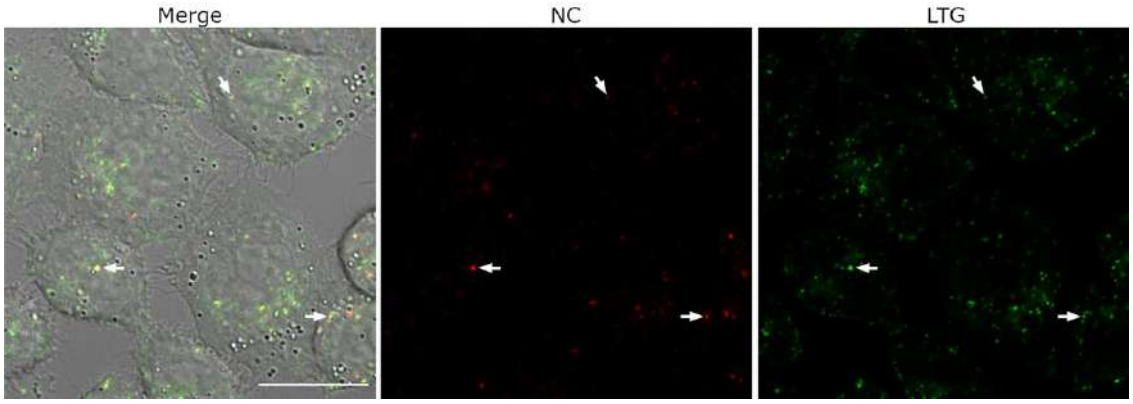

Figura 12: Imágenes de microscopia confocal de **Zn(Pc)-NCs** colocalizadas con LTG. **Zn(Pc)-NCs** fueron excitadas usando el láser centrado a 561 nm. Las flechas blancas representan localizaciones significativas donde la señal de fluorescencia proveniente de **Zn(Pc)-NCs** en el canal rojo colocaliza con la señal verde de fluorescencia proveniente de LTG. La barra de escala representa 20 μM.

Acto seguido, se ensayaron la cito- y fototoxicidad de **Zn(Pc)**, **Ir-Zn(Pc)**, **Zn(Pc)-NCs** e **Ir-Zn(Pc)-NCs** en la línea celular HeLa. En este caso, se planteó un tratamiento de irradiación con luz roja centrada en 620 nm, ya que ambos compuestos muestran una fuerte absorción a esta longitud de onda.

Tabla 7: Valores de IC_{50} (μM) y de PI para **Zn(Pc)**, **Ir-Zn(Pc)**, **Zn(Pc)-NCs** e **Ir-Zn(Pc)-NCs** en células HeLa en condiciones de oscuridad y bajo irradiación con luz roja centrada a 620 nm.

HeLa				
	Zn(Pc)-NCs		**Zn(Pc)**	
	IC_{50}	*PI*	*IC_{50}*	*PI*
Oscuridad	>100	-	>100	-
620 nm	0.72 ± 0,2	>138.9	56 ± 4	1.8
	Ir-Zn(Pc)-NCs		**Ir-Zn(Pc)**	
	IC_{50}	*PI*	*IC_{50}*	*PI*
Oscuridad	>100	-	>100	-
620 nm	1.2 ± 0,2	>83.3	95 ± 8	1.,0

La Tabla 7 pone de manifiesto el extraordinario efecto de la nanoencapsulación de los compuestos **Zn(Pc)** e **Ir-Zn(Pc)** en nanocápsulas híbridas de poliuretano-poliurea como medio para mejorar su actividad fototóxica que, de por sí, es prácticamente nula debido a su escasa internalización celular. Así, mientras **Zn(Pc)-NCs** e **Ir-Zn(Pc)-NCs** exhiben una nula toxicidad en condiciones de oscuridad, son capaces de vehiculizar ambos fotosensibilizadores al interior de las células, permitiendo que generen toxicidad tras irradiación con luz roja.

Conclusiones

A lo largo del Capítulo I se ha abordado satisfactoriamente la encapsulación de diferentes fotosensibilizadores en nanocápsulas híbridas de poliuretano-poliurea para su aplicación en PDT anticancerígena. En el subcapítulo Ia, se presentan los resultados de la encapsulación de un fotosensibilizador orgánico basado en un derivado COUPY, así como su caracterización biológica; en el subcapítulo Ib, los resultados asociados a la encapsulación y evaluación biológica de dos fotosensibilizadores basados en complejos de rutenio(II) tipo polipiridilo, fotoactivables con luz visible y NIR; por último, en el subcapítulo Ic, se describe la encapsulación de un fotosensibilizador zinc-ftalocianina y de su conjugado a un compuesto ciclometalado de iridio(III), así como los correspondientes estudios de fototoxicidad. Las conclusiones concretas de este Capítulo I se muestran a continuación:

- Se ha conseguido encapsular de forma satisfactoria el fotosensibilizador liposoluble **COUPY 2** en nanocápsulas híbridas de poliuretano y poliurea.
- La encapsulación condujo a una mejora tanto de la fotoestabilidad como del rendimiento cuántico de fluorescencia de **COUPY 2** en medio acuoso.
- Se ha confirmado la generación de ROS tras irradiación con luz visible para las formas libre y encapsulada del fotosensibilizador **COUPY 2** en modelos *in vitro* 2D y 3D de células cancerígenas.
- La apoptosis fue identificada como el principal mecanismo de muerte celular inducido por **NC-COUPY-2** tras la irradiación.
- La encapsulación de los complejos de rutenio(II) de tipo polipiridilo (**Ru1** y **Ru2**) también transcurrió satisfactoriamente, lo que permitió mejorar su fotoestabilidad para una óptima operabilidad bajo irradiación con luz roja lejana/NIR.
- Los estudios biológicos realizados en varias líneas celulares cancerígenas y sanas confirmaron el potencial de **Ru1-NCs** y **Ru2-NCs** en PDT, mostrando una extraordinaria actividad fototóxica contra células CT-26 cancerígenas, incluso bajo irradiación en la zona del NIR en el caso de **Ru2-NCs**, dando lugar a valores de PI sustancialmente superiores a los de los compuestos no encapsulados.
- También se identificó una toxicidad atenuada en líneas celulares sanas para las **Ru1/Ru2-NCs**, aumentando así el factor de selectividad frente a las células cancerígenas en comparación con los compuestos no encapsulados.
- La encapsulación de **Zn(Pc)** e **Ir-Zn(Pc)** en nanocápsulas híbridas de poliuretano-poliurea también transcurrió de forma satisfactoria, aunque con una eficacia moderada en comparación con los otros fotosensibilizadores.
- Se logró la vehiculización *in vitro* de **Zn(Pc)** e **Ir-Zn(Pc)** hacia células tumorales gracias a la nanoencapsulación, lo que permitió confirmar una elevada

fototoxicidad para ambos compuestos nanoencapsulados bajo irradiación con luz roja.

Resumen del capítulo II

Introducción y objetivos

Los metalofármacos son una de las familias de compuestos más utilizadas en oncología como agentes quimiterapéticos[18]. Entre ellos, destacan los complejos de platino(II) y, en particular, el cisplatino, considerado como uno de los fármacos más eficaces y de primera línea de acción en quimioterapia contra diferentes tumores[19]. A raíz de la aparición del cisplatino, y de su demostrada eficacia en este tipo de tratamientos, empezó una búsqueda de nuevos compuestos de base metálica capaces de paliar la problemática del cisplatino y sus derivados. Dicha problemática reside, sobre todo, en la inespecificidad de este tipo de compuestos hacia las lesiones tumorales, lo que suele acarrear graves problemas de toxicidad sistémica en muchos pacientes oncológicos, así como la aparición de resistencia inherente o adquirida[20].

En este escenario, se ha estudiado la incorporación de diversas funcionalizaciones en los compuestos de platino(II) con el objetivo de incrementar su direccionalidad hacia las lesiones tumorales desde el torrente sanguíneo. Como se muestra en la Figura 13, muchas de ellas se basan en la incorporación de ligandos de receptores sobre expresados en la membrana de las células tumorales[21].

Otras aproximaciones estudian la oxidación del núcleo central de platino(II) a platino(IV), lo que inactiva temporalmente su actividad citotóxica, ya que el estado de oxidación +2 y los ligandos presentes en cisplatino y derivados, son cruciales para desencadenar el mecanismo que conduce a la muerte celular, causada por la unión del platino a las cadenas de ADN a través de la reacción con la posición *N7* de las bases púricas. En general, los complejos de Pt(IV) están racionalmente diseñados para ser activados bajo las condiciones intracelulares reductoras presentes en células tumorales[22]. Ahora bien, muchos de estos compuestos suelen presentar una desventaja competitiva frente a los derivados de platino(II) relacionada con la pérdida de solubilidad en medio acuoso que provoca, en muchos casos, la necesidad de acudir a construcciones nanomédicas para su vehiculización[23].

Muchas otras soluciones emergentes basan su aproximación en la utilización de compuestos metálicos con diferente metal central. En las últimas décadas, un gran número de complejos de iridio, rutenio, paladio u osmio han sido evaluados como potenciales agentes quimioterapéuticos.

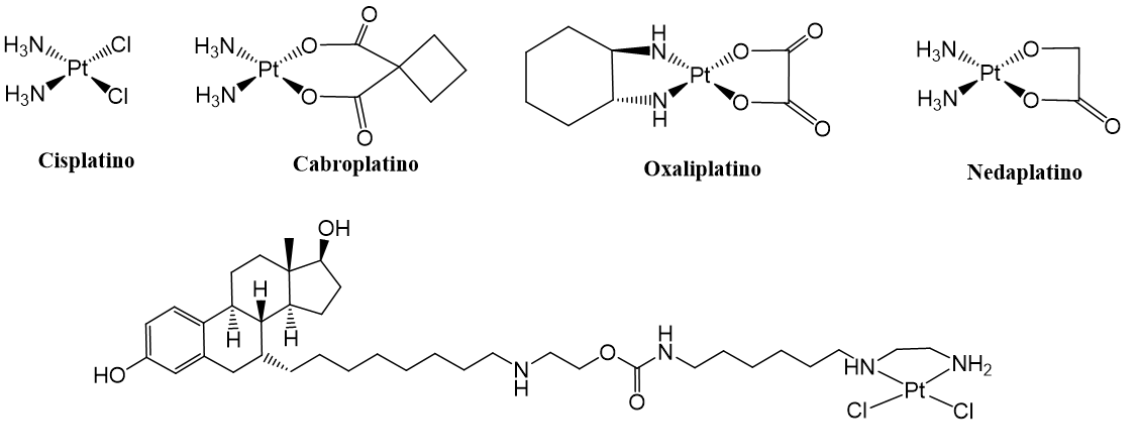

Compuestos de platino(II) que incluyen ligandos direccionadores de receptores de estrógeno

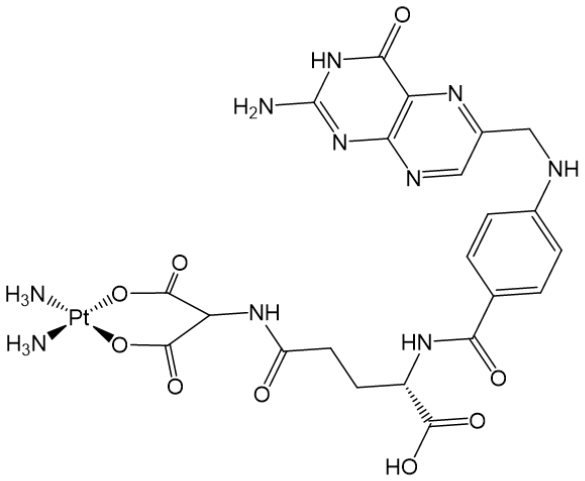

Compuestos de platino(II) direccionados a receptores folato

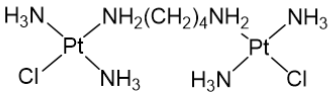

Compuestos de platino(II) polinucleares

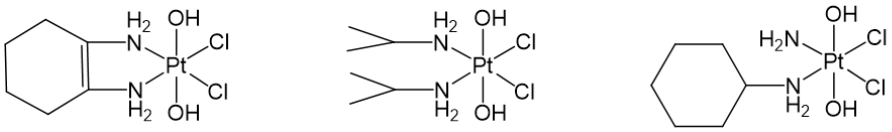

Profármacos de platino(IV) evaluados en ensayos clínicos

Figura 13: Ejemplos de complejos de Pt(II) y Pt(IV) con actividad anticancerígena.

De entre todos los metales mencionados anteriormente, el iridio es uno de los más ampliamente estudiados en quimioterapia, ya que la química de coordinación basada en dicho metal ofrece una amplia gama de posibilidades [24].

En esta línea, el grupo del Prof. José Ruiz, en la Universidad de Murcia, se ha centrado en el desarrollo de nuevos complejos ciclometalados de iridio(III) y en el estudio de sus propiedades biológicas como nuevos candidatos en quimioterapia [25].

De entre los compuestos desarrollados en el laboratorio del Prof. Ruiz, destacó un compuesto ciclometalado de iridio(III), compuesto A de la Figura 14, que mostró una elevada toxicidad en células tumorales. Ahora bien, los compuestos B y C no generaron toxicidad en células tumorales. Posteriores experimentos de microscopia confocal confirmaron una muy escasa internalización celular, verificando así el porqué de su baja actividad citotóxica. Esta escasa internalización se asoció a una muy baja solubilidad en agua como consecuencia de la inclusión de un tercer ligando ciclometalado en sustitución de un ligando N^N polipiridilo, lo que generaba compuestos sin carga[26].

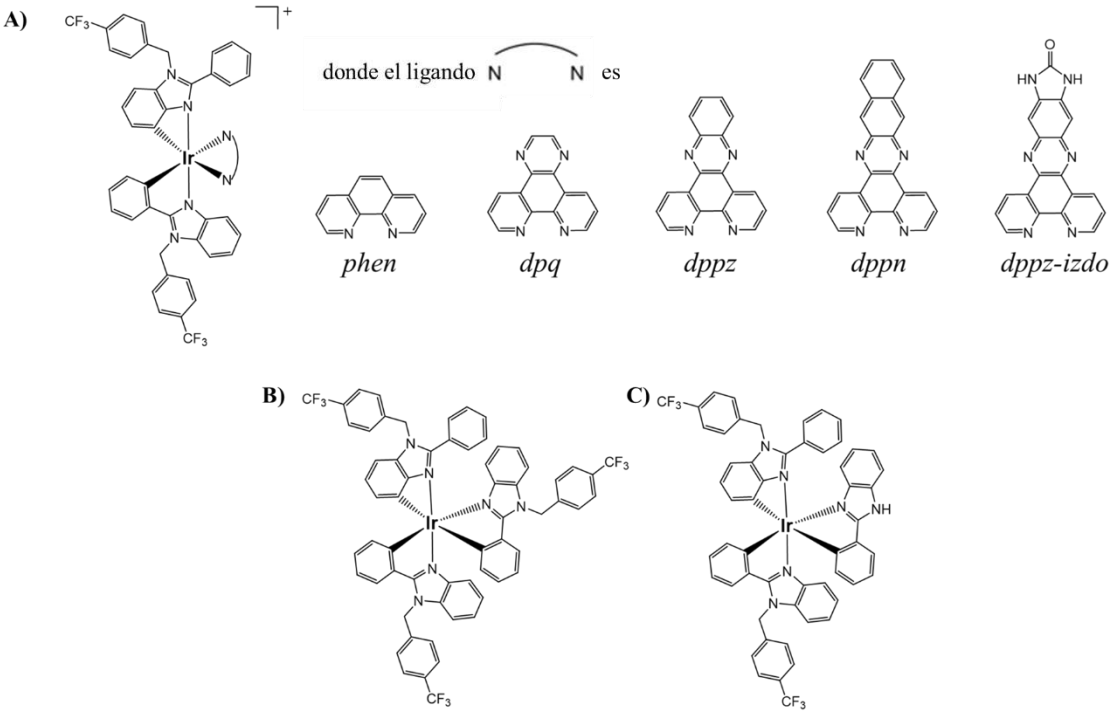

Figura 14: Ejemplos de compuestos ciclometalados de Ir(III).

Así pues, en este capítulo se ha explorado la encapsulación de los compuestos B y C de la Figura 14, denominados **Ir1** e **Ir2** respectivamente, y en el estudio de sus propiedades biológicas en colaboración con el grupo del Prof. Ruiz con el objetivo de evaluar su potencial como agentes antitumorales.

Resultados y discusión

Publicación II: Bonelli, J.; Ortega-Forte, E.; Vigueras, G.; Bosch, M.; Cutillas, N.; Rocas, J.; Ruiz, J.; Marchán, V. Polyurethane–Polyurea Hybrid Nanocapsules as Efficient Delivery Systems of Anticancer Ir(III) Metallodrugs. *Inorg. Chem. Front.* **2022**, *9*, 2123–2138.

Como se ha comentado en la anterior sección, con visos a incrementar la pobre internalización celular que ofrecían los complejos ciclometalados de Ir(III) homoléptico (**Ir1**) y heteroléptico (**Ir2**), se procedió a su incorporación en el núcleo de nanopartículas de poliuretano-poliurea capaces de acumularse en localizaciones ácidas del organismo, como las presentes en el TME de tumores sólidos, así como de liberarse preferentemente en aquellos medios intracelulares donde exista una sobreexpresión de agentes reductores. La publicación derivada de este trabajo fue portada del número 10 del volumen 9 de la revista *Inorganic Chemistry Frontiers*, en mayo del 2022.

Síntesis de **NC-Ir1** y **NC-Ir2**

La metodología de síntesis de nanocápsulas híbridas de poliuretano-poliurea para compuestos liposolubles descrita en el Resumen del Capítulo I se empleó también para obtener de forma satisfactoria **NC-Ir1** y **NC-Ir2**. El radio hidrodinámico de ambos productos se encontró alrededor de unos 18 nm, confirmado posteriormente por TEM.

En cuanto a los resultados de carga superficial en función del pH, evaluados a través de medidas de potencial Z, cabe indicar que esta gama de nanocápsulas también mostró un comportamiento anfotérico, protonándose al acidificar las condiciones del medio. A diferencia de, por ejemplo, el rango de valores reportado en el apartado de resultados y discusión del Capítulo Ia, en el que los valores de carga superficial según el pH se movían entre 15/20 mV a pH bajo y -5/-10 mV a pH fisiológico, las **NC-Ir2** descienden hasta aproximadamente -25 mV a pH fisiólogico, hecho atribuible a un pequeño desajuste en el ratio de grupos catiónicos provenientes del prepolímero P1 y los equivalentes libres superficiales de grupos carboxilato provenientes de la adición de lisina al esqueleto de poliuretano-poliurea durante la síntesis.

El análisis de la carga efectiva y de la eficacia de encapsulación se llevó a cabo mediante el análisis de la concentración de iridio en sendas emulsiones por ICP-OES. Ambos productos presentan unas concentraciones de complejo metálico y unas eficacias de encapsulación muy similares, como se recoge en la Tabla 8, sugiriendo que la hidrofobia/hidrofilia relativa del compuesto ciclometalado de iridio(III) no se ve afectada por la coordinación de un ligando u otro.

Tabla 8: Valores de concentración de cápsulas, carga efectiva y eficacia de encapsulación para cada producto

	[NCs] (mg/mL)	**Carga efectiva (DL, μM)**	**Eficacia de encapsulación (EE, %)**
NC-GTCC	64.8 ± 0.5	-	-
NC-Ir1	45.4 ± 3.1	130.5 ± 16.2	41.4
NC-Ir2	64.8 ± 0.5	206.2 ± 16.8	40.0

Con el objetivo de estudiar la degradación selectiva de la pared de **NC-Ir1** y **NC-Ir2** se empleó la microscopia electrónica de transmisión (TEM), más concretamente se pretendía dilucidar la integridad de las nanocápsulas después de diferentes tratamientos en PBS con y sin tripéptido glutatión. Los resultados de dichos ensayos, que se muestran en la Figura 15, confirman la degradación total de las muestras incubadas durante 48 h a 37 ºC en PBS suplementado con 10 mM de GSH, mientras que las muestras incubadas en medio no-reductor mantienen por completo su integridad estructural y morfológica.

Estos resultados confirman los obtenidos en el anterior Capítulo Ia, dónde la descarga de las nanocápsulas híbridas de poliuretano-poliurea se produce mediante la degradación de las mismas, promovida por la sobreexpresión de especies reductoras en el medio, como es el caso de glutatión.

Se llevaron también a cabo experimentos para una completa caracterización fotofísica de los productos y, a la vez, comprobar si la encapsulación permitía mejorar de algún modo las propiedades espectroscópicas de los compuestos metálicos. Con este fin, se registraron los espectros de absorción y emisión de **Ir1** e **Ir2**, en su forma libre, en sendas soluciones de DCM y DMSO, con y sin desgasificar. En paralelo, se midieron los mismos parámetros en agua para las muestras de **NC-Ir1** y **NC-Ir2**, también en condiciones con y sin desgasificación. Seguidamente también se calcularon los tiempos de vida media de fosforescencia y el rendimiento cuántico de la misma para todos los compuestos, observando una mejora sustancial de estos parámetros para los compuestos encapsulados en condiciones de aireado.

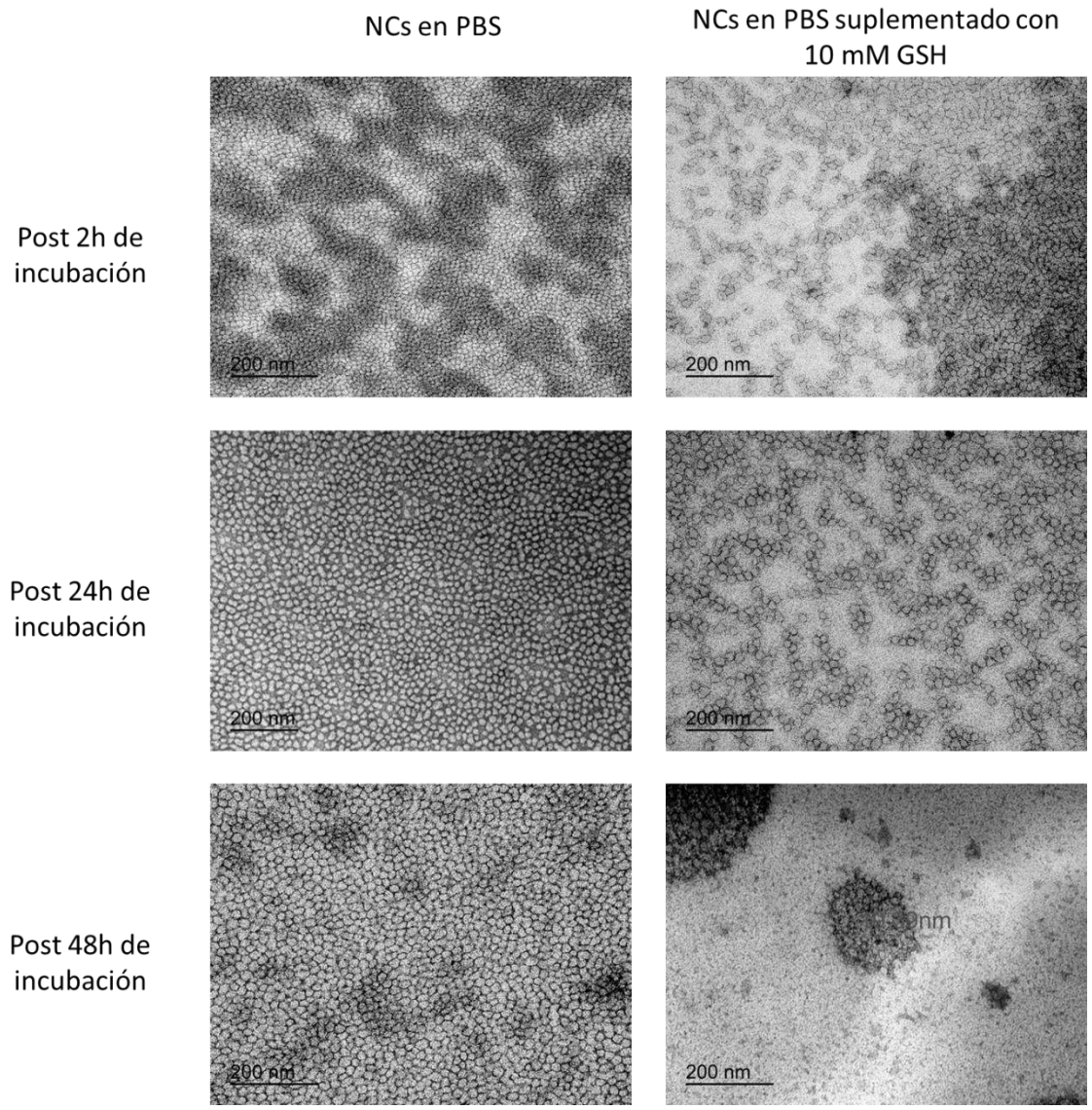

Figura 15: Imágenes de TEM de la comparativa de las **NC-Ir2** incubadas a 16 mg/mL en PBS (izquierda) o en PBS suplementado con una concentración 10 mM de GSH (derecha) durante un total de 48 h.

Evaluación de las propiedades biológicas de **NC-Ir1** y **NC-Ir2**

Las imágenes de microscopia confocal de los complejos de Ir(III) libres, **Ir1** e **Ir2**, tras 30 minutos de incubación en células HeLa, confirmó la nula penetración de éstos a través de la membrana celular. En las imágenes de la Figura 16 se puede observar cómo los compuestos agregan y quedan aislados en el medio extracelular. Por el contrario, en las imágenes de la Figura 17 se puede observar cómo ambas nanocápsulas, **NC-Ir1** y **NC-Ir2**, permiten detectar sendos compuestos en el interior de las células, logrando así uno de los principales objetivos de este trabajo.

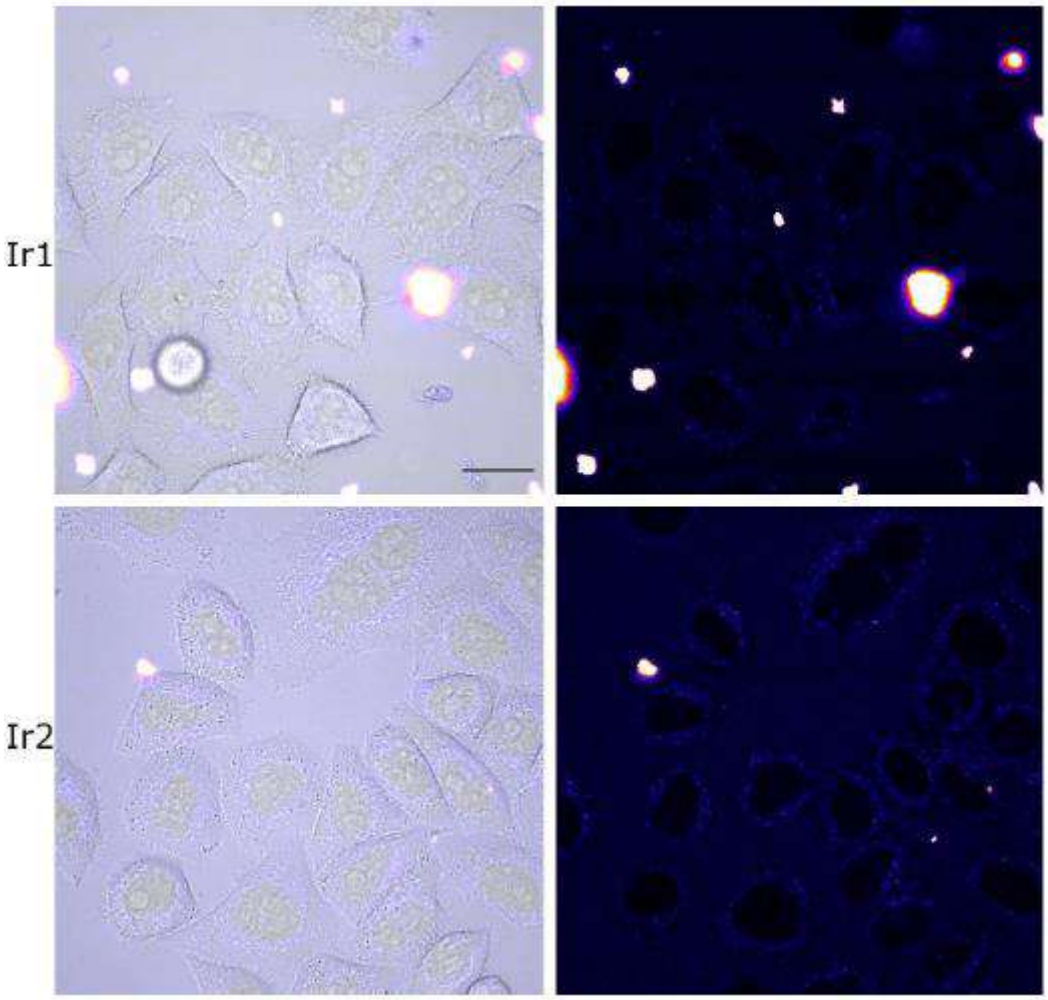

Figura 16: Imágenes de microscopia confocal de los compuestos libres **Ir1** e **Ir2** incubados 30 minutos en células HeLa a una concentración de 5 μM.

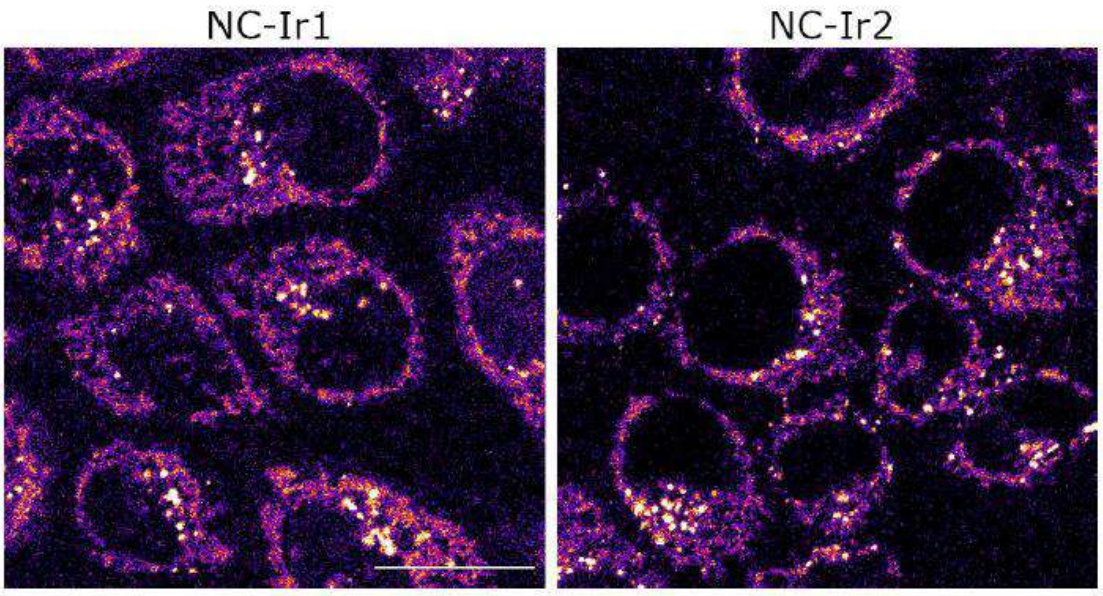

Figura 17: Imágenes de microscopia confocal de los compuestos encapsulados **NC-Ir1** y **NC-Ir2** incubados 30 minutos en células HeLa a una concentración de 5 μM para cada compuesto.

Con el objetivo de cuantificar las diferencias en el grado de internalización entre los complejos de Ir(III) libres, **Ir1** e **Ir2**, y las correspondientes versiones nanoencapsuladas, **NC-Ir1** y **NC-Ir2**, se llevaron a cabo unos experimentos en los que se incubaron los compuestos a una concentración de 6 μM, durante 30 minutos en células HeLa para después limpiar y cambiar el medio de cultivo, generar un pellet con las células incubadas, digerirlas con ácido nítrico concentrado y analizar el contenido en iridio por ICP-OES.

Este estudio reveló que, para la misma cantidad de compuesto incubada, la cantidad de iridio en 1 millón de células era unas 4 veces mayor para la muestra de **NC-Ir1** que para la de **Ir1** y del orden de unas 8 veces mayor para la muestra de **NC-Ir2** frente a la muestra de **Ir2**, confirmando así los datos obtenidos por microscopia confocal.

A partir de estos buenos resultados de internalización se procedió a evaluar la actividad citotóxica de estos compuestos en modelos *in vitro*, primero en 2D y posteriormente en 3D usando microesferas tumorales. Un screening del IC_{50} de **NC-Ir1** y **NC-Ir2**, usando como control positivo cisplatino, en las líneas celulares tumorales HeLa, A2780 y la versión de A2780 resistente a cisplatino (A2780cis), como también en la línea celular sana BGM ofreció unos resultados muy esperanzadores. En células HeLa, **NC-Ir1** y NC-Ir2 mostraron unos valores de IC_{50} sustancialmente más bajos que el cisplatino, alrededor de 2 μM frente a 33 μM para el fármaco de platino(II). En el caso de A2780 y A2780cis, las diferencias no fueron tan sustanciales, aunque los productos nanoencapulados **NC-Ir1** y **NC-Ir2** mostraron una mejor actividad que el cisplatino en la línea tumoral A2780cis, y los valores de citotoxicidad resultaron similares. En cambio, y para nuestro deleite, **NC-Ir1** y **NC-Ir2** prácticamente no presentaron citotoxicidad en células BGM sanas en contraposición con cisplatino. Los resultados de los estudios de citotoxicidad en modelos 2D se recopilan en la siguiente Tabla 9:

Tabla 9: Valores de citotoxicidad de **NC-Ir1**, **NC-Ir2** y cisplatino en diferentes líneas celulares

	HeLa			**A2780**	**A2780cis**	**BGM**
	2 h	24 h	48 h		24 h	
NC-Ir1	23 ± 1	2.9 ± 0.2	1.77 ± 0.06	3.7 ± 0.9	10 ± 1	>85
NC-Ir2	47 ± 6	3.6 ± 0.2	2.9 ± 0.1	2.5 ± 0.6	9.8± 0.9	>85
Cisplatino	-	-	33 ± 6	1.4 ± 0.2	16 ± 1	16.6 ± 0.2

El análisis de citotoxicidad en modelos 3D de microesferas tumorales también reveló un importante efecto citotóxico de las **NC-Ir1** y **NC-Ir2**, en comparación con el control negativo. La Figura 18 muestra como ambos productos nanoencapsulados son capaces de generar una destrucción total o casi total del esferoide 15 días después de su administración.

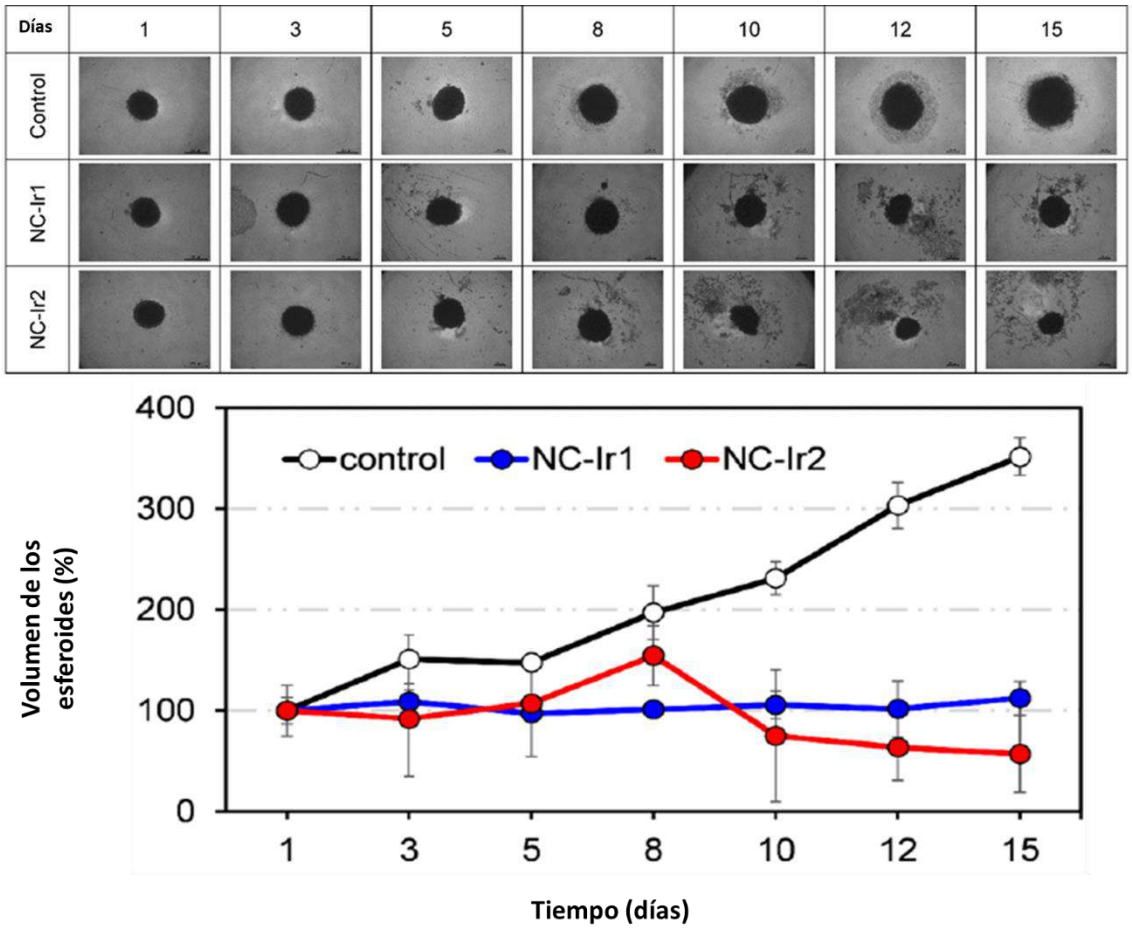

Figura 18: Imágenes del cambio de morfología de los esferoides a lo largo del tratamiento con **NC-Ir1** y **NC-Ir2** (arriba). Cuantificación porcentual del volumen de los esferoides a lo largo del tratamiento con las nanocápsulas (abajo).

Experimentos de visualización directa de las células en el microscopio de confocal revelaron los cambios morfológicos que sufren las células, durante el tratamiento con **NC-Ir1** y **NC-Ir2**, que las conducen a eventos de muerte celular (Figura 19).

Para elucidar los mecanismos provocados por las nanocápsulas que conducen hacia la muerte celular se llevaron a cabo diversos experimentos. En el primero, se compararon los eventos de apoptosis temprana, apoptosis tardía y necrosis. En este experimento se utilizó cisplatino control positivo y permitió concluir que, mientras este fármaco de platino(II) promocionaba los eventos de muerte celular por apoptosis temprana, **NC-Ir1** y **NC-Ir2** lo hacían por apoptosis tardía y, en especial, necrosis (Figura 20).

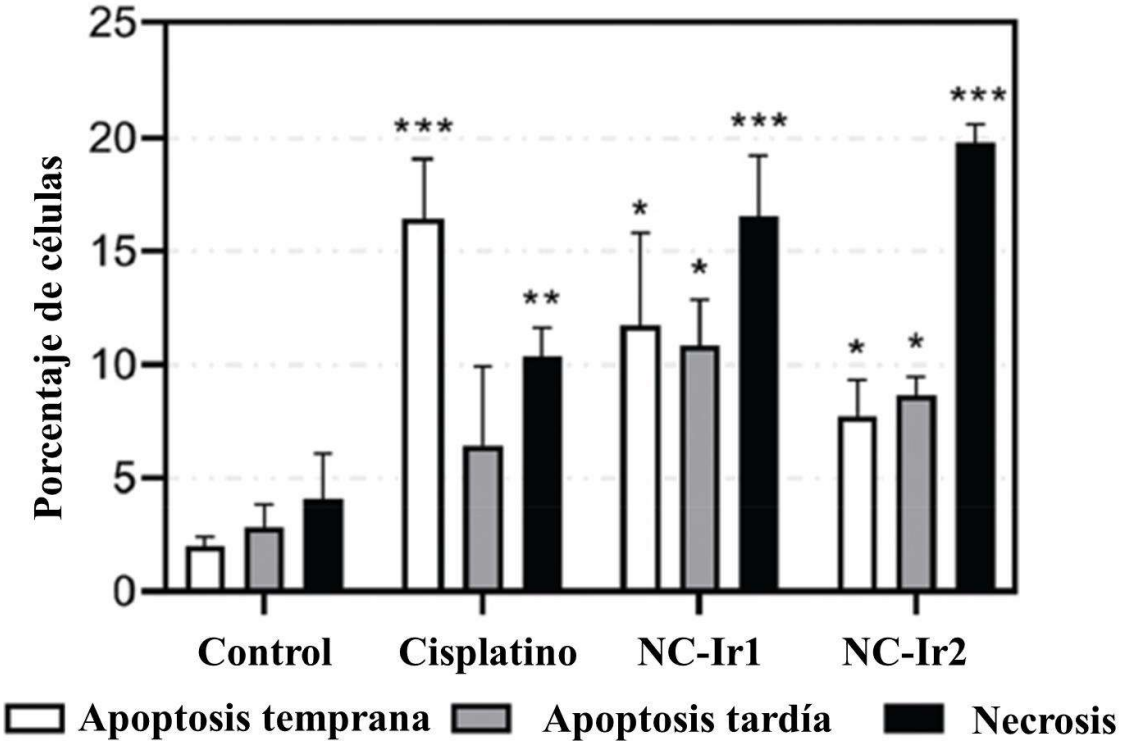

Figura 20: Cuantificación de los mecanismos de muerte celular producidos por el cisplatino (20 μM), **NC-Ir1** y **NC-Ir2** (6 μM) en células HeLa, después de 24 h de tratamiento.

A su vez se ensayó la disfunción que provocan los tratamientos con **NC-Ir1** y **NC-Ir2** a concentraciones 6 μM en células HeLa mediante la medición del MMP, concluyendo que ambos compuestos encapsulados ejercen un papel fundamental en la disrupción de la correcta función mitocondrial. En paralelo, se llevaron a cabo ensayos de los niveles de estrés oxidativo en células HeLa, provocados por los tratamientos de 24 h con las nanocápsulas a diferentes concentraciones, mediante la medición del daño en las cadenas de ADN con el marcador de fosforilación γH2AX, concluyendo que ambos compuestos encapsulados generan un daño similar al provocado por el cisplatino en las cadenas de ADN.

Con todos estos ensayos se puede confirmar que ambos productos, **NC-Ir1** y **NC-Ir2**, generan una fuerte toxicidad en células cancerígenas, permitiendo que los compuestos atraviesen la membrana celular y sean liberados en el medio intracelular para activar mecanismos de muerte celular, preferencialmente de apoptosis tardía y necrosis.

Conclusiones

El trabajo desarrollado en el Capítulo II consistió en la obtención y evaluación biológica de unas nanocápsulas híbridas de poliuretano-poliurea que contuviesen dos complejos ciclometalados de iridio(III), **Ir1** e **Ir2**, desarrollados en el laboratorio del Prof. José Ruiz en la Universidad de Murcia. Las conclusiones concretas de este Capítulo son las siguientes:

- Se logró la encapsulación de complejos anticancerígenos de iridio(III) liposolubles homolépticos y heterolepticos (**Ir1** e **Ir2**) con alta eficacia, manteniendo sus propiedades espectroscópicas en la dispersión acuosa.
- Se confirmó una eficiente internalización celular de las nanocápsulas correspondientes, **NC-Ir1** y **NC-Ir2**, tanto por ICP-MS como por microscopía confocal en células HeLa.
- La fuerte actividad citotóxica de ambas nanoformulaciones se confirmó mediante ensayos *in vitro* basados en resazurina.
- Las vías de muerte celular promovidas por **NC-Ir1** y **NC-Ir2** se asociaron con eventos apoptóticos tardíos y necróticos.
- Tano el daño al ADN como la disfunción de la respiración celular fueron identificados como procesos promovidos por el tratamiento con **NC-Ir1** y **NC-Ir2** en las células HeLa.

Resumen del Capítulo III

Introducción y objetivos

En capítulos previos se ha abordado la encapsulación en nanocápsulas híbridas de poliuretano-poliurea de compuestos liposolubles, ya sean moléculas orgánicas o complejos metálicos, pero ¿qué ocurre cuando se pretende encapsular un compuesto hidrosoluble?

La bibliografía está repleta de soluciones basadas en nanovehículos que facilitan la estabilización y biodisponibilidad de compuestos liposolubles, pero se reduce drásticamente cuando el objetivo se traslada a la encapsulación de compuestos hidrosolubles. Ello es debido a la dificultad que entraña el aislar un compuesto en una fase dispersa que es, en gran medida, o bien totalmente, afín a la fase dispersante. Se trata de una paradoja física, porque estás dos fases siempre tenderán a la miscibilidad y nunca se podrá formar entre ellas una fase definida, dado que no existe un gradiente de HLB entre ellas.

Es interesante destacar que la naturaleza ya diseñó un sistema para ello: se trata de las bicapas lipídicas, las cuales son capaces de aislar, por ejemplo, el medio intra- y extracelular, aunque ambos tengan naturalezas similares. Las estructuras químicas de los lípidos son anfifílicas por definición y se auto ordenan entre ellas, mediante interacciones no-iónicas, para formar cadenas contrapuestas que interactúan en medio acuoso para minimizar las fuerzas de repulsión. En base a esta teoría se conforman los liposomas que, como se ha explicado en secciones anteriores, son los primeros sistemas de liberación controlada de fármacos aprobados en oncología para la entrega de doxorrubicina.

Para llevar a cabo la encapsulación de compuestos hidrosolubles, los lípidos que constituyen la pared de un liposoma adoptan una conformación bicapa que les permite rodear el núcleo donde se encuentra el compuesto encapsulado, creando así un gradiente decreciente desde el centro de la nanoestructura, de alto HLB, hacia una posición tangencial de la pared de la estructura liposómica de HLB bajo, para luego volver a incrementarse hacia el medio externo de alto HLB.

Tomando como base la estructura de los liposomas, nacen muchos diseños basados en polímeros que mimetizan esta estratificación *in situ* y permiten el aislamiento de compuestos hidrosolubles en medio acuoso[27]. Algunos de estos procesos emplean metodologías sintéticas a través de emulsiones dobles agua aceite en agua (W/O/W, por sus siglas en inglés), como la representada en la Figura 21.

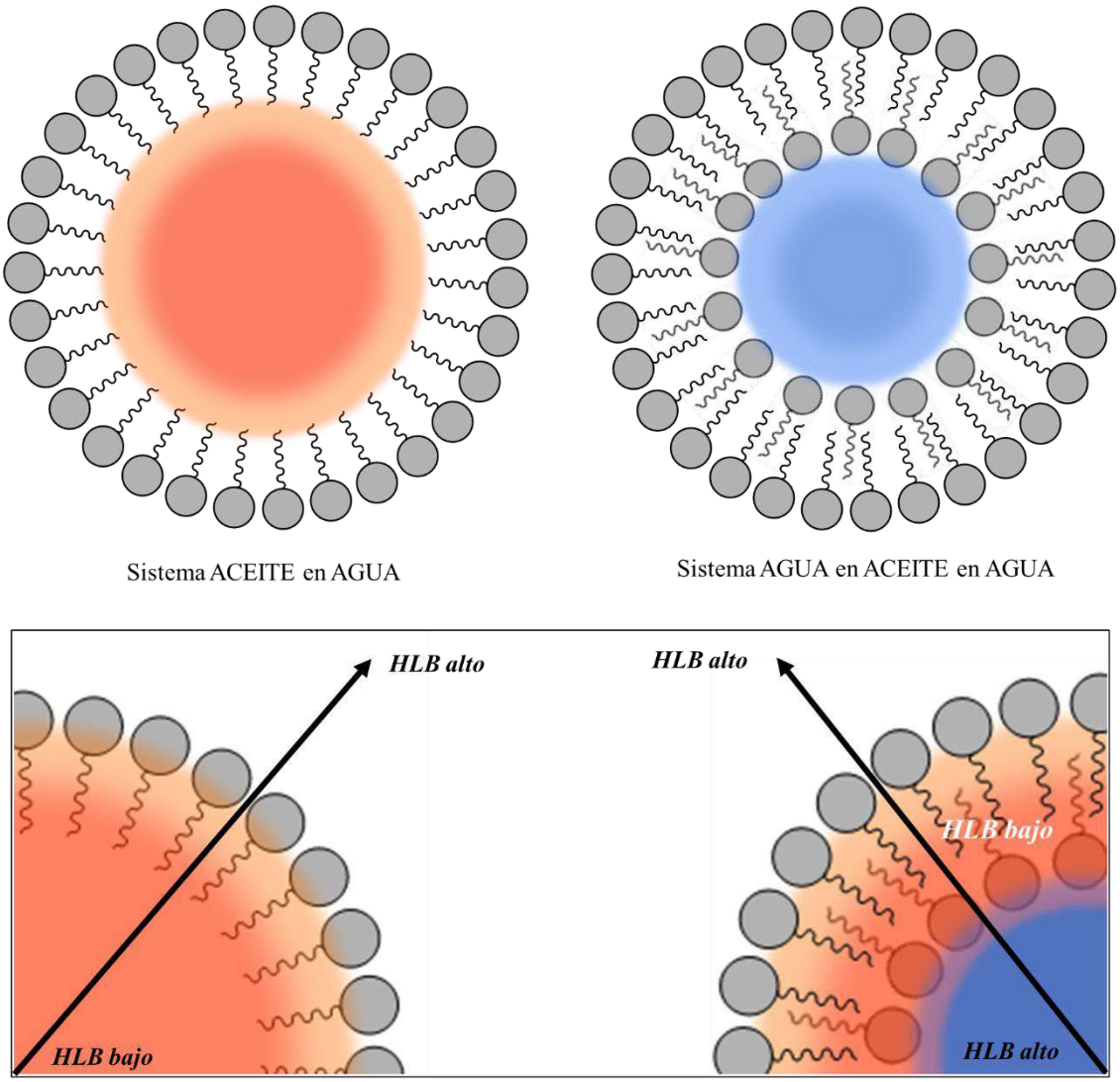

Figura 21: Disección de los gradientes de HLB en un sistema O/W y en un sistema W/O/W

Aunque los compuestos hidrosolubles presentan grandes ventajas en términos de biodisponibilidad respecto a los compuestos liposolubles en terapia, muchos de ellos presentan una baja especificidad, tal y como se mencionó en el Resumen del Capítulo II para el caso del cisplatino, lo que dificulta un uso óptimo en tratamientos oncológicos.

Uno de los ejemplos más claros de moléculas bioactivas que padecen dicha problemática es la gama de fluoróforos orgánicos hidrosolubles, que son ampliamente usados en medicina como herramientas de bioimagen gracias a sus excelentes propiedades espectroscópicas. A pesar de que muchos de ellos presentan una aceptable estabilidad en medio acuoso y son capaces de permanecer íntegros en el torrente sanguíneo durante un notable periodo de tiempo, carecen de capacidad para acumularse selectivamente en una localización concreta del organismo[28]. Así pues, la única sonda fluorescente aprobada hasta la fecha para su uso en oncología en las resecciones de glioma es el GLIOLAN®, basado en el hidrocloruro del ácido 5-aminolevulínico[29].

Esta problemática, dificulta su uso como agentes de imagen en aplicaciones oncológicas y, por este motivo, en la literatura se ha abordado la modificación estructural de dichas sondas fluorescentes para incrementar su acumulación preferencial en lesiones tumorales[30], tal y como se esquematiza en la Figura 22.

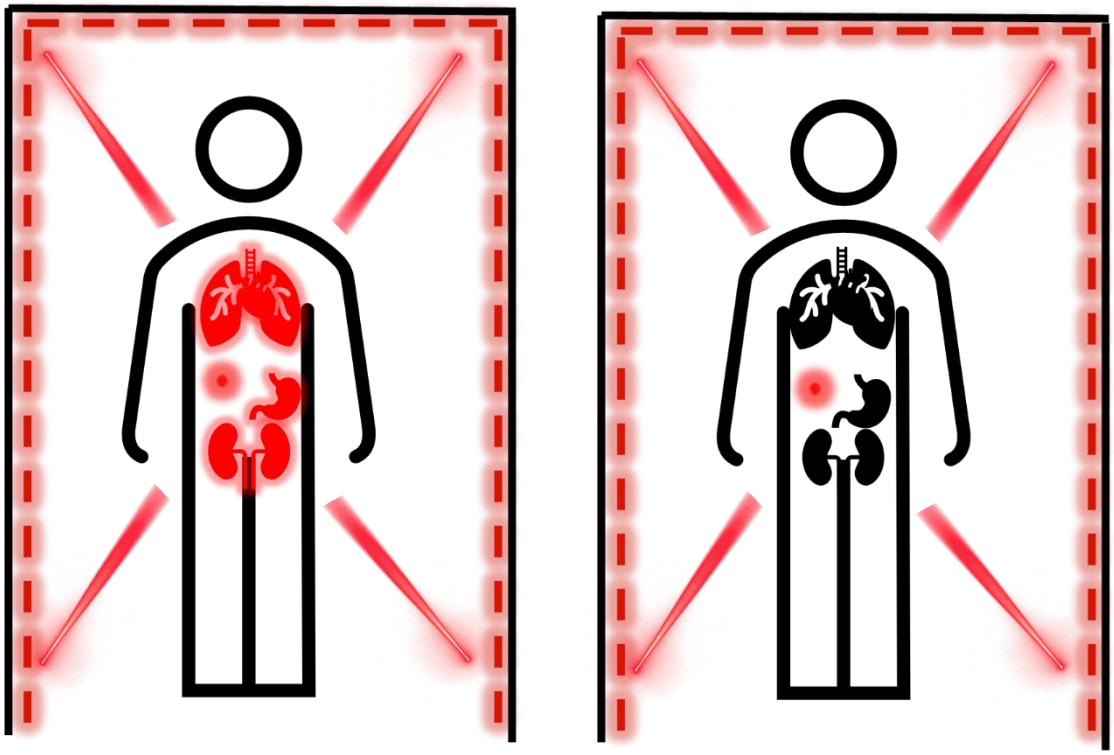

Figura 22: El objetivo de toda sonda fluorescente para aplicaciones oncológicas es ser capaz de pasar de un modelo farmacocinético inespecífico a un modelo dónde quede señalada de manera inequívoca la localización de la lesión tumoral, incluso si ésta se encuentra en una zona de difícil acceso en el organismo.

En el caso concreto del compuesto verde de indocianina (ICG, por sus siglas en inglés), que fue la primera sonda fluorescente aprobada para uso clínico, se han abordado diferentes estrategias para aumentar su potencial en diferentes aplicaciones oncológicas debido a su escasa selectividad frente a tumores[31].

El marco de aplicación de las sondas fluorescentes de nueva generación en oncología no se reduce únicamente a la visualización de la lesión tumoral. Como en el caso del GLIOLAN, se pretenden usar como "perros lazarillos" para intervenciones intra-operativas de resección tumoral, la llamada cirugía guiada por fluorescencia (FGS, por sus siglas en inglés). Es por ello por lo que este tipo de compuestos deben cumplir una serie de requisitos para su uso como agentes teragnósticos:

1. Deben ser inocuos para las células bajo irradiación, es decir, no pueden actuar como los fotosensibilizadores en PDT y generar ROS.
2. Su ventana de absorción y emisión debe situarse por encima de los 650-700 nm, lo que permite una irradiación extracorpórea cualitativa.

3. Deben presentar una acumulación específica en células o lesiones tumorales.
4. Su biodisponibilidad debe ser lo suficientemente buena para que permita una primera administración para después proseguir con la intervención quirúrgica (un mínimo de 48 h en cuanto a biodisponibilidad).
5. Evitar una degradación prematura en el torrente sanguíneo.

Con todos estos requisitos sobre la mesa, la nanomedicina se ha postulado como una de las grandes herramientas para la síntesis de productos que cumplan con estos criterios[32]. En el caso concreto de la vehiculización de fluoróforos orgánicos hidrosolubles en entidades nanométricas, que es una de las aproximaciones preferidas ya que brinda una elevada protección frente a la biodegradación prematura, varios autores reportan diversas metodologías de gran interés[33–35].

Nuestro grupo de investigación en Ecopol Tech, en colaboración con diversos grupos de la Universidad de Barcelona, se ha centrado recientemente en el desarrollo de nanocápsulas de doble pared, mediante emulsiones W/O/W, que permitieran incorporar en el núcleo hidrosoluble de las mismas a la sonda fluorescente ICG. Estas nanocápsulas se han diseñado para permitir una acumulación de manera selectiva en lesiones causadas por tumores sólidos, permitiendo así la rápida identificación de los mismos con técnicas de monitorización no-invasivas. Es por ello por lo que se seleccionó como agente a encapsular a la sonda fluorescente ICG debido a sus excelentes propiedades espectroscópicas.

Cabe mencionar que, aunque este capítulo está centrado en el desarrollo de nanocápsulas con sondas fluorescentes, la investigación para la vehiculización biológica de compuestos hidrosolubles tiene una amplia aplicabilidad para su uso con compuestos de naturaleza delicada y de baja estabilidad, como es el caso de los oligonucleótidos, especialmente en terapia oncológica[36].

Resultados y discusión

Publicación III (manuscrito enviado para publicación): Bonelli, J.; Velasco- de Andrés, M.; Isidro, N.; Bayó, C.; Chumillas, S.; Carrillo-Serradell, L.; Casadó-Llombart, S.; Mok, C.; Benítez, D.; Lozano, F.; Rocas, J.; Marchán, V.

Novel tumor-targeted self-nanostructured and compartmentalized water-in-oil-in-water polyurethane-polyurea nanocapsules for cancer theragnosis.

Este proyecto ha sido desarrollado en colaboración con los grupos de investigación del Dr. Daniel Benítez y el Dr. Francisco Lozano del centro de investigación IDIBAPS, en el Hospital Clínico de Barcelona. Todos los ensayos en animales contenidos en este capítulo han sido aprobados por el comité ético de la Fundació Clínic per a la Recerca Biomédica (FCRB).

Síntesis de las ICG-NCs catiónicas y de las ICG-NCs anfotéricas

La metodología de encapsulación utilizada en este proyecto ha implicado también la síntesis racional de polímeros híbridos de poliuretano-poliurea para su uso como entidades auto-emulsionables que sean capaces de formar *in situ* una pared polimérica robusta en una localización interfacial.

Dado que en esta aproximación se pretende la nanoencapsulación de un compuesto hidrosoluble, el esquema sintético viaja a través de la formación, en dos etapas, de una doble pared multifuncional y robusta de poliuretano-poliurea, estructurada mediante un proceso de doble emulsión W/O/W.

Para llevar a cabo esta síntesis, en primer lugar, es necesario preparar un prepolímero de bajo HLB, P1, capaz de emulsionar una fase acuosa en un medio orgánico inmiscible. El proceso sintético empieza por el secado y adición de un diol que incorpora una cadena lateral PEG_{1000} (de nombre comercial YMER N-120), y un diol de cadena corta que incorpora de manera lineal un enlace disulfuro (2,2′-Ditiodietanol, de nombre comercial DEDS) sobre un exceso de diisocianato de isoforona (IPDI), a una ratio determinada. Esta polimerización se lleva a cabo sin necesidad de calentar el matraz de reacción y en ausencia de disolvente.

Una vez comprobada la desaparición de la banda de isocianato mediante análisis or FTIR (sobre unos 2250 cm^{-1}) y la aparición de la banda de uretano (alrededor de 1530 cm^{-1}), se procede a la adición de acetona como disolvente debido a la elevada viscosidad de la muestra. En un balón a parte se prepara una disolución en acetona en exceso de 1,3-

diamino-N-octadecilpropano (de nombre comercial Genamin TAP 100D), respecto a los equivalentes libres de isocianato presentes en el poliuretano anteriormente preparado. En el paso final, se añade lentamente la disolución del poliuretano en acetona sobre el exceso en equivalentes de la diamina grasa, dando lugar a la formación de enlaces urea (confirmado por la aparición de la correspondiente banda de carbonilo de la urea sobre 1630 cm^{-1}) por reacción entre los grupos amina e isocianato, consumiéndose este último en su totalidad y conduciendo a la formación del prepolímero P1 de estructura híbrida poliuretano-poliurea. **El prepolímero P1 formará la primera pared de las nanocápsulas**.

En paralelo, se precisa llevar a cabo la síntesis de un prepolímero de alto HLB, descrito como P1 en la sección de Resultados y Discusión del Capítulo Ia de esta Tesis, al que ahora llamaremos **prepolímero P2 y que formará la segunda pared de las nanocápsulas**.

En el primer paso del proceso de encapsulación propiamente dicho, una vez tenemos preparados los dos prepolímeros intermedios **P1** y **P2**, se agita una cantidad determinada del compuesto a encapsular en agua (ICG en este caso), una disolución de dietielentriamina y una alícuota del prepolímero **P1** disuelto en acetona. Esta mezcla se homogeniza con agitación magnética y, si es necesario, con ciclos cortos de ultrasonicación. Bajo una agitación controlada, se añade gota a gota una cantidad determinada de ciclohexano para producir la primera emulsión W/O (agua/ciclohexano) por inversión de fase a la que luego se le añade una cantidad de IPDI ligeramente superior en equivalentes de isocianato frente a los equivalentes de amina presentes en la mezcla. Estos equivalentes de isocianato en exceso reaccionan rápidamente con las aminas de la mezcla (tanto provenientes de **P1** como de la dietilentriamina) para generar una polimerización entrecruzada que forma la primera pared de la doble encapsulación. Una vez finalizado este proceso, se utiliza esta fase orgánica de nanocápsulas dispersadas como fase dispersa de una encapsulación O/W al uso, como las descritas en capítulos anteriores, utilizando el **P2** como emulsionante y precursor de la segunda pared para generar la estructura deseada de W/O/W. Todo este proceso sintético de encapsulación se muestra en la Figura 23.

Cabe decir que pensando en la validación del sistema de protonación superficial de las nanocápsulas en medio ácido con el objetivo de promover la direccionalidad al TME, también se abordó la síntesis de unas nanocápsulas puramente catiónicas que nos servirían como control "no-direccionado" a lesiones tumorales *in vivo*. Así pues, en este caso, la adición de lisina durante el proceso sintético es un elemento clave para controlar la inclusión o no de grupos carboxilato en superficie, lo que permite generar **ICG-NCs anfotéricas** o **ICG-NCs catiónicas**, respectivamente.

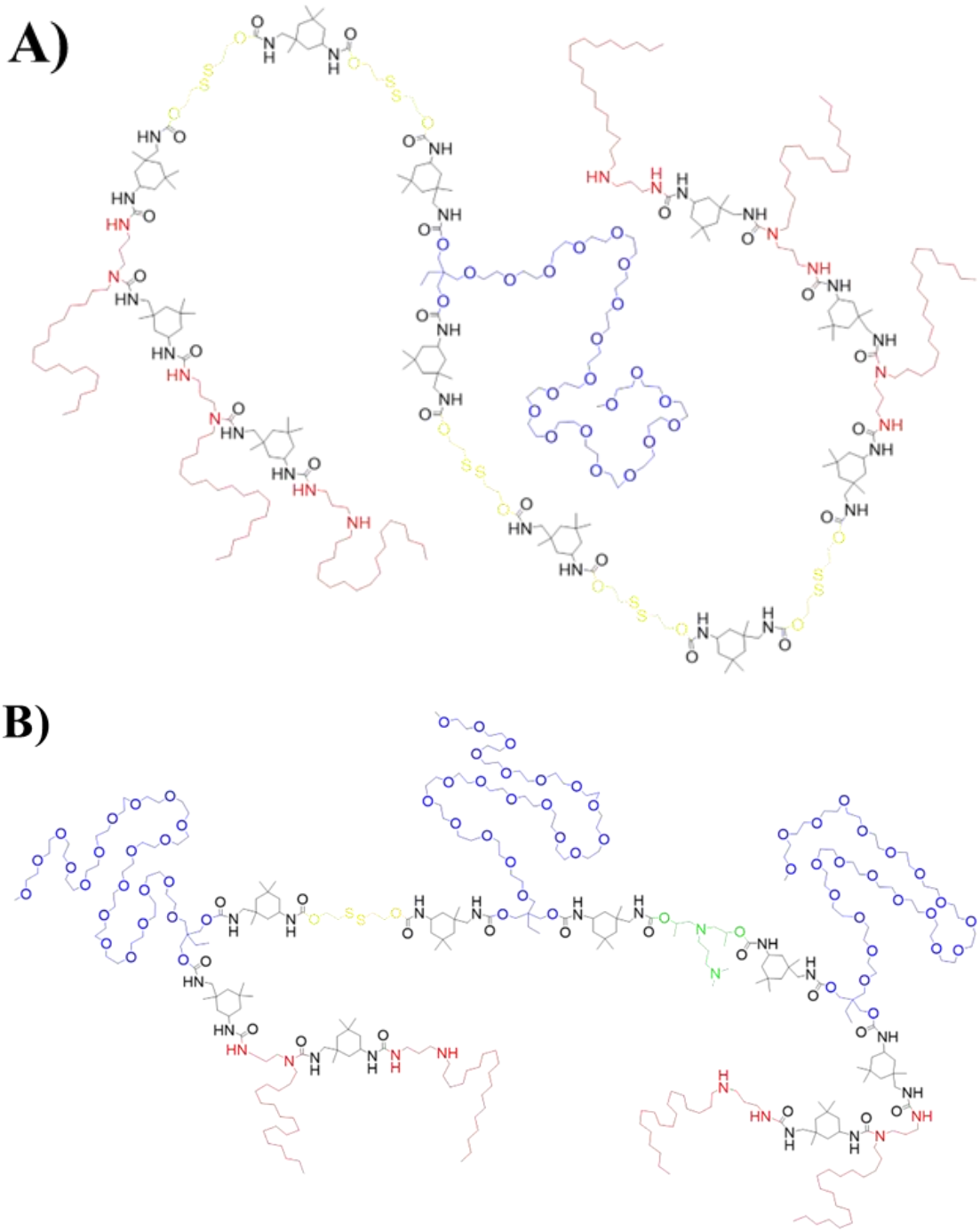

Figura 22: Representación de posibles estructuras químicas para los prepolímeros de peso molecular medio que se generan en la síntesis de A) **P1** y B) **P2**.

Cabe destacar que el proceso de inversión de fase producido durante la segunda etapa del proceso de encapsulación atraviesa un periodo de alta viscosidad, justamente en el cambio de fase dispersante de ciclohexano a agua debido a que, en ese momento y paradójicamente, en la fase dispersante ya existe una dispersión formada y estabilizada. Al final de la síntesis se elimina el ciclohexano de la muestra por evaporación suave en vacío y se purifica el producto final por un proceso de diálisis.

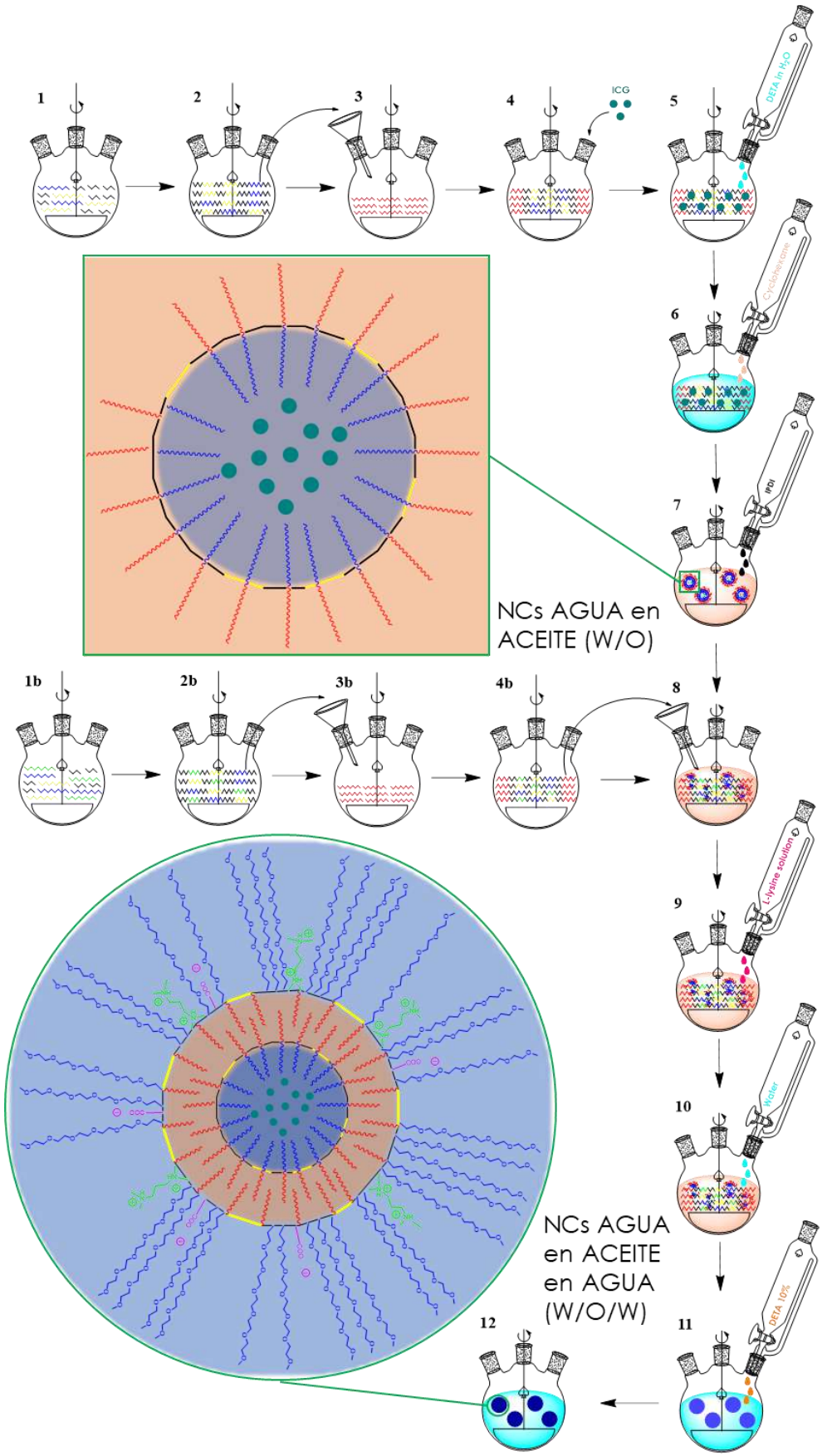

Figura 23: Síntesis detallada del proceso de nanoencapsulación por doble emulsión (W/O/W)

Ambos productos, ICG-NCs anfotéricas o ICG-NCs catiónicas, se caracterizaron por DLS y TEM para conocer su tamaño tanto en un entorno hidrodinámico como seco. Siendo ambos tamaños superiores a los obtenidos en los procesos de encapsulación de compuestos liposolubles (hecho esperable debido a la dificultad que acarrea la estabilización de una emulsión tan pequeña y mucho más compleja), el tamaño de las ICG-NCs catiónicas resultó ser de unos 55 nm, mientras que el tamaño de las ICG-NCs anfotéricas, que incorporan motivos carboxilato en superficie provenientes de la reacción con la lisina, disminuyó hasta unos 30 nm. Este hecho concuerda perfectamente con el diseño experimental ya que, a igual cantidad de polímero P2 en ambos procesos, la adición de lisina aporta un poder emulsionante extra como ionómero en la estructura del polímero. Así, aumenta el HLB del polímero *in situ*, disminuye su concentración micelar crítica y permite estabilizar micelas de menor tamaño.

La modificación de la carga superficial en base a las variaciones de pH del medio se verificó con experimentos de potencial Z. Como era de esperar, mientras que las ICG-NCs anfotéricas mostraban una variación de carga superficial sustancial dependiente del pH, las ICG-NCs catiónicas mantienen elevados valores de carga positiva durante todas las mediciones, tal y como se muestra en la gráfica de la Figura 24.

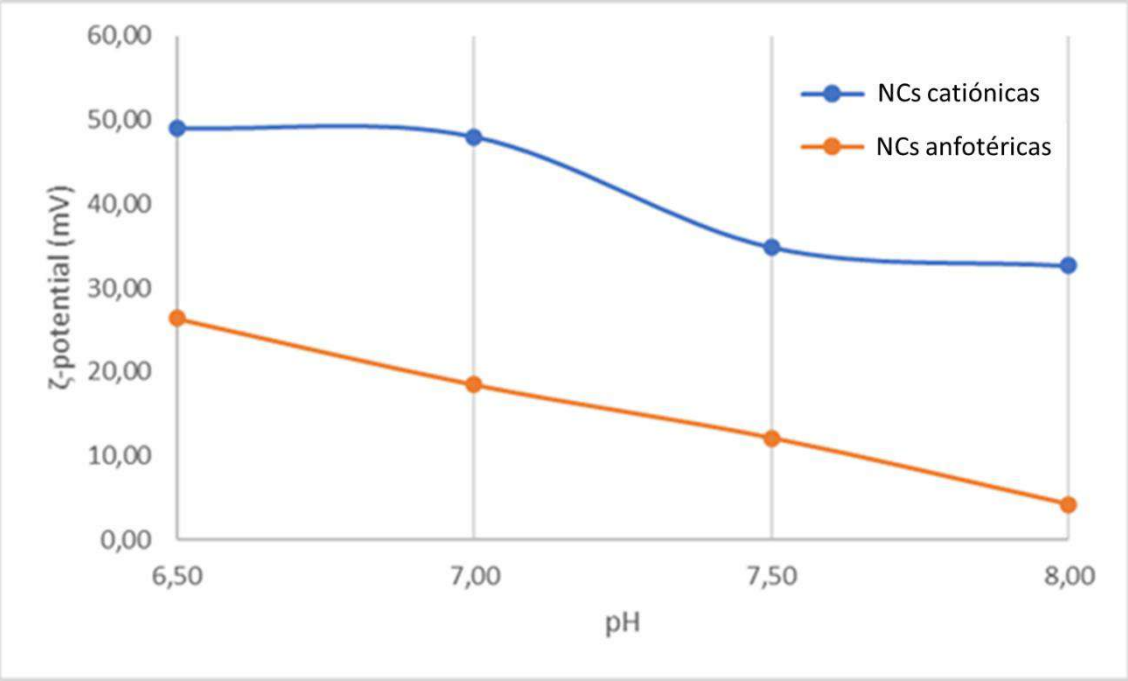

Figura 24: Representación gráfica de la variación de carga superficial dependiente de pH medida por potencial Z para las ICG-NCs catiónicas y las ICG-NCs anfotéricas.

La determinación de la carga efectiva de ICG y de la eficacia de encapsulación en ambas muestras se llevó a cabo mediante el análisis por espectroscopia UV-visible. Los valores obtenidos fueron de 215 μM para ICG-NCs catiónicas y de 237 μM para ICG-NCs anfotéricas, siendo los valores de eficacia de encapsulación 54% y 62%, respectivamente.

Como se menciona en el apartado de introducción, uno de los principales objetivos de la encapsulación de sondas fluorescentes es incrementar su estabilidad en medio acuoso, manteniendo sus propiedades durante periodos más largos de tiempo. Para evaluar el efecto de la encapsulación sobre dicho parámetro, se comparó la estabilidad entre una solución acuosa de ICG y una dispersión de nanocápsulas del mismo a igual concentración, aplicando diferentes tratamientos: i) calentamiento en estufa a 37 ºC, ii) exposición a la luz a 25 ºC, iii) almacenamiento a 4 ºC en la oscuridad durante 7 días. En todos ellos se evaluó la intensidad de la absorbancia de la sonda ICG, concluyéndose que, en todos los casos, **la nanoencapsulación mitiga enormemente la degradación de la sonda ICG en medio acuoso**.

Evaluación de las propiedades biológicas de las ICG-NCs anfotéricas y ICG-NCs catiónicas

La evaluación, primero por microscopía confocal y después por citometría de flujo, reveló una elevada internalización en células dendríticas primaras derivadas de monocitos (moDCs, por sus siglas en inglés) tanto para las ICG-NCs anfotéricas como para las ICG-NCs catiónicas.

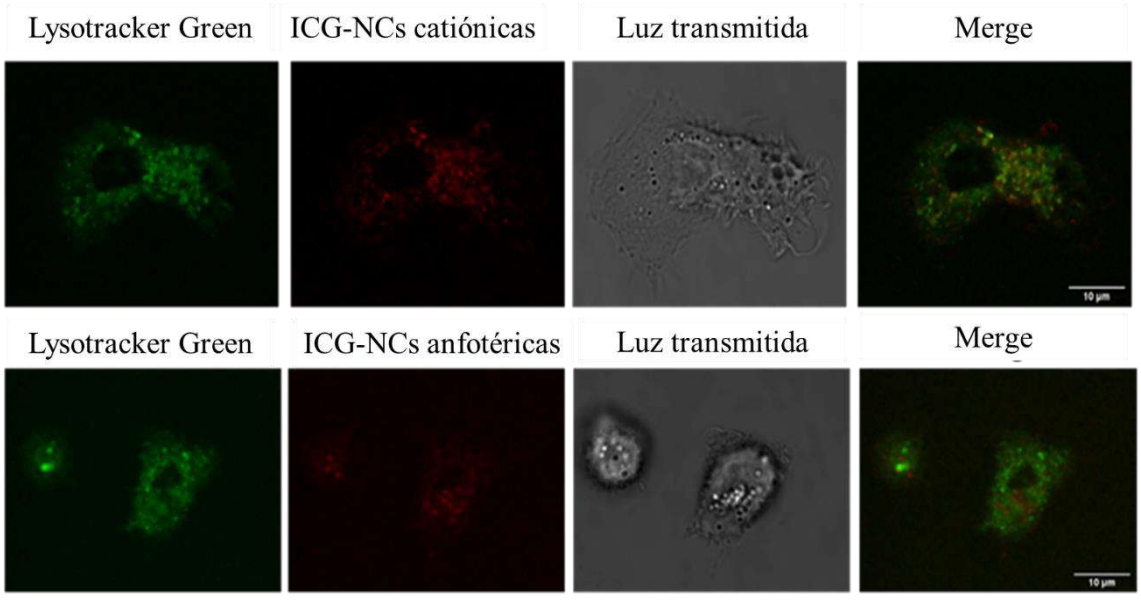

Figura 25: Experimentos de microscopia confocal llevados a cabo con ICG-NCs anfotéricas a una concentración 2 μM de ICG y con incubaciones de 2 h en cultivos de moDCs. En la imagen se muestran los canales del verde (LTG), el rojo (ICG), el campo claro (células) y la superposición de verde y rojo (*merge*).

La ventana de operabilidad del ICG nos permite trabajar con tecnologías de visualización que emplean irradiaciones muy penetrantes y completamente inocuas para las células (otro de los objetivos inicialmente planteados). En el caso de las imágenes de microscopia confocal mostradas en la Figura 25, la monitorización de ICG se llevó a cabo empleando un láser multifotón que permite excitar a 790 nm y con detección de la emisión centrada a 810 nm. Aunque los coeficientes de colocalización de Pearson y Manders no fueron calculados en esta ocasión, los patrones de señal de fluorescencia de los canales verde (LTG) y rojo (ICG) sugieren que la mayor parte de ICG está situada en localizaciones lisosomales en las muestras.

Para cuantificar si existían diferencias significativas de internalización celular entre las nanocápsulas anfotéricas y las catiónicas se sintetizaron, siguiendo el método descrito en el apartado de síntesis, unas nanocápsulas análogas que contenían un derivado COUPY idóneo para su uso en citometría de flujo (FACS, por sus siglas en inglés), ya que la visualización de ICG mediante esta técnica era imposible debido a que opera a unas longitudes de onda fuera del rango de excitación y detección que ofrecía el equipo del que disponíamos en ese momento. Los resultados de dichos estudios nos permitieron concluir que no existen diferencias significativas entre la internalización en moDCs de las nanocápsulas anfotéricas y catiónicas tras 24 h de incubación. Ahora bien, sí que revelaron, como era previsible en base a estudios anteriores, que el mecanismo de internalización de ambas nanoestructuras implica un transporte activo dependiente de energía a través de la membrana celular.

Una vez confirmada la correcta visualización *in vitro* de las ICG-NCs anfotéricas y de las ICG-NCs catiónicas, se diseñaron una serie de experimentos *in vivo* en modelos de ratón NSG inmunodeprimidos, implantados con células de melanoma A375 de forma subcutánea en el flanco trasero derecho. En el paso previo a estos ensayos se realizó un análisis toxicológico completo, también en modelos roedores, donde ambas nanocápsulas mostraron una nula toxicidad a las concentraciones de trabajo.

Los experimentos de eficacia en el modelo tumoral de ratón se realizaron implantando células de melanoma A375, por inyección subcutánea, en el flanco derecho trasero del animal. Se permitió proliferar a las células tumorales durante 14 días en un régimen de dieta occidental del ratón y se procedió entonces a las inyecciones intravenosas, a través la vena de la cola, de las muestras con las ICG-NCs anfotéricas y las ICG-NCs catiónicas en PBS. El patrón de biodistribución de las nanocápsulas fue fácilmente monitorizado mediante la tecnología IVIS®, en la que se emplea el uso de radiación infrarroja extracorpórea del animal, para el posterior análisis de la fluorescencia emitida y su interpretación en un mapa de calor del animal a cuerpo entero.

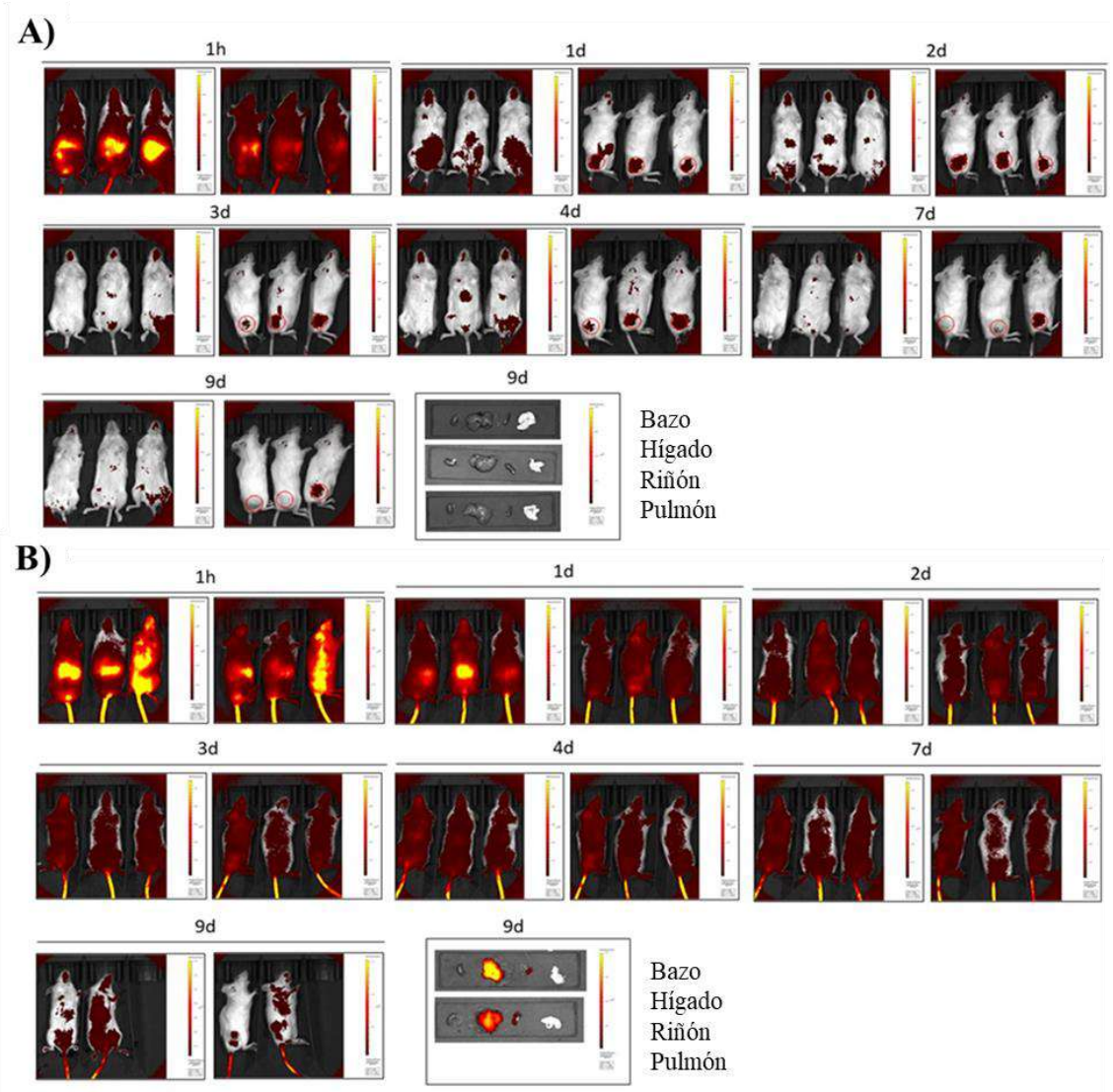

Figura 26: Patrón de monitorización de la biodistribución del ICG durante 9 días post inyección en A) Ratones NSG implantados con células de melanoma A375 tratados con ICG-NCs anfotéricas (n=3/grupo) a 40 µM ICG y B) Ratones NSG implantados con células de melanoma A375 tratados con ICG-NCs catiónicas (n=3/grupo) a 40 µM ICG. Las localizaciones tumorales están señalizadas con círculos rojos punteados.

Como se puede observar en la Figura 26, la monitorización de la sonda ICG se llevó a cabo durante 9 días después de la inyección de las nanocápsulas y, después de este periodo, los ratones fueron sacrificados para obtener los datos de acumulación cualitativa en sus principales órganos excretores: bazo, hígado, riñón y pulmón.

Los resultados de este análisis esclarecieron que, si bien el ICG libre en solución salina no puede ser identificado a las 48 h después de su inyección intravenosa (datos no mostrados en la Figura 26), tanto las ICG-NCs anfotéricas como las ICG-NCs catiónicas son monitorizables durante más de una semana mediante la tecnología IVIS® de irradiación infrarroja.

Para nuestro deleite, los análisis llevados a cabo durante el tratamiento revelan que las ICG-NCs anfotéricas empiezan a mostrar un patrón selectivo de acumulación tumoral

a las 24 h-48 h después de la inyección, concentrando la señal de fluorescencia en el flanco derecho trasero de los animales. Por el contrario, la muestra con ICG-NCs catiónicas genera una señal inespecífica a lo largo de todo el animal, que no permite discernir las localizaciones de las lesiones tumorales. Esto nos permite verificar que la aproximación biológica de **acumulación selectiva de las nanocápsulas por su protonación superficial selectiva en el microambiente tumoral se produce de manera satisfactoria** en modelos tumorales de ratones implantados con células de melanoma A375, tal y como ilustra la Figura 27.

Además, el análisis *ex vivo* de los principales órganos excretores después de 9 días del tratamiento confirma una acumulación inespecífica de ICG-NCs catiónicas en los mismos, mientras que no se observa señal alguna proveniente del análisis con ICG-NCs anfotéricas. Estos resultados son muy positivos de cara a un potencial tratamiento basado en la liberación controlada de fármacos en localizaciones tumorales, ya que evitaría toxicidades indeseadas por acumulación en los principales órganos de excreción.

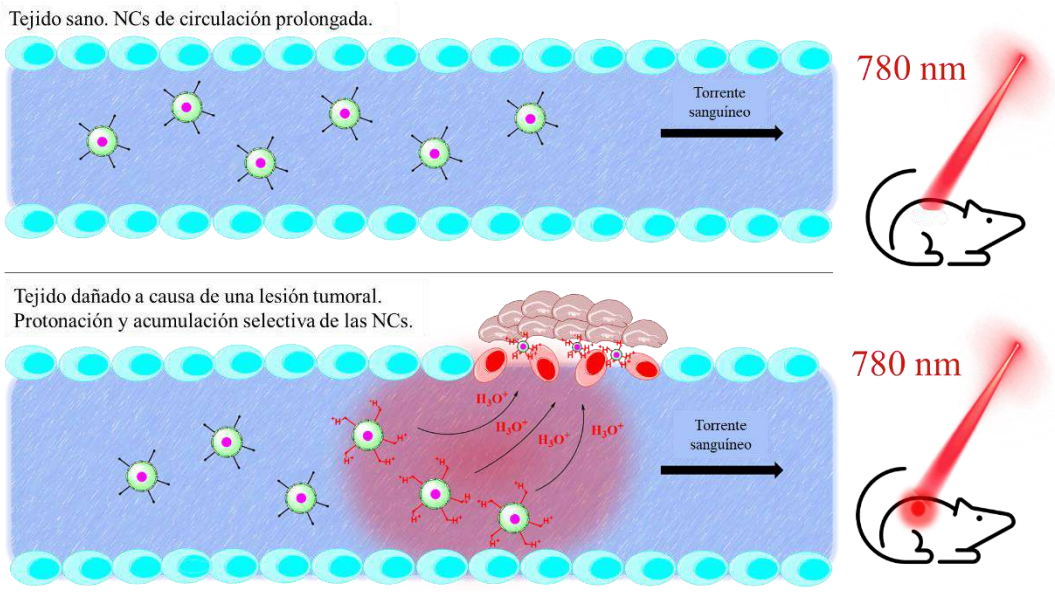

Figura 27: Simplificación del mecanismo de acumulación de las nanocápsulas en el microambiente tumoral, causado por la presencia de una lesión tumoral adyacente.

El trabajo basado en la encapsulación de compuestos hidrosolubles mediante el uso de nanocápsulas híbridas de poliuretano-poliurea, junto con otras aproximaciones basadas también en esta tecnología, fue declarado novedoso en un informe emitido por la Oficina de Patentes Europeas a finales de 2021. La correspondiente PCT ha sido aceptada a inicios de septiembre de 2022 y será publicada a finales del mismo año.

Conclusiones

El trabajo desarrollado en el Capítulo III se focalizó en el desarrollo de una nueva metodología sintética que permitiese la encapsulación de compuestos hidrosolubles en nanocápsulas híbridas de poliuretano-poliurea, promoviendo su acumulación específica en lesiones tumorales. La validación y evaluación de este tipo de nanocápsulas en un medio *in vivo* relevante se realizó mediante la encapsulación de la sonda fluorescente *Indocyanine Green* (ICG) en un modelo tumoral de ratón inoculado con células A375 de melanoma, lo que abre la puerta a su empleo como posible agente teragnóstico. Este estudio cristalizó en la presentación de una patente titulada "*Nanotechnological platform based on polyurethane/polyurea chemistry to furnish water-oil-water multi walled and functionalizable nanocapsules and their preparation process*". Inventores: Bonelli, J.; Rocas, J. PCT/EP2022/058801. Solicitante: Ecopol Tech S.L.

Las conclusiones concretas extraídas de este trabajo se muestran a continuación:

- Se desarrolló con éxito una metodología sintética para encapsular compuestos bioactivos hidrosolubles utilizando nanocápsulas híbridas de poliuretano-poliurea de doble pared, empleando un sistema de emulsión doble de agua en aceite en agua (W/O/W).
- La encapsulación de la sonda fluorescente ICG se abordó exitosamente y con un alto rendimiento.
- Se validó la monitorización extracorpórea *in vivo* de la sonda nanoestructurada mediante la tecnología IVIS®.
- La funcionalización anfotérica en las nanocápsulas cargadas con ICG se reveló como un importante punto de partida para la promoción de la acumulación *in vivo* selectiva de nanomedicinas en el TME en un modelo de ratón con melanoma.
- La administración intravenosa de ICG-NCs anfótericas no condujo, tras un tratamiento de 9 días, a una acumulación inespecífica en los principales órganos de excreción, al contrario de lo que se observó con la versión de ICG-NCs catiónicas.
- Además de su posible aplicación en bioimagen, la acumulación *in vivo* de las nanocápsulas cargadas con ICG anfotéricas en el TME respalda su posible uso para la administración de agentes anticancerígenos hidrosolubles.

Referencias

(1) Food and Drug Administration. *Doxil Label*; 1995.

(2) Blanco, E.; Shen, H.; Ferrari, M. Principles of Nanoparticle Design for Overcoming Biological Barriers to Drug Delivery. *Nat. Biotechnol.* **2015**, *33*, 941–951. https://doi.org/10.1038/nbt.3330.

(3) Shi, J.; Kantoff, P. W.; Wooster, R.; Farokhzad, O. C. Cancer Nanomedicine: Progress, Challenges and Opportunities. *Nat. Rev. Cancer* **2017**, *17*, 20–37. https://doi.org/10.1038/nrc.2016.108.

(4) Liu, C.; Jin, Y.; Fan, Z. The Mechanism of Warburg Effect-Induced Chemoresistance in Cancer. *Front. Oncol.* **2021**, *11*. https://doi.org/10.3389/fonc.2021.698023.

(5) Kennedy, L.; Sandhu, J. K.; Harper, M. E.; Cuperlovic-culf, M. Role of Glutathione in Cancer: From Mechanisms to Therapies. *Biomolecules* **2020**, *10*, 1–27. https://doi.org/10.3390/biom10101429.

(6) Allison, R. R.; Moghissi, K. Photodynamic Therapy (PDT): PDT Mechanisms. *Clin. Endosc.* **2013**, *46*, 24–29. https://doi.org/10.5946/ce.2013.46.1.24.

(7) Liu, M.; Li, C. Recent Advances in Activatable Organic Photosensitizers for Specific Photodynamic Therapy. *Chempluschem.* **2020**, *85*, 948–957. https://doi.org/10.1002/cplu.202000203.

(8) Gandioso, A.; Bresolí-Obach, R.; Nin-Hill, A.; Bosch, M.; Palau, M.; Galindo, A.; Contreras, S.; Rovira, A.; Rovira, C.; Nonell, S.; Marchán, V. Redesigning the Coumarin Scaffold into Small Bright Fluorophores with Far-Red to Near-Infrared Emission and Large Stokes Shifts Useful for Cell Imaging. *J. Org. Chem.* **2018**, *83*, 1185–1195. https://doi.org/10.1021/acs.joc.7b02660.

(9) Ortega-Forte, E.; Rovira, A.; Gandioso, A.; Bonelli, J.; Bosch, M.; Ruiz, J.; Marchán, V. COUPY Coumarins as Novel Mitochondria-Targeted Photodynamic Therapy Anticancer Agents. *J. Med. Chem.* **2021**, *64*, 17209–17220. https://doi.org/10.1021/acs.jmedchem.1c01254.

(10) McKenzie, L. K.; Bryant, H. E.; Weinstein, J. A. Transition Metal Complexes as Photosensitisers in One- and Two-Photon Photodynamic Therapy. *Coord. Chem. Rev.* **2019**, *379*, 2–29. https://doi.org/10.1016/j.ccr.2018.03.020.

(11) Karges, J. Clinical Development of Metal Complexes as Photosensitizers for Photodynamic Therapy of Cancer. *Angew. Chem. – Int. Ed.* **2022**, *61*. https://doi.org/10.1002/anie.202112236.

(12) Huang, H.; Banerjee, S.; Sadler, P. J. Recent Advances in the Design of Targeted Iridium(III) Photosensitizers for Photodynamic Therapy. *ChemBioChem* **2018**, *19*, 1574–1589. https://doi.org/10.1002/cbic.201800182.

(13) Howerton, B. S.; Heidary, D. K.; Glazer, E. C. Strained Ruthenium Complexes Are Potent Light-Activated Anticancer Agents. *J. Am. Chem. Soc.* **2012**, *134*, 8324–8327. https://doi.org/10.1021/ja3009677.

(14) McFarland, S. A. Metal-Based Thiophene Photodynamic Compounds and Their Use. US 9,676,806 B2, December 14, 2013. https://doi.org/10.1016/j.molstruc.2011.09.021.

(15) Novohradsky, V.; Rovira, A.; Hally, C.; Galindo, A.; Vigueras, G.; Gandioso, A.; Svitelova, M.; Bresolí-Obach, R.; Kostrhunova, H.; Markova, L.; Kasparkova, J.; Nonell, S.; Ruiz, J.; Brabec, V.; Marchán, V. Towards Novel Photodynamic Anticancer Agents Generating Superoxide Anion Radicals: A Cyclometalated Ir III Complex Conjugated to a Far-Red Emitting Coumarin. *Angew. Chem.* **2019**, *131*, 6377–6381. https://doi.org/10.1002/ange.201901268.

(16) Martins, T. J.; Negri, L. B.; Pernomian, L.; Faial, K. do C. F.; Xue, C.; Akhimie, R. N.; Hamblin, M. R.; Turro, C.; da Silva, R. S. The Influence of Some Axial Ligands on Ruthenium–Phthalocyanine Complexes: Chemical, Photochemical, and Photobiological Properties. *Front. Mol. Biosci.* **2021**, *7*. https://doi.org/10.3389/fmolb.2020.595830.

(17) Roguin, L. P.; Chiarante, N.; García Vior, M. C.; Marino, J. Zinc(II) Phthalocyanines as Photosensitizers for Antitumor Photodynamic Therapy. *Int. J. Biochem. Cell B.* **2019**, *114*. https://doi.org/10.1016/j.biocel.2019.105575.

(18) Nayeem, N.; Contel, M. Exploring the Potential of Metallodrugs as Chemotherapeutics for Triple Negative Breast Cancer. *Chem. Eur. J.* **2021**, *27*, 8891–8917. https://doi.org/10.1002/chem.202100438.

(19) Rosenberg, B.; VanCamp, L. The Successful Regression of Large Solid Sarcoma 180 Tumors by Platinum Compounds. *Cancer Res.* **1970**, *30*, 1799–1802.

(20) Oberoi, H. S.; Nukolova, N. v.; Kabanov, A. v.; Bronich, T. K. Nanocarriers for Delivery of Platinum Anticancer Drugs. *Adv. Drug Deliv. Rev.* **2013**, *65*, 1667–1685. https://doi.org/10.1016/j.addr.2013.09.014.

(21) Kelland, L. The Resurgence of Platinum-Based Cancer Chemotherapy. *Nat. Rev. Cancer* **2007**, *7*, 573–584. https://doi.org/10.1038/nrc2167.

(22) Zheng, Y. R.; Suntharalingam, K.; Johnstone, T. C.; Yoo, H.; Lin, W.; Brooks, J. G.; Lippard, S. J. Pt(IV) Prodrugs Designed to Bind Non-Covalently to Human Serum Albumin for Drug Delivery. *J. Am. Chem. Soc.* **2014**, *136*, 8790–8798. https://doi.org/10.1021/ja5038269.

(23) Johnstone, T. C.; Lippard, S. J. The Effect of Ligand Lipophilicity on the Nanoparticle Encapsulation of Pt(IV) Prodrugs. *Inorg. Chem.* **2013**, *52*, 9915–9920. https://doi.org/10.1021/ic4010642.

(24) Millett, A. J.; Habtemariam, A.; Romero-Canelón, I.; Clarkson, G. J.; Sadler, P. J. Contrasting Anticancer Activity of Half-Sandwich Iridium(III) Complexes Bearing Functionally Diverse 2-Phenylpyridine Ligands. *Organometallics* **2015**, *34*, 2683–2694. https://doi.org/10.1021/acs.organomet.5b00097.

(25) Zamora, A.; Vigueras, G.; Rodríguez, V.; Santana, M. D.; Ruiz, J. Cyclometalated Iridium(III) Luminescent Complexes in Therapy and Phototherapy. *Coord. Chem. Rev.* **2018**, *360*, 34–76. https://doi.org/10.1016/j.ccr.2018.01.010.

(26) Pracharova, J.; Vigueras, G.; Novohradsky, V.; Cutillas, N.; Janiak, C.; Kostrhunova, H.; Kasparkova, J.; Ruiz, J.; Brabec, V. Exploring the Effect of Polypyridyl Ligands on the Anticancer Activity of Phosphorescent Iridium(III) Complexes: From Proteosynthesis Inhibitors to Photodynamic Therapy Agents. *Chem. Eur. J.* **2018**, *24*, 4607–4619. https://doi.org/10.1002/chem.201705362.

(27) Becker Peres, L.; Becker Peres, L.; de Araújo, P. H. H.; Sayer, C. Solid Lipid Nanoparticles for Encapsulation of Hydrophilic Drugs by an Organic Solvent Free Double Emulsion Technique. *Colloids Surf. B. Biointerfaces* **2016**, *140*, 317–323. https://doi.org/10.1016/j.colsurfb.2015.12.033.

(28) Onda, N.; Kimura, M.; Yoshida, T.; Shibutani, M. Preferential Tumor Cellular Uptake and Retention of Indocyanine Green for in Vivo Tumor Imaging. *Int. J. Cancer* **2016**, *139*, 673–682. https://doi.org/10.1002/ijc.30102.

(29) Mieog, J. S. D.; Achterberg, F. B.; Zlitni, A.; Hutteman, M.; Burggraaf, J.; Swijnenburg, R. J.; Gioux, S.; Vahrmeijer, A. L. Fundamentals and Developments

in Fluorescence-Guided Cancer Surgery. *Nat. Rev. Clin. Oncol.* **2022**, *19*, 9–22. https://doi.org/10.1038/s41571-021-00548-3.

(30) Jung, D.; Maiti, S.; Lee, J. H.; Lee, J. H.; Kim, J. S. Rational Design of Biotin-Disulfide-Coumarin Conjugates: A Cancer Targeted Thiol Probe and Bioimaging. *Chem. Commun.* **2014**, *50*, 3044–3047. https://doi.org/10.1039/c3cc49790a.

(31) Boni, L.; David, G.; Mangano, A.; Dionigi, G.; Rausei, S.; Spampatti, S.; Cassinotti, E.; Fingerhut, A. Clinical Applications of Indocyanine Green (ICG) Enhanced Fluorescence in Laparoscopic Surgery. *Surg. Endosc.* **2015**, *29*, 2046–2055. https://doi.org/10.1007/s00464-014-3895-x.

(32) Hu, X.; Dong, X.; Lu, Y.; Qi, J.; Zhao, W.; Wu, W. Bioimaging of Nanoparticles: The Crucial Role of Discriminating Nanoparticles from Free Probes. *Drug Discov. Today* **2017**, *22*, 382–387. https://doi.org/10.1016/j.drudis.2016.10.002.

(33) Makino, A.; Kizaka-Kondoh, S.; Yamahara, R.; Hara, I.; Kanzaki, T.; Ozeki, E.; Hiraoka, M.; Kimura, S. Near-Infrared Fluorescence Tumor Imaging Using Nanocarrier Composed of Poly(l-Lactic Acid)-Block-Poly(Sarcosine) Amphiphilic Polydepsipeptide. *Biomaterials* **2009**, *30*, 5156–5160. https://doi.org/10.1016/j.biomaterials.2009.05.046.

(34) Funayama, T.; Sakane, M.; Abe, T.; Hara, I.; Ozeki, E.; Ochiai, N. Intraoperative Near-Infrared Fluorescence Imaging with Novel Indocyanine Green-Loaded Nanocarrier for Spinal Metastasis: A Preliminary Animal Study. *Open Biomed. Eng. J.* **2012**, *6*, 80–84.

(35) Souchek, J. J.; Wojtynek, N. E.; Payne, W. M.; Holmes, M. B.; Dutta, S.; Qi, B.; Datta, K.; LaGrange, C. A.; Mohs, A. M. Hyaluronic Acid Formulation of near Infrared Fluorophores Optimizes Surgical Imaging in a Prostate Tumor Xenograft. *Acta Biomater.* **2018**, *75*, 323–333. https://doi.org/10.1016/j.actbio.2018.06.016.

(36) Duschmalé, J.; Hansen, H. F.; Duschmalé, M.; Koller, E.; Albaek, N.; Møller, M. R.; Jensen, K.; Koch, T.; Wengel, J.; Bleicher, K. In Vitro and in Vivo Properties of Therapeutic Oligonucleotides Containing Non-Chiral 3′ and 5′ Thiophosphate Linkages. *Nucleic Acids Res.* **2020**, *48*, 63–74. https://doi.org/10.1093/nar/gkz1099.